NIS-Elements AI

Intelligent Imaging with Deep Learning

NIS-Elements AI

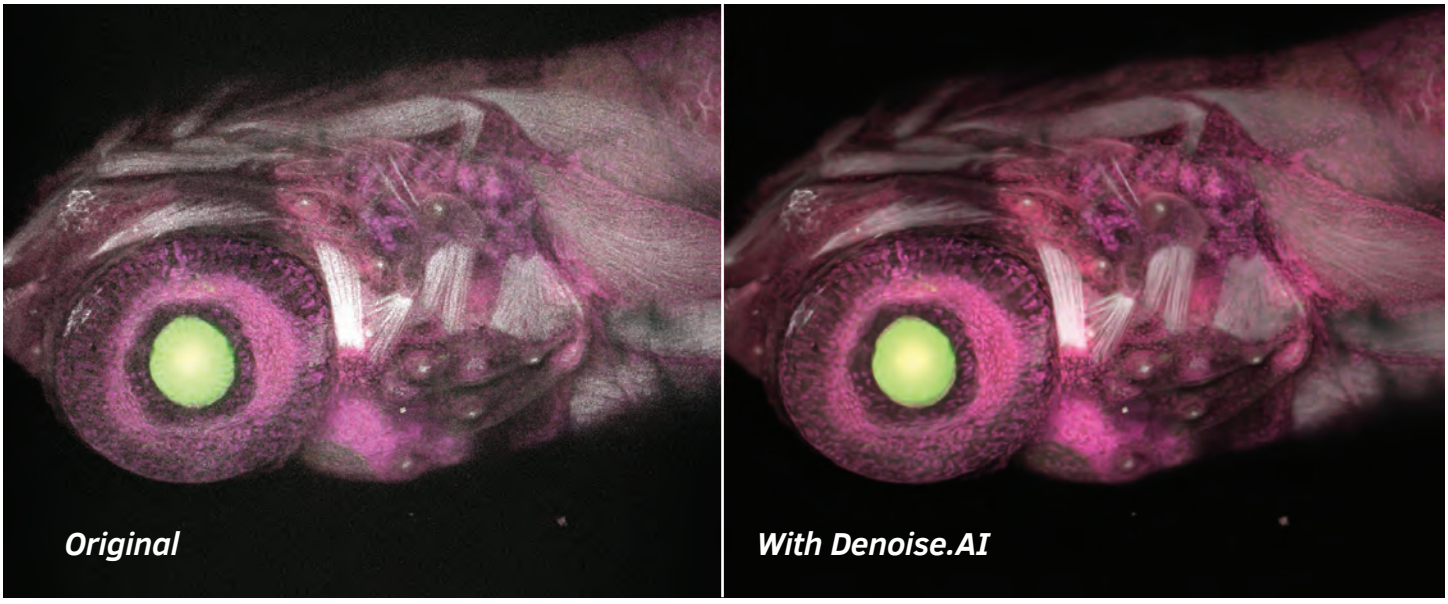

Nikon's new Artificial Intelligence (AI) feature for its NIS-Elements imaging software leverages deep learning to remove shot noise from resonant confocal images in real-time, resulting in breathtakingly clear images using minimal excitation power.

See Nikon at the ASCB|EMBO 2019 Meeting
Booth #900

To see how Nikon is using AI to transform your imaging,
visit www.microscope.healthcare.nikon.com/nis-elements-ai

Nikon Instruments Inc. | www.microscope.healthcare.nikon.com | nikoninstruments@nikon.net

Cell

Best of 2019

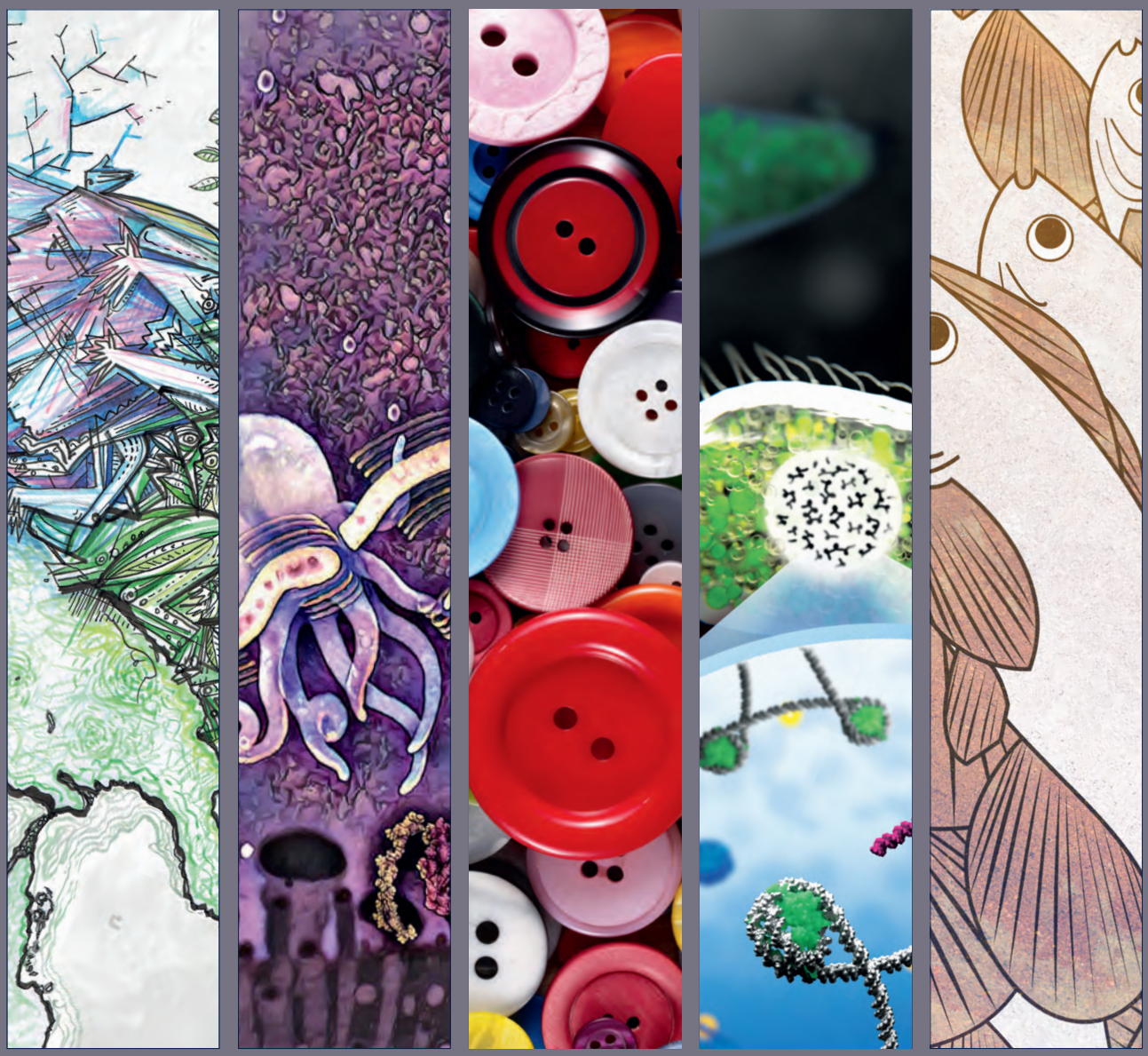

Featuring a Collection of SnapShots

CellPress
www.cell.com
CELLBO 2019

Be Brilliant. Single Molecule Localization / Voltage Sensitive Dyes / Lightsheet Microscopy / Spinning Disk Confocal / Live Cell Fluorescence / Total Internal Reflection Fluorescence / Calcium Imaging / Super Resolution / Expansion Microscopy / Fluorescence Resonance Energy Transfer / Structured Illumination / Multi-dimensional Imaging / Optogenetics / Point Accumulation for Imaging in Nanoscale Topography. **Do Dim Things.**

ROCKLAND
antibodies & assays

Do what matters for your matter

Neurological research relies heavily on quality antibodies for isolation, characterization, and localization of target proteins. Choose from our extensive collection of multi-assay validated neuroscience antibodies to propel your research further than ever before.

Learn more at:
rockland-inc.com/neuro

CellDrop™

Count Cells Without Slides

Reduce Plastic Waste In Your Lab

Eliminate Disposable Slide Costs

Automated Cell Counting and Viability in Seconds

Patent US 10,302,568

Dual Fluorescence and Brightfield or Brightfield Only Models

DirectPipette™ Technology

DeNovix' unique innovation creates a variable height, wipe-clean sample chamber with micron-level precision. CellDrop eliminates the need for plastic slides and hemocytometers and delivers the fastest, most accurate counts across the widest range of cells - from $7x10^2$ to $2.5x10^7$ cells per ml and cell diameters down to 4µm. CellDrop is stand-alone and fully connected with built-in WiFi, Ethernet & USB Exporting. Pre-installed EasyApps® software provides powerful analysis options and one-touch use for common applications such as Trypan blue, AO/PI, GFP, yeast and more.

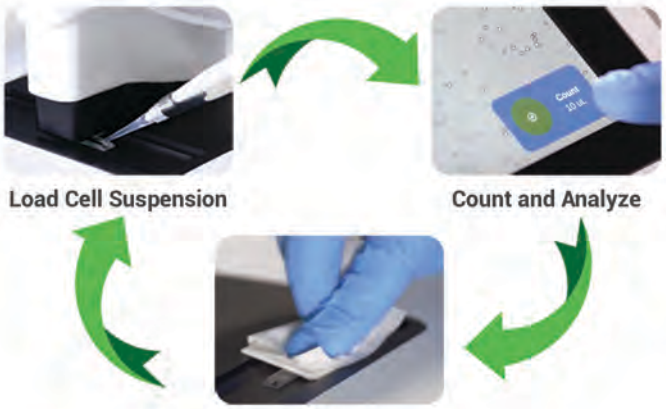

Advanced Image Analysis

High Definition cell outlining and Declustering for accurate counts of regular and irregular cells, even at high density.

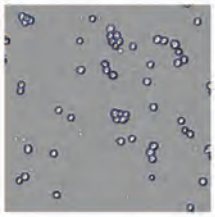

Primary Cells

Viability measurements of PBMCs in the presence of debris and red blood cells.

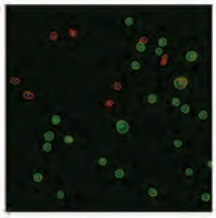

Request a Free One-Week Trial:
www.denovix.com/celldrop

DeNovix®

Profile Organ-Specific Toxicity

Enzo Life Sciences provides innovative research tools for early safety assessment. Our CELLESTIAL® Fluorescence Assays for live cell analysis are designed to help assess the impact of toxic agents on overall cell function, and our SCREEN-WELL® Toxicity Libraries are useful for high-throughput screening of organ-associated toxicity profiles. With this perfect pair, Enzo offers novel solutions for the discovery, analysis and quantification of biomarkers relevant to predictive toxicology.

Cardiotoxicity | Hematotoxicity | Hepatotoxicity | Myotoxicity | Nephrotoxicity

Enzo

www.enzolifesciences.com/toxicology

OLYMPUS®

Optical Performance Without Tradeoffs

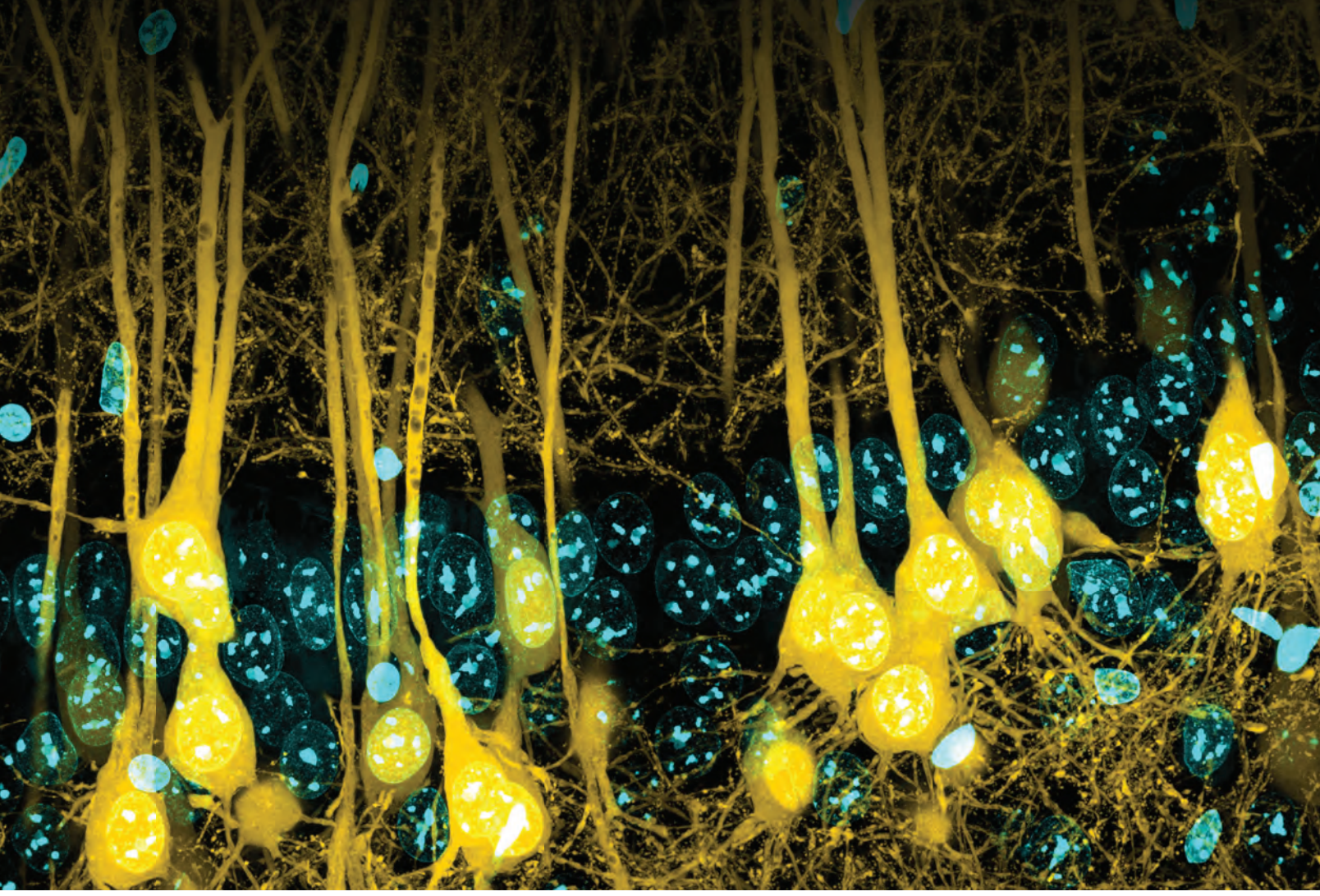

Built with innovative lens polishing technology, our new X Line™ objectives break optical barriers with simultaneously improved performance in three areas:

- Expanded flatness for uniform images in a large field of view
- Exceptional color accuracy with enhanced chromatic correction
- Excellent image quality with a high numerical aperture

X LINE

Your Science Matters™

www.olympus-lifescience.com

Foreword

In 2012, Cell Press launched the “Best of” reprint collections across a number of journals, most notably *Ce*⊠ Now, we are happy to bring you a new *Best o*⊠*Ce*⊠that focuses on articles published over the course of 2019.

For this edition, we made our selection by looking at reviews and research articles that garnered wide attention or captured editorial interest for conceptual impact. Looking back over the year, we discovered that winnowing down the list to only a few required hard choices from among papers that we were excited to publish. In the end, we⊠ve chosen papers, at the frontiers of their respective fields, that represent the broad sweep of today⊠s biology. We’ve also included reviews that provide authoritative views on immunotherapy, genomic medicine, and autophagy and a collection of SnapShots that present up-to-date, quick-read summaries to highlight several key areas of biology; we hope these SnapShots will be useful reference tools for the scientific community. The papers collected here also feature exciting methodologies and experimental procedures⊠ including a platform for identifying small molecules that modulate CRISPR-Cas9 activity, an optics-free imaging technique, and use of nanoparticles to allow mice to see near-infrared light.

We hope that highlighting these articles will provide an overview of the science that we published from the end of 2018 to this point in 2019. We recognize that no single measurement can be indicative of the “best” papers over a given period of time, especially when the articles are relatively new and their true significance will only be established with time. Regardless of whether they will be highly cited papers in their fields, we believe they are noteworthy, and we hope you enjoy reading them.

You can access the entire “Best of” collection online at www.cell.com/bestof. Visit www.cell.com/cell to learn about the latest findings that Cell has had the privilege to publish and www.cell.com to find other high-quality life science papers published in the full portfolio of Cell Press journals. Please feel free to contact us at cell⊠ cell.com to tell us about your latest work or to provide feedback. We look forward to working with you in 2020 and beyond⊠

As a final note, we are grateful for the generosity of our sponsors, who helped to make this reprint collection possible.

John Pham
Editor-in-Chief, *Ce*⊠

Cell

For information for the Best of Series, please contact:
⊠onathan Christison
⊠rogram Director, ⊠est of Cell ⊠ress
e: ⊠christison⊠ cell.com
p: 617-⊠97-289⊠
t: ⊠ Cell⊠ress⊠ ⊠

StressMarq Biosciences INC.

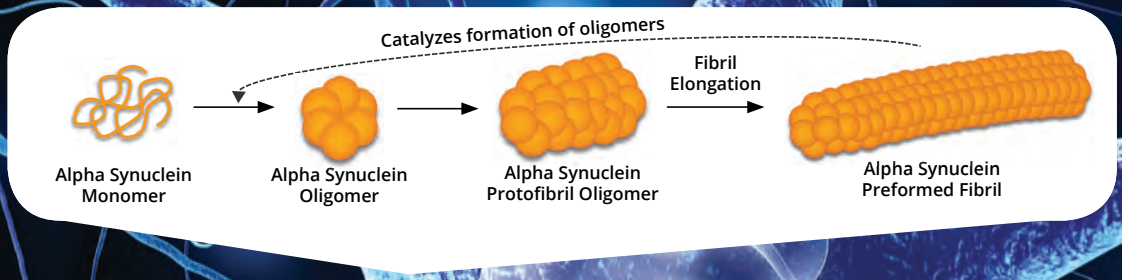

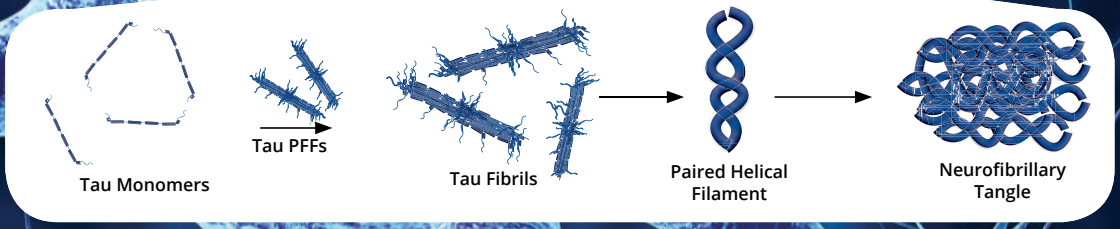

Alpha Synuclein & Tau

Preformed fibrils (PFFs) for neurodegeneration research

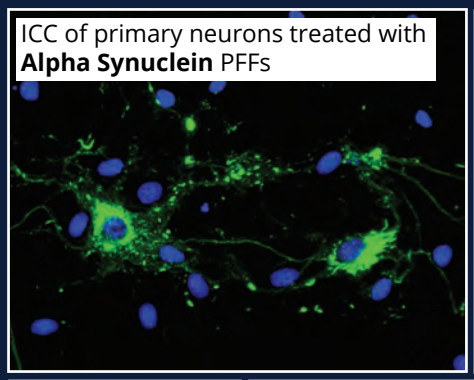

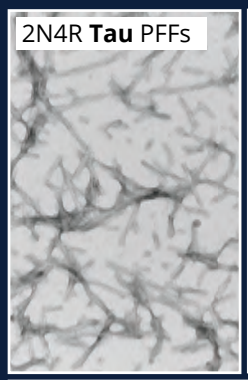

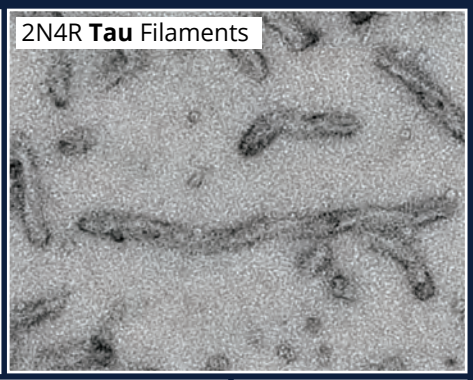

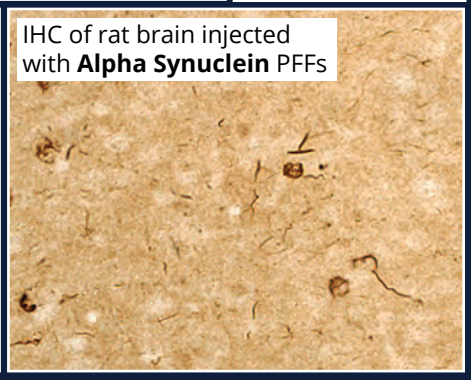

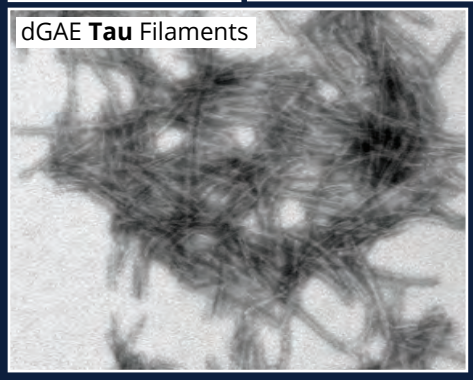

Learn more: www.stressmarq.com/PFFs | info@stressmarq.com | 1.250.294.9065

CELLECTA

Gene functional analysis. Simplified.

CELLECTA

YOUR INPUT

Cell or Animal Models
Biological Samples

YOUR BRIDGE TO DISCOVERY

- **CRISPR / RNAi** Libraries & Genetic Screens
- **DriverMap™** Targeted RNA Expression Profiling
- **CloneTracker™** Barcode Libraries

YOUR RESULTS

Functionally Important Genes & Biomarkers

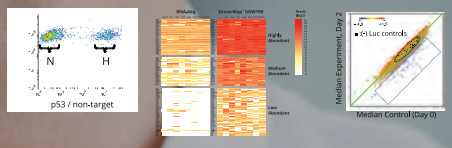

Real expertise delivering results. Visit www.cellecta.com today.

Who we are

Cellecta is a leading provider of genomic products and services. Our functional genomics portfolio includes gene knockout and knockdown screens, custom and genome-wide CRISPR and RNAi libraries, construct services, cell engineering, NGS kits and targeted expression profiling products and services.

CELLECTA

We can help your discovery efforts.
www.cellecta.com info@cellecta.com +1 877-938-3910 or +1 650-938-3910

F · S · T®

FINE SCIENCE TOOLS

FLAWLESS PRECISION

For over forty years, we have built our reputation on intertwining stringent quality standards with exemplary customer service. By working closely with the world's leading scientific and biomedical research communities, we are able to provide you with a complete range of innovative, precision surgical and microsurgical instruments. At Fine Science Tools, you can always expect flawless product quality that is backed by our 100% satisfaction guarantee. Take your research further, faster—with Fine Science Tools.

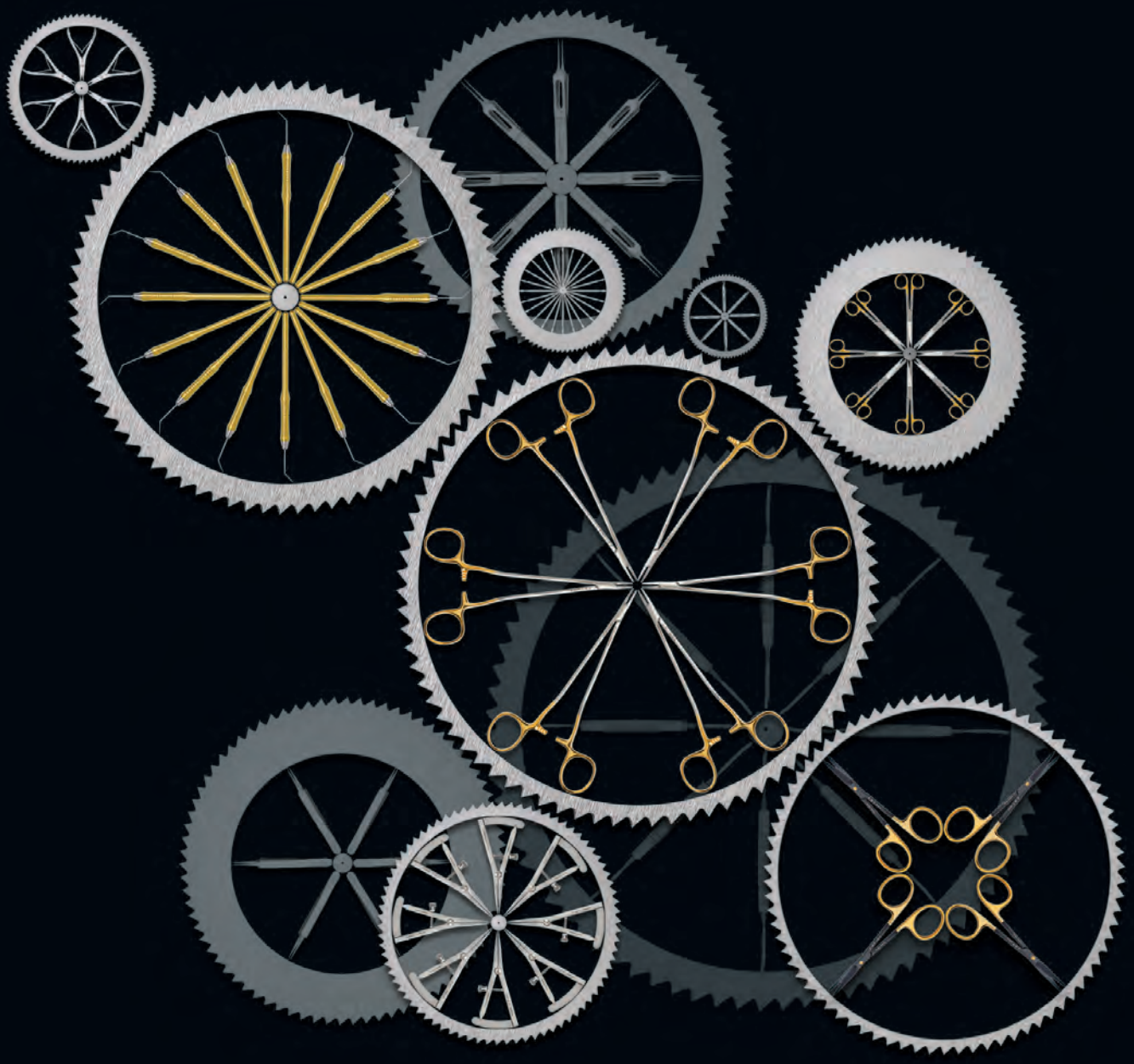

FINE SURGICAL INSTRUMENTS FOR RESEARCH™

VISIT US AT FINESCIENCE.COM OR CALL 800 521 2109

Cell

Best of 2019

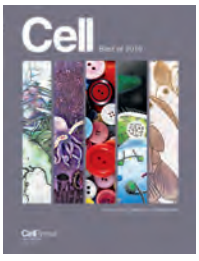

On the cover: Featured on the cover is a cross-section of visually striking images published on the cover of *Cell* in 2018 and 2019. Images are courtesy of (from left to right): Markus Kasemaa (volume 177, issue 4), Weinhäupl et al. (volume 175, issue 5), iStock/kemalbas (volume 176, issue 6), Myles Marshall (volume 177, issue 7), and Design and Creative Services, Katharina Link (volume 178, issue 2).

Agilent

Trusted Answers

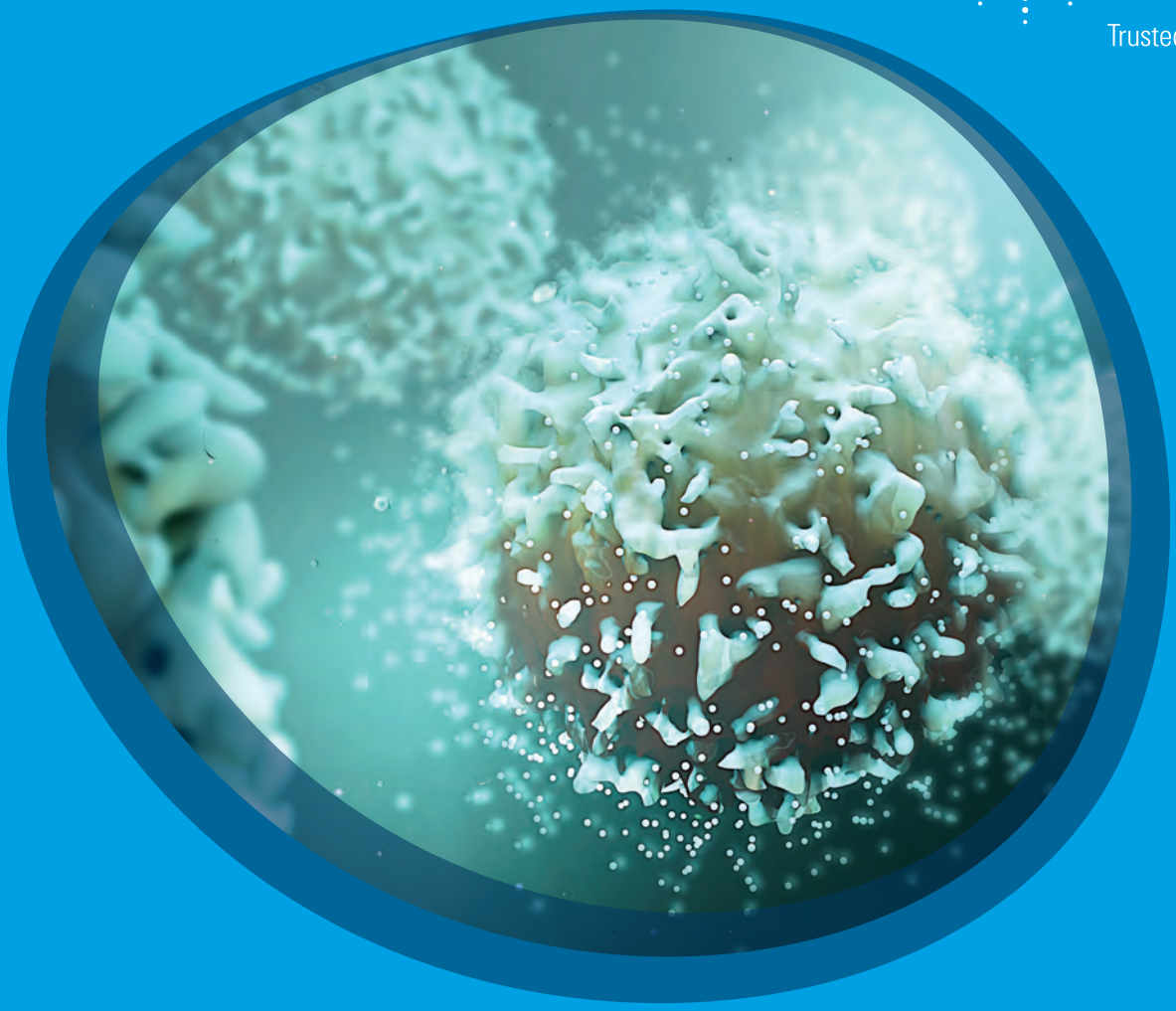

Master the Potency of Immune Cell Therapies

Develop more effective, potent, and persistent immune cell products with the Agilent immunotherapy tool bench.

Get confident control of key aspects of immune cell function. By accessing this suite of advanced gene editing and cell analysis technologies, you'll gain greater command over phenotype, function, potency, and persistence at all phases of development, for unprecedented insight to accelerate therapeutic discovery and development.

To learn more about this tool bench consisting of the Agilent xCELLigence RTCA eSight, Agilent Seahorse XF Analyzers, Agilent NovoCyte flow cytometers, and Agilent SureGuide CRISPR, visit agilent.com/chem/immune-cell-therapy and register to download our e-book entitled Breakthroughs in Immunotherapy.

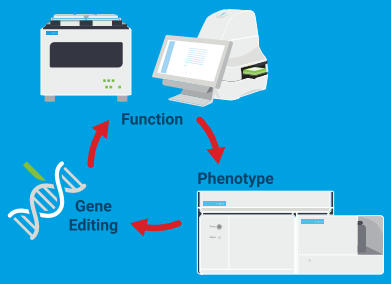

For Research Use Only. Not for use in diagnostic procedures.

ZYMO RESEARCH | CELEBRATING 25 YEARS

ZymoBIOMICS®

The Complete Microbiomics Solution

The findings of microbiomics studies have far-reaching implications in human health, agriculture, and environmental safety. Such impactful work requires controls and tools validated to accurately and reproducibly assess the most complex microbial communities.

A Total Solution
The only complete microbiomics workflow from sample collection/preservation to unbiased NGS-ready libraries.

Microbiomics-Grade Kits
Eliminate bias and bioburden for the most accurate microbiome measurements.

Streamlined Workflow
Simple and fast protocols produce high-quality data from any sample type.

ZymoBIOMICS® The Complete Microbiomics Solution

To learn more, visit **www.zymoresearch.com/pages/zymobiomics-portfolio**

info@zymoresearch.com | www.zymoresearch.com | Toll Free: (888) 882-9682

CELL CULTURE

REPORTER CELL LINES

The family keeps growing.

- PRR, Transcription Factor, Cytokine, Autophagy
- Thoroughly tested for viability and biological activity
- Compatible with High-Throughput Screening

InvivoGen offers a large panel of cell lines stably transfected with innate immunity-specific pathway reporter constructs. Our cells express one or two reporter proteins, secreted embryonic alkaline phosphatase (SEAP) and/or Lucia luciferase.Both systems offer the advantage of being secreted outside the cell,allowing for multiple and non-destructive readings over time.

Recombinant cells of various origins:

RAW 264.7 Macrophages
A549 Lung Carcinoma
Jurkat T Lymphocytes
HepG2 Hepatoma
THP-1 Monocytes
HEK293
And more...

InvivoGen

WWW.INVIVOGEN.COM/REPORTER-CELLS

Track immune cell-mediated killing label-free and in real-time

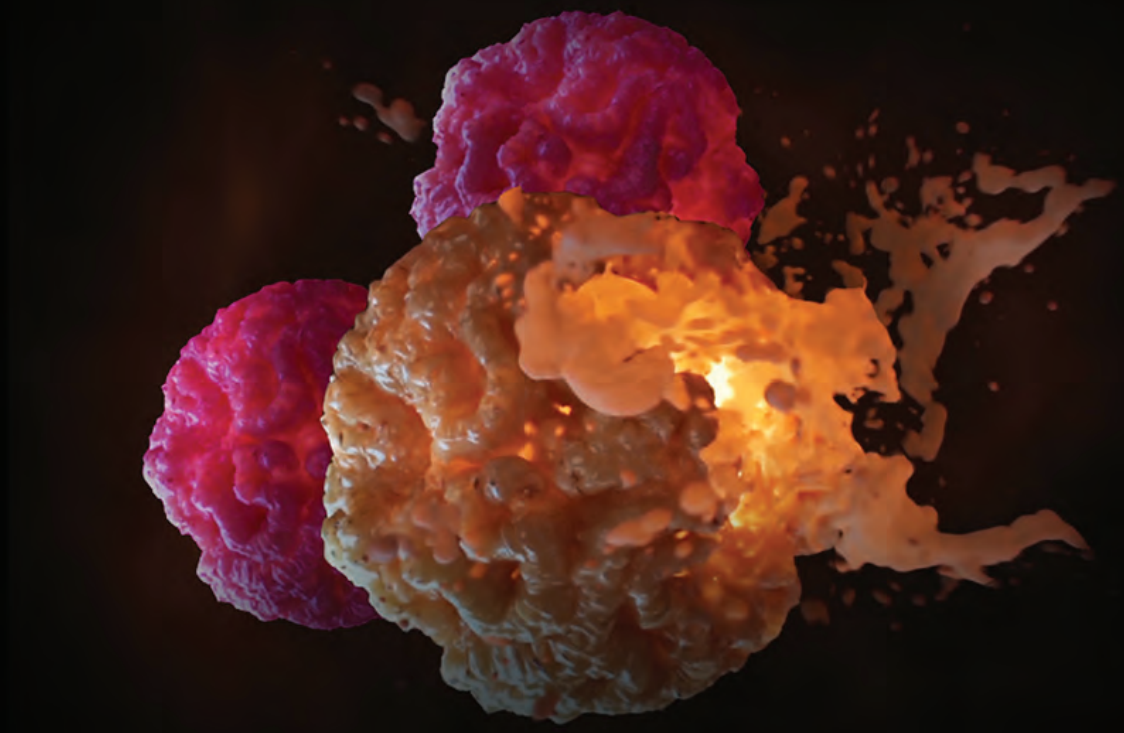

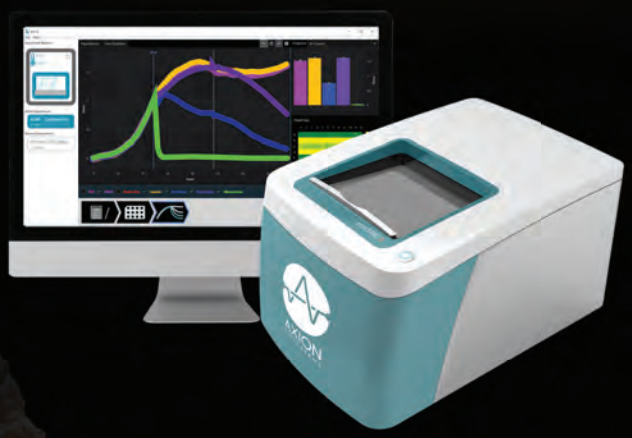

Maestro Z platform measuring the kinetics of immune cell-mediated killing in a 96-well plate.

AXION BIOSYSTEMS
Imagine • Explore • Discover

MAESTRO Z™

impedance assay platform
real-time, label-free cell analysis

Want to evaluate killing kinetics with physiologically relevant effector cell to target cell ratios? Concerned about the possible confounding effects of labeling your cells?

Introducing Maestro Z, the world's most advanced impedance-based real-time cell analysis platform. Over minutes or weeks gain unprecedented access to the kinetics of your biology.

Straightforward and easy to use, any researcher can now track immune cell-mediated killing in a 96-well plate.

www.axionbio.com/immuno-oncology

SnapShot: RNA Structure Probing Technologies

Cell

Paul D. Carlson,[1,2] Molly E. Evans,[3] Angela M Yu,[2,4] Eric J. Strobel,[3] and Julius B. Lucks[2,3]
[1]Robert F. Smith School of Chemical and Biomolecular Engineering, Cornell University, Ithaca NY; [2]Center for Synthetic Biology, Northwestern University, Evanston IL; [3]Department of Chemical and Biological Engineering, Northwestern University, Evanston IL; [4]Tri-Institutional Training Program in Computational Biology and Medicine, Weill Cornell Medicine, New York, NY

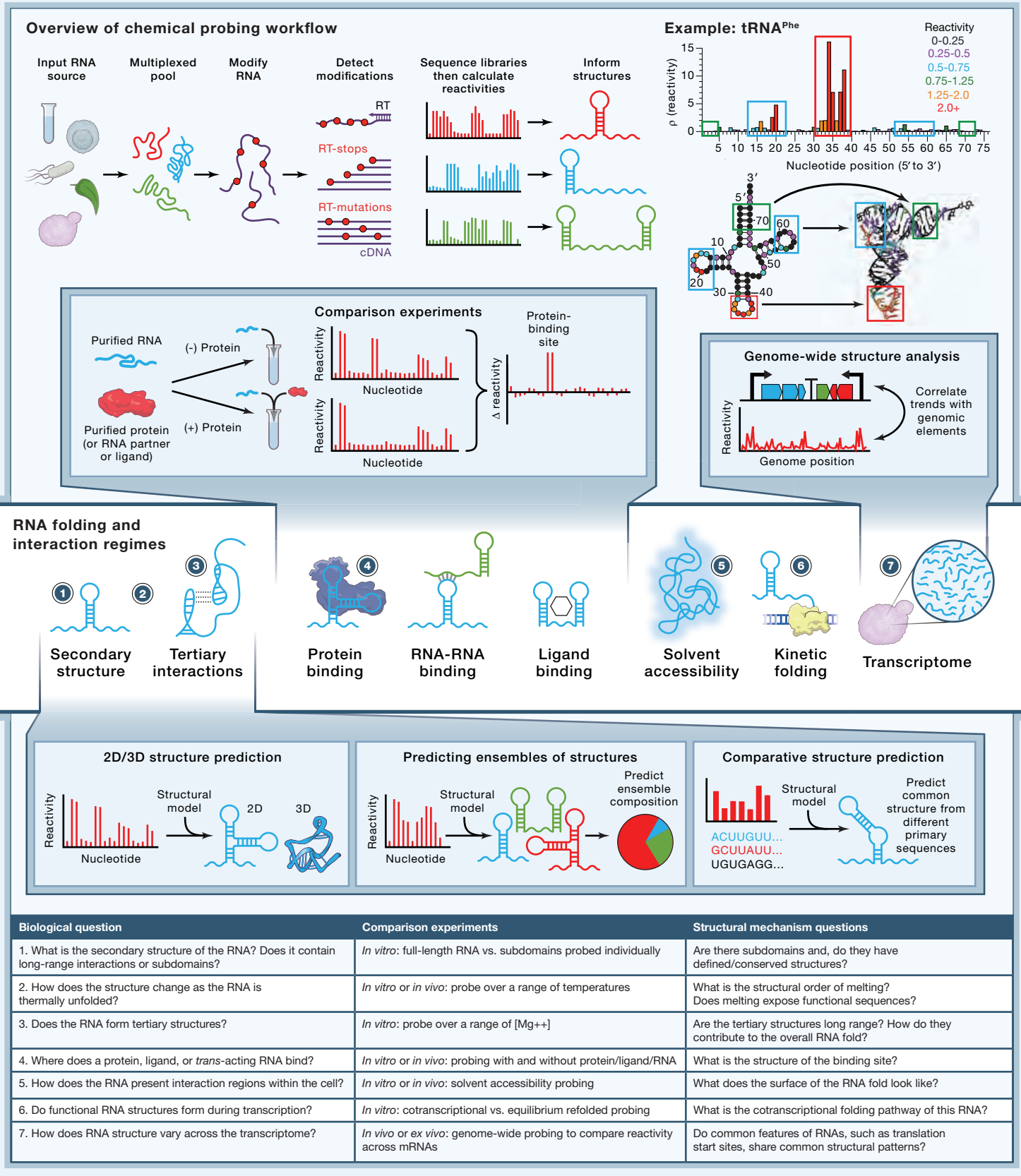

Biological question	Comparison experiments	Structural mechanism questions
1. What is the secondary structure of the RNA? Does it contain long-range interactions or subdomains?	*In vitro*: full-length RNA vs. subdomains probed individually	Are there subdomains and, do they have defined/conserved structures?
2. How does the structure change as the RNA is thermally unfolded?	*In vitro* or *in vivo*: probe over a range of temperatures	What is the structural order of melting? Does melting expose functional sequences?
3. Does the RNA form tertiary structures?	*In vitro*: probe over a range of [Mg++]	Are the tertiary structures long range? How do they contribute to the overall RNA fold?
4. Where does a protein, ligand, or *trans*-acting RNA bind?	*In vitro* or *in vivo*: probing with and without protein/ligand/RNA	What is the structure of the binding site?
5. How does the RNA present interaction regions within the cell?	*In vitro* or *in vivo*: solvent accessibility probing	What does the surface of the RNA fold look like?
6. Do functional RNA structures form during transcription?	*In vitro*: cotranscriptional vs. equilibrium refolded probing	What is the cotranscriptional folding pathway of this RNA?
7. How does RNA structure vary across the transcriptome?	*In vivo* or *ex vivo*: genome-wide probing to compare reactivity across mRNAs	Do common features of RNAs, such as translation start sites, share common structural patterns?

See online version for legends and references

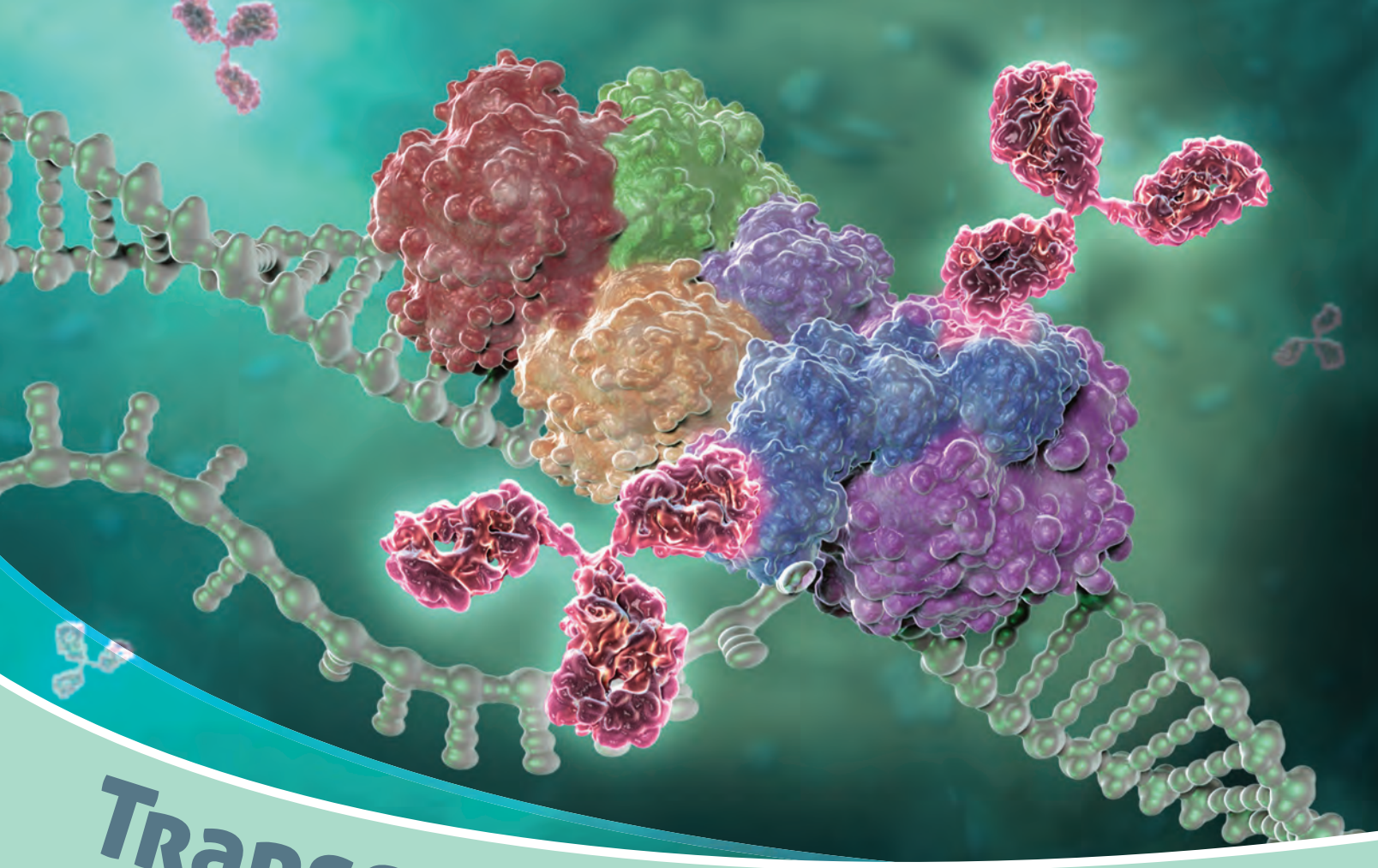

Transcription Factors

Discover what controls a cell's fate.

BioLegend has over 800 highly specific antibodies to help explore the many facets of transcriptional regulation that govern a cell's fate. We validate our antibodies across multiple applications to provide value and convenience to the scientific community.

Use BioLegend Transcription Factor Antibodies for:

- Chromatin Immunoprecipitation
- Flow Cytometry
- Immunocytochemistry
- Immunohistochemistry
- Immunoprecipitation
- Western Blotting

For nuclear protein flow cytometry staining, BioLegend's True-Nuclear™ Transcription Factor Buffer Set has been specially formulated for intracellular staining with minimal effect on surface fluorochrome staining.

Learn more at: biolegend.com/en-us/transcription-factors

Optimal Resolution of T-bet with True-Nuclear™ Transcription Factor Buffer Set

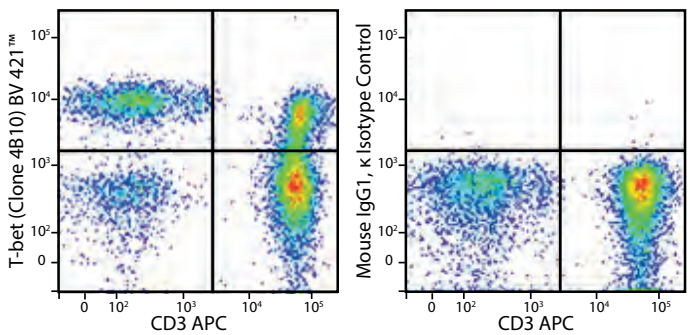

Human peripheral blood lymphocytes surface stained with anti-CD3 APC, treated with True-Nuclear™ Transcription Factor Buffer Set, then stained with anti-T-bet (clone 4B10) Brilliant Violet 421™ (left) or mouse IgG1, κ BV421™ isotype control (right).

BioLegend is ISO 13485:2016 Certified

Toll-Free Tel (US & Canada): 1.877.BIOLEGEND (246.5343)
Tel: 858.768.5800
biolegend.com

08-0082-02

BioLegend®

World-Class Quality | Superior Customer Support | Outstanding Value

1240 Cell 176, February 21, 2019 © 2019 Published by Elsevier Inc. DOI https://doi.org/10.1016/j.cell.2019.01.051

SnapShot: Cancer Immunotherapy with Oncolytic Viruses

Cell

Shashi Gujar,[1] John Bell,[2,3] and Jean-Simon Diallo[2,3]
[1]Departments of Pathology, Biology, and Microbiology & Immunolgy, Faculty of Medicine, Dalhousie University, Halifax, NS, Canada; [2]Departments of Medicine & Biochemistry and Microbiology & Immunology, University of Ottawa, ON, Canada; [3]Cancer Therapeutics Program, Ottawa Hospital Research Institute, Ottawa, ON, Canada

Therapeutic advantages

Tumor selectivity
- Leaky vasculature
- Defective antiviral defenses
- High metabolism
- Expression of viral receptors (e.g., CAR)

Broad spectrum
- Tissue tropism inherent to some viruses
- Other viruses employ ubiquitous receptors (e.g., LDLR by rhabdovirus)

Abscopal effect
- Anti-tumor effects observed in uninfected tumor lesions
- Can be both cytokine (e.g., TNF) or immune cell (NK, CTL) mediated

Design flexibility
- OVs (e.g., vaccinia and rhabdovirus) can accommodate transgenes
- Deliver cytokines, antibodies, enzymes, and reporters

Four modes of action for OV therapy

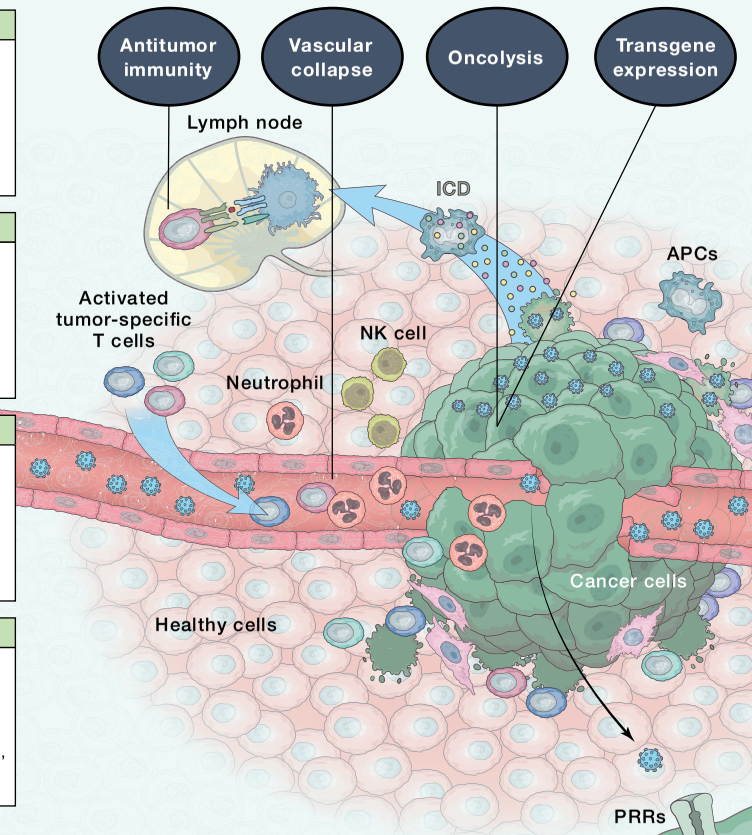

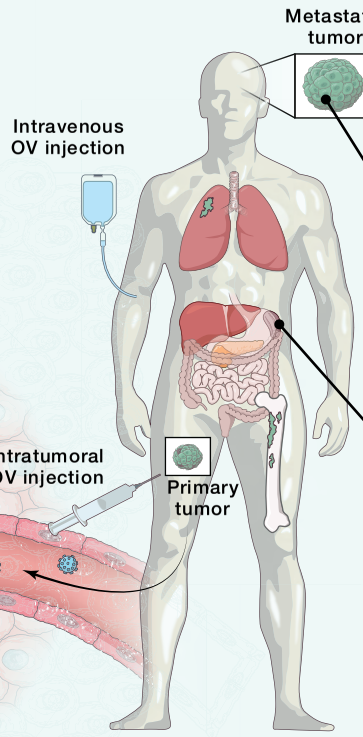

Therapeutic barriers and solutions

Manufacturing
- Barrier: inefficient production can limit maximum feasible dose
- Solutions: novel culture supplements, designer cell lines, and bioreactors

Physical barriers
- Barrier: capture of viruses by tissue-resident macrophages in organs like liver, reaching distant metastases
- Solutions: clodronate, cell carriers, liver de-targeting

Immune response to virus
- Barrier: immune response to virus reduces its capacity to spread and blocks re-dosing
- Solutions: serotype swap and immune-suppressants

Cellular antiviral response
- Barrier: OVs susceptible to antiviral response (e.g., IFN)
- Solutions: genetic engineering and small molecules (e.g., viral sensitizers)

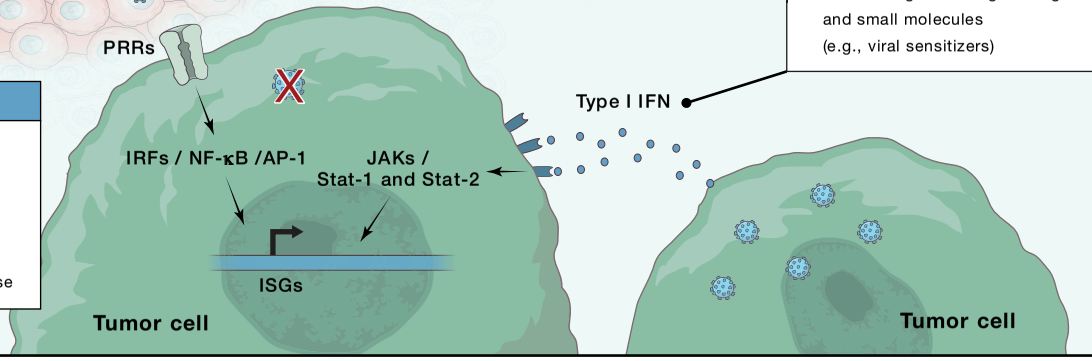

OV-induced anticancer immunotherapeutic effects

Innate immunity
- IFN and pro-inflammation response
- Induction of ICD in cancer cells
- Recruitment of immune cells in TME
- Maturation of APCs
- Activation and recruitment of NK and NKT cells

Adaptive immunity
- Oncolysis exposes tumor antigens
- Matured APCs capture tumor antigens, migrate to LN, and activate T cells
- Activation of tumor-specific T cells
- Establishment of memory against relapse

See online version for legends and references

Brilliant visualization

See the difference to make big breakthroughs in your tumor microenvironment research

In the world of next generation immuno-oncology research, having confidence in your immunoassay results is vital. Unfortunately, 75% of antibodies in today's market are non-specific or simply do not work at all.* That's why at Bethyl, we manufacture and validate every antibody on-site to ensure target specificity and sensitivity. More than 10,000 independent citations over the past 15 years have proven that our antibodies will function as designed in your assay — and we offer a 100% guarantee. Work with Bethyl to bring your discovery into full focus.

See our data at bethyl.com/immuno-oncology

Ask About Our PathPlex™ MULTIPLEX Antibody Panels

*Weller, MG, Analytical Chemistry Insights:11, 21-27 (2016).
Antibodies shown: PD-L1 (A700-016) & Lamin A/C (A303-430A)

BETHYL LABORATORIES, INC

Really Good Antibodies

SnapShot: The RNA Exosome

M. Rhyan Puno[1], Eva-Maria Weick[1], Mom Das[1], Christopher D. Lima[1,2]
[1] Structural Biology Program, Sloan Kettering Institute, Memorial Sloan Kettering Cancer Center, New York, New York 10065; [2]Howard Hughes Medical Institute, 1275 York Avenue, New York, NY 10065

Cell

Exosome-mediated 3′ to 5′ decay

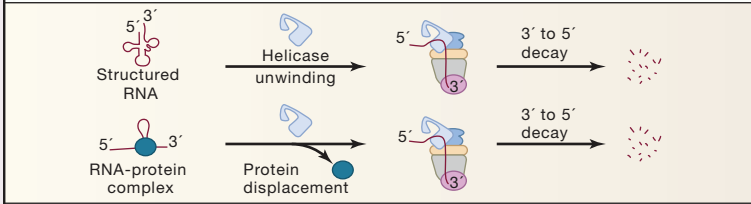

Exosome-mediated 3′ to 5′ processing

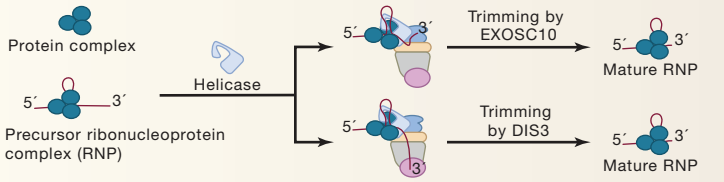

Exosome and human diseases

Protein	Disease
EXOSC2	Syndrome characterized by retinitis pigmentosa, hearing loss, hypothyroidism, short stature, premature aging, mild intellectual disability
EXOSC3	Pontocerebellar hypolasia type 1b
EXOSC8	Pontocerebellar hypolasia type 1c
DIS3	Multiple myeloma
SKIV2L	Syndromic diarrhea (SD) or trichohepatoenteric (THES1) syndrome
TTC37	Syndromic diarrhea (SD) or trichohepatoenteric (THES1) syndrome
RBM7	Spinal muscular atrophy-like syndrome
ZCCHC8	Congenital glioblastoma multiforme, lung adenocarcinoma, Spitz tumor, familial pulmonary fibrosis

mRNA quality control/ribosome stress

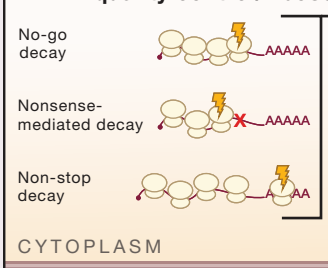

mRNA turnover

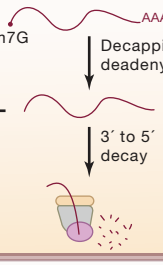

AU-rich mRNA decay

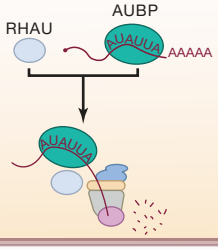

Viral RNA decay

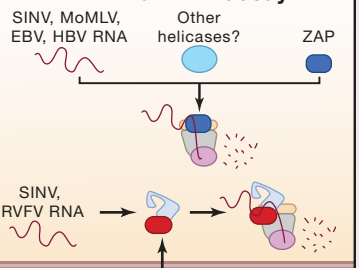

NUCLEUS

rRNA processing

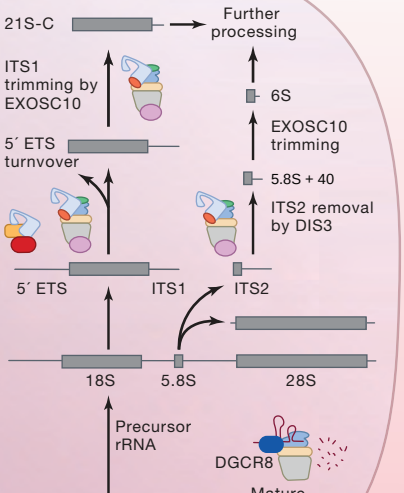

Nuclear RNA turnover and quality control

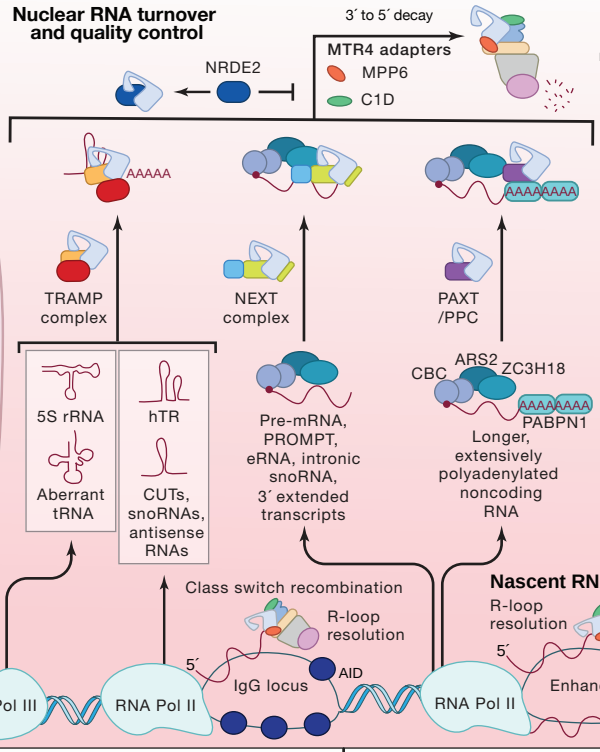

Small ncRNA processing

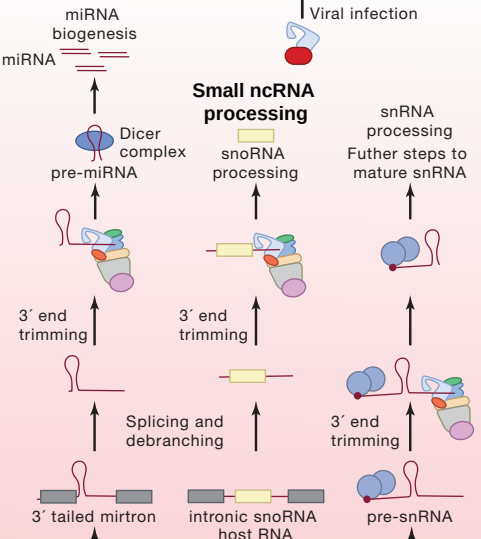

Viral infection

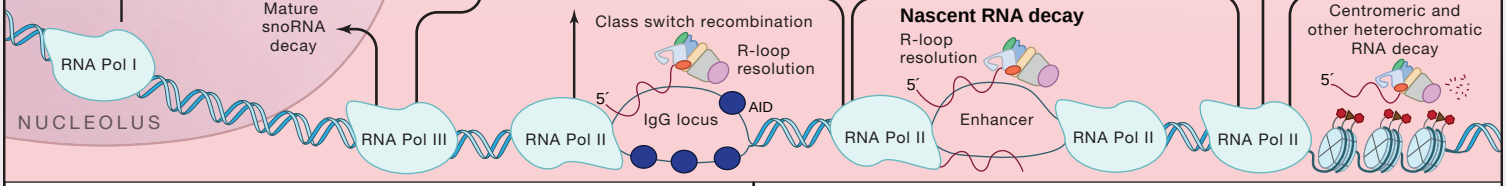

RNA exosome subunits and architecture

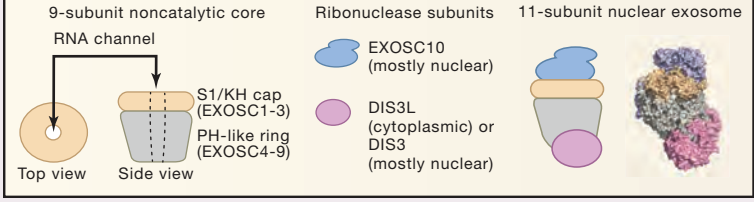

RNA exosome co-factors

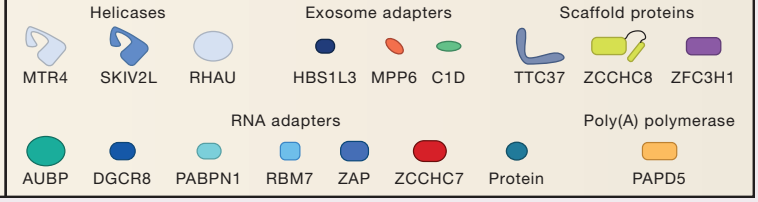

 DOI https://doi.org/10.1016/j.cell.2019.09.005

See online version for legends and references

R&D SYSTEMS
a bio-techne brand

Get A Great Assay

Go from good to great by following our ELISA guide

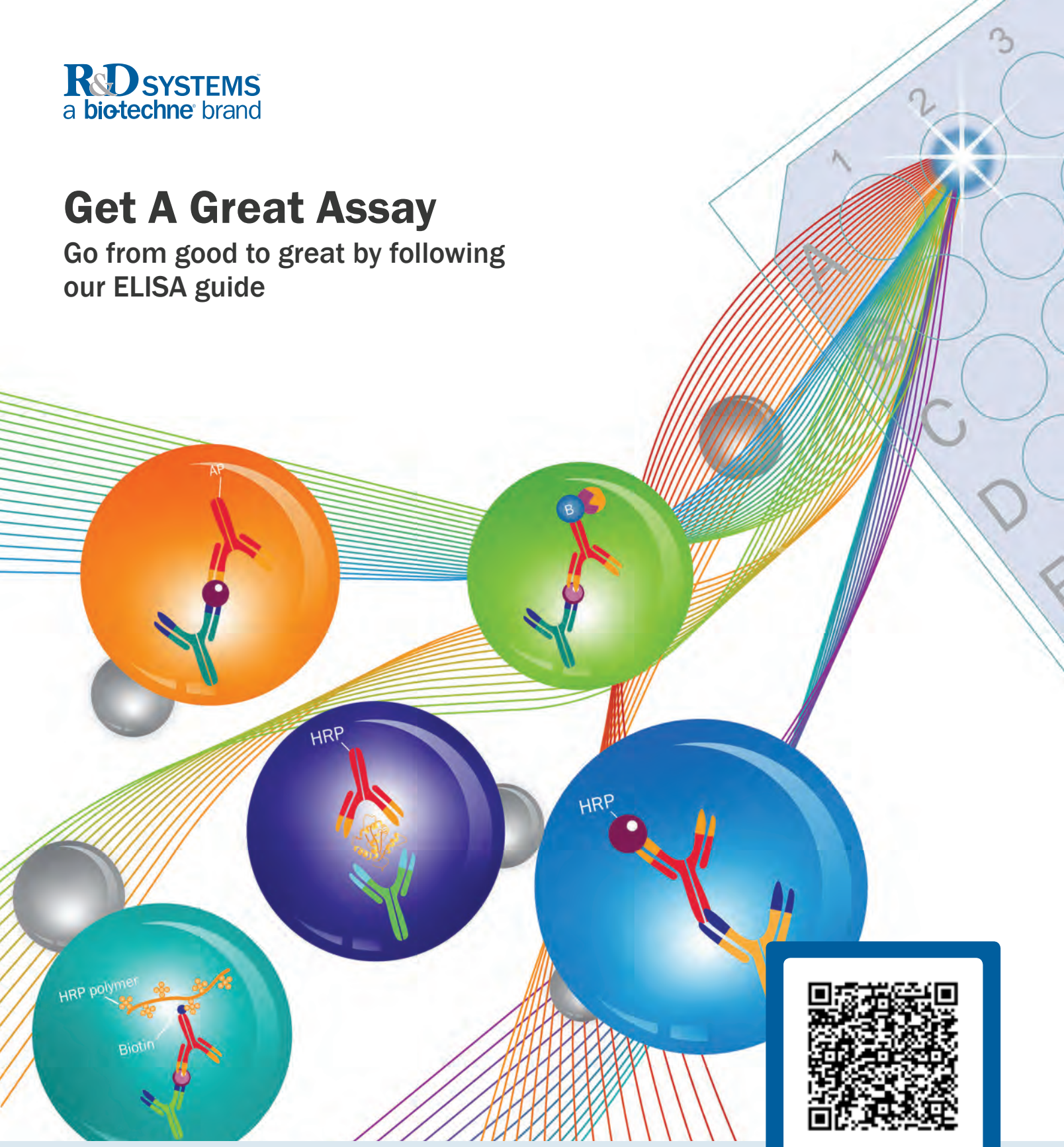

Learn more at **rndsystems.com/elisa**

DOWNLOAD
The ELISA Guide

bio-techne®

Global bio-techne.com info@bio-techne.com TEL +1 612 379 2956 **USA** TEL 800 343 7475 **Canada** TEL 855 668 8722
Europe | Middle East | Africa TEL +44 (0)1235 529449 **China** TEL +86 (21) 52380373

SnapShot: Biology of Genetic Ataxias

Cell

Ilse Eidhof,[1] Bart P. van de Warrenburg,[2] and Annette Schenck[1]
[1]Department of Human Genetics and [2]Department of Neurology, Donders Institute for Brain, Cognition, and Behaviour, Radboud University Medical Center, Nijmegen, the Netherlands

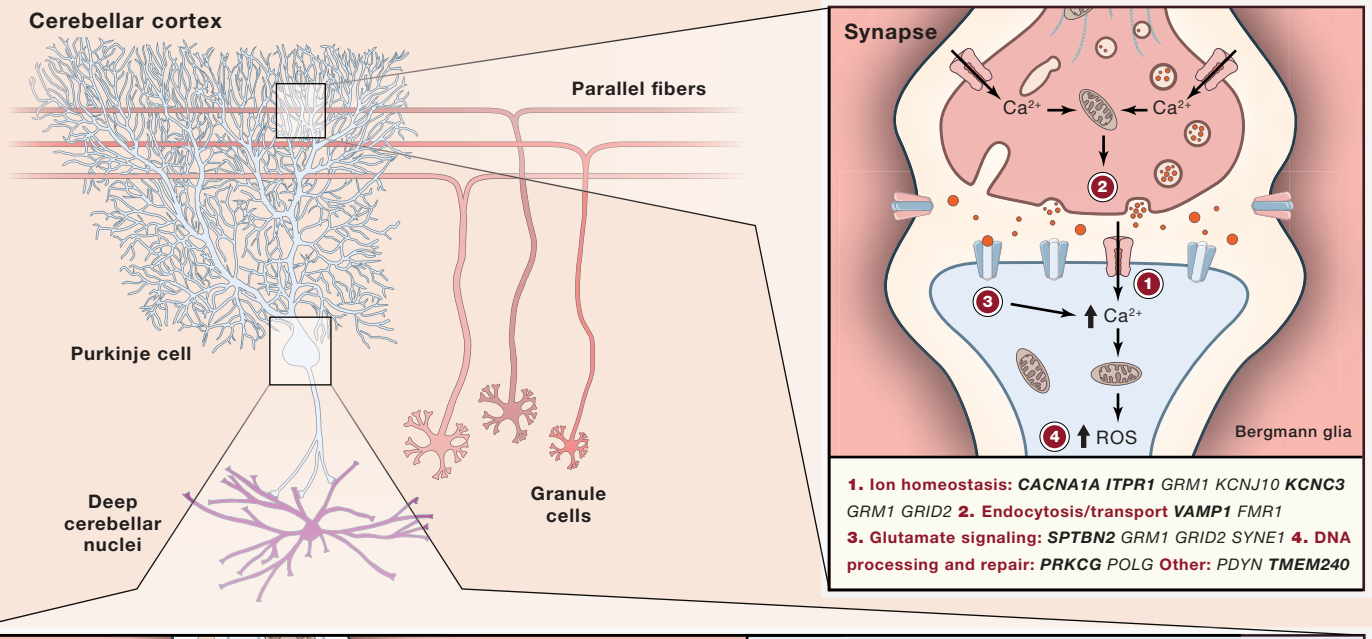

1. Ion homeostasis: ***CACNA1A ITPR1*** *GRM1 KCNJ10* ***KCNC3*** *GRM1 GRID2* **2. Endocytosis/transport** ***VAMP1*** *FMR1* **3. Glutamate signaling:** ***SPTBN2*** *GRM1 GRID2 SYNE1* **4. DNA processing and repair:** ***PRKCG*** *POLG* **Other:** *PDYN* ***TMEM240***

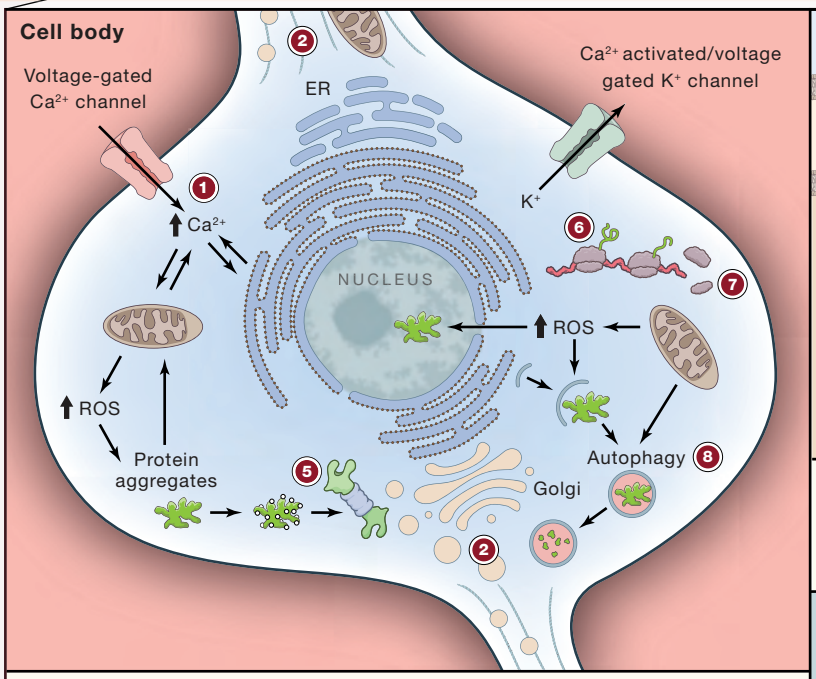

1. Ion homeostasis: *ATP2B3 SLC9A1* ***TRPC3 AFG3L2 CACNA1A ITPR1*** *GRM1 FXN KCNJ10* ***FGF14 KCNC3 KCND3*** *GRID2 ANO10* **2. Endocytosis/transport:** *FMR1* ***FGF14*** *DNAJC3 GOSR2* ***PRKCG*** *KIF1C* ***VAMP1 CACNA1A*** *SYT14* ***EEF2 SPTBN2 ATXN2***
5. Proteasome/ubiquitin-mediated protein degradation: ***ATXN3*** *STUB1 UCHL1 SACS* ***ATXN8OS*** **6. RNA processing/translation:** *FMR1 DNAJC3* ***EEF2 ATXN2*** *MARS2* ***NOP56***
7. RNA toxicity: ***ATXN8OS ATXN10*** *FMR1* ***BEAN1 NOP56 PPP2R2B***
8. Autophagy: *DNAJC3 SCARB2 KIAA0226 TPP1 POLR3A ATM* ***ITPR1*** *UCHL1*

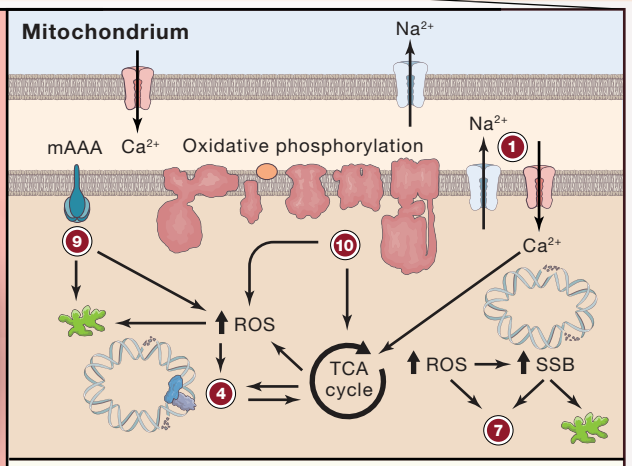

1. Ion homeostasis: *SLC9A1* ***AFG3L2*** *FXN* **4. DNA processing and repair:** *PNKP POLG C100RF2 MTPAP* **7. RNA toxicity:** *TPP1* **9. mAAA complex-mediated mitochondrial proteostasis:** ***AFG3L2*** *SPG7* **10. Energy transport:** *TTC19 ADCK3* **Other:** *MARS2 SACS WWOX* ***ATXN3 PPP2R2B***

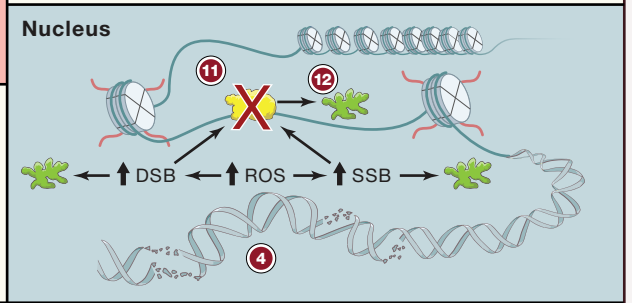

4. DNA processing and repair: *MRE11A PNKP TDP1* ***ATXN3*** *STUB1 SETX TDP2* ***PRKCG*** *PCNA APTX ATM* **11. Transcription:** ***ATN1 ATXN1 ATXN3 ATXN7 DNMT1*** *POLR3A* ***TBP*** *WWOX* **12. Nuclear inclusion body formation:** ***ATXN1 ATXN3*** *STUB1*

The function of the following genes implicated in ataxia did not match the depicted molecular processes: *ATP8A2* ***CCDC88C ELOVL4 ELOVL5*** *GBA2 PIK3R5 PRICKLE1 SIL1* ***TGM6 TTBK2***
Genes associated with dominantly inherited ataxias are depicted in bold, with recessively inherited forms in regular font.

See online version for legends and references

LIPIDOMIC PROFILING

TARGETED AND DISCOVERY

BY LIPID EXPERTS

Cayman's lipidomics services are based upon well-established methods for targeted and untargeted lipid analysis backed by a team with more than 35 years of experience in lipid synthesis, purification, and characterization.

ASK US ABOUT A PILOT STUDY
CAYMANCHEM.COM/LIPIDOMICS

Cayman CHEMICAL

BIOMEDICAL RESEARCH PRODUCTS

CONTRACT SERVICES

ANALYTICAL STANDARDS

ACTIVE PHARMACEUTICAL INGREDIENTS

Leading Edge
Perspective

Cell

A Paradigm Shift in Cancer Immunotherapy: From Enhancement to Normalization

Miguel F. Sanmamed[1] and Lieping Chen[1,*]
[1]Department of Immunobiology and Yale Cancer Center, Yale University School of Medicine, New Haven, CT, USA
*Correspondence: lieping.chen@yale.edu
https://doi.org/10.1016/j.cell.2018.09.035

Harnessing an antitumor immune response has been a fundamental strategy in cancer immunotherapy. For over a century, efforts have primarily focused on amplifying immune activation mechanisms that are employed by humans to eliminate invaders such as viruses and bacteria. This "immune enhancement" strategy often results in rare objective responses and frequent immune-related adverse events (irAEs). However, in the last decade, cancer immunotherapies targeting the B7-H1/PD-1 pathway (anti-PD therapy), have achieved higher objective response rates in patients with much fewer irAEs. This more beneficial tumor response-to-toxicity profile stems from distinct mechanisms of action that restore tumor-induced immune deficiency selectively in the tumor microenvironment, here termed "immune normalization," which has led to its FDA approval in more than 10 cancer indications and facilitated its combination with different therapies. In this article, we wish to highlight the principles of immune normalization and learn from it, with the ultimate goal to guide better designs for future cancer immunotherapies.

Introduction

Successful generation of a T cell-mediated immunity to eliminate antigen includes but it is not limited to the following steps: (1) tumor-antigen uptake and processing by antigen-presenting cells (APCs), (2) migration of APCs to lymphoid organs, (3) tumor-antigen presentation fine-tuned by co-stimulation and co-inhibitory signals that regulate the activation of tumor-specific naive T cells to become effector T cells in lymphoid organs, (4) the regression of tumor-specific effector T cells from lymphoid organs into peripheral blood and trafficking to tumor tissues, (5) tumor-antigen recognition and tumor lysis, and (6) death of effector T cells and the generation of tumor-specific memory T cells. Based on the understanding of these cellular and molecular mechanisms, various types of immunotherapies were developed to "push" immune activation through the modulation of general regulatory and/or activatory mechanisms governing these steps to improve antitumor immune responses in quantity and/or quality. This general approach aims to activate and increase the immune response, and we have termed this as "enhancement immunotherapies."

However, cancer does not simply grow to race with the development of immune responses, but rather actively employs various tactics to delay, alter, or even stop antitumor immunity. These tactics, collectively termed "immune evasion mechanisms," often defeat intrinsically developed antitumor immunity, leading to a failure in the control of tumor growth. These mechanisms develop continuously during the progression of cancer and become more diverse and complex in late-stage cancers. New approaches to improve the immune response against cancer consist of blocking these immune evasion mechanisms. One of the first and most characterized immune evasion mechanisms is the programmed cell death (PD) pathway. This pathway inhibits an effector T cell antitumor immune response when it is upregulated in the tumor microenvironment, and therapies blocking this pathway have proven effective at improving an antitumor immune response against multiple tumor types. This approach is conceptually different from the previous enhancement approach. While enhancement approaches are designed based on the knowledge of the general activation process, anti-PD therapy exploits new knowledge based on immune evasion mechanisms. Furthermore, while in the enhancement approach, we assume that the general mechanisms of immune system activation are always the same, anti-PD therapy first requires a careful study of the tumor microenvironment (TME) to identify that the PD pathway is upregulated, making this therapy more "personalized." We believe that this approach represents the first of an emerging group of strategies in the future of cancer immunology research and will expand as we understand better mechanisms of immune escape. Because this new approach aims to restore a lost antitumor immunity, we have termed it "normalization cancer immunotherapy."

The Beginning: Enhancement Cancer Immunotherapy

Starting from its inception, mainstream cancer immunotherapy has involved enhancing the processes believed to be necessary for a successful and powerful immune response. These enhancement strategies have generally been grouped in two: the first approach is to use effector cells/molecules of the immune system to directly attack tumor cells, which is called "passive" immunotherapy. This category includes antibody-targeted therapy and its derivatives (e.g., antibody-drug conjugates), as well as adoptive immune cell therapies and, more recently, genetically engineered T cells (chimeric antigen

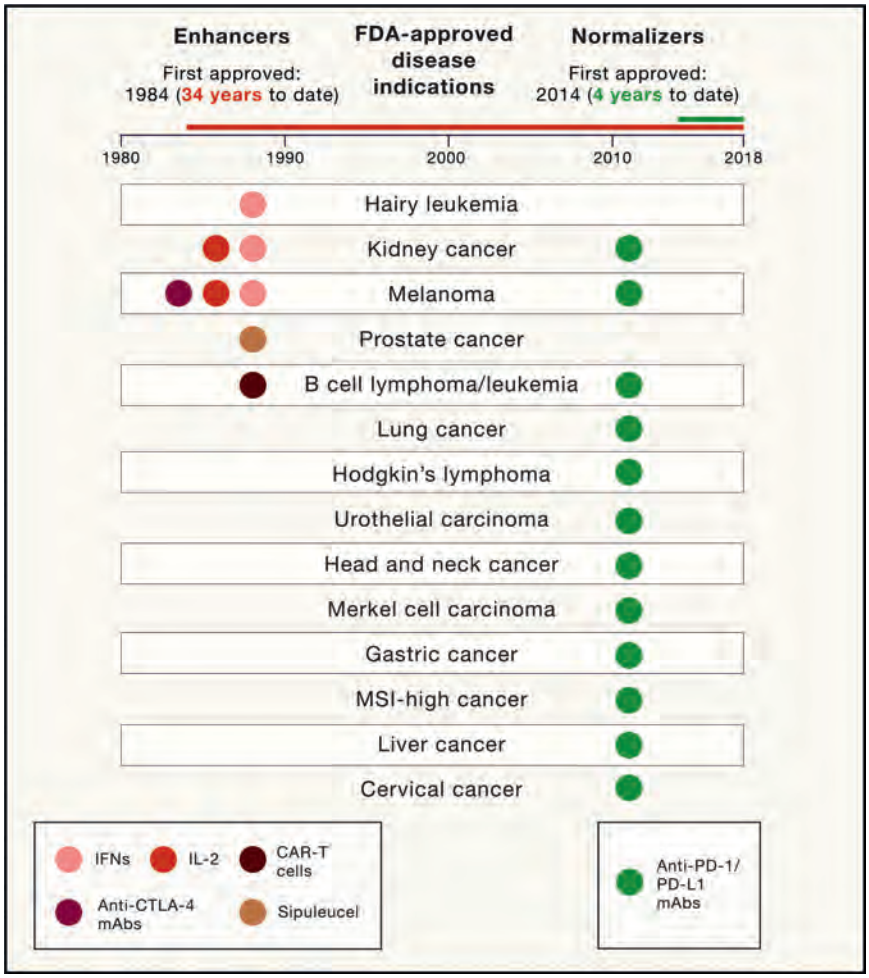

Figure 1. FDA-Approved Cancer Immunotherapies and Their Indications under the Categories of the Immune Enhancement versus Immune Normalization

All FDA-approved cancer immunotherapies are illustrated. These cancer immunotherapies are divided into two categories. The immune enhancement category (IFNs, IL-2, anti-CTLA-4, cancer vaccine, and CAR-T cells) is listed in the left panel with the first approval of type I IFN for the treatment of hairy cell leukemia in 1984. The immune normalization category (anti-PD-1/PD-L1 mAbs) is listed in the right panel with the first approval of anti-PD-1 mAb nivolumab in 2014. Approved disease indications are listed in the middle panel.

receptor [CAR]-T, T cell receptor [TCR]-T, etc.). Passive immunotherapy employs the power of modern technology and brings the immune system to much higher, sometimes extraordinary levels. The most well-known examples are anti-Her2/neu monoclonal antibody (mAb) for breast cancer, anti-EGFR mAb for colorectal or head and neck cancer, and anti-CD20 mAb for B lymphoma, among others. The second approach is to enhance immune system activation through the modulation of endogenous regulatory and/or activatory immune mechanisms, which is also called "active" immunotherapy. In accordance with the immune response step that these strategies enhance, we can (1) enhance antigen uptake, processing, and presentation to T cells by APCs, such as antigen/adjuvant vaccines and dendritic cell vaccines—this could also extend to cytokines or agents that promote APC activity such as type I interferons (IFNs), Toll-like receptor (TLR) agonists, and stimulator of interferon genes (STINGs) agonists; (2) enhance the activation and expansion of naive T cells: examples are dendritic cell vaccines and anti-cytotoxic T lymphocyte antigen-4 (CTLA-4) mAb; and (3) intensify the effector phase of the immune response: examples are adoptive cell therapy using *ex vivo* stimulated and expanded tumor infiltrate T cells to infuse back into cancer patients. In this article, we will focus our discussion and analysis mainly on active immunotherapies, as well as CAR-T cell therapy. For antibody-targeted therapy, we will refer to several excellent review articles (Scott et al., 2012; Weiner, 2015; Weiner et al., 2010), and it will not be discussed in depth here.

It is important to understand that the enhancement strategies are not designed to correct or overcome an existing or known deficiency during the development of the antitumor immune response. For instance, interleukin-2 (IL-2) therapy was not chosen based on a defective expression on IL-2 and its receptors in cancer patients. It is also unknown whether or not CTLA-4 overexpression or altered B7-1/B7-2 expression constitutes a tumor-induced immune-deficient mechanism in patients treated with anti-CTLA-4 mAbs. Likewise, cancer vaccines or adoptive therapy are also given to patients without knowledge of any defects in presentation/priming in patients. This suggests that perhaps, in some patients, these enhancement strategies are indeed providing a needed supply to the immune activation process. Therefore, these patients may benefit greatly from this treatment. However, in most of these cases, these strategies may simply be general activators of the immune system that are increasing the immune response against tumors but that are also pushing the immune system to supraphysiological levels with a subsequent risk of increasing immune-related adverse events (irAEs). This may explain the low tumor response-to-toxicity profile during enhancement immunotherapy.

Despite these conceptual limitations, these early strategies resulted in objective tumor responses and subsequent FDA approvals for the treatment of a few tumors (Grupp et al., 2013; Kantoff et al., 2010; Parkinson et al., 1990; Porter et al., 2011; Rosenberg et al., 1987), as summarized in Figure 1. However, it became evident that successful treatment was the exception (only a small portion of patients showed objective responses), and often, these strategies failed to demonstrate a

significant clinical benefit in multiple tumor types. In most of the cases, these therapies failed to extend their approval beyond classically immunogenic tumors due to an unfavorable response/toxicity ratio (i.e., IL-2 and anti-CTLA-4 mAbs). We focus this discussion on why we consider these therapies as ''enhancement'' and the reasons for their less favorable response-to-toxicity ratio. Because it is well beyond this Perspective to review all possible immunotherapies that failed during past and present years, we have chosen to focus our analysis here only on FDA-approved cancer immunotherapies that have demonstrated a significant antitumor activity in at least one tumor type.

Cancer Vaccines

Following the idea of vaccination in infectious diseases, the most popular cancer immunotherapy practice has been to immunize patients against tumor antigens through many different approaches, including cell-based, DNA-based, and protein/peptide-based preparations. Unfortunately, after thousands of cancer vaccine trials have been conducted and tested in multiple tumor types, only one cancer vaccine has been approved with moderate effect (sipuleucel in prostate cancer) (Kantoff et al., 2010). Ironically, many of these vaccination strategies were able to induce a peripheral tumor-specific T cell response while failing to show objective antitumor activity (Melero et al., 2014; Rosenberg et al., 2004). These findings suggest that tumor-specific T cell priming may not be the major hurdle in these cancer patients. Furthermore, the appearance of vitiligo, a sign of autoimmunity, is often associated with objective tumor response after cancer vaccination in some melanoma patients, indicating that tumor response and autoimmunity are frequently associated (Overwijk and Restifo, 2000). With the advent of neoantigen tumor vaccines, this strategy has been reinvigorated proposing the need for new antigens without central tolerance and higher T cell affinity (Ott et al., 2017; Sahin et al., 2017).

Cytokines

One of the most illustrative examples of the enhancement of cancer immunotherapy is the use of IL-2. IL-2 is a growth factor for antigen-specific T cells and natural killer (NK) cells. IL-2 was first identified in 1976 (Morgan et al., 1976), and isolation of the cDNA clone was described in 1983 (Taniguchi et al., 1983). Subsequently, recombinant IL-2 was shown to have antitumor activity in a number of murine tumor models (Rosenberg et al., 1985). Based on animal model data, IL-2 was tested in cancer patients and received FDA approval to treat renal cell carcinoma (1992) and melanoma (1998) with a 5%–15% objective response rate (Rosenberg, 2014). While IL-2 induces an effective antitumor immune response in a few cases, in most patients, IL-2 induces a significant toxicity in multiple organs and tissues, mostly related with general capillary leak syndrome (Atkins et al., 1999). Thus, the antitumor effect seems to be the exception, while broad stimulation of the immune system seems to be the rule. With the arrival of new versions of IL-2 receptor agonists, efficacy and toxicity are expected to be improved, based first on the design of engineered IL-2 that preferentially binds CD8 and NK IL-2 receptor over Treg IL-2 receptor (Charych et al., 2016) and second on bispecific constructs targeting tumor antigens and refocusing most of the effect of IL-2 into the tumor microenvironment (Klein et al., 2017).

Anti-CTLA-4 mAbs

CTLA-4 is a cell-surface receptor induced in conventional T cells after TCR engagement that acts as a regulator of naive and effector antigen-specific T cell activation (Leach et al., 1996; Walunas et al., 1994). Additionally, CTLA-4 is highly expressed in Tregs and has proven to be critical for the development and function of induced Tregs (Takahashi et al., 2000). Mice lacking CTLA-4 develop an early-onset general T cell activation, resulting in inflammatory infiltration and death around 3 weeks of age, highlighting the importance of CTLA-4 to control self-reactive T cell responses (Waterhouse et al., 1995). In the clinic, anti-CTLA-4 mAbs induce frequent autoimmune reactions that confirm the importance of this pathway in controlling self-reactive T cells. Whether these autoimmune reactions occur due to the loss of CTLA-4 function in conventional T cells, regulatory T cells, or both is under debate. A recent study using a humanized CTLA-4 mouse model casts doubt on the blockade of the B7s/CTLA-4 interaction using clinical-grade anti-CTLA-4 mAbs (ipilimumab) (Du et al., 2018), and numerous works during recent years suggest that the main effect of anti-CTLA-4 mAbs may be mediated by Treg depletion (Bulliard et al., 2013; Selby et al., 2013; Simpson et al., 2013, Arce Vargas et al., 2018). These results thus call for a reassessment of the ''immune checkpoint blockade'' concept for anti-CTLA-4 therapy. On the other hand, while a small group of melanoma patients developed an objective tumor response (15%–20%), severe toxicities (grades 3–5) were more common (30%), suggesting that this agent more effectively activates self-reactive rather than tumor-specific T cells. Judging from the mechanisms of action, the CTLA-4 blocking strategy may be another type of enhancement cancer immunotherapy, because there is no evidence that this pathway is induced by tumors as an immune evasion mechanism, and furthermore, we do not have evidence that anti-CTLA-4 mAbs preferentially activate tumor-specific T cells over self-reactive T cells in patients. In contrast, clinical data illustrate that irAEs are more frequent than tumor response (ORR) as it happens with the use of unspecific T cell growth factor IL-2 (Table 1). This unfavorable response/toxicity ratio most likely is the reason why ipilimumab has been approved to treat metastatic melanoma (Hodi et al., 2010) but failed to show clinical benefit in other tumor types where it was tested as a single-agent therapy (Bilusic et al., 2017; Lynch et al., 2012).

Chimeric Antigen Receptor

CAR-T cells are genetically engineered T cells with an antigen-binding domain (typically a single-chain variable fragment [scFv]) and additional intracellular costimulatory domains from receptors, such as CD28 and/or CD137. The advantage of these engineered T cells is that the recognition of antigens by CAR-T is not restricted by major histocompatibility complex (MHC) expression. This design is one of the most paradigmatic examples of using engineered effector immune cells to more effectively attack tumor cells, and the infusion of a large number of these cells is an illustrative case of the enhancement strategy. A main disadvantage is that it requires extracellular surface expression of the targets on the tumor cells, and this limits CAR-T cells' specificity and broadness of application. Since the invention of hybridoma technology, numerous mAbs have been generated against tumor cells with the hope to discover

Table 1. ORR and Severe Treatment-Related AEs in Metastatic Melanoma Patients Treated with FDA-Approved Immunotherapies

Drug	Phase	Drug and Schedule	Number of Patients[a]	Objective Response Rate (%)	Treatment-Related Toxicities[b]		Reference
					Any Grade (%)	Grades 3–4 (%)	
IL-2							
	II	high dose IL-2	46	10 (24)	>32 (>68)	>17 (>35)	Parkinson et al. (1990)
	II	high dose IL-2	134	23 (17)	134 (100)	>78 (>37)	Rosenberg et al. (1994)
	II[c]	high dose IL-2	270	43 (16)	>64 (>24)	>45 (>17)	Atkins et al. (1999)
	II	high dose IL-2	26	5 (19)	26 (100)	13 (50)	Tarhini et al. (2007)
	III	low dose IL-2	153	5 (3)	N/A	59 (39)	Agarwala et al. (2002)
	III	high dose IL-2	93	6 (6)	>36 (>39)	74 (80)	Schwartzentruber et al. (2011)
Average				(14)		(>43)	
Anti-CTLA-4 mAbs							
	II	ipilimumab	57	9 (16)	54 (95)	27 (47)	Weber et al. (2009)
	III	ipilimumab	137	15 (11)	105 (80)	30 (23)	Hodi et al. (2010)
	III	ipilimumab	278	33 (12)	187 (73)	51 (20)	Robert et al. (2015a)
	III	ipilimumab	315	60 (19)	268 (85)	85 (27)	Larkin et al. (2015)
	II	ipilimumab	47	5 (11)	34 (74)	9 (19)	Hodi et al. (2016)
	III	ipilimumab	727	100 (14)	324 (45)	190 (26)	Ascierto et al. (2017)
Average				(14)		(27)	
Anti-PD-1 mAbs							
	I	pembrolizumab	135	44 (38)	107 (79)	17 (13)	Hamid et al. (2013)
	II	nivolumab	107	33 (31)	90 (84)	24 (22)	Topalian et al. (2014)
	I	pembrolizumab	173	41 (26)	142 (82)	20 (12)	Robert et al. (2014)
	III	nivolumab	316	138 (44)	257 (82)	51 (16)	Larkin et al. (2015)
	III	pembrolizumab	556	185 (33)	423 (76)	65 (12)	Robert et al. (2015a)
	III	nivolumab	210	84 (40)	153 (74)	24 (12)	Robert et al. (2015b)
	II	pembrolizumab	357	84 (23)	252 (76)	45 (13)	Ribas et al. (2015)
	III	nivolumab	227	74 (27)	206 (77)	37 (14)	Larkin et al. (2018)
Average				(33)		(14)	

N/A, not available.

[a]Number of patients available for ORR or treatment-related AE assessment vary across the studies.

[b]Indicated as ">" when frequency per toxicity grade was not available, and it was estimated based on the most common treatment-related adverse event reported.

[c]Data combination of eight phase II clinical trials.

"magic bullets," and it is now clear that there are very few tumor-specific cell-surface antigens. CAR-T cells are extremely effective at recognizing and destroying target cells. In this regard, this type of adoptive cell therapy is equally effective to clear tumor as normal cells when the target antigen is shared by tumor and non-tumor tissues. For instance, CAR-T cells targeting CD19 proteins are very effective at recognizing and destroying B cell lymphoma and leukemia cells but also destroying all the normal CD19+ B cells in the body of the patient. While this off-target effect is acceptable, since B cell depletion in patients can be functionally replaced by administering polyclonal human immunoglobulin Gs (IgGs), the consequences can be more dramatic when the target is expressed in normal epithelial cells. In addition to this off-target toxicity, the most important irAE related with CAR-T cells is acute cytokine release syndrome (CRS) as a consequence of producing supraphysiologic levels of cytokines via CAR-T cells upon antigen recognition (Brudno and Kochenderfer, 2016; Namuduri and Brentjens, 2016). All of these are important limitations to the extension of these therapies to solid tumors as was shown in the preliminary results of HER2-specific CAR-T cells (Ahmed et al., 2015; Morgan et al., 2010).

In summary, the common experience for the use of enhancement cancer immunotherapy is that general activation of the immune system leads to more frequent irAEs than objective antitumor responses (with the exception of CAR-T therapy in hematological malignancies). This unfavorable response-to-toxicity ratio has limited the use for most of these therapies, and none of these agents have had a broad spectrum of indications thus far (Figure 1).

The Normalization Cancer Immunotherapy Has Come of Age

An important clinical observation in the last decade is that systemic immune activation does not necessarily result in cancer

regression, especially in solid tumors. In fact, ample evidence exists that the presence of fully activated tumor-specific T cells in peripheral blood does not often correlate with the regression of tumors or a better prognosis in cancer patients (Melero et al., 2014; Rosenberg et al., 2005). This discrepancy has been better understood recently with the discovery and characterization of immune escape mechanisms developed by tumors that lead to a local, rather than a systemic, immunosuppression (Taube et al., 2012, Chen and Han, 2015). It has been well documented that human cancer can develop various mechanisms to escape specific and non-specific immune attacks (Vinay et al., 2015). These mechanisms prevent immune attack, inhibiting T cell activity in the TME. Unfortunately, the mechanisms governing immune escape in tumors discovered thus far are often similar, if not identical, to those governing self-tolerance (Phan et al., 2001), making it difficult to develop a therapeutic that generates an antitumor response but avoids irAEs. This limitation, however, has recently been challenged by encouraging basic and clinical findings using mAbs to block B7-H1 and PD-1 interactions (collectively named anti-PD therapy) (Chen and Han, 2015). Indeed, anti-PD therapies are the first FDA-approved immunotherapies to demonstrate more frequent objective tumor responses than severe treatment-related AEs in cancer patients, illustrating that it is possible to increase efficacy without increasing toxicity. We have highlighted this achievement by comparing the objective response rate and treatment-related AEs across clinical trials using FDA-approved IL-2, anti-CTLA-4, and anti-PD-1 mAbs as single agents to treat metastatic melanoma patients (Table 1). Also, a recent side-by-side comparison of nivolumab (anti-PD-1) and ipilimumab in a randomized clinical trial of advanced and localized melanoma patients confirmed that nivolumab has three times more activity and three times less toxicity than ipilimumab (Larkin et al., 2015; Robert et al., 2015a; Weber et al., 2017). Furthermore, clinical results have repeatedly demonstrated that this strategy can induce durable responses in a broad spectrum of large and disseminated late-stage human malignancies, increasing the frontiers of immunotherapy beyond the traditional set of previously categorized immunogenic tumors, such as melanoma (Callahan et al., 2016; Zou et al., 2016). Currently, anti-PD therapy has been approved by the FDA for the treatment of metastatic melanoma, lung cancer, head and neck cancer, renal cell carcinoma, urothelial carcinoma, liver cancer, gastric cancer, Hodgkin's lymphoma, Merkel cell carcinoma, large B cell lymphoma, cervical cancer, and any MSI+ tumors (Ribas and Wolchok, 2018) (Figure 1). Moreover, anti-PD therapy is effective in >25 different types of solid tumors and several hematopoietic malignancies, which will likely lead to future FDA approval (Ribas and Wolchok, 2018). One of the factors that facilitated this unprecedented success is a more favorable response-to-toxicity profile, with a 40% objective tumor response rate and a 7%–12% grades 3–5 irAEs across multiple tumor types (Naidoo et al., 2015; Ribas and Wolchok, 2018). This new tumor response-to-toxicity profile and this antitumor activity across multiple tumor types (beyond those classically considered "immunogenic tumors") reflect a different mechanism of action, termed here immune normalization, which we will discuss in detail in the following section. We believe that there are other potential immune normalizers, and learning from the principles of anti-PD therapies, we can choose immunotherapies that can reproduce the success of anti-PD therapy.

Principles of Normalization Cancer Immunotherapy

The concept of immune normalization emphasizes the importance of identifying the particular defects or dysfunctions of the immune response during tumor progression and to develop strategies to specifically correct these deficiencies to restore a natural antitumor immune capacity. Although the end result of the normalization strategy may lead to elevated immune responses, these responses should fluctuate transiently in limited ranges and, in theory, should not cause permanent damage to normal organs/tissues. This "controlled" elevation of immune responses during normalization immunotherapy may be due to immune responses under normal feedback regulation. While there are some cases where severe irAEs occur in patients treated with anti-PD therapy, under a normalization immunotherapy approach, these patients may be predisposed to or in a "subclinical" status of inflammatory or autoimmune disease in which anti-PD therapy will serve as a "final nail in the coffin."

Normalization strategies aim to unblock a blocked immune response to increase the antitumor responses in contrast to enhancers that aim to generally activate the immune system to improve the antitumor responses. To illustrate this concept, we can think of the process of immune response as a big pipeline with water flow. Normal immune response, in this case, would be proper drainage. Thus, if the pipeline gets blocked, the flow would be impaired, and the pipeline would not drain sufficiently. In this situation, the "enhancer" approach can be illustrated as an increase in the pressure on the pipeline to overcome deficient drainage with the associated risk of breaking the pipeline if we increase the pressure too much. In contrast, the normalizer approach can be illustrated by strategies that aim to identify and unlock the blockade to restore the normal flow without risking the pipeline walls (Figure 2).

Anti-PD therapy is the clearest example of this approach thus far. Immune inhibitory B7-H1 protein is overexpressed in the TME leading to an overregulation of tumor-specific effector T cells, thus creating a locally deficient immune response that prevents tumor cell destruction. Blocking the B7-H1/PD-1 pathway results in selective repair of this defect and restores immune competence against tumors without leading to a general immune activation. Taking the B7-H1/PD-1 pathway as an example, we can illustrate three main principles that explain why the normalization approach is more suitable to reach antitumor immunity with reduced adverse events.

Targeting a Tumor-Induced Immune Escape Mechanism

Ample evidence indicates that B7-H1/PD-1 is a major counter-receptor interaction that leads to suppression of immune responses in both preclinical and clinical settings (Chen and Han, 2015; Ribas and Wolchok, 2018; Zou et al., 2016). Although either B7-H1 or PD-1 could also interact with other proteins (B7-H1/B7-1, PD-1/PD-L2), the biological significance of these interactions in humans is not yet fully understood. While T cells are a primary target for suppression, as shown in the majority of studies, the PD pathway could also impair the functions of dendritic cells (Yao et al., 2009), macrophages (Yao et al., 2009), and

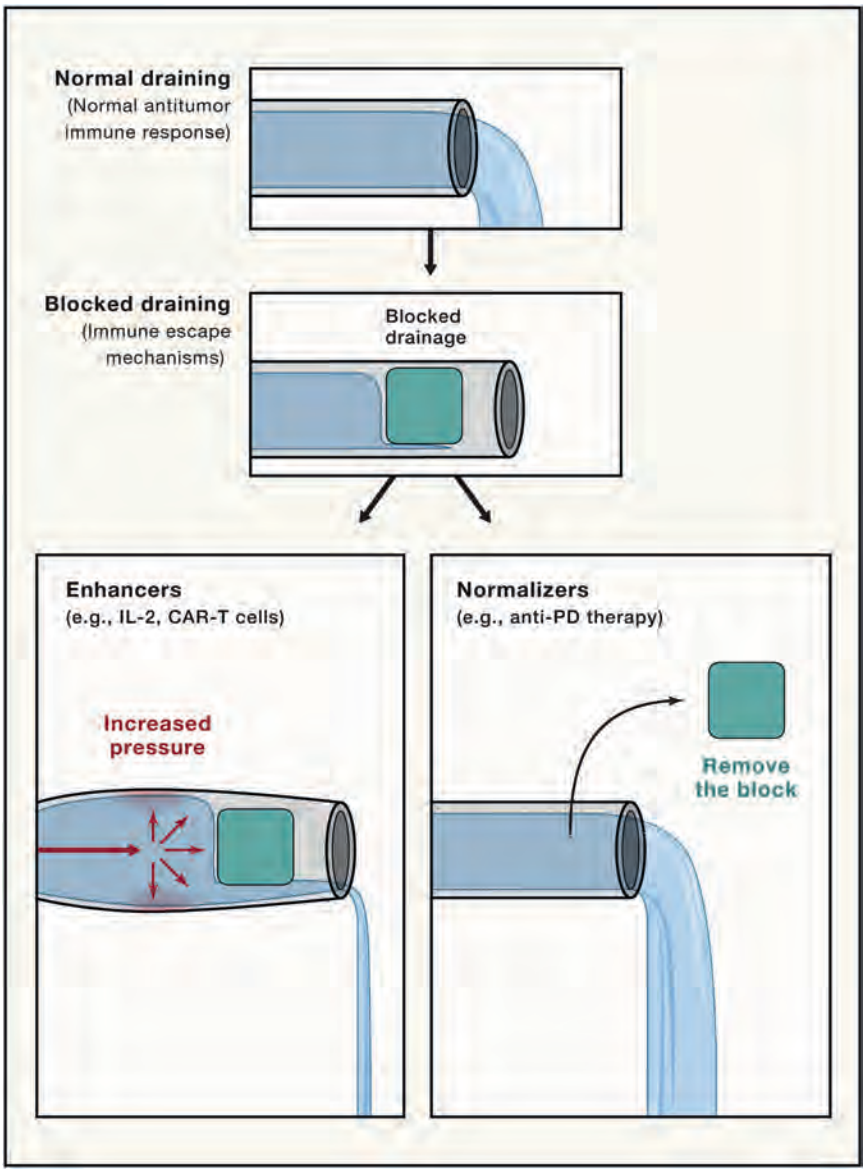

Figure 2. Illustration of the Immune-Normalization versus Immune-Enhancement Approaches

Using proper flow and drainage of a pipeline as a comparison for the antitumor immune response. The flow of the pipeline can be insufficient when a blockade impairs flow, as the antitumor immune response can be insufficient when there is an immune impairment. The immune enhancement approach is illustrated as an increase in flow or pressure to return to proper function/flow with the risk of breaking the pipe (adverse effects). In contrast, the immune normalization approach would be to identify and try to unblock this specific blockage and restore the flow.

NK cells (Benson et al., 2010; Huang et al., 2015; Vari et al., 2018). The PD-1 mediated suppression mechanisms appear to be complex, including apoptosis, induction of suppressive cytokines, anergy, exhaustion, and Treg induction (Chen and Han, 2015; Zou and Chen, 2008; Zou et al., 2016). It is also evident that B7-H1 could also act as a receptor to transmit an anti-apoptotic signal to various types of cells, which may be responsible for the resistance of tumor cells to T cell-mediated lysis (Azuma et al., 2008; Chin et al., 2018). How these potential mechanisms contribute to human cancer progression, as well as new mechanistic insights, are under intensive investigation. The B7-H1/PD-1 pathway represents the archetypal tumor-adaptive immune escape mechanism. Upon recognition of tumor antigens, tumor-specific effector T cells upregulate PD-1 and release IFN-γ that induces B7-H1 in tumor and myeloid cells in the TME. B7-H1 inhibits T cells through PD-1 engagement, interrupting antitumor T cell attack. This interruption of the antitumor T cell response represents a form of local immunodeficiency that allows tumors to escape and has been termed "adaptive immune resistance" (Dong et al., 2002, Taube et al., 2012). This interruption of the antitumor immune response can be restored by terminating B7-H1/PD-1 pathway signaling, described first in preclinical tumor models (Dong et al., 2002). Additionally, chronic viral infection models (e.g., hepatitis B virus [HBV] or lymphocytic choriomeningitis virus [LCMV]) demonstrated that chronic expression of B7-H1 is associated with T cell dysfunction, which can be restored when the B7-H1/PD-1 pathway is blocked (Barber et al., 2006). These findings have also been explored in human chronic viral infections (Gardiner et al., 2013; Gay et al., 2017). Although ample evidence indicates that chronic viral infection also utilizes the B7-H1/PD-1 pathway to suppress anti-viral immunity, the lessons learned from these studies are not always applicable to understanding the B7-H1/PD-1-mediated tumor escape mechanisms. In contrast to frequent systemic immune suppression in peripheral organs and lymphoid organs during viral infection, tumor escape mechanisms occur frequently at tumor sites, while immune responses in peripheral organs, as well as lymphoid organs, are relatively normal. This may explain, in part, the dichotomy of progressive tumor growth accompanied with elevated tumor immunity in blood, indicating that the priming of T cell immune responses are not impaired, as described above. This led to the second important principle of the normalization cancer immunotherapy: selectively modulating immunity in the tumor microenvironment.

Selectively Modulating Immunity in the Tumor Microenvironment

A major difference of the B7-H1/PD-1 pathway with other immune inhibitory pathways is that B7-H1/PD-1 is minimally active in non-lymphoid tissues under normal physiological conditions.

In this regard, B7-H1 protein is not expressed in steady-state normal human tissues (with the exception of placenta, tonsil, and a small portion of macrophage-like cells in lung and liver), although the mRNA of B7-H1 is broadly present in various normal tissues/cells (Chen and Flies, 2013; Dong et al., 2002; Petroff et al., 2002). In contrast, this membrane receptor can be broadly induced by type I and type II IFNs (Lee et al., 2006; Sanmamed and Chen, 2014) and displayed on the cell membrane of hematopoietic and non-hematopoietic cells within inflammatory tissues, including tumoral and virally infected tissues (Chen and Han, 2015). Because PD-1 is broadly present on effector memory T cells in peripheral blood and in tumor and non-tumor lymphoid organs (Gros et al., 2014), the TME-specific effect of anti-PD therapy is determined by selective expression of B7-H1 in the TME.

This minimal expression of B7-H1 in non-inflamed tissues ensures a TME-selective effect of anti-PD therapy by preventing damage to normal tissues and allows for a more focused and precise immune response with less systemic immune activation (Sanmamed and Chen, 2014). Such minimal systemic toxicity was demonstrated in early phase I clinical trials with anti-PD therapy when a maximum tolerated dose was not reached during dose escalation of anti-PD-1 or anti-B7-H1 mAbs (Brahmer et al., 2010, 2012; Topalian et al., 2012). A dose-dependent increase in toxicity was similarly absent, as the 10-mg/kg dose did not show a significant increase in the frequency of severe adverse events when compared with the 1-mg/kg dose (Brahmer et al., 2010, 2012; Topalian et al., 2012).

The tumor-site specificity of the pathway is, therefore, mainly determined by the localized induction of B7-H1 by IFN-γ. In this manner, B7-H1 expression is often a sign of a local ongoing but impaired antitumor immune response. Histological analyses corroborate this concept, as most human tumors show a pattern of B7-H1 expression that is focal or clustered rather than diffused and is often co-localized with T cell infiltration (Taube et al., 2012). It is still not well understood why a soluble cytokine like IFN-γ does not diffuse to a large area of tissues to have a more profound effect. One possible explanation could be the broad distribution of IFN-γ receptor on various types of cells in the TME (Bach et al., 1997), which may prevent IFN-γ from traveling further. Additional evidence supporting tumor selectivity of the immune response during anti-PD therapy is the selective expansion and functional improvement of T cells, mainly at the tumor site, and a lack of correlation between tumor regression and immune cell activation markers detected in the peripheral blood (Das et al., 2015; Herbst et al., 2014). This is in sharp contrast with enhancement immunotherapies that are often effective in activating a systemic immune response but show weak immune activation at the tumor site.

Resetting Immunity in the Tumor Microenvironment

A most-intriguing but less-understood observation in basic and clinical research in anti-PD therapy is its capacity to reset or reprogram antitumor immunity in the TME. The B7-H1/PD-1 pathway seems like a ''master switch'' that determines the fate of the entire TME in some cancer patients, since manipulation of a single pathway (the blockade of the B7-H1/PD-1 interaction) and, in some cases, even with a single dose of anti-PD therapy, can change from an initially highly suppressive TME to a highly active inflammatory site. During phase 1 clinical trials with anti-PD therapy, some patients showed objective tumor shrinkage with a single dose of anti-PD therapy (Gainor et al., 2016). Because immune dysfunction or deficiency in the TME are often multifaceted at the cellular and molecular levels (Zou, 2005; Zou and Chen, 2008; Zou et al., 2016), these observations are encouraging and implicate that, at least in some patients, normalizing a single master pathway is sufficient to trigger the resetting process, and it is not necessary to correct all defects in the TME.

From the currently available data, we speculate that the majority of, if not all, patients with late-stage cancer do not have systemic immune defects, and their immune systems still work to continuously provide newly generated effector T cells into the TME. This constitutes an important immunological basis for normalization immunotherapy. The TME in late-stage cancer patients could be considered a hostile work environment where various tactics of immune evasion mechanisms have already developed during tumor progression. The mechanisms of action for anti-PD therapy are likely multifaceted, including restoring functions of those already dysfunctional T cells, as well as preventing newly arrived effector T cells from becoming dysfunctional in the TME. These reinvigorated T cells, upon PD-pathway blockade, and newly arriving immune cells protected against PD-pathway inhibition may contribute to the resetting of immune responses in the TME while behaving as effector cells against tumor cells. An important but less-understood consequence of this normalization process is the generation of memory T cells, which are believed to give the durable antitumor effect of anti-PD therapy. Currently, we do not know the origin of tumor-antigen-specific memory T cells, how and why they become memory T cells, and how to modulate them. Understanding these issues will determine how and when we can use these therapies with precision.

The Normalization of Cancer Immunotherapy: The End of the Beginning

Beyond B7-H1, there are arrays of molecular pathways that cause immune defects in the antitumor immune response that can be targeted to restore the competence of this response. A new classification system of human cancer, termed tumor immunity in the microenvironment (TIME) was proposed based on the level of tumor-infiltrating leukocytes (TILs) and B7-H1 expression levels in the TME as a road map to search for potential immune defects that need to be normalized (Sznol and Chen, 2013; Taube et al., 2012; Zhang and Chen, 2016) (Figure 3). Molecular entities and mechanisms of these immune defects, once identified and characterized, could be potential targets for normalization immunotherapies and should provide an alternative for those patients that do not respond to anti-PD therapy. Among the potential different antitumor immunity defects, we can broadly classify cancer patients into three categories: (1) defects in the entry and/or proliferation of immune cells in which there is a lack of significant TILs in the TME, as indicated in TIME types I and IV, (2) overregulation of activated TILs, largely due to the effect of the B7-H1/PD-1 pathway and potentially other T cell regulatory pathways, indicated as type II, and (3) dysfunctional TILs in the TME due to suppression by molecular pathways (non-B7-H1/PD-1), indicated

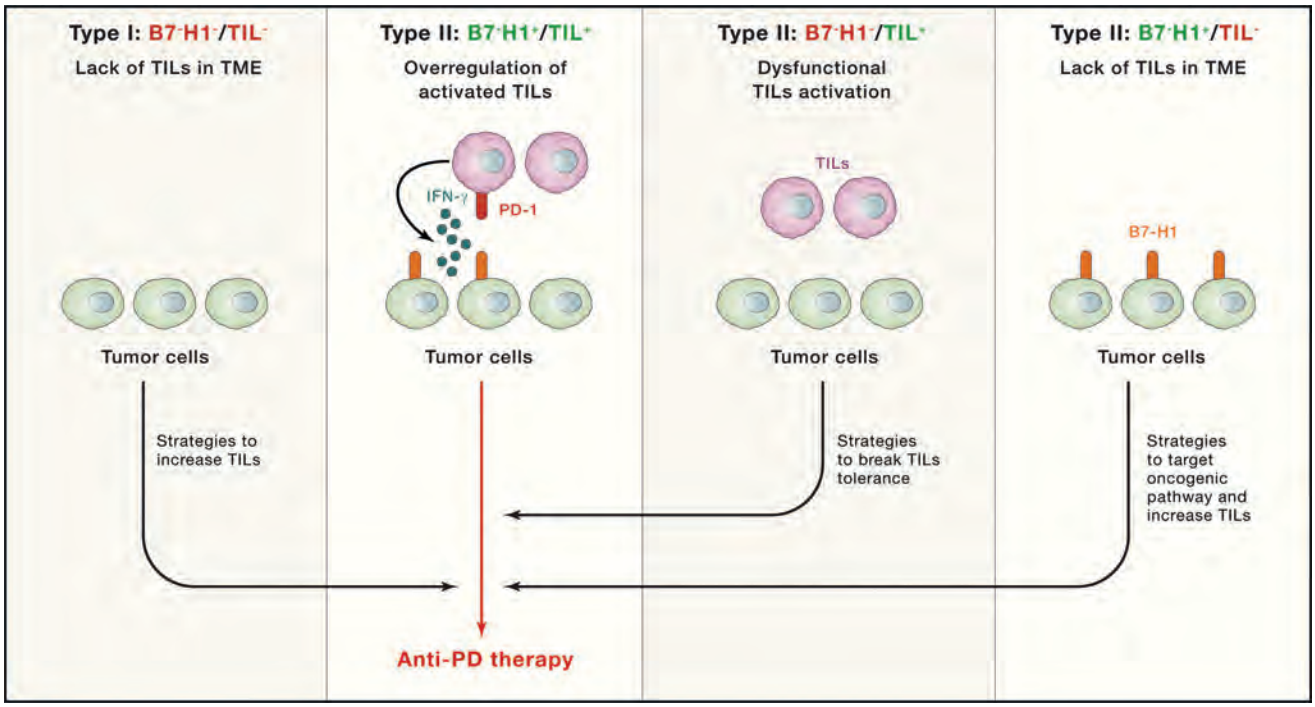

Figure 3. Tumor Immunity in the Microenvironment Classification

Four different TME groups with potential implications for mechanism and therapy have been identified according to B7-H1 (PD-L1) expression and the presence of TILs in tumor biopsies: (1) B7-H1-negative tumors without TILs, considered immunological ignorant because immune cells do not accumulate at the tumor site, (2) B7-H1-positive tumors with TILs, considered a paradigm of adaptive resistance of tumors mediated by the B7-H1/PD-1 pathway, (3) B7-H1-negative tumors with TILs, considered a situation of tolerance because TILs are present, but they do not induce B7-H1 expression in the tumor microenvironment through IFN-γ production, and (4) B7-H1-positive tumors without TILs, considered as a scenario of intrinsic induction of B7-H1 expression in tumor cells through oncogenic pathways that may be susceptible to be targeted. Groups 1, 3, and 4 can be converted into group 2 through different strategies, synergizing with the action of anti-PD therapies that are more effective in the presence of TILs and B7-H1 expression.

as type III. It is critical to identify which antitumor immune defect is predominant in each patient, since using the same strategy for all patients will be inefficient, costly, and wasteful. For instance, targeting local immune inhibitory pathways like the B7-H1/PD-1 pathway in a patient with a cancer that lacks immune infiltration may be pointless as a single therapy.

Since we are just starting to understand the complexity of the TME in the regulation of immune responses, it is obvious that this TIME classification for human cancer is preliminary, and this may also raise more questions than answers. For example, in type II and type III TIME, we do not know which kinds of TIL components and other regulatory cells will determine the outcomes and responses to immunotherapy. In addition to IFNs, are there any other cytokines and molecular pathways that could regulate the expression of B7-H1? In types I and IV, what makes the TME stop the entry of TILs, and what are the mechanisms that prevent the proliferation of TILs? It is unlikely that these human cancer types do not have sufficient antigens, because our previous data have shown that among melanomas, which have the highest mutation burden of nearly all human cancers, up to 45% fall into this category (Taube et al., 2012). Extensive studies of the identification and characterization of molecular pathways and detailed molecular profiling of the TME may help address these questions and provide targets for future normalization cancer immunotherapy.

Challenges in Developing New Normalization Cancer Immunotherapies

With the success of anti-PD therapy, immune normalization as an approach for cancer immunotherapy has already shown great promise. However, there are still quite a few hurdles that hinder the development of new normalization over enhancement immunotherapies. Some of these limitations are conceptual, while others may be more technical.

Identification of the Dominant Antitumor Immune Defect

The development of normalization immunotherapy relies on identifying specific defects in the antitumor immune response. However, tumor-induced immune defects are highly heterogeneous (Schalper et al., 2017). This heterogeneity of immune defects not only occurs among different patients, but also extends to different areas in a single tumor lesion. These observations speak to the importance of identifying which of the immune defects is the dominant or master switch ultimately facilitating tumor escape. However, the definition of master switch may be patient specific and should be functionally demonstrated based on the capacity to reset the tumor microenvironment when this is modulated. Selecting the right master switch in each patient is the real challenge. Currently, the only way to demonstrate among all immune defects identified in a TME which factor is dominant is empirically. We then need better

in vivo models to characterize the dominance of the different immune pathways in a patient TME and the effect of their modulation. Humanized mouse models or explant 3D culture models may provide support in this way (Jenkins et al., 2018; Sanmamed et al., 2016; Zitvogel et al., 2016).

Technological Difficulties to Study Immune Defects in the TME

Similar to the B7-H1/PD-1 pathway, many other immunosuppressive mechanisms that favor tumor progression occur in the local TME. One major challenge to characterize these mechanisms will be the capacity to evaluate immune responses at the TME level, requiring sequential tumor tissue collection and analyses. This is distinct from enhancement immunotherapies, whose systemic effects can be more readily monitored largely via blood analysis. Tumor tissue analysis represents a tremendous technical challenge, as sequential biopsies in cancer patients are not always possible, and most samples obtained are tiny and have large areas of necrosis.

The study of these immune defects requires the use of technology that can perform single-cell analyses with high phenotypical resolutions. New platforms such as single-cell sequencing, mass cytometry, and *in vivo* imaging techniques (e.g., PET imaging) may help uncover the complexity of the TME (Burel et al., 2016). With rapid progress in the identification and characterization of various immune defects in the TME, a future challenge will be how to identify among the multiple immune inhibitory pathways one or few that are dominant in a specific patient to decide on the best therapeutic approach.

The Principles to Combine Other Therapeutics with Anti-PD Therapy

Anti-PD therapy as a representative of an immune normalization approach has an inherent and significant advantage in the context of its broad therapeutic effect and minimal toxicity, which facilitates its use in combinatorial treatment. While combination therapy represents a popular, current strategy for the treatment of cancer, this strategy is largely driven by a mix of demands in clinical cancer care, corporate finance, and market competition with limited or modest scientific rationales. Currently, >1,500 clinical trials are ongoing that combine anti-PD therapy with nearly all available cancer therapeutics, including chemotherapy, radiotherapy, oncolytic virus, targeted therapy, and other immunotherapies (Tang et al., 2018). However, many of these clinical trials are not designed based on the basic principles of anti-PD therapy, and some of them may even impair the effects of anti-PD therapies. The future direction of combination cancer immunotherapies should mainly be guided by science. For example, a minimal requirement for a successful combination with anti-PD therapy should be chosen based on the biology of the pathway. It is important to keep in mind that our main driving force here is immune cells—specifically effector T cells and memory T cells, for which survival and activation of effector T cells in the TME and the generation of memory T cells for long-term effect need to be respected and potentiated. We will not cover all ongoing combinatorial approaches here, because it is beyond the scope of our Perspective, but we will mention some examples for consideration.

Combination with Radiotherapy and Chemotherapy

Radiotherapy may potentially destroy valuable tumor-specific T cells present in the tumor tissue, whereas it would be safer to perform local radiotherapy in those tumors without tumor-infiltrated T cells at the moment of starting radiotherapy (TIME classification types I and IV). Similarly, some chemotherapy drugs may also damage the function of effector T cells in the TME, which may lead to a less-than-additive effect of the combination therapy. In this case, a sequential treatment, rather than combination therapy, may be a better approach, since immunotherapy treatments may promote tumor-specific T cell proliferation while we are providing cytotoxic agents that target critical processes for cell division. Furthermore, currently, it is unknown whether or not radiotherapy or chemotherapy can affect the generation of memory T cells, which is the holy grail of adaptive immunity and may directly determine the durability of immunotherapy. This issue should also be addressed in the future. In the context of this concern, overall survival may be a better indicator than tumor response rate to appraise the impact of tumor-specific memory formation. It is encouraging that anti-PD therapy plus chemotherapy showed an improved overall survival over chemotherapy alone during a short period of time (1–2 years) (Gandhi et al., 2018). It is more important to compare this combination therapy with anti-PD therapy alone, as well as the evaluation of the generation of memory T cells, a major force for durable immune responses.

Combination with Local Therapies

Direct injection of various biological and chemical agents into tumors as an approach for cancer therapy has a longstanding history with William B. Coley's efforts in the late 19th century (Aznar et al., 2017; Marabelle et al., 2017). These agents include but are not limited to TLRs, RIG-I-like receptor (RLR) agonists, STING pathway modulators (Corrales et al., 2016; Li et al., 2017), and oncolytic viruses (Lawler et al., 2017). Local therapies are believed to (1) trigger innate immunity so as to initiate adaptive immunity, (2) induce death of tumor cells, which could make more tumor antigens available to the immune system, and (3) generate a more inflammatory environment, which may support a better T cell response. These therapies can induce the regression of injected and distal tumors in experimental models. Very promising results have been reported in clinical trials with local injection of oncolytic viruses in melanoma lesions (Tang et al., 2018) and brain tumors (Desjardins et al., 2018; Lang et al., 2018). The roles of local therapies in long-term survival and the regression of distal metastases remain to be studied in the clinic. Furthermore, some fundamental questions on the immunological effect of these approaches in the patients' TMEs remain to be fully characterized. In normal tissue, these local therapies could generate potential innate immunity, which helps initiate antigen-specific responses. However, in the TME, various tumor escaping mechanisms may impair antigen-specific responses, explaining infrequent objective response rates observed in the clinic using these therapies alone. In the context of these observations, it seems reasonable to combine local therapies with anti-PD therapy to neutralize the immunosuppressive mechanisms developed in the TME as long as the B7-H1/PD-1 pathway is one of the major immunosuppressive mechanisms. It is also possible that this combination may deviate the T cell response

against viral antigens instead of tumor antigens due to possible immunological dominancy by anti-PD therapy (Martínez-Usatorre et al., 2018; Chen et al., 2018). Local treatment, on the other hand, has shown to be an effective approach to increase T cell infiltration into tumors. Recently, some promising results were published that illustrated the synergistic effect of local virotherapy as a way to increase tumor T cell infiltration and synergize with anti-PD therapy (Ribas et al., 2017).

Combination with Targeted Therapies

The combination between anti-PD therapy and targeted therapies (antibody or small molecules) has been explored extensively in animal models and currently in the clinic (Hughes et al., 2016; Vanneman and Dranoff, 2012). While these therapies are not capable of achieving durable, complete responses as single agents, in most cases, they are useful at inhibiting tumor growth and changing or even resetting the TME. It is possible that rapid lysis of tumor cells by targeted therapies generates an acute inflammation environment that may boost tumor immunity. It could not be excluded that in this context, B7-H1 may be upregulated. If this is the case, the combination of target therapies and anti-PD therapy seems reasonable, since at least an additive effect is expected. Target therapies, however, should be chosen carefully to avoid intrinsic metabolic and activation pathways that are required for TILs's proliferation and survival. Also, pathways required for tumor-specific T cell memory formation should be considered.

Combination with Adoptive Cell Therapies

One of the reasons that adoptive cell therapy fails in some patients could be the suppression of transferred activated T cells when they enter the TME. Before adoptive transfer, T cells are activated *in vitro*, leading to PD-1 expression. Activated effector T cells upon tumor-antigen recognition in the TME can rapidly release IFN-γ; therefore, B7-H1 upregulation is expected, although this needs to be validated in the clinic. Therefore, as long as *in vitro* activated T cells can arrive in the TME, TILs and anti-PD therapy may represent an attractive direction for future cancer immunotherapy.

Combination with Other Immunotherapies

Currently, there are multiple immunotherapies under development that could be combined with anti-PD therapy. These potential combinations have been reviewed elsewhere (Melero et al., 2015; Smyth et al., 2016). To select the immunotherapy strategies most likely to succeed by combining with anti-PD therapies, some aspects need to be considered. First, as was explained in the principles section above, a favorable response-to-toxicity ratio of anti-PD therapy is attributed to the selective expression of B7-H1 in the TME, with minimal expression in normal tissues in the steady state. However, therapies that promote inflammation in normal tissues may trigger an anti-PD therapy effect out of the TME, losing this favorable response-to-toxicity ratio. An example is the combination with anti-CTLA-4 mAb. CTLA-4 mAbs, as we reviewed before, as a single therapy show more frequent irAEs than objective tumor responses. These irAEs in non-tumoral tissues can be amplified by anti-PD therapy (Larkin et al., 2015), which could explain why anti-CTLA-4 plus anti-PD therapy shows a synergistic toxic effect but an additive antitumor effect. Immunotherapies with a more selective treatment in the TME but a different mechanism of action (e.g., targeting myeloid cells or other immune escape mechanisms) may be better immunotherapy partners to be combined with anti-PD therapy. It is important to have a better understanding of how T cell memory formation is developed and collaborated to not only achieve strong effector T cell responses, but also to build strong T cell memory that ensures a long-lasting immune response.

An ideal scenario for combination therapy is synergism, which is commonly formulated as "1 + 1 > 2." Without such a synergistic effect with two or more drugs, sequential use of these drugs may achieve the same goals. With an understanding of the mechanisms and limitations of anti-PD therapy, it is ideal that the TIME classification type I, type III, and type IV tumors be treated differently, with a goal to convert them to type II tumors. In this case, these treatments are likely to synergize with anti-PD therapy, since anti-PD therapies are most likely to be effective in the presence of TILs and B7-H1 expression. Therefore, a future effort would be to carefully analyze the defects of the antitumor immune response for each patient with a set of biomarkers and design a rationale for an effective combinatorial treatment that will achieve a potential synergistic efficacy. For instance, types I and IV will require strategies that increase the trafficking of T cells into the TME, while type III will require strategies to break TIL tolerance or reversal of TIL dysfunction (Figure 3).

Concluding Remarks

Cancer immunotherapy is undergoing an important transition from traditional immune enhancement approaches that activate systemic immune responses based on general knowledge of immune-activation processes to a more effective and less toxic treatment of immune normalization that targets the tumor microenvironment based on tumor-induced immune escape mechanisms. Anti-PD therapy has set an example that it is possible to increase the antitumor effect while minimizing irAEs. These results set a new standard in the field of cancer immunotherapy, and we believe that future cancer immunotherapy should aim not only to boost antitumor immunity, but also to understand the specific defects in tumor immunity and then normalize them to selectively modify a specific type of antitumor response in the right location rather than exacerbate a systemic immune response with the risk of increased irAEs. Our analyses reveal multiple principles that are fundamental and essential for the success of anti-PD therapy. Therefore, a simplistic description of the B7-H1/PD-1 pathway as another "immune checkpoint" may deviate our efforts to target those pathways that have low therapeutic value. The principles we have learned from the immunology of the B7-H1/PD-1 pathway and the development of anti-PD therapy will lead us to design more effective normalization cancer immunotherapies, allowing for optimal combinatorial therapies and to extend the frontiers of more successful cancer treatment.

ACKNOWLEDGMENTS

We thank Beth Cadugan for editing the manuscript. This work is partially supported by US NIH grants P50 CA196530 and P30 CA16359 and a Yale University endowed chair from the United Technologies Corporation. M.F.S. is supported by a Miguel Servet contract from Instituto de Salud Carlos III, Fondo de Investigación Sanitaria (Spain).

DECLARATION OF INTERESTS

L.C. is a consultant/board member of NextCure, Pfizer, Tayu, Vcanbio, and GenomiCare and currently has sponsored research funds from NextCure.

REFERENCES

Agarwala, S.S., Glaspy, J., O'Day, S.J., Mitchell, M., Gutheil, J., Whitman, E., Gonzalez, R., Hersh, E., Feun, L., Belt, R., et al. (2002). Results from a randomized phase III study comparing combined treatment with histamine dihydrochloride plus interleukin-2 versus interleukin-2 alone in patients with metastatic melanoma. J. Clin. Oncol. *20*, 125–133.

Ahmed, N., Brawley, V.S., Hegde, M., Robertson, C., Ghazi, A., Gerken, C., Liu, E., Dakhova, O., Ashoori, A., Corder, A., et al. (2015). Human Epidermal Growth Factor Receptor 2 (HER2) -Specific Chimeric Antigen Receptor-Modified T Cells for the Immunotherapy of HER2-Positive Sarcoma. J. Clin. Oncol. *33*, 1688–1696.

Arce Vargas, F., Furness, A.J.S., Litchfield, K., Joshi, K., Rosenthal, R., Ghorani, E., Solomon, I., Lesko, M.H., Ruef, N., Roddie, C., et al. (2018). Fc Effector Function Contributes to the Activity of Human Anti-CTLA-4 Antibodies. Cancer Cell *33*, 649–663.

Ascierto, P.A., Del Vecchio, M., Robert, C., Mackiewicz, A., Chiarion-Sileni, V., Arance, A., Lebbé, C., Bastholt, L., Hamit, O., Rutkowski, P., et al. (2017). Ipilimumab 10 mg/kg versus ipilimumab 3 mg/kg in patients with unresectable or metastaticmelanoma: a randomised, double-blind, multicentre, phase 3 trial. Lancet Oncol. *18*, 611–622.

Atkins, M.B., Lotze, M.T., Dutcher, J.P., Fisher, R.I., Weiss, G., Margolin, K., Abrams, J., Sznol, M., Parkinson, D., Hawkins, M., et al. (1999). High-dose recombinant interleukin 2 therapy for patients with metastatic melanoma: analysis of 270 patients treated between 1985 and 1993. J. Clin. Oncol. *17*, 2105–2116.

Aznar, M.A., Tinari, N., Rullán, A.J., Sánchez-Paulete, A.R., Rodriguez-Ruiz, M.E., and Melero, I. (2017). Intratumoral Delivery of Immunotherapy-Act Locally, Think Globally. J. Immunol. *198*, 31–39.

Azuma, T., Yao, S., Zhu, G., Flies, A.S., Flies, S.J., and Chen, L. (2008). B7-H1 is a ubiquitous antiapoptotic receptor on cancer cells. Blood *111*, 3635–3643.

Bach, E.A., Aguet, M., and Schreiber, R.D. (1997). The IFN γ receptor: a paradigm for cytokine receptor signaling. Annu. Rev. Immunol. *15*, 563–591.

Barber, D.L., Wherry, E.J., Masopust, D., Zhu, B., Allison, J.P., Sharpe, A.H., Freeman, G.J., and Ahmed, R. (2006). Restoring function in exhausted CD8 T cells during chronic viral infection. Nature *439*, 682–687.

Benson, D.M., Jr., Bakan, C.E., Mishra, A., Hofmeister, C.C., Efebera, Y., Becknell, B., Baiocchi, R.A., Zhang, J., Yu, J., Smith, M.K., et al. (2010). The PD-1/PD-L1 axis modulates the natural killer cell versus multiple myeloma effect: a therapeutic target for CT-011, a novel monoclonal anti-PD-1 antibody. Blood *116*, 2286–2294.

Bilusic, M., Madan, R.A., and Gulley, J.L. (2017). Immunotherapy of Prostate Cancer: Facts and Hopes. Clin. Cancer Res. *23*, 6764–6770.

Brahmer, J.R., Drake, C.G., Wollner, I., Powderly, J.D., Picus, J., Sharfman, W.H., Stankevich, E., Pons, A., Salay, T.M., McMiller, T.L., et al. (2010). Phase I study of single-agent anti-programmed death-1 (MDX-1106) in refractory solid tumors: safety, clinical activity, pharmacodynamics, and immunologic correlates. J. Clin. Oncol. *28*, 3167–3175.

Brahmer, J.R., Tykodi, S.S., Chow, L.Q.M., Hwu, W.-J., Topalian, S.L., Hwu, P., Drake, C.G., Camacho, L.H., Kauh, J., Odunsi, K., et al. (2012). Safety and activity of anti-PD-L1 antibody in patients with advanced cancer. N. Engl. J. Med. *366*, 2455–2465.

Brudno, J.N., and Kochenderfer, J.N. (2016). Toxicities of chimeric antigen receptor T cells: recognition and management. Blood *127*, 3321–3330.

Bulliard, Y., Jolicoeur, R., Windman, M., Rue, S.M., Ettenberg, S., Knee, D.A., Wilson, N.S., Dranoff, G., and Brogdon, J.L. (2013). Activating Fc γ receptors contribute to the antitumor activities of immunoregulatory receptor-targeting antibodies. J. Exp. Med. *210*, 1685–1693.

Burel, J.G., Apte, S.H., and Doolan, D.L. (2016). Systems Approaches towards Molecular Profiling of Human Immunity. Trends Immunol. *37*, 53–67.

Callahan, M.K., Postow, M.A., and Wolchok, J.D. (2016). Targeting T Cell Co-receptors for Cancer Therapy. Immunity *44*, 1069–1078.

Charych, D.H., Hoch, U., Langowski, J.L., Lee, S.R., Addepalli, M.K., Kirk, P.B., Sheng, D., Liu, X., Sims, P.W., Vanderveen, L.A., et al. (2016). NKTR-214, an Engineered Cytokine with Biased IL2 Receptor Binding (Increased Tumor Exposure, and Marked Efficacy in Mouse Tumor Models).

Chen, L., and Flies, D.B. (2013). Molecular mechanisms of T cell co-stimulation and co-inhibition. Nat. Rev. Immunol. *13*, 227–242.

Chen, L., and Han, X. (2015). Anti-PD-1/PD-L1 therapy of human cancer: past, present, and future. J. Clin. Invest. *125*, 3384–3391.

Chen, L., Azuma, T., Yu, W., Zheng, X., Luo, L., and Chen, L. (2018). B7-H1 maintains the polyclonal T cell response by protecting dendritic cells from cytotoxic T lymphocyte destruction. Proc. Natl. Acad. Sci. USA *115*, 3126–3131.

Chin, Y.T., Wei, P.L., Ho, Y., Nana, A.W., Changou, C.A., Chen, Y.R., Yang, Y.S., Hsieh, M.T., Hercbergs, A., Davis, P.J., et al. (2018). Thyroxine inhibits resveratrol-caused apoptosis by PD-L1 in ovarian cancer cells. Endocr. Relat. Cancer *25*, 533–545.

Corrales, L., McWhirter, S.M., Dubensky, T.W., Jr., and Gajewski, T.F. (2016). The host STING pathway at the interface of cancer and immunity. J. Clin. Invest. *126*, 2404–2411.

Das, R., Verma, R., Sznol, M., Boddupalli, C.S., Gettinger, S.N., Kluger, H., Callahan, M., Wolchok, J.D., Halaban, R., Dhodapkar, M.V., and Dhodapkar, K.M. (2015). Combination therapy with anti-CTLA-4 and anti-PD-1 leads to distinct immunologic changes in vivo. J. Immunol. *194*, 950–959.

Desjardins, A., Gromeier, M., Herndon, J.E., 2nd, Beaubier, N., Bolognesi, D.P., Friedman, A.H., Friedman, H.S., McSherry, F., Muscat, A.M., Nair, S., et al. (2018). Recurrent Glioblastoma Treated with Recombinant Poliovirus. N. Engl. J. Med. *379*, 150–161.

Dong, H., Strome, S.E., Salomao, D.R., Tamura, H., Hirano, F., Flies, D.B., Roche, P.C., Lu, J., Zhu, G., Tamada, K., et al. (2002). Tumor-associated B7-H1 promotes T-cell apoptosis: a potential mechanism of immune evasion. Nat. Med. *8*, 793–800.

Du, X., Tang, F., Liu, M., Su, J., Zhang, Y., Wu, W., Devenport, M., Lazarski, C.A., Zhang, P., Wang, X., et al. (2018). A reappraisal of CTLA-4 checkpoint blockade in cancer immunotherapy. Cell Res. *28*, 416–432.

Gainor, J.F., Shaw, A.T., Sequist, L.V., Fu, X., Azzoli, C.G., Piotrowska, Z., Huynh, T.G., Zhao, L., Fulton, L., Schultz, K.R., et al. (2016). EGFR Mutations and ALK Rearrangements Are Associated with Low Response Rates to PD-1 Pathway Blockade in Non-Small Cell Lung Cancer: A Retrospective Analysis. Clin. Cancer Res. *22*, 4585–4593.

Gandhi, L., Rodríguez-Abreu, D., Gadgeel, S., Esteban, E., Felip, E., De Angelis, F., Domine, M., Clingan, P., Hochmair, M.J., Powell, S.F., et al.; KEYNOTE-189 Investigators (2018). Pembrolizumab plus Chemotherapy in Metastatic Non-Small-Cell Lung Cancer. N. Engl. J. Med. *378*, 2078–2092.

Gardiner, D., Lalezari, J., Lawitz, E., DiMicco, M., Ghalib, R., Reddy, K.R., Chang, K.-M., Sulkowski, M., Marro, S.O., Anderson, J., et al. (2013). A randomized, double-blind, placebo-controlled assessment of BMS-936558, a fully human monoclonal antibody to programmed death-1 (PD-1), in patients with chronic hepatitis C virus infection. PLoS ONE *8*, e63818.

Gay, C.L., Bosch, R.J., Ritz, J., Hataye, J.M., Aga, E., Tressler, R.L., Mason, S.W., Hwang, C.K., Grasela, D.M., Ray, N., et al.; AIDS Clinical Trials 5326 Study Team (2017). Clinical Trial of the Anti-PD-L1 Antibody BMS-936559 in HIV-1 Infected Participants on Suppressive Antiretroviral Therapy. J. Infect. Dis. *215*, 1725–1733.

Gros, A., Robbins, P.F., Yao, X., Li, Y.F., Turcotte, S., Tran, E., Wunderlich, J.R., Mixon, A., Farid, S., Dudley, M.E., et al. (2014). PD-1 identifies the patient-specific CD8^{+} tumor-reactive repertoire infiltrating human tumors. J. Clin. Invest. *124*, 2246–2259.

Grupp, S.A., Kalos, M., Barrett, D., Aplenc, R., Porter, D.L., Rheingold, S.R., Teachey, D.T., Chew, A., Hauck, B., Wright, J.F., et al. (2013). Chimeric antigen

receptor-modified T cells for acute lymphoid leukemia. N. Engl. J. Med. *368*, 1509–1518.

Hamid, O., Robert, C., Daud, A., Hodi, F.S., Hwu, W.-J., Kefford, R., Wolchok, J.D., Hersey, P., Joseph, R.W., Weber, J.S., et al. (2013). Safety and tumor responses with lambrolizumab (anti-PD-1) in melanoma. N. Engl. J. Med. *369*, 134–144.

Herbst, R.S., Soria, J.-C., Kowanetz, M., Fine, G.D., Hamid, O., Gordon, M.S., Sosman, J.A., McDermott, D.F., Powderly, J.D., Gettinger, S.N., et al. (2014). Predictive correlates of response to the anti-PD-L1 antibody MPDL3280A in cancer patients. Nature *515*, 563–567.

Hodi, F.S., Chesney, J., Pavlick, A.C., Robert, C., Grossmann, K.F., McDermott, D.F., Linette, G.P., Meyer, N., Giguere, J.K., Argarwala, S.S., et al. (2016). Combined nivolumab and ipilimumab versus ipilimumab alone in patients with advancedmelanoma: 2-year overall survival outcomes in a multicentre, randomised, controlled, phase 2trial. Lancet Oncol. *17*, 1558–1568.

Hodi, F.S., O'Day, S.J., McDermott, D.F., Weber, R.W., Sosman, J.A., Haanen, J.B., Gonzalez, R., Robert, C., Schadendorf, D., Hassel, J.C., et al. (2010). Improved survival with ipilimumab in patients with metastatic melanoma. N. Engl. J. Med. *363*, 711–723.

Huang, B.Y., Zhan, Y.P., Zong, W.J., Yu, C.J., Li, J.F., Qu, Y.M., and Han, S. (2015). The PD-1/B7-H1 pathway modulates the natural killer cells versus mouse glioma stem cells. PLoS ONE *10*, e0134715.

Hughes, P.E., Caenepeel, S., and Wu, L.C. (2016). Targeted Therapy and Checkpoint Immunotherapy Combinations for the Treatment of Cancer. Trends Immunol. *37*, 462–476.

Jenkins, R.W., Aref, A.R., Lizotte, P.H., Ivanova, E., Stinson, S., Zhou, C.W., Bowden, M., Deng, J., Liu, H., Miao, D., et al. (2018). *Ex Vivo* Profiling of PD-1 Blockade Using Organotypic Tumor Spheroids. Cancer Discov. *8*, 196–215.

Kantoff, P.W., Higano, C.S., Shore, N.D., Berger, E.R., Small, E.J., Penson, D.F., Redfern, C.H., Ferrari, A.C., Dreicer, R., Sims, R.B., et al.; IMPACT Study Investigators (2010). Sipuleucel-T immunotherapy for castration-resistant prostate cancer. N. Engl. J. Med. *363*, 411–422.

Klein, C., Waldhauer, I., Nicolini, V.G., Freimoser-Grundschober, A., Nayak, T., Vugts, D.J., Dunn, C., Bolijn, M., Benz, J., Stihle, M., et al. (2017). Cergutuzumab amunaleukin (CEA-IL2v), a CEA-targeted IL-2 variant-based immunocytokine for combination cancer immunotherapy: Overcoming limitations of aldesleukin and conventional IL-2-based immunocytokines. OncoImmunology *6*, e1277306.

Lang, F.F., Conrad, C., Gomez-Manzano, C., Yung, W.K.A., Sawaya, R., Weinberg, J.S., Prabhu, S.S., Rao, G., Fuller, G.N., Aldape, K.D., et al. (2018). Phase I Study of DNX-2401 (Delta-24-RGD) Oncolytic Adenovirus: Replication and Immunotherapeutic Effects in Recurrent Malignant Glioma. J. Clin. Oncol. *36*, 1419–1427.

Larkin, J., Chiarion-Sileni, V., Gonzalez, R., Grob, J.J., Cowey, C.L., Lao, C.D., Schadendorf, D., Dummer, R., Smylie, M., Rutkowski, P., et al. (2015). Combined Nivolumab and Ipilimumab or Monotherapy in Untreated Melanoma. N. Engl. J. Med. *373*, 23–34.

Larkin, J., Minor, D., D'Angelo, S., Neyns, B., Smylie, M., Miller, W.H., Jr., Gutzmer, R., Linette, G., Chmielowski, B., Lao, C.D., et al. (2018). Overall Survival in Patients With Advanced Melanoma Who Received Nivolumab VersusInvestigator's Choice Chemotherapy in CheckMate 037: A Randomized, Controlled, Open-LabelPhase III Trial. J. Clin. Oncol. *36*, 383–390.

Lawler, S.E., Speranza, M.-C., Cho, C.-F., and Chiocca, E.A. (2017). Oncolytic Viruses in Cancer Treatment: A Review. JAMA Oncol. *3*, 841–849.

Leach, D.R., Krummel, M.F., and Allison, J.P. (1996). Enhancement of antitumor immunity by CTLA-4 blockade. Science *271*, 1734–1736.

Lee, S.-J., Jang, B.-C., Lee, S.-W., Yang, Y.-I., Suh, S.-I., Park, Y.-M., Oh, S., Shin, J.-G., Yao, S., Chen, L., and Choi, I.H. (2006). Interferon regulatory factor-1 is prerequisite to the constitutive expression and IFN-gamma-induced upregulation of B7-H1 (CD274). FEBS Lett. *580*, 755–762.

Li, K., Qu, S., Chen, X., Wu, Q., and Shi, M. (2017). Promising Targets for Cancer Immunotherapy: TLRs, RLRs, and STING-Mediated Innate Immune Pathways. Int. J. Mol. Sci. *18*.

Lynch, T.J., Bondarenko, I., Luft, A., Serwatowski, P., Barlesi, F., Chacko, R., Sebastian, M., Neal, J., Lu, H., Cuillerot, J.-M., and Reck, M. (2012). Ipilimumab in combination with paclitaxel and carboplatin as first-line treatment in stage IIIB/IV non-small-cell lung cancer: results from a randomized, double-blind, multicenter phase II study. J. Clin. Oncol. *30*, 2046–2054.

Marabelle, A., Tselikas, L., de Baere, T., and Houot, R. (2017). Intratumoral immunotherapy: using the tumor as the remedy. Ann. Oncol. *28* (suppl_12), xii33–xii43.

Martínez-Usatorre, A., Donda, A., Zehn, D., and Romero, P. (2018). PD-1 Blockade Unleashes Effector Potential of Both High- and Low-Affinity Tumor-Infiltrating T Cells. J Immunol. *201*, 792–803.

Melero, I., Gaudernack, G., Gerritsen, W., Huber, C., Parmiani, G., Scholl, S., Thatcher, N., Wagstaff, J., Zielinski, C., Faulkner, I., et al. (2014). Therapeutic vaccines for cancer: an overview of clinical trials. Nat. Rev. Clin. Oncol *11*, 509–524.

Melero, I., Berman, D.M., Aznar, M.A., Korman, A.J., Pérez Gracia, J.L., and Haanen, J. (2015). Evolving synergistic combinations of targeted immunotherapies to combat cancer. Nat. Rev. Cancer *15*, 457–472.

Morgan, D.A., Ruscetti, F.W., and Gallo, R. (1976). Selective in vitro growth of T lymphocytes from normal human bone marrows. Science *193*, 1007–1008.

Morgan, R.A., Yang, J.C., Kitano, M., Dudley, M.E., Laurencot, C.M., and Rosenberg, S.A. (2010). Case report of a serious adverse event following the administration of T cells transduced with a chimeric antigen receptor recognizing ERBB2. Mol. Ther. *18*, 843–851.

Naidoo, J., Page, D.B., Li, B.T., Connell, L.C., Schindler, K., Lacouture, M.E., Postow, M.A., and Wolchok, J.D. (2015). Toxicities of the anti-PD-1 and anti-PD-L1 immune checkpoint antibodies. Ann. Oncol. *26*, 2375–2391.

Namuduri, M., and Brentjens, R.J. (2016). Medical management of side effects related to CAR T cell therapy in hematologic malignancies. Expert Rev. Hematol. *9*, 511–513.

Ott, P.A., Hu, Z., Keskin, D.B., Shukla, S.A., Sun, J., Bozym, D.J., Zhang, W., Luoma, A., Giobbie-Hurder, A., Peter, L., et al. (2017). An immunogenic personal neoantigen vaccine for patients with melanoma. Nature *547*, 217–221.

Overwijk, W.W., and Restifo, N.P. (2000). Autoimmunity and the immunotherapy of cancer: targeting the "self" to destroy the "other". Crit. Rev. Immunol. *20*, 433–450.

Parkinson, D.R., Abrams, J.S., Wiernik, P.H., Rayner, A.A., Margolin, K.A., Van Echo, D.A., Sznol, M., Dutcher, J.P., Aronson, F.R., Doroshow, J.H., et al. (1990). Interleukin-2 therapy in patients with metastatic malignant melanoma: a phase II study. J. Clin. Oncol. *8*, 1650–1656.

Petroff, M.G., Chen, L., Phillips, T.A., and Hunt, J.S. (2002). B7 family molecules: novel immunomodulators at the maternal-fetal interface. Placenta *23* (*Suppl A*), S95–S101.

Phan, G.Q., Wang, E., and Marincola, F.M. (2001). T-cell-directed cancer vaccines: mechanisms of immune escape and immune tolerance. Expert Opin. Biol. Ther. *1*, 511–523.

Porter, D.L., Levine, B.L., Kalos, M., Bagg, A., and June, C.H. (2011). Chimeric antigen receptor-modified T cells in chronic lymphoid leukemia. N. Engl. J. Med. *365*, 725–733.

Ribas, A., and Wolchok, J.D. (2018). Cancer immunotherapy using checkpoint blockade. Science *359*, 1350–1355.

Ribas, A., Puzanov, I., Dummer, R., Schadendorf, D., Hamid, O., Robert, C., Hodi, F.S., Schachter, J., Pavlick, A.C., Lewis, K.D., et al. (2015). Pembrolizumab versus investigator-choice chemotherapy for ipilimumab-refractory melanoma (KEYNOTE-002): a randomised, controlled, phase 2 trial. Lancet Oncol. *16*, 908–918.

Ribas, A., Dummer, R., Puzanov, I., VanderWalde, A., Andtbacka, R.H.I., Michielin, O., Olszanski, A.J., Malvehy, J., Cebon, J., Fernandez, E., et al. (2017).

Oncolytic Virotherapy Promotes Intratumoral T Cell Infiltration and Improves Anti-PD-1 Immunotherapy. Cell *170*, 1109–1119.

Robert, C., Ribas, A., Wolchok, J.D., Hodi, F.S., Hamid, O., Kefford, R., Weber, J.S., Joshua, A.M., Hwu, W.-J., Gangadhar, T.C., et al. (2014). Anti-programmed-death-receptor-1 treatment with pembrolizumab in ipilimumab-refractory advanced melanoma: a randomised dose-comparison cohort of a phase 1 trial. Lancet *384*, 1109–1117.

Robert, C., Schachter, J., Long, G.V., Arance, A., Grob, J.J., Mortier, L., Daud, A., Carlino, M.S., McNeil, C., Lotem, M., et al.; KEYNOTE-006 investigators (2015a). Pembrolizumab versus Ipilimumab in Advanced Melanoma. N. Engl. J. Med. *372*, 2521–2532.

Robert, C., Long, G.V., Brady, B., Dutriaux, C., Maio, M., Mortier, L., Hassel, J.C., Rutkowski, P., McNeil, C., Kalinka-Warzocha, E., et al. (2015b). Nivolumab in previously untreated melanoma without BRAF mutation. N. Engl. J. Med. *372*, 320–330.

Rosenberg, S.A. (2014). IL-2: the first effective immunotherapy for human cancer. J. Immunol. *192*, 5451–5458.

Rosenberg, S.A., Mulé, J.J., Spiess, P.J., Reichert, C.M., and Schwarz, S.L. (1985). Regression of established pulmonary metastases and subcutaneous tumor mediated by the systemic administration of high-dose recombinant interleukin 2. J. Exp. Med. *161*, 1169–1188.

Rosenberg, S.A., Lotze, M.T., Muul, L.M., Chang, A.E., Avis, F.P., Leitman, S., Linehan, W.M., Robertson, C.N., Lee, R.E., Rubin, J.T., et al. (1987). A progress report on the treatment of 157 patients with advanced cancer using lymphokine-activated killer cells and interleukin-2 or high-dose interleukin-2 alone. N. Engl. J. Med. *316*, 889–897.

Rosenberg, S.A., Yang, J.C., Topalian, S.L., Schwartzentruber, D.J., Weber, J.S., Parkinson, D.R., Seipp, C.A., Einhorn, J.H., and White, D.E. (1994). Treatment of 283 consecutive patients with metastatic melanoma or renal cell cancer using high-dose bolus interleukin 2. JAMA *271*, 907–913.

Rosenberg, S.A., Yang, J.C., and Restifo, N.P. (2004). Cancer immunotherapy: moving beyond current vaccines. Nat. Med. *10*, 909–915.

Rosenberg, S.A., Sherry, R.M., Morton, K.E., Scharfman, W.J., Yang, J.C., Topalian, S.L., Royal, R.E., Kammula, U., Restifo, N.P., Hughes, M.S., et al. (2005). Tumor progression can occur despite the induction of very high levels of self/tumor antigen-specific CD8+ T cells in patients with melanoma. J. Immunol. *175*, 6169–6176.

Sahin, U., Derhovanessian, E., Miller, M., Kloke, B.-P., Simon, P., Löwer, M., Bukur, V., Tadmor, A.D., Luxemburger, U., Schrörs, B., et al. (2017). Personalized RNA mutanome vaccines mobilize poly-specific therapeutic immunity against cancer. Nature *547*, 222–226.

Sanmamed, M.F., and Chen, L. (2014). Inducible expression of B7-H1 (PD-L1) and its selective role in tumor site immune modulation. Cancer J. *20*, 256–261.

Sanmamed, M.F., Chester, C., Melero, I., and Kohrt, H. (2016). Defining the optimal murine models to investigate immune checkpoint blockers and their combination with other immunotherapies. Ann. Oncol. *27*, 1190–1198.

Schalper, K.A., Carvajal-Hausdorf, D., McLaughlin, J., Altan, M., Velcheti, V., Gaule, P., Sanmamed, M.F., Chen, L., Herbst, R.S., and Rimm, D.L. (2017). Differential Expression and Significance of PD-L1, IDO-1, and B7-H4 in Human Lung Cancer. Clin. Cancer Res. *23*, 370–378.

Schwartzentruber, D.J., Lawson, D.H., Richards, J.M., Conry, R.M., Miller, D.M., Treisman, J., Gailani, F., Riley, L., Conlon, K., Pockaj, B., et al. (2011). gp100 peptide vaccine and interleukin-2 in patients with advanced melanoma. N. Engl. J. Med. *364*, 2119–2127.

Scott, A.M., Wolchok, J.D., and Old, L.J. (2012). Antibody therapy of cancer. Nat. Rev. Cancer *12*, 278–287.

Selby, M.J., Engelhardt, J.J., Quigley, M., Henning, K.A., Chen, T., Srinivasan, M., and Korman, A.J. (2013). Anti-CTLA-4 antibodies of IgG2a isotype enhance antitumor activity through reduction of intratumoral regulatory T cells. Cancer Immunol. Res. *1*, 32–42.

Simpson, T.R., Li, F., Montalvo-Ortiz, W., Sepulveda, M.A., Bergerhoff, K., Arce, F., Roddie, C., Henry, J.Y., Yagita, H., Wolchok, J.D., et al. (2013). Fc-dependent depletion of tumor-infiltrating regulatory T cells co-defines the efficacy of anti-CTLA-4 therapy against melanoma. J. Exp. Med. *210*, 1695–1710.

Smyth, M.J., Ngiow, S.F., Ribas, A., and Teng, M.W.L. (2016). Combination cancer immunotherapies tailored to the tumour microenvironment. Nat. Rev. Clin. Oncol. *13*, 143–158.

Sznol, M., and Chen, L. (2013). Antagonist antibodies to PD-1 and B7-H1 (PD-L1) in the treatment of advanced human cancer–response. Clin. Cancer Res. *19*, 5542.

Takahashi, T., Tagami, T., Yamazaki, S., Uede, T., Shimizu, J., Sakaguchi, N., Mak, T.W., and Sakaguchi, S. (2000). Immunologic self-tolerance maintained by CD25(+)CD4(+) regulatory T cells constitutively expressing cytotoxic T lymphocyte-associated antigen 4. J. Exp. Med. *192*, 303–310.

Tang, J., Shalabi, A., and Hubbard-Lucey, V.M. (2018). Comprehensive analysis of the clinical immuno-oncology landscape. Ann. Oncol. *29*, 84–91.

Taniguchi, T., Matsui, H., Fujita, T., Takaoka, C., Kashima, N., Yoshimoto, R., and Hamuro, J. (1983). Structure and expression of a cloned cDNA for human interleukin-2. Nature *302*, 305–310.

Tarhini, A.A., Kirkwood, J.M., Gooding, W.E., Cai, C., and Agarwala, S.S. (2007). Durable complete responses with high-dose bolus interleukin-2 in patients with metastatic melanoma who have experienced progression after biochemotherapy. J. Clin. Oncol. *25*, 3802–3807.

Taube, J.M., Anders, R.A., Young, G.D., Xu, H., Sharma, R., McMiller, T.L., Chen, S., Klein, A.P., Pardoll, D.M., Topalian, S.L., and Chen, L. (2012). Colocalization of inflammatory response with B7-h1 expression in human melanocytic lesions supports an adaptive resistance mechanism of immune escape. Sci. Transl. Med. *4*, 127ra37.

Topalian, S.L., Hodi, F.S., Brahmer, J.R., Gettinger, S.N., Smith, D.C., McDermott, D.F., Powderly, J.D., Carvajal, R.D., Sosman, J.A., Atkins, M.B., et al. (2012). Safety, activity, and immune correlates of anti-PD-1 antibody in cancer. N. Engl. J. Med. *366*, 2443–2454.

Topalian, S.L., Sznol, M., McDermott, D.F., Kluger, H.M., Carvajal, R.D., Sharfman, W.H., Brahmer, J.R., Lawrence, D.P., Atkins, M.B., Powderly, J.D., et al. (2014). Survival, durable tumor remission, and long-term safety in patients with advanced melanoma receiving nivolumab. J. Clin. Oncol. *32*, 1020–1030.

Vanneman, M., and Dranoff, G. (2012). Combining immunotherapy and targeted therapies in cancer treatment. Nat. Rev. Cancer *12*, 237–251.

Vari, F., Arpon, D., Keane, C., Hertzberg, M.S., Talaulikar, D., Jain, S., Cui, Q., Han, E., Tobin, J., Bird, R., et al. (2018). Immune evasion via PD-1/PD-L1 on NK cells and monocyte/macrophages is more prominent in Hodgkin lymphoma than DLBCL. Blood *131*, 1809–1819.

Vinay, D.S., Ryan, E.P., Pawelec, G., Talib, W.H., Stagg, J., Elkord, E., Lichtor, T., Decker, W.K., Whelan, R.L., Kumara, H.M.C.S., et al. (2015). Immune evasion in cancer: Mechanistic basis and therapeutic strategies. Semin. Cancer Biol. *35* (*Suppl*), S185–S198.

Walunas, T.L., Lenschow, D.J., Bakker, C.Y., Linsley, P.S., Freeman, G.J., Green, J.M., Thompson, C.B., and Bluestone, J.A. (1994). CTLA-4 can function as a negative regulator of T cell activation. Immunity *1*, 405–413.

Waterhouse, P., Penninger, J.M., Timms, E., Wakeham, A., Shahinian, A., Lee, K.P., Thompson, C.B., Griesser, H., and Mak, T.W. (1995). Lymphoproliferative disorders with early lethality in mice deficient in Ctla-4. Science *270*, 985–988.

Weber, J., Thompson, J.A., Hamid, O., Minor, D., Amin, A., Ron, I., Ridolfi, R., Assi, H., Maraveyas, A., Berman, D., et al. (2009). A randomized, double-blind, placebo-controlled, phase II study comparing the tolerability and efficacy of ipilimumab administered with or without prophylactic budesonide in patients with unresectable stage III or IV melanoma. Clin. Cancer Res. *15*, 5591–5598.

Weber, J., Mandala, M., Del Vecchio, M., Gogas, H.J., Arance, A.M., Cowey, C.L., Dalle, S., Schenker, M., Chiarion-Sileni, V., Marquez-Rodas, I., et al. (2017). Adjuvant Nivolumab versus Ipilimumab in Resected Stage III or IV Melanoma. N. Engl. J. Med. *377*, 1824–1835.

Weiner, G.J. (2015). Building better monoclonal antibody-based therapeutics. Nat. Rev. Cancer *15*, 361–370.

Weiner, L.M., Surana, R., and Wang, S. (2010). Monoclonal antibodies: versatile platforms for cancer immunotherapy. Nat. Rev. Immunol. *10*, 317–327.

Yao, S., Wang, S., Zhu, Y., Luo, L., Zhu, G., Flies, S., Xu, H., Ruff, W., Broadwater, M., Choi, I.-H., et al. (2009). PD-1 on dendritic cells impedes innate immunity against bacterial infection. Blood *113*, 5811–5818.

Zhang, Y., and Chen, L. (2016). Classification of Advanced Human Cancers Based on Tumor Immunity in the MicroEnvironment (TIME) for Cancer Immunotherapy. JAMA Oncol. *2*, 1403–1404.

Zitvogel, L., Pitt, J.M., Daillère, R., Smyth, M.J., and Kroemer, G. (2016). Mouse models in oncoimmunology. Nat. Rev. Cancer *16*, 759–773.

Zou, W. (2005). Immunosuppressive networks in the tumour environment and their therapeutic relevance. Nat. Rev. Cancer *5*, 263–274.

Zou, W., and Chen, L. (2008). Inhibitory B7-family molecules in the tumour microenvironment. Nat. Rev. Immunol. *8*, 467–477.

Zou, W., Wolchok, J.D., and Chen, L. (2016). PD-L1 (B7-H1) and PD-1 pathway blockade for cancer therapy: Mechanisms, response biomarkers, and combinations. Sci. Transl. Med. *8*, 328rv4.

Cell

Biological Functions of Autophagy Genes: A Disease Perspective

Beth Levine[1,2,3,*] and Guido Kroemer[4,5,6,7,8,9,10,*]
[1]Center for Autophagy Research, Department of Internal Medicine, University of Texas Southwestern Medical Center, Dallas, TX 75390, USA
[2]Howard Hughes Medical Institute, University of Texas Southwestern Medical Center, Dallas, TX 75390, USA
[3]Department of Microbiology, University of Texas Southwestern Medical Center, Dallas, TX 75390, USA
[4]Equipe 11 labellisée par la Ligue contre le Cancer, Centre de Recherche des Cordeliers, 75006 Paris, France
[5]Cell Biology and Metabolomics platforms, Gustave Roussy Cancer Campus, 94805 Villejuif, France
[6]INSERM, U1138, 75006 Paris, France
[7]Université Paris Descartes, Sorbonne Paris Cité, 75006 Paris, France
[8]Université Pierre et Marie Curie, Sorbonne Université, 75006 Paris, France
[9]Pôle de Biologie, Hôpital Européen Georges Pompidou, AP-HP, 75015 Paris, France
[10]Karolinska Institute, Department of Women's and Children's Health, Karolinska University Hospital, 17176 Stockholm, Sweden
*Correspondence: beth.levine@utsouthwestern.edu (B.L.), kroemer@orange.fr (G.K.)
https://doi.org/10.1016/j.cell.2018.09.048

The lysosomal degradation pathway of autophagy plays a fundamental role in cellular, tissue, and organismal homeostasis and is mediated by evolutionarily conserved autophagy-related (*ATG*) genes. Definitive etiological links exist between mutations in genes that control autophagy and human disease, especially neurodegenerative, inflammatory disorders and cancer. Autophagy selectively targets dysfunctional organelles, intracellular microbes, and pathogenic proteins, and deficiencies in these processes may lead to disease. Moreover, *ATG* genes have diverse physiologically important roles in other membrane-trafficking and signaling pathways. This Review discusses the biological functions of autophagy genes from the perspective of understanding—and potentially reversing—the pathophysiology of human disease and aging.

Introduction

A decade has elapsed since our 2008 Review in *Cell*, "Autophagy in the Pathogenesis of Disease" (Levine and Kroemer, 2008). During this period, more than 33,000 new articles related to autophagy were published, a Nobel prize was awarded for the discovery of the molecular mechanisms of autophagy (Levine and Klionsky, 2017; Mizushima, 2018), and considerable interest has emerged in autophagy modulation as a potential target in clinical medicine (Galluzzi et al., 2017a).

The fundamental concepts discussed in our 2008 Review (Levine and Kroemer, 2008) remain unchanged. The lysosomal degradation pathway of macroautophagy (herein referred to as autophagy) plays a crucial role in cellular physiology, including adaptation to metabolic stress, removal of dangerous cargo (e.g., protein aggregates, damaged organelles, intracellular pathogens), renovation during differentiation and development, and prevention of genomic damage. Generally, these and other functions protect against numerous diseases, including infections, cancer, neurodegeneration, cardiovascular disorders, and aging (Mizushima and Komatsu, 2011). Under certain circumstances, autophagy may be detrimental either via its pro-survival effects (such as in cancer progression [Amaravadi et al., 2016]) or via possible cell-death-promoting effects (Mariño et al., 2014a).

Over the past 10 years, significant progress has been made in understanding the molecular mechanisms of autophagy, the regulation of autophagy, and the effects of autophagy on physiology and pathophysiology (Dikic and Elazar, 2018; Galluzzi et al., 2014; Mizushima, 2018). New major conceptual advances underscore the plurality of functions of the autophagic core machinery in various membrane-trafficking and signaling events (Cadwell and Debnath, 2018) and delineate the exquisite specificity with which autophagy targets selected cargo for degradation (Gatica et al., 2018). These advances, together with discoveries in human genetics linking autophagy-related (*ATG*) gene mutations to specific diseases (Jiang and Mizushima, 2014; van Beek et al., 2018), provide a multidimensional perspective of mechanisms by which *ATG* gene-dependent pathways protect against mammalian disease.

Herein, we review selected highlights of the past decade of research on the biological functions of autophagy genes, primarily from a perspective of understanding and treating human disease.

Autophagy and Other Autophagy Gene-Dependent Pathways

The original scientific definition of autophagy (Greek, "self-eating") is the delivery of cytoplasmic cargo to the lysosome for degradation. There are at least three distinct forms of autophagy—chaperone-mediated autophagy, microautophagy, and macroautophagy—that differ in terms of mode of cargo delivery to the lysosome. Macroautophagy is the major catabolic mechanism used by eukaryotic cells to maintain nutrient homeostasis and organellar quality control. It is mediated by a set of

evolutionarily conserved genes, the *ATG* genes (Klionsky et al., 2003), originally discovered in yeast genetic screens (Mizushima, 2018). With a few exceptions, all *ATG* genes are required for the efficient formation of sealed autophagosomes that proceed to fuse with lysosomes.

In higher eukaryotes, many *ATG* genes functionally diversified to facilitate delivery of extracellular cargo to the lysosome, to promote the plasma membrane localization or extracellular release of intracellular cargo, and to coordinate intracellular communication with various cell-signaling pathways (Figure 1). These other functions are not, *sensu stricto*, autophagy and, accordingly, will be referred to as *ATG* gene-dependent pathways. There are broad implications of *ATG* gene functions in different membrane-trafficking and signaling pathways for mammalian cell biology, physiology, and disease.

Degradative Autophagy: The "Raison d'Être" of Autophagy Genes

The originally discovered function of *ATG* genes is to orchestrate and mediate the formation of double-membraned structures that deliver intracytoplasmic contents to the lysosome for degradation. This process is conserved in all eukaryotic organisms, occurs at basal levels in nearly all cell types, and is increased by diverse intracellular and extracellular cues. It is essential for cellular homeostasis, cellular protein and organelle quality control, and organismal adaptation to environmental stress. These principles are firmly supported by nearly 2 decades of studies involving genetic ablation of the autophagy machinery in diverse eukaryotic species (Levine and Kroemer, 2008; Mizushima and Komatsu, 2011).

This lysosomal degradation pathway is usually described as involving a set of ~16–20 core conserved *ATG* genes. The ATG proteins encoded by these genes are traditionally classified into distinct biochemical and functional groups that act at specific stages of autophagosome initiation or formation. In this scheme (see other recent reviews for details [Dikic and Elazar, 2018; Yu et al., 2018]), the ULK1 serine threonine kinase complex (involving ULK1, FIP200, ATG13, and ATG101) plays a major role in autophagy initiation, phosphorylating multiple downstream factors. Two distinct Beclin 1/class III phosphatidylinositol 3-kinase (PI3KC3) complexes generate phosphatidylinositol 3-phosphate (PI3P) to act in autophagosome nucleation (PI3KC3-C1 involving Beclin 1, VPS34, VPS15, and ATG14) or endolysosomal and autophagolysosomal maturation (PI3KC3-C2 involving Beclin 1, VPS34, VPS15, and UVRAG). Vesicles containing ATG9A, the only transmembrane core ATG protein, supply membrane to autophagosomes. WIPI (WD repeat domain phosphoinositide-interacting) proteins and their binding partners, ATG2A or ATG2B, function in early stages of membrane elongation at the site of PI3P generation. Autophagosome membrane expansion and completion involves two ubiquitin-like protein conjugation systems: the Ub-like ATG12 conjugates with ATG5 and ATL16L1 and the Ub-like LC3 subfamily (ATG8 in yeast) conjugates with membrane-resident phosphatidylethanoloamine (PE). Unlike in yeast, the ubiquitin-like protein conjugation systems are not essential for autophagosomal membrane completion in mammalian cells, although they determine the efficiency of the process (Tsuboyama et al., 2016).

This classification of the ATG proteins has provided a useful framework for studying and understanding autophagy. However, its apparent simplicity is at variance with extensive data indicating a highly complex level of interconnectivity among the ATG proteins and newly described functions of ATG proteins at different stages of autophagy. Based on unbiased proteomic analyses, most ATG proteins interact with other ATG proteins that reside outside of their "classic" functional complex (Behrends et al., 2010). Experimentally, some of these interactions are known to be important for autophagosome formation. For example, FIP200 (a member of the ULK1 kinase complex) interacts with ATG16L1 to properly target it to the isolation membrane (also known as the phagophore) of the nascent autophagosome (Nishimura et al., 2013). ATG14 (a component of the autophagy-specific PI3KC3-C1 complex) also functions in SNARE-driven membrane fusion (Diao et al., 2015). Similarly, Atg13 (a component of the yeast Atg1/mammalian ULK1 kinase complex) interacts with Atg9 to recruit Atg9 vesicles to the pre-autophagosomal structure (Suzuki et al., 2015). The broader interconnectivity and functional multiplicity of core autophagy proteins in autophagosomal biogenesis requires further elucidation. Moreover, as indicated by a recent conditional genetic interactions study using diverse yeast –omics datasets (Kramer et al., 2017), new systems biology approaches will likely identify additional genes required for autophagy, especially those that may function in a stimulus-dependent, cell-type-dependent, or species-specific manner.

The core ATG proteins, conserved from yeast to humans, are necessary but not sufficient for degradative autophagy. The degradation of autophagosomal cargo cannot proceed without successful fusion to an available and functional lysosome. Research in the past decade has unmasked some of the key factors required for lysosomal biogenesis (Settembre et al., 2013b), autophagolysosomal fusion (Yu et al., 2018), lysosomal function during autophagy (Shen and Mizushima, 2014), and autophagic lysosome reformation (Chen and Yu, 2017). Adenoviral-mediated gene delivery of *TFEB*, a master transcriptional regulator of lysosomal biogenesis, improves outcomes in various rodent disease models, including Parkinson's disease, lysosomal storage disorders, tauopathies, α1-antitrypsin deficiency, and hepatic hyperammonemia (Napolitano and Ballabio 2016; Soria et al., 2018). Autophagolysosomal fusion requires changes in lysosomal pH, certain cytoskeleton motor proteins (dynein), tethering factors (the HOPS complex, the Rab GTPase, RAB7), SNARE proteins (the Q-SNARE, syntaxin 17 on autophagosomes that interacts with R-SNARE proteins, SNAP29, and VAMP8 on endosomes/lysosomes), phospholipids, and members of the LC3/GABARAP family (Kriegenburg et al., 2018) that are bridged to tethering factors or SNARES by adaptor proteins. Screens in *C. elegans* identified novel metazoan-specific genes required for fusion steps in degradative autophagy (Tian et al., 2010). One example relevant to human disease is *EPG5*, which encodes a RAB7 effector. Autosomal recessive mutation of *EPG5* results in Vici syndrome, a neurodevelopmental and multisystem disorder (Table 1). Mutations in genes that regulate lysosomal acidification such as *ATP6AP2* and *presenilin 1* are associated with X-linked Parkinsonism and Alzheimer's disease (Table 1). Thus, we must consider regulators of lysosomal

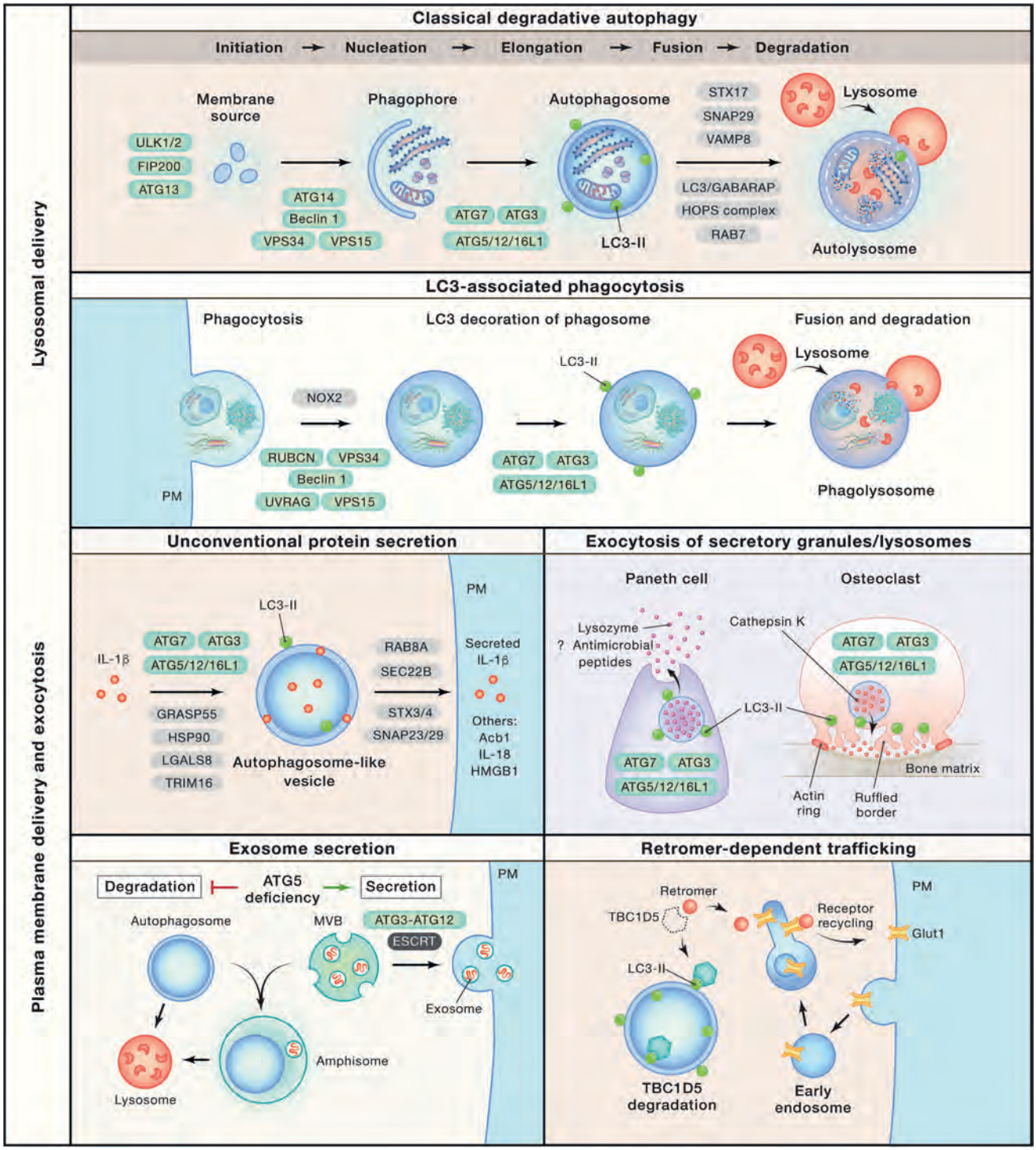

Figure 1. Autophagy Gene-Dependent Membrane-Trafficking Pathways

Shown are schematic illustrations of different membrane-trafficking pathways that involve autophagy (ATG) proteins (green ovals). See text for explanations of each pathway and a discussion of their physiological functions. See Table 1 for examples of genetic mutations that impair autophagy-related pathways that are associated with human disease. The major type of autophagy, macroautophagy, is labeled as "classical degradative autophagy" to distinguish it from other trafficking pathways that utilize overlapping ATG proteins. Due to space limitations, not all ATG proteins, proteins involved in vesicle fusion, or secretary cargo are depicted. PM, plasma membrane. LC3-II (green circle) is the phosphatidylethanolamine-conjugated form of the autophagy protein LC3.

Table 1. Examples of Genetic Mutations in Human Disease that Impair Autophagy

Gene	Disease	Mechanism	References
Mutations in Genes Required for Autophagy and Lysosomal Function			
ATG16L1	Crohn's Disease (CD)	ATGL16L1 T300A is a major risk allele for CD. The T300A polymorphism has a caspase 3 cleavage site that decreases protein levels. T300A knockin or hypomorphic or intestinal knockout mice show decreased intestinal bacterial clearance, increased cytokine responses, reduced Paneth cell lysozyme secretion and clearance of IRE1α protein aggregates during ER stress, enhanced enterocyte TNFα-induced necroptosis, dendritic cell defects in regulatory T cell induction and suppression of mucosal inflammation	(Bel et al., 2017; Chu et al., 2016; Jiang and Mizushima, 2014; Lassen et al., 2014; Murthy et al., 2014; Matsuzawa-Ishimoto et al., 2017; Tschurtschenthaler et al., 2017)
ATG16L2	Systemic lupus erythematosus (SLE)	ATG16L2 R114W allele is a disease susceptibility gene	(Molineros et al., 2017)
ATG5	Childhood ataxia, systemic sclerosis, SLE	Loss-of-function mutation reduces autophagy and causes ataxia. Intronic variants are associated with susceptibility to systemic sclerosis. Polymorphisms associated with SLE susceptibility; mouse studies suggest mechanism may involve deficient LC3-associated phagocytosis	(Kim et al., 2016; Martinez et al., 2016)
ATP6AP2	X-linked Parkinsonism with spasticity; multisystem disorder	Exon skipping mutations linked to Parkinsonism. Missense mutations associated with immunodeficiency, liver disease, and psychomotor impairment lead to defective lysosomal acidification due to impaired v-ATPase assembly, resulting in defects in autophagy	(Korvatska et al., 2013; Rujano et al., 2017)
BECN1	Breast and ovarian cancer	Monoallelic deletion associated with risk and poor prognosis of sporadic breast and ovarian cancer; monoallelic deletion in mice leads to decreased autophagy and increased tumors, including basal-like breast cancer	(Qu et al., 2003; Tang et al., 2015; Valente et al., 2014; Yue et al., 2003)
CLEC16A	Diabetes; multiple sclerosis	*CLEC16A* variants associated with multiple autoimmune diseases. Mice deficient in *Clec16a* have autophagy defects associated with Purkinje degeneration and ataxia, impaired β cell mitophagy, and autoimmunity	(Bronson et al., 2016; Redmann et al., 2016; Schuster et al., 2015; Soleimanpour et al., 2014)
CTNS	Cystinosis	Recessive loss-of-function mutations in *CTNS*, a gene encoding a proton transporter that exports cysteine from lysosomes, associated with renal lysosomal storage disease; gene deletion in mice results in deficient autophagy, altered lysosomal dynamics, and accumulation of dysfunctional ROS overproducing mitochondria	(Festa et al., 2018)
EPG5	Vici syndrome	Recessive mutations in *EPG5*, a gene required for autophagolysosomal fusion, results in a neurodevelopmental disorder with multisystem involvement	(Cullup et al., 2013; Hori et al., 2017)

(*Continued on next page*)

Table 1. ***Continued***

Gene	Disease	Mechanism	References
GBA1	Gaucher's disease; Parkinson's disease (PD)	*GBA1* encodes the lysosomal enzyme glucocerebrosidase. Homozygous GBA defects cause Gaucher's disease, and heterozygous defects predispose to PD. Mutations in GBA1 decrease glucocerebrosidase activity, leading to defects in autophagic-lysosomal function and a-synuclein aggregate accumulation	(Aflaki et al., 2017; Schapira, 2015)
GRN	Frontotemporal dementia (heterozygous) or neuronal ceroid lipofuscinosis (homozygous)	Loss-of-function mutations compromise lysosomal function and autophagic flux	(Chang et al., 2017)
LAMP2	Danon's cardiomyopathy	X-linked deletion results in vacuolar cardiomyopathy and myopathy; Lamp2 deletion in mice results in autophagosome accumulation and cardiomyopathy	(Nishino et al., 2000; Tanaka et al., 2000)
PIK3R4 (VPS15)	Cortical atrophy and epilepsy	Mutations in PIK3R4, a component of the Beclin 1 complex required for endosomal-lysosomal trafficking and autophagy, associated with human neurodevelopmental disease	(Gstrein et al., 2018)
SNX14	Autosomal recessive spinocerebellar ataxia	SNX14 binds lysosomal phosphatidylinositol (3,5)-bisphosphate and is required for autophagosomal clearance	(Akizu et al., 2015)
SPG11, SPG15 (ZFYVE26), SPG49 (TECPR2)	Hereditary spastic paraplegia	SPG15 binds phosphatidylinositol 3-phosphate, and SPG49 binds LC3 to function in autophagolysosomal trafficking	(Ebrahimi-Fakhari et al., 2016)
WDR45 (WIPI4)	Beta-propeller protein-associated neurodegeneration	WDR45 (WIPI4) binds to phosphoinositide 3-phosphate and interacts with ATG2 and ATG9; disease-associated mutations impair autophagy	(Ebrahimi-Fakhari et al., 2016; Haack et al., 2012; Saitsu et al., 2013)
Mutations in Genes that Regulate Autophagy and Lysosomal Function			
APP	Alzheimer's disease	Mutant amyloid precursor protein expressed in mouse hippocampal neurons inhibits mitophagy and autophagy	(Reddy et al., 2018)
AT-1 (SLC33A1)	Spastic paraplegia, developmental delay; autism spectrum disorders	AT-1 translocates cytosolic acetyl coA into ER lumen; mutations and duplications associated with a variety of CNS phenotypes in humans; in mice, overexpression blocks Atg9a-Fam134b-LC3 interactions, leading to defective ER-phagy and progeria	(Peng et al., 2018)
C9orf72	Amyotrophic lateral sclerosis (ALS); frontotemporal dementia (FTD)	Hexanucleotide repeat expansion in C9orf72 gene is most common genetic cause of ALS and FTD; regulates autophagy and lysosomal homeostasis through interactions with SMCR8, ULK1 and Rab-GTPases	(Corrionero and Horvitz, 2018; Nassif et al., 2017)
ERBB2	Breast cancer	Amplification of *ERBB2* and consequent overexpression of ERBB2 (HER2) interacts with Beclin 1 and inhibits autophagy	(Vega-Rubín-de-Celis et al., 2018)
GPR65	Inflammatory bowel disease (IBD)	GPR65 I231L risk variant of this proton-sensing G protein-coupled receptor impairs lysosomal acidification, decreases intracellular bacterial clearance, and alters lipid droplet turnover	(Lassen et al., 2016)

(*Continued on next page*)

Table 1. ***Continued***

Gene	Disease	Mechanism	References
HTT (Huntingtin)	Huntington's disease	PolyQ extension in HTT competitively disrupts interaction between the deubiquitinase ataxin 3 and Beclin 1, leading to enhanced Beclin 1 proteasomal degradation and reduced autophagy	(Ashkenazi et al., 2017)
IRGM	Non-alcoholic fatty liver disease (NAFLD); CD; tuberculosis	IRGM functions in assembly and activation of autophagy machinery; a synonymous variant reduces protein expression, leading to reduced autophagy and lipophagy in NAFLD; polymorphisms are associated with risk of CD and tuberculosis	(Chauhan et al., 2016b; Jiang and Mizushima, 2014; Lin et al., 2016)
LRRK2	CD; PD	Risk alleles for CD and PD increase kinase activity of leucine-rich repeat kinase 2 and reduce autophagic flux; a protective allele increases flux	(Cooper et al., 2012; Hui et al., 2018)
MeCP2	Rett syndrome (X-linked neuro-developmental disorder)	Deficiency of methyl-CpG-binding protein-2 (MeCP2), a transcriptional regulator, results in defective autophagy in patient fibroblasts and knockout mouse cerebellum and mitochondrial retention in erythrocytes	(Sbardella et al., 2017)
MTMR3	IBD	MMTR is a PI3P phosphatase that decreases autophagy. Macrophages from carriers of the risk allele express higher MTMR3 protein levels and have increased pathogen recognition receptor-induced caspase-1 activation and IL-1β secretion	(Lahiri et al., 2015)
PLEKHM1	Osteopetrosis	Disease-associated mutants impair binding to RAB7A and secretory lysosome trafficking in osteoclasts	(Stenbeck and Coxon, 2014)
RAB7A	Charcot-Marie-Tooth type 2B disease	Disease-associated RAB7A mutants reduce autophagic flux in HeLa cells and patient-derived fibroblasts are autophagy deficient	(Colecchia et al., 2018)
PS1	Alzheimer's disease	Mutations in presenilin 1 that disrupt v-ATPase assembly, lysosomal acidification, and autophagy cause early-onset Alzheimer's disease	(Lee et al., 2010)
PTPN2	IBD; type 1 diabetes; juvenile arthritis	Disease-associated SNP in *PTPN2*, a gene encoding protein tyrosine phosphatase non-receptor type 2 causes impaired autophagosome formation and defective bacterial handling in macrophages and intestinal epithelial cells	(Scharl et al., 2012)
SMS	Snyder-Robinson syndrome (SRS)	Loss-of-function mutations in spermine synthase (SMS) cause SRS, an X-linked intellectual disability syndrome; deficiency in SMS generates toxic metabolites that impair lysosomal function and autophagic flux	(Li et al., 2017a)
TMEM230	Parkinson's disease	Transmembrane protein involved in retromer function; loss reduces autophagic cargo degradation and secretory autophagy	(Kim et al., 2017)
v-ATPase	Autosomal recessive osteoporosis	Mutations in the α3 subunit encoded by *TCIRG1* impair lysosomal acidification at the ruffled border of osteoclasts, leading to defects in bone resorption	(Ochotny et al., 2013)
WASP	Wiskott-Aldrich syndrome	Deficiency of the actin cytoskeleton-regulatory WASP protein impairs formation of autophagosomes, resulting in deficient xenophagy and excessive inflammasome activation and pyroptosis	(Lee et al., 2017b)

(*Continued on next page*)

Table 1. ***Continued***

Gene	Disease	Mechanism	References
Mutations in Genes Required for Cargo Delivery in Selective Autophagy			
ALFY	Primary microcephaly	Dominant mutation in this autophagy scaffold protein causes human microcephaly	(Kadir et al., 2016)
CALCOCO2(NDP52)	CD	Missense mutation of this autophagy adaptor reduces its function and enhances NF-kB activation of inflammatory genes	(Ellinghaus et al., 2013)
FAM134B	Hereditary sensory and autonomic neuropathy type II	Mutations disrupt the interaction of this ER protein with LC3 and GABARP to impair ER-phagy	(Khaminets et al., 2015)
FANC genes	Fanconi anemia (FA) congenital syndrome; hereditary breast and ovarian cancer; sporadic cancers	FA pathway genes required for clearing damaged mitochondria (mitophagy) and preventing aberrant inflammasome activation	(Sumpter et al., 2016)
OPTN1	Amyotrophic lateral sclerosis (ALS); primary open angle glaucoma (POAG); Paget's disease of the bone (PGD)	Mutations in ALS reduce interaction of this autophagy adaptor with TBK1 and reduce Parkin-dependent mitophagy; mutations in POAG increase interaction with TBK1, activate Bax-dependent apoptosis, and are associated with mitochondrial dysfunction. Truncated protein mutation associated with PGD	(Li et al., 2016; Shim et al., 2016; Silva et al., 2018; (Wong and Holzbaur, 2014)
PARK2/Parkin	Autosomal recessive and sporadic early-onset PD; colon, lung, and brain cancer	Parkin is an E3 ligase that functions in mitophagy and xenophagy; mutations are associated with PD and cancer risk; polymorphisms associated with increased susceptibility to intracellular bacterial infections	(Kitada et al., 1998; Mira et al., 2004; Xu et al., 2014)
PARK6/PINK1	Autosomal recessive and sporadic early-onset PD	PINK1 is a serine-threonine kinase that translocates to the outer mitochondrial membrane upon damage, mediating Parkin recruitment and mitophagy	(Jiang and Mizushima, 2014)
PEX13	Zellweger syndrome spectrum disorders	Disease-associated mutations impair mitophagy, and patients with mutations have accumulation of abnormal mitochondria	(Lee et al., 2017a)
SQSTM1 (p62)	ALS; FTD; PGD; distal myopathy	SQSTM1 is an autophagy adaptor that binds ubiquitin and LC3; mutations in the ubiquitin-binding association domain result in a spectrum of multisystem proteinopathies	(Goode et al., 2014; Lee et al., 2018)
SMURF1	Ulcerative colitis	*SMURF1*, a susceptibility gene for ulcerative colitis, encodes an E3 ligase that functions in mitophagy, virophagy, and xenophagy of intracellular bacteria	(Franco et al., 2017)
TBK1	ALS; frontotemporal dementia; other neurodegenerative phenotypes; POAG	TBK1 kinase phosphorylates the autophagy receptor OPTN1, increasing its interaction with ATG8 proteins and polyubiquitinated proteins	(Cirulli et al., 2015; van Beek et al., 2018)
TRIM20	Familial Mediterranean fever	Disease-associated TRIM20 mutants fail to interact with inflammasome components and target them for autophagic destruction	(Kimura et al., 2015)
VPS13D	Ataxia with spasticity	Recessively inherited defects in this ubiquitin-binding protein cause failure in mitophagy and mitochondrial dysfunction	(Seong et al., 2018)

biogenesis, the fusion machinery, and determinants of lysosomal function in our efforts to decipher how deficient autophagy leads to disease and how autophagy can be regulated to prevent or treat disease.

Beyond Self-Eating: Autophagy Genes Function in Phagocytosis

Several core *ATG* genes function in a process that shares some similarities with autophagy but involves digestion of unwanted extracellular (rather than intracellular) material. During this process, termed LC3-associated phagocytosis (LAP), single-membraned macroendocytic vacuoles (macropinosomes, phagosomes, and entotic vacuoles) engulf extracellular cargo (such as bacteria, dead cells, or live cells), become decorated by lipidated LC3, and are directed to the lysosome for degradation (Cadwell and Debnath, 2018; Heckmann et al., 2017). LAP is distinguished from autophagy by four main features: (1) the origin of the vacuolar contents (extracellular versus intracellular), (2) the requirement of cargo engagement of an extracellular receptor for activation, (3) the type of membrane that fuses with the lysosome (single membrane versus double membrane), and (4) the utilization of a subset versus all the core ATG proteins. LAP requires NADPH-oxidase (NOX2) to generate reactive oxygen species (ROS), certain components of the Beclin 1/VPS34 complexes, PI3P generation, LC3-conjugation to the single membrane of the phagosome, and all components of the LC3 conjugation machinery (Martinez et al., 2011, 2015; Sanjuan et al., 2007). However, it does not require other core ATG proteins, such as components of the ULK1 complex or the autophagy-specific Beclin 1/VPS34 complex component, ATG14. Somewhat enigmatically, LAP requires Rubicon, an inhibitory component of the autophagy-specific Beclin 1/VPS34 complex. The precise effects of LC3 decoration of phagosomes on their fusion with lysosomes and on lysosomal function are unknown. The presence of LC3 on phagosomes may enhance efficiency of phagolysosomal maturation, perhaps through a mechanism similar to that of LC3/GABARAP family members in autophagolysosomal maturation.

LAP was originally described in murine macrophages during phagocytosis of particles that engage Toll-like receptors (TLRs) (Sanjuan et al., 2007) and is involved in type I interferon (IFN) secretion in response to DNA immune complexes and other TLR9 ligands (Hayashi et al., 2018; Henault et al., 2012). Physiologically important functions of LAP have been identified by comparing phenotypes of mice with myeloid-specific deletion of LAP-specific genes (e.g., *Rubicon* or *NOX2*) and autophagy-specific *ATG* genes (e.g., *FIP200* or *Atg14*). LAP is required for degradation of photoreceptor outer segments by retinal pigment epithelium (RPE), a process necessary for intact vision (Kim et al., 2013b). LAP is induced by the fungus *A. fumigatus* and the intracellular bacterium *L. monocytogenes* and enhances host defense against these pathogens (Gluschko et al., 2018; Martinez et al., 2015). Mice lacking several components of the LAP pathway develop an autoimmune systemic lupus erythematosus (SLE)-like disease, perhaps due to a defect in the clearance of dying cells that triggers enhanced proinflammatory signaling and autoantibody production (Martinez et al., 2016).

Given the crucial roles of receptor-activated phagocytosis in human physiology, it is likely that LAP, like classical autophagy, will emerge as an important pathway in human disease. While the two pathways utilize overlapping genetic machinery, a critical distinction renders them antagonistic. Specifically, Rubicon is required for LAP but suppresses autophagy, and recent studies confirm a mutually inhibitory relationship between LAP and autophagy in photoreceptor degradation in RPE cells (Muniz-Feliciano et al., 2017). It is not clear why these two pathways are counter-regulated; possibly, cells may need to shut off the alternative pathway during stress to avoid competition for overlapping resources (Muniz-Feliciano et al., 2017). At a mechanistic level, it is uncertain how Rubicon functions to promote Beclin 1/VPS34 kinase activity at the phagosome (Martinez et al., 2015) but inhibit it at other organellar sites (Matsunaga et al., 2009). Interestingly, the WD repeat-containing C-terminal domain of ATG16L1 is essential for LC3 recruitment to endolysosomal membranes in LAP but dispensable for canonical autophagy (Fletcher et al., 2018), illustrating another difference in the molecular roles of an ATG protein in autophagy and LAP.

The genetic overlap and mutual antagonism of LAP and autophagy have practical implications for autophagy-targeted therapies. Theoretically, specificity in autophagy induction might be enhanced by activating the ULK1 complex rather than downstream shared nodes in autophagy and LAP (although the ULK1 kinase complex may have substrates outside of autophagy). The appeal of targeting Rubicon—a negative regulator of autophagy whose knockout in mice has beneficial effects (e.g., improved high-fat-diet-induced hepatic steatosis [Tanaka et al., 2016] and increased cardiac protection during lipopolysaccharide-induced sepsis [Zi et al., 2015])—may be tempered by potential adverse effects of LAP inhibition, such as increased susceptibility to fungal diseases and autoimmunity. Furthermore, treatments that target shared ATG proteins may result in unpredictable effects on each pathway, assuming that these proteins are rate-limiting and that the two pathways compete for access to these shared core ATG proteins.

The identification of LAP as a lysosomal degradation pathway that utilizes certain core *ATG* genes requires us to adopt a wider interpretative lens for studies of mice with deletions of these genes. Does deficient LAP versus deficient autophagy contribute to pathological phenotypes in mice with whole-body or tissue-specific deficiency of genes such as *beclin 1*, *ATG5*, *ATG7*, or *ATG16L1*? To what extent does increased autophagy versus decreased LAP contribute to Rubicon knockout phenotypes? Do the genome-wide association study links between polymorphisms in some of these genes and diseases that involve disordered immune regulation (such as asthma, SLE, and inflammatory bowel disease) (see Table 1) suggest a role for altered LAP in their pathogenesis? The observation that a deficiency of LAP-associated (but not of non-LAP-associated) *ATG* genes results in a SLE-like syndrome in mice (Martinez et al., 2016) underscores the importance of this question. Specific molecular markers to distinguish LAP from autophagy in both animal models and human disease are needed.

Beyond Lysosomal Degradation: Autophagy Genes Function in Secretion and Exocytosis

ATG genes are used not only for targeting intracellular cargo to the lysosome for degradation but also for pathways that involve the targeting of intracellular cargo to either the plasma membrane or extracellular environment (Figure 1). Generally, these

pathways have been grouped under the umbrella term "secretory autophagy"; however, as the "phagy" part is missing from the process, we prefer the more linguistically precise term of *ATG* gene-dependent secretion. There are many different types of *ATG* gene-dependent secretion (reviewed elsewhere from a cell biology perspective [Cadwell and Debnath, 2018]), but the mechanisms governing most of these processes are not well understood. Here, we focus on these pathways as they may relate to mammalian physiology and disease.

Unconventional secretion involves the extracellular release of proteins that lack amino-terminal signal peptide leader sequences and bypass "conventional" transit through the endoplasmic-reticulum (ER)-Golgi apparatus to reach the plasma membrane. A role for ATG proteins (Atg1/5/6/7/8/9/12/17) in this process was first discovered in yeast secretion of the acyl-CoA-binding protein, Acb1 (Duran et al., 2010; Manjithaya et al., 2010). In mammalian cells, unconventional secretion of leaderless proteins, such as the pro-inflammatory cytokines processed by the inflammasome, IL-1β and IL-18, also require the autophagy protein, ATG5 (Dupont et al., 2011). The precise mechanisms underlying *ATG* gene-dependent unconventional secretion remain unclear. It is not certain whether targets are captured in an autophagosomal lumen (Dupont et al., 2011) and/or the intermembrane space between the double membrane of the autophagosome (Zhang et al., 2015b), nor is it certain how targets are delivered to and released from the plasma membrane. Autophagosome-like vesicles containing IL-1β bypass syntaxin 17-dependent fusion with lysosomes and instead use specific SNAREs and syntaxins involved in vesicle fusion with the plasma membrane for cargo secretion (Kimura et al., 2017).

A function of *ATG* genes in secretion of pro-inflammatory mediators (and more broadly, other leaderless proteins) could have vast importance for inflammatory disorders and a wide range of other diseases. However, it is currently difficult to assess the physiological importance of *ATG* gene-dependent secretion of IL-1β and IL-18 *in vivo*, as macrophage (or hematopoietic cell)-specific deletion of *Atg5*, *Atg16l1*, and *Atg7* in mice is associated with increased, rather than decreased, levels of IL-1β and IL-18 production (Kimmey et al., 2015; Martinez et al., 2016; Saitoh et al., 2008). These findings may reflect basal functions of *ATG* genes in the negative control of inflammasome activation (Zhou et al., 2011), whereas the *ATG* gene-dependent secretion of pro-inflammatory mediators may be unmasked during certain stress conditions, such as inflammasome activation triggered by lysosomal membrane damage (Kimura et al., 2017). The possibility of an autophagy-dependent secretome *in vivo* warrants further investigation and may lead to the identification of proteomic signatures of autophagy activation as clinically useful serum biomarkers. Theoretically, autophagy-inducing therapies might lead to untoward effects via the unconventional secretion of pro-inflammatory mediators or other pathogenic proteins.

Perhaps the best-established link between *ATG* gene-dependent secretion and mammalian physiology and disease relates to the exocytosis of secretory granules and lysosomes. Notably, human genome-wide association studies that revealed a polymorphism in a core *ATG* gene, *ATG16L1T300A*, as a major risk allele for Crohn's disease (Barrett et al., 2008) spurred the discovery of a fundamental role for the ATG protein conjugation machinery in secretory granule exocytosis (Cadwell et al., 2008). In mice, hypomorphic expression of *Atg16l1*, *Atg16l1*^{T300A} knockin mutation; Paneth cell-specific deletion of *Atg16l1*, *Atg5*, or *Atg7*; or whole-body deletion of *Atg4b* results in abnormal granule morphology and a defect in granule exocytosis and lysozyme secretion by Paneth cells (Bel et al., 2017; Cabrera et al., 2013; Cadwell et al., 2008; Lassen et al., 2014), a specialized ileal epithelial cell type that controls the intestinal microbiota by secreting lysozyme and antimicrobial peptides. Similar defects in Paneth cell morphology are observed in patients with (but not those without) the ATG16L1T300A Crohn's disease risk allele (Cadwell et al., 2008). The precise membrane-trafficking mechanisms by which ATG proteins facilitate secretory granule exocytosis in Paneth cells or other cell types remain unknown. However, a recent study indicates that lysozyme is localized in large LC3-positive vesicles in Paneth cells from wild-type but not *Atg16l1*^{T300A} mice (Bel et al., 2017). Thus, in a manner similar to autophagosome-like vesicles involved in unconventional protein secretion, secretory granules may be earmarked for exocytosis by the presence of LC3 on their surface.

A related, but topologically distinct, link between autophagy and secretory lysosome exocytosis was uncovered in another specialized type of secretory cell, the osteoclast. Osteoclasts resorb bone by a mechanism that involves secretory lysosome fusion with bone-apposed plasma membrane composed of ruffled borders, with the discharge of matrix-degrading molecules into the site of osteal degradation. In mice, the ATG protein conjugation machinery and the Rab GTPase, Rab7, are essential for generating an LC3-labeled ruffled border, cathepsin K release, and normal bone resorption (DeSelm et al., 2011), thus indicating a role for *ATG* genes in mediating polarized secretion of lysosomal contents to the extracellular space. In this scenario, the plasma membrane, not the secretory lysosome, is labeled by LC3. Thus, during secretion, the ATG protein conjugation machinery and resulting lipidated LC3 can function either in the formation of normal secretory granules that properly fuse with the plasma membrane or in the creation of a specialized plasma membrane that fuses with secretory lysosomes.

The predicted clinical outcome of defects in *ATG* gene-dependent osteoclast functions would be osteopetrosis, a disease marked by abnormally dense bone. Consistent with this prediction, mutations in PLEKHM1, a Rab7 effector, and the v-ATPase α3 subunit involved in lysosomal acidification are each associated with osteopetrosis in patients (Stenbeck and Coxon, 2014). In contrast, aging, which is associated with reduced autophagy in most cell types (Hansen et al., 2018), is accompanied by osteopenia and osteoporosis in mice and humans. This may reflect the roles of *ATG* genes in other cell types in the bone that favor bone growth and normal bone density, including protection against ER and oxidative stress in osteoblasts and osteocytes (Li et al., 2018b; Liu et al., 2013a; Onal et al., 2013) and maintenance of the proper function of bone mesenchymal stem cells (Ma et al., 2018). Thus, studies in bone represent an elegant example of how the autophagic machinery can exert different specialized functions in distinct cell types within a given organ—functions that may have opposite effects (such as bone resorption and bone formation)—to orchestrate overall tissue homeostasis. As osteopenia/osteoporosis and associated

skeletal fractures are a major cause of morbidity and mortality in aging humans, this area warrants further investigation as a potential clinical target for autophagy upregulation.

Numerous other defects in protein secretion in *ATG* gene knockout mice have been described, although it is unclear whether they reflect a direct role for *ATG* genes in autophagy-independent trafficking or more indirect consequences of autophagy deficiency on secretory processes. These include defects in the assembly and secretion of octogonial core proteins, which lead to abnormalities in vestibular development (Mariño et al., 2010) and defects in pancreatic β cell insulin granule morphology and secretion (Watada and Fujitani, 2015), melanogenesis and pigmentation (Ganesan et al., 2008), and mucus secretion of airway epithelial cells and intestinal goblet cells (Patel et al., 2013).

Accumulating evidence suggests that ATG proteins also have pleiotropic effects on the cellular release of exosomes, a process that is mediated by fusion of the multivesicular body (MVB) with the plasma membrane (Baixauli et al., 2014; Hessvik and Llorente, 2018). Autophagy induction can prevent—whereas *ATG* gene silencing or pharmacological inhibition can increase—extracellular release of exosomes, including those containing pathogenic protein cargoes, such as α-synuclein (Fussi et al., 2018), prions (Abdulrahman et al., 2018), and amyloid precursor protein (Miranda et al., 2018). This regulatory mechanism is presumed to involve MVB fusion with autophagosomes, thereby diverting MVB transport away from the plasma membrane. Increased exosome release in the setting of impaired autophagy may function as an alternative quality-control pathway to maintain cellular homeostasis and prevent cell death due to proteotoxicity. However, there are also examples in which *ATG* genes stimulate exosome production. *Atg5*, but not *Atg7*, has been shown to decrease late endosome acidification by disrupting the v-ATPase, thereby promoting the production of exosomes that enhance tumor metastasis (Guo et al., 2017). Similarly, the ATG3-ATG12 conjugate, which is required for LC3 lipidation during basal (but not starvation) conditions, interacts with the ESCRT protein Alix and positively controls Alix-dependent exosome biogenesis (Murrow et al., 2015). Given the expanding repertoire of exosome-dependent processes (including neurodegeneration, immune signaling, metabolism, tumor metastasis, and viral infection), the effects of the autophagic machinery on the fate of the MVB—lysosomal degradation or exocytosis—may partly underlie the pathophysiological effects of *ATG* gene mutation.

The ATG machinery modulates retromer function to control the endosome-to-cell-surface recycling pathway (Roy et al., 2017). During metabolic stress (e.g., glucose withdrawal, hypoxia, Ras transformation), LC3 on autophagic structures binds to the RabGAP protein TBC1D5 to sequester it away from an inhibitory interaction with the retromer complex. This sequestration allows retromers to associate with endosomal membranes and mediate plasma membrane translocation of the glucose transporter, GLUT1, a facilitator of glucose uptake. GLUT1 is required for the low levels of basal glucose uptake required to sustain cellular respiration, and its plasma membrane localization normally increases when cells are exposed to low glucose. Perturbation in ATG protein conjugation may significantly cripple this metabolic homeostatic mechanism involving GLUT1 trafficking and, in addition, affect the cell-surface localization of other as-yet-unidentified receptors.

Autophagy Genes in Other Dynamic Membrane Events

Non-autophagic functions of *ATG* genes in membrane trafficking modulate the infection of host cells by viruses, bacteria, and other pathogens. These include processes described above such as LAP (which may be partially antagonized by virulent micro-organisms that enter professional phagocytes) and LC3-regulated exocytosis (which is involved in the egress of viruses that either reside inside autophagosomes or whose envelopes become decorated with LC3) (reviewed in Cadwell and Debnath [2018]). Many additional *ATG* gene-dependent membrane reorganization events—or interference with such events—also regulate infection. For example, several *ATG* genes are required for the formation of intracytoplasmic membrane-associated replication factories of certain medically important RNA viruses, such as hepatitis C virus (Dreux et al., 2009). Similarly, the formation of multi-membranous vacuoles that support replication of the bacterium *Brucella abortus* involves *ATG* genes required for class III PI3K activity but not those required for LC3 conjugation (Starr et al., 2012). In contrast, IFN-γ inhibits *Toxoplasma gondii* replication by a process involving LC3/GABARAP lipidation and recruitment of IFN-γ-inducible GTPases to the parasitophorous vacuole, where they disrupt the membrane and destroy the parasite's replicative niche (Choi et al., 2014). Similarly, IFN-γ mediated control of murine norovirus (a model for human epidemics of gastroenteritis) involves labeling membrane-associated viral-replication complexes with lipidated LC3 and recruitment of IFN-γ-inducible GTPases (Biering et al., 2017). Thus, marking replication-associated membrane structures by LC3 conjugation may represent a conserved mechanism underlying IFN-γ-mediated control of intracellular pathogen replication. Further understanding of the precise processes by which different subsets of ATG proteins provide or destroy host membranes necessary for different stages of pathogen replication may lead to the development of new anti-infective strategies.

Beyond Membrane Trafficking: Autophagy Proteins Have Other Functions

The autophagy proteins not only help orchestrate the crosstalk of diverse vesicular trafficking pathways but also interface with multiple other cellular pathways, including (but not limited to) cell-death pathways, cell-cycle regulation, and innate immune signaling. The interaction of FIP200 with Atg13 is essential for autophagy *in vivo* and neonatal survival in mice, but the non-autophagic function is sufficient to maintain embryogenesis through a mechanism involving protection against TNFα-induced apoptosis (Chen et al., 2016). Atg7, independently of its E1-like enzymatic activity and function in autophagy, regulates p53-dependent cell-cycle arrest and apoptosis, and the neonatal lethality of Atg7 knockout mice is partially rescued by inhibition of the DNA damage response through deletion of the protein kinase Chk2 (Lee et al., 2012). In mice, deletion of Atg9a, but not Atg5, results in a defect in necrosis at the bone surface during developmental morphogenesis (Imagawa et al., 2016). The precise mechanisms underlying these (and additional) functions of individual ATG proteins in cell death and cell-cycle regulation are not well understood.

ATG proteins regulate inflammatory and immune signaling both through autophagy-dependent mechanisms (such as by the autophagic removal of damaged mitochondria that produce ROS and activate RIG-I signaling and the NLRP3 inflammasome) and autophagy-independent mechanisms that generally involve ATG protein interactions with immune-signaling molecules. For example, the ATG5-ATG12 conjugate inhibits type I IFN signaling in response to viral infection by binding to the CARDs (caspase activation and recruitment domains) of RNA-recognition molecules such as RIG-I and MAVs (Jounai et al., 2007). Similarly, the cytosolic DNA-sensing innate immunity pathway mediated by cGAS (cyclic GMP-AMP [cGAMP] synthase) and STING (stimulator of interferon genes) is regulated by autophagy proteins. The generation of cGAMP by cGAS activates ULK1, which phosphorylates and inhibits STING-dependent cytokine production (Konno et al., 2013). As unrestrained STING signaling (either via inherited mutations in the ADAR (adenosine deaminase, RNA specific) and ribonuclease H2 complex or gain-of-function mutations in STING) causes human autoinflammatory diseases, ULK1 activating agents have been proposed as potential treatments for such disorders (Konno et al., 2018). Beclin 1 binds cGAS to suppress cGAMP synthesis and halt interferon production (Liang et al., 2014). Atg9a may also function as a negative regulator of innate immune signaling by decreasing the assembly of STING and TBK1 in the presence of double-stranded DNA (Saitoh et al., 2009). Of note, these same RNA-sensing and cytosolic DNA-sensing signaling pathways are activators of autophagy, which is itself an important innate immune effector pathway (Deretic and Levine, 2018). Thus, ATG proteins play a crucial role in both mediating innate immunity and in providing feedback inhibition to fine-tune inflammatory signaling so as to avoid deleterious consequences.

The Selectivity of Autophagy: A Guardian of Cellular Homeostasis

For nearly half a century, the process of macroautophagy was believed to lack cargo specificity. In fact, the morphological identification of an autophagosome required visualizing the simultaneous presence of diverse cytoplasmic contents, such as ER, ribosomes, and mitochondria inside a double-membraned vacuole. However, a transformative body of work over the past decade has fully dispelled this notion. We now know that there can be extreme specificity in governing the choice of cargo that is degraded by the autophagosome and an intricate system for earmarking and capturing such cargo. This process, termed selective autophagy, may be more crucial in protection against most mammalian diseases than ''bulk autophagy,'' which is primarily a homeostatic mechanism during nutrient stress.

Many parts of the cell can be ''selected'' for degradation by autophagy (Figure 2; Table 2). Numerous studies have reported the selective autophagy of various organelles, including mitochondria, ER, peroxisomes, lipid droplets, ribosomes, midbody rings, and the nucleus. Autophagy selectively degrades aggregation-prone misfolded proteins such as those involved in the pathogenesis of certain neurodegenerative, skeletal and cardiac muscle, and liver diseases. In addition, it degrades the individual proteins that serve as adaptors to bridge cargo with the nascent phagophore as well as specific inflammatory and immune signaling molecules. Moreover, selective autophagy can target pathogens that reside inside vacuoles or directly inside the cytosol for lysosomal degradation. Once captured, cargo degradation proceeds through a route that involves the same molecular machinery as bulk autophagy. Different forms of selective autophagy are often named by a term comprising a prefix derived from the cargo (e.g., mito-, ER-, ribo-, nucleo-, pexo-, lipo-) and the suffix ''phagy.'' For selective autophagy of microbial invaders, the term xenophagy is commonly used.

Major advances have been made in understanding certain aspects of selective autophagy, particularly how cargo binds to the forming phagophore (Figure 2). In most known instances, the cargo either contains an identifiable LC3-interacting region or LIR motif ($W/F/Y_1x_2x_3L/I/V_4$) that directly binds LC3, or it must be labeled with a tag such as ubiquitin, which then binds adaptor proteins that contain both a ubiquitin-binding domain and a LIR motif, thus serving as a bridge between the cargo and the LC3 (or GABARAPs) conjugated to the phagophore membrane. Alternatively, specific proteins (particularly those involved in the inflammasome or IFN signaling) can bind to TRIM (tripartite motif) family members, which serve as adaptors that interact with GABARAPs to target such proteins for autophagic degradation (Kimura et al., 2017). Of note, the proteins we refer to as ''adaptors'' are often called autophagy ''receptors''; however, as these are bridging molecules that are not integral parts of cellular membranes that undergo ligand-dependent activation, the designation as ''receptors'' can be confusing.

Several layers of control are needed to properly dictate the targeting of cargo for autophagy. In theory, cargo should be disposed of when it is constitutively harmful (e.g., intracellular pathogens), potentially dangerous to the cell (e.g., mitochondrial damage), or obsolete as a result of cellular differentiation (e.g., organelles during erythrocyte maturation). In the scenario where LC3 directly binds to a protein on an organelle containing a LIR motif, there must exist ways to hide or expose the LIR motif in a regulated fashion. Two mechanisms identified thus far include (1) stimulatory and inhibitory phosphorylations of residues near or in the LIR motif (such as occurs for the mitochondrial outer membrane protein, FUNDC1, that mediates hypoxia-stimulated mitophagy [Lv et al., 2017]) and (2) the exposure of a normally hidden LIR motif (such as occurs when proteasomal-dependent rupture of the outer mitochondrial membrane exposes the inner mitochondrial membrane LC3-binding protein, prohibitin 2 [Wei et al., 2017]). Under circumstances where LC3 binds to an adaptor protein, there must exist ways to recruit the adaptor to the cargo destined for degradation. This process generally involves the concerted action of E3 ligases that ubiquitinate targets (e.g., Parkin, SMURF1), kinases that recruit E3 ligases (e.g., PINK1) or that phosphorylate LIR domains of adaptors (e.g., TBK1), deubiquitinating enzymes (DUBs) that counter E3 ligase activity (e.g., USP30, USP15) (Gatica et al., 2018), and acetylation/deacetylation of mitochondrial and ER target proteins (Peng et al., 2018; Webster et al., 2013).

All mechanisms for earmarking cargo must be tightly coordinated with the formation of autophagosomes to ensure final cargo disposal. Some potential nodes of coordination have recently been described. Certain autophagy adaptors, most notably the TRIM family proteins, bind not only substrate

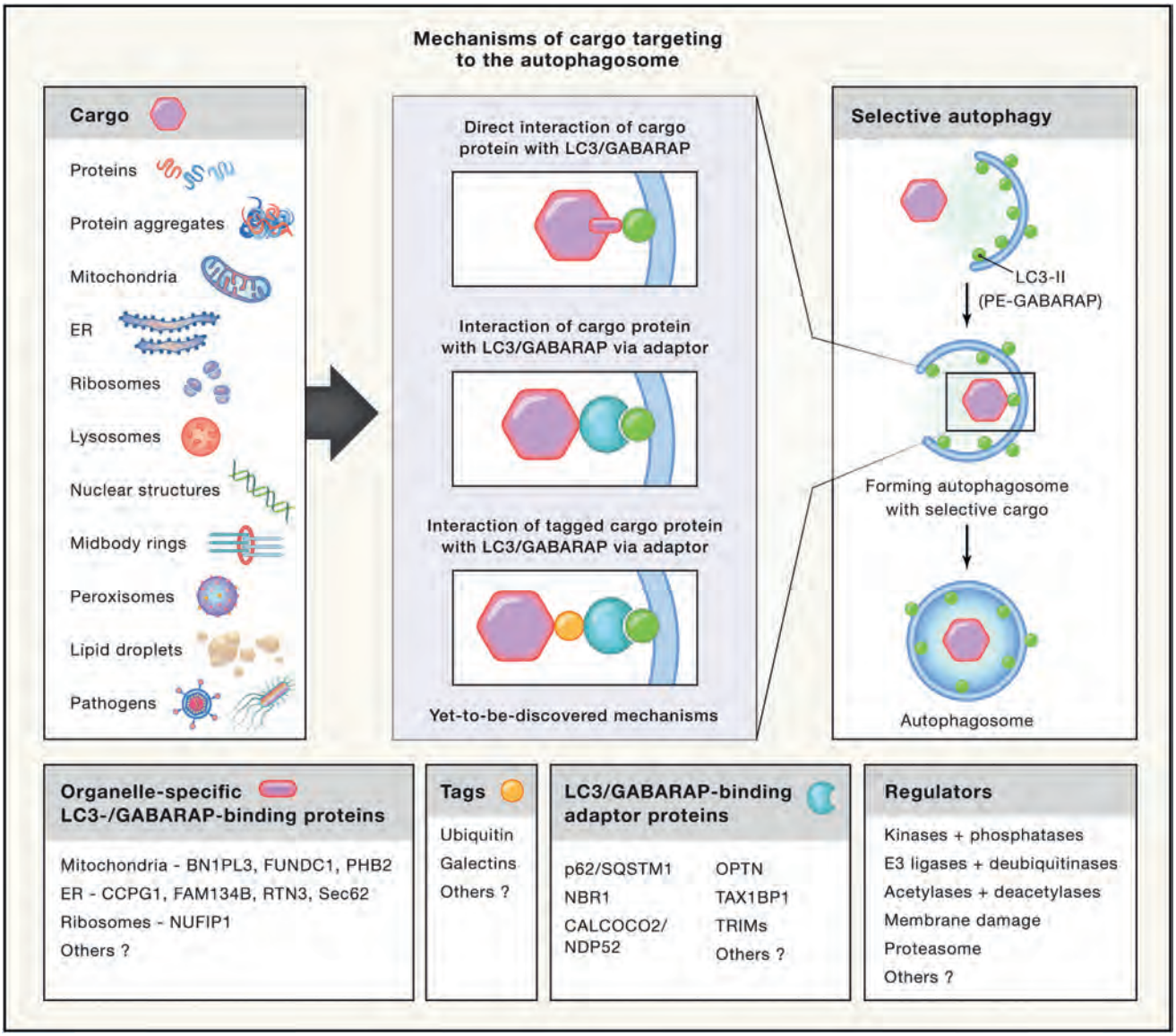

Figure 2. Conceptual Overview of Selective Autophagy

Shown are the diverse cargoes that are degraded by autophagy and the major known mechanisms by which cargo are attached to LC3 or GABARAP family members on the phagophore membrane. Also listed are currently known organelle-specific LC3/GABARAP-binding proteins, tags that label cargo destined for selective autophagic degradation, LC3/GABRAP-binding adaptor proteins, and factors that regulate the recognition of cargo by adaptors or LC3/GABARAP. Organelle-specific LC3/GABARAP-binding proteins and LC3/GABARAP-binding adaptor proteins interact with LC3/GABARAP via conserved W/F/YxxL/I/V motifs. See Table 2 for information about different types of selective autophagy and their possible roles in physiology and disease.

proteins and LC3/GABARAP family members but also assemble the ULK1 and class III PI3K complexes to initiate autophagosome formation (Kimura et al., 2017). ULK1, a "master kinase" that phosphorylates multiple sites on downstream core autophagy proteins, is recruited to and phosphorylates proteins involved in selective autophagy, such as the LIR domain of the mitochondrial membrane protein, FUNDC1 (Wu et al., 2014). An organelle-specific LC3/GABARAP-binding protein, the ER membrane protein CCPG1, interacts with a key component of the autophagy-initiating ULK1 complex, FIP200 (Smith et al., 2018). Thus, the machinery involved in selective autophagy substrate recognition may play an active role in autophagy initiation.

For selective autophagy targeting events that involve substrate ubiquitination, the precise mechanisms that dictate the choice between autophagic versus proteasomal degradation are uncertain. In yeast, substrate aggregation and oligmerization of the ubiquitin-binding proteins may favor autophagic degradation (Lu et al., 2017). The lysine residues used for linkage and the length and nature of the ubiquitin chains have also been proposed to contribute to pathway selection (Gatica et al., 2018), but definitive evidence is lacking. Moreover, despite elegant

Table 2. Types of Selective Autophagy and Possible Roles in Physiology and Disease

Process (Cargo)	Physiological Function	Possible Pathological Consequences of Defects	References
Proteins	Proteostasis	Aberrant signaling/cellular functions related to effects of increased protein (e.g., p62/SQSTM1 inflammatory and pro-tumorigenic signaling; autoinflammatory disorders with defects in TRIM-mediated autophagy of inflammasome components; abnormal iron accumulation and ferroptosis in tissues with defects in ferritin degradation)	(Kimura et al., 2015; Latunde-Dada, 2017; Liu et al., 2016; Moscat et al., 2016)
Aggrephagy (protein aggregates)	Removal of misfolded aggregate-prone proteins labeled by ubiquitin	Enhanced accumulation and detrimental consequences of pathogenic proteins targeted by this mechanism (e.g., β-amyloid, mutant huntingtin, α-synuclein, mutant α1-antitrypsin)	(Gatica et al., 2018; Ueno and Komatsu, 2017)
Mitophagy (mitochondria)	Mitochondrial quality control and homeostasis. Removal of damaged mitochondria, paternal mitochondria during embryogenesis, and mitochondria during erythrocyte differentiation; piecemeal degradation for respiratory chain turnover	Defective mitophagy may contribute to neurodegenerative diseases, aging, cancer, increased ROS-dependent inflammasome activation, and genotoxic stress	(Drake et al., 2017; Rojansky et al., 2016)
ER-phagy (endoplasmic reticulum)	Control of ER morphology, turnover, ER luminal proteostasis, and recovery from stress	Pathological consequences of defects not defined, but hypothetical role in pathologies associated with abnormal UPR and ER intraluminal proteostasis, including pancreatitis and certain metabolic disorders and aggregopathies. Mutation in ER LC3/GABARAP-binding protein FAM134B leads to hereditary neuropathy in patients; loss of ER LC3-binding protein CCPG1 leads to injury of exocrine pancreas in mice. Defective ER-phagy in mice (due to AT-1 overexpression) leads to segmental progeria with multiple metabolic and inflammatory phenotypes	(Grumati et al., 2017; Khaminets et al., 2015; Peng et al., 2018; Smith et al., 2018)
Ribophagy (ribosomes)	Required for survival during nutrient starvation, providing source of nucleosides to cell	Not yet known whether defects in pathway occur *in vivo*; if so, would be predicted to disrupt adaptive responses to starvation	(Wyant et al., 2018)
Lysophagy (lysosomes)	Prevents cell destruction and inflammation due to leakage of lysosomal contents when lysosomal membranes are damaged or ruptured	Defects predicted to be associated with increased cytosol invasion of pathogens, increased lysosomal cell death, and inflammation as well as disruption of lysosomal homeostasis (latter postulated to participate in neurodegeneration); lysosomal damage in autophagy-deficient mice results in acute kidney injury	(Chauhan et al., 2016a; Maejima et al., 2013; Yoshida et al., 2017)
Nucleophagy (entire nucleus)	Nuclear destruction necessary for terminal differentiation of keratinocytes; unknown whether required for nuclear removal in red blood cells and lens fiber cells	Perturbations may occur in psoriasis, causing parakeratosis (retention of nuclei in stratum corneum of epidermis)	(Akinduro et al., 2016)
Nuclear lamina	Promotes Ras-oncogene-induced senescence	Autophagic degradation of lamin B proposed to be a mechanism of tumor suppression; defects may promote oncogenesis and phenotypes associated with decreased cellular senescence.	(Dou et al., 2015)

(*Continued on next page*)

Table 2. ***Continued***

Process (Cargo)	Physiological Function	Possible Pathological Consequences of Defects	References
Micronuclei	Removal of micronuclei generated by mitotic aberration (and cytosolic DNA aggregates that resemble micronuclei)	Defects may contribute to genomic instability associated with autophagy deficiency and pro-inflammatory signaling via cGAS activation; neuroinflammatory autoimmune disorder Aicardi-Goutieres syndrome caused by mutation of DNA repair enzyme RNase H2, resulting in accumulation of micronuclei-like cytosolic DNA aggregates	(Bartsch et al., 2017; Rello-Varona et al., 2012)
Retrotransposon RNA	Degradation of RNA granules containing retrotransposons may favor genomic stability	Deficiency results in increased retrotransposon insertions into the genome	(Guo et al., 2014)
Midbody rings	Degradation of the midbody, an organelle that contains the remnants of cell division machinery, may regulate cellular fate	Deficiency predicted to alter cellular fate; several mutations affecting midbody proteins cause primary encephalopathies, which is also observed with genetically inherited syndromes associated with defects in autophagic flux	(Kuo et al., 2011; Mandell et al., 2016)
Pexophagy (peroxisomes)	Perixosomal quality control	Defects may contribute to neurodevelopmental disorders associated with mutations in genes involved in pexophagy, inflammation, aging and age-related diseases, diabetes, cancer, and neurodegenerative disorders	(Cipolla and Lodhi, 2017)
Lipophagy (lipid droplets)	Facilitates transport of lipid droplets to lysosomes for catabolism by lysosomal acid lipase; contributes to lipid homeostasis	Defects are postulated to contribute to pathogenesis of metabolic syndrome, NAFLD, and alcoholic fatty liver disease; however, role of defects in lipophagy versus general autophagy pathway remain to be elucidated	(Zechner et al., 2017; Zhang et al., 2018b)
Xenophagy (intracellular pathogens)	Removal of cytoplasmic bacteria or viruses functions in cell-intrinsic immunity	Mutations in genes required for selective autophagy of pathogens result in enhanced microbial virulence in mouse models of tuberculosis and viral infections	(Franco et al., 2017; Mitchell and Isberg, 2017; Sumpter et al., 2016)

studies characterizing the ubiquitylome of selective autophagy cargo (such as mitochondria and intracellular pathogens) (Grumati and Dikic, 2018), the ubiquitin substrates required for autophagic targeting remain largely undefined.

Selective autophagy seems to involve multiple concurrent targeting mechanisms that act in a cooperative, potentially hierarchical and/or partially redundant manner to ensure proper removal of cargo. This ''combinatorial design'' may allow specific cell types to more precisely regulate when and how selective autophagy occurs for a given cargo. The partial redundancy also renders it more feasible to study loss-of-function phenotypes of genes required for selective autophagy but dispensable for bulk autophagy (as compared to those required for bulk autophagy), as they are less likely to be lethal to the cell or organism. As selective autophagy genes are partially redundant, this may explain why their loss-of-function mutation seems to be better tolerated in the human population than loss-of-function mutation of core *ATG* genes.

Indeed, mutations in many of the known molecules involved in selective autophagy are associated with susceptibility to a variety of human diseases (Table 1). Mutations in the genes encoding the adaptor proteins p62/SQSTM and optineurin, the E3 ligase Parkin, and the kinases PINK1 and TBK1 are among the most common causes of familial and early onset neurodegenerative diseases, including Parkinson's disease, frontotemporal dementia, and amyotrophic lateral sclerosis. Hereditary sensory and autonomic neuropathy type II is caused by mutations in an ER-specific LC3-binding protein, FAM134B, required for ER-phagy. Mutations in TRIM20 (also known as pyrin) that impair its ability to target inflammasome components for autophagic degradation result in an inherited autoinflammatory disorder, familial Mediterranean fever. Inflammatory bowel disease-associated genes encode proteins that function in multiple steps of autophagy, including the selective targeting of bacteria by the adaptor CALCOCO2/NDP52 and the E3 ligase SMURF1.

The numerous links between mutations in selective autophagy genes and human diseases underscore the likely physiological importance of different forms of selective autophagy (Table 2). However, the precise mechanisms that connect genotype to phenotype remain largely undefined. For example, it is not known why mutations in Parkin and PINK1 are associated with Parkinson's disease whereas mutations in optineurin, TBK1, and p62/SQSTM1 are associated with amyotrophic lateral sclerosis and frontotemporal dementia (Table 1). In addition to potential non-cell-autonomous effects of mutations in these genes in tissues outside of the brain, cell-type-specific differences in various populations of neurons and glia may exist with respect to (1) dependency on subsets of selective autophagy genes, (2) expression and activity of DUBs and other negative feedback mechanisms that regulate selective autophagy, and/or (3) levels and types of stress that mandate different types of selective autophagy responses to maintain homeostasis (e.g., mitophagy or other forms of selective autophagy such as aggrephagy that are relevant to neurodegenerative diseases). Parkin knockout mice (unlike flies lacking Parkin) do not develop spontaneous neurodegeneration, but they do develop dopaminergic neuronal degeneration (resembling that observed in human Parkinson's disease) when crossed with ''mutator'' mice with a proofreading-defective mitochondrial DNA polymerase (PolG) that accumulate mitochondrial mutations (Pickrell et al., 2015). The localization of disease in dopaminergic neurons may be related to increased mitochondrial stress in these cells as compared to other neuronal populations in the brain. Intriguingly, the motor defect and neurodegeneration in Parkin null/mutator mice can be rescued by deletion of STING, a regulator of type I IFN responses to cytosolic DNA (Sliter et al., 2018). Thus, aberrant inflammatory signaling as a result of defects in mitophagy may contribute to the pathogenesis of neurodegenerative disease in patients with Parkin or PINK1 mutations.

While most, if not all, forms of selective autophagy are likely to contribute to normal physiology and protection against disease, mitophagy has been the most extensively studied. Mitophagy is an essential component of mammalian developmental and differentiation processes, including elimination of paternal mitochondria from the fertilized egg (Rojansky et al., 2016), removal of mitochondria during red blood cell maturation (Sandoval et al., 2008), and beige-to-white adipocyte differentiation (Lu et al., 2018). In addition to Parkinson's and other neurodegenerative diseases, defective mitophagy is thought to contribute to organ-specific and systemic inflammatory diseases (Zhao et al., 2018), cancer development and/or progression (Drake et al., 2017), and potentially aging (López-Otín et al., 2016). The removal of damaged mitochondria by mitophagy maintains normal cellular metabolism, reduces mitochondrial generation of ROS that triggers inflammation and genotoxic stress, and prevents mitochondrial release of pro-apoptotic factors. Thus, maintenance of proper mitochondrial function by mitophagy is crucial for cellular and organismal health. Other forms of selective autophagy (including xenophagy) likely operate in a manner analogous to mitophagy in that the mechanisms by which they regulate physiology and disease are a function of the normal ''duties'' of their substrate and the ensuing pathological consequences of abnormal substrate accumulation (see Table 2).

Our expanding knowledge of the mechanisms and physiological functions of selective autophagy may open up new—albeit unchartered—pathways for drug discovery. Knockdown of the mitochondrial deubiquitinase USP30 rescues mitophagy defects and disease in flies with pathogenic mutations in Parkin (Bingol et al., 2014), suggesting a potential role for the inhibition of DUBs that target selective autophagy E3 ligases in the treatment of Parkinson's and other diseases. Indeed, novel highly selective inhibitors of USP30 that accelerate mitophagy have recently been reported (Kluge et al., 2018). As phosphorylation of substrates is also a common mechanism involved in selective autophagic targeting, it may be possible to activate specific kinases to enhance selective autophagy. Potentially, it may also be possible to develop novel strategies to attach high-affinity LIR domains selectively to harmful cargo so that they can be more efficiently captured by an LC3-decorated nascent autophagosome.

Autophagy Regulation: A Nexus for Therapeutics?

Autophagy was originally studied in yeast and mammalian cells as a nutrient stress-response pathway. During the past decade, we have dramatically expanded our knowledge of autophagy regulation, particularly the spectrum of physiological

and pathophysiological stimuli that control autophagy, the mechanisms that regulate the activity of the core autophagy proteins (Grumati and Dikic, 2018), and the interconnectivity of autophagy with other cellular stress-response pathways (Kroemer et al., 2010). These concepts have been reviewed elsewhere; here, we highlight selected aspects relevant to physiology and disease.

Post-translational protein modifications such as phosphorylation, ubiquitination, and acetylation play a central role in coordinating the activity of ATG proteins. In most cases, the upstream kinases/phosphatases, ubiquitin ligases/DUBs, and acetyltransferases simultaneously modify both ATG proteins and proteins involved in other cellular stress-response pathways that are co-regulated with autophagy. As a result, pharmacological targeting of these enzymes will elicit broad-based modulation of multiple intertwined stress-response pathways. Depending on the enzyme and its substrates, such nonspecific targeting may be harmful in some instances and useful in others.

One important example is the stimulation of AMPK, a low-energy-sensing kinase activated by ATP depletion, which phosphorylates multiple proteins to both stimulate catabolic pathways (including autophagy) and restrain anabolic pathways (including mTORC1 signaling), thereby ensuring limitation of ATP consumption and generation of new ATP via breakdown of metabolic products (Herzig and Shaw, 2018). In recent years, AMPK has been shown to not only activate autophagy through inhibition of mTORC1 but also directly phosphorylate several ATG proteins, including ULK1, ATG9A, Beclin 1, and VPS34 (Egan et al., 2011; Kim et al., 2013a). In addition, AMPK promotes mitophagy through effects on ULK1 and stimulates TFEB-dependent activation of the CLEAR (coordinated lysosomal expression and regulation) network of genes required for autophagy (Herzig and Shaw, 2018). This pro-autophagic activity of AMPK occurs concurrently with its effects on mitochondrial homeostasis and on lipid and glucose metabolism.

AMPK activation may underlie the beneficial effects of metformin, a drug widely prescribed for the treatment of diabetes (Herzig and Shaw, 2018). Metformin activates AMPK indirectly through mitochondrial depletion of ATP, and direct AMPK activators that yield effects similar to metformin are in preclinical development. The extent to which autophagy stimulation contributes to beneficial effects of AMPK activation in mice or patients is not known, but it seems likely that autophagy represents a critical part of an AMPK-activated hub that protects against various metabolic diseases, including diabetes, obesity, and non-alcoholic fatty liver disorders as well as certain cancers and aging-related phenotypes. In *Drosophila*, deficiency of the Beclin 1 ortholog (ATG6) impairs the ability of metformin to prevent intestinal stem cell aging (Na et al., 2018), and lifespan extension by neuronal AMPK expression requires the fly ULK1 ortholog, ATG1 (Ulgherait et al., 2014). In mice, AMPK upregulation of autophagy is correlated with improved function of aging muscle stem cells (White et al., 2018); additionally, muscle-specific AMPK deficiency results in defective autophagy, fasting-induced hypoglycemia, and aging-associated myopathy (Bujak et al., 2015). In yeast, core *ATG* genes are required for AMPK-mediated lipid droplet degradation and survival during acute glucose deprivation (Seo et al., 2017).

The lysine acetylation/deacetylation of ATG proteins has emerged as a central node of autophagic control regulated by metabolic sensors involved in lipid, glucose, and protein metabolism. Moreover, this control center may function independently from, but intertwined with, AMPK and mTORC1 (Mariño et al., 2014b; Su et al., 2017). During acute nutrient depletion, cells undergo a rapid decrease in levels of cytosolic acetyl coenzyme A (AcCoA), which leads to the deacetylation of cellular proteins (Mariño et al., 2014b). Sirtuin 1 (which is downstream of AMPK) deacetylates multiple ATGs (e.g., ATG5, ATG7, ATG12, Beclin 1, VPS34, LC3) and thereby promotes autophagy, as does reduced activity of the acetyl transferase EP300 (Madeo et al., 2014; Su et al., 2017). Hence, endogenous activators of sirtuin 1 (e.g., nicotine adenine dinucleotide [NAD^+]), endogenous inhibitors of EP300 (e.g., spermidine, a dietary polyamine), and reduced availability of AcCoA (a rate-limiting step for EP300 function) all stimulate autophagy (Madeo et al., 2014).

Compounds that act on these pathways, thereby mimicking the effects of caloric restriction (so-called caloric restriction mimetics), are an active area of investigation, and genetic evidence suggests that autophagy is essential for their beneficial effects *in vivo*. Reservatrol, an indirect sirtuin 1 activator, requires the autophagy machinery for its favorable effects on longevity in nematodes (Morselli et al., 2010). Spermidine-induced autophagy is required for several of its beneficial health effects in model organisms, including lifespan extension in flies, worms, and mice; prevention of cardiac aging in mice; improvement in neuronal function in aging flies; and preservation of myocyte stemness in mice (reviewed in Madeo et al. [2018]). Moreover, caloric restriction mimetics improve anti-tumor immune surveillance and enhance chemotherapy responses in autophagy-competent, but not autophagy-incompetent, mouse tumor allografts (Pietrocola et al., 2016).

Over the past decade, the lysosome—an organelle traditionally viewed as the downstream ''workhorse'' for autophagosomal cargo degradation—has been shown to also play a crucial role in the upstream regulation of autophagy (Napolitano and Ballabio, 2016; Shen and Mizushima, 2014). The nutrient-sensing kinase complex mTORC1 detects both cytosolic and intra-lysosomal amino acids through distinct mechanisms to inhibit autophagy (Saxton and Sabatini, 2017). Amino acids (such as arginine) inside the lysosomal lumen are sensed by the amino acid transporter SLC38A9, which interacts with the lysosomal v-ATPase/Rag/Ragulator complex to activate mTORC1. This both restrains autophagy during baseline conditions and provides feedback inhibition to terminate autophagic responses to acute nutrient depletion. mTORC1 activation in the fed state and/or hyperactivation (as a result of mutations in regulatory signals) switches the cell to a state of anabolic growth and energy storage. Although essential for cell growth and proper metabolic regulation, sustained mTORC1 activation at the organismal level is associated with a variety of pathophysiological consequences, including impaired neonatal gluconeogenesis and survival (Efeyan et al., 2013), accelerated age-related decline in pancreatic β cell function (Shigeyama et al., 2008), late-onset muscle atrophy (Castets et al., 2013), altered lipogenesis and adipogenesis (Lee et al., 2016), immune suppression, epileptic seizures and autistic traits, tumorigenesis,

and aging (Saxton and Sabatini, 2017). While in some cases, impaired induction of autophagy has been documented in mice with hyperactive mTORC1 signaling and is postulated to contribute to pathological phenotypes (e.g., impaired neonatal gluconeogenesis, late-onset muscle atrophy), the precise role of autophagy inhibition in most diseases associated with mTORC1 signaling remains unknown. There has been some interest in using US Food and Drug Administration [FDA]-approved mTOR inhibitors for the treatment of neurodegenerative disorders that may benefit from autophagy induction (Sarkar, 2013). However, the safety and efficacy of using mTOR inhibitors to induce therapeutic autophagy is uncertain, given the broad range of essential catabolic functions regulated by mTORC1 along with the lack of full specificity of existing agents to target mTORC1 rather than mTORC2 (which functions primarily as an effector of insulin/PI3K signaling).

Both AMPK and mTORC1 participate (in opposite directions) in a signaling axis that links autophagy, the lysosome, and the transcription factor EB (TFEB) and related family members. During the acute response to autophagic stimuli, transcriptional activation is not required, as evidenced by the observation that enucleated cells (cytoplasts) undergo autophagy (Morselli et al., 2011). However, sustained autophagy requires TFEB, a transcription factor that (when inactive) binds to Ragulator at the lysosomal membrane, is phosphorylated by mTORC1, and is retained in the cytoplasm by 14-3-3 proteins. Following mTORC1 inhibition, TFEB dephosphorylation releases it from the cytoplasm, allowing its nuclear translocation and subsequent activation of the CLEAR gene network, which includes genes encoding lysosomal hydrolases, lysosomal v-ATPase pumps, lysosomal regulators and autophagy regulators (Puertollano et al., 2018). As noted above, AMPK also activates TFEB-dependent gene expression; this occurs through multiple different mechanisms. In addition, a recent study showed that phosphorylation of acetyl-CoA synthetase 2 (ACSS2) promotes its transport into the nucleus, where it binds to TFEB and favors the acetylation of histone H3 residues within the promoters of TFEB target genes (Li et al., 2017b).

In addition to TFEB, other transcription factors from the same family (such as micropthalmia-associated transcription factor [MITF] and TFE3) (Perera et al., 2015) or from other families (e.g., FOXO3A, HSF1, or TP53) stimulate autophagy (Cai et al., 2018; Kenzelmann Broz et al., 2013). Bromodomain 4 (BRD4), a transcription factor that represses autophagy and lysosomal genes, is displaced from chromatin in response to starvation by a signaling cascade involving an AMPK-SIRT1 axis (Sakamaki et al., 2017). Thus, multiple known (and probably yet-to-be-identified) transcription factors regulate the synthesis of genes required for autophagy (including both the formation of the autophagosome and degradation of its contents by lysosomes). Not surprisingly, the activity of these transcription factors is tightly regulated by numerous signaling factors that also regulate core ATG protein function by post-translational modifications.

Modulation of the activity of TFEB, a master regulator of both lysosomal biogenesis and autophagy, has emerged as a potential therapeutic strategy. Conceptually, this approach is attractive, since limitations in lysosomal numbers and function either occur intrinsically as part of many rare, but devastating, difficult-to-treat, primary diseases (such as lysosomal storage disorders [LSDs]) or are acquired during the progression of diseases associated with the clearance of toxic aggregates progress (such as Huntington's, Parkinson's, and Alzheimer's diseases and tauopathies). In mice, TFEB overexpression ameliorates several LSDs, neurodegenerative diseases, and α1-antitrypsin deficiency, and it also promotes lipophagy, thereby reducing obesity and associated metabolic syndrome (Napolitano and Ballabio, 2016). The mechanisms by which TFEB overexpression partially corrects lysosomal malfunction in LSDs are not fully understood but may involve induction of lysosomal exocytosis for the secretion of undigested material.

One potential obstacle to strategies for enhancing TFEB family activity is the risk of tumorigenesis associated with constitutive activation (e.g., renal clear cell carcinoma with TFEB and pancreatic cancer with MITF, TFE3, and TFEB) (Napolitano and Ballabio, 2016). While MITF/TFE3/TFEB-dependent autophagy-lysosomal activation is thought to sustain metabolic reprogramming in pancreatic cancer cells by maintaining intracellular amino acid pools (Perera et al., 2015), further genetic investigations are warranted to confirm that *ATG* genes are involved in these effects. Moreover, enhanced activity of BRD4, a transcriptional repressor of autophagy, drives another type of cancer, NUT midline carcinoma (Sakamaki et al., 2017), suggesting that the effects of transcriptional regulators of autophagy on tumorigenesis may be cell-type specific. It is unclear whether specific subsets of the TFEB-regulated gene network can be induced to avoid genes that contribute to tumorigenesis without losing beneficial effects on the autophagy-lysosomal pathway. An alternative strategy is to activate TFEB on an intermittent basis and/or for limited periods to avoid potential oncogenic effects.

Intriguingly, one of the most widely used medications in the world—aspirin—has been reported to upregulate TFEB in brain cells (via activation of PPARα), induce lysosomal biogenesis, and decrease amyloid plaque pathology in a mouse model of Alzheimer's-like disease (Chandra et al., 2018). Aspirin (and its active metabolite salicylate) also induces autophagy via inhibition of the acetyltransferase EP300 (Pietrocola et al., 2018) and via AMPK activation/mTORC1 inactivation (Din et al., 2012). However, there is as of yet no direct genetic evidence that autophagy contributes to the health benefits of aspirin.

Highly specific activation of autophagy may be possible through strategies that enhance the activity of the upstream components in the core autophagy pathway, i.e., the ULK1 serine/threonine kinase complex and/or Beclin 1/VPS34 lipid kinase complexes. As a key allosteric regulator of VPS34 lipid kinase activity, Beclin 1 activity is tightly regulated by multiple post-translational modifications (ubiquitination, acetylation, phosphorylation), which govern its stability, heterodimeric binding to ATG14 or UVRAG, homodimerization in an inactive form, and/or binding to negative regulators, such as Bcl-2/Bcl-xL (Grumati and Dikic, 2018; Levine et al., 2015). Diverse stress kinases, including AMPK and MAPKAPK2/3 as well as the upstream ATG protein, ULK1, mediate stimulatory phosphorylations of Beclin 1 (Kim et al., 2013a; Park et al., 2018; Wei et al., 2015). The oncogenic kinases, Akt and EGFR, and the EP300 acetylase inhibit the autophagic activity of Beclin 1; mutation of their target

post-translational sites in Beclin 1 demonstrates that suppression of Beclin 1-dependent autophagy promotes tumor growth in mouse xenograft models (Sun et al., 2015; Wang et al., 2012; Wei et al., 2013). Enhanced proteasome-mediated degradation of Beclin 1 due to decreased binding of the deubiquitinase ataxin 3 may contribute to dysregulated autophagy in cells of patients with polyglutamine-expansion-protein-related diseases, such as Huntington's and spinocerebellar ataxia type 3 (Ashkenazi et al., 2017).

Disruption of Bcl-2 binding to Beclin 1 represents a central mechanism by which autophagy is activated in response to stress stimuli (such as starvation, exercise, and immune signaling) (He et al., 2012; Wei et al., 2008). This disruption can be triggered by phosphorylation of the BH3 domain of Beclin 1 by DAPK, ubiquitination of the Beclin 1 BH3 domain by the E3 ligase TRAF6, phosphorylation of Bcl-2 by JNK1, or competition by BH3-only proteins (reviewed in Levine et al. [2015]). Mice containing knockin non-phosphorylatable mutations in Bcl-2 that prevent disruption of its binding to Beclin 1 are deficient in starvation- and exercise-induced autophagy, have decreased exercise endurance, and fail to manifest the beneficial effects of exercise on glucose metabolism (He et al., 2012). Conversely, mice with a knockin mutation in Beclin 1 that decreases Bcl-2 binding exhibit increased autophagy and extended lifespan and healthspan, including protection against Alzheimer's-like disease and HER2-mediated breast cancer (Fernández et al., 2018; Rocchi et al., 2017; Vega-Rubín-de-Celis et al., 2018). Thus, disruption of Beclin 1/Bcl-2 binding may be a safe and effective approach to induce autophagy *in vivo*; preclinical studies are in progress to develop agents that act through this mechanism (Chiang et al., 2018).

Cell-penetrating peptides (Tat-Beclin 1) derived from a flexible hinge region of Beclin 1 important for VPS34 membrane association and lipid kinase activity (Rostislavleva et al., 2015) are sufficient to induce autophagy *in vitro* and *in vivo* (Shoji-Kawata et al., 2013). In mice, Tat-Beclin 1 protects against West Nile virus, chikungunya virus, and *E. coli* bacterial infections; lipopolysaccharide-induced cardiac dysfunction; pressure-overload-induced heart failure; hyperammonemia in liver failure and urea cycle disorders; and bone loss in LSDs and in fibroblast growth factor (FGF) deficiency (Bartolomeo et al., 2017; Cinque et al., 2015; Shoji-Kawata et al., 2013; Soria et al., 2018; Sun et al., 2018). It also enhances chemotherapeutic effects of murine cancers in immune-competent mice (Pietrocola et al., 2016), reduces the growth of human HER2-positive breast cancer xenografts in immune-deficient mice (Vega-Rubín-de-Celis et al., 2018), and acts synergistically with erastin to increase animal survival in an orthotopic pancreatic cancer model (Song et al., 2018). In rats, intrahippocampal injection of Tat-Beclin 1 improves long-term spatial memory (Hylin et al., 2018). In a zebrafish model of human polycystic kidney disease, Tat-Beclin 1 ameliorates renal cyst formation (Zhu et al., 2017). Further studies are needed to examine whether Tat-Beclin 1 induces these effects through autophagy, autophagy-independent effects of Beclin 1, or alternative mechanisms. Moreover, precise definition of its mechanism of action may lead to the development of novel small drug-like molecules that mimic its activity. Recent structural advances elucidating the atomic details of the Beclin 1/VPS34 complexes (reviewed in Hurley and Young [2017]) may provide a basis for rational drug design to selectively activate autophagy-specific Beclin 1-associated VP34 lipid kinase activity.

Autophagy in Tissue and Whole-Body Homeostasis

The health of multicellular organisms requires the coordinated regulation of cellular life and death decisions, cell fate determinations, preservation of genomic integrity, immune responses, and metabolic circuitries. The autophagy machinery, via its diverse functions described above (and yet-to-be-discovered mechanisms), plays a crucial role in these processes. Herein, we highlight some recent advances related to the role of autophagy in cell death, preservation of stem cells, tumor suppression, longevity, and defense against metabolic diseases.

Autophagy as a Homeostat

During both routine "housekeeping" and responses to acute stress, cells must find ways to maintain adaptive cytoprotective levels of autophagy while simultaneously avoiding potentially maladaptive levels and/or detrimental effects of autophagy. This balance involves self-control of the levels of autophagy, mechanisms of preventing degradation products from becoming toxic to cells, avoidance of degrading essential cargo, and suppression of unwarranted cell death—which likely is a combined function of the aforementioned processes. Cellular self-titration of levels of autophagy involves multiple different inhibitory feedback loops, including feedback regulation of nutrient-sensing signals by the generation of amino acids, acetyl-CoA, and respiratory substrates (Galluzzi et al., 2014); cytosolic retention of pro-autophagic transcription factors by ATG7 (Simon et al., 2017); and TFEB-mediated activation of mTORC1 (Simon et al., 2017). Cellular toxicity by degradation products may be avoided during autophagy, as evidenced by the observation that the generation of lipid droplets generated by autophagy-dependent dismantling of lipid membranes during starvation-induced autophagy sequesters fatty acids, thereby protecting mitochondria against lipotoxicity and preserving cellular viability (Nguyen et al., 2017). It is not known whether starvation-induced autophagy preferentially induces removal of certain, perhaps aged, structures (and if so, by what mechanisms) or whether it is nonspecific. Mitochondria elongate during starvation, which spares them from the autophagic capture that generally occurs after fission (Gomes et al., 2011). Numerous yet-to-be-discovered mechanisms likely protect mitochondria and other organelles from excessive autophagic capture during stress-induced autophagy.

The aforementioned negative feedback loops restrain autophagy to adaptive (rather than maladaptive) levels, allowing this homeostatic pathway to exert cytoprotective effects during stress, and thereby prevent apoptotic and necroptotic cell death (Mariño et al., 2014a). In addition, *ATG* gene-dependent processes, such as increased plasma membrane localization of the GLUT1 glucose transporter (Roy et al., 2017), may increase the threshold of damage required to kill cells and thereby promote successful organismal adaptation to stress. Promotion of cell survival *in vivo* during stress-induced autophagy may depend on concurrent antagonism of the Na^+,K^+-ATPase pump, which normally consumes a large fraction of the ATP

available to the cell (Kheloufi et al., 2015). Interestingly, during acute bouts of exercise or nutrient limitation (potent physiological stimuli of autophagy that generally do not result in cell death), endogenous cardiac glycosides that target Na^+,K^+-ATPase are upregulated 50- to 500-fold, resulting in decreased cellular ATP consumption (Schoner, 2002).

However, when organisms are pushed beyond physiological limits of energy deprivation, adaptive mechanisms are insufficient to keep cells alive and to prevent tissue damage. In the liver of patients with anorexia nervosa or in neonatal rodents subjected to severe cerebral ischemic injury, a morphologically and genetically distinct form of cell death occurs called autosis, which requires both *ATG* genes and Na^+,K^+-ATPase activity (Kheloufi et al., 2015; Liu et al., 2013b). It is not clear how the cell's major consumer of ATP (i.e., the Na^+,K^+-ATPase pump) and the cell's major mobilizer of ATP-generating substrates during stress conditions (i.e., autophagy) interact to regulate life and death decisions of the cell. However, this interaction may represent a fundamental energy homeostatic mechanism that becomes pathologic during different types of ischemic conditions.

Another recently identified bona fide form of autophagic cell death (i.e., demonstrating a genetic requirement for *ATG* genes) involves *GBA1*—the gene encoding the lysosomal enzyme, glucocerebrosidase (GCase)—which metabolizes glucosylceramide (GlcCer) to ceramide and glucose. *GBA1* knockdown blocks autophagic cell death in resveratrol-treated lung cancer cells *in vitro* and developmental midgut death in *Drosophila in vivo* (Dasari et al., 2017). In humans, homozygous *GBA1* mutations lead to Gaucher's disease, a lysosomal storage disorder, while heterozygous mutations are the most important risk factor for Parkinson's disease (Schapira, 2015). Interestingly, GBA1 deficiency in the brains of flies and mice leads to an accumulation of GlcCer, impaired autophagic-lysosomal flux, α-synuclein aggregate accumulation, and neurodegeneration; these features are similar to those observed in patients with Parkinson's disease (Aflaki et al., 2017).

Thus, levels of cellular GCase are crucial for homeostasis; insufficient GCase activity results in a defect in autophagic-lysosomal function and neurodegeneration, whereas excessive GCase activity results in autophagic cell death. It is not yet known how GCase levels are physiologically titrated or how an excess of GCase activity converts adaptive autophagy into lethal autophagy. One possibility is that death occurs as a result of the generation of a metabolic intermediate, sphingosine, which affects lysosomal membrane permeabilization, as lysosome-membrane permeabilization by lysosomal-targeted Bax facilitates autophagic cell death in Bax/Bax knockout murine embryonic fibroblasts (Karch et al., 2017). Future studies are needed to determine the precise mechanisms that convert autophagy from a pro-survival to a cell-death pathway, to specifically delineate the role of autophagic cell-death pathways in pathophysiology, and to devise therapeutic strategies to block such death *in vivo*.

Autophagy in Stemness

Accumulating evidence indicates that autophagy is required for stem cell quality control (especially via mitophagy-mediated reduction in ROS levels), energy homeostasis, metabolic reprogramming, and the preservation of fitness. This requirement has multiple disease-related implications, depending on the type of stem cell (e.g., embryonic, adult, cancer) (see Boya et al. [2018] for a detailed recent review). In general, autophagy functions in adult stem cells, including muscle stem cells (satellite cells), hematopoietic stem cells (HSCs), and neural stem cells (NSCs), as a mechanism to prevent exhaustion and aging and to promote quiescence, allowing either self-renewal or differentiation (as needed). Conditional Atg7 deletion leads to a reduction of the muscle satellite cell pool in young mice and hallmarks of premature muscle aging (senescence and DNA damage), and autophagy activation reverses senescence and restores regenerative functions in satellite cells in aged animals (García-Prat et al., 2016). Loss of Atg12 in HSCs impairs maintenance of HSC quiescence and stemness (Ho et al., 2017). Loss of FIP200 results in a progressive loss of NSCs and reduced neurogenesis in the adult brain (Wang et al., 2013). Thus, upregulation of autophagy may help stimulate muscle regeneration in sarcopenia, prevent late-onset diseases associated with immune cell senescence, and/or promote adult neurogenesis.

Several studies suggest a role for autophagy in the reprogramming of somatic cells to generate induced pluripotent stem cells (iPSCs) (Boya et al., 2018). The precise mechanisms by which autophagy functions in pluripotency reprogramming are debated but may involve degradation of transcription factors, ability to sustain glycolytic metabolism (which favors stemness), degradation of mitochondria and other organelles, and mitophagy-mediated limitation of cellular ROS production. While the deletion of core *ATG* genes or loss of PINK1-dependent mitophagy impairs the reprogramming process (Boya et al., 2018), it is not known whether autophagy upregulation improves the efficiency of pluripotent reprogramming for the optimization of stem cell-based therapies.

Additionally, autophagy is important in the origin, differentiation, and survival of cancer stem cells (CSCs), a unique niche that (similar to other stem cell populations) has the potential for self-renewal but also has the potential for malignancy, initiation of tumor metastasis, and enhanced chemotherapy resistance (Pattabiraman and Weinberg, 2014). CSC formation is enhanced in regions of tumors that are hypoxic, nutrient depleted, and acidic—conditions that favor enhanced autophagy—and CSCs usually have higher rates of basal autophagy than non-cancer stem cells (Boya et al., 2018). Knockdown of core *ATG* genes in breast CSCs impairs their self-renewal *in vitro* and impairs their growth when xenografted into mice (Boya et al., 2018). This observation has raised interest in the therapeutic potential of autophagy inhibition of CSCs. However, it is not clear how such cells could be selectively targeted *in vivo*, and systemic inhibition of autophagy, even in adult mice, is associated with multiple severe toxicities, including multi-organ degeneration and fatal hypoglycemia during fasting (Karsli-Uzunbas et al., 2014). Moreover, this concept is further complicated by the plasticity of CSCs, i.e., the ability to convert to non-cancer stem cells and vice versa. In addition, the depletion of autophagy in HSCs favors the expansion of acute myeloid progenitor cells and development of frank hematological malignancies (Auberger and Puissant, 2017). Given these complexities, it may be premature to consider targeting autophagy in CSCs as an anti-cancer strategy.

Autophagy in Genomic Stability and Tumor Suppression

Besides eliminating ROS-producing dysfunctional mitochondria that are potentially mutagenic, autophagy may promote genomic stability through several additional mechanisms. In the setting of impaired autophagy, the accumulation of the autophagy adaptor and substrate p62/SQSTM1 (1) inhibits the E3 ligase RNA168 that is essential for histone and chromatin ubiquitination and DNA damage responses (Wang et al., 2016) and (2) activates NRF2 transcription factor of MDM2, which acts through p53-dependent and p53-independent mechanisms to abrogate normal cell-cycle checkpoints (Todoric et al., 2017). Genetic inhibition of autophagosome formation or lysosomal function results in a failure to degrade the small GTPase, RHOA, which leads to cytokinesis failure, multinucleation, and aneuploidy (Belaid et al., 2013). Selective autophagic removal of micronuclei and endogenous retrotransposons may also promote genomic stability (Table 2). Intriguingly, DNA damage repair pathway genes are involved in the selective autophagy of ROS-generating organelles, including pexophagy (e.g., ATM kinase [Zhang et al., 2015a]) and mitophagy (e.g., Fanconi anemia proteins [Sumpter et al., 2016]). Thus, there may be selective pressure for nuclear DNA damage pathways and autophagy proteins to function at multiple levels to protect the genome, both in the cytoplasmic removal of dysfunctional organelles that threaten genomic integrity and, more directly, in the regulation of nuclear events that maintain genomic stability.

The role of autophagy in promoting genomic stability is consistent with its role in tumor suppression. One of the most frequent genetic alterations in sporadic human breast and ovarian cancer is the allelic loss of *beclin 1*, which is associated with more aggressive cancers and worse patient survival (independently of allelic loss of the nearby tumor suppressor *BRCA1*) (Liang et al., 1999; Tang et al., 2015; Valente et al., 2014). Mice lacking a copy of *beclin 1* develop spontaneous malignancies, demonstrating that it is a haploinsufficient tumor suppressor gene (Cicchini et al., 2014; Qu et al., 2003; Yue et al., 2003), and allelic loss of *beclin 1* in immortalized mouse mammary epithelial cells promotes mammary tumorigenesis, DNA damage, and genomic instability *in vivo* (Karantza-Wadsworth et al., 2007). Similarly, partial autophagy defects in other mouse models (*Ambra1*$^{+/-}$, *Atg4c*$^{-/-}$, *Sh3glb1*$^{-/-}$, and mosaic *Atg5*$^{-/-}$) are associated with an increased incidence of spontaneous or chemically induced tumors (Rybstein et al., 2018). In mice, loss of the mitophagy receptor, BNIP3, accelerates progression to metastatic breast cancer (Chourasia et al., 2015), and loss of Parkin results in spontaneous liver tumors, increased radiation-induced lymphoma, enhanced colorectal adenoma development in Apc mutant mice and accelerated KRas-driven pancreatic tumorigenesis (Drake et al., 2017; Li et al., 2018a; Poulogiannis et al., 2010). In patients, PARKIN-inactivating mutations are observed in glioblastomas, colorectal carcinoma, and other malignancies (Drake et al., 2017). Numerous oncogenic mutations suppress autophagy through mTORC1 activation (e.g., activating mutations in Akt/class I PI3K, PTEN loss, LKB1 loss), ULK1 and Parkin inhibition (e.g., cytoplasmic accumulation of TP53 mutant proteins), and/or inhibition of the activity of Beclin 1/class III PI3K complex (e.g., Akt, EGFR, HER2, Bcl-2 amplification or activation) (Levine et al., 2015; Rybstein et al., 2018; Vega-Rubín-de-Celis et al., 2018).

Autophagy has additional cell-autonomous and non-cell-autonomous functions in tumor suppression. At the cell-autonomous level, together with its promotion of genomic instability, autophagy degrades the nuclear lamina (through an interaction with LC3 and lamin B) to promote oncogene-induced senescence (Dou et al., 2015), and it negatively regulates inflammatory signaling, which is a strong oncogenic driver (Zhong et al., 2016). It has been proposed that deregulated inflammatory signaling due to defective autophagy may represent a common pro-oncogenic pathway for several cancer risk factors, including obesity, aging, alcohol abuse, chronic infections, and ATG16L1 deficiency/Crohn's disease (Zhong et al., 2016).

At the non-cell-autonomous level, autophagy acts to suppress tumor-promoting inflammatory signaling and to enhance anti-cancer immunity in myeloid cells in the tumor microenvironment. Autophagy in cancer cells is important for cross-presentation as well as facilitating the release of tumor antigens from dying cells and increasing their extracellular availability (Ma et al., 2013). The phenomenon of autophagy-dependent "immunogenic cell death" also leads to the release of ATP and other danger-associated molecular patterns (Michaud et al., 2011), enhancing anti-tumor cytotoxic T lymphocyte (CTL) responses and contributing to the anti-cancer efficacy of chemotherapy and radiation therapy (Galluzzi et al., 2017b). Interestingly, the incidence of KRAS-induced non-small lung cancer is increased by genetic inhibition of autophagy and reduced by autophagy induction through a mechanism that requires T cell-dependent anti-tumor immunity (Pietrocola et al., 2016). Taken together, autophagy acts both in cancer cells and myeloid cells to dampen pro-tumorigenic inflammation and to augment adaptive immunity that curtails cancer growth and progression. It is not yet known whether autophagy induction will act synergistically with immune checkpoint inhibitors to boost anti-cancer therapeutic responses.

In parallel with delineation of mechanisms of autophagy in tumor suppression and the promotion of anti-tumor immunity, numerous reports have demonstrated pro-tumorigenic roles of autophagy, primarily in cancers driven by KRAS that require high cellular metabolic activity to sustain survival (Kimmelman and White, 2017). The pro-tumorigenic effects are generally believed to result from the ability of autophagy to sustain tumor cell survival during metabolic stress in a cell-intrinsic fashion and/or in a cell-extrinsic fashion via the provision of nutrients to malignant cells by autophagy in stromal cells in the tumor microenvironment (Katheder et al., 2017; Kimmelman and White, 2017; Yang et al., 2018). These observations have piqued interest in developing autophagy inhibitors for treating certain cancers, a concept that has been explored in mice using two principal approaches: (1) tissue-specific or whole-body-inducible deletion of *ATG* genes and (2) lysosomotropic agents such as a chloroquine and hyxdroxychloroquine that inhibit autophagic flux (along with other pharmacological effects). While both approaches reduce KRAS-driven tumor growth in mice (Kimmelman and White, 2017), *ATG* gene deletion results in inflammation and/or destruction of the organ (i.e., in pancreatic-specific or lung-specific knockouts) or in multisystem degeneration (in whole-body knockouts) (Guo et al., 2013; Karsli-Uzunbas et al.,

2014; Rosenfeldt et al., 2013). Furthermore, an extensive examination of the effects of chloroquine on a panel of KRAS mutant tumors failed to show any *ATG* gene-dependent growth inhibition (Eng et al., 2016). Thus, despite the crucial role of autophagy in malignant cells and stromal cells in promoting tumor growth, conclusive data are lacking to support autophagy inhibition as a viable therapeutic approach, although a recent study of KRAS-driven pancreatic cancer using only mosaic genetic inhibition of autophagy may suggest efficacy with tolerable toxicity (Yang et al., 2018). This issue is further complicated by the aforementioned multiple roles of autophagy in tumor suppression and anti-tumor immunity, along with emerging evidence that autophagy inhibition may promote tumor metastasis (reviewed in Dower et al. [2018]).

Autophagy in Metabolic Diseases

Growing evidence implicates functional defects in autophagy in various metabolic disorders, including obesity, diabetes, atherosclerosis, and non-alcoholic fatty liver disease (NAFLD) (reviewed in Ueno and Komatsu [2017]; Zhang et al. [2018a]). While these disorders involve genetic and epigenetic factors, excess caloric intake and decreased physical activity are principal driving forces, both of which suppress autophagy. Although there are divergent reports of whether autophagy is enhanced or suppressed in obesity, the preponderance of mouse genetic data indicate that decreased autophagy facilitates the transition from obesity to diabetes and increases the risk of atherosclerosis and NAFLD. Specifically, mice with whole-body partial mutation or tissue-specific (liver or pancreas) deletion of *ATG* genes or *TFEB* gain more weight when fed a high-fat diet and have an increased propensity to develop systemic inflammation, diabetes, and hepatic steatosis (Fernández et al., 2017; Jung et al., 2008; Lim et al., 2014; Settembre et al., 2013a; Singh et al., 2009). In addition, mice with macrophage-specific deletion of *Atg5* are more prone to the development of atherosclerotic plaques (Liao et al., 2012; Razani et al., 2012). In humans, genetic variants of *IRGM1*, a gene required for assembly and activation of the autophagy machinery, are associated with increased risk of NAFLD (Lin et al., 2016). Moreover, patients with NAFLD have elevated hepatic levels of Rubicon, an inhibitor of Beclin 1/VPS34 PI3KC3 activity, and hepatocyte-specific knockout of Rubicon protects mice against high-fat-diet-induced impaired autophagy and steatosis (Tanaka et al., 2016). Interestingly, ethanol exposure also inhibits hepatocyte lipophagy by inactivating Rab7 (Schulze et al., 2017), raising the question of whether defective autophagy (lipophagy) may also contribute to alcoholic fatty liver disease.

The precise mechanisms by which deficient autophagy (and *ATG* gene functions) promote obesity and its metabolic complications are complex and may involve a variety of cell-intrinsic effects (e.g., nutrient metabolism; mitochondria, peroxisome, ER, and lipid droplet homeostasis), cell-extrinsic effects (e.g., release of pro-inflammatory cytokines by aberrant inflammasome activation), and potentially, lack of feedback inhibition of insulin and mTORC1 signaling pathways. The mechanisms by which autophagy is inhibited during obesity are not well understood but may involve a combination of abnormal lysosomal function in cells with lipid accumulation (Koga et al., 2010) as well as dysregulated endocrine signaling (Zhang et al., 2018a). Autophagy is normally tightly regulated by neuroendocrine signals that are decreased (e.g., insulin and insulin-like growth factors) or increased (e.g., glucagon, fibroblast growth factor 21 [FGF21]) during fasting, and the initiation of and cellular response to these signals are commonly dysregulated in obesity. In mice, deficiency of the fasting hormone FGF21 impairs TFEB activation in hepatocytes, resulting in defective autophagic-lysosomal function and increased lipid accumulation, demonstrating a nutrient-sensing hormonal link between the FGF21-TFEB signaling axis, lysosomal function, and lipid metabolism (Chen et al., 2017). Interestingly, not only do neuroendocrine signals regulate autophagy, but *ATG* genes may act within subpopulations of neurons to regulate metabolism and feeding behavior. Genetic ablation of certain *ATG* genes in hypothalamic proopiomelanocortin neurons results in adiposity, glucose intolerance, and hyperphagia (Coupé et al., 2012; Malhotra et al., 2015; Quan et al., 2012). Postulated (and potentially non-autophagic) mechanisms involve leptin resistance as well as defects in the unconventional secretion of α-melanocyte-stimulating hormone.

Further studies are needed to determine whether general inducers of autophagy, specific activators of lipophagy, and/or regulators of anti-obesogenic CNS functions of *ATG* genes may be useful in reducing the morbidity and mortality due to obesity and its associated metabolic disorders. At least in mice, nutritional interventions and physical exercise exert favorable metabolic effects through *ATG* gene-dependent mechanisms. The benefits of intermittent fasting on high-fat-diet-induced loss of pancreatic cells are blocked in autophagy-deficient *Lamp2a*$^{-/-}$ and *Becn1*$^{+/-}$ mice (Liu et al., 2017). Moreover, the benefits of prolongation of the intermeal time interval (i.e., feeding mice an isocaloric diet twice a day) on adiposity, lipid levels, gluconeogenesis, and age/obesity-associated metabolic defects are impaired in animals with knockout of *Atg7* in different organs (proopiomelanocortin neurons, hepatocytes, white adipose tissue, skeletal muscle) (Martinez-Lopez et al., 2017). The ability of chronic exercise to protect against HFD-induced glucose intolerance is compromised in mice that cannot increase autophagy by virtue of a knockin mutation in Bcl-2 that prevents its disruption from Beclin 1 (He et al., 2012). Physical exercise induces TFEB translocation into muscle fiber nuclei, allowing muscle to adapt by changes in the expression of glucose transporters, glycolytic enzymes, and other metabolism-relevant genes (Mansueto et al., 2017). Whether TFEB activation is causally involved in exercise-induced autophagy induction remains to be explored, but its dual role in coordinating insulin sensitivity and glucose homeostasis during exercise and as a master regulator of autophagic-lysosomal function is intriguing. Thus, lifestyle interventions (e.g., dietary and exercise) that are important interventions in preventing metabolic disease may exert such effects, at least in part, through autophagy.

Autophagy in Longevity

Genetic studies using yeasts, worms, flies, and mice demonstrate the *ATG* genes are required for lifespan extension requirement in caloric restriction, loss-of-function insulin signaling, and other conserved longevity paradigms (reviewed in Hansen et al. [2018]). Systemic autophagy induction exerts anti-aging effects in worms, flies, and mice (López-Otín et al., 2016), and

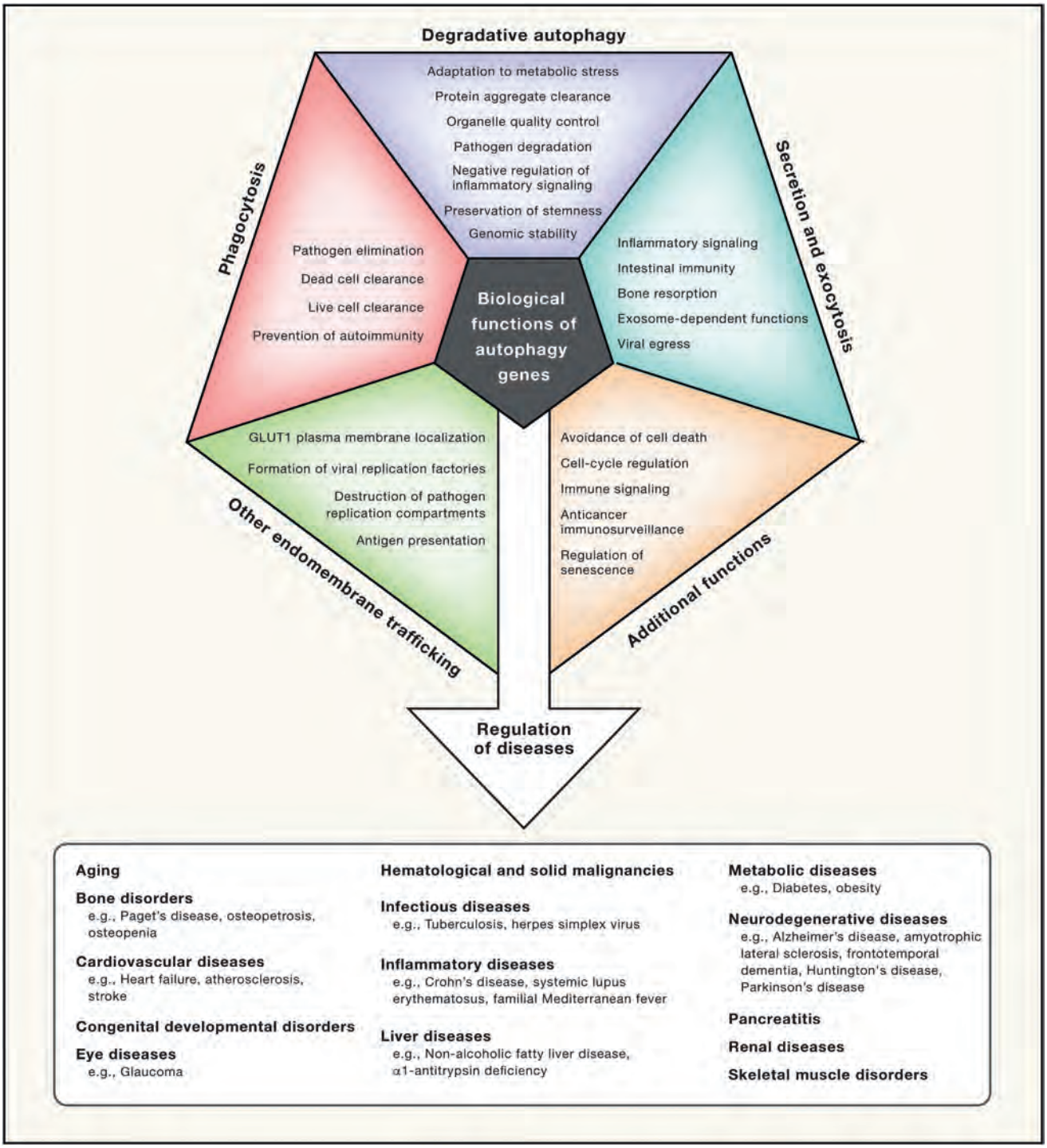

Figure 3. Diverse Biological Functions of Autophagy Genes Contribute to Their Roles in the Regulation of Mammalian Disease
Shown are the major known biological functions of *ATG* genes and the broad categories of diseases that they regulate as predicted based on mouse experimental data and human genetic associations. Below major disease categories, some representative specific diseases are noted. Many other examples exist but are not shown due to space limitations.

genetically engineered mice with constitutively increased autophagy have extended lifespan and improved healthspan (e.g., leanness, increased insulin sensitivity, improved muscle function, reduced cardiac and renal fibrosis, and decreased age-related spontaneous tumorigenesis) (Fernández et al., 2018; Pyo et al., 2013). Interestingly, the offspring of people with

exceptional longevity have enhanced activation-induced T cell autophagy and immune function compared to age-matched controls (Raz et al., 2017). Autophagy may prevent aging through improved organellar quality control and homeostasis (e.g., via selective autophagy pathways such as mitophagy, lipophagy, lysophagy, aggrephagy), enhanced insulin sensitivity, maintenance of stemness, and promotion of genomic stability. Interestingly, tissue-specific autophagy in certain tissues (e.g., in the muscle, intestine, and brain) may also exert favorable effects on longevity, potentially by modulating a range of inter-tissue interactions (Hansen et al., 2018). It is possible that *ATG* genes may have autophagy-independent effects that promote longevity; for example, their roles in secretion and exocytosis might contribute to inter-tissue effects.

Autophagy gene expression and lysosomal function decline with aging in a range of tissues in worms, flies, and mammals (including in human brains), resulting in an age-related decline in autophagic capacity (Hansen et al., 2018). This age-related decline likely contributes both to the aging process itself as well as the development of age-related diseases such as neurodegenerative diseases and cancer. Aside from autophagy inhibition produced by obesity, it is not known what factors contribute to this age-related decline. The molecular mechanisms underlying age-related declines in distinct steps in the autophagic-lysosomal pathway is a fascinating area of future autophagy research.

Concluding Remarks

Autophagy genes function in diverse cell biological pathways, not only in autophagy but also in other processes, to exert widespread physiological functions that protect mammals against aging and a broad range of medically important diseases (Figure 3). Accordingly, a large spectrum of mutations in genes required for autophagy-related pathways have now been implicated in the pathogenesis of human diseases (Table 1).

Some general mechanisms of disease pathogenesis emerge from these links: (1) mutations in genes that regulate mitophagy, such as PARKIN and PINK1, are causally linked to hereditary forms of Parkinson's disease (and also observed in some cancers), suggesting a crucial role for the consequences of impaired mitophagy (e.g., cellular ROS accumulation, mitochondrial DNA accumulation provoking cGAS/STING-dependent inflammatory signaling); (2) mutations in genes encoding autophagy adaptor proteins or their activating kinases (e.g., p62/SQSTM1, optineurin, TBK) contribute to familial forms of amyotrophic lateral sclerosis, frontotemproal dementia, and primary open glaucoma, implying a role for deficient selective autophagy in their pathogenesis; (3) mutations in genes that disrupt lysosomal function perturb autophagy and contribute to lysosomal storage disorders (including those with CNS and bone manifestations), Alzheimer's disease, and Parkinson's disease; (4) mutations in genes that disrupt autophagolysosomal fusion are often associated with congenital neurodevelopmental disorders; (5) mutations in genes that result in the accumulation of excess protein cargo (e.g., polyglutamine expansion proteins, presenilin 1, amyloid precursor protein, αB-crystallin, α1-anti-trypsin) exceed the turnover capacity of autophagy, leading to end-organ proteotoxicity and degeneration; (6) hypomorphic mutations in core autophagy or selective autophagy machinery increase the risk of cancer; (7) dysregulated inflammatory signaling (as a result of defective mitophagy and enhanced inflammasome activation and/or cGAS/STING-mediated interferon signaling) may represent a common downstream event that contributes to diseases that are associated with mutations in the autophagy pathway (e.g., Crohn's disease, Parkinson's disease, SLE); (8) specific disorders, such as Crohn's disease, are associated with several different mutations/polymorphisms in genes (e.g., *ATG16L1*, *CALCOCO2*/*NDP62*, *GPR65*, *IRGM*, *LRRK2*, *NOD2*) that simultaneously compromise intertwined pathways (e.g., bacterial autophagy, inflammasome regulation, secretion of antimicrobial peptides by Paneth cells) that govern their pathological and clinical manifestations. These genetic links illustrate the wide-ranging impact of autophagy-related pathways on distinct cell types and homeostatic processes.

Therapeutic interventions may aim to restore the wild-type function of the mutated protein, to reverse the specific defects or downstream pathogenetic consequences caused by the gene mutation, and/or to broadly upregulate autophagic activity and lysosomal function. Preclinical studies in animal models with mutations in genes that impair autophagy and lysosomal function will be necessary to determine the optimal therapeutic approaches for diseases due to defects in autophagy-related pathways. Moreover, the intriguing possibility emerges that selectively enhancing or blocking autophagy-related sub-routines might indirectly influence other sub-routines, thus affecting a therapeutically relevant ecosystem of intersecting pathways involving ATG proteins.

ACKOWLEDGMENTS

The authors thank H. Smith for assistance with manuscript preparation and A. Diehl for expert medical illustration. The work in the authors' laboratories was supported by NIH grants RO1 CA109618 and U19 AI109725 (B.L.), Cancer Prevention Research Institute of Texas (CPRIT) grant RP120718 (B.L.), and Fondation Leducq grant 15CBD04 (B.L., G.K.). G.K. was supported by Ligue contre le Cancer (équipe labelisée); Agence National de la Recherche (ANR) – Projets blancs; ANR under the frame of E-Rare-2, the ERA-Net for Research on Rare Diseases; Association pour la recherche sur le cancer (ARC); Cancéropôle Ile-de-France; Chancelerie des universités de Paris (Legs Poix); Fondation pour la Recherche Médicale (FRM); European Research Area Network on Cardiovascular Diseases (ERA-CVD, MINOTAUR); the European Research Council (ERC); Fondation Carrefour; Institut National du Cancer (INCa); Inserm (HTE); Institut Universitaire de France; the LabEx Immuno-Oncology; the RHU Torino Lumière; the Seerave Foundation; the SIRIC Stratified Oncology Cell DNA Repair and Tumor Immune Elimination (SOCRATE); and the SIRIC Cancer Research and Personalized Medicine (CARPEM). We apologize to all those authors whose work could not be cited due to space limitations.

DECLARATION OF INTERESTS

B.L. is a scientific co-founder of Casma Therapeutics. G.K. is a scientific co-founder of Samsara Therapeutics.

REFERENCES

Abdulrahman, B.A., Abdelaziz, D.H., and Schatzl, H.M. (2018). Autophagy regulates exosomal release of prions in neuronal cells. J. Biol. Chem. *293*, 8956–8968.

Aflaki, E., Westbroek, W., and Sidransky, E. (2017). The complicated relationship between Gaucher disease and Parkinsonism: Insights from a rare disease. Neuron *93*, 737–746.

Akinduro, O., Sully, K., Patel, A., Robinson, D.J., Chikh, A., McPhail, G., Braun, K.M., Philpott, M.P., Harwood, C.A., Byrne, C., et al. (2016). Constitutive autophagy and nucleophagy during epidermal differentiation. J. Invest. Dermatol. *136*, 1460–1470.

Akizu, N., Cantagrel, V., Zaki, M.S., Al-Gazali, L., Wang, X., Rosti, R.O., Dikoglu, E., Gelot, A.B., Rosti, B., Vaux, K.K., et al. (2015). Biallelic mutations in *SNX14* cause a syndromic form of cerebellar atrophy and lysosome-autophagosome dysfunction. Nat. Genet. *47*, 528–534.

Amaravadi, R., Kimmelman, A.C., and White, E. (2016). Recent insights into the function of autophagy in cancer. Genes Dev. *30*, 1913–1930.

Ashkenazi, A., Bento, C.F., Ricketts, T., Vicinanza, M., Siddiqi, F., Pavel, M., Squitieri, F., Hardenberg, M.C., Imarisio, S., Menzies, F.M., and Rubinsztein, D.C. (2017). Polyglutamine tracts regulate beclin 1-dependent autophagy. Nature *545*, 108–111.

Auberger, P., and Puissant, A. (2017). Autophagy, a key mechanism of oncogenesis and resistance in leukemia. Blood *129*, 547–552.

Baixauli, F., López-Otín, C., and Mittelbrunn, M. (2014). Exosomes and autophagy: coordinated mechanisms for the maintenance of cellular fitness. Front. Immunol. *5*, 403.

Barrett, J.C., Hansoul, S., Nicolae, D.L., Cho, J.H., Duerr, R.H., Rioux, J.D., Brant, S.R., Silverberg, M.S., Taylor, K.D., Barmada, M.M., et al.; NIDDK IBD Genetics Consortium; Belgian-French IBD Consortium; Wellcome Trust Case Control Consortium (2008). Genome-wide association defines more than 30 distinct susceptibility loci for Crohn's disease. Nat. Genet. *40*, 955–962.

Bartolomeo, R., Cinque, L., De Leonibus, C., Forrester, A., Salzano, A.C., Monfregola, J., De Gennaro, E., Nusco, E., Azario, I., Lanzara, C., et al. (2017). mTORC1 hyperactivation arrests bone growth in lysosomal storage disorders by suppressing autophagy. J. Clin. Invest. *127*, 3717–3729.

Bartsch, K., Knittler, K., Borowski, C., Rudnik, S., Damme, M., Aden, K., Spehlmann, M.E., Frey, N., Saftig, P., Chalaris, A., and Rabe, B. (2017). Absence of RNase H2 triggers generation of immunogenic micronuclei removed by autophagy. Hum. Mol. Genet. *26*, 3960–3972.

Behrends, C., Sowa, M.E., Gygi, S.P., and Harper, J.W. (2010). Network organization of the human autophagy system. Nature *466*, 68–76.

Bel, S., Pendse, M., Wang, Y., Li, Y., Ruhn, K.A., Hassell, B., Leal, T., Winter, S.E., Xavier, R.J., and Hooper, L.V. (2017). Paneth cells secrete lysozyme via secretory autophagy during bacterial infection of the intestine. Science *357*, 1047–1052.

Belaid, A., Cerezo, M., Chargui, A., Corcelle-Termeau, E., Pedeutour, F., Giuliano, S., Ilie, M., Rubera, I., Tauc, M., Barale, S., et al. (2013). Autophagy plays a critical role in the degradation of active RHOA, the control of cell cytokinesis, and genomic stability. Cancer Res. *73*, 4311–4322.

Biering, S.B., Choi, J., Halstrom, R.A., Brown, H.M., Beatty, W.L., Lee, S., McCune, B.T., Dominici, E., Williams, L.E., Orchard, R.C., et al. (2017). Viral replication complexes are targeted by LC3-guided interferon-inducible GTPases. Cell Host Microbe *22*, 74–85.e7.

Bingol, B., Tea, J.S., Phu, L., Reichelt, M., Bakalarski, C.E., Song, Q., Foreman, O., Kirkpatrick, D.S., and Sheng, M. (2014). The mitochondrial deubiquitinase USP30 opposes parkin-mediated mitophagy. Nature *510*, 370–375.

Boya, P., Codogno, P., and Rodriguez-Muela, N. (2018). Autophagy in stem cells: repair, remodelling and metabolic reprogramming. Development *145*. https://doi.org/10.1242/dev.146506.

Bronson, P.G., Chang, D., Bhangale, T., Seldin, M.F., Ortmann, W., Ferreira, R.C., Urcelay, E., Pereira, L.F., Martin, J., Plebani, A., et al. (2016). Common variants at *PVT1*, *ATG13-AMBRA1*, *AHI1* and *CLEC16A* are associated with selective IgA deficiency. Nat. Genet. *48*, 1425–1429.

Bujak, A.L., Crane, J.D., Lally, J.S., Ford, R.J., Kang, S.J., Rebalka, I.A., Green, A.E., Kemp, B.E., Hawke, T.J., Schertzer, J.D., and Steinberg, G.R. (2015). AMPK activation of muscle autophagy prevents fasting-induced hypoglycemia and myopathy during aging. Cell Metab. *21*, 883–890.

Cabrera, S., Fernández, A.F., Mariño, G., Aguirre, A., Suárez, M.F., Español, Y., Vega, J.A., Laurà, R., Fueyo, A., Fernández-García, M.S., et al. (2013). ATG4B/autophagin-1 regulates intestinal homeostasis and protects mice from experimental colitis. Autophagy *9*, 1188–1200.

Cadwell, K., and Debnath, J. (2018). Beyond self-eating: The control of nonautophagic functions and signaling pathways by autophagy-related proteins. J. Cell Biol. *217*, 813–822.

Cadwell, K., Liu, J.Y., Brown, S.L., Miyoshi, H., Loh, J., Lennerz, J.K., Kishi, C., Kc, W., Carrero, J.A., Hunt, S., et al. (2008). A key role for autophagy and the autophagy gene *Atg16l1* in mouse and human intestinal Paneth cells. Nature *456*, 259–263.

Cai, J., Li, R., Xu, X., Zhang, L., Lian, R., Fang, L., Huang, Y., Feng, X., Liu, X., Li, X., et al. (2018). CK1α suppresses lung tumour growth by stabilizing PTEN and inducing autophagy. Nat. Cell Biol. *20*, 465–478.

Castets, P., Lin, S., Rion, N., Di Fulvio, S., Romanino, K., Guridi, M., Frank, S., Tintignac, L.A., Sinnreich, M., and Rüegg, M.A. (2013). Sustained activation of mTORC1 in skeletal muscle inhibits constitutive and starvation-induced autophagy and causes a severe, late-onset myopathy. Cell Metab. *17*, 731–744.

Chandra, S., Jana, M., and Pahan, K. (2018). Aspirin induces lysosomal biogenesis and attenuates amyloid plaque pathology in a mouse model of Alzheimer's disease via PPARα. J. Neurosci. *38*, 6682–6699.

Chang, M.C., Srinivasan, K., Friedman, B.A., Suto, E., Modrusan, Z., Lee, W.P., Kaminker, J.S., Hansen, D.V., and Sheng, M. (2017). Progranulin deficiency causes impairment of autophagy and TDP-43 accumulation. J. Exp. Med. *214*, 2611–2628.

Chauhan, S., Kumar, S., Jain, A., Ponpuak, M., Mudd, M.H., Kimura, T., Choi, S.W., Peters, R., Mandell, M., Bruun, J.A., et al. (2016a). TRIMs and Galectins globally cooperate and TRIM16 and Galectin-3 co-direct autophagy in endomembrane damage homeostasis. Dev. Cell *39*, 13–27.

Chauhan, S., Mandell, M.A., and Deretic, V. (2016b). Mechanism of action of the tuberculosis and Crohn disease risk factor IRGM in autophagy. Autophagy *12*, 429–431.

Chen, Y., and Yu, L. (2017). Recent progress in autophagic lysosome reformation. Traffic *18*, 358–361.

Chen, S., Wang, C., Yeo, S., Liang, C.C., Okamoto, T., Sun, S., Wen, J., and Guan, J.L. (2016). Distinct roles of autophagy-dependent and -independent functions of FIP200 revealed by generation and analysis of a mutant knock-in mouse model. Genes Dev. *30*, 856–869.

Chen, L., Wang, K., Long, A., Jia, L., Zhang, Y., Deng, H., Li, Y., Han, J., and Wang, Y. (2017). Fasting-induced hormonal regulation of lysosomal function. Cell Res. *27*, 748–763.

Chiang, W.C., Wei, Y., Kuo, Y.C., Wei, S., Zhou, A., Zou, Z., Yehl, J., Ranaghan, M.J., Skepner, A., Bittker, J.A., et al. (2018). High-throughput screens to identify autophagy inducers that function by disrupting Beclin 1/Bcl-2 binding. ACS Chem. Biol. *13*, 2247–2260.

Choi, J., Park, S., Biering, S.B., Selleck, E., Liu, C.Y., Zhang, X., Fujita, N., Saitoh, T., Akira, S., Yoshimori, T., et al. (2014). The parasitophorous vacuole membrane of *Toxoplasma gondii* is targeted for disruption by ubiquitin-like conjugation systems of autophagy. Immunity *40*, 924–935.

Chourasia, A.H., Tracy, K., Frankenberger, C., Boland, M.L., Sharifi, M.N., Drake, L.E., Sachleben, J.R., Asara, J.M., Locasale, J.W., Karczmar, G.S., and Macleod, K.F. (2015). Mitophagy defects arising from BNip3 loss promote mammary tumor progression to metastasis. EMBO Rep. *16*, 1145–1163.

Chu, H., Khosravi, A., Kusumawardhani, I.P., Kwon, A.H., Vasconcelos, A.C., Cunha, L.D., Mayer, A.E., Shen, Y., Wu, W.L., Kambal, A., et al. (2016). Gene-microbiota interactions contribute to the pathogenesis of inflammatory bowel disease. Science *352*, 1116–1120.

Cicchini, M., Chakrabarti, R., Kongara, S., Price, S., Nahar, R., Lozy, F., Zhong, H., Vazquez, A., Kang, Y., and Karantza, V. (2014). Autophagy regulator BECN1 suppresses mammary tumorigenesis driven by WNT1 activation and following parity. Autophagy *10*, 2036–2052.

Cinque, L., Forrester, A., Bartolomeo, R., Svelto, M., Venditti, R., Montefusco, S., Polishchuk, E., Nusco, E., Rossi, A., Medina, D.L., et al. (2015). FGF signalling regulates bone growth through autophagy. Nature *528*, 272–275.

Cipolla, C.M., and Lodhi, I.J. (2017). Peroxisomal dysfunction in age-related diseases. Trends Endocrinol. Metab. *28*, 297–308.

Cirulli, E.T., Lasseigne, B.N., Petrovski, S., Sapp, P.C., Dion, P.A., Leblond, C.S., Couthouis, J., Lu, Y.F., Wang, Q., Krueger, B.J., et al.; FALS Sequencing Consortium (2015). Exome sequencing in amyotrophic lateral sclerosis identifies risk genes and pathways. Science *347*, 1436–1441.

Colecchia, D., Stasi, M., Leonardi, M., Manganelli, F., Nolano, M., Veneziani, B.M., Santoro, L., Eskelinen, E.L., Chiariello, M., and Bucci, C. (2018). Alterations of autophagy in the peripheral neuropathy Charcot-Marie-Tooth type 2B. Autophagy *14*, 930–941.

Cooper, O., Seo, H., Andrabi, S., Guardia-Laguarta, C., Graziotto, J., Sundberg, M., McLean, J.R., Carrillo-Reid, L., Xie, Z., Osborn, T., et al. (2012). Pharmacological rescue of mitochondrial deficits in iPSC-derived neural cells from patients with familial Parkinson's disease. Sci. Transl. Med. *4*, 141ra90.

Corrionero, A., and Horvitz, H.R. (2018). A C9orf72 ALS/FTD ortholog acts in endolysosomal degradation and lysosomal homeostasis. Curr. Biol. *28*, 1522–1535.e5.

Coupé, B., Ishii, Y., Dietrich, M.O., Komatsu, M., Horvath, T.L., and Bouret, S.G. (2012). Loss of autophagy in pro-opiomelanocortin neurons perturbs axon growth and causes metabolic dysregulation. Cell Metab. *15*, 247–255.

Cullup, T., Kho, A.L., Dionisi-Vici, C., Brandmeier, B., Smith, F., Urry, Z., Simpson, M.A., Yau, S., Bertini, E., McClelland, V., et al. (2013). Recessive mutations in *EPG5* cause Vici syndrome, a multisystem disorder with defective autophagy. Nat. Genet. *45*, 83–87.

Dasari, S.K., Bialik, S., Levin-Zaidman, S., Levin-Salomon, V., Merrill, A.H., Jr., Futerman, A.H., and Kimchi, A. (2017). Signalome-wide RNAi screen identifies GBA1 as a positive mediator of autophagic cell death. Cell Death Differ. *24*, 1288–1302.

Deretic, V., and Levine, B. (2018). Autophagy balances inflammation in innate immunity. Autophagy *14*, 243–251.

DeSelm, C.J., Miller, B.C., Zou, W., Beatty, W.L., van Meel, E., Takahata, Y., Klumperman, J., Tooze, S.A., Teitelbaum, S.L., and Virgin, H.W. (2011). Autophagy proteins regulate the secretory component of osteoclastic bone resorption. Dev. Cell *21*, 966–974.

Diao, J., Liu, R., Rong, Y., Zhao, M., Zhang, J., Lai, Y., Zhou, Q., Wilz, L.M., Li, J., Vivona, S., et al. (2015). ATG14 promotes membrane tethering and fusion of autophagosomes to endolysosomes. Nature *520*, 563–566.

Dikic, I., and Elazar, Z. (2018). Mechanism and medical implications of mammalian autophagy. Nat. Rev. Mol. Cell Biol. *19*, 349–364.

Din, F.V., Valanciute, A., Houde, V.P., Zibrova, D., Green, K.A., Sakamoto, K., Alessi, D.R., and Dunlop, M.G. (2012). Aspirin inhibits mTOR signaling, activates AMP-activated protein kinase, and induces autophagy in colorectal cancer cells. Gastroenterology *142*, 1504–1515.e3.

Dou, Z., Xu, C., Donahue, G., Shimi, T., Pan, J.A., Zhu, J., Ivanov, A., Capell, B.C., Drake, A.M., Shah, P.P., et al. (2015). Autophagy mediates degradation of nuclear lamina. Nature *527*, 105–109.

Dower, C.M., Wills, C.A., Frisch, S.M., and Wang, H.G. (2018). Mechanisms and context underlying the role of autophagy in cancer metastasis. Autophagy *14*, 1110–1128.

Drake, L.E., Springer, M.Z., Poole, L.P., Kim, C.J., and Macleod, K.F. (2017). Expanding perspectives on the significance of mitophagy in cancer. Semin. Cancer Biol. *47*, 110–124.

Dreux, M., Gastaminza, P., Wieland, S.F., and Chisari, F.V. (2009). The autophagy machinery is required to initiate hepatitis C virus replication. Proc. Natl. Acad. Sci. USA *106*, 14046–14051.

Dupont, N., Jiang, S., Pilli, M., Ornatowski, W., Bhattacharya, D., and Deretic, V. (2011). Autophagy-based unconventional secretory pathway for extracellular delivery of IL-1β. EMBO J. *30*, 4701–4711.

Duran, J.M., Anjard, C., Stefan, C., Loomis, W.F., and Malhotra, V. (2010). Unconventional secretion of Acb1 is mediated by autophagosomes. J. Cell Biol. *188*, 527–536.

Ebrahimi-Fakhari, D., Saffari, A., Wahlster, L., Lu, J., Byrne, S., Hoffmann, G.F., Jungbluth, H., and Sahin, M. (2016). Congenital disorders of autophagy: an emerging novel class of inborn errors of neuro-metabolism. Brain *139*, 317–337.

Efeyan, A., Zoncu, R., Chang, S., Gumper, I., Snitkin, H., Wolfson, R.L., Kirak, O., Sabatini, D.D., and Sabatini, D.M. (2013). Regulation of mTORC1 by the Rag GTPases is necessary for neonatal autophagy and survival. Nature *493*, 679–683.

Egan, D.F., Shackelford, D.B., Mihaylova, M.M., Gelino, S., Kohnz, R.A., Mair, W., Vasquez, D.S., Joshi, A., Gwinn, D.M., Taylor, R., et al. (2011). Phosphorylation of ULK1 (hATG1) by AMP-activated protein kinase connects energy sensing to mitophagy. Science *331*, 456–461.

Ellinghaus, D., Zhang, H., Zeissig, S., Lipinski, S., Till, A., Jiang, T., Stade, B., Bromberg, Y., Ellinghaus, E., Keller, A., et al. (2013). Association between variants of *PRDM1* and NDP_{52} and Crohn's disease, based on exome sequencing and functional studies. Gastroenterology *145*, 339–347.

Eng, C.H., Wang, Z., Tkach, D., Toral-Barza, L., Ugwonali, S., Liu, S., Fitzgerald, S.L., George, E., Frias, E., Cochran, N., et al. (2016). Macroautophagy is dispensable for growth of KRAS mutant tumors and chloroquine efficacy. Proc. Natl. Acad. Sci. USA *113*, 182–187.

Fernández, A.F., Bárcena, C., Martínez-García, G.G., Tamargo-Gómez, I., Suárez, M.F., Pietrocola, F., Castoldi, F., Esteban, L., Sierra-Filardi, E., Boya, P., et al. (2017). Autophagy couteracts weight gain, lipotoxicity and pancreatic β-cell death upon hypercaloric pro-diabetic regimens. Cell Death Dis. *8*, e2970.

Fernández, A.F., Sebti, S., Wei, Y., Zou, Z., Shi, M., McMillan, K.L., He, C., Ting, T., Liu, Y., Chiang, W.C., et al. (2018). Disruption of the beclin 1-BCL2 autophagy regulatory complex promotes longevity in mice. Nature *558*, 136–140.

Festa, B.P., Chen, Z., Berquez, M., Debaix, H., Tokonami, N., Prange, J.A., Hoek, G.V., Alessio, C., Raimondi, A., Nevo, N., et al. (2018). Impaired autophagy bridges lysosomal storage disease and epithelial dysfunction in the kidney. Nat. Commun. *9*, 161.

Fletcher, K., Ulferts, R., Jacquin, E., Veith, T., Gammoh, N., Arasteh, J.M., Mayer, U., Carding, S.R., Wileman, T., Beale, R., and Florey, O. (2018). The WD40 domain of ATG16L1 is required for its non-canonical role in lipidation of LC3 at single membranes. EMBO J. *37*, e97840.

Franco, L.H., Nair, V.R., Scharn, C.R., Xavier, R.J., Torrealba, J.R., Shiloh, M.U., and Levine, B. (2017). The ubiquitin ligase Smurf1 functions in selective autophagy of *Mycobacterium tuberculosis* and anti-tuberculous host defense. Cell Host Microbe *21*, 59–72.

Fussi, N., Höllerhage, M., Chakroun, T., Nykänen, N.P., Rösler, T.W., Koeglsperger, T., Wurst, W., Behrends, C., and Höglinger, G.U. (2018). Exosomal secretion of α-synuclein as protective mechanism after upstream blockage of macroautophagy. Cell Death Dis. *9*, 757.

Galluzzi, L., Pietrocola, F., Levine, B., and Kroemer, G. (2014). Metabolic control of autophagy. Cell *159*, 1263–1276.

Galluzzi, L., Bravo-San Pedro, J.M., Levine, B., Green, D.R., and Kroemer, G. (2017a). Pharmacological modulation of autophagy: therapeutic potential and persisting obstacles. Nat. Rev. Drug Discov. *16*, 487–511.

Galluzzi, L., Buqué, A., Kepp, O., Zitvogel, L., and Kroemer, G. (2017b). Immunogenic cell death in cancer and infectious disease. Nat. Rev. Immunol. *17*, 97–111.

Ganesan, A.K., Ho, H., Bodemann, B., Petersen, S., Aruri, J., Koshy, S., Richardson, Z., Le, L.Q., Krasieva, T., Roth, M.G., et al. (2008). Genome-wide siRNA-based functional genomics of pigmentation identifies novel genes and pathways that impact melanogenesis in human cells. PLoS Genet. *4*, e1000298.

García-Prat, L., Martínez-Vicente, M., Perdiguero, E., Ortet, L., Rodríguez-Ubreva, J., Rebollo, E., Ruiz-Bonilla, V., Gutarra, S., Ballestar, E., Serrano,

A.L., et al. (2016). Autophagy maintains stemness by preventing senescence. Nature *529*, 37–42.

Gatica, D., Lahiri, V., and Klionsky, D.J. (2018). Cargo recognition and degradation by selective autophagy. Nat. Cell Biol. *20*, 233–242.

Gluschko, A., Herb, M., Wiegmann, K., Krut, O., Neiss, W.F., Utermohlen, O., Kronke, M., and Schramm, M. (2018). The β2 integrin Mac-1 induces protective LC3-associated phagocytosis of *Listeria monocytogenes*. Cell Host Microbe *23*, 324–337.e5.

Gomes, L.C., Di Benedetto, G., and Scorrano, L. (2011). During autophagy mitochondria elongate, are spared from degradation and sustain cell viability. Nat. Cell Biol. *13*, 589–598.

Goode, A., Long, J.E., Shaw, B., Ralston, S.H., Visconti, M.R., Gianfrancesco, F., Esposito, T., Gennari, L., Merlotti, D., Rendina, D., et al. (2014). Paget disease of bone-associated UBA domain mutations of *SQSTM1* exert distinct effects on protein structure and function. Biochim. Biophys. Acta *1842*, 992–1000.

Grumati, P., and Dikic, I. (2018). Ubiquitin signaling and autophagy. J. Biol. Chem. *293*, 5404–5413.

Grumati, P., Morozzi, G., Hölper, S., Mari, M., Harwardt, M.I., Yan, R., Müller, S., Reggiori, F., Heilemann, M., and Dikic, I. (2017). Full length RTN3 regulates turnover of tubular endoplasmic reticulum via selective autophagy. eLife *6*. https://doi.org/10.7554/eLife.25555.

Gstrein, T., Edwards, A., Přistoupilová, A., Leca, I., Breuss, M., Pilat-Carotta, S., Hansen, A.H., Tripathy, R., Traunbauer, A.K., Hochstoeger, T., et al. (2018). Mutations in *Vps15* perturb neuronal migration in mice and are associated with neurodevelopmental disease in humans. Nat. Neurosci. *21*, 207–217.

Guo, J.Y., Karsli-Uzunbas, G., Mathew, R., Aisner, S.C., Kamphorst, J.J., Strohecker, A.M., Chen, G., Price, S., Lu, W., Teng, X., et al. (2013). Autophagy suppresses progression of K-ras-induced lung tumors to oncocytomas and maintains lipid homeostasis. Genes Dev. *27*, 1447–1461.

Guo, H., Chitiprolu, M., Gagnon, D., Meng, L., Perez-Iratxeta, C., Lagace, D., and Gibbings, D. (2014). Autophagy supports genomic stability by degrading retrotransposon RNA. Nat. Commun. *5*, 5276.

Guo, H., Chitiprolu, M., Roncevic, L., Javalet, C., Hemming, F.J., Trung, M.T., Meng, L., Latreille, E., Tanese de Souza, C., McCulloch, D., et al. (2017). Atg5 disassociates the V1V0-ATPase to promote exosome production and tumor metastasis independent of canonical macroautophagy. Dev Cell *43*, 716–730.e7.

Haack, T.B., Hogarth, P., Kruer, M.C., Gregory, A., Wieland, T., Schwarzmayr, T., Graf, E., Sanford, L., Meyer, E., Kara, E., et al. (2012). Exome sequencing reveals de novo *WDR45* mutations causing a phenotypically distinct, X-linked dominant form of NBIA. Am. J. Hum. Genet. *91*, 1144–1149.

Hansen, M., Rubinsztein, D.C., and Walker, D.W. (2018). Autophagy as a promoter of longevity: insights from model organisms. Nat. Rev. Mol. Cell Biol. *19*, 579–593.

Hayashi, K., Taura, M., and Iwasaki, A. (2018). The interaction between IKKα and LC3 promotes type I interferon production through the TLR9-containing LAPosome. Sci. Signal. *11*, eaan4144.

He, C., Bassik, M.C., Moresi, V., Sun, K., Wei, Y., Zou, Z., An, Z., Loh, J., Fisher, J., Sun, Q., et al. (2012). Exercise-induced BCL2-regulated autophagy is required for muscle glucose homeostasis. Nature *481*, 511–515.

Heckmann, B.L., Boada-Romero, E., Cunha, L.D., Magne, J., and Green, D.R. (2017). LC3-associated phagocytosis and inflammation. J. Mol. Biol. *429*, 3561–3576.

Henault, J., Martinez, J., Riggs, J.M., Tian, J., Mehta, P., Clarke, L., Sasai, M., Latz, E., Brinkmann, M.M., Iwasaki, A., et al. (2012). Noncanonical autophagy is required for type I interferon secretion in response to DNA-immune complexes. Immunity *37*, 986–997.

Herzig, S., and Shaw, R.J. (2018). AMPK: guardian of metabolism and mitochondrial homeostasis. Nat. Rev. Mol. Cell Biol. *19*, 121–135.

Hessvik, N.P., and Llorente, A. (2018). Current knowledge on exosome biogenesis and release. Cell. Mol. Life Sci. *75*, 193–208.

Ho, T.T., Warr, M.R., Adelman, E.R., Lansinger, O.M., Flach, J., Verovskaya, E.V., Figueroa, M.E., and Passegué, E. (2017). Autophagy maintains the metabolism and function of young and old stem cells. Nature *543*, 205–210.

Hori, I., Otomo, T., Nakashima, M., Miya, F., Negishi, Y., Shiraishi, H., Nonoda, Y., Magara, S., Tohyama, J., Okamoto, N., et al. (2017). Defects in autophagosome-lysosome fusion underlie Vici syndrome, a neurodevelopmental disorder with multisystem involvement. Sci. Rep. *7*, 3552.

Hui, K.Y., Fernandez-Hernandez, H., Hu, J., Schaffner, A., Pankratz, N., Hsu, N.Y., Chuang, L.S., Carmi, S., Villaverde, N., Li, X., et al. (2018). Functional variants in the *LRRK2* gene confer shared effects on risk for Crohn's disease and Parkinson's disease. Sci. Transl. Med. *10*, eaai7795.

Hurley, J.H., and Young, L.N. (2017). Mechanisms of autophagy initiation. Annu. Rev. Biochem. *86*, 225–244.

Hylin, M.J., Zhao, J., Tangavelou, K., Rozas, N.S., Hood, K.N., MacGowan, J.S., Moore, A.N., and Dash, P.K. (2018). A role for autophagy in long-term spatial memory formation in male rodents. J. Neurosci. Res. *96*, 416–426.

Imagawa, Y., Saitoh, T., and Tsujimoto, Y. (2016). Vital staining for cell death identifies Atg9a-dependent necrosis in developmental bone formation in mouse. Nat. Commun. *7*, 13391.

Jiang, P., and Mizushima, N. (2014). Autophagy and human diseases. Cell Res. *24*, 69–79.

Jounai, N., Takeshita, F., Kobiyama, K., Sawano, A., Miyawaki, A., Xin, K.Q., Ishii, K.J., Kawai, T., Akira, S., Suzuki, K., and Okuda, K. (2007). The Atg5 Atg12 conjugate associates with innate antiviral immune responses. Proc. Natl. Acad. Sci. USA *104*, 14050–14055.

Jung, H.S., Chung, K.W., Won Kim, J., Kim, J., Komatsu, M., Tanaka, K., Nguyen, Y.H., Kang, T.M., Yoon, K.H., Kim, J.W., et al. (2008). Loss of autophagy diminishes pancreatic beta cell mass and function with resultant hyperglycemia. Cell Metab. *8*, 318–324.

Kadir, R., Harel, T., Markus, B., Perez, Y., Bakhrat, A., Cohen, I., Volodarsky, M., Feintsein-Linial, M., Chervinski, E., Zlotogora, J., et al. (2016). ALFY-controlled DVL3 autophagy regulates Wnt signaling, determining human brain size. PLoS Genet. *12*, e1005919.

Karantza-Wadsworth, V., Patel, S., Kravchuk, O., Chen, G., Mathew, R., Jin, S., and White, E. (2007). Autophagy mitigates metabolic stress and genome damage in mammary tumorigenesis. Genes Dev. *21*, 1621–1635.

Karch, J., Schips, T.G., Maliken, B.D., Brody, M.J., Sargent, M.A., Kanisicak, O., and Molkentin, J.D. (2017). Autophagic cell death is dependent on lysosomal membrane permeability through Bax and Bak. eLife *6*, e30543.

Karsli-Uzunbas, G., Guo, J.Y., Price, S., Teng, X., Laddha, S.V., Khor, S., Kalaany, N.Y., Jacks, T., Chan, C.S., Rabinowitz, J.D., and White, E. (2014). Autophagy is required for glucose homeostasis and lung tumor maintenance. Cancer Discov. *4*, 914–927.

Katheder, N.S., Khezri, R., O'Farrell, F., Schultz, S.W., Jain, A., Rahman, M.M., Schink, K.O., Theodossiou, T.A., Johansen, T., Juhász, G., et al. (2017). Microenvironmental autophagy promotes tumour growth. Nature *541*, 417–420.

Kenzelmann Broz, D., Spano Mello, S., Bieging, K.T., Jiang, D., Dusek, R.L., Brady, C.A., Sidow, A., and Attardi, L.D. (2013). Global genomic profiling reveals an extensive p53-regulated autophagy program contributing to key p53 responses. Genes Dev. *27*, 1016–1031.

Khaminets, A., Heinrich, T., Mari, M., Grumati, P., Huebner, A.K., Akutsu, M., Liebmann, L., Stolz, A., Nietzsche, S., Koch, N., et al. (2015). Regulation of endoplasmic reticulum turnover by selective autophagy. Nature *522*, 354–358.

Kheloufi, M., Boulanger, C.M., Codogno, P., and Rautou, P.E. (2015). Autosis occurs in the liver of patients with severe anorexia nervosa. Hepatology *62*, 657–658.

Kim, J., Kim, Y.C., Fang, C., Russell, R.C., Kim, J.H., Fan, W., Liu, R., Zhong, Q., and Guan, K.L. (2013a). Differential regulation of distinct Vps34 complexes by AMPK in nutrient stress and autophagy. Cell *152*, 290–303.

Kim, J.Y., Zhao, H., Martinez, J., Doggett, T.A., Kolesnikov, A.V., Tang, P.H., Ablonczy, Z., Chan, C.C., Zhou, Z., Green, D.R., and Ferguson, T.A. (2013b). Noncanonical autophagy promotes the visual cycle. Cell *154*, 365–376.

Kim, M., Sandford, E., Gatica, D., Qiu, Y., Liu, X., Zheng, Y., Schulman, B.A., Xu, J., Semple, I., Ro, S.H., et al. (2016). Mutation in *ATG5* reduces autophagy and leads to ataxia with developmental delay. eLife *5*, e12245.

Kim, M.J., Deng, H.X., Wong, Y.C., Siddique, T., and Krainc, D. (2017). The Parkinson's disease-linked protein TMEM230 is required for Rab8a-mediated secretory vesicle trafficking and retromer trafficking. Hum. Mol. Genet. *26*, 729–741.

Kimmelman, A.C., and White, E. (2017). Autophagy and tumor metabolism. Cell Metab. *25*, 1037–1043.

Kimmey, J.M., Huynh, J.P., Weiss, L.A., Park, S., Kambal, A., Debnath, J., Virgin, H.W., and Stallings, C.L. (2015). Unique role for ATG5 in neutrophil-mediated immunopathology during *M. tuberculosis* infection. Nature *528*, 565–569.

Kimura, T., Jain, A., Choi, S.W., Mandell, M.A., Schroder, K., Johansen, T., and Deretic, V. (2015). TRIM-mediated precision autophagy targets cytoplasmic regulators of innate immunity. J. Cell Biol. *210*, 973–989.

Kimura, T., Jia, J., Kumar, S., Choi, S.W., Gu, Y., Mudd, M., Dupont, N., Jiang, S., Peters, R., Farzam, F., et al. (2017). Dedicated SNAREs and specialized TRIM cargo receptors mediate secretory autophagy. EMBO J. *36*, 42–60.

Kitada, T., Asakawa, S., Hattori, N., Matsumine, H., Yamamura, Y., Minoshima, S., Yokochi, M., Mizuno, Y., and Shimizu, N. (1998). Mutations in the *parkin* gene cause autosomal recessive juvenile parkinsonism. Nature *392*, 605–608.

Klionsky, D.J., Cregg, J.M., Dunn, W.A., Jr., Emr, S.D., Sakai, Y., Sandoval, I.V., Sibirny, A., Subramani, S., Thumm, M., Veenhuis, M., and Ohsumi, Y. (2003). A unified nomenclature for yeast autophagy-related genes. Dev. Cell *5*, 539–545.

Kluge, A.F., Lagu, B.R., Maiti, P., Jaleel, M., Webb, M., Malhotra, J., Mallat, A., Srinivas, P.A., and Thompson, J.E. (2018). Novel highly selective inhibitors of ubiquitin specific protease 30 (USP30) accelerate mitophagy. Bioorg. Med. Chem. Lett. *28*, 2655–2659.

Koga, H., Kaushik, S., and Cuervo, A.M. (2010). Altered lipid content inhibits autophagic vesicular fusion. FASEB J. *24*, 3052–3065.

Konno, H., Konno, K., and Barber, G.N. (2013). Cyclic dinucleotides trigger ULK1 (ATG1) phosphorylation of STING to prevent sustained innate immune signaling. Cell *155*, 688–698.

Konno, H., Chinn, I.K., Hong, D., Orange, J.S., Lupski, J.R., Mendoza, A., Pedroza, L.A., and Barber, G.N. (2018). Pro-inflammation associated with a gain-of-function mutation (R284S) in the innate immune sensor STING. Cell Rep. *23*, 1112–1123.

Korvatska, O., Strand, N.S., Berndt, J.D., Strovas, T., Chen, D.H., Leverenz, J.B., Kiianitsa, K., Mata, I.F., Karakoc, E., Greenup, J.L., et al. (2013). Altered splicing of *ATP6AP2* causes X-linked parkinsonism with spasticity (XPDS). Hum. Mol. Genet. *22*, 3259–3268.

Kramer, M.H., Farre, J.C., Mitra, K., Yu, M.K., Ono, K., Demchak, B., Licon, K., Flagg, M., Balakrishnan, R., Cherry, J.M., et al. (2017). Active interaction mapping reveals the hierarchical organization of autophagy. Mol Cell *65*, 761–774.e5.

Kriegenburg, F., Ungermann, C., and Reggiori, F. (2018). Coordination of autophagosome-lysosome fusion by Atg8 family members. Curr. Biol. *28*, R512–R518.

Kroemer, G., Mariño, G., and Levine, B. (2010). Autophagy and the integrated stress response. Mol. Cell *40*, 280–293.

Kuo, T.C., Chen, C.T., Baron, D., Onder, T.T., Loewer, S., Almeida, S., Weismann, C.M., Xu, P., Houghton, J.M., Gao, F.B., et al. (2011). Midbody accumulation through evasion of autophagy contributes to cellular reprogramming and tumorigenicity. Nat. Cell Biol. *13*, 1214–1223.

Lahiri, A., Hedl, M., and Abraham, C. (2015). *MTMR3* risk allele enhances innate receptor-induced signaling and cytokines by decreasing autophagy and increasing caspase-1 activation. Proc. Natl. Acad. Sci. USA *112*, 10461–10466.

Lassen, K.G., Kuballa, P., Conway, K.L., Patel, K.K., Becker, C.E., Peloquin, J.M., Villablanca, E.J., Norman, J.M., Liu, T.C., Heath, R.J., et al. (2014). Atg16L1 T300A variant decreases selective autophagy resulting in altered cytokine signaling and decreased antibacterial defense. Proc. Natl. Acad. Sci. USA *111*, 7741–7746.

Lassen, K.G., McKenzie, C.I., Mari, M., Murano, T., Begun, J., Baxt, L.A., Goel, G., Villablanca, E.J., Kuo, S.Y., Huang, H., et al. (2016). Genetic coding variant in GPR65 alters lysosomal pH and links lysosomal dysfunction with colitis risk. Immunity *44*, 1392–1405.

Latunde-Dada, G.O. (2017). Ferroptosis: Role of lipid peroxidation, iron and ferritinophagy. Biochim. Biophys. Acta, Gen. Subj. *1861*, 1893–1900.

Lee, J.H., Yu, W.H., Kumar, A., Lee, S., Mohan, P.S., Peterhoff, C.M., Wolfe, D.M., Martinez-Vicente, M., Massey, A.C., Sovak, G., et al. (2010). Lysosomal proteolysis and autophagy require presenilin 1 and are disrupted by Alzheimer-related PS1 mutations. Cell *141*, 1146–1158.

Lee, I.H., Kawai, Y., Fergusson, M.M., Rovira, I.I., Bishop, A.J., Motoyama, N., Cao, L., and Finkel, T. (2012). Atg7 modulates p53 activity to regulate cell cycle and survival during metabolic stress. Science *336*, 225–228.

Lee, P.L., Tang, Y., Li, H., and Guertin, D.A. (2016). Raptor/mTORC1 loss in adipocytes causes progressive lipodystrophy and fatty liver disease. Mol. Metab. *5*, 422–432.

Lee, M.Y., Sumpter, R., Jr., Zou, Z., Sirasanagandla, S., Wei, Y., Mishra, P., Rosewich, H., Crane, D.I., and Levine, B. (2017a). Peroxisomal protein PEX13 functions in selective autophagy. EMBO Rep. *18*, 48–60.

Lee, P.P., Lobato-Márquez, D., Pramanik, N., Sirianni, A., Daza-Cajigal, V., Rivers, E., Cavazza, A., Bouma, G., Moulding, D., Hultenby, K., et al. (2017b). Wiskott-Aldrich syndrome protein regulates autophagy and inflammasome activity in innate immune cells. Nat. Commun. *8*, 1576.

Lee, Y., Jonson, P.H., Sarparanta, J., Palmio, J., Sarkar, M., Vihola, A., Evilä, A., Suominen, T., Penttilä, S., Savarese, M., et al. (2018). *TIA1* variant drives myodegeneration in multisystem proteinopathy with *SQSTM1* mutations. J. Clin. Invest. *128*, 1164–1177.

Levine, B., and Klionsky, D.J. (2017). Autophagy wins the 2016 Nobel Prize in Physiology or Medicine: Breakthroughs in baker's yeast fuel advances in biomedical research. Proc. Natl. Acad. Sci. USA *114*, 201–205.

Levine, B., and Kroemer, G. (2008). Autophagy in the pathogenesis of disease. Cell *132*, 27–42.

Levine, B., Liu, R., Dong, X., and Zhong, Q. (2015). Beclin orthologs: integrative hubs of cell signaling, membrane trafficking, and physiology. Trends Cell Biol. *25*, 533–544.

Li, F., Xie, X., Wang, Y., Liu, J., Cheng, X., Guo, Y., Gong, Y., Hu, S., and Pan, L. (2016). Structural insights into the interaction and disease mechanism of neurodegenerative disease-associated optineurin and TBK1 proteins. Nat. Commun. *7*, 12708.

Li, C., Brazill, J.M., Liu, S., Bello, C., Zhu, Y., Morimoto, M., Cascio, L., Pauly, R., Diaz-Perez, Z., Malicdan, M.C.V., et al. (2017a). Spermine synthase deficiency causes lysosomal dysfunction and oxidative stress in models of Snyder-Robinson syndrome. Nat. Commun. *8*, 1257.

Li, X., Yu, W., Qian, X., Xia, Y., Zheng, Y., Lee, J.H., Li, W., Lyu, J., Rao, G., Zhang, X., et al. (2017b). Nucleus-translocated ACSS2 promotes gene transcription for lysosomal biogenesis and autophagy. Mol Cell *66*, 684–697.e9.

Li, C., Zhang, Y., Cheng, X., Yuan, H., Zhu, S., Liu, J., Wen, Q., Xie, Y., Liu, J., Kroemer, G., et al. (2018a). PINK1 and PARK2 suppress pancreatic tumorigenesis through control of mitochondrial iron-mediated immunometabolism. Dev. Cell *46*, 441–455.e8.

Li, H., Li, D., Ma, Z., Qian, Z., Kang, X., Jin, X., Li, F., Wang, X., Chen, Q., Sun, H., and Wu, S. (2018b). Defective autophagy in osteoblasts induces endoplasmic reticulum stress and causes remarkable bone loss. Autophagy *14*, 1726–1741.

Liang, X.H., Jackson, S., Seaman, M., Brown, K., Kempkes, B., Hibshoosh, H., and Levine, B. (1999). Induction of autophagy and inhibition of tumorigenesis by *beclin 1*. Nature *402*, 672–676.

Liang, Q., Seo, G.J., Choi, Y.J., Kwak, M.J., Ge, J., Rodgers, M.A., Shi, M., Leslie, B.J., Hopfner, K.P., Ha, T., et al. (2014). Crosstalk between the cGAS DNA sensor and Beclin-1 autophagy protein shapes innate antimicrobial immune responses. Cell Host Microbe *15*, 228–238.

Liao, X., Sluimer, J.C., Wang, Y., Subramanian, M., Brown, K., Pattison, J.S., Robbins, J., Martinez, J., and Tabas, I. (2012). Macrophage autophagy plays a protective role in advanced atherosclerosis. Cell Metab. *15*, 545–553.

Lim, Y.M., Lim, H., Hur, K.Y., Quan, W., Lee, H.Y., Cheon, H., Ryu, D., Koo, S.H., Kim, H.L., Kim, J., et al. (2014). Systemic autophagy insufficiency compromises adaptation to metabolic stress and facilitates progression from obesity to diabetes. Nat. Commun. *5*, 4934.

Lin, Y.C., Chang, P.F., Lin, H.F., Liu, K., Chang, M.H., and Ni, Y.H. (2016). Variants in the autophagy-related gene *IRGM* confer susceptibility to non-alcoholic fatty liver disease by modulating lipophagy. J. Hepatol. *65*, 1209–1216.

Liu, F., Fang, F., Yuan, H., Yang, D., Chen, Y., Williams, L., Goldstein, S.A., Krebsbach, P.H., and Guan, J.L. (2013a). Suppression of autophagy by FIP200 deletion leads to osteopenia in mice through the inhibition of osteoblast terminal differentiation. J. Bone Miner. Res. *28*, 2414–2430.

Liu, Y., Shoji-Kawata, S., Sumpter, R.M., Jr., Wei, Y., Ginet, V., Zhang, L., Posner, B., Tran, K.A., Green, D.R., Xavier, R.J., et al. (2013b). Autosis is a Na^+,K^+-ATPase-regulated form of cell death triggered by autophagy-inducing peptides, starvation, and hypoxia-ischemia. Proc. Natl. Acad. Sci. USA *110*, 20364–20371.

Liu, T., Tang, Q., Liu, K., Xie, W., Liu, X., Wang, H., Wang, R.F., and Cui, J. (2016). TRIM11 suppresses AIM2 inflammasome by degrading AIM2 via p62-dependent selective autophagy. Cell Rep. *16*, 1988–2002.

Liu, H., Javaheri, A., Godar, R.J., Murphy, J., Ma, X., Rohatgi, N., Mahadevan, J., Hyrc, K., Saftig, P., Marshall, C., et al. (2017). Intermittent fasting preserves beta-cell mass in obesity-induced diabetes via the autophagy-lysosome pathway. Autophagy *13*, 1952–1968.

López-Otín, C., Galluzzi, L., Freije, J.M.P., Madeo, F., and Kroemer, G. (2016). Metabolic control of longevity. Cell *166*, 802–821.

Lu, K., den Brave, F., and Jentsch, S. (2017). Receptor oligomerization guides pathway choice between proteasomal and autophagic degradation. Nat. Cell Biol. *19*, 732–739.

Lu, X., Altshuler-Keylin, S., Wang, Q., Chen, Y., Henrique Sponton, C., Ikeda, K., Maretich, P., Yoneshiro, T., and Kajimura, S. (2018). Mitophagy controls beige adipocyte maintenance through a Parkin-dependent and UCP1-independent mechanism. Sci. Signal. *11*, eaap8526.

Lv, M., Wang, C., Li, F., Peng, J., Wen, B., Gong, Q., Shi, Y., and Tang, Y. (2017). Structural insights into the recognition of phosphorylated FUNDC1 by LC3B in mitophagy. Protein Cell *8*, 25–38.

Ma, Y., Galluzzi, L., Zitvogel, L., and Kroemer, G. (2013). Autophagy and cellular immune responses. Immunity *39*, 211–227.

Ma, Y., Qi, M., An, Y., Zhang, L., Yang, R., Doro, D.H., Liu, W., and Jin, Y. (2018). Autophagy controls mesenchymal stem cell properties and senescence during bone aging. Aging Cell *17*. https://doi.org/10.1111/acel.12709.

Madeo, F., Eisenberg, T., Pietrocola, F., and Kroemer, G. (2018). Spermidine in health and disease. Science *359*. https://doi.org/10.1126/science.aan2788.

Madeo, F., Pietrocola, F., Eisenberg, T., and Kroemer, G. (2014). Caloric restriction mimetics: towards a molecular definition. Nat. Rev. Drug Discov. *13*, 727–740.

Maejima, I., Takahashi, A., Omori, H., Kimura, T., Takabatake, Y., Saitoh, T., Yamamoto, A., Hamasaki, M., Noda, T., Isaka, Y., and Yoshimori, T. (2013). Autophagy sequesters damaged lysosomes to control lysosomal biogenesis and kidney injury. EMBO J. *32*, 2336–2347.

Malhotra, R., Warne, J.P., Salas, E., Xu, A.W., and Debnath, J. (2015). Loss of *Atg12*, but not *Atg5*, in pro-opiomelanocortin neurons exacerbates diet-induced obesity. Autophagy *11*, 145–154.

Mandell, M.A., Jain, A., Kumar, S., Castleman, M.J., Anwar, T., Eskelinen, E.L., Johansen, T., Prekeris, R., and Deretic, V. (2016). TRIM17 contributes to autophagy of midbodies while actively sparing other targets from degradation. J. Cell Sci. *129*, 3562–3573.

Manjithaya, R., Anjard, C., Loomis, W.F., and Subramani, S. (2010). Unconventional secretion of *Pichia pastoris* Acb1 is dependent on GRASP protein, peroxisomal functions, and autophagosome formation. J. Cell Biol. *188*, 537–546.

Mansueto, G., Armani, A., Viscomi, C., D'Orsi, L., De Cegli, R., Polishchuk, E.V., Lamperti, C., Di Meo, I., Romanello, V., Marchet, S., et al. (2017). Transcription factor EB controls metabolic flexibility during exercise. Cell Metab. *25*, 182–196.

Mariño, G., Fernández, A.F., Cabrera, S., Lundberg, Y.W., Cabanillas, R., Rodríguez, F., Salvador-Montoliu, N., Vega, J.A., Germanà, A., Fueyo, A., et al. (2010). Autophagy is essential for mouse sense of balance. J. Clin. Invest. *120*, 2331–2344.

Mariño, G., Niso-Santano, M., Baehrecke, E.H., and Kroemer, G. (2014a). Self-consumption: the interplay of autophagy and apoptosis. Nat. Rev. Mol. Cell Biol. *15*, 81–94.

Mariño, G., Pietrocola, F., Eisenberg, T., Kong, Y., Malik, S.A., Andryushkova, A., Schroeder, S., Pendl, T., Harger, A., Niso-Santano, M., et al. (2014b). Regulation of autophagy by cytosolic acetyl-coenzyme A. Mol. Cell *53*, 710–725.

Martinez, J., Almendinger, J., Oberst, A., Ness, R., Dillon, C.P., Fitzgerald, P., Hengartner, M.O., and Green, D.R. (2011). Microtubule-associated protein 1 light chain 3 alpha (LC3)-associated phagocytosis is required for the efficient clearance of dead cells. Proc. Natl. Acad. Sci. USA *108*, 17396–17401.

Martinez, J., Malireddi, R.K., Lu, Q., Cunha, L.D., Pelletier, S., Gingras, S., Orchard, R., Guan, J.L., Tan, H., Peng, J., et al. (2015). Molecular characterization of LC3-associated phagocytosis reveals distinct roles for Rubicon, NOX2 and autophagy proteins. Nat. Cell Biol. *17*, 893–906.

Martinez, J., Cunha, L.D., Park, S., Yang, M., Lu, Q., Orchard, R., Li, Q.Z., Yan, M., Janke, L., Guy, C., et al. (2016). Noncanonical autophagy inhibits the autoinflammatory, lupus-like response to dying cells. Nature *533*, 115–119.

Martinez-Lopez, N., Tarabra, E., Toledo, M., Garcia-Macia, M., Sahu, S., Coletto, L., Batista-Gonzalez, A., Barzilai, N., Pessin, J.E., Schwartz, G.J., et al. (2017). System-wide benefits of intermeal fasting by autophagy. Cell Metab *26*, 856–871.e5.

Matsunaga, K., Saitoh, T., Tabata, K., Omori, H., Satoh, T., Kurotori, N., Maejima, I., Shirahama-Noda, K., Ichimura, T., Isobe, T., et al. (2009). Two Beclin 1-binding proteins, Atg14L and Rubicon, reciprocally regulate autophagy at different stages. Nat. Cell Biol. *11*, 385–396.

Matsuzawa-Ishimoto, Y., Shono, Y., Gomez, L.E., Hubbard-Lucey, V.M., Cammer, M., Neil, J., Dewan, M.Z., Lieberman, S.R., Lazrak, A., Marinis, J.M., et al. (2017). Autophagy protein ATG16L1 prevents necroptosis in the intestinal epithelium. J. Exp. Med. *214*, 3687–3705.

Michaud, M., Martins, I., Sukkurwala, A.Q., Adjemian, S., Ma, Y., Pellegatti, P., Shen, S., Kepp, O., Scoazec, M., Mignot, G., et al. (2011). Autophagy-dependent anticancer immune responses induced by chemotherapeutic agents in mice. Science *334*, 1573–1577.

Mira, M.T., Alcaïs, A., Nguyen, V.T., Moraes, M.O., Di Flumeri, C., Vu, H.T., Mai, C.P., Nguyen, T.H., Nguyen, N.B., Pham, X.K., et al. (2004). Susceptibility to leprosy is associated with *PARK2* and *PACRG*. Nature *427*, 636–640.

Miranda, A.M., Lasiecka, Z.M., Xu, Y., Neufeld, J., Shahriar, S., Simoes, S., Chan, R.B., Oliveira, T.G., Small, S.A., and Di Paolo, G. (2018). Neuronal lysosomal dysfunction releases exosomes harboring APP C-terminal fragments and unique lipid signatures. Nat. Commun. *9*, 291.

Mitchell, G., and Isberg, R.R. (2017). Innate immunity to intracellular pathogens: Balancing microbial elimination and inflammation. Cell Host Microbe *22*, 166–175.

Mizushima, N. (2018). A brief history of autophagy from cell biology to physiology and disease. Nat. Cell Biol. *20*, 521–527.

Mizushima, N., and Komatsu, M. (2011). Autophagy: renovation of cells and tissues. Cell *147*, 728–741.

Molineros, J.E., Yang, W., Zhou, X.J., Sun, C., Okada, Y., Zhang, H., Heng Chua, K., Lau, Y.L., Kochi, Y., Suzuki, A., et al. (2017). Confirmation of five novel susceptibility loci for systemic lupus erythematosus (SLE) and integrated network analysis of 82 SLE susceptibility loci. Hum. Mol. Genet. *26*, 1205–1216.

Morselli, E., Maiuri, M.C., Markaki, M., Megalou, E., Pasparaki, A., Palikaras, K., Criollo, A., Galluzzi, L., Malik, S.A., Vitale, I., et al. (2010). Caloric restriction

and resveratrol promote longevity through the Sirtuin-1-dependent induction of autophagy. Cell Death Dis. *1*, e10.

Morselli, E., Mariño, G., Bennetzen, M.V., Eisenberg, T., Megalou, E., Schroeder, S., Cabrera, S., Bénit, P., Rustin, P., Criollo, A., et al. (2011). Spermidine and resveratrol induce autophagy by distinct pathways converging on the acetylproteome. J. Cell Biol. *192*, 615–629.

Moscat, J., Karin, M., and Diaz-Meco, M.T. (2016). p62 in cancer: Signaling adaptor beyond autophagy. Cell *167*, 606–609.

Muniz-Feliciano, L., Doggett, T.A., Zhou, Z., and Ferguson, T.A. (2017). RUBCN/rubicon and EGFR regulate lysosomal degradative processes in the retinal pigment epithelium (RPE) of the eye. Autophagy *13*, 2072–2085.

Murrow, L., Malhotra, R., and Debnath, J. (2015). ATG12-ATG3 interacts with Alix to promote basal autophagic flux and late endosome function. Nat. Cell Biol. *17*, 300–310.

Murthy, A., Li, Y., Peng, I., Reichelt, M., Katakam, A.K., Noubade, R., Roose-Girma, M., DeVoss, J., Diehl, L., Graham, R.R., and van Lookeren Campagne, M. (2014). A Crohn's disease variant in *Atg16l1* enhances its degradation by caspase 3. Nature *506*, 456–462.

Na, H.J., Pyo, J.H., Jeon, H.J., Park, J.S., Chung, H.Y., and Yoo, M.A. (2018). Deficiency of Atg6 impairs beneficial effect of metformin on intestinal stem cell aging in Drosophila. Biochem. Biophys. Res. Commun. *498*, 18–24.

Napolitano, G., and Ballabio, A. (2016). TFEB at a glance. J. Cell Sci. *129*, 2475–2481.

Nassif, M., Woehlbier, U., and Manque, P.A. (2017). The enigmatic role of C9ORF72 in autophagy. Front. Neurosci. *11*, 442.

Nguyen, T.B., Louie, S.M., Daniele, J.R., Tran, Q., Dillin, A., Zoncu, R., Nomura, D.K., and Olzmann, J.A. (2017). DGAT1-dependent lipid droplet biogenesis protects mitochondrial function during starvation-induced autophagy. Dev Cell *42*, 9–21.e5.

Nishimura, T., Kaizuka, T., Cadwell, K., Sahani, M.H., Saitoh, T., Akira, S., Virgin, H.W., and Mizushima, N. (2013). FIP200 regulates targeting of Atg16L1 to the isolation membrane. EMBO Rep. *14*, 284–291.

Nishino, I., Fu, J., Tanji, K., Yamada, T., Shimojo, S., Koori, T., Mora, M., Riggs, J.E., Oh, S.J., Koga, Y., et al. (2000). Primary LAMP-2 deficiency causes X-linked vacuolar cardiomyopathy and myopathy (Danon disease). Nature *406*, 906–910.

Ochotny, N., Voronov, I., Owen, C., Aubin, J.E., and Manolson, M.F. (2013). The R740S mutation in the V-ATPase a3 subunit results in osteoclast apoptosis and defective early-stage autophagy. J. Cell. Biochem. *114*, 2823–2833.

Onal, M., Piemontese, M., Xiong, J., Wang, Y., Han, L., Ye, S., Komatsu, M., Selig, M., Weinstein, R.S., Zhao, H., et al. (2013). Suppression of autophagy in osteocytes mimics skeletal aging. J. Biol. Chem. *288*, 17432–17440.

Park, J.M., Seo, M., Jung, C.H., Grunwald, D., Stone, M., Otto, N.M., Toso, E., Ahn, Y., Kyba, M., Griffin, T.J., et al. (2018). ULK1 phosphorylates Ser30 of BECN1 in association with ATG14 to stimulate autophagy induction. Autophagy *14*, 584–597.

Patel, K.K., Miyoshi, H., Beatty, W.L., Head, R.D., Malvin, N.P., Cadwell, K., Guan, J.L., Saitoh, T., Akira, S., Seglen, P.O., et al. (2013). Autophagy proteins control goblet cell function by potentiating reactive oxygen species production. EMBO J. *32*, 3130–3144.

Pattabiraman, D.R., and Weinberg, R.A. (2014). Tackling the cancer stem cells - what challenges do they pose? Nat. Rev. Drug Discov. *13*, 497–512.

Peng, Y., Shapiro, S.L., Banduseela, V.C., Dieterich, I.A., Hewitt, K.J., Bresnick, E.H., Kong, G., Zhang, J., Schueler, K.L., Keller, M.P., et al. (2018). Increased transport of acetyl-CoA into the endoplasmic reticulum causes a progeria-like phenotype. Aging Cell *17*, e12820.

Perera, R.M., Stoykova, S., Nicolay, B.N., Ross, K.N., Fitamant, J., Boukhali, M., Lengrand, J., Deshpande, V., Selig, M.K., Ferrone, C.R., et al. (2015). Transcriptional control of autophagy-lysosome function drives pancreatic cancer metabolism. Nature *524*, 361–365.

Pickrell, A.M., Huang, C.H., Kennedy, S.R., Ordureau, A., Sideris, D.P., Hoekstra, J.G., Harper, J.W., and Youle, R.J. (2015). Endogenous parkin preserves dopaminergic substantia Nigral neurons following mitochondrial DNA mutagenic stress. Neuron *87*, 371–381.

Pietrocola, F., Pol, J., Vacchelli, E., Rao, S., Enot, D.P., Baracco, E.E., Levesque, S., Castoldi, F., Jacquelot, N., Yamazaki, T., et al. (2016). Caloric restriction mimetics enhance anticancer immunosurveillance. Cancer Cell *30*, 147–160.

Pietrocola, F., Castoldi, F., Markaki, M., Lachkar, S., Chen, G., Enot, D.P., Durand, S., Bossut, N., Tong, M., Malik, S.A., et al. (2018). Aspirin recapitulates features of caloric restriction. Cell Rep. *22*, 2395–2407.

Poulogiannis, G., McIntyre, R.E., Dimitriadi, M., Apps, J.R., Wilson, C.H., Ichimura, K., Luo, F., Cantley, L.C., Wyllie, A.H., Adams, D.J., and Arends, M.J. (2010). *PARK2* deletions occur frequently in sporadic colorectal cancer and accelerate adenoma development in *Apc* mutant mice. Proc. Natl. Acad. Sci. USA *107*, 15145–15150.

Puertollano, R., Ferguson, S.M., Brugarolas, J., and Ballabio, A. (2018). The complex relationship between TFEB transcription factor phosphorylation and subcellular localization. EMBO J. *37*, e98804.

Pyo, J.O., Yoo, S.M., Ahn, H.H., Nah, J., Hong, S.H., Kam, T.I., Jung, S., and Jung, Y.K. (2013). Overexpression of Atg5 in mice activates autophagy and extends lifespan. Nat. Commun. *4*, 2300.

Qu, X., Yu, J., Bhagat, G., Furuya, N., Hibshoosh, H., Troxel, A., Rosen, J., Eskelinen, E.L., Mizushima, N., Ohsumi, Y., et al. (2003). Promotion of tumorigenesis by heterozygous disruption of the *beclin 1* autophagy gene. J. Clin. Invest. *112*, 1809–1820.

Quan, W., Kim, H.K., Moon, E.Y., Kim, S.S., Choi, C.S., Komatsu, M., Jeong, Y.T., Lee, M.K., Kim, K.W., Kim, M.S., and Lee, M.S. (2012). Role of hypothalamic proopiomelanocortin neuron autophagy in the control of appetite and leptin response. Endocrinology *153*, 1817–1826.

Raz, Y., Guerrero-Ros, I., Maier, A., Slagboom, P.E., Atzmon, G., Barzilai, N., and Macian, F. (2017). Activation-induced autophagy is preserved in CD4+ T-cells in familial longevity. J. Gerontol. A Biol. Sci. Med. Sci. *72*, 1201–1206.

Razani, B., Feng, C., Coleman, T., Emanuel, R., Wen, H., Hwang, S., Ting, J.P., Virgin, H.W., Kastan, M.B., and Semenkovich, C.F. (2012). Autophagy links inflammasomes to atherosclerotic progression. Cell Metab. *15*, 534–544.

Reddy, P.H., Yin, X., Manczak, M., Kumar, S., Pradeepkiran, J.A., Vijayan, M., and Reddy, A.P. (2018). Mutant APP and amyloid beta-induced defective autophagy, mitophagy, mitochondrial structural and functional changes and synaptic damage in hippocampal neurons from Alzheimer's disease. Hum. Mol. Genet. *27*, 2502–2516.

Redmann, V., Lamb, C.A., Hwang, S., Orchard, R.C., Kim, S., Razi, M., Milam, A., Park, S., Yokoyama, C.C., Kambal, A., et al. (2016). Clec16a is critical for autolysosome function and Purkinje cell survival. Sci. Rep. *6*, 23326.

Rello-Varona, S., Lissa, D., Shen, S., Niso-Santano, M., Senovilla, L., Mariño, G., Vitale, I., Jemaá, M., Harper, F., Pierron, G., et al. (2012). Autophagic removal of micronuclei. Cell Cycle *11*, 170–176.

Rocchi, A., Yamamoto, S., Ting, T., Fan, Y., Sadleir, K., Wang, Y., Zhang, W., Huang, S., Levine, B., Vassar, R., and He, C. (2017). A *Becn1* mutation mediates hyperactive autophagic sequestration of amyloid oligomers and improved cognition in Alzheimer's disease. PLoS Genet. *13*, e1006962.

Rojansky, R., Cha, M.Y., and Chan, D.C. (2016). Elimination of paternal mitochondria in mouse embryos occurs through autophagic degradation dependent on PARKIN and MUL1. eLife *5*, e17896.

Rosenfeldt, M.T., O'Prey, J., Morton, J.P., Nixon, C., MacKay, G., Mrowinska, A., Au, A., Rai, T.S., Zheng, L., Ridgway, R., et al. (2013). p53 status determines the role of autophagy in pancreatic tumour development. Nature *504*, 296–300.

Rostislavleva, K., Soler, N., Ohashi, Y., Zhang, L., Pardon, E., Burke, J.E., Masson, G.R., Johnson, C., Steyaert, J., Ktistakis, N.T., and Williams, R.L. (2015).

Structure and flexibility of the endosomal Vps34 complex reveals the basis of its function on membranes. Science *350*, aac7365.

Roy, S., Leidal, A.M., Ye, J., Ronen, S.M., and Debnath, J. (2017). Autophagy-dependent shuttling of TBC1D5 controls plasma membrane translocation of GLUT1 and glucose uptake. Mol Cell *67*, 84–95 e85.

Rujano, M.A., Cannata Serio, M., Panasyuk, G., Péanne, R., Reunert, J., Rymen, D., Hauser, V., Park, J.H., Freisinger, P., Souche, E., et al. (2017). Mutations in the X-linked *ATP6AP2* cause a glycosylation disorder with autophagic defects. J. Exp. Med. *214*, 3707–3729.

Rybstein, M.D., Bravo-San Pedro, J.M., Kroemer, G., and Galluzzi, L. (2018). The autophagic network and cancer. Nat. Cell Biol. *20*, 243–251.

Saitoh, T., Fujita, N., Jang, M.H., Uematsu, S., Yang, B.G., Satoh, T., Omori, H., Noda, T., Yamamoto, N., Komatsu, M., et al. (2008). Loss of the autophagy protein Atg16L1 enhances endotoxin-induced IL-1β production. Nature *456*, 264–268.

Saitoh, T., Fujita, N., Hayashi, T., Takahara, K., Satoh, T., Lee, H., Matsunaga, K., Kageyama, S., Omori, H., Noda, T., et al. (2009). Atg9a controls dsDNA-driven dynamic translocation of STING and the innate immune response. Proc. Natl. Acad. Sci. USA *106*, 20842–20846.

Saitsu, H., Nishimura, T., Muramatsu, K., Kodera, H., Kumada, S., Sugai, K., Kasai-Yoshida, E., Sawaura, N., Nishida, H., Hoshino, A., et al. (2013). *De novo* mutations in the autophagy gene *WDR45* cause static encephalopathy of childhood with neurodegeneration in adulthood. Nat Genet *45*, 445–449.e1.

Sakamaki, J.I., Wilkinson, S., Hahn, M., Tasdemir, N., O'Prey, J., Clark, W., Hedley, A., Nixon, C., Long, J.S., New, M., et al. (2017). Bromodomain protein BRD4 is a transcriptional repressor of autophagy and lysosomal function. Mol Cell *66*, 517–532.e9.

Sandoval, H., Thiagarajan, P., Dasgupta, S.K., Schumacher, A., Prchal, J.T., Chen, M., and Wang, J. (2008). Essential role for Nix in autophagic maturation of erythroid cells. Nature *454*, 232–235.

Sanjuan, M.A., Dillon, C.P., Tait, S.W., Moshiach, S., Dorsey, F., Connell, S., Komatsu, M., Tanaka, K., Cleveland, J.L., Withoff, S., and Green, D.R. (2007). Toll-like receptor signalling in macrophages links the autophagy pathway to phagocytosis. Nature *450*, 1253–1257.

Sarkar, S. (2013). Regulation of autophagy by mTOR-dependent and mTOR-independent pathways: autophagy dysfunction in neurodegenerative diseases and therapeutic application of autophagy enhancers. Biochem. Soc. Trans. *41*, 1103–1130.

Saxton, R.A., and Sabatini, D.M. (2017). mTOR signaling in growth, metabolism, and disease. Cell *169*, 361–371.

Sbardella, D., Tundo, G.R., Campagnolo, L., Valacchi, G., Orlandi, A., Curatolo, P., Borsellino, G., D'Esposito, M., Ciaccio, C., Cesare, S.D., et al. (2017). Retention of mitochondria in mature human red blood cells as the result of autophagy impairment in Rett Syndrome. Sci. Rep. *7*, 12297.

Schapira, A.H. (2015). Glucocerebrosidase and Parkinson disease: Recent advances. Mol. Cell. Neurosci. *66* (Pt A), 37–42.

Scharl, M., Wojtal, K.A., Becker, H.M., Fischbeck, A., Frei, P., Arikkat, J., Pesch, T., Kellermeier, S., Boone, D.L., Weber, A., et al. (2012). Protein tyrosine phosphatase nonreceptor type 2 regulates autophagosome formation in human intestinal cells. Inflamm. Bowel Dis. *18*, 1287–1302.

Schoner, W. (2002). Endogenous cardiac glycosides, a new class of steroid hormones. Eur. J. Biochem. *269*, 2440–2448.

Schulze, R.J., Rasineni, K., Weller, S.G., Schott, M.B., Schroeder, B., Casey, C.A., and McNiven, M.A. (2017). Ethanol exposure inhibits hepatocyte lipophagy by inactivating the small guanosine triphosphatase Rab7. Hepatol Commun *1*, 140–152.

Schuster, C., Gerold, K.D., Schober, K., Probst, L., Boerner, K., Kim, M.J., Ruckdeschel, A., Serwold, T., and Kissler, S. (2015). The autoimmunity-associated gene *CLEC16A* modulates thymic epithelial cell autophagy and alters T cell selection. Immunity *42*, 942–952.

Seo, A.Y., Lau, P.W., Feliciano, D., Sengupta, P., Gros, M.A.L., Cinquin, B., Larabell, C.A., and Lippincott-Schwartz, J. (2017). AMPK and vacuole-associated Atg14p orchestrate μ-lipophagy for energy production and long-term survival under glucose starvation. eLife *6*, e21690.

Seong, E., Insolera, R., Dulovic, M., Kamsteeg, E.J., Trinh, J., Brüggemann, N., Sandford, E., Li, S., Ozel, A.B., Li, J.Z., et al. (2018). Mutations in *VPS13D* lead to a new recessive ataxia with spasticity and mitochondrial defects. Ann. Neurol. *83*, 1075–1088.

Settembre, C., De Cegli, R., Mansueto, G., Saha, P.K., Vetrini, F., Visvikis, O., Huynh, T., Carissimo, A., Palmer, D., Klisch, T.J., et al. (2013a). TFEB controls cellular lipid metabolism through a starvation-induced autoregulatory loop. Nat. Cell Biol. *15*, 647–658.

Settembre, C., Fraldi, A., Medina, D.L., and Ballabio, A. (2013b). Signals from the lysosome: a control centre for cellular clearance and energy metabolism. Nat. Rev. Mol. Cell Biol. *14*, 283–296.

Shen, H.M., and Mizushima, N. (2014). At the end of the autophagic road: an emerging understanding of lysosomal functions in autophagy. Trends Biochem. Sci. *39*, 61–71.

Shigeyama, Y., Kobayashi, T., Kido, Y., Hashimoto, N., Asahara, S., Matsuda, T., Takeda, A., Inoue, T., Shibutani, Y., Koyanagi, M., et al. (2008). Biphasic response of pancreatic β-cell mass to ablation of tuberous sclerosis complex 2 in mice. Mol. Cell. Biol. *28*, 2971–2979.

Shim, M.S., Takihara, Y., Kim, K.Y., Iwata, T., Yue, B.Y., Inatani, M., Weinreb, R.N., Perkins, G.A., and Ju, W.K. (2016). Mitochondrial pathogenic mechanism and degradation in optineurin E50K mutation-mediated retinal ganglion cell degeneration. Sci. Rep. *6*, 33830.

Shoji-Kawata, S., Sumpter, R., Leveno, M., Campbell, G.R., Zou, Z., Kinch, L., Wilkins, A.D., Sun, Q., Pallauf, K., MacDuff, D., et al. (2013). Identification of a candidate therapeutic autophagy-inducing peptide. Nature *494*, 201–206.

Silva, I.A.L., Conceição, N., Gagnon, É., Caiado, H., Brown, J.P., Gianfrancesco, F., Michou, L., and Cancela, M.L. (2018). Effect of genetic variants of OPTN in the pathophysiology of Paget's disease of bone. Biochim Biophys Acta Mol Basis Dis *1864*, 143–151.

Simon, H.U., Friis, R., Tait, S.W., and Ryan, K.M. (2017). Retrograde signaling from autophagy modulates stress responses. Sci. Signal. *10*, eaag2791.

Singh, R., Kaushik, S., Wang, Y., Xiang, Y., Novak, I., Komatsu, M., Tanaka, K., Cuervo, A.M., and Czaja, M.J. (2009). Autophagy regulates lipid metabolism. Nature *458*, 1131–1135.

Sliter, D.A., Martinez, J., Hao, L., Chen, X., Sun, N., Fischer, T.D., Burman, J.L., Li, Y., Zhang, Z., Narendra, D.P., et al. (2018). Parkin and PINK1 mitigate STING-induced inflammation. Nature *561*, 258–262.

Smith, M.D., Harley, M.E., Kemp, A.J., Wills, J., Lee, M., Arends, M., von Kriegsheim, A., Behrends, C., and Wilkinson, S. (2018). CCPG1 is a non-canonical autophagy cargo receptor essential for ER-phagy and pancreatic ER proteostasis. Dev Cell *44*, 217–232.e11.

Soleimanpour, S.A., Gupta, A., Bakay, M., Ferrari, A.M., Groff, D.N., Fadista, J., Spruce, L.A., Kushner, J.A., Groop, L., Seeholzer, S.H., et al. (2014). The diabetes susceptibility gene *Clec16a* regulates mitophagy. Cell *157*, 1577–1590.

Song, X., Zhu, S., Chen, P., Hou, W., Wen, Q., Liu, J., Xie, Y., Liu, J., Klionsky, D.J., Kroemer, G., et al. (2018). AMPK-mediated BECN1 phosphorylation promotes ferroptosis by directly blocking system Xc(-) activity. Curr. Biol. *28*, 2388–2399.e5.

Soria, L.R., Allegri, G., Melck, D., Pastore, N., Annunziata, P., Paris, D., Polishchuk, E., Nusco, E., Thöny, B., Motta, A., et al. (2018). Enhancement of hepatic autophagy increases ureagenesis and protects against hyperammonemia. Proc. Natl. Acad. Sci. USA *115*, 391–396.

Starr, T., Child, R., Wehrly, T.D., Hansen, B., Hwang, S., López-Otin, C., Virgin, H.W., and Celli, J. (2012). Selective subversion of autophagy complexes facilitates completion of the *Brucella* intracellular cycle. Cell Host Microbe *11*, 33–45.

Stenbeck, G., and Coxon, F.P. (2014). Role of vesicular trafficking in skeletal dynamics. Curr. Opin. Pharmacol. *16*, 7–14.

Su, H., Yang, F., Wang, Q., Shen, Q., Huang, J., Peng, C., Zhang, Y., Wan, W., Wong, C.C.L., Sun, Q., et al. (2017). VPS34 acetylation controls its lipid kinase

activity and the initiation of canonical and non-canonical autophagy. Mol Cell *67*, 907–921.e7.

Sumpter, R., Jr., Sirasanagandla, S., Fernández, A.F., Wei, Y., Dong, X., Franco, L., Zou, Z., Marchal, C., Lee, M.Y., Clapp, D.W., et al. (2016). Fanconi anemia proteins function in mitophagy and immunity. Cell *165*, 867–881.

Sun, T., Li, X., Zhang, P., Chen, W.D., Zhang, H.L., Li, D.D., Deng, R., Qian, X.J., Jiao, L., Ji, J., et al. (2015). Acetylation of Beclin 1 inhibits autophagosome maturation and promotes tumour growth. Nat. Commun. *6*, 7215.

Sun, Y., Yao, X., Zhang, Q.J., Zhu, M., Liu, Z.P., Ci, B., Xie, Y., Carlson, D., Rothermel, B.A., Sun, Y., et al. (2018). Beclin-1-dependent autophagy protects the heart during sepsis. Circulation *138*, 2247–2262.

Suzuki, S.W., Yamamoto, H., Oikawa, Y., Kondo-Kakuta, C., Kimura, Y., Hirano, H., and Ohsumi, Y. (2015). Atg13 HORMA domain recruits Atg9 vesicles during autophagosome formation. Proc. Natl. Acad. Sci. USA *112*, 3350–3355.

Tanaka, Y., Guhde, G., Suter, A., Eskelinen, E.L., Hartmann, D., Lüllmann-Rauch, R., Janssen, P.M., Blanz, J., von Figura, K., and Saftig, P. (2000). Accumulation of autophagic vacuoles and cardiomyopathy in LAMP-2-deficient mice. Nature *406*, 902–906.

Tanaka, S., Hikita, H., Tatsumi, T., Sakamori, R., Nozaki, Y., Sakane, S., Shiode, Y., Nakabori, T., Saito, Y., Hiramatsu, N., et al. (2016). Rubicon inhibits autophagy and accelerates hepatocyte apoptosis and lipid accumulation in nonalcoholic fatty liver disease in mice. Hepatology *64*, 1994–2014.

Tang, H., Sebti, S., Titone, R., Zhou, Y., Isidoro, C., Ross, T.S., Hibshoosh, H., Xiao, G., Packer, M., Xie, Y., et al. (2015). Decreased *BECN1* mRNA expression in human breast cancer is associated with estrogen receptor-negative subtypes and poor prognosis. EBioMedicine *2*, 255–263.

Tian, Y., Li, Z., Hu, W., Ren, H., Tian, E., Zhao, Y., Lu, Q., Huang, X., Yang, P., Li, X., et al. (2010). *C. elegans* screen identifies autophagy genes specific to multicellular organisms. Cell *141*, 1042–1055.

Todoric, J., Antonucci, L., Di Caro, G., Li, N., Wu, X., Lytle, N.K., Dhar, D., Banerjee, S., Fagman, J.B., Browne, C.D., et al. (2017). Stress-activated NRF2-MDM2 cascade controls neoplastic progression in pancreas. Cancer Cell *32*, 824–839.e8.

Tschurtschenthaler, M., Adolph, T.E., Ashcroft, J.W., Niederreiter, L., Bharti, R., Saveljeva, S., Bhattacharyya, J., Flak, M.B., Shih, D.Q., Fuhler, G.M., et al. (2017). Defective ATG16L1-mediated removal of IRE1α drives Crohn's disease-like ileitis. J. Exp. Med. *214*, 401–422.

Tsuboyama, K., Koyama-Honda, I., Sakamaki, Y., Koike, M., Morishita, H., and Mizushima, N. (2016). The ATG conjugation systems are important for degradation of the inner autophagosomal membrane. Science *354*, 1036–1041.

Ueno, T., and Komatsu, M. (2017). Autophagy in the liver: functions in health and disease. Nat. Rev. Gastroenterol. Hepatol. *14*, 170–184.

Ulgherait, M., Rana, A., Rera, M., Graniel, J., and Walker, D.W. (2014). AMPK modulates tissue and organismal aging in a non-cell-autonomous manner. Cell Rep. *8*, 1767–1780.

Valente, G., Morani, F., Nicotra, G., Fusco, N., Peracchio, C., Titone, R., Alabiso, O., Arisio, R., Katsaros, D., Benedetto, C., and Isidoro, C. (2014). Expression and clinical significance of the autophagy proteins BECLIN 1 and LC3 in ovarian cancer. BioMed Res. Int. *2014*, 462658.

van Beek, N., Klionsky, D.J., and Reggiori, F. (2018). Genetic aberrations in macroautophagy genes leading to diseases. Biochim Biophys Acta Mol Cell Res *1865*, 803–816.

Vega-Rubín-de-Celis, S., Zou, Z., Fernández, A.F., Ci, B., Kim, M., Xiao, G., Xie, Y., and Levine, B. (2018). Increased autophagy blocks HER2-mediated breast tumorigenesis. Proc. Natl. Acad. Sci. USA *115*, 4176–4181.

Wang, R.C., Wei, Y., An, Z., Zou, Z., Xiao, G., Bhagat, G., White, M., Reichelt, J., and Levine, B. (2012). Akt-mediated regulation of autophagy and tumorigenesis through Beclin 1 phosphorylation. Science *338*, 956–959.

Wang, C., Liang, C.C., Bian, Z.C., Zhu, Y., and Guan, J.L. (2013). FIP200 is required for maintenance and differentiation of postnatal neural stem cells. Nat. Neurosci. *16*, 532–542.

Wang, Y., Zhang, N., Zhang, L., Li, R., Fu, W., Ma, K., Li, X., Wang, L., Wang, J., Zhang, H., et al. (2016). Autophagy regulates chromatin ubiquitination in DNA damage response through elimination of SQSTM1/p62. Mol. Cell *63*, 34–48.

Watada, H., and Fujitani, Y. (2015). Minireview: Autophagy in pancreatic β-cells and its implication in diabetes. Mol. Endocrinol. *29*, 338–348.

Webster, B.R., Scott, I., Han, K., Li, J.H., Lu, Z., Stevens, M.V., Malide, D., Chen, Y., Samsel, L., Connelly, P.S., et al. (2013). Restricted mitochondrial protein acetylation initiates mitochondrial autophagy. J. Cell Sci. *126*, 4843–4849.

Wei, Y., Pattingre, S., Sinha, S., Bassik, M., and Levine, B. (2008). JNK1-mediated phosphorylation of Bcl-2 regulates starvation-induced autophagy. Mol. Cell *30*, 678–688.

Wei, Y., Zou, Z., Becker, N., Anderson, M., Sumpter, R., Xiao, G., Kinch, L., Koduru, P., Christudass, C.S., Veltri, R.W., et al. (2013). EGFR-mediated Beclin 1 phosphorylation in autophagy suppression, tumor progression, and tumor chemoresistance. Cell *154*, 1269–1284.

Wei, Y., An, Z., Zou, Z., Sumpter, R., Su, M., Zang, X., Sinha, S., Gaestel, M., and Levine, B. (2015). The stress-responsive kinases MAPKAPK2/MAPKAPK3 activate starvation-induced autophagy through Beclin 1 phosphorylation. eLife *4*.. https://doi.org/10.7554/eLife.05289.

Wei, Y., Chiang, W.C., Sumpter, R., Jr., Mishra, P., and Levine, B. (2017). Prohibitin 2 is an inner mitochondrial membrane mitophagy receptor. Cell *168*, 224–238.e10.

White, J.P., Billin, A.N., Campbell, M.E., Russell, A.J., Huffman, K.M., and Kraus, W.E. (2018). The AMPK/p27(Kip1) axis regulates autophagy/apoptosis decisions in aged skeletal muscle stem cells. Stem Cell Reports *11*, 425–439.

Wong, Y.C., and Holzbaur, E.L. (2014). Optineurin is an autophagy receptor for damaged mitochondria in parkin-mediated mitophagy that is disrupted by an ALS-linked mutation. Proc. Natl. Acad. Sci. USA *111*, E4439–E4448.

Wu, W., Tian, W., Hu, Z., Chen, G., Huang, L., Li, W., Zhang, X., Xue, P., Zhou, C., Liu, L., et al. (2014). ULK1 translocates to mitochondria and phosphorylates FUNDC1 to regulate mitophagy. EMBO Rep. *15*, 566–575.

Wyant, G.A., Abu-Remaileh, M., Frenkel, E.M., Laqtom, N.N., Dharamdasani, V., Lewis, C.A., Chan, S.H., Heinze, I., Ori, A., and Sabatini, D.M. (2018). NUFIP1 is a ribosome receptor for starvation-induced ribophagy. Science *360*, 751–758.

Xu, L., Lin, D.C., Yin, D., and Koeffler, H.P. (2014). An emerging role of PARK2 in cancer. J. Mol. Med. (Berl.) *92*, 31–42.

Yang, A., Herter-Sprie, G., Zhang, H., Lin, E.Y., Biancur, D., Wang, X., Deng, J., Hai, J., Yang, S., Wong, K.K., and Kimmelman, A.C. (2018). Autophagy sustains pancreatic cancer growth through both cell-autonomous and nonautonomous mechanisms. Cancer Discov. *8*, 276–287.

Yoshida, Y., Yasuda, S., Fujita, T., Hamasaki, M., Murakami, A., Kawawaki, J., Iwai, K., Saeki, Y., Yoshimori, T., Matsuda, N., and Tanaka, K. (2017). Ubiquitination of exposed glycoproteins by SCF^{FBXO27} directs damaged lysosomes for autophagy. Proc. Natl. Acad. Sci. USA *114*, 8574–8579.

Yu, L., Chen, Y., and Tooze, S.A. (2018). Autophagy pathway: Cellular and molecular mechanisms. Autophagy *14*, 207–215.

Yue, Z., Jin, S., Yang, C., Levine, A.J., and Heintz, N. (2003). *Beclin 1*, an autophagy gene essential for early embryonic development, is a haploinsufficient tumor suppressor. Proc. Natl. Acad. Sci. USA *100*, 15077–15082.

Zechner, R., Madeo, F., and Kratky, D. (2017). Cytosolic lipolysis and lipophagy: two sides of the same coin. Nat. Rev. Mol. Cell Biol. *18*, 671–684.

Zhang, J., Tripathi, D.N., Jing, J., Alexander, A., Kim, J., Powell, R.T., Dere, R., Tait-Mulder, J., Lee, J.H., Paull, T.T., et al. (2015a). ATM functions at the peroxisome to induce pexophagy in response to ROS. Nat. Cell Biol. *17*, 1259–1269.

Zhang, M., Kenny, S.J., Ge, L., Xu, K., and Schekman, R. (2015b). Translocation of interleukin-1β into a vesicle intermediate in autophagy-mediated secretion. eLife *4*, e11205.

Zhang, Y., Sowers, J.R., and Ren, J. (2018a). Targeting autophagy in obesity: from pathophysiology to management. Nat. Rev. Endocrinol. *14*, 356–376.

Zhang, Z., Yao, Z., Chen, Y., Qian, L., Jiang, S., Zhou, J., Shao, J., Chen, A., Zhang, F., and Zheng, S. (2018b). Lipophagy and liver disease: New perspectives to better understanding and therapy. Biomed. Pharmacother. *97*, 339–348.

Zhao, Y., Huang, S., Liu, J., Wu, X., Zhou, S., Dai, K., and Kou, Y. (2018). Mitophagy contributes to the pathogenesis of inflammatory diseases. Inflammation *41*, 1590–1600.

Zhong, Z., Sanchez-Lopez, E., and Karin, M. (2016). Autophagy, inflammation, and immunity: A troika governing cancer and its treatment. Cell *166*, 288–298.

Zhou, R., Yazdi, A.S., Menu, P., and Tschopp, J. (2011). A role for mitochondria in NLRP3 inflammasome activation. Nature *469*, 221–225.

Zhu, P., Sieben, C.J., Xu, X., Harris, P.C., and Lin, X. (2017). Autophagy activators suppress cystogenesis in an autosomal dominant polycystic kidney disease model. Hum. Mol. Genet. *26*, 158–172.

Zi, Z., Song, Z., Zhang, S., Ye, Y., Li, C., Xu, M., Zou, Y., He, L., and Zhu, H. (2015). Rubicon deficiency enhances cardiac autophagy and protects mice from lipopolysaccharide-induced lethality and reduction in stroke volume. J. Cardiovasc. Pharmacol. *65*, 252–261.

Leading Edge
Perspective

Cell

Genomic Medicine–Progress, Pitfalls, and Promise

Jay Shendure,[1,2,3,*] Gregory M. Findlay,[1] and Matthew W. Snyder[1,4]
[1]Department of Genome Sciences, University of Washington, Seattle, WA 98195, USA
[2]Howard Hughes Medical Institute, Seattle, WA 98195, USA
[3]Brotman Baty Institute for Precision Medicine, Seattle, WA 98195, USA
[4]Present address: Bellwether Bio, Inc., Seattle, WA 98104, USA
*Correspondence: shendure@uw.edu
https://doi.org/10.1016/j.cell.2019.02.003

In the wake of the Human Genome Project (HGP), strong expectations were set for the timeline and impact of genomics on medicine—an anticipated transformation in the diagnosis, treatment, and prevention of disease. In this Perspective, we take stock of the nascent field of genomic medicine. In what areas, if any, is genomics delivering on this promise, or is the path to success clear? Where are we falling short, and why? What have been the unanticipated developments? Overall, we argue that the optimism surrounding the transformational potential of genomics on medicine remains justified, albeit with a considerably different form and timescale than originally projected. We also argue that the field needs to pivot back to basics, as understanding the entirety of the genotype-to-phenotype equation is a likely prerequisite for delivering on the full potential of the human genome to advance the human condition.

It is worth reminding ourselves that regardless of its impact on medicine, the sequencing of the human genome represents a monumental achievement. It is the blueprint that quite literally specifies how to build a human, even if we do not yet fully understand the means by which it does so. To have gone from observing the double helix to the assembly and rudimentary understanding of the human genome's 3 billion nucleotides in 50 years is a stunning trajectory, with no obvious equivalent other than our progression from the first powered flight to a moon landing in about the same amount of time. Furthermore, although it has only been 15 years since an achievement that will be remembered for millennia, the Human Genome Project (HGP) has already had scientific and economic impacts that more than amply justify its cost (National Human Genome Research Institute, 2013).

This praise notwithstanding, we should not forget that the prioritization and cost of the HGP were justified by, and its completion celebrated with, the setting of ambitious expectations about the time frame on which it would transform the diagnosis, treatment, and prevention of a broad swath of human diseases. In this Perspective, we attempt to take stock of the progress made, as well as the hurdles to, the clinical translation of the human genome—the nascent field of genomic medicine. For the citizens that funded it, has the bet of the HGP paid off? If it has not, will it ever? Is the value proposition as originally laid out still justified, or do we need to recalibrate?

This is a large topic to undertake, and we have organized this review as follows. First, we summarize the key technological developments since the HGP. Second, we consider the successes and challenges to genomic medicine in four areas: common inherited diseases, rare inherited diseases, reproductive health, and cancer (Figures 1 and 2). Finally, we take stock of the field as a whole and suggest areas that warrant further investment to fully unlock its potential.

Beyond the HGP: From One to Millions of Human Genomes

The HGP was completed in 2003 at an estimated cost of $2.7 billion, primarily through the brute-force scaling of automated Sanger sequencing of large insert clones, followed by hierarchical assembly (International Human Genome Sequencing Consortium, 2004). The commonplace use of the article "the" in conjunction with "human genome" emphasizes the nearly perfect similarity of individual humans to one another (~99.9%) but downplays the millions of differences (~0.1%) that make each of us genetically unique. However, the *raison d'etre* for the field of human genetics lies not with our similarities but our differences—more specifically, with disentangling how our genotypic differences underlie our phenotypic differences.

If there is one area where we have over-delivered as a field since the HGP, it is in the development and deployment of technologies for ascertaining interindividual genetic differences. Two technologies now critically underpin nearly every aspect of genomic medicine. First, high-density DNA microarrays can be used to genotype millions of specific positions in each of many human genomes. Coupled with population-based maps of linkage disequilibrium (LD), array-based genotyping enables the ascertainment of most common genetic variation in a human genome for a remarkably low cost (initially hundreds, now tens, of dollars per individual) (Gunderson et al., 2005). Second, massively parallel DNA sequencing technologies, which have steadily improved since their introduction in 2005, can generate billions of short sequencing reads within a day or less (Shendure et al., 2017). Also known as next-generation sequencing (NGS),

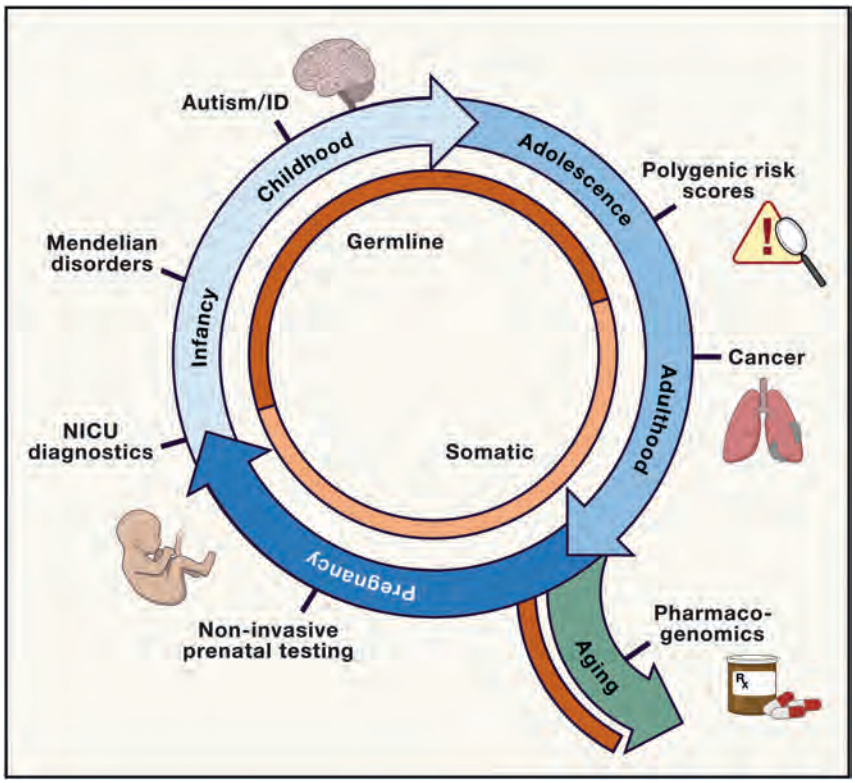

Figure 1. Genomic Medicine throughout the Human Life Cycle
There are many modalities for genomics to have an impact on clinical care, with entry points for application that span the human life cycle from conception to death.

such platforms now permit the near-comprehensive ascertainment of both rare and common genetic variation for about $1,000 per individual (or a few hundred dollars, if one selectively sequences the exome or coding regions of the genome). Importantly, both array-based genotyping and NGS depend heavily on the availability of a high-quality reference genome such as the one generated by the HGP, the former for designing probes with which to query positions of common variation and the latter for mapping short reads to, so as to localize *bona fide* variants and distinguish them from sequencing errors. Of note, NGS has also become an incredibly powerful tool for quantifying a broad range of molecular phenomena, e.g., transcriptomes (RNA sequencing, RNA-seq), protein-DNA binding (chromatin immunoprecipitation sequencing, ChIP-seq), etc., essentially through the counting of molecules (Shendure and Lieberman Aiden, 2012).

The precipitous rate at which genotyping and sequencing costs have dropped was scarcely anticipated at the completion of the HGP in 2003. Given that it has only been a few years since the full maturation of these technologies, the number of humans that have been already been genotyped by arrays or subjected to exome or genome sequencing is staggering. Although a comprehensive count is not easily achieved, it is estimated that the number of individuals genotyped by direct-to-consumer genealogy companies was less than 1 million as recently as 2014 but 3 million by 2016 and 12 million by 2018 (Figure 3, left). The number of individual humans whose genomes have been sequenced is estimated to have gone from 1 in 2003 to over 50,000 by 2015 and over 1.5 million by 2018 (Figure 3, right).

These trends are driven by distinct forces in the research, medical, and direct-to-consumer fields and do not show any signs of abating. For example, large cohorts, including nationwide efforts such as the UK Biobank and US All of Us programs, are collectively targeting the genome sequencing of over 25 million humans (Global Genomic Medicine Collaborative, 2018).

Genomic Medicine → Common Disease

Whether fairly or not, much of the discussion about the perceived shortcomings of genomic medicine has centered on genome-wide association studies (GWASs). In brief, most genetic variants in individual human genomes are common (allele frequency > 1%), leading to the hypothesis that our individual genetic risk for common diseases derives mostly from common variants, as opposed to the rare variants or *de novo* mutations that underlie Mendelian disorders (Manolio et al., 2009). The GWAS framework, first proposed by Risch and Merikangas in 1996 as an alternative to linkage studies (which had succeeded for Mendelian diseases but largely failed for common diseases), is designed to detect even subtle associations between common variants and common diseases on a systematic, genome-wide basis (Risch and Merikangas, 1996). Around 2005, several developments converged to enable well-powered GWAS, including public catalogs of common human genetic variants, initial maps of LD among common variants in human populations, and cost-effective array-based genotyping technologies (Collins et al., 1997; Gunderson et al., 2005; International HapMap Consortium, 2005). Over the ensuing decade, through the genome-wide genotyping of increasingly large cohorts of cases and controls, the imputation of additional genotypes based on LD maps, and the application of appropriately corrected statistical tests, the field has collectively discovered over 100,000 unique, robust associations between common variants and common diseases (Burdett et al., 2018).

This sounds like success—why are we so unhappy? It is worth taking a step back and asking: for what reasons do we want to investigate the genetic basis for common human diseases in the first place? One motivation is risk prediction—that is, using genetic factors to better stratify which individuals are at higher risk for specific common diseases, which may facilitate preventative measures and/or the better allocation of resources across a heterogeneously susceptible population. A second motivation

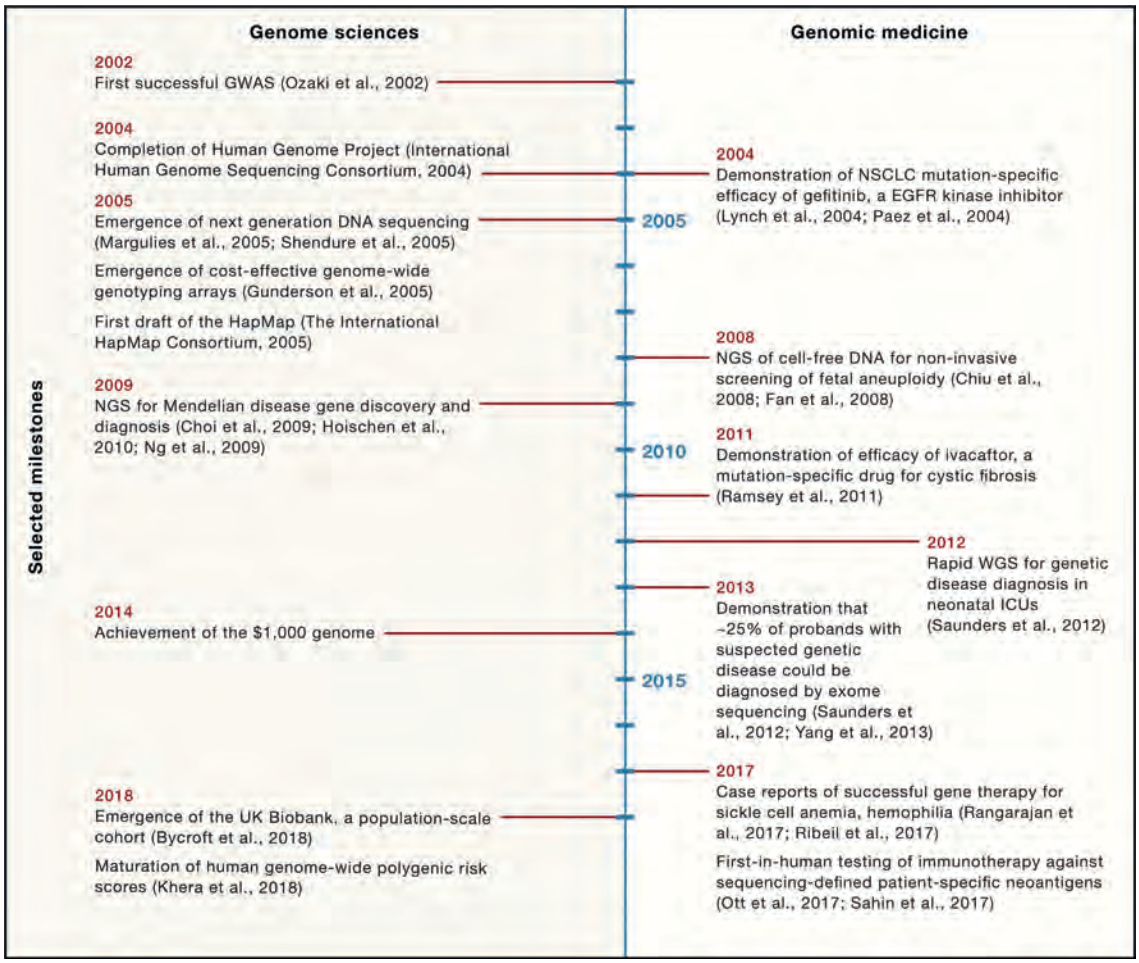

Figure 2. Past Milestones for Genome Sciences and Genomic Medicine
A timeline on selected milestones in the progression of the genome sciences (left) and genomic medicine (right).

is target identification, grounded in the view that our historical approach to understanding the pathogenesis of common diseases has been largely *ad hoc* and therefore prone to false positives and negatives. In contrast, GWASs provide a systematic, genome-wide approach for identifying genes that play a role in each disease. As this should result in a longer, higher-quality list of potential drug targets, GWASs were/are expected by some to accelerate our ability to develop effective therapies.

So what has gone wrong? A first challenge, primarily to the goal of risk prediction, has been that with few exceptions, the genetic component of common human disease risk consists of an extremely large number of variants of small effects, the vast majority of which would require astronomically large study sizes to definitively implicate. A subset of these weakly associated variants achieves genome-wide significance, but the effect sizes are usually modest even for these, and they have limited predictive power whether taken individually or considered together.

A second challenge is that for most common diseases, genome-wide-significant common variants turn out to explain only a small minority of their heritability. This was recognized relatively early in the GWAS era, and many potential explanations were put forth (Manolio et al., 2009). A leading hypothesis that emerged was that rare variants might explain a substantial fraction of this "missing heritability," motivating large-scale exome- and genome-sequencing studies of common diseases. However, even when reasonably well-powered studies are conducted, this hypothesis has not borne out, or at least not yet. For example, in type II diabetes, it was shown that lower-frequency variants are collectively likely to contribute less to heritability than common variants (Fuchsberger et al., 2016). Recently, the mystery of missing heritability has been solved to a large extent by the demonstration that common variants *as a class* account for a much larger proportion of heritability than the subset that achieve genome-wide significance (Yang et al., 2010).

A third challenge, primarily to the goal of therapeutic target identification, has been that the same LD structure that makes GWAS considerably cheaper to execute ironically limits its resolution, the consequence being that we have succeeded in implicating tens of thousands of haplotypes rather than tens of thousands of specific variants. Although considerable effort has been invested in fine-mapping, the task of confidently dissecting which variants are causally responsible for each

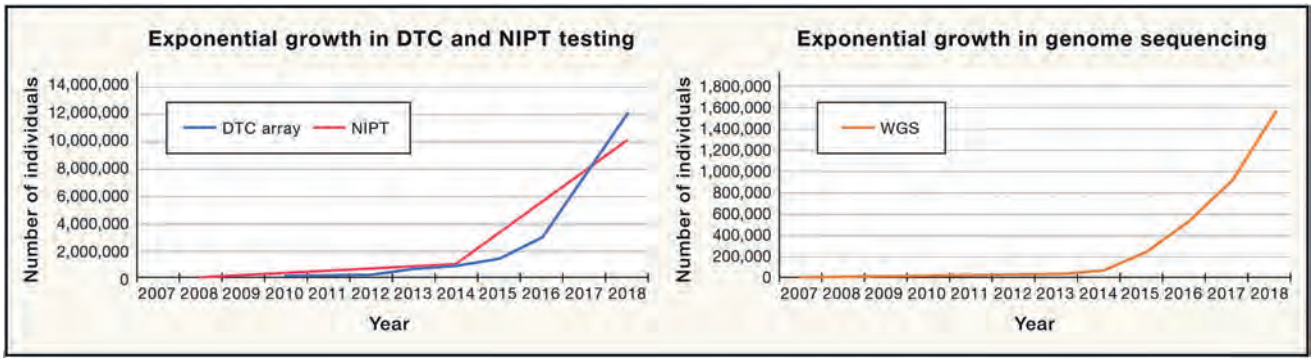

Figure 3. Exponential Growth in Genomic Testing

We show estimates of number of individuals that have been received genetic testing in the form of direct-to-consumer microarrays (DTC) and non-invasive prenatal testing (NIPT) (left) and whole-genome sequencing (WGS) (right) as a function of time. For NIPT, estimates are from Chiu et al. (2008), Fan et al. (2008), Liu et al. (2018), and Yuzuki (2015). For DTC and WGS, estimates are from Illumina (personal communication), with estimates of WGS based on equivalents of 30X coverage.

observed association between a haplotype and a common disease can be maddening.

A fourth challenge, also more relevant to the goal of target identification, is that the vast majority of the GWAS-defined heritability signal partitions to non-coding regions of the genome, and much of it to cell-type-specific regulatory elements (Finucane et al., 2015). As most enhancers are not definitively linked to genes, even if one is successful in pinpointing a causal regulatory variant, identifying the gene through which it mediates its subtle effects on disease risk, not to mention the mechanisms by which the gene acts, represents additional hurdles. A major rate limiter to further progress in this field is that we lack scalable solutions for any of these tasks, in part because they require non-trivial experiments incorporating disease-specific biology.

A fifth challenge, raised in a recent perspective by Boyle & Pritchard, is that gene regulatory networks are so densely interconnected, and GWAS so well-powered to detect subtle effects, that many *bona fide* associations may be due to genes that subtly impact genes in core pathways but themselves are only peripherally relevant to the phenotype (Boyle et al., 2017). An implication of this "omnigenic" model is that many if not the vast majority of GWAS signals, even if successfully fine-mapped, may not meaningfully inform target identification nor our understanding of disease.

Finally, as the cohorts required to identify additional GWAS signals grow larger and larger, a broader question is when do we stop caring? How can one credibly argue for the marginal value of the 100th significant association with type II diabetes, when the vast majority of the first 99 have larger effect sizes but have yet to be effectively followed up on with respect to identifying the causal variants and genes?

On one hand, we feel that these are fair concerns to raise, provided that they are raised constructively. At the same time, for a goal as audacious as dissecting the basis of all common human diseases, we should not expect that the solution to every obstacle should have been established in advance, or we would have never gotten started. Furthermore, despite these non-trivial challenges, we actually remain quite positive with regard to the ultimate impact that GWASs will have on the diagnosis, treatment, and prevention of common diseases. There are four main reasons for our optimism.

First, it is retrospectively unsurprising that many of the strongest GWAS associations came early, as smaller studies were only powered to detect large effects, and large effects seem more likely to be mediated through core genes and pathways. The vast majority of GWASs have been conducted in European populations (Visscher et al., 2017), and with the exception of some unique subpopulations, we are skeptical of the marginal value of ever-larger studies in these same populations for the purpose of gene discovery. However, each non-European population represents a fresh source of variants common to that population, and comparatively smaller studies in these populations may yield additional large-effect signals (presumably easier to fine-map and more likely to be therapeutically relevant) for a reasonable cost. Furthermore, smaller studies in populations with less LD (e.g., African ancestry) can facilitate the fine-mapping of associations identified in other populations (Willer et al., 2013).

Second, there are an increasing number of clear examples of GWASs shedding light on the specific pathways and cell types that are most relevant for particular common diseases, of association signals being followed up on to implicate specific variants and genes, and of these insights having meaningful consequences for how the disease will be approached from a drug-discovery perspective. These are reviewed elsewhere (Visscher et al., 2017), but a particularly compelling example is the use of GWAS together with Mendelian randomization to convincingly demonstrate that the associations of LDL cholesterol and triglyceride levels with coronary artery disease (CAD) reflect causal relationships, whereas the association of HDL cholesterol levels with CAD does not (Do et al., 2013; Voight et al., 2012). A more general observation is that the pharmaceutical industry is an increasingly sophisticated consumer of GWAS analyses in order to make maximally well-informed decisions about target selection for drug discovery (Nelson et al., 2015). On a related topic, the list of genetic variants that impact drug response, i.e., pharmacogenomic interactions, is growing, with many of the newer discoveries made via GWASs (Motsinger-Reif et al.,

2013). Of note, despite their clear clinical utility and often large effect sizes, pharmacogenomics has been slow to achieve clinical adoption, illustrating how the science is often only the first of many challenges.

Third, although we are still far from where we need to be, the toolkit for identifying the variants and genes that causally underlie GWAS signals is steadily improving. These include statistical methods that incorporate biochemical annotations (to identify which variants lie in *bona fide* regulatory regions), expression quantitative trait locus (QTL) studies (to locate genes whose expression is modulated by the same haplotype as a disease), massively parallel reporter assays (to pinpoint variants with regulatory effects), and CRISPR/Cas9 genome editing (to test the functional consequences of a specific variant, or potentially libraries of variants, in their endogenous genomic context). Methods are also advancing for linking regulatory elements to the gene(s) that they regulate, e.g., by 3C-based identification of ''loops'' or by coupling CRISPR/Cas9 perturbations and single-cell readouts (Gasperini et al., 2019; Mumbach et al., 2016). To date, such tools have been applied to investigate only a small number of GWAS signals. However, as they become more widely used and more scalable, the number of common disease associations for which the causal variants and genes are known is likely to grow.

Fourth, as long evidenced by plant and animal breeding programs, we need not restrict ourselves to genome-wide significant associations to build phenotypic predictors from GWAS results. Polygenic risk scores (PRSs) are not a new concept (Wray et al., 2013), but an increasing number of studies are showing that PRSs that incorporate information from common variants throughout the genome (including from vast numbers of single nucleotide variants [SNVs] that fail to achieve genome-wide significance) achieve reasonable performance in stratifying risk for complex diseases in humans. For example, Khera et al. recently reported that a PRS trained on a portion of the UK Biobank (training set) identifies 2.5% of the remaining participants (test set) that are at 4-fold higher risk for CAD, essentially equivalent to monogenic hypercholesterolemia but impacting a much larger proportion of the population (Khera et al., 2018). Analogous results were obtained for breast cancer and obesity. Through PRS, we may more effectively deliver on the HGP's promise of better predicting individual risk for common diseases, without necessarily requiring any understanding of the biology on which those predictors are based.

In summary, with respect to the genetic study of common diseases, the glass is both half empty and half full. We are not saying that there is not more to be learned from additional GWASs, but in a world of finite resources, we should be skeptical of the commitment to ever-larger GWASs of specific diseases when we are already drowning in robust associations that remain incompletely followed up on. It is clear that following up *bona fide* associations can provide insights, both for biology and drug discovery. Shifting resources toward developing and implementing the necessary computational and experimental tools for pinpointing the specific variants, genes, and mechanisms that underlie established association signals should be prioritized, in hopes of finishing our incomplete sentences at a faster rate than we are starting new ones. A qualification is that the developments around PRSs, which are potentially clinically useful without requiring fine-mapping or biological understanding, are exciting and warrant further exploration. It is notable that the training and validation of PRSs for a broad range of human traits and diseases has been strongly enabled by the effectively unrestricted availability of a massive, population-scale cohort, the UK Biobank (Bycroft et al., 2018). Such cohorts, and their amalgamation, likely represent the future of common disease genetics, as opposed to disease-specific cohorts.

Genomic Medicine → Rare Disease

An area in which the glass is clearly much fuller is that of rare disease. It is estimated that there are ~7,000 Mendelian or monogenic disorders that collectively impact ~0.4% of live births (~8% if congenital anomalies are included) but account for a much larger proportion of morbidity and mortality (e.g., by one study, 71% of pediatric hospital admissions) (Baird et al., 1988; Chong et al., 2015; McCandless et al., 2004). To better serve these patients as well as to advance knowledge, a defining quest for human genetics has been to comprehensively delineate the genetic basis of Mendelian disorders. In the era prior to the HGP, linkage mapping followed by arduous molecular cloning was used to ''solve'' over 1,000 Mendelian disorders. The reference human genome greatly accelerated the latter task, enabling a steady rate of discovery throughout the 2000s. Since 2009, exome or genome sequencing, facilitated by NGS, the reference human genome, and catalogs of common genetic variation, have driven a renaissance in this field (Choi et al., 2009; Hoischen et al., 2010; Ng et al., 2009). These approaches have been particularly useful for diseases whose inheritance patterns are not amenable to linkage analysis, e.g., those predominantly caused by *de novo* dominant mutations or somatic mosaicism, resolvable by ''trio-based sequencing'' of unaffected parents and an affected offspring.

One of the larger surprises of this renaissance has been the substantial proportion of cases of neurodevelopmental disorders—in particular, diagnoses of intellectual disability (ID) and/or autism spectrum disorder (ASD)—that are attributable to *de novo* mutations. For example, it was recently estimated that *de novo* events including point mutations and copy-number variants (CNVs) account for at least 30% and possibly as much as 60% of simplex ASD (Iossifov et al., 2014). Although the waters muddy considerably for patients in whom causal mutations cannot yet be identified, both Mendelian disease and neurodevelopmental disorders are broadly considered to be areas of solid and ongoing success, at least with respect to elucidating the underlying genetic factors.

For Mendelian and neurodevelopmental disorders, NGS, coupled with the reference human genome, are transforming not only gene discovery but also how clinical diagnoses are made. Particularly given that the diagnosis of many or most Mendelian disorders based on clinical features alone remains challenging, directly sequencing a patient's and/or family's exome(s) can provide a definitive answer and circumvent so-called diagnostic odysseys. A landmark study in 2013 showed that ~25% of probands with potentially genetic conditions could be diagnosed by exome sequencing, a proportion that will only rise as our understanding of monogenic disease becomes

more comprehensive (Yang et al., 2013). A more recent study from the same group showed that over one-third of cases that were unsolved by a standardized pipeline could be resolved by focused investigation (Eldomery et al., 2017).

A recurrent criticism is that diagnoses are not terribly useful when ''cures'' are not available, as is the case for the vast majority of Mendelian diseases. This is misguided, as accurate diagnoses can provide meaningful resolution for patients and families, connect them to disease-specific support networks, inform prognosis and co-morbidities, and facilitate family planning. For ID and ASD as well, ''molecular stratification,'' i.e., the identification of what specific gene underlies a particular patient's condition, is useful for exactly the same reasons (Bernier et al., 2014).

Particularly given the contribution of Mendelian disorders to infant mortality in developed countries (by one study, 23% of infant deaths), the pioneering efforts of Kingsmore and colleagues toward sub-24 h diagnoses of rare genetic conditions in neonatal intensive care unit (NICU) patients warrants mention. Studies from multiple groups have shown that rapid whole-genome sequencing can result in diagnoses for as many as half of acutely ill inpatient infants, informing clinical management as well as reducing inpatient costs in about half those cases. Given the stakes, we would be unsurprised to see this further develop into the standard of care in the near future (Farnaes et al., 2018; Meng et al., 2017; Saunders et al., 2012; Willig et al., 2015).

A noteworthy set of genes are the 59 designated by the American College of Medical Genetics (ACMG) to be sufficiently ''medically actionable'' so as to merit reporting as secondary findings in the context of clinical genetic testing done for other purposes (Kalia et al., 2017). The paradigmatic examples from the ACMG 59 are *BRCA1* and *BRCA2*, wherein pathogenic mutations are associated with early-onset breast and ovarian cancers, the risk for which can be mitigated by appropriate interventions (e.g., mastectomy, oophorectomy). Other examples include *BMPR1A* and *SMAD4*, wherein pathogenic mutations are associated with polyps and ultimately colon cancer, morbidity from which can be mitigated by frequent screening. Genes like *BRCA1* and *BRCA2* have already been sequenced in millions of individuals; most other genes on this list are far behind but are increasingly included on gene panels and naturally ascertained through exome or genome sequencing. Although the development of guidelines for reporting and actionability around these genes is an unquestionably positive development, at least two major challenges remain.

A first challenge is that of variant interpretation. A key distinction between secondary findings in ACMG 59 genes versus conventional findings in Mendelian disorders is that with the former, the patient has not yet developed the phenotype, such that the prior probability that a rare variant or *de novo* mutation is pathogenic is much lower. Although nonsense mutations are generally interpretable as pathogenic, missense and other mutations in these genes are typically classified as variants of unknown significance (VUS), a label that is confusing for physicians and anxiety-provoking for patients. Particularly as sequencing is extended to ever-larger populations, and as more genes become medically actionable, the number of VUS will exponentially grow (Starita et al., 2017). The problem is mitigated by public data sharing, but by no means solved, as the vast majority of rare variants may occur in only a handful of living humans, insufficient for the definitive assignment of risk. Toward solving this, we and others are pursuing scalable approaches for experimentally testing the functional consequences of variants, the vast majority of which have yet to be observed in a patient, via *in vitro* assays that capture the gene's disease-relevant function (Starita et al., 2017). As one example, for *BRCA1*, we and colleagues recently used saturation genome editing to experimentally test >96% of all possible SNVs in the gene's RING and BRCT domains, with results that strongly correlate with available clinical interpretations (Findlay et al., 2018).

A second challenge is that of penetrance, i.e., the proportion of individuals with a mutation in a gene that will actually express the associated phenotype. Historically, we have estimated the penetrance of mutations in genes such as *BRCA1* and *BRCA2* by studying patients and their families. However, these families may be enriched for modifiers in a way that results in penetrance being overestimated. Through cohorts such as the UK Biobank and All of Us, sufficiently powered studies on unselected populations are increasingly realistic, potentially allowing for a correction of penetrance estimates for genes such as *BRCA1* and *BRCA2* and the first such estimates for rare diseases for which they have heretofore not been possible. On a related point, it seems that we will increasingly be in a position to identify and exploit modifiers of penetrance for disorders caused by rare variants. There is accumulating evidence that common genetic variants, in aggregate, are formidable modifiers of penetrance and expressivity. For example, *BRCA1* mutation carriers can be stratified into those at high versus low risk for breast or ovarian cancer on the basis of common variants (Couch et al., 2013). Common genetic variants also appear to contribute substantially to risk for neurodevelopmental disorders including autism (Niemi et al., 2018; Weiner et al., 2017). These findings suggest that the PRS approach highlighted above will be relevant for not only common diseases but also Mendelian and neurodevelopmental disorders.

In the past few years, with increasing investment from pharma in rare diseases (Litterman et al., 2014), the second coming of gene therapy (Dunbar et al., 2018), and the third wave of genome editing platforms (Gaj et al., 2013), there is justified excitement about the development of therapies, and possibly even cures, for select Mendelian disorders. A full consideration of these is beyond the scope of this Perspective, but we briefly highlight four examples. (1) Cystic fibrosis: In 2011, over 2 decades after the gene underlying cystic fibrosis (CF) was mapped, a new drug, ivacaftor, was demonstrated to be efficacious in improving lung function for CF patients bearing a mutation for which the drug was designed (Ramsey et al., 2011). Compounds directed at modulating the activity of other CFTR alleles, e.g., lumacaftor for the common delta-F508 mutation, are actively being developed. (2) Sickle cell anemia: A recent single-patient report described effective, sustained remission of sickle cell anemia subsequent to lentiviral transfer of an antisickling beta-globin variant (Ribeil et al., 2017). (3) Hemophilia: A recent phase 1-2 trial in patients with severe hemophilia A showed that a single dose of an adeno-associated virus (AAV) vector bearing human *F8* consistently resulted in stable levels of factor VIII, reduced

bleeding, few adverse events, and no neutralizing antibodies (Rangarajan et al., 2017). (4) Muscular dystrophy: Although still unpublished, early results from three patients with Duchenne muscular dystrophy, treated by AAV delivery of a shortened form of dystrophin, included surprisingly high dystrophin levels, reduced creatine kinase, and anecdotes of massive clinical improvement (Herper, 2018). These and other recent reports, together with major recent investments in the clinical translation of genome editing, suggest that we are in for an exciting few years in this space. Although Mendelian diseases are rare, and it will likely only be a small subset for which effective treatments will be developed in the near future, their impact on young patients and their families can be profound and should not be discounted. These developments also illustrate the decades-long road, but one that can ultimately prove very worthwhile, between the basic science of mapping disease genes and the translational science of developing effective therapies.

The study of rare diseases can also have major implications for common diseases, including for guiding therapeutic strategies. The classic example is familial hypercholesterolemia, an autosomal dominant condition whose mapping to the LDL receptor helped make the case for statins, now used by millions of individuals for primary prevention of atherosclerotic cardiovascular disease (Stossel, 2008). A more recent example is *PCSK9*, wherein loss-of-function (LOF) mutations are associated with lower cholesterol, motivating the development of agents to inhibit its protein product, several of which were recently shown to be effective in lowering LDL cholesterol levels more effectively than statins (Chaudhary et al., 2017).

Motivated by these and other successes, there are now several efforts to systematically discover instances in which LOF mutations in living humans might inform drug development. For example, through ''hypothesis-free'' exome sequencing of a cohort of ~50,000 individuals for which healthcare records were available, Dewey and colleagues discovered that heterozygous LOF mutations in *ANGPTL3* were associated with lower cholesterol levels. Correspondingly, a monoclonal antibody against this same gene lowered cholesterol in animal models and healthy human volunteers (Chaudhary et al., 2017; Dewey et al., 2017).

Whereas heterozygous LOF carriers for nearly any haplosufficient gene can be found in such large cohorts, there are also efforts underway to leverage high levels of consanguinity in some populations to identify and deeply phenotype humans bearing homozygous LOF mutations for as many genes as possible (Perdigoto, 2017). As an unconventional example of how insights from such homozygous LOF patients can inform even common infectious diseases, consider *CCR5*, a gene for which LOF results in resistance to HIV acquisition. A brilliant study showed that a stem cell transplant from a donor with homozygous LOF of *CCR5* to a patient with HIV resulted in long-term control of viral load without antiretroviral therapy (Hütter et al., 2009). An obvious next step to explore is whether gene editing of *CCR5* in autologous cells is an effective strategy for long-term control of HIV (Tebas et al., 2014), i.e., as a potential alternative to lifelong antiretroviral treatment.

Most of the threads on the road between rare disease genetics and effective therapies for rare and common diseases are still works in progress. However, there is now ample reason, much more so than even 2 years ago, to believe that a reasonable fraction of them will succeed.

Genomic Medicine → Prenatal and Reproductive Health

Nowhere has the impact of genomic medicine on clinical practice been stronger than in prenatal and reproductive diagnostics. A sea change has already occurred in non-invasive screening for fetal trisomies (i.e., non-invasive prenatal testing, NIPT), both in terms of the screening methodologies themselves and in the risk categories of the pregnancies being tested. Assisted reproductive technology is offering prospective parents increasing quantities of genetic information on fertilized embryos before implantation. However, the information provided can sometimes complicate, rather than clarify, clinical decision-making. In this section, we briefly summarize the technologies underlying these tests, the types of information they provide to clinicians and patients, and the implications—clinical and ethical—of their continued growth.

Following its discovery in 1948 (Mandel and Metais, 1948), plasma-borne DNA remained essentially a curiosity until the discovery that the variable tissue sources of these fragments provide a window into malignancy and pregnancy (Leon et al., 1977; Lo et al., 1997; Stroun et al., 1987). While non-invasive screening for fetal abnormalities is not new, the accuracy and resolution of cell-free DNA (cfDNA)-based genetic tests for trisomies led to their emergence as the fastest adopted molecular test in the history of medicine and arguably the largest success story of genomic medicine to date. NIPT directed at identifying common fetal aneuploidies include ''chromosomal counting'' methods based on low-pass whole-genome sequencing (Chiu et al., 2008; Fan et al., 2008), targeted sequencing derivatives that potentially reduce the likelihood of incidental findings (Sparks et al., 2012; Zimmermann et al., 2012), and purely microarray-based assays (Juneau et al., 2014). The performance of tests implementing each of these approaches has been consistently strong in both high- and low-risk cohorts (Bianchi et al., 2014; Dar et al., 2016; Norton and Wapner, 2015), which has, together with the comparatively poor performance of contemporary alternatives, no doubt accelerated their widespread and rapid adoption.

The resolution of NIPT continues to improve, enabling clinicians to evaluate the risk of additional classes of genetic lesions beyond chromosomal aneuploidy. Recently, cfDNA-based tests able to detect sub-chromosomal abnormalities, such as microdeletions implicated in Prader-Willi or Angelman syndromes, were described and added to some existing commercial NIPT offerings (Srinivasan et al., 2013; Wapner et al., 2015). These tests mirror the growth in non-invasive testing for single-gene disorders, wherein the detection of specific risk alleles is obtained through more targeted means (Camunas-Soler et al., 2018). In proof-of-concept studies, we and others have shown that the whole-genome sequence of a fetus can be ascertained with samples obtained non-invasively from the parents (Chan et al., 2016; Fan et al., 2012; Kitzman et al., 2012). For prospective parents with difficulties with conception or with known risk of recessive disease, preimplantation genetic diagnosis (PGD) offers the *in vitro* fertilization and profiling of multiple embryos

prior to implantation. Mirroring the advances in NIPT, the resolution of PGD has increased in recent years, such that determination of the whole genome of each embryo is now possible (Hou et al., 2013; Kumar et al., 2015).

Looking forward, it seems plausible to suggest that the future of reproductive genetics may be a single, comprehensive test that simultaneously interrogates a pregnancy or fertilized zygote for aneuploidy, structural variants, and inherited variants or *de novo* mutations potentially causing any one of the >3,000 Mendelian disorders with known causes. While such whole-genome tests are technically within reach, multiple challenges remain to their widespread adoption. First and foremost is the challenge of interpretation of exhaustive test results: given the inevitably large number of VUSs as well as the challenges in quantifying penetrance discussed above, how much information is too much for a clinician, a genetic counselor, or a prospective parent? Second, substantial technical and logistical obstacles—including experimental complexity, scalability, necessary expertise, and cost—remain significant impediments to clinical adoption. Finally, the ethical considerations surrounding prenatal testing, which are not unique to cfDNA-based NIPT, are magnified in light of increasing resolution as well as the development of PRS, with potential for prenatal prediction of adult-onset diseases as well as non-disease traits. Greater scrutiny and regulatory oversight of the reproductive genetics industry is sorely needed.

Genomic Medicine → Cancer

The public's perception of the successes and struggles of genomic medicine has largely focused on cancer, which competes with heart disease for status as the leading cause of death in developed countries. Here, we consider cancer separately from other common diseases, because although there are inherited factors that can modulate risk (e.g., common variants, *BRCA1* mutations, etc.), it is ultimately a disease of somatic mutation. With NGS and projects such as The Cancer Genome Atlas (TCGA), the past decade has witnessed enormous strides toward comprehensively cataloging the genes and mutations that can serve as drivers of oncogenesis, essentially by exome or genome sequencing of thousands of tumor-normal matched sample pairs. A recent pan-cancer analysis across the entire TCGA dataset identified a consensus list of 299 driver genes of common cancers (Bailey et al., 2018). Furthermore, we have not yet saturated discovery of such drivers, potentially motivating a much larger version of the TCGA (Lawrence et al., 2014). However, given finite resources and analogous to GWASs, one wonders about the marginal value of the 300th driver gene, which is likely mutated in only a very small fraction of cancers, particularly when the first 299 remain understudied and therapeutically underexploited. Nonetheless, the catalog achieved to date is a wonderful accomplishment, a necessary prelude to a rational attack on the so-called emperor of maladies.

Far more so than in the other areas discussed above, driver genes and mutations in cancer provide clear molecular targets for therapeutic agents. The paradigmatic example is that non-small cell lung cancers with activating somatic mutations in the EGFR kinase, but not those without, are effectively treated with the EGFR kinase inhibitor gefitinib (Paez et al., 2004). Taking the TCGA as a reasonably representative broad survey, about half of common tumors contain one or more clinically relevant mutations, predicting sensitivity or resistance to specific agents or suggesting clinical trial eligibility (Bailey et al., 2018). But how efficacious are such "precision therapies"? On the one hand, there are accumulating anecdotes of patients who have had remarkable responses, including complete remissions, to agents whose selection was guided by genomic information. On the other hand, to the extent that it has been systematically studied, treating patients with therapies that are molecularly matched to their tumors more typically extends progression-free survival by weeks or months, rather than years (Radovich et al., 2016; Wheler et al., 2015). Clearly, at least for the vast majority of cancer patients, we have yet to deliver.

Cancer immunotherapy—leveraging the immune system to treat cancer—is an overlapping area showing terrific promise. It has many modalities, one of which is to actively reengineer a patient's immune cells to target tumor-specific antigens, and another of which involves vaccination with "neoantigens," i.e., peptides that are unequivocally unique to the tumor because they arose through somatic mutation. For the latter, a combination of exome sequencing and computational design can be used to generate a set of patient- and tumor-specific epitopes that are predicted to bind MHC class I and induce T cell-mediated immunity. In a recent small-scale study, four of six stage III/IV melanoma patients treated with such immunogenic personal vaccines followed by surgery had no recurrence 25 months post-vaccination, while the two that recurred were effectively treated with checkpoint blockade (Ott et al., 2017). This kind of approach obviously requires testing on larger numbers of patients and more tumor types before its efficacy is proven, but it potentially represents a new genome-centric paradigm for cancer treatment.

The observation that the early detection of many common cancers leads to substantially better outcomes predated the genomic era; this is of course the motivation for screening measures including colonoscopy and mammography. Even for those cancer types for which screens are available, the modest proportion of cases detected when the tumor is localized—less than four in ten colorectal tumors, and about six in ten breast cancers—argues both for the refinement and continued use of existing screening methodologies and for the development of new, minimally invasive biomarkers (Noone et al., 2018). As such, there has been considerable investment over the past decade into the use of DNA as such a biomarker—not just for early detection but also for detection of recurrence, for monitoring response to treatment, and as a companion diagnostic to select appropriate therapies.

Tumors shed DNA, just like a fetus or placenta sheds DNA, into circulation. This circulating tumor DNA (ctDNA) reflects the mutational profile of the tumor: the ensemble of somatic point mutations, copy-number changes, aneuploidy, and other genomic aberrations that distinguish the tumor from the healthy tissue. In the context of late-stage cancer recurrence detection, the presence of disease can be surveilled via the ctDNA in bespoke fashion by first sequencing the patient's tumor, i.e., after a conventional biopsy, to define a list of mutated loci to

follow over time, or in a more generic assay focused on regions commonly mutated across many cancers. Whether either of these approaches will translate to the goal of early detection is less clear, owing to a number of factors. First, the proportion of ctDNA in the circulation is, on average, substantially lower for early, localized tumors than for the late-stage tumors typically monitored in this way (Bettegowda et al., 2014; Haque and Elemento, 2017). Second, the bespoke model is effectively impossible to apply to early detection, and approaches based on lists of the most frequent mutations are inherently limited in their scope. Third, the bar is high for the performance characteristics of a screening test that will be applied to healthy individuals, and appropriately so, as each false positive will incur unnecessary anxiety and expensive follow up. Fourth, some recent studies suggest that for at least some cancer types, metastases may be seeded through early-stage dissemination (Hosseini et al., 2016).

Of course, these reasons for caution are balanced in part by countervailing reasons for optimism. First, any meaningful shift toward earlier detection, even if it falls short of stage I, is likely to improve outcomes for a broad range of cancer types. Second, complementary strategies being developed by us and others involve focusing on epigenetic signals, such as aberrant ctDNA fragmentation or methylation, as additional sources of information that can be used to detect the presence of a tumor and localize it to an anatomical compartment (Guo et al., 2017; Snyder et al., 2016; Sun et al., 2015). Third, even further additional signals, e.g., protein biomarkers, can be combined with information from ctDNA to improve predictive performance (Cohen et al., 2018). Fourth, even further information from the same patient (e.g., monitoring of their immune system, their likelihood of disease based on medical history, other risk factors, or even their PRS for each cancer type), could effectively be used as a prior while interpreting the results of a ctDNA screening test.

Initially, such screens are likely to be focused on detection of a specific type of tumor, for example, measuring promoter methylation of *SEPT9* for colorectal cancer (deVos et al., 2009) or quantifying circulating fragments of the Epstein-Barr viral genome for nasopharyngeal carcinoma (Chan et al., 2017). Indeed, such tests are already in limited clinical use, either in geographic areas with high incidence of a certain cancer or in patient groups reluctant to be screened by more established means. Looking forward, one possible outcome is the development of a pan-cancer (or at least multi-cancer) screen capable of simultaneously detecting and localizing a large number of tumor types at early stage. Even a partial achievement of this goal has the potential to radically change the way that we screen for cancer.

The Future of Genomic Medicine

Amidst the excitement around the HGP, there was perhaps a naive hope that the human genome would somehow magically solve everything. It obviously has not—but it is having an impact. We have gone from sequencing one human genome to over a million, with tens of millions more genotyped, in just 15 years. We have a more grounded understanding of the complexities of the genetic component of common disease risk, including the roadblocks between association signals and the development of meaningful therapies. We have a vastly more comprehensive catalog of the molecular lesions underlying cancer and can apply "precision therapies" in as many as half of patients, albeit only to be stymied in nearly all cases by cancer's remarkable ability to evolve. We are on the path to understanding the genetic basis of nearly all Mendelian disorders and to making meaningful impacts on the lives of those patients through diagnoses and, for at least a small subset of patients, through cures. In retrospect, the initial expectations were clearly set too high. But at the same time, what we have accomplished, and the trajectory that we are on as a field, are nothing to sneeze at. Furthermore, in certain areas (e.g., the cost of sequencing, NIPT, Mendelian disease), the field has advanced much more quickly than anyone anticipated.

We should not shy from setting high expectations, but one concern about promising aggressive timelines for therapies and cures is that it results in an excessive focus on often-unrealistic short-term objectives, which is in turn a disservice to the longer journey that this inevitably will be. Furthermore, as NGS, genome editing, and other breakthroughs clearly show, the human genome sequence is not enough, and achieving maximal impact for our field demands that we expand our investment in basic science, foundational resources, and technologies that are designed and calibrated to serve the long-term view. Grand challenges for the future of the genome sciences that we are particularly excited about in the sense that we think that they could serve to accelerate progress across the board, include (1) understanding, at least at some basic level, the function of every gene in the human genome; (2) scaling the identification of causal variants, genes, and mechanisms for existing GWAS signals from a handful to thousands; (3) a spatially resolved molecular atlas of all human cell types, from birth to death, e.g., including their chromatin landscape, gene expression, and protein expression signatures; and (4) developing accurate, quantitative models for predicting the impact of arbitrary sequence variants on gene expression and/or protein function in any one of these cell types. A fuller list of potential grand challenges for both genome sciences and genomic medicine in the coming decade is shown in Figure 4.

We are well along the path to a future in which a substantial fraction of the human population, at least in the developed world, will have their genomes genotyped or sequenced, and where that information is available together with their electronic healthcare records for both clinical and research uses (Topol, 2014). The phenotypes to which many of these genomes are linked will outgrow the conventional medical record, e.g., longitudinal molecular profiles and imaging, recording of activity and exposures, etc. Sequencing in some form is likely to become routine for all cancers and possibly for prospective parents and the unborn as well. We may even be recurrently sequenced, e.g., routine monitoring of cfDNA for cancer or other conditions. Finally, we have focused here on human genomes, but the genomes of commensal and pathogenic microorganisms are likely to be routinely interrogated as well.

Much of the value of an individual's genetic information lasts throughout their lifetime, meaning that advances in our ability to interpret variation will continue to provide benefits. Although genome sequencing may only have marginal benefits for many if not most patients, the improved understanding of human

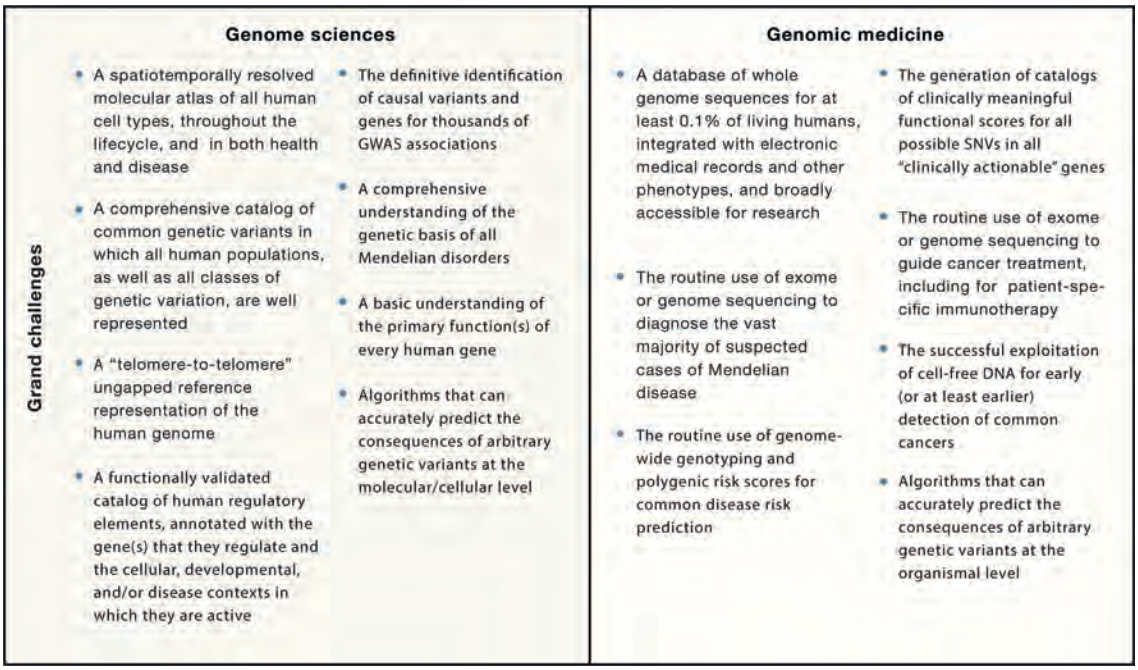

Figure 4. Future Grand Challenges for Genome Sciences and Genomic Medicine
A selection of future grand challenges for the genome sciences (left) and genomic medicine (right).

biology that comes from conducting genetics on humans will have an impact that lasts as long as our species does. Combined with other advances (e.g., PRSs, gene therapy, immunotherapy, etc.), our collective genomes will serve as a basis not only for advancing our understanding of disease but also for the development of new preventative and therapeutic strategies.

At some level, we worry that the above framing is again setting high expectations, so we should be clear. We continue to believe in the transformative potential of genomics on medicine and argue that the progress of the last 15 years, although poorly aligned with oft-criticized predictions made in the past, provides more-than-ample evidence to support this potential. At the same time, the reality will be nuanced, and there are no guarantees here. Large hurdles remain, and continued investment in basic science and technology is unquestionably necessary to overcome them. In our view, much of the biomedical research enterprise, including genomics, should be thought of as long-term bets for our society and our species, investments whose payoffs may not be fully realized for many decades or even in our lifetimes. That does not make these investments any less worthwhile.

In closing, we note that the Human Genome Project was accompanied by an early recognition of the ethical, legal, and social implications (ELSIs) that it would raise. These concerns have never been more paramount. We are increasingly identifiable, even if we have never volunteered our own DNA, through the combination of proliferating ancestry tests and pedigree searches (Erlich et al., 2018). Scientific racism, which continues to misappropriate studies of human genetics, is alive and well. Individual scientists have flaunted norms, and perhaps laws, to perform medically unnecessary genetic modifications to the human germline (Belluck, 2018). The life insurance industry has taken a strong interest in PRS (Russell, 2018), while US-based startup companies purport to offer embryo selection for non-disease traits (Belluck, 2018; Wilson, 2018). As we grapple with these and other ethically and socially alarming developments, it is incumbent on our field to much more proactively assume responsibility not only for maximizing the benefits associated with the human genome and genomic medicine but also for minimizing the harms.

ACKNOWLEDGMENTS

We thank the Shendure Lab and many colleagues for many useful discussions on these topics. We are greatly appreciative of the Illumina marketing department for their assistance with estimates of the number of individuals who have received genomic testing. This work was funded in part by grant 5DP1HG007811 from the National Institutes of Health. J.S. is an investigator of the Howard Hughes Medical Institute.

DECLARATION OF INTERESTS

J.S. has financial interests in companies working on subjects related to genomic medicine, including Adaptive Biotechnologies, Bellwether Bio, Camp4 Therapeutics, Cambridge Epigenetix, GenePeeks, Maze Therapeutics, Nanostring, Phase Genomics, and Stratos Genomics. His lab has an unfunded collaborative research agreement with Illumina. M.W.S. is a founder and employee of Bellwether Bio.

SUPPORTING CITATIONS

The following references appear in Figure 2: Lynch et al. (2004); Margulies et al. (2005); Ozaki et al. (2002); Sahin et al. (2017); Shendure et al. (2005).

REFERENCES

Bailey, M.H., Tokheim, C., Porta-Pardo, E., Sengupta, S., Bertrand, D., Weerasinghe, A., Colaprico, A., Wendl, M.C., Kim, J., Reardon, B., et al.; MC3 Working Group; Cancer Genome Atlas Research Network (2018). Comprehensive Characterization of Cancer Driver Genes and Mutations. Cell *173*, 371–385.e18.

Baird, P.A., Anderson, T.W., Newcombe, H.B., and Lowry, R.B. (1988). Genetic disorders in children and young adults: a population study. Am. J. Hum. Genet. *42*, 677–693.

Bernier, R., Golzio, C., Xiong, B., Stessman, H.A., Coe, B.P., Penn, O., Witherspoon, K., Gerdts, J., Baker, C., Vulto-van Silfhout, A.T., et al. (2014). Disruptive CHD8 mutations define a subtype of autism early in development. Cell *158*, 263–276.

Bettegowda, C., Sausen, M., Leary, R.J., Kinde, I., Wang, Y., Agrawal, N., Bartlett, B.R., Wang, H., Luber, B., Alani, R.M., et al. (2014). Detection of circulating tumor DNA in early- and late-stage human malignancies. Sci. Transl. Med. *6*, 224ra24.

Bianchi, D.W., Parker, R.L., Wentworth, J., Madankumar, R., Saffer, C., Das, A.F., Craig, J.A., Chudova, D.I., Devers, P.L., Jones, K.W., et al.; CARE Study Group (2014). DNA sequencing versus standard prenatal aneuploidy screening. N. Engl. J. Med. *370*, 799–808.

Boyle, E.A., Li, Y.I., and Pritchard, J.K. (2017). An Expanded View of Complex Traits: From Polygenic to Omnigenic. Cell *169*, 1177–1186.

Burdett, T., Hastings, E., and Welter, D. (2018). SPOT, EMBL-EBI, and NHGRI (GWAS Catalog).

Bycroft, C., Freeman, C., Petkova, D., Band, G., Elliott, L.T., Sharp, K., Motyer, A., Vukcevic, D., Delaneau, O., O'Connell, J., et al. (2018). The UK Biobank resource with deep phenotyping and genomic data. Nature *562*, 203–209.

Camunas-Soler, J., Lee, H., Hudgins, L., Hintz, S.R., Blumenfeld, Y.J., El-Sayed, Y.Y., and Quake, S.R. (2018). Noninvasive Prenatal Diagnosis of Single-Gene Disorders by Use of Droplet Digital PCR. Clin. Chem. *64*, 336–345.

Chan, K.C.A., Jiang, P., Sun, K., Cheng, Y.K.Y., Tong, Y.K., Cheng, S.H., Wong, A.I.C., Hudecova, I., Leung, T.Y., Chiu, R.W.K., and Lo, Y.M. (2016). Second generation noninvasive fetal genome analysis reveals de novo mutations, single-base parental inheritance, and preferred DNA ends. Proc. Natl. Acad. Sci. USA *113*, E8159–E8168.

Chan, K.C.A., Woo, J.K.S., King, A., Zee, B.C.Y., Lam, W.K.J., Chan, S.L., Chu, S.W.I., Mak, C., Tse, I.O.L., Leung, S.Y.M., et al. (2017). Analysis of Plasma Epstein-Barr Virus DNA to Screen for Nasopharyngeal Cancer. N. Engl. J. Med. *377*, 513–522.

Chaudhary, R., Garg, J., Shah, N., and Sumner, A. (2017). PCSK9 inhibitors: A new era of lipid lowering therapy. World J. Cardiol. *9*, 76–91.

Chiu, R.W.K., Chan, K.C.A., Gao, Y., Lau, V.Y.M., Zheng, W., Leung, T.Y., Foo, C.H.F., Xie, B., Tsui, N.B.Y., Lun, F.M.F., et al. (2008). Noninvasive prenatal diagnosis of fetal chromosomal aneuploidy by massively parallel genomic sequencing of DNA in maternal plasma. Proc. Natl. Acad. Sci. USA *105*, 20458–20463.

Choi, M., Scholl, U.I., Ji, W., Liu, T., Tikhonova, I.R., Zumbo, P., Nayir, A., Bakkaloğlu, A., Ozen, S., Sanjad, S., et al. (2009). Genetic diagnosis by whole exome capture and massively parallel DNA sequencing. Proc. Natl. Acad. Sci. USA *106*, 19096–19101.

Chong, J.X., Buckingham, K.J., Jhangiani, S.N., Boehm, C., Sobreira, N., Smith, J.D., Harrell, T.M., McMillin, M.J., Wiszniewski, W., Gambin, T., et al.; Centers for Mendelian Genomics (2015). The Genetic Basis of Mendelian Phenotypes: Discoveries, Challenges, and Opportunities. Am. J. Hum. Genet. *97*, 199–215.

Cohen, J.D., Li, L., Wang, Y., Thoburn, C., Afsari, B., Danilova, L., Douville, C., Javed, A.A., Wong, F., Mattox, A., et al. (2018). Detection and localization of surgically resectable cancers with a multi-analyte blood test. Science *359*, 926–930.

Collins, F.S., Guyer, M.S., and Charkravarti, A. (1997). Variations on a theme: cataloging human DNA sequence variation. Science *278*, 1580–1581.

Couch, F.J., Wang, X., McGuffog, L., Lee, A., Olswold, C., Kuchenbaecker, K.B., Soucy, P., Fredericksen, Z., Barrowdale, D., Dennis, J., et al.; kConFab Investigators; SWE-BRCA; Ontario Cancer Genetics Network; HEBON; EMBRACE; GEMO Study Collaborators; BCFR; CIMBA (2013). Genome-wide association study in BRCA1 mutation carriers identifies novel loci associated with breast and ovarian cancer risk. PLoS Genet. *9*, e1003212.

Dar, P., Shani, H., and Evans, M.I. (2016). Cell-free DNA: Comparison of Technologies. Clin. Lab. Med. *36*, 199–211.

deVos, T., Tetzner, R., Model, F., Weiss, G., Schuster, M., Distler, J., Steiger, K.V., Grützmann, R., Pilarsky, C., Habermann, J.K., et al. (2009). Circulating methylated SEPT9 DNA in plasma is a biomarker for colorectal cancer. Clin. Chem. *55*, 1337–1346.

Dewey, F.E., Gusarova, V., Dunbar, R.L., O'Dushlaine, C., Schurmann, C., Gottesman, O., McCarthy, S., Van Hout, C.V., Bruse, S., Dansky, H.M., et al. (2017). Genetic and Pharmacologic Inactivation of ANGPTL3 and Cardiovascular Disease. N. Engl. J. Med. *377*, 211–221.

Do, R., Willer, C.J., Schmidt, E.M., Sengupta, S., Gao, C., Peloso, G.M., Gustafsson, S., Kanoni, S., Ganna, A., Chen, J., et al. (2013). Common variants associated with plasma triglycerides and risk for coronary artery disease. Nat. Genet. *45*, 1345–1352.

Dunbar, C.E., High, K.A., Joung, J.K., Kohn, D.B., Ozawa, K., and Sadelain, M. (2018). Gene therapy comes of age. Science *359*, eaan4672.

Eldomery, M.K., Coban-Akdemir, Z., Harel, T., Rosenfeld, J.A., Gambin, T., Stray-Pedersen, A., Küry, S., Mercier, S., Lessel, D., Denecke, J., et al. (2017). Lessons learned from additional research analyses of unsolved clinical exome cases. Genome Med. *9*, 26.

Erlich, Y., Shor, T., Pe'er, I., and Carmi, S. (2018). Identity inference of genomic data using long-range familial searches. Science *362*, 690–694.

Fan, H.C., Blumenfeld, Y.J., Chitkara, U., Hudgins, L., and Quake, S.R. (2008). Noninvasive diagnosis of fetal aneuploidy by shotgun sequencing DNA from maternal blood. Proc. Natl. Acad. Sci. USA *105*, 16266–16271.

Fan, H.C., Gu, W., Wang, J., Blumenfeld, Y.J., El-Sayed, Y.Y., and Quake, S.R. (2012). Non-invasive prenatal measurement of the fetal genome. Nature *487*, 320–324.

Farnaes, L., Hildreth, A., Sweeney, N.M., Clark, M.M., Chowdhury, S., Nahas, S., Cakici, J.A., Benson, W., Kaplan, R.H., Kronick, R., et al. (2018). Rapid whole-genome sequencing decreases infant morbidity and cost of hospitalization. NPJ Genom Med *3*, 10.

Findlay, G.M., Daza, R.M., Martin, B., Zhang, M.D., Leith, A.P., Gasperini, M., Janizek, J.D., Huang, X., Starita, L.M., and Shendure, J. (2018). Accurate functional classification of thousands of BRCA1 variants with saturation genome editing. Nature *562*, 217–222.

Finucane, H.K., Bulik-Sullivan, B., Gusev, A., Trynka, G., Reshef, Y., Loh, P.-R., Anttila, V., Xu, H., Zang, C., Farh, K., et al.; ReproGen Consortium; Schizophrenia Working Group of the Psychiatric Genomics Consortium; RACI Consortium (2015). Partitioning heritability by functional annotation using genome-wide association summary statistics. Nat. Genet. *47*, 1228–1235.

Fuchsberger, C., Flannick, J., Teslovich, T.M., Mahajan, A., Agarwala, V., Gaulton, K.J., Ma, C., Fontanillas, P., Moutsianas, L., McCarthy, D.J., et al. (2016). The genetic architecture of type 2 diabetes. Nature *536*, 41–47.

Gaj, T., Gersbach, C.A., and Barbas, C.F., 3rd. (2013). ZFN, TALEN, and CRISPR/Cas-based methods for genome engineering. Trends Biotechnol. *31*, 397–405.

Gasperini, M., Hill, A.J., McFaline-Figueroa, J.L., Martin, B., Kim, S., Zhang, M.D., Jackson, D., Leith, A., Schreiber, J., Noble, W.S., et al. (2019). A Genome-wide Framework for Mapping Gene Regulation via Cellular Genetic Screens. Cell *176*, 377–390.e19.

Gitlin, J.M. (2013). Calculating the economic impact of the Human Genome Project. National Human Genome Research Institute (NHGRI), last updated June 12, 2013. https://www.genome.gov/27544383/calculating-the-economic-impact-of-the-human-genome-project/.

Global Genomic Medicine Collaborative (2018). Improving the implementation of: Global Genomic Medicine. https://g2mc.org/.

Gunderson, K.L., Steemers, F.J., Lee, G., Mendoza, L.G., and Chee, M.S. (2005). A genome-wide scalable SNP genotyping assay using microarray technology. Nat. Genet. *37*, 549–554.

Guo, S., Diep, D., Plongthongkum, N., Fung, H.-L., Zhang, K., and Zhang, K. (2017). Identification of methylation haplotype blocks aids in deconvolution of heterogeneous tissue samples and tumor tissue-of-origin mapping from plasma DNA. Nat. Genet. *49*, 635–642.

Haque, I.S., and Elemento, O. (2017). Challenges in Using ctDNA to Achieve Early Detection of Cancer. bioRxiv. https://doi.org/10.1101/237578.

Herper, M. (2018). A Gene Therapy Appears To Replace Missing Protein In Muscular Dystrophy Patients. Forbes, June 19, 2018. https://www.forbes.com/sites/matthewherper/2018/06/19/a-gene-therapy-appears-to-replace-missing-protein-in-muscular-dystrophy-patients/#55e0ddfc5225.

Hoischen, A., van Bon, B.W.M., Gilissen, C., Arts, P., van Lier, B., Steehouwer, M., de Vries, P., de Reuver, R., Wieskamp, N., Mortier, G., et al. (2010). De novo mutations of SETBP1 cause Schinzel-Giedion syndrome. Nat. Genet. *42*, 483–485.

Hosseini, H., Obradović, M.M.S., Hoffmann, M., Harper, K.L., Sosa, M.S., Werner-Klein, M., Nanduri, L.K., Werno, C., Ehrl, C., Maneck, M., et al. (2016). Early dissemination seeds metastasis in breast cancer. Nature *540*, 552–558.

Hou, Y., Fan, W., Yan, L., Li, R., Lian, Y., Huang, J., Li, J., Xu, L., Tang, F., Xie, X.S., and Qiao, J. (2013). Genome analyses of single human oocytes. Cell *155*, 1492–1506.

Hütter, G., Nowak, D., Mossner, M., Ganepola, S., Müssig, A., Allers, K., Schneider, T., Hofmann, J., Kücherer, C., Blau, O., et al. (2009). Long-term control of HIV by CCR5 Delta32/Delta32 stem-cell transplantation. N. Engl. J. Med. *360*, 692–698.

International HapMap Consortium (2005). A haplotype map of the human genome. Nature *437*, 1299–1320.

International Human Genome Sequencing Consortium (2004). Finishing the euchromatic sequence of the human genome. Nature *431*, 931–945.

Iossifov, I., O'Roak, B.J., Sanders, S.J., Ronemus, M., Krumm, N., Levy, D., Stessman, H.A., Witherspoon, K.T., Vives, L., Patterson, K.E., et al. (2014). The contribution of de novo coding mutations to autism spectrum disorder. Nature *515*, 216–221.

Juneau, K., Bogard, P.E., Huang, S., Mohseni, M., Wang, E.T., Ryvkin, P., Kingsley, C., Struble, C.A., Oliphant, A., and Zahn, J.M. (2014). Microarray-based cell-free DNA analysis improves noninvasive prenatal testing. Fetal Diagn. Ther. *36*, 282–286.

Kalia, S.S., Adelman, K., Bale, S.J., Chung, W.K., Eng, C., Evans, J.P., Herman, G.E., Hufnagel, S.B., Klein, T.E., Korf, B.R., et al. (2017). Recommendations for reporting of secondary findings in clinical exome and genome sequencing, 2016 update (ACMG SF v2.0): a policy statement of the American College of Medical Genetics and Genomics. Genet. Med. *19*, 249–255.

Khera, A.V., Chaffin, M., Aragam, K.G., Haas, M.E., Roselli, C., Choi, S.H., Natarajan, P., Lander, E.S., Lubitz, S.A., Ellinor, P.T., and Kathiresan, S. (2018). Genome-wide polygenic scores for common diseases identify individuals with risk equivalent to monogenic mutations. Nat. Genet. *50*, 1219–1224.

Kitzman, J.O., Snyder, M.W., Ventura, M., Lewis, A.P., Qiu, R., Simmons, L.E., Gammill, H.S., Rubens, C.E., Santillan, D.A., Murray, J.C., et al. (2012). Noninvasive Whole-Genome Sequencing of a Human Fetus. Sci. Transl. Med. *4*, 137ra76.

Kolata, G., Wee, S.-L., and Belluck, P. (2018). Chinese Scientist Claims to Use Crispr to Make First Genetically Edited Babies. The New York Times, November 26, 2018. https://www.nytimes.com/2018/11/26/health/gene-editing-babies-china.html.

Kumar, A., Ryan, A., Kitzman, J.O., Wemmer, N., Snyder, M.W., Sigurjonsson, S., Lee, C., Banjevic, M., Zarutskie, P.W., Lewis, A.P., et al. (2015). Whole genome prediction for preimplantation genetic diagnosis. Genome Med. *7*, 35.

Lawrence, M.S., Stojanov, P., Mermel, C.H., Robinson, J.T., Garraway, L.A., Golub, T.R., Meyerson, M., Gabriel, S.B., Lander, E.S., and Getz, G. (2014). Discovery and saturation analysis of cancer genes across 21 tumour types. Nature *505*, 495–501.

Leon, S.A., Shapiro, B., Sklaroff, D.M., and Yaros, M.J. (1977). Free DNA in the serum of cancer patients and the effect of therapy. Cancer Res. *37*, 646–650.

Litterman, N.K., Rhee, M., Swinney, D.C., and Ekins, S. (2014). Collaboration for rare disease drug discovery research. F1000Res. *3*, 261.

Liu, S., Huang, S., Chen, F., Zhao, L., Yuan, Y., Francis, S.S., Fang, L., Li, Z., Lin, L., Liu, R., et al. (2018). Genomic Analyses from Non-invasive Prenatal Testing Reveal Genetic Associations, Patterns of Viral Infections, and Chinese Population History. Cell *175*, 347–359.e14.

Lo, Y.M., Corbetta, N., Chamberlain, P.F., Rai, V., Sargent, I.L., Redman, C.W., and Wainscoat, J.S. (1997). Presence of fetal DNA in maternal plasma and serum. Lancet *350*, 485–487.

Lynch, T.J., Bell, D.W., Sordella, R., Gurubhagavatula, S., Okimoto, R.A., Brannigan, B.W., Harris, P.L., Haserlat, S.M., Supko, J.G., Haluska, F.G., et al. (2004). Activating mutations in the epidermal growth factor receptor underlying responsiveness of non-small-cell lung cancer to gefitinib. N. Engl. J. Med. *350*, 2129–2139.

Mandel, P., and Metais, P. (1948). Les acides nucléiques du plasma sanguin chez l'homme. C. R. Seances Soc. Biol. Fil. *142*, 241–243.

Manolio, T.A., Collins, F.S., Cox, N.J., Goldstein, D.B., Hindorff, L.A., Hunter, D.J., McCarthy, M.I., Ramos, E.M., Cardon, L.R., Chakravarti, A., et al. (2009). Finding the missing heritability of complex diseases. Nature *461*, 747–753.

Margulies, M., Egholm, M., Altman, W.E., Attiya, S., Bader, J.S., Bemben, L.A., Berka, J., Braverman, M.S., Chen, Y.-J., Chen, Z., et al. (2005). Genome sequencing in microfabricated high-density picolitre reactors. Nature *437*, 376–380.

McCandless, S.E., Brunger, J.W., and Cassidy, S.B. (2004). The burden of genetic disease on inpatient care in a children's hospital. Am. J. Hum. Genet. *74*, 121–127.

Meng, L., Pammi, M., Saronwala, A., Magoulas, P., Ghazi, A.R., Vetrini, F., Zhang, J., He, W., Dharmadhikari, A.V., Qu, C., et al. (2017). Use of Exome Sequencing for Infants in Intensive Care Units: Ascertainment of Severe Single-Gene Disorders and Effect on Medical Management. JAMA Pediatr. *171*, e173438.

Motsinger-Reif, A.A., Jorgenson, E., Relling, M.V., Kroetz, D.L., Weinshilboum, R., Cox, N.J., and Roden, D.M. (2013). Genome-wide association studies in pharmacogenomics: successes and lessons. Pharmacogenet. Genomics *23*, 383–394.

Mumbach, M.R., Rubin, A.J., Flynn, R.A., Dai, C., Khavari, P.A., Greenleaf, W.J., and Chang, H.Y. (2016). HiChIP: efficient and sensitive analysis of protein-directed genome architecture. Nat. Methods *13*, 919–922.

Nelson, M.R., Tipney, H., Painter, J.L., Shen, J., Nicoletti, P., Shen, Y., Floratos, A., Sham, P.C., Li, M.J., Wang, J., et al. (2015). The support of human genetic evidence for approved drug indications. Nat. Genet. *47*, 856–860.

Ng, S.B., Turner, E.H., Robertson, P.D., Flygare, S.D., Bigham, A.W., Lee, C., Shaffer, T., Wong, M., Bhattacharjee, A., Eichler, E.E., et al. (2009). Targeted capture and massively parallel sequencing of 12 human exomes. Nature *461*, 272–276.

Niemi, M.E.K., Martin, H.C., Rice, D.L., Gallone, G., Gordon, S., Kelemen, M., McAloney, K., McRae, J., Radford, E.J., Yu, S., et al. (2018). Common genetic variants contribute to risk of rare severe neurodevelopmental disorders. Nature *562*, 268–271.

Noone, A.M., Howlader, N., Krapcho, M., Miller, D., Brest, A., Yu, M., Ruhl, J., Tatalovich, Z., Mariotto, A., Lewis, D.R., et al. (2018). SEER Cancer Statistics Review, 1975–2015. National Cancer Institute, last updated September 10, 2018. https://seer.cancer.gov/csr/1975_2015/.

Norton, M.E., and Wapner, R.J. (2015). Cell-free DNA Analysis for Noninvasive Examination of Trisomy. N. Engl. J. Med. *373*, 2582.

Ott, P.A., Hu, Z., Keskin, D.B., Shukla, S.A., Sun, J., Bozym, D.J., Zhang, W., Luoma, A., Giobbie-Hurder, A., Peter, L., et al. (2017). An immunogenic personal neoantigen vaccine for patients with melanoma. Nature *547*, 217–221.

Ozaki, K., Ohnishi, Y., Iida, A., Sekine, A., Yamada, R., Tsunoda, T., Sato, H., Sato, H., Hori, M., Nakamura, Y., and Tanaka, T. (2002). Functional SNPs in the

lymphotoxin-alpha gene that are associated with susceptibility to myocardial infarction. Nat. Genet. *32*, 650–654.

Paez, J.G., Jänne, P.A., Lee, J.C., Tracy, S., Greulich, H., Gabriel, S., Herman, P., Kaye, F.J., Lindeman, N., Boggon, T.J., et al. (2004). EGFR mutations in lung cancer: correlation with clinical response to gefitinib therapy. Science *304*, 1497–1500.

Perdigoto, C. (2017). Mutations: Dawn of the Human Knockout Project. Nat. Rev. Genet. *18*, 328–329.

Radovich, M., Kiel, P.J., Nance, S.M., Niland, E.E., Parsley, M.E., Ferguson, M.E., Jiang, G., Ammakkanavar, N.R., Einhorn, L.H., Cheng, L., et al. (2016). Clinical benefit of a precision medicine based approach for guiding treatment of refractory cancers. Oncotarget *7*, 56491–56500.

Ramsey, B.W., Davies, J., McElvaney, N.G., Tullis, E., Bell, S.C., Dřevínek, P., Griese, M., McKone, E.F., Wainwright, C.E., Konstan, M.W., et al.; VX08-770-102 Study Group (2011). A CFTR potentiator in patients with cystic fibrosis and the G551D mutation. N. Engl. J. Med. *365*, 1663–1672.

Rangarajan, S., Walsh, L., Lester, W., Perry, D., Madan, B., Laffan, M., Yu, H., Vettermann, C., Pierce, G.F., Wong, W.Y., and Pasi, K.J. (2017). AAV5-Factor VIII Gene Transfer in Severe Hemophilia A. N. Engl. J. Med. *377*, 2519–2530.

Ribeil, J.-A., Hacein-Bey-Abina, S., Payen, E., Magnani, A., Semeraro, M., Magrin, E., Caccavelli, L., Neven, B., Bourget, P., El Nemer, W., et al. (2017). Gene Therapy in a Patient with Sickle Cell Disease. N. Engl. J. Med. *376*, 848–855.

Risch, N., and Merikangas, K. (1996). The future of genetic studies of complex human diseases. Science *273*, 1516–1517.

Russell, R. (2018). Polygenic Risk Scores: Combining Thousands of Genetic Variants to Predict Disease. Reinsurance Group of America, Inc., September 10, 2018. https://www.rgare.com/knowledge-center/media/articles/polygenic-risk-scores-combining-thousands-of-genetic-variants-to-predict-disease.

Sahin, U., Derhovanessian, E., Miller, M., Kloke, B.-P., Simon, P., Löwer, M., Bukur, V., Tadmor, A.D., Luxemburger, U., Schrörs, B., et al. (2017). Personalized RNA mutanome vaccines mobilize poly-specific therapeutic immunity against cancer. Nature *547*, 222–226.

Saunders, C.J., Miller, N.A., Soden, S.E., Dinwiddie, D.L., Noll, A., Alnadi, N.A., Andraws, N., Patterson, M.L., Krivohlavek, L.A., Fellis, J., et al. (2012). Rapid whole-genome sequencing for genetic disease diagnosis in neonatal intensive care units. Sci. Transl. Med. *4*, 154ra135.

Shendure, J., and Lieberman Aiden, E. (2012). The expanding scope of DNA sequencing. Nat. Biotechnol. *30*, 1084–1094.

Shendure, J., Porreca, G.J., Reppas, N.B., Lin, X., McCutcheon, J.P., Rosenbaum, A.M., Wang, M.D., Zhang, K., Mitra, R.D., and Church, G.M. (2005). Accurate multiplex polony sequencing of an evolved bacterial genome. Science *309*, 1728–1732.

Shendure, J., Balasubramanian, S., Church, G.M., Gilbert, W., Rogers, J., Schloss, J.A., and Waterston, R.H. (2017). DNA sequencing at 40: past, present and future. Nature *550*, 345–353.

Snyder, M.W., Kircher, M., Hill, A.J., Daza, R.M., and Shendure, J. (2016). Cell-free DNA Comprises an In Vivo Nucleosome Footprint that Informs Its Tissues-Of-Origin. Cell *164*, 57–68.

Sparks, A.B., Wang, E.T., Struble, C.A., Barrett, W., Stokowski, R., McBride, C., Zahn, J., Lee, K., Shen, N., Doshi, J., et al. (2012). Selective analysis of cell-free DNA in maternal blood for evaluation of fetal trisomy. Prenat. Diagn. *32*, 3–9.

Srinivasan, A., Bianchi, D.W., Huang, H., Sehnert, A.J., and Rava, R.P. (2013). Noninvasive detection of fetal subchromosome abnormalities via deep sequencing of maternal plasma. Am. J. Hum. Genet. *92*, 167–176.

Starita, L.M., Ahituv, N., Dunham, M.J., Kitzman, J.O., Roth, F.P., Seelig, G., Shendure, J., and Fowler, D.M. (2017). Variant Interpretation: Functional Assays to the Rescue. Am. J. Hum. Genet. *101*, 315–325.

Stossel, T.P. (2008). The discovery of statins. Cell *134*, 903–905.

Stroun, M., Anker, P., Lyautey, J., Lederrey, C., and Maurice, P.A. (1987). Isolation and characterization of DNA from the plasma of cancer patients. Eur. J. Cancer Clin. Oncol. *23*, 707–712.

Sun, K., Jiang, P., Chan, K.C.A., Wong, J., Cheng, Y.K.Y., Liang, R.H.S., Chan, W.-K., Ma, E.S.K., Chan, S.L., Cheng, S.H., et al. (2015). Plasma DNA tissue mapping by genome-wide methylation sequencing for noninvasive prenatal, cancer, and transplantation assessments. Proc. Natl. Acad. Sci. USA *112*, E5503–E5512.

Tebas, P., Stein, D., Tang, W.W., Frank, I., Wang, S.Q., Lee, G., Spratt, S.K., Surosky, R.T., Giedlin, M.A., Nichol, G., et al. (2014). Gene editing of CCR5 in autologous CD4 T cells of persons infected with HIV. N. Engl. J. Med. *370*, 901–910.

Topol, E.J. (2014). Individualized medicine from prewomb to tomb. Cell *157*, 241–253.

Visscher, P.M., Wray, N.R., Zhang, Q., Sklar, P., McCarthy, M.I., Brown, M.A., and Yang, J. (2017). 10 Years of GWAS Discovery: Biology, Function, and Translation. Am. J. Hum. Genet. *101*, 5–22.

Voight, B.F., Peloso, G.M., Orho-Melander, M., Frikke-Schmidt, R., Barbalic, M., Jensen, M.K., Hindy, G., Hólm, H., Ding, E.L., Johnson, T., et al. (2012). Plasma HDL cholesterol and risk of myocardial infarction: a mendelian randomisation study. Lancet *380*, 572–580.

Wapner, R.J., Babiarz, J.E., Levy, B., Stosic, M., Zimmermann, B., Sigurjonsson, S., Wayham, N., Ryan, A., Banjevic, M., Lacroute, P., et al. (2015). Expanding the scope of noninvasive prenatal testing: detection of fetal microdeletion syndromes. Am. J. Obstet. Gynecol. *212*, 332.e1–332.e9.

Weiner, D.J., Wigdor, E.M., Ripke, S., Walters, R.K., Kosmicki, J.A., Grove, J., Samocha, K.E., Goldstein, J., Okbay, A., Bybjerg-Gauholm, J., et al. (2017). Polygenic transmission disequilibrium confirms that common and rare variation act additively to create risk for autism spectrum disorders. Nat Genet. *49*, 978–985.

Wheler, J.J., Yelensky, R., Stephen, B., Hong, D.S., Zinner, R., Subbiah, V., Fu, S., Karp, D.D., Falchook, G.S., Naing, A., et al. (2015). Prospective study comparing outcomes in patients with advanced malignancies on molecular alteration-matched versus non-matched therapy. J Clin Oncol. *33*, 11019.

Willer, C.J., Schmidt, E.M., Sengupta, S., Peloso, G.M., Gustafsson, S., Kanoni, S., Ganna, A., Chen, J., Buchkovich, M.L., Mora, S., et al.; Global Lipids Genetics Consortium (2013). Discovery and refinement of loci associated with lipid levels. Nat. Genet. *45*, 1274–1283.

Willig, L.K., Petrikin, J.E., Smith, L.D., Saunders, C.J., Thiffault, I., Miller, N.A., Soden, S.E., Cakici, J.A., Herd, S.M., Twist, G., et al. (2015). Whole-genome sequencing for identification of Mendelian disorders in critically ill infants: a retrospective analysis of diagnostic and clinical findings. Lancet Respir. Med. *3*, 377–387.

Wilson, C. (2018). Exclusive: A new test can predict IVF embryos' risk of having a low IQ. New Scientist., November 15, 2018. https://www.newscientist.com/article/mg24032041-900-exclusive-a-new-test-can-predict-ivf-embryos-risk-of-having-a-low-iq/.

Wray, N.R., Yang, J., Hayes, B.J., Price, A.L., Goddard, M.E., and Visscher, P.M. (2013). Pitfalls of predicting complex traits from SNPs. Nat. Rev. Genet. *14*, 507–515.

Yang, J., Benyamin, B., McEvoy, B.P., Gordon, S., Henders, A.K., Nyholt, D.R., Madden, P.A., Heath, A.C., Martin, N.G., Montgomery, G.W., et al. (2010). Common SNPs explain a large proportion of the heritability for human height. Nat. Genet. *42*, 565–569.

Yang, Y., Muzny, D.M., Reid, J.G., Bainbridge, M.N., Willis, A., Ward, P.A., Braxton, A., Beuten, J., Xia, F., Niu, Z., et al. (2013). Clinical whole-exome sequencing for the diagnosis of mendelian disorders. N. Engl. J. Med. *369*, 1502–1511.

Yuzuki, D. (2015). What is Non-Invasive Prenatal Testing (NIPT)? Genomic Precision, SeraCare blog, November 17, 2015. https://blog.seracare.com/home/tabid/294/artmid/989/articleid/23/what-is-non-invasive-prenatal-testing-nipt.aspx.

Zimmermann, B., Hill, M., Gemelos, G., Demko, Z., Banjevic, M., Baner, J., Ryan, A., Sigurjonsson, S., Chopra, N., Dodd, M., et al. (2012). Noninvasive prenatal aneuploidy testing of chromosomes 13, 18, 21, X, and Y, using targeted sequencing of polymorphic loci. Prenat. Diagn. *32*, 1233–1241.

Sino Biological
Biological Solution Specialist

ASCB Booth #319

Emerging Leader in Biological Reagents & Services

Elite Reagents & One-stop CRO Services

Proteins 6000+

Antibodies 10,000+

CRO Services
Recombinant protein production service
Antibody production service
Biopharmaceutical service

ELISA Kits 800+

Genes 400,000+

Technology Platforms

Virus Technologies
Virus Vector
Pseudo Virus
Virus-like Particle
Neutralizing Antibody

Antibody Technologies
Antibody Library
Mouse & Rabbit Mab
Antibody Engineering
Single Cell PCR

Protein Technologies
Five Expression Systems
Experience of 6000+ Protein Production
1000+ Bio-activity Assays
Validated Formulation Methods

Cell Technologies
Tumor Cells
T Cells
Stem Cells
Stable Cell Lines

Gene Technologies
cDNA Library
Gene Knock-out
Expression-ready Vector
qPCR

Sino Biological US Inc.
Tel: 215-583-7898
Address: 1400 Liberty Ridge Drive, Suite 101, Wayne, PA 19087

Website: www.sinobiological.com
Email: Order_us@Sinobiological.com;
cro-service@Sinobiological.com

Resource

Cell

In Toto Imaging and Reconstruction of Post-Implantation Mouse Development at the Single-Cell Level

Katie McDole,[1,*] Léo Guignard,[1,*] Fernando Amat,[1] Andrew Berger,[1] Grégoire Malandain,[2] Loïc A. Royer,[3] Srinivas C. Turaga,[1] Kristin Branson,[1] and Philipp J. Keller[1,4,*]

[1]Janelia Research Campus, Howard Hughes Medical Institute, Ashburn, VA 20147, USA

[2]Université Côte d'Azur, Inria, CNRS, I3S, 06900 Sophia Antipolis, France

[3]Chan Zuckerberg Biohub, San Francisco, CA 94158, USA

[4]Lead Contact

*Correspondence: mcdolek@janelia.hhmi.org (K.M.), guignardl@janelia.hhmi.org (L.G.), kellerp@janelia.hhmi.org (P.J.K.)

https://doi.org/10.1016/j.cell.2018.09.031

SUMMARY

The mouse embryo has long been central to the study of mammalian development; however, elucidating the cell behaviors governing gastrulation and the formation of tissues and organs remains a fundamental challenge. A major obstacle is the lack of live imaging and image analysis technologies capable of systematically following cellular dynamics across the developing embryo. We developed a light-sheet microscope that adapts itself to the dramatic changes in size, shape, and optical properties of the post-implantation mouse embryo and captures its development from gastrulation to early organogenesis at the cellular level. We furthermore developed a computational framework for reconstructing long-term cell tracks, cell divisions, dynamic fate maps, and maps of tissue morphogenesis across the entire embryo. By jointly analyzing cellular dynamics in multiple embryos registered in space and time, we built a dynamic atlas of post-implantation mouse development that, together with our microscopy and computational methods, is provided as a resource.

INTRODUCTION

Mammalian development has been an area of intense study for many decades, but for all our efforts to elucidate the developmental mechanisms that enable the transition from a single cell to a fully formed organism, we have only limited knowledge of the dynamic processes that shape the embryo. The study of mouse embryogenesis, though an ideal candidate to investigate early mammalian development due to its size, relative accessibility, and genetic tractability, remains largely limited to snapshots in time. In particular, the period from gastrulation to organogenesis (E6.5 to E8.5 d.p.c., Figures S1A–S1C), when cells from the pluripotent epiblast migrate out of the primitive streak and begin to differentiate into various tissues and organ systems, is an area of keen interest for stem cell biology and tissue engineering. However, owing to the technical challenges associated with the visualization and quantification of dynamic cell behaviors *in vivo*, it is still largely unknown how cells migrate, how they organize during the formation of tissues, what dynamic behaviors they exhibit, how cells interact with their neighbors, and how stereotyped cell behaviors are across individuals (Herion et al., 2014; Lawson and Pedersen, 1992; Rivera-Pérez and Hadjantonakis, 2014; Tam and Beddington, 1992). The ability to image and computationally reconstruct whole-embryo development at the cellular level would enable the detailed analysis of these morphodynamic events and reveal developmental processes never before visualized *in vivo*.

Standing in the way of this goal, however, is that mouse embryos and their culture present a unique set of challenges. First, the rapid growth, complex optical properties, and often dense cell structures of the embryo, which change during development, present fundamental obstacles for high-resolution imaging. Second, the embryo requires optically scattering, autofluorescent serum to develop properly. Third, due to its rapid expansion in volume, the embryo cannot be mechanically constrained. Finally, mouse embryos are very photosensitive, limiting the amount of light they can tolerate without compromising development. Widely used confocal microscopes, for example, are limited to observing sub-regions of the embryo, with large steps in time and space, and cannot sustain normal development beyond 24 hr due to phototoxicity. To address even the most fundamental questions in post-implantation mouse development will require not only customized solutions, but entirely new imaging strategies.

Recent technological advances, such as the introduction of light-sheet microscopy for developmental imaging (Huisken et al., 2004; Keller et al., 2008), have provided a major opportunity for advancing our understanding in the field. The unique benefits of light-sheet microscopy make it ideal for studying sensitive, developing organisms. A sheet of laser light illuminates the embryo selectively along the detection focal plane an entire section at a time. This scheme greatly reduces the amount of light the embryo is exposed to and allows for significantly higher temporal resolution without compromising viability. Early efforts toward adapting light-sheet microscopy to mouse embryogenesis enabled the imaging of early developmental stages

(Ichikawa et al., 2014; Strnad et al., 2016) and sub-regions of larger, sparsely labeled embryos (Udan et al., 2014). However, methods capable of imaging post-implantation development beyond a short period of time, or even entire embryos at the single-cell level, are still lacking. Here, we developed a light-sheet microscope for long-term imaging of entire mouse embryos from gastrulation to early organogenesis at the high spatial and temporal resolution required to systematically follow single-cell behavior. We designed an adaptive imaging approach, custom optics, and an integrated culturing system to build a multi-view light-sheet microscope that tracks the changing shape, size, and optical properties of the mouse embryo as it grows over 250-fold in volume.

Overcoming these challenges in live imaging is, however, only the first step needed for reconstructing a cellular-resolution, dynamic atlas of development. A single 48 hr light-sheet recording of gastrulation and early organogenesis captures tens of thousands of cells with diverse shapes and dynamic properties over hundreds of time points, as they form an embryo 10–70 times larger than zebrafish or *Drosophila* embryos at comparable stages. To extract biologically meaningful information from images of such complexity and size, we developed a computational framework for the following: (1) automated long-term cell tracking over the full 48 hr period with an average precision of two cell diameters; (2) robust detection of cell divisions across the embryo; (3) construction of high-resolution dynamic fate maps and spatiotemporal maps of tissue morphodynamics; (4) spatiotemporal registration of multiple embryos to enable statistical quantifications of cellular dynamics and variability in developmental processes across individuals; and (5) the construction of an average mouse embryo. We used these methods to reconstruct the development of entire mouse embryos across scales, from single-cell dynamics to whole-embryo morphogenesis, and jointly analyze these data to build a statistical, dynamic atlas of gastrulation and early organogenesis in the mouse embryo. We applied these resources to the analysis of specific cell and tissue behaviors, including migration of primordial germ cells, embryo-wide spatiotemporal patterns and geometric properties of cell divisions, and cellular dynamics during elongation and folding of the neural tube.

While this study focuses on *in toto* imaging, dynamic analysis, and atlas construction for the stages of mouse development covering gastrulation to early organogenesis, we designed our imaging and computational tools to be broadly applicable across organisms and developmental systems, including organoids, stem cell systems, and tissue explants. Moreover, the tools and resources presented here should not only enable the analysis of broader developmental timescales, but also support a wide spectrum of applications—from mutant phenotyping, real-time analysis of cell signaling, morphodynamics, and force measurements to atlas-guided transcriptional analyses, optical manipulations, and perturbations.

RESULTS

Adaptive Multi-view Light-Sheet Microscope for Imaging Mouse Development

We developed a light-sheet microscope capable of culturing and imaging mouse embryos from gastrulation to early organogenesis at high spatiotemporal resolution (Figures 1A–1C, S1D–S1H; Data S1A). The microscope adapts itself to the rapid growth and complex optical properties of the embryo while maintaining viability over days of continuous imaging. The instrument does the following: (1) optimizing spatial resolution by automatically measuring and compensating for the continuously changing optical properties and geometry of the embryo; (2) minimizing optical path lengths in light-scattering serum through the use of custom-designed objectives; (3) continuously tracking the three-dimensional (3D) movements and growth of the embryo; and (4) supporting proper embryonic development, with minimal phototoxicity and a mounting strategy that does not interfere with embryonic growth.

Conceptually, our microscope design advances the principles introduced in simultaneous multi-view (SiMView) light-sheet microscopy (Tomer et al., 2012) and the AutoPilot light-sheet microscopy framework (Royer et al., 2016), which enable the imaging of externally developing organisms such as *Drosophila* and zebrafish. In our present work, we introduced a wide spectrum of improvements required to sustain and image normal mouse embryonic development at high resolution over a period of days (STAR Methods; Figure 1; Videos S1 and S2). While necessary for proper embryo development, the loose mounting strategy required by the mouse embryo complicates time-lapse live imaging. Not only does the embryo position drift slowly over time, but the embryo expands in volume more than 250-fold over 48 hr and dramatically changes in shape and composition. If the system were to be left in its initial configuration, image quality and spatial resolution would not only degrade over time, but the embryo may drift out of the field of view (Video S1B; Table S1). We thus developed an adaptive imaging framework suitable for dynamic specimens that simultaneously compensates for drift, growth, and changing optical properties (Figures 1D and 1E; STAR Methods). This method improves over our earlier AutoPilot system (Royer et al., 2016), which was limited to imaging developing specimens with approximately constant size and shape. We found that the AutoPilot corrects for only 37% of the aberration-induced defocus error in developing mouse embryos and suffers from an average defocus-induced mismatch between light sheets and detection focal planes of 1.90 ± 0.81 μm (n = 680,000 focus measurements across 20 time-lapse experiments) (Table S1; Figure S2). A fully uncorrected microscope produces an even higher average defocus error of 2.99 ± 1.34 μm (same statistics). Existing imaging methods therefore yield aberrated images that lack cellular resolution in more than 50% of the embryo (Figure 1F). In addition, existing light-sheet microscopes lack the ability to track the embryo and expand the imaging volume to match its growth, leading to a loss of 64.4% ± 11.9% of the embryo's volume over 24 hr when using mechanically unconstrained sample mounting (n = 20 time-lapse experiments) (Table S1).

We developed algorithms for image-based tracking of embryo position and mapping of embryo size (Figures 1D and 1E), which achieve the following: (1) ensure that no part of the embryo is lost during imaging, and (2) facilitate building a dynamic geometrical model of the embryo that automatically defines reference locations for aberration measurements throughout the embryo. These algorithms perform real-time processing of the time-lapse

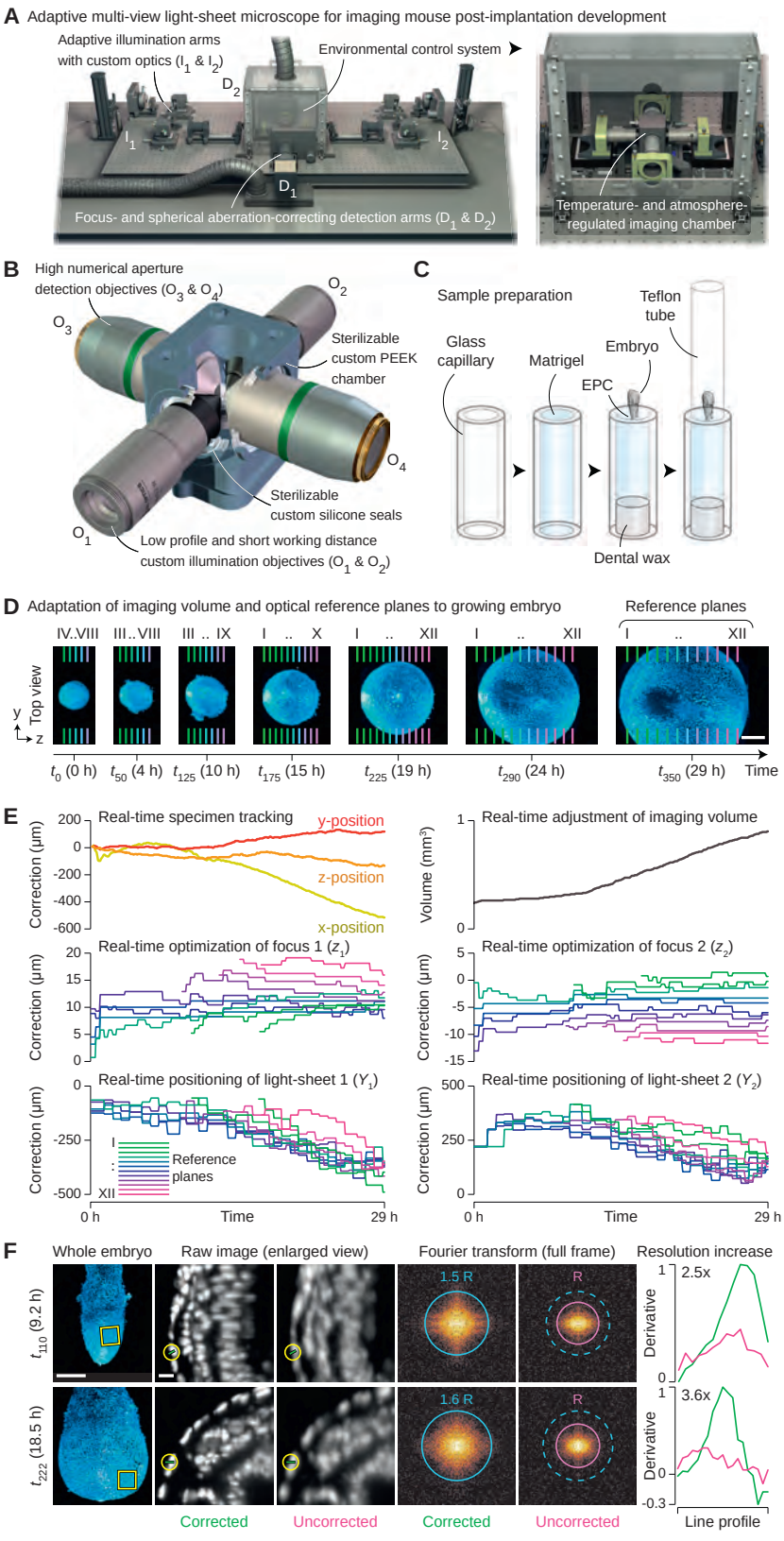

Figure 1. Light-Sheet Microscope for Adaptive Imaging of Mouse Embryo Development

(A) Adaptive multi-view light-sheet microscope for live imaging of mouse embryos, including Maus Haus environmental control system.

(B) Sample chamber and objectives. Custom illumination objectives (O_1, O_2) provide short working distance and spatial compatibility with high numerical aperture detection objectives (O_3, O_4).

(C) Mounting of post-implantation embryos. A glass capillary with Matrigel is sealed on one end with dental wax. The embryo's EPC is embedded in the opposite end. This assembly is placed either directly into the chamber for open culture or surrounded by a 25-µm-thin FEP cylinder.

(D) Automated expansion of imaging volume and positioning of reference planes for adaptive imaging with optimal image quality during embryo development and growth.

(E) Adaptive correction of embryo position and imaging volume, focus optimization for light sheets and detection objectives (z_1, z_2), and optimization of light-sheet waist positions (Y_1, Y_2) for all dynamic reference planes in one imaging experiment.

(F) Left: comparison of image quality with ("Corrected") or without ("Uncorrected") adaptive corrections. Right: Fourier transforms and quantifications of resolution improvements (for regions marked by green lines, as described in Royer et al. [2016]).

Scale bars (µm): 200 (D; F, embryo), 15 (F, enlarged view).

See also Video S1 and Figures S1 and S2.

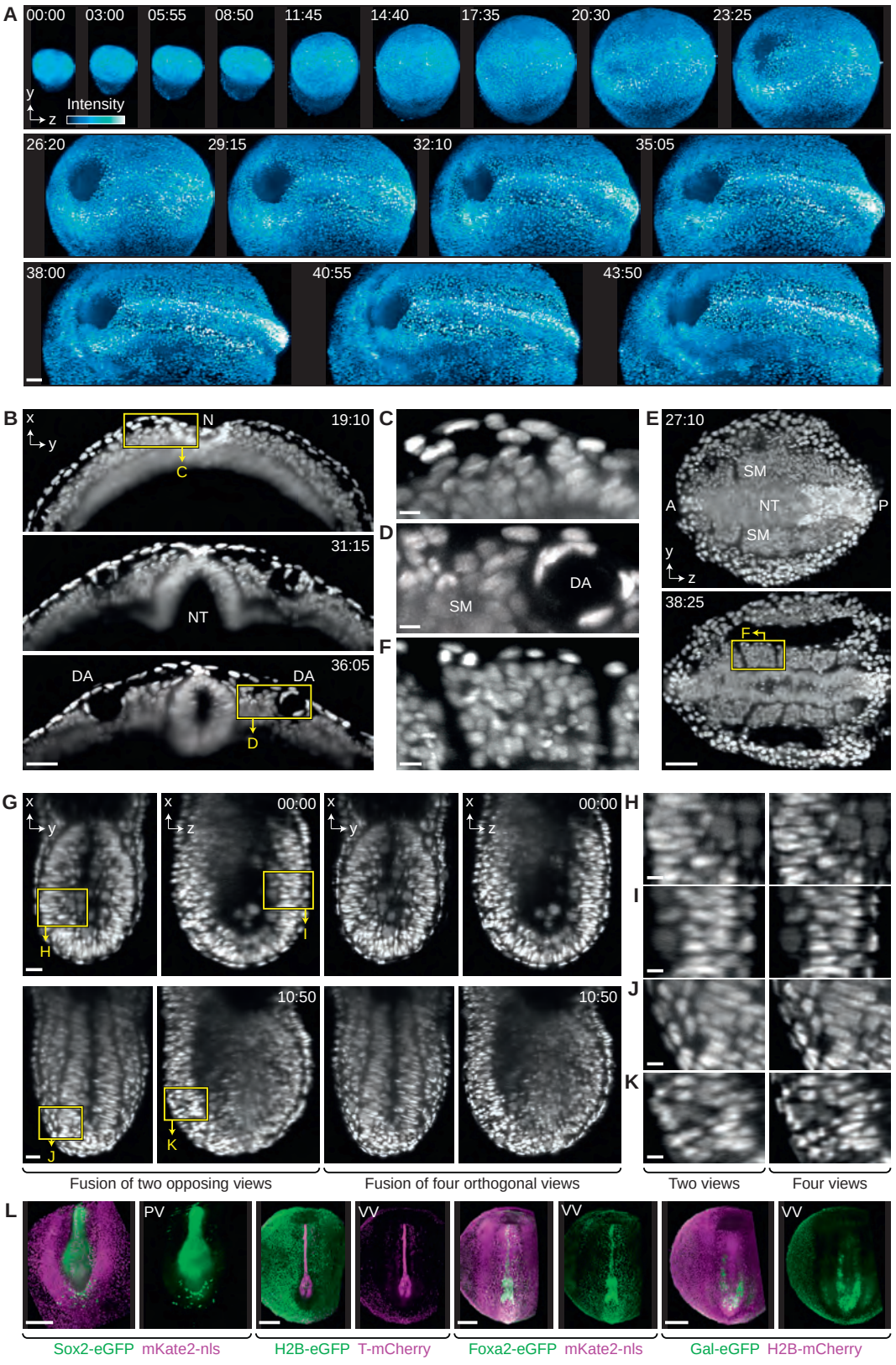

(legend on next page)

volumetric imaging data acquired by the microscope, stabilize the 3D position of the embryo in the center of the field of view, and continuously adjust the size of the imaging volume to match the growth rate of the embryo. Using the dynamic geometrical sample model, the adaptive imaging framework then divides the specimen volume into a set of reference regions, for which it determines the locally optimal light-sheet geometry and geometrically matches detection focal planes to illumination planes (Figure 1E; Video S1B). Thereby, the average defocus-induced mismatch between light sheets and detection focal planes is reduced to 0.06 ± 0.04 μm (Table S1), spatial resolution is increased 3.3-fold, and signal strength is increased 2.1-fold (Figure 1F; Video S1C). This continuous, automated adaptation also allows the microscope to run unattended for days and greatly reduces the data rate.

To minimize light exposure of the specimen, all measurements of the adaptive imaging framework are performed with low laser power and structured illumination. Enabling full system optimization with all degrees of freedom increases the number of images recorded per experiment by 5.2% and the energy load on the sample by 2.3% (n = 11 time-lapse experiments), which is negligible with respect to specimen viability. The total energy load in our microscope is so low that fluorescent protein production outperforms photobleaching in all experiments reported in this study, leading to a doubling of fluorescence levels every 10 hr on average.

Multi-day High-Resolution Imaging of Post-Implantation Mouse Development

These advancements in microscope design, algorithmic strategies for real-time adaptive imaging, and embryo culture allowed us to capture the development of the mouse embryo in high resolution from gastrulation to organogenesis *in toto* over the course of nearly 48 hr (from E6.5 d.p.c. to E8.5 d.p.c.; Video S2A; Figures 2A and S1A–S1C). We acquired opposing views of the embryo for up to two color channels in 5 min intervals, visualizing and tracking individual cells across the embryo at varying depths and observing morphodynamic processes and tissue formation as they occur (Figures 2B–2F). Notably, although we achieved single-cell resolution in endoderm and mesodermal tissues, the ectoderm presents a particular challenge due to its dense and highly scattering structure. More ventral ectodermal structures and those closest to the detection objectives could generally be resolved at the single-cell level; however, the dorsal-most and internal structures such as the surface ectoderm and medial head folds are not easily accessible (Figure 2B). Careful selection of fluorescent reporters proved essential to achieve cellular resolution in these optically complex areas and in deeper tissues such as the heart. Selective lineage labeling strategies can be used to generate a compelling overview of heart development (Video S3A) but lack the high resolution at later stages to clearly distinguish individual cells. While far-red reporters such as mKate2 provide a slight advantage in discerning individual cells and structures (Video S2B), bright near-infrared fluorescent reporter lines are needed to achieve greater depth and contrast. To demonstrate these advantages, we utilized a Histone2B-miRFP703 reporter line (Gu et al., 2018) to image the developing heart in greater cellular detail than has been previously possible (Video S3B). Using this line, we were able to image up to 600 μm deep into the anterior region of the embryo, encapsulating nearly the entire linear heart tube at single-cell resolution, as well as regions of the head-fold and foregut pocket that were previously inaccessible.

Spatial resolution, particularly in crowded, low-contrast regions such as the disorganized, rapidly mixing primitive streak (Figures S3A and S3B), can be further improved by orthogonal four-view imaging (Video S2C; Figures 2G–2K; STAR Methods). Alternatively, mosaic reporter strategies provide an excellent opportunity to track and visualize individual cell behaviors in a crowded and dynamic environment. The reconstruction of lineages had previously been accomplished by manual single-cell labeling (Lawson and Pedersen, 1987; Tam et al., 1997); however, this approach lacks the spatial and temporal resolution provided by live imaging and adds additional manipulations to the embryo. By using a mosaic Cre/loxP reporter strategy, we created detailed lineage trees for single cells as they migrate through the primitive streak (Figures S3C and S3D). Cells can be tracked starting from their positions in the epiblast and as they mix, divide, and migrate through the streak.

Although these recordings appear to represent "normal" and expected embryonic development over the stages imaged, the post-implantation embryo cannot be returned to the uterus to verify competency. We thus sought to ensure that imaging conditions did not perturb normal developmental processes by utilizing a range of existing fluorescent reporters known to spatially recapitulate endogenous gene expression in various tissues (Figures S3E–S3H and 2L; Video S3C and S3D). These experiments show that embryos not only develop normally with respect

Figure 2. Long-Term Live Imaging of Post-Implantation Mouse Development at the Cellular Level

(A) Selected projections from H2B-eGFP channel of a CAGTAG1 expressing mouse embryo over 44 h of continuous imaging, from early streak (E6.5) to somite stages (E8.5).

(B–D) (B) Projections of 45-μm-thick cross-section through mid-plane of embryo in (A), demonstrating ability to resolve individual cells across germ layers. Cross-section and zoomed-in segment (C) highlight node (N), mesoderm, and endoderm regions. (D) shows cross-section of angioblasts assembling dorsal aortae (DA).

(E and F) (E) Projections of 45-μm thick cross-sections of neural tube (NT) and somitic mesoderm, with surrounding regions in lateral plate and endoderm. (F) Zoomed-in region showing single somite.

(G) En face (XY) and lateral (XZ) slices of two-view (left) and four-view (right) image data of streak-stage embryo expressing mKate2-nls.

(H–K) Enlarged views of regions marked in (G), showing contrast and resolution improvement by four-view deconvolution (right) versus two-view content-based fusion (left).

(L) Live-reporter expression in developing embryos for Sox2-eGFP, T-mCherry, Foxa2-eGFP, Gal-eGFP, displaying expected expression and localization after long-term imaging.

Time (hh:mm). SM, somite. NT, neural tube. A, anterior. P, posterior. PV, posterior view. VV, ventral view.

Scale bars (μm): 200 (L), 100 (A, E), 50 (B), 25 (G), 15 (F), 10 (C, D, H–K).

See also Videos S2 and S3 and Figures S1 and S3.

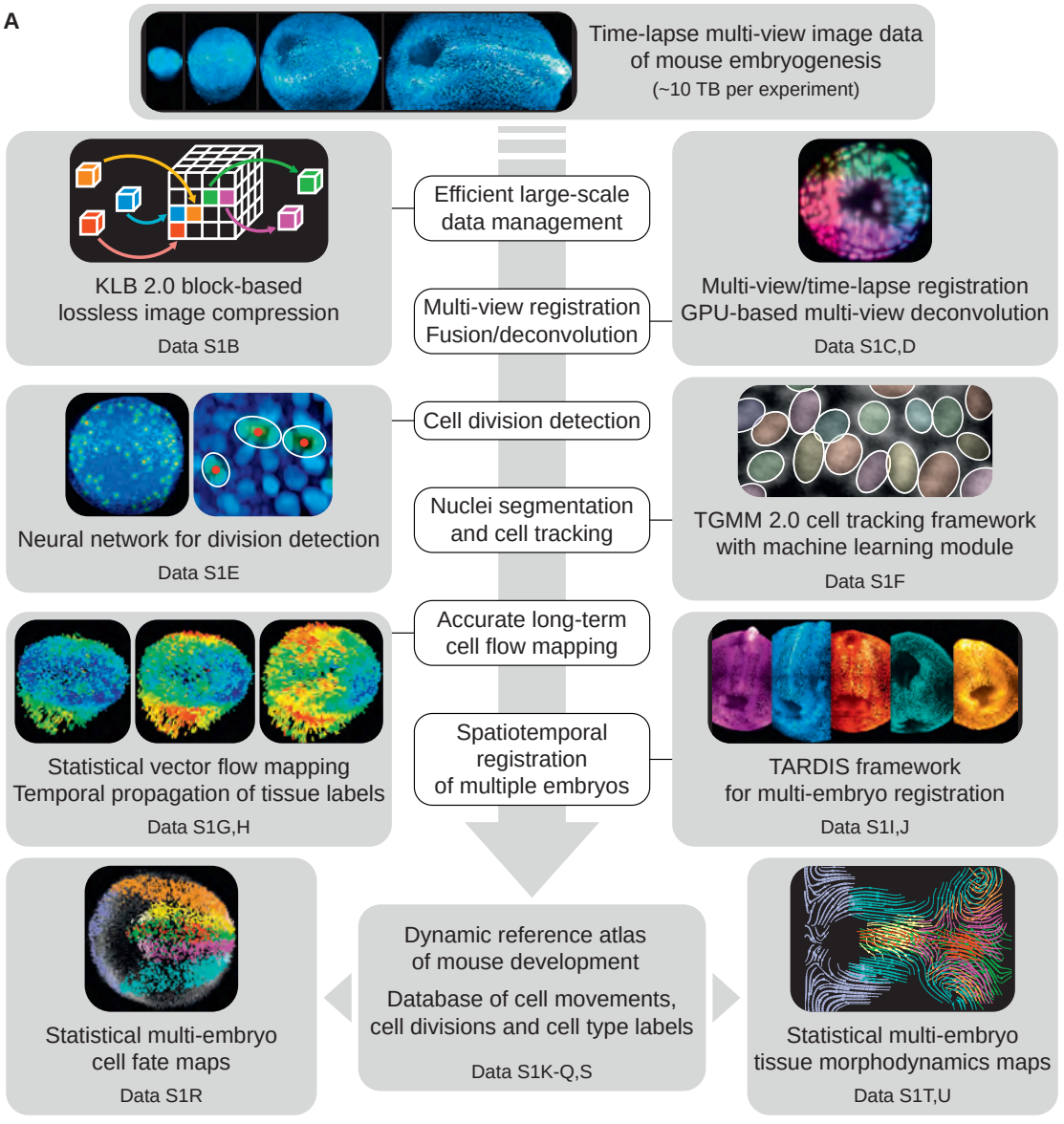

(legend on next page)

to their morphology, but also properly express patterning genes over the course of development. The viability of these dual reporters greatly expands the avenues of study for early mouse development.

To conclude this section, we present an example of the versatility of this technique to image specific cell types or populations over long timescales. We used a Sox2-eGFP reporter line (Video S3C) to visualize the migration of primordial germ cells (PGCs) (Campolo et al., 2013). Primordial germ cells first arise at around E6.5 d.p.c. in the proximal posterior bordering the extra-embryonic and embryonic regions (Saitou and Yamaji, 2012) and later migrate to the genital ridge (Molyneaux et al., 2001). The use of the Sox2-eGFP reporter allowed us to clearly distinguish PGCs as they arose from a small cluster in the proximal posterior, migrated into the endoderm layer, and began to actively wander about, sending out small membrane protrusions (Video S3C) until they were drawn inward by the formation of the hindgut portal. During amnion inflation, a few of the more proximal PGCs were pulled along with the allantois toward the extra-embryonic region (ExE). These cells never rejoined their embryonic counterparts during imaging and are presumably the origin of PGCs found in the extra-embryonic region (Anderson et al., 2000; Ginsburg et al., 1990). This segregation of PGCs into the extra-embryonic region appears to be an unintended consequence of the rapidly expanding amnion, as embryos will exhibit multiple different behaviors regarding the more proximal PGCs in this region. In every embryo examined (n = 4), we observed two or three PGCs to act in one of four ways: (1) join the ExE; (2) be drawn along with the allantois proximally but then turn around and rejoin the embryonic PGCs; (3) one rejoins while the other remains in the ExE; or (4) yet another one rejoins, while the other undergoes apoptosis. It is unclear why, with such a small initial population size, the fate of these cells would seemingly be left to chance. The power of the adaptive imaging methodology presented here enabled us to visualize this population over long timescales, with a richness and detail that has previously been unattainable.

Automated Cell Tracking Across the Post-Implantation Mouse Embryo

Post-implantation mouse development presents a unique challenge not only for live imaging, but also for the analysis of the resulting image datasets. To systematically extract quantitative information on cellular dynamics and—ultimately—biological insights from the image data, we developed a modular computational framework (Figure 3A). Our tools facilitate efficient and accurate cell segmentation, long-term cell tracking, detection of cell divisions, reconstruction of high-resolution dynamic fate maps, high-resolution mapping of tissue morphodynamics, and registration and quantitative comparison of cellular dynamics across multiple embryos (STAR Methods; Videos S4, S5, S6, and S7; Data S1B–S1U). We provide a comprehensive guide that explains the practical use of this framework and includes example data (STAR Methods). In the following sections, we briefly describe each module and the respective biological analyses they enable, starting here with automated, whole-embryo cell tracking.

A 48 hr recording of gastrulation and early organogenesis in the mouse embryo captures the dynamic behavior of tens of thousands of cells over hundreds of time points. Conventional cell segmentation and tracking algorithms are not equipped to handle the size and complexity of these datasets, and manual annotation by a human would ostensibly take years for a single dataset. We thus developed an improved version of our Bayesian cell tracking framework TGMM (Tracking with Gaussian Mixture Models), which was originally designed for automated cell tracking in developing zebrafish and *Drosophila* embryos. We successfully tested TGMM on short-term recordings of early streak-stage mouse embryos comprising less than 1,000 cells (Amat et al., 2014) but found that it failed on our long-term recordings of the up to 200-fold larger embryo volumes and 20-fold higher cell counts encountered in the present study. We thus developed TGMM 2.0, which employs a machine learning approach to division detection utilizing both lineage-based and image-based features (STAR Methods; Data S1F).

Over the full 48 hr imaging period and across all tissues in the mouse embryo, TGMM 2.0 achieved an average linkage accuracy of 93.0%–94.8% and an average segmentation accuracy of 96.7%–97.6% (n = 8,982–30,962 cell position and linkage annotations), depending on the fluorescent marker strategy (Table S1). We note that while we designed TGMM 2.0 as a tool for cell tracking and recommend its use for this purpose, we discourage its use as a cell division detector (except in smaller model systems, such as zebrafish and *Drosophila*). Even with the improvements introduced in TGMM 2.0, cell division detection performance itself is still limited and cannot easily be improved within the scope of the current algorithmic design. We thus set out to develop a new computational tool that complements TGMM and offers a robust and automated way of identifying cell divisions in the raw image data of developing embryos.

Efficient Detection of Cell Divisions Using Deep Learning

Cell proliferation rates and timing are of critical importance to cell differentiation and tissue formation, but little is known about tissue- and embryo-wide division patterns or how they might evolve over time. Although TGMM 2.0 incorporates a classifier for identifying dividing cells and linking a parent cell with its daughters, this approach faces the same challenges as those

Figure 3. Data Processing Framework and Neural Network for Cell Division Detection

(A) Overview of image processing and data analysis modules.

(B) Cell division prediction with a convolutional neural network (CNN). Top: projection of example image region. Middle: predicted locations of dividing cells (intensity reflects prediction confidence). Bottom: images overlaid with predictions, showing correct identification of two neighboring dividing cells.

(C) Precision-recall curves of CNN division detector for two embryos at three time points (training on embryo A only). TGMM 2.0 machine learning classifier shown for comparison.

Scale bar (μm): 10 (B).

See also Video S4A.

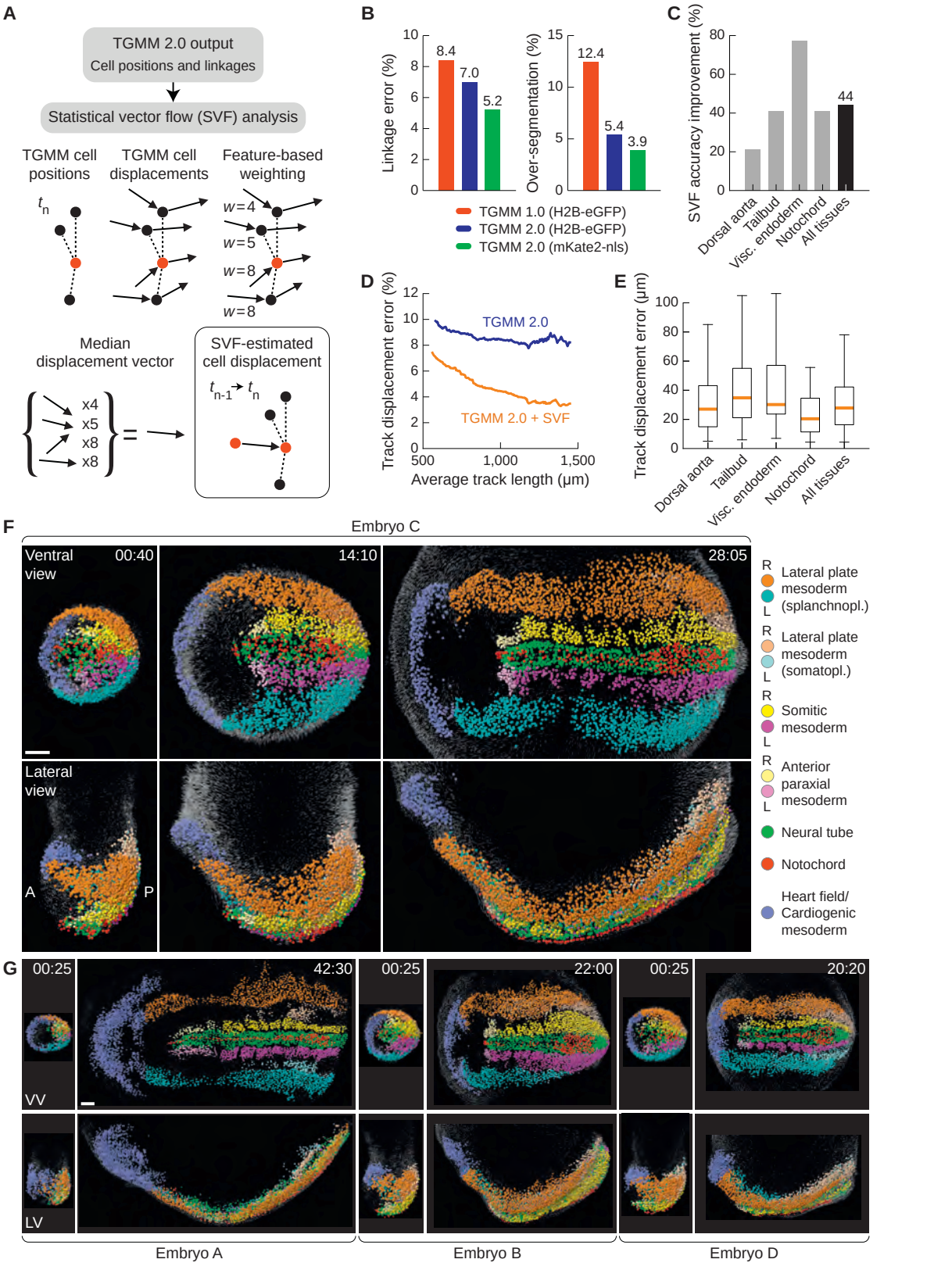

(legend on next page)

confronting the tracking algorithm itself; rapid cell movements and heterogenous nuclear shapes and sizes complicate image analysis. Fortunately, the use of histone reporters for tracking cell nuclei provides an additional benefit: divisions are readily identifiable by the condensation and increase in brightness of chromatin as the metaphase plate appears, followed by the appearance of two smaller, bright daughters. This stereotyped event can be easily identified, even in regions of poor contrast and between different cell types. We thus sought to leverage the strength of deep learning and train a convolutional neural network (CNN) to automatically and accurately identify cellular divisions in 3D and time (STAR Methods; Data S1E).

Our network correctly locates and identifies the presence of a single metaphase plate even in a highly crowded cellular environment or where multiple divisions are occurring in the same spatiotemporal window (Figure 3B). We determined the precision and recall of this detector to be 0.81 and 0.81, respectively; i.e., 81% of all detections are true cell divisions, and 81% of all true divisions in the embryo are retrieved by the CNN (*f*-score = 0.81; n = 381 annotated divisions in three volumes), which corresponds to a detection accuracy of 99.8%. This represents a 3.7-fold improvement in precision and a 24% increase in recall compared to TGMM 2.0 (Table S1). We confirmed that the CNN can be effectively applied to new data without the need for retraining: application to data from a second embryo produced an *f*-score of 0.80 (n = 479 annotated divisions in three volumes), indicating that the network generalizes well to new experiments (Figure 3C). Notably, the CNN was able to retrieve on average more than twice the number of cell divisions found by a human annotator. A time-lapse reconstruction of cell divisions across an entire developing embryo is shown in Video S4A and included in Data S1P.

Reconstructing High-Resolution Dynamic Cell Fate Maps Across the Mouse Embryo

Because nuclei of even the same lineage can experience huge variations in size, shape, and intensity, we performed a detailed parameter sweep to determine the regime of optimal TGMM performance in post-implantation development (Figure S4). Even still, the photosensitivity of the mouse embryo limits temporal resolution, and rapid cell movements in the mouse embryo combined with their complex, fluctuating shapes introduce temporal gaps and/or linkage errors in cell tracks over long timescales. While the shorter, fragmented tracks generated by TGMM faithfully recapitulate the movements of individual cells, TGMM alone is insufficient to reconstruct cell fates over an entire 48 hr experiment. We thus took advantage of the high-quality data TGMM provides for local spatiotemporal windows and enhanced the accuracy of long-term cell tracking by augmenting individual cell tracks through a statistical assessment of cell behavior in a cell's local neighborhood (Figure 4A). The integration of TGMM 2.0 with this statistical vector flow (SVF) analysis not only improves spatial accuracy of cell tracks, but also reconstructs continuous cell tracks (rather than sets of short, disconnected tracks) for the full duration of the experiment (Video S4B; STAR Methods; Data S1G and S1H).

Compared to TGMM 2.0 alone (Figure 4B), combined use of TGMM and SVF has a positive effect on cell tracking performance across all tissues (Table S1), including difficult cases such as the thin notochord, and results in a 44% improvement in accuracy across all cell tracks (Figure 4C; n = 285 annotated cell tracks). This number reflects the decrease in spatial mismatch between automatically versus manually reconstructed cell tracks. This performance boost increases with track length and tracking period: for tracks with a length of 1,500 μm, SVF improves accuracy by as much as 140%, reducing track displacement errors (versus ground truth) to 3% (Figure 4D). Overall, we determined that our combined TGMM and SVF approach reconstructs individual cell tracks with an average error of 34.2 μm (two cell diameters) over 48 hr and across all tissues (Figure 4E).

With the ability to accurately reconstruct cell tracks from beginning to end we systematically queried the origin of cell fates by doing the following: (1) manually segmenting individual tissues or regions of interest in the image data at the last time point of the experiment, (2) then locating the corresponding SVF objects within these manual tissue labels, and (3) following the labeled cell tracks backward in time to the beginning of the experiment. This approach provides a complete reconstruction of the trajectories of cells as they migrate out of the primitive streak and assemble into their corresponding tissues. As a first

Figure 4. Long-Term Cell Tracking and Reconstruction of Cell Fates in the Mouse Embryo

(A) SVF workflow: SVF-based cell displacement estimate is computed from TGMM-based cell displacements using feature-based weighting. The degree of neighborhood conservation is considered to calculate median displacement vectors for each cell.

(B) Linkage errors and over-segmentation in TGMM 1.0 versus 2.0 (n = 8,982/30,962 cell position and linkage annotations for H2B-eGFP and mKate2-nls data, respectively).

(C) SVF post-processing improves TGMM cell tracking accuracy on average by 44% across all cell types (n = 285 cell tracks spanning all stages, H2B-eGFP reporter).

(D) Average track displacement error (versus ground truth) as a function of track length when using TGMM 2.0 + SVF versus TGMM 2.0 alone. Statistics as in C.

(E) Track displacement error for different cell types using TGMM 2.0 + SVF (orange line: mean, box: $25^{th}/75^{th}$ percentiles, whiskers: extremum data within 1.5 × interquartile range). Average error across all cell types is 34.2 μm over full imaging experiment. Statistics as in C.

(F) Reconstruction of an embryo shown at three time points of an experiment from mid/late-streak stage to early somite stage, using TGMM 2.0 + SVF. The dynamic fate map was created by labeling tissues in the image data at the last time point, transferring labels to SVF objects (spheres) and propagating labels backward in time.

(G) Cell-fate reconstructions for three additional embryos ("A," "B," "D"). Similar tissue locations and patterning are seen across embryos and are consistent across developmental stages.

Time (hh:mm). VV = ventral view, LV = lateral view.

Scale bars (μm): 200 (F, G).

See also Videos S4B and S5 and Figure S4.

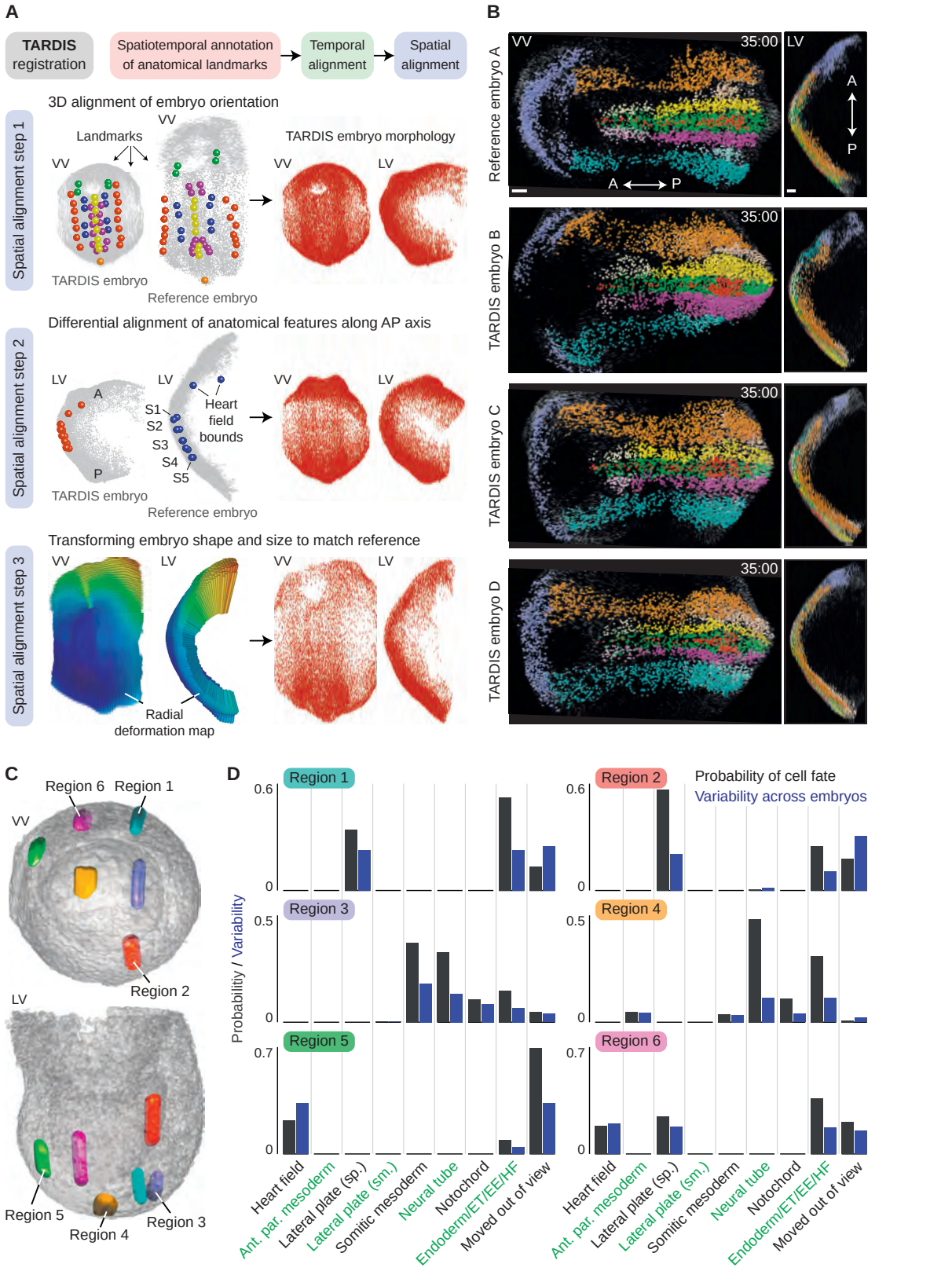

(legend on next page)

demonstration, we labeled a set of tissues based on their easily identifiable anatomical features, but we note that our method is not limited to this selection. The heart field, lateral plate mesoderm (split into splanchnopleure and somatopleure), somitic mesoderm (including condensed somites and pre-somitic mesoderm), anterior paraxial mesoderm (mesoderm anterior of first somite), endoderm, neural tube, and notochord were manually labeled and dynamically reconstructed in four embryos (Video S5A; Figures 4F and 4G). By comparing results across embryos, we found a strong similarity between origins and movements of individual tissue types, regardless of size and shape of the embryo (Video S6A). A time-lapse visualization of a dynamic fate map including the endoderm is shown in Video S5B and an interactive 4D visualization is provided as Data S1O.

Notably, our spatiotemporal fate maps are also in agreement with the individual snapshots that were laboriously generated by others prior to the availability of live imaging techniques (Lawson and Pedersen, 1992; Takaoka et al., 2011; Tam and Beddington, 1992; Tam et al., 1997) and confirm that there is little mixing of the different mesodermal layers once cells exit the primitive streak. This suggests that when and where a cell exits the streak is of critical importance to determining its final fate, an order that is strongly maintained by its local environment. In contrast to early static maps, however, and as shown in the next sections, our dynamic, high-resolution reconstructions allow us to visualize the interactions of multiple cell types over time, comprehensively follow cell behavior in a single embryo, determine the degree of variability between embryos in establishing cell fates, and require no additional physical manipulation or perturbation of the embryo.

Importantly, this technique can be applied to any tissue, cell type, time period, or region of interest within the embryo. In our next example, we used reporters for Brachyury and Foxa2 to further demonstrate the accuracy of SVF and trace the origins of cells that give rise to the node and notochord. We visualized and quantified single-cell behaviors in the convergent extension of the anterior portion of the notochord and subsequent elongation as the posterior axis expands (Video S3D). Using dual-expressing T-mCherry and H2B-eGFP embryos, we tracked cells in the ubiquitous nuclear channel and masked the last time point with the location of T-mCherry positive cells in the node and notochord to seed SVF propagation (Video S5C). Thereby, we verified by direct comparison with the image data that cells tracked over a period of more than 24 h with SVF precisely matched the location and dynamics of the T-mCherry live reporter (Figures S5A and S5B): 94% of all cell tracks matched the dynamic expression pattern and the remaining 6% exhibited an average mismatch of only 5.0 ± 4.4 μm.

Building a Dynamic Atlas of Development by Spatiotemporal Registration of Multiple Embryos

Although we can accurately track and characterize cell fates and tissue dynamics in individual embryos, in order to employ meaningful statistical analyses or measure variability of developmental processes, it is necessary to jointly analyze data from multiple embryos. However, the wide variation in size, shape, and even rate of tissue formation across normal mouse development makes direct comparisons between embryos even of the same developmental stage problematic. We thus developed the registration method TARDIS (time and relative dimension in space) that combines manually annotated spatiotemporal landmarks and information on local cell distributions obtained from TGMM to map multiple embryos in space and time onto a single reference embryo (Figure 5A; Video S6C; STAR Methods; Data S1I).

Using TARDIS, we registered in space and time four different embryos, which encompass a range of developmental timescales and size and shape variations, with an average registration error of 41.5 μm (Video S6D; Figures 5B, S5C, and S5D; unregistered embryos are shown in Figures 4F and 4G). Despite these dramatic differences in size and shape, the resulting TARDIS embryos preserve the motion and morphology of different tissues as compared to their original form. We note that our quantifications of cell dynamics, such as movement speed, movement direction, and cell density, are performed in the original, untransformed embryos to ensure that these quantifications are not biased by the registration procedure itself. Equipped with these registered datasets, we set out to generate a reference atlas of mouse embryonic development (Data S1K–S1O). The purpose of this atlas is not only to assess quantitatively how conserved or variable cellular dynamics are across different individuals, but also to create a statistically average embryo that can be used as a point of comparison between normal embryos (e.g., to query a region of interest before cells in that region are fully specified) or for the quantitative analysis of mutant phenotypes or otherwise perturbed embryos.

A Statistical Fate Map of the Post-Implantation Mouse Embryo

TARDIS makes it possible to assess cell behavior in the developing mouse embryo in a statistically meaningful way. As the first application of this approach, we constructed a whole-embryo statistical fate map (STAR Methods; Data S1R) based on the

Figure 5. Spatiotemporal Registration of Mouse Embryo Development Using TARDIS

(A) TARDIS overview: embryos are aligned in time using manual annotations, then aligned in space by rigid registration to a reference embryo using spatial landmarks (step 1), differential alignment of anatomical features along anterior-posterior axis (step 2), and transformation of their shape and size to match the reference embryo (step 3). Left: examples of landmarks and transformation maps are shown. Right: resulting embryo morphology.

(B) TARDIS registered embryos A–D shown side-by-side. Although embryos can vary dramatically in size and shape prior to registration (Figures 4F and 4G), they are closely aligned post-registration while maintaining overall tissue morphology and movements. Colors as in Figure 4F.

(C and D) Statistical cell fate predictions (D) for six example regions in an embryo selected at an early time point (C) and computed from combined dynamic fate maps of four TARDIS-registered embryos. Dark gray bars represent average probability for a region to become a specific tissue. Blue bars represent variability between embryos (standard deviation of probabilities). Category "Moved out of view" represents cells that moved outside imaging volume during recording.

VV, ventral view. LV, lateral view. A, anterior. P, posterior. ET, endothelial. EE, extra-embryonic. HF, head fold.

Scale bar (μm): 200 (B).

See also Video S6 and Figure S5.

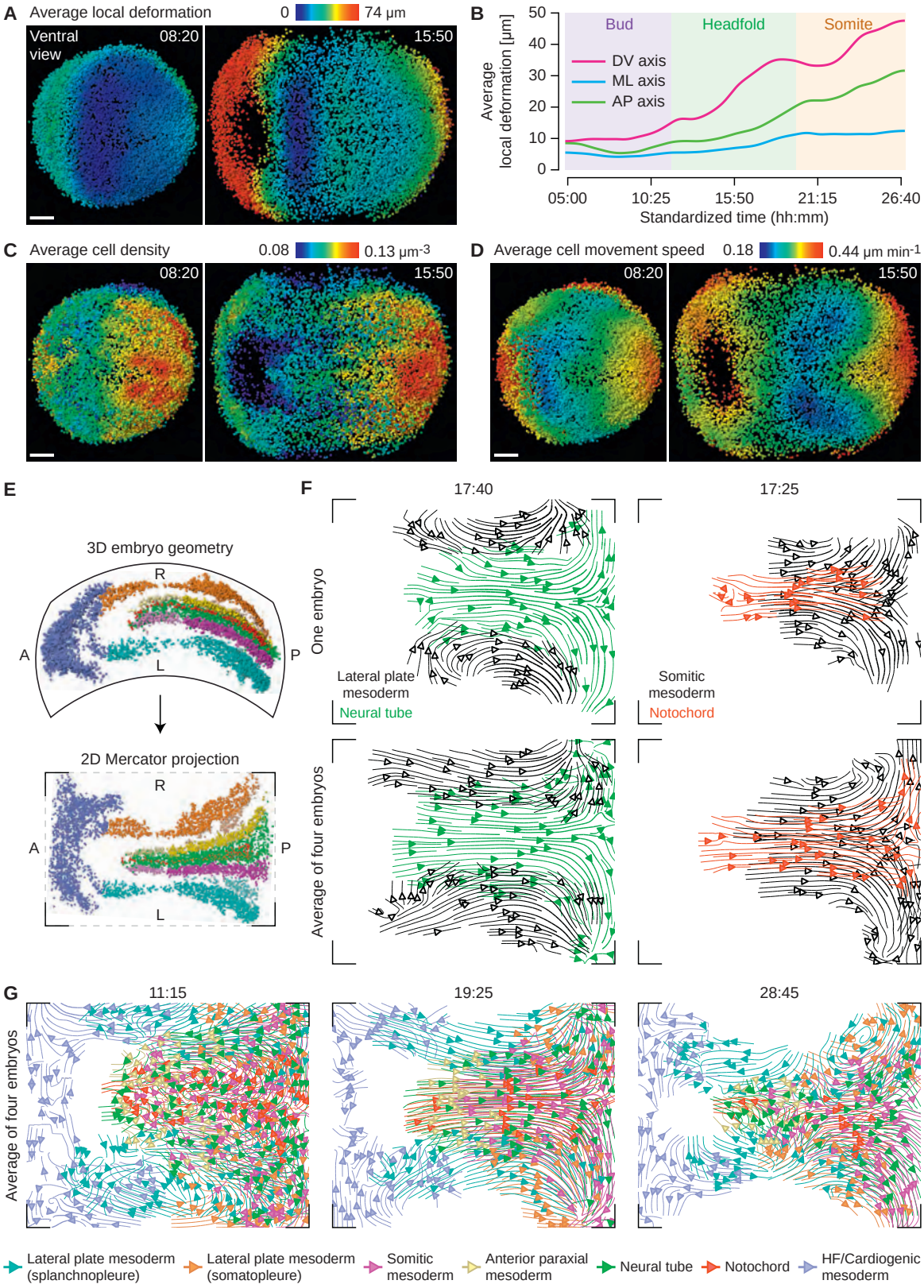

(legend on next page)

tissue annotations we generated for four individual embryos by jointly analyzing the data of the respective TARDIS-registered embryos. We systematically computed the average percentages of local cell fate contributions across all TARDIS embryos for all labeled tissues (Video S6E). These combined statistical results closely correspond with and support what has been observed for past tissue or single-cell labeling of individual embryos (Lawson, 1999; Lawson and Pedersen, 1992; Tam and Beddington, 1992). However, while past observations relied on small cell populations or individually labeled cells, our method enables us not only to visualize cell fate dynamics and establishment of all cell populations in an embryo simultaneously, but also to make direct comparisons between multiple embryos.

Although it is usually possible to determine the identity of a cell at the end of an experiment, this is not helpful if one wishes to know in real time where a cell might end up before arriving at that location. Labeling, isolating, optogenetically manipulating, or otherwise perturbing cell fates requires *a priori* knowledge of the probability of cells to assume a particular fate. Using the TARDIS atlas, we queried the probability that certain cell populations in a mid- to late-streak stage embryo would assume the fate of one of the previously labeled tissue groups by manually selecting regions of interest in the query embryo and visualizing the final predicted contribution to different tissues 24 hours later (Figures 5C and 5D). We included difficult "edge" cases, such as the endoderm (region 1), as well as locations in the mesoderm (region 2), ectoderm (region 4), and combinations of both (region 3) (Figures 5C and 5D). Correct statistical classification of the endoderm region is exceptionally difficult, as it requires both accurate long-term tracking of this single-cell-layer thick tissue and precise registration of all TARDIS embryos with an accuracy approaching a single-cell diameter. Nevertheless, even for this challenging setting, the majority of TARDIS predictions were indeed in the endoderm-containing category, with a smaller contribution from the underlying lateral plate mesoderm. Additionally, we tracked a set of individual cells through the developing embryo and showed how the TARDIS database can be used to measure, as a function of time, the cell fate composition in the local neighborhoods of these tracked cells as well as the variability of cell fate composition across embryos (Video S5D).

While TARDIS provides a useful tool to enable the mapping of multiple embryos onto one reference scaffold, we also designed a complementary method to combine the information from multiple embryos into a single, average embryo (STAR Methods). Related concepts have been successfully employed for later developmental stages, using fixed embryos imaged with micro-CT (Wong et al., 2014). By contrast, our approach relies on dynamic cellular information obtained from fluorescence imaging, using live embryos at earlier stages. This approach creates a statistically "average" embryo (Data S1S, Video S7), avoiding the use of a reference embryo as a physical scaffold for data visualization and analysis, and allows for the direct measurement and visualization of average embryo shape and development as well as of the variability of shape and developmental parameters across individuals (Figures S3E–S3G; Video S7A–S7C). We built this average embryo as the mean of our four reconstructed embryos after registering all embryos to their global center of mass.

As an example of the different metrics that can be quantified from the average embryo, we examined the average local deformation, cell density, and cell movement speed across the development of the average embryo (Figures 6A–6D and S5E–S5G; Video S7A–S7C). The average local deformation (Figures 6A and 6B) reports to which extent the contributing embryos had to be deformed in a given area to match the average embryo shape, i.e., it quantifies variability in local shape of individuals. Across the DV, ML, and AP axes, average variability in shape is less than 50 μm, and local deformations are generally significantly smaller, particularly at early developmental stages or along the ML and AP axes. As with the TARDIS registration, individual points or tissue regions can be labeled in the average embryo and propagated in time (Data S1J, STAR Methods) to determine their developmental origin, fate, or the variability in cell neighborhood over time and across embryos (Video S7D). The unique strength of performing such analyses in the average embryo is that the results represent the statistically average cell behaviors across individuals.

It is important to note here that the labeling scheme for the query regions and predictions for both TARDIS and the average embryo can be entirely arbitrary. For example, labeling criteria could include anatomical features, a second fluorescent reporter, or the expression of genes of interest. To demonstrate the latter strategy, we used the T-mCherry reporter and masking scheme for SVF described previously to map a single time point of an H2B-eGFP and T-mCherry expressing embryo onto the average embryo. Using a single time point from the T-mCherry expressing embryo to label corresponding T-positive locations

Figure 6. Quantifying Stereotypy and Variability of Local Cell Dynamics Across Embryos

(A and B) Visualization and quantification of differences in local embryo shape across four rigidly aligned embryos. DV, dorsoventral, ML, mediolateral, AP, anteroposterior.

(C) Average local cell densities and (D) average local cell movement speeds at two time points in the average embryo.

(E) 2D flattening of a 3D embryo using the Mercator projection. The 3D embryo geometry is represented using a spherical coordinate system with radial dimension ρ and angular dimensions θ and ϕ (corresponding to the horizontal and vertical dimensions of the Mercator map). A, anterior. P, posterior. L/R, left/right side of embryo.

(F) Overlay of cell movements in lateral plate mesoderm and neural tube (left) and in somitic mesoderm and notochord (right), for a single embryo (top) and averaged across four embryos at the early head fold stage. 3D tissue movements were computed from respective cell movements reconstructed with TGMM 2.0 + SVF over 100 min and visualized in 2D using Mercator projection.

(G) Overlay of movements for all labeled tissues combined into one morphodynamic fate map, shown at mid-bud, early head fold, and early somite stages. Top: map for single embryo, bottom: average map for four embryos.

Time (hh:mm).

Scale bars (μm): 100 (A, C, D).

See also Videos S4C, S4D, and S7 and Figure S5.

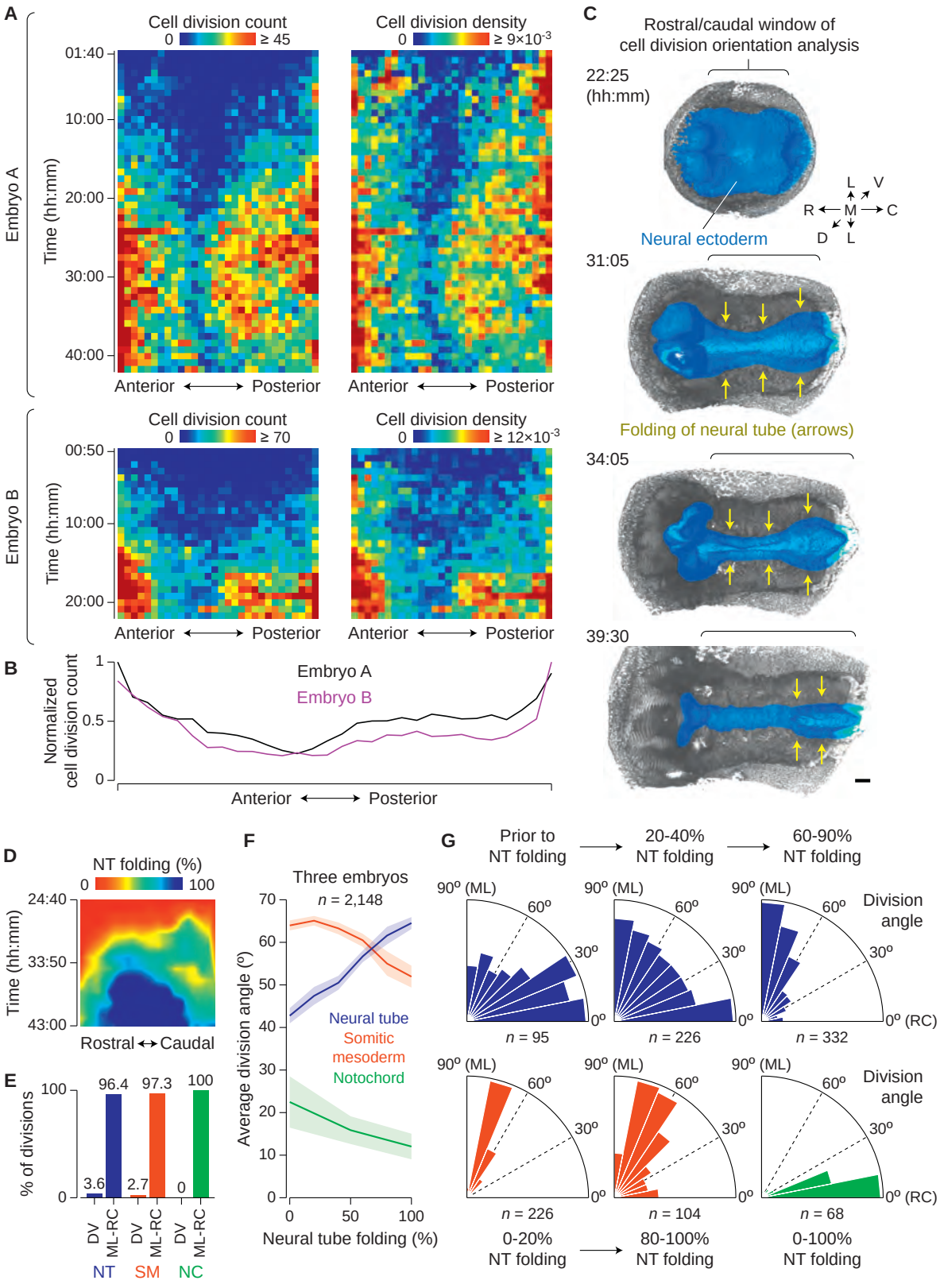

(legend on next page)

in the average embryo, we tracked the progression and location of T-positive cells in the average embryo backward and forward in time (Video S7D). These results are in close agreement with the expected expression patterns and dynamics of notochord development visualized in live embryos (Video S3D). To facilitate the general use of our average embryo database for reconstructing the developmental history and fate of arbitrary cell populations defined by image data obtained from other imaging experiments (using live or fixed embryos), we provide software tools for mapping snapshot image data of gene expression patterns and other types of label masks onto the average embryo database (Data S1J).

Mapping Tissue Morphodynamics

Using TARDIS, we combined quantitative measurements of the behavior of individual cells and tissues across individuals and made comparisons where they might otherwise be prevented by differences in embryo geometry or developmental timing. Complementing our statistical analysis of cell fate described above, we developed a similar approach for the quantitative investigation of cell movements, specifically the direction and speed of cell populations during the formation of tissues (STAR Methods; Data S1T and S1U). The construction of such maps of tissue morphodynamics allows us not only to visualize the flow of different tissues in comparison to their neighbors, but to measure changes in velocity and tissue size over the course of development as well as variability in tissue movements across individuals (Figures 6E–6G; Video S4C and S4D).

A Spatiotemporal Switch in the Orientation of Cell Divisions during Neural Tube Morphogenesis

In this final section, we combined our dynamic fate maps created with TGMM 2.0 and SVF, our maps of tissue morphodynamics and our CNN-based reconstruction of cell divisions across the developing embryo into a single database (STAR Methods). With this resource, we can jointly analyze the spatiotemporal distribution of cell divisions, local cell movements, and cell fates and large-scale morphogenetic changes over the course of development. A visualization of the combined data in this database (Video S6B) showed that the vast majority of cell divisions in later stages of development occur in the anterior- and posterior-most regions of the embryo (Figure 7A). Comparative analysis of a second embryo confirmed that divisions generally cluster at the leading edge of growing tissues (Figure 7A) and revealed similarities not only at the ends but along the entire AP axis (Figure 7B).

The high spatiotemporal resolution of our image data enabled the analysis of cell divisions not just by their location in the embryo but also with respect to their orientation. For example, the striking changes in tissue geometry during neural tube formation led us to ask whether the rate and orientation of divisions in the neural tube changed as a function of elongation and closure. The first site of neural tube closure can be visualized at the hindbrain/cervical boundary, after which the neural tube progressively closes in a zipper-like fashion in both rostral and caudal directions (Video S2D). An examination of division orientation using fixed tissues in chick and mouse (Sausedo et al., 1997) determined that a large percentage of cells divided along the RC axis, with some dividing along the ML axis during bending, but was unable to correlate this with the progression of neural tube closure. The image data and computational reconstructions generated here allowed us to examine this dynamic, mechanical process in detail (Figures 7C–7F). While the neural ectoderm is the most challenging part of the embryo to capture at a single-cell level, the vast majority of divisions occur on the luminal surface, making these events well separated and easily identifiable. Additionally, we quantified the orientation of cell divisions in neighboring tissues to determine if division orientation was a shared function of axis elongation or unique to the developmental stage of the tissue in question.

Prior to neural tube closure, when the primary tissue-wide morphogenetic process in the neural tube is tissue elongation, cells in the neural tube preferentially orient their divisions along the RC axis (Figure 7G). Division orientation subsequently becomes more uniformly distributed as folding progresses. Then, as the neural tube reaches the final stages of closure, cells exhibit a strong tendency to divide along the ML axis. As elongation proceeds and the neural plate narrows, it begins to bend dorsally, elevating the neural folds toward the midline, and divisions reorient to divide along the ML axis. We furthermore observed what appears to be significant 90° spindle rotation prior to division in the neural tube during these stages; however, higher temporal resolution will be necessary to quantify this behavior.

Finally, we examined neighboring tissues to determine if they too showed a preference for division orientation or a change in division angle preference as a function of their development (Figure 7G). In the somitic mesoderm, newly condensed or condensing somites appear to display a preference for ML divisions. However, this preference is lost over time as somites mature. By contrast, notochord cells, while largely quiescent, divide almost exclusively along the rostral-caudal axis. While the embryo-wide process of axis elongation almost certainly

Figure 7. A Temporal Switch in Cell Division Orientation During Neural Tube Closure

(A) Spatiotemporal distributions (left) and densities (right) of cell divisions in two embryos. As a function of time, embryos were subdivided along anterior-posterior axis into 30 sectors with equal cell counts (horizontal axis).

(B) Time-integrated, normalized cell division distributions for embryos in (A).

(C) Surface rendering of neural tube (NT) development as seen from inside of embryo.

(D) Neural tube folding map obtained by manual annotations of local NT folding angles (n = 564). 100% folding corresponds to NT closure at that location.

(E) Percentages of divisions that occur primarily along dorso-ventral axis (DV) versus within mediolateral-rostrocaudal plane (ML-RC) for three tissues.

(F) Division angle versus NT folding progression for three tissues, based on division data from three embryos.

(G) Distribution of division angles as a function of NT folding.

R, rostral. C, caudal. D, dorsal. V, ventral. M, medial. L, lateral. SM, somitic mesoderm. NC, notochord.

Scale bar (μm): 100 (C).

See also Videos S2D, S4A, and S6B.

imposes some degree of physical force on these tissues, our observations here imply that cell division orientation, at least, is a more local feature distinct to each tissue in space and time.

DISCUSSION

A Framework for Studying Whole-Embryo Development at the Single-Cell Level

The light-sheet microscope presented and applied here enabled, for the first time, imaging of mouse development *in toto* and with cellular resolution from gastrulation to early organogenesis. The resulting image data allowed us to generate the first dynamic fate maps, systematically visualize tissue formation and developmental processes at an unprecedented level of detail, and quantitatively examine dynamic processes such as the embryo-wide patterns of cell division and cell behavior during neural tube formation. In the future, further advances of this technique and the use of new, brighter, and near-infrared fluorescent reporters will aid in our ability to resolve with even greater detail those anatomical regions with the most challenging optical properties, such as the deepest layers of the ectoderm. Such advances may also enable the imaging of later stages in development, large explants or small organ cultures, where lack of transparency becomes the major limitation for light microscopy.

With the ability to systematically image the dynamic behavior of individual cells throughout the embryo came a need to develop a suite of computational methods capable of processing and analyzing the massive and highly complex image data. The result of this synergy between advances in imaging and computational image analysis is the generation of a statistical atlas of mouse development, which systematically maps cell movements, cell proliferation, cell fates, and tissue-level morphodynamic processes across the embryo and furthermore quantifies variability of these developmental parameters across individuals. These datasets and tools provide a wealth of information that can be used to address a wide range of questions on post-implantation development. For example, the ability to predict the final positions and fates of cells will allow for sampling individual cell populations at different points in time and profiling or altering their various transcriptional and behavioral states as they develop. Additionally, our dynamic atlas can be used as a platform for high-resolution mutant phenotyping by providing a systematic, quantitative comparison of "normal" development to mutants or altered states.

Dissemination and application of microscopy and image analysis methods

The ability to quantitatively examine the morphodynamic events patterning a developing embryo is of substantial value to any field. Importantly, the imaging system, computational tools, and resources we provide here are not limited to the study of post-implantation mouse development, or even to only mouse development, and may be broadly adopted for a wide range of developmental organisms and timescales, including tissue and stem cell systems, organoids or 3D culture systems. The software tools developed in this work for data management, multi-view image processing, and TGMM-based cell segmentation and tracking are applicable to a wide spectrum of live imaging data and are now also used routinely in fruit flies, zebrafish, crustaceans, and organ explants. In future work, we furthermore envision an extension of the CNN-based cell division detector, SVF cell tracking method, and TARDIS framework for multi-embryo registration to other model systems.

Considering this wide application space, we have designed all tools and resources accordingly so that they may serve a wide spectrum of groups and users. The documented code of all computational tools (Data S1B–S1J), a comprehensive practical guide to using our software including example image datasets (STAR Methods), the blueprints of the microscope (Data S1A), all databases of mouse embryonic development generated in this study (Data S1K–S1U), and interactive 4D visualizations of our cellular-resolution dynamic atlas (Data S1O) are available as a public repository. Future work will focus on continued improvements to this computational toolkit to enable new analyses of complex image data, as well as developing a new cell lineaging framework based in its entirely on a deep learning paradigm.

Access to the custom—and often highly experimental—microscopes that enable such advancements has been notoriously difficult. However, it is of critical importance that such instruments are made available to the community immediately and independently of any need for synergy or collaborative coordination. As such, we have partnered with the Janelia Advanced Imaging Center and built a copy of our adaptive light-sheet microscope with all capabilities and functions described in this work. This instrument is dedicated solely to the free use by the general scientific community and maintained by a team of experts that guide users through sample preparation, imaging, and image analysis (https://www.aicjanelia.org/).

The steady march of advancing imaging technologies and new computational methods makes this a truly exciting time for the field of mouse development, which has largely been left behind by new imaging strategies in favor of more 'amenable' organisms like D*rosophila* or zebrafish. The comprehensive methodological framework we have presented here and the generation of a dynamic atlas of early mouse development will hopefully serve as the first step in the next phase of our understanding of mammalian development as a whole.

STAR★METHODS

Detailed methods are provided in the online version of this paper and include the following:

- KEY RESOURCES TABLE
- CONTACT FOR REAGENT AND RESOURCE SHARING
- EXPERIMENTAL MODEL AND SUBJECT DETAILS
  - Transgenic mice and reporters
  - Sample preparation, embryo culture and imaging of mouse embryos
- METHOD DETAILS
  - Adaptive light-sheet microscope for imaging post-implantation mouse development
  - Large-scale image data management
  - Robust affine 3D registration of multi-view and time-lapse image data
  - TGMM 2.0 framework for cell nuclei segmentation and tracking

- Long-term tracking of cell movements with Statistical Vector Flow (SVF)
- Convolutional neural network for automated detection of cell divisions
- TARDIS algorithm for spatiotemporal registration of multiple embryos
- Constructing an average embryo from multiple reconstructed embryos
- Probabilistic and statistical cell fate maps
- Computation of tissue morphodynamics maps
- A practical guide to the framework for analyzing image data of mouse development

SUPPLEMENTAL INFORMATION

Supplemental Information includes five figures, one table, seven videos, two data files, and one methods file and can be found with this article online at https://doi.org/10.1016/j.cell.2018.09.031.

A video abstract is available at https://doi.org/10.1016/j.cell.2018.09.031#mmc12.

ACKNOWLEDGMENTS

We thank N. Clack and A. Taylor for help with developing MVD and TGMM 2.0 software; B. Coop and Janelia jET for mechanical designs and custom parts; M. Coleman for LabVIEW software; Janelia AIC for providing free microscope access; J. Kuhl for illustrations in Figures S1A–S1C; C. Wang for help with custom objective designs; B. Höckendorf for help with developing KLB; S. Preibisch for helpful discussions about image registration; J. Liu for Brachyury-H2B-mCherry mice; B. Gu, E. Posfai, and J. Rossant for H2B-miRFP703 mice; S. Srinivas, T. Watanabe, W. Lemon and A. Hantman for help with exploring mouse live imaging assays; J. Green and S. Srinivas for helpful comments on the manuscript; and Janelia Vivarium Team for animal care. All aspects of this work were funded by the Howard Hughes Medical Institute. G.M. acknowledges additional funding from the French National Research Agency (Project Dig-Em: ANR-14-CE11-0013) and L.A.R. from the Chan Zuckerberg Biohub.

AUTHOR CONTRIBUTIONS

Conceptualization: P.J.K., K.M., and L.G.; Methodology: K.M., P.J.K., L.G., F.A., K.B., A.B., L.A.R., S.C.T., and G.M.; Software: L.G., P.J.K., F.A., A.B., L.A.R., K.B., and G.M.; Formal Analysis: L.G., P.J.K., F.A., and K.M.; Investigation: K.M., L.G., F.A., and A.B.; Data Curation: K.M.; Writing: P.J.K., K.M., and L.G.; Visualization: P.J.K., K.M., and L.G.; Supervision: P.J.K., S.C.T., and K.B.; Project Administration: P.J.K., K.M., S.C.T., and K.B.; Funding: P.J.K.

DECLARATION OF INTERESTS

P.J.K., L.A.R., and R. Chhetri filed provisional US patent application 62,354,384 for adaptive light-sheet microscopy on June 24, 2016. P.J.K. holds US patent 9,404,869 for simultaneous multi-view light-sheet microscopy issued on August 2, 2016.

Received: December 1, 2017
Revised: May 12, 2018
Accepted: September 13, 2018
Published: October 11, 2018

REFERENCES

Abadi, M., Agarwal, A., Barham, P., Brevedo, E., Chen, Z., Citro, C., Corrado, G.S., Davis, A., Dean, J., Devin, M., et al. (2016). TensorFlow: Large-Scale Machine Learning on Heterogeneous Distributed Systems. arXiv, 1603.04467. https://arxiv.org/abs/1603.04467.

Abe, T., Kiyonari, H., Shioi, G., Inoue, K., Nakao, K., Aizawa, S., and Fujimori, T. (2011). Establishment of conditional reporter mouse lines at ROSA26 locus for live cell imaging. Genesis *49*, 579–590.

Amat, F., and Keller, P.J. (2013). 3D Haar-Like Elliptical Features for Object Classification in Microscopy. ISBI, 1194–1197.

Amat, F., Lemon, W., Mossing, D.P., McDole, K., Wan, Y., Branson, K., Myers, E.W., and Keller, P.J. (2014). Fast, accurate reconstruction of cell lineages from large-scale fluorescence microscopy data. Nat. Methods *11*, 951–958.

Amat, F., Höckendorf, B., Wan, Y., Lemon, W.C., McDole, K., and Keller, P.J. (2015). Efficient processing and analysis of large-scale light-sheet microscopy data. Nat. Protoc. *10*, 1679–1696.

Anderson, R., Copeland, T.K., Schöler, H., Heasman, J., and Wylie, C. (2000). The onset of germ cell migration in the mouse embryo. Mech. Dev. *91*, 61–68.

Astola, J., Haavisto, P., and Neuvo, Y. (1990). Vector Median Filters. Proc. IEEE *78*, 678–689.

Attali, D., and Boissonnat, J.D. (2003). Complexity of the Delaunay triangulation of points on polyhedral surfaces. Discrete. Comput. Geom. *30*, 437–452.

Besl, P.J., and Mckay, N.D. (1992). A Method for Registration of 3-D Shapes. PAMI *14*, 239–256.

Campolo, F., Gori, M., Favaro, R., Nicolis, S., Pellegrini, M., Botti, F., Rossi, P., Jannini, E.A., and Dolci, S. (2013). Essential role of Sox2 for the establishment and maintenance of the germ cell line. Stem Cells *31*, 1408–1421.

Chhetri, R.K., Amat, F., Wan, Y., Höckendorf, B., Lemon, W.C., and Keller, P.J. (2015). Whole-animal functional and developmental imaging with isotropic spatial resolution. Nat. Methods *12*, 1171–1178.

Gabriel, K.R., and Sokal, R.R. (1969). A new statistical approach to geographic variation analysis. Syst. Zool. *18*, 259–278.

Ginsburg, M., Snow, M.H., and McLaren, A. (1990). Primordial germ cells in the mouse embryo during gastrulation. Development *110*, 521–528.

Gu, B., Posfai, E., and Rossant, J. (2018). Efficient generation of targeted large insertions by microinjection into two-cell-stage mouse embryos. Nat. Biotechnol. *36*, 632–637.

Guignard, L., Godin, C., Fiuza, U.M., Hufnagel, L., Lemaire, P., and Malandain, G. (2014). Spatio-temporal registration of embryo images. ISBI, 778–781.

Guimond, A., Meunier, J., and Thirion, J.P. (2000). Average brain models: A convergence study. Comput. Vis. Image Underst. *77*, 192–210.

Herion, N.J., Salbaum, J.M., and Kappen, C. (2014). Traffic jam in the primitive streak: the role of defective mesoderm migration in birth defects. Birth Defects Res. A Clin. Mol. Teratol. *100*, 608–622.

Huh, S., Ker, D.F.E., Bise, R., Chen, M., and Kanade, T. (2011). Automated Mitosis Detection of Stem Cell Populations in Phase-Contrast Microscopy Images. IEEE Trans. Med. Imaging *30*, 586–596.

Huisken, J., Swoger, J., Del Bene, F., Wittbrodt, J., and Stelzer, E.H.K. (2004). Optical sectioning deep inside live embryos by selective plane illumination microscopy. Science *305*, 1007–1009.

Ichikawa, T., Nakazato, K., Keller, P.J., Kajiura-Kobayashi, H., Stelzer, E.H., Mochizuki, A., and Nonaka, S. (2014). Live imaging and quantitative analysis of gastrulation in mouse embryos using light-sheet microscopy and 3D tracking tools. Nat. Protoc. *9*, 575–585.

Imuta, Y., Kiyonari, H., Jang, C.W., Behringer, R.R., and Sasaki, H. (2013). Generation of knock-in mice that express nuclear enhanced green fluorescent protein and tamoxifen-inducible Cre recombinase in the notochord from Foxa2 and T loci. Genesis *51*, 210–218.

Ioffe, S., and Szegedy, C. (2015). Batch normalization: Accelerating deep network training by reducing internal covariate shift. ICML, 448–456.

Jones, E.A., Crotty, D., Kulesa, P.M., Waters, C.W., Baron, M.H., Fraser, S.E., and Dickinson, M.E. (2002). Dynamic in vivo imaging of postimplantation mammalian embryos using whole embryo culture. Genesis *34*, 228–235.

Kabra, M., Robie, A.A., Rivera-Alba, M., Branson, S., and Branson, K. (2013). JAABA: interactive machine learning for automatic annotation of animal behavior. Nat. Methods *10*, 64–67.

Keller, P.J., Schmidt, A.D., Wittbrodt, J., and Stelzer, E.H.K. (2008). Reconstruction of zebrafish early embryonic development by scanned light sheet microscopy. Science *322*, 1065–1069.

Kingma, D., and Ba, J. (2014). Adam: A method for stochastic optimization. arXiv, 1412.6980. https://arxiv.org/abs/1412.6980.

Kuhn, H.W. (1955). The Hungarian method for the assignment problem. Nav. Res. Log. *2*, 83–97.

Lawson, K.A. (1999). Fate mapping the mouse embryo. Int. J. Dev. Biol. *43*, 773–775.

Lawson, K.A., and Pedersen, R.A. (1987). Cell fate, morphogenetic movement and population kinetics of embryonic endoderm at the time of germ layer formation in the mouse. Development *101*, 627–652.

Lawson, K.A., and Pedersen, R.A. (1992). Clonal analysis of cell fate during gastrulation and early neurulation in the mouse. Ciba Found. Symp. *165*, 3–26.

Liu, Y.K. (2013). Noise reduction by vector median filtering. Geophysics *78*, V79–V86.

Lolas, M., Valenzuela, P.D., Tjian, R., and Liu, Z. (2014). Charting Brachyury-mediated developmental pathways during early mouse embryogenesis. Proc. Natl. Acad. Sci. USA *111*, 4478–4483.

Matula, D.W., and Sokal, R.R. (1980). Properties of Gabriel graphs relevant to geographic variation research and the clustering of points in the plane. Geogr. Anal. *12*, 205–222.

Molyneaux, K.A., Stallock, J., Schaible, K., and Wylie, C. (2001). Time-lapse analysis of living mouse germ cell migration. Dev. Biol. *240*, 488–498.

Ourselin, S., Roche, A., Prima, S., and Ayache, N. (2000). Block matching: A general framework to improve robustness of rigid registration of medical images. MICCAI *1935*, 557–566.

Piliszek, A., Kwon, G.S., and Hadjantonakis, A.K. (2011). Ex utero culture and live imaging of mouse embryos. Methods Mol. Biol. *770*, 243–257.

Rivera-Pérez, J.A., and Hadjantonakis, A.K. (2014). The dynamics of morphogenesis in the early mouse embryo. Cold Spring Harb. Perspect. Biol. *7*. https://doi.org/10.1101/cshperspect.a015867.

Royer, L.A., Lemon, W.C., Chhetri, R.K., Wan, Y., Coleman, M., Myers, E.W., and Keller, P.J. (2016). Adaptive light-sheet microscopy for long-term, high-resolution imaging in living organisms. Nat. Biotechnol. *34*, 1267–1278.

Saitou, M., and Yamaji, M. (2012). Primordial germ cells in mice. Cold Spring Harb. Perspect. Biol. *4*. https://doi.org/10.1101/cshperspect.a008375.

Sausedo, R.A., Smith, J.L., and Schoenwolf, G.C. (1997). Role of nonrandomly oriented cell division in shaping and bending of the neural plate. J. Comp. Neurol. *381*, 473–488.

Shoemake, K. (1985). Animating rotation with quaternion curves. SIGGRAPH *19*, 245–254.

Strnad, P., Gunther, S., Reichmann, J., Krzic, U., Balazs, B., de Medeiros, G., Norlin, N., Hiiragi, T., Hufnagel, L., and Ellenberg, J. (2016). Inverted light-sheet microscope for imaging mouse pre-implantation development. Nat. Methods *13*, 139–142.

Susaki, E.A., Tainaka, K., Perrin, D., Yukinaga, H., Kuno, A., and Ueda, H.R. (2015). Advanced CUBIC protocols for whole-brain and whole-body clearing and imaging. Nat. Protoc. *10*, 1709–1727.

Takaoka, K., Yamamoto, M., and Hamada, H. (2011). Origin and role of distal visceral endoderm, a group of cells that determines anterior-posterior polarity of the mouse embryo. Nat. Cell Biol. *13*, 743–752.

Tam, P.P., and Beddington, R.S. (1992). Establishment and organization of germ layers in the gastrulating mouse embryo. Ciba Found. Symp. *165*, 27–41, discussion 42–49.

Tam, P.P., Parameswaran, M., Kinder, S.J., and Weinberger, R.P. (1997). The allocation of epiblast cells to the embryonic heart and other mesodermal lineages: the role of ingression and tissue movement during gastrulation. Development *124*, 1631–1642.

Tomer, R., Khairy, K., Amat, F., and Keller, P.J. (2012). Quantitative high-speed imaging of entire developing embryos with simultaneous multiview light-sheet microscopy. Nat. Methods *9*, 755–763.

Trichas, G., Begbie, J., and Srinivas, S. (2008). Use of the viral 2A peptide for bicistronic expression in transgenic mice. BMC Biol. *6*, 40.

Udan, R.S., Piazza, V.G., Hsu, C.W., Hadjantonakis, A.K., and Dickinson, M.E. (2014). Quantitative imaging of cell dynamics in mouse embryos using light-sheet microscopy. Development *141*, 4406–4414.

Wolff, C., Tinevez, J.Y., Pietzsch, T., Stamataki, E., Harich, B., Guignard, L., Preibisch, S., Shorte, S., Keller, P.J., Tomancak, P., et al. (2018). Multi-view light-sheet imaging and tracking with the MaMuT software reveals the cell lineage of a direct developing arthropod limb. Elife *7*, e34410.

Wong, M.D., Maezawa, Y., Lerch, J.P., and Henkelman, R.M. (2014). Automated pipeline for anatomical phenotyping of mouse embryos using micro-CT. Development *141*, 2533–2541.

Article

Cell

Predicting Splicing from Primary Sequence with Deep Learning

Kishore Jaganathan,[1,6] Sofia Kyriazopoulou Panagiotopoulou,[1,6] Jeremy F. McRae,[1,6] Siavash Fazel Darbandi,[2] David Knowles,[3] Yang I. Li,[3] Jack A. Kosmicki,[1,4] Juan Arbelaez,[2] Wenwu Cui,[1] Grace B. Schwartz,[2] Eric D. Chow,[5] Efstathios Kanterakis,[1] Hong Gao,[1] Amirali Kia,[1] Serafim Batzoglou,[1] Stephan J. Sanders,[2] and Kyle Kai-How Farh[1,7,*]

[1]Illumina Artificial Intelligence Laboratory, Illumina, Inc., San Diego, CA, USA
[2]Department of Psychiatry, University of California, San Francisco, San Francisco, CA, USA
[3]Department of Genetics, Stanford University, Stanford, CA, USA
[4]Broad Institute of MIT and Harvard, Cambridge, MA, USA
[5]Department of Biochemistry and Biophysics, University of California, San Francisco, San Francisco, CA, USA
[6]These authors contributed equally
[7]Lead Contact
*Correspondence: kfarh@illumina.com
https://doi.org/10.1016/j.cell.2018.12.015

SUMMARY

The splicing of pre-mRNAs into mature transcripts is remarkable for its precision, but the mechanisms by which the cellular machinery achieves such specificity are incompletely understood. Here, we describe a deep neural network that accurately predicts splice junctions from an arbitrary pre-mRNA transcript sequence, enabling precise prediction of noncoding genetic variants that cause cryptic splicing. Synonymous and intronic mutations with predicted splice-altering consequence validate at a high rate on RNA-seq and are strongly deleterious in the human population. *De novo* mutations with predicted splice-altering consequence are significantly enriched in patients with autism and intellectual disability compared to healthy controls and validate against RNA-seq in 21 out of 28 of these patients. We estimate that 9%–11% of pathogenic mutations in patients with rare genetic disorders are caused by this previously underappreciated class of disease variation.

INTRODUCTION

Exome sequencing has transformed the clinical diagnosis of patients and families with rare genetic disorders and, when employed as a first-line test, significantly reduces the time and costs of the diagnostic odyssey (Tan et al., 2017). However, the diagnostic yield of exome sequencing is ~25%–30% in rare genetic disease cohorts, leaving the majority of patients without a diagnosis even after combined exome and microarray testing (Lee et al., 2014; Yang et al., 2014). Noncoding regions play a significant role in gene regulation and account for 90% of causal disease loci discovered in unbiased genome-wide association studies of human complex diseases (Farh et al., 2015; Maurano et al., 2012), suggesting that penetrant noncoding variants may also account for a significant burden of causal mutations in rare genetic diseases. Indeed, penetrant noncoding variants that disrupt the normal pattern of mRNA splicing despite lying outside the essential GT and AG splice dinucleotides, often referred to as cryptic splice variants, have long been recognized to play a significant role in rare genetic diseases (Cooper et al., 2009). However, cryptic splice mutations are often overlooked in clinical practice, due to our incomplete understanding of the splicing code and the resulting difficulty in accurately identifying splice-altering variants outside the essential GT and AG dinucleotides (Wang and Burge, 2008).

Recently, RNA sequencing (RNA-seq) has emerged as a promising assay for detecting splicing abnormalities in Mendelian disorders (Cummings et al., 2017), but thus far its utility in a clinical setting remains limited to a minority of cases where the relevant cell type is known and accessible to biopsy. High-throughput screening assays of potential splice-altering variants (Soemedi et al., 2017) have expanded the characterization of splicing variation but are less practical for evaluating random *de novo* mutations in genetic diseases, since the genomic space where splice-altering mutations may occur is extremely large. General prediction of splicing from an arbitrary pre-mRNA sequence would potentially allow precise prediction of the splice-altering consequences of noncoding variants, substantially improving diagnosis in patients with genetic diseases. To date, a general predictive model of splicing from a raw sequence that approaches the specificity of the spliceosome remains elusive, despite progress in specific applications, such as modeling the sequence characteristics of the core splicing motifs (Yeo and Burge, 2004), characterizing exonic splice enhancers and silencers (Fairbrother et al., 2002; Wang et al., 2004), and predicting cassette exon inclusion (Xiong et al., 2015).

RESULTS

Accurate Prediction of Splicing from a Primary Sequence Using Deep Learning

We constructed SpliceAI, a deep residual neural network (He et al., 2016) that predicts whether each position in a pre-mRNA

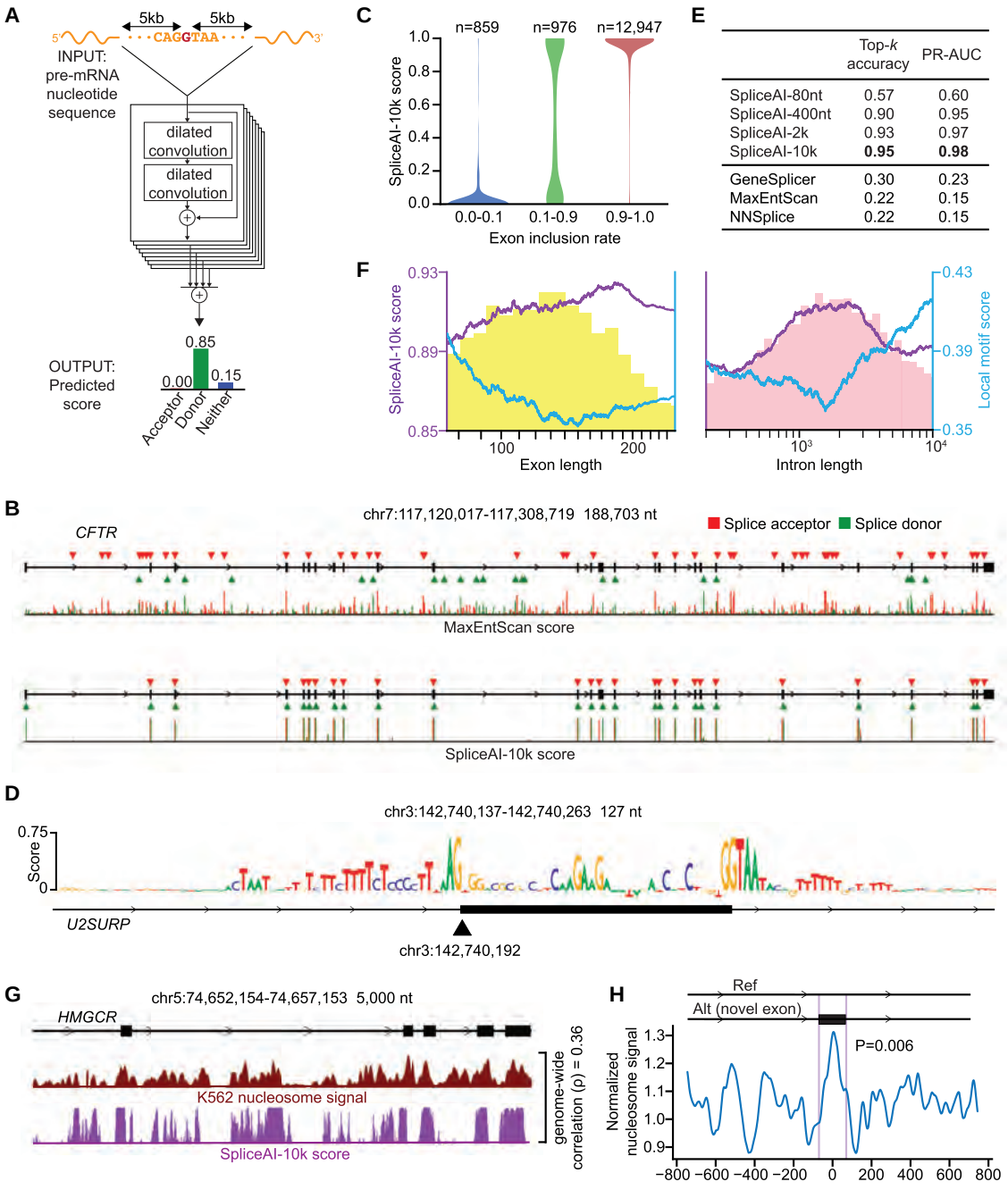

Figure 1. Predicting Splicing from Primary Sequence with Deep Learning

(A) For each position in the pre-mRNA transcript, SpliceAI-10k uses 10,000 nucleotides of flanking sequence as input and predicts whether that position is a splice acceptor, splice donor, or neither.

(B) The full pre-mRNA transcript for the *CFTR* gene scored using MaxEntScan (top) and SpliceAI-10k (bottom) is shown, along with predicted acceptor (red arrows) and donor (green arrows) sites and the actual positions of the exons (black boxes). For each method, we applied the threshold that made the number of predicted sites equal to the total number of actual sites.

(C) We measured the inclusion rate of each exon on RNA-seq and show the SpliceAI-10k score distribution for exons at different inclusion rates. Shown are the maximum of the exon's acceptor and donor scores.

(D) Impact of *in silico* mutating each nucleotide around exon 9 in the *U2SURP* gene. The vertical size of each nucleotide shows the decrease in the predicted strength of the acceptor site (black arrow) when that nucleotide is mutated (Δ score).

(E) Effect of the size of the input sequence context on the accuracy of the network. Top-*k* accuracy is the fraction of correctly predicted splice sites at the threshold where the number of predicted sites is equal to the actual number of sites present. PR-AUC is the area under the precision-recall curve. We also show the top-*k* accuracy and PR-AUC for three other algorithms for splice-site detection.

(legend continued on next page)

transcript is a splice donor, splice acceptor, or neither (Figures 1A and S1), using as input only the genomic sequence of the pre-mRNA transcript. Because splice donors and splice acceptors may be separated by tens of thousands of nucleotides, we employed a network architecture consisting of 32 dilated convolutional layers that can recognize sequence determinants spanning very large genomic distances. In contrast to previous methods that have only considered short nucleotide windows adjoining exon-intron boundaries (Yeo and Burge, 2004), or relied on human-engineered features, our neural network learns splicing determinants directly from the primary sequence by evaluating 10,000 nucleotides of the flanking context sequence to predict the splice function of each position in the pre-mRNA transcript.

We used GENCODE-annotated pre-mRNA transcript sequences (Harrow et al., 2012) on a subset of the human chromosomes to train the parameters of the neural network, and transcripts on the remaining chromosomes, with paralogs excluded, to test the network's predictions. For pre-mRNA transcripts in the test dataset, the network predicts splice junctions with 95% top-*k* accuracy, which is the fraction of correctly predicted splice sites at the threshold where the number of predicted sites is equal to the actual number of splice sites present in the test dataset (Boyd et al., 2012; Yeo and Burge, 2004). Even genes in excess of 100 kb such as *CFTR* are often reconstructed perfectly to nucleotide precision (Figure 1B). To confirm that the network is not simply relying on exonic sequence biases, we also tested the network on long noncoding RNAs. Despite the incompleteness of noncoding transcript annotations, which is expected to reduce our accuracy, the network predicts known splice junctions in long noncoding RNAs (lincRNAs) with 84% top-*k* accuracy (Figures S2A and S2B), indicating that it can approximate the behavior of the spliceosome on arbitrary sequences that are free from protein-coding selective pressures.

For each GENCODE-annotated exon in the test dataset (excluding the first and last exons of each gene), we also examined whether the network's prediction scores correlate with the fraction of reads supporting exon inclusion versus exon skipping, based on RNA-seq data from the Gene and Tissue Expression (GTEx) atlas (The GTEx Consortium et al., 2015; Lonsdale et al., 2013) (Figure 1C). Exons that were constitutively spliced in or spliced out across GTEx tissues had prediction scores that were close to 1 or 0, respectively, whereas exons that underwent a substantial degree of alternative splicing (between 10% and 90% exon inclusion averaged across samples) tended toward intermediate scores (Pearson correlation = 0.78, $p \approx 0$).

We next sought to understand the sequence determinants utilized by the network to achieve its remarkable accuracy. We performed systematic *in silico* substitutions of each nucleotide near annotated exons, measuring the effects on the network's prediction scores at the adjoining splice sites (Figure 1D). We found that disrupting the sequence of a splice donor motif frequently caused the network to predict that the upstream splice acceptor site will also be lost, as is observed with exon-skipping events *in vivo*, indicating that a significant degree of specificity is imparted by exon definition between a paired upstream acceptor motif and a downstream donor motif set at an optimal distance (Berget, 1995). Additional motifs that contribute to the splicing signal include the well-characterized binding motifs of the branchpoint and the SR-protein family (Figures S2C and S2D) (Fairbrother et al., 2002). The effects of these motifs are highly dependent on their position in the exon, suggesting that their roles include specifying the precise positioning of intron-exon boundaries by differentiating between competing acceptor and donor sites.

Training the network with varying input sequence context markedly impacts the accuracy of the splice predictions (Figure 1E), indicating that long-range sequence determinants thousands of nucleotides away from the splice site are essential for discerning functional splice junctions from the large number of nonfunctional sites with near-optimal motifs. To examine long-range and short-range specificity determinants, we compared the scores assigned to annotated junctions by a model trained on 80 nt of the sequence context (SpliceAI-80nt) versus the full model that is trained on 10,000 nt of context (SpliceAI-10k). The network trained on 80 nt of the sequence context assigns lower scores to junctions adjoining exons or introns of typical length (150 nt for exons, ~1,000 nt for introns) (Figure 1F), in agreement with earlier observations that such sites tend to have weaker splice motifs compared to the splice sites of exons and introns, which are unusually long or short (Amit et al., 2012). In contrast, the network trained on 10,000 nt of the sequence context shows preference for introns and exons of average length, despite their weaker splice motifs, because it can account for long-range specificity conferred by exon or intron length. The skipping of weaker motifs in long uninterrupted introns is consistent with the faster RNA polymerase II elongation experimentally observed in the absence of exon pausing, which may allow the spliceosome less time to recognize suboptimal motifs (Close et al., 2012; Jonkers et al., 2014). Our findings suggest that the average splice junction possesses favorable long-range sequence determinants that confer substantial specificity, explaining the high degree of sequence degeneracy tolerated at most splice motifs.

Because splicing occurs co-transcriptionally, interactions between chromatin state and co-transcriptional splicing might also guide exon definition (Luco et al., 2010) and have the potential to be utilized by the network to the extent that chromatin state is predictable from the primary sequence. In particular, genome-wide studies of nucleosome positioning have shown that

(F) Relationship between exon-intron length and the strength of the adjoining splice sites, as predicted by SpliceAI-80 nt (local motif score) and SpliceAI-10k. The genome-wide distributions of exon length (yellow) and intron length (pink) are shown in the background. The x axis is in log-scale.
(G) A pair of splice acceptor and donor motifs, placed 150 nt apart, are walked along the *HMGCR* gene. Shown are, at each position, K562 nucleosome signal and the likelihood of the pair forming an exon at that position, as predicted by SpliceAI-10k. The genome-wide Spearman correlation between the two tracks is shown.
(H) Average K562 and GM12878 nucleosome signal near private mutations that are predicted by the SpliceAI-10k model to create novel exons in the GTEx cohort. The p value by permutation test is shown.
See also Figures S1 and S2.

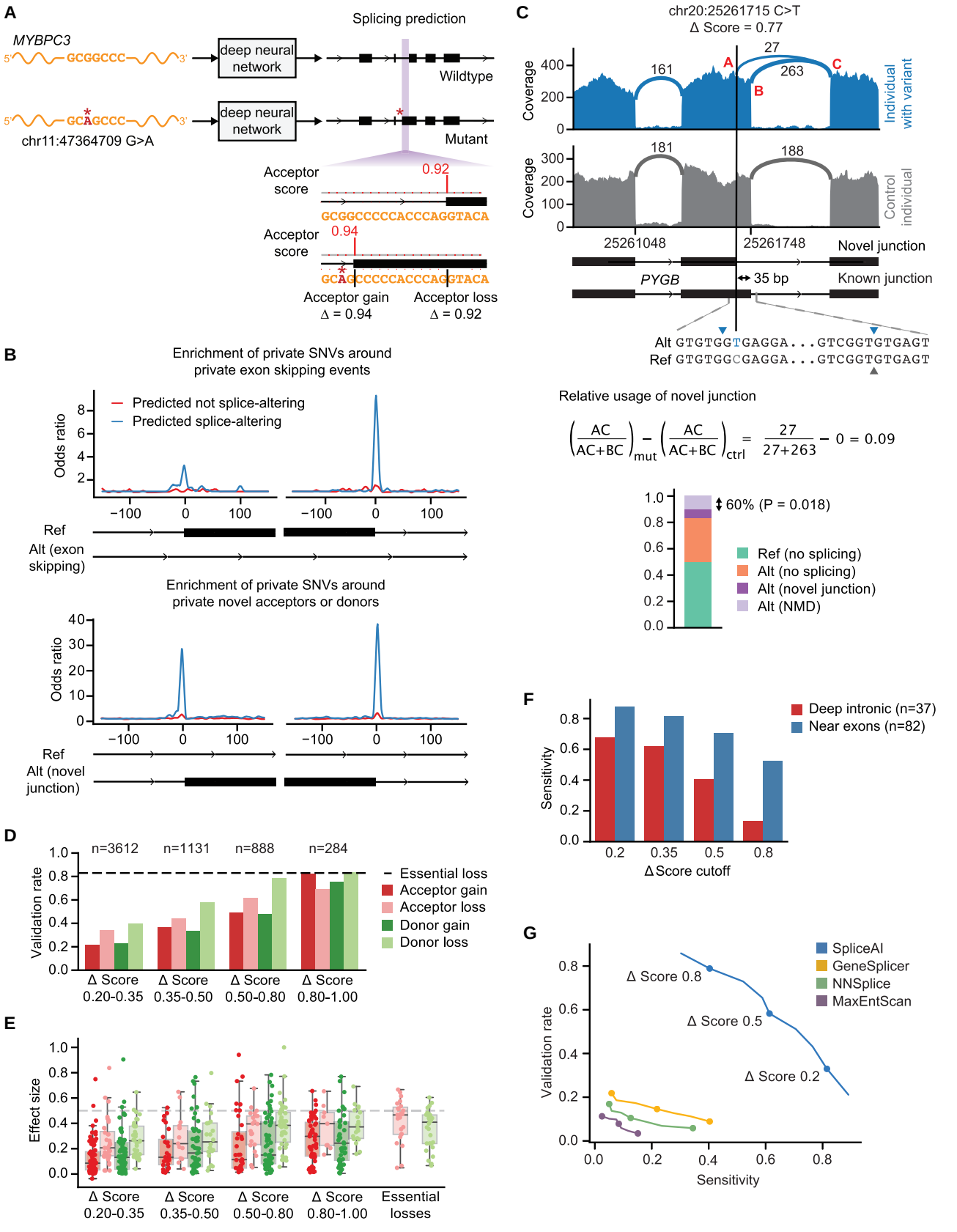

(legend on next page)

nucleosome occupancy is higher in exons (Schwartz et al., 2009; Spies et al., 2009). To test whether the network uses sequence determinants of nucleosome positioning for splice site prediction, we walked a pair of optimal acceptor and donor motifs separated by 150 nt (roughly the size of the average exon) across the genome and asked the network to predict whether the pair of motifs would result in exon inclusion at that locus (Figure 1G). We find that positions predicted to be favorable for exon inclusion correlated with positions of high nucleosome occupancy, even in intergenic regions (Spearman correlation = 0.36, $p \approx 0$), and this effect persists after controlling for GC content (Figure S2E). These results suggest that the network has implicitly learned to predict nucleosome positioning from the primary sequence and utilizes it as a specificity determinant in exon definition. Similar to exons and introns of average length, exons positioned over nucleosomes have weaker local splice motifs (Figure S2F), consistent with greater tolerance for degenerate motifs in the presence of compensatory factors (Spies et al., 2009).

Although multiple studies have reported a correlation between exons and nucleosome occupancy, a causal role for nucleosome positioning in exon definition has not been firmly established. Using data from 149 individuals with both RNA-seq and whole-genome sequencing from the Genotype-Tissue Expression (GTEx) cohort (The GTEx Consortium et al., 2015; Lonsdale et al., 2013), we identified novel exons that were private to a single individual, and corresponded to a private splice site-creating genetic mutation. These private exon-creation events were significantly associated with existing nucleosome positioning in K562 and GM12878 cells ($p = 0.006$ by permutation test, Figure 1H), even though these cell lines most likely lack the corresponding private genetic mutations. Our results indicate that genetic variants are more likely to trigger creation of a novel exon if the resulting novel exon would overlay a region of existing nucleosome occupancy, supporting a causal role for nucleosome positioning in promoting exon definition.

Verification of Predicted Cryptic Splice Mutations in RNA-Seq Data

We extended the deep learning network to the evaluation of genetic variants for splice-altering function by predicting exon-intron boundaries for both the reference pre-mRNA transcript sequence and the alternate transcript sequence containing the variant, and taking the difference between the scores (Δ score, Figure 2A). Importantly, the network was only trained on reference transcript sequences and splice junction annotations, and never saw variant data during training, making prediction of variant effects a challenging test of the network's ability to accurately model the sequence determinants of splicing.

We looked for the effects of cryptic splice variants in RNA-seq data in the GTEx cohort, comprising 149 individuals with both whole-genome sequencing and RNA-seq from multiple tissues. To approximate the scenario encountered in rare disease sequencing, we first focused on rare, private mutations (present in only one individual in the GTEx cohort). We find that private mutations predicted to have functional consequences by the neural network are strongly enriched at private novel splice junctions and at the boundaries of skipped-over exons in private exon-skipping events (Figure 2B), suggesting that a large fraction of these predictions are functional.

To quantify the effects of splice-site creating variants on the relative production of normal and aberrant splice isoforms, we measured the number of reads supporting the novel splice event as a fraction of the total number of reads covering the site (Figure 2C). We calculated both the decrease in the fraction of reads that spliced at the disrupted junction and the increase in the

Figure 2. Validation of Rare Cryptic Splice Mutations in RNA-Seq Data

(A) To assess the splice-altering impact of a mutation, SpliceAI-10k predicts acceptor and donor scores at each position in the pre-mRNA sequence of the gene with and without the mutation, as shown here for rs397515893, a pathogenic cryptic splice variant in the *MYBPC3* intron associated with cardiomyopathy. The Δ score value for the mutation is the largest change in splice prediction scores within 50 nt from the variant.

(B) We scored private genetic variants (observed in only one out of 149 individuals in the GTEx cohort) with SpliceAI-10k. Shown are the enrichment of private variants predicted to alter splicing (Δ score >0.2, blue) or to have no effect on splicing (Δ score <0.01, red) in the vicinity of private exon-skipping junctions (top) or private acceptor and donor sites (bottom). The y axis shows the number of times a private splice event and a nearby private genetic variant co-occur in the same individual, compared to expected numbers obtained through permutations.

(C) Example of a heterozygous synonymous variant in the *PYGB* gene that creates a novel donor site with incomplete penetrance. RNA-seq coverage, junction read counts, and the positions of junctions (blue and gray arrows) are shown for the individual with the variant and a control individual. The effect size is computed as the difference in the usage of the novel junction (AC) between individuals with the variant and individuals without the variant. In the stacked bar graph below, we show the number of reads with the reference or alternate allele that used the annotated or the novel junction ("no splicing" and "novel junction" respectively). The total number of reference reads differed significantly from the total number of alternate reads ($p = 0.018$, Binomial test), suggesting that 60% of transcripts splicing at the novel junction are missing in the RNA-seq data, presumably due to nonsense mediated decay (NMD).

(D) Fraction of cryptic splice mutations predicted by SpliceAI-10k that validated against the GTEx RNA-seq data. The validation rate of disruptions of essential acceptor or donor dinucleotides (dashed line) is less than 100% due to insufficient coverage and nonsense mediated decay.

(E) Distribution of effect sizes for validated cryptic splice predictions. The dashed line (50%) corresponds to the expected effect size of fully penetrant heterozygous variants. The measured effect size of essential acceptor or donor dinucleotide disruptions is less than 50% due to nonsense-mediated decay or unaccounted-for isoform changes.

(F) Sensitivity of SpliceAI-10k at detecting splice-altering private variants in the GTEx cohort at different Δ score cutoffs. Variants are split into deep intronic variants (>50 nt from exons) and variants near exons (overlapping exons or ≤50 nt from exon-intron boundaries).

(G) Validation rate and sensitivity of SpliceAI-10k and three other methods for splice site prediction at different confidence cutoffs. The three dots on the SpliceAI-10k curve show the performance of SpliceAI-10k at Δ score cutoffs of 0.2, 0.5, and 0.8. For the other three algorithms, the three dots on the curve indicate their performance at the thresholds where they predict the same number of cryptic splice variants as SpliceAI-10k at Δ score cutoffs of 0.2, 0.5, and 0.8.

See also Figures S3 and S4 and Tables S1 and S2.

fraction of reads that skipped the exon, taking the larger of the two effects (Figure S3A; STAR Methods).

Confidently predicted cryptic splice variants (Δ score $\geq$0.5) validate on RNA-seq at three-quarters the rate of essential GT or AG splice disruptions (Figure 2D). Both the validation rate and effect size of cryptic splice variants closely track their Δ scores (Figures 2D and 2E), demonstrating that the model's prediction score is a good proxy for the splice-altering potential of a variant. Validated variants, especially those with lower scores (Δ score <0.5), are often incompletely penetrant, and result in alternative splicing with production of a mixture of both aberrant and normal transcripts in the RNA-seq data (Figure 2E). Our estimates of validation rates and effect sizes are conservative and likely underestimate the true values, due to both unaccounted-for splice isoform changes and nonsense-mediated decay (Figures 2C and S3A). This is evidenced by the average effect sizes of variants that disrupt essential GT and AG splice dinucleotides being less than the 50% expected for fully penetrant heterozygous variants.

For cryptic splice variants that produce aberrant splice isoforms in at least three-tenths of the observed copies of the mRNA transcript, the network has a sensitivity of 71% when the variant is near exons, and 41% when the variant is in the deep intronic sequence (Δ score $\geq$0.5, Figure 2F). These findings indicate that deep intronic variants are more challenging to predict, possibly because deep intronic regions contain fewer of the specificity determinants that have been selected to be present near exons.

To benchmark the performance of our network against existing methods, we selected three popular classifiers that have been referenced in the literature for rare genetic disease diagnosis, GeneSplicer (Pertea et al., 2001), MaxEntScan (Yeo and Burge, 2004), and NNSplice (Reese et al., 1997), and plotted the RNA-seq validation rate and sensitivity at varying thresholds (Figure 2G). As has been the experience of others in the field (Cummings et al., 2017), we find that existing classifiers have insufficient specificity given the very large number of noncoding variants genome-wide that can possibly affect splicing, presumably because they focus on local motifs and largely do not account for long-range specificity determinants.

Given the large gap in performance compared with existing methods, we performed additional controls to exclude the possibility that our results in the RNA-seq data could be confounded by overfitting. First, we repeated the validation and sensitivity analyses separately for private variants and variants present in more than one individual in the GTEx cohort (Figures S3B–S3D) and verified that, at the same Δ score thresholds, private and common variants show no significant differences in their validation rate ($p > 0.05$, Fisher's exact test). Second, we also saw no significant differences in the validation rates of cryptic splice variants that create new GT or AG dinucleotides, variants that affect the extended acceptor or donor motif, and variants that occur in more distal regions ($p > 0.3$ χ^2 test of uniformity and $p > 0.3$ Mann-Whitney U test, respectively, Figures S3E and S3F). Third, we performed the RNA-seq validation and sensitivity analyses separately for variants on the chromosomes used for training and variants on the rest of the chromosomes (Figures S4A and S4B). Although the network was trained only on the reference genomic sequence and splice annotations, and was not exposed to variant data during training, we wanted to rule out the possibility of biases in variant predictions arising from the fact that the network has seen the reference sequence in the training chromosomes. We found that the network performs equally well on variants from the training and testing chromosomes, with no significant difference in validation rate or sensitivity ($p > 0.05$, Fisher's exact test), indicating that the network's variant predictions are unlikely to be explained by overfitting the training sequences.

Tissue-Specific Alternative Splicing Frequently Arises from Weak Cryptic Splice Variants

Alternative splicing is a major mode of gene regulation that serves to increase the diversity of transcripts in different tissues and developmental stages, and its dysregulation is associated with disease processes (Irimia et al., 2014; Wang et al., 2008). Unexpectedly, we find that the relative usage of novel splice junctions created by cryptic splice mutations can vary substantially across tissues (Figure 3A). Moreover, variants that cause tissue-specific differences in splicing are reproducible across multiple individuals (Figure 3B), indicating that tissue-specific biology likely underlies these differences, rather than stochastic effects. We find that 35% of cryptic splice variants with weak and intermediate predicted scores (Δ score 0.35–0.8) exhibit significant differences in the fraction of normal and aberrant transcripts produced across tissues (Bonferroni corrected $p < 0.01$ for a χ^2 test, Figure 3C). This contrasted with variants with high predicted scores (Δ score >0.8), which were significantly less likely to produce tissue-specific effects ($p = 0.015$). Our findings align with the earlier observation that alternatively spliced exons tend to have intermediate prediction scores (Figure 1C), compared to exons that are constitutively spliced in or spliced out, which have scores that are close to 1 or 0, respectively.

These results support a model where tissue-specific factors, such as the chromatin context and binding of RNA-binding proteins, may swing the contest between two splice junctions that are close in favorability (Luco et al., 2010; Ule et al., 2003). Strong cryptic splice variants are likely to fully shift splicing from the normal to the aberrant isoform irrespective of the epigenetic context, whereas weaker variants bring splice junction selection closer to the decision boundary, resulting in alternative junction usage in different tissue types and cell contexts. This highlights the unexpected role played by cryptic splice mutations in generating novel alternative splicing diversity, as natural selection would then have the opportunity to preserve mutations that create useful tissue-specific alternative splicing.

Predicted Cryptic Splice Variants Are Strongly Deleterious in Human Populations

Although predicted cryptic splice variants validate at a high rate in RNA-seq, in many cases the effects are not fully penetrant and a mixture of both normal and aberrant splice isoforms are produced, raising the possibility that a fraction of these cryptic splice-altering variants may not be functionally significant. To explore the signature of natural selection on predicted cryptic splice variants, we scored each variant present in 60,706 human exomes from the Exome Aggregation Consortium (ExAC)

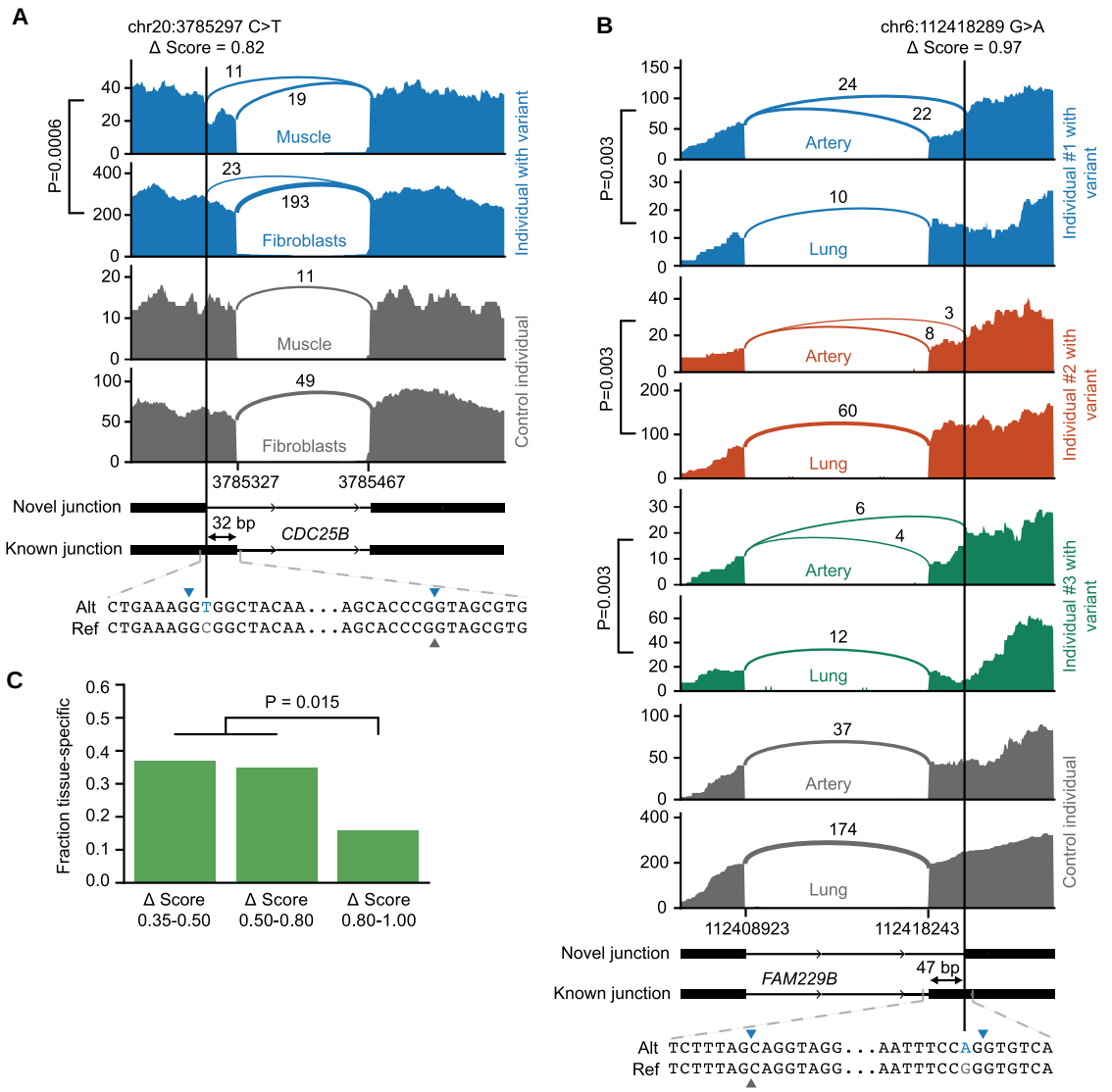

Figure 3. Cryptic Splice Variants Frequently Create Tissue-Specific Alternative Splicing

(A) Example of a heterozygous exonic variant in the *CDC25B* gene, which creates a novel donor site. The variant is private to a single individual in the GTEx cohort and exhibits tissue-specific alternative splicing that favors a greater fraction of the novel splice isoform in muscle compared to fibroblasts (p = 0.006 by Fisher's exact test). RNA-seq coverage, junction read counts, and the positions of junctions (blue and gray arrows) are shown for the individual with the variant and a control individual, in both muscle and fibroblasts.

(B) Example of a heterozygous exonic acceptor-creating variant in the *FAM229B* gene, which exhibits consistent tissue-specific effects across all three individuals in the GTEx cohort who harbor the variant. RNA-seq for artery and lung are shown for the three individuals with the variant and a control individual.

(C) Fraction of splice site-creating variants in the GTEx cohort that are associated with significantly non-uniform usage of the novel junction across expressing tissues, evaluated by the chi-square test for homogeneity. Validated cryptic splice variants with low to intermediate Δ score values were more likely to result in tissue-specific alternative splicing (p = 0.015, Fisher's exact test).

database (Lek et al., 2016) and identified variants that were predicted to alter exon-intron boundaries.

To measure the extent of negative selection acting on predicted splice-altering variants, we counted the number of predicted splice-altering variants found at common allele frequencies (≥0.1% in the human population) and compared it to the number of predicted splice-altering variants at singleton allele frequencies in ExAC (i.e., in 1 out of 60,706 individuals). Because of the recent exponential expansion in human population size, singleton variants represent recently created mutations that have been minimally filtered by purifying selection (Tennessen et al., 2012). In contrast, common variants represent a subset of neutral mutations that have passed through the sieve of purifying selection. Hence, depletion of predicted splice-altering variants in the common allele frequency spectrum relative to singleton variants provides an estimate of the fraction of

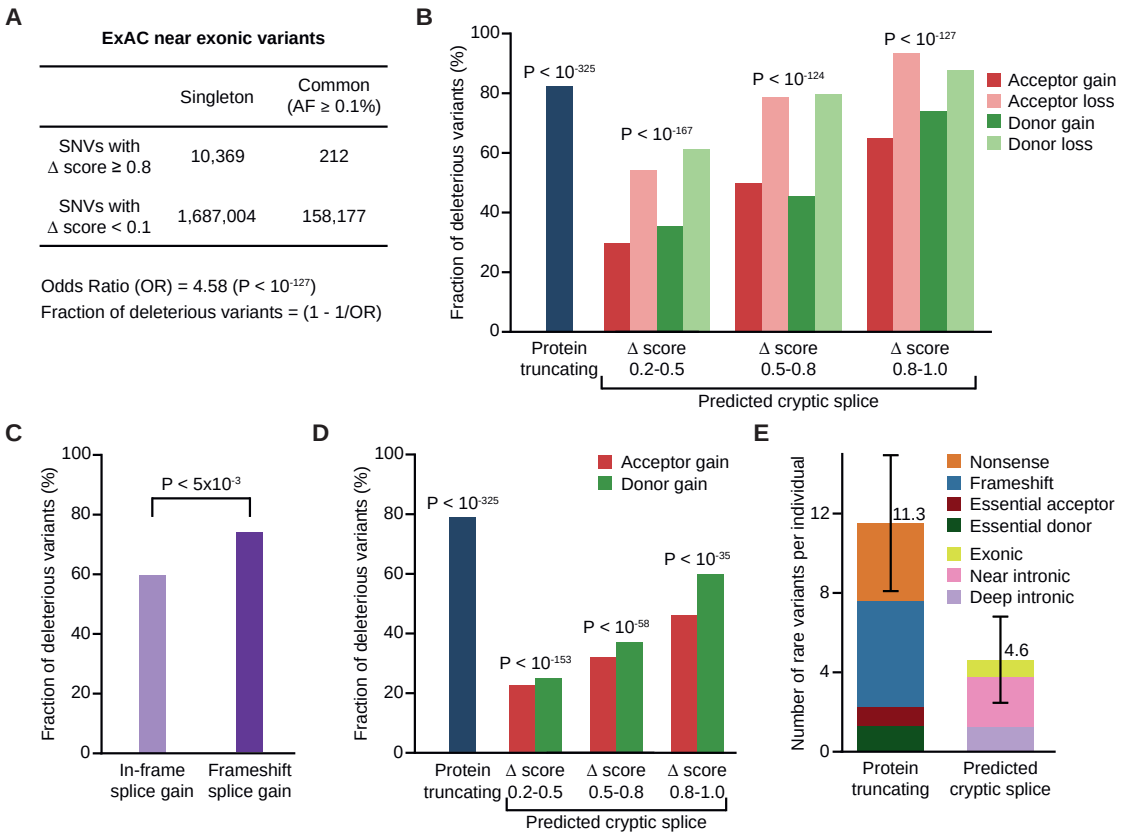

Figure 4. Predicted Cryptic Splice Variants Are Strongly Deleterious in Human Populations

(A) Synonymous and intronic variants (≤50 nt from known exon-intron boundaries and excluding the essential GT or AG dinucleotides) with confidently predicted splice-altering effects (Δ score ≥0.8) are strongly depleted at common allele frequencies (≥0.1%) in the human population relative to rare variants observed only once in 60,706 individuals. The 4.58 odds ratio ($p < 10^{-127}$ by χ^2 test) indicates that 78% of recently arising predicted cryptic splice variants are sufficiently deleterious to be removed by natural selection.

(B) Fraction of protein-truncating variants and predicted synonymous and intronic cryptic splice variants in the ExAC dataset that are deleterious, calculated as in (A).

(C) Fraction of synonymous and intronic cryptic splice gain variants in the ExAC dataset that are deleterious (Δ score ≥0.8), split based on whether the variant is expected to cause a frameshift or not ($p < 0.005$ by χ^2 test).

(D) Fraction of protein-truncating variants and predicted deep intronic (>50 nt from known exon-intron boundaries) cryptic splice variants in the gnomAD dataset that are deleterious, calculated as in (A).

(E) Average number of rare (allele frequency <0.1%) protein-truncating variants and rare functional cryptic splice variants per individual human genome. The number of cryptic splice mutations that are expected to be functional is estimated based on the fraction of predictions that are deleterious. The total number of predictions is higher. Error bars represent SD.

See also Figure S4.

predicted splice-altering variants that are deleterious, and therefore functional. To avoid confounding effects on the protein-coding sequence, we restricted our analysis to synonymous variants and intronic variants lying outside the essential GT or AG dinucleotides, excluding missense mutations that are also predicted to have splice-altering effects.

At common allele frequencies, high-scoring predicted cryptic splice variants (Δ score ≥0.8) are under strong negative selection, as evidenced by their relative depletion compared to expectation (Figure 4A). At this threshold, where most variants are expected to be close to fully penetrant in the RNA-seq data (Figure 2D), predicted synonymous and intronic cryptic splice mutations are depleted by 78% at common allele frequencies, which is comparable with the 82% depletion of frameshift, stop-gain, and essential GT or AG splice-disrupting variants (Figure 4B). The impact of negative selection is larger when considering cryptic splice variants that would cause frameshifts over those that cause in-frame changes (Figure 4C). The depletion of cryptic splice variants with frameshift consequence is nearly identical to that of other classes of protein-truncating variation, indicating that the vast majority of confidently predicted cryptic splice mutations in the exonic and near-intronic regions (≤50 nt from known exon-intron boundaries) are functional and have strongly deleterious effects in the human population.

To extend this analysis into deep intronic regions (>50 nt from known exon-intron boundaries), we used aggregated

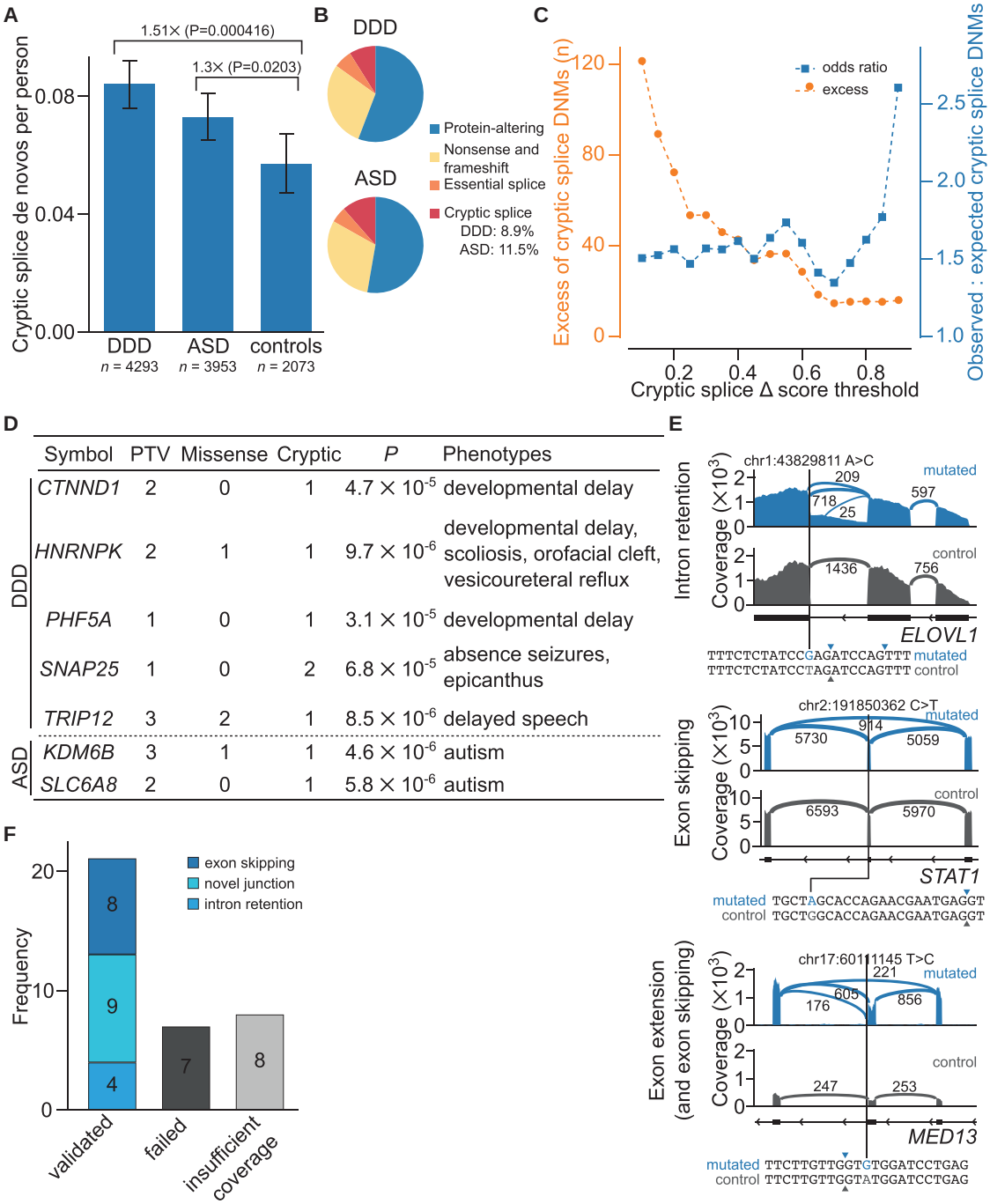

Figure 5. *De Novo* Cryptic Splice Mutations in Patients with Rare Genetic Disease

(A) Predicted cryptic splice *de novo* mutations per person for patients from the Deciphering Developmental Disorders cohort (DDD), individuals with autism spectrum disorders (ASDs) from the Simons Simplex Collection and the Autism Sequencing Consortium, as well as healthy controls. Enrichment in the DDD and ASD cohorts above healthy controls is shown, adjusting for variant ascertainment between cohorts. Error bars show 95% confidence intervals.

(B) Estimated proportion of pathogenic *de novo* mutations by functional category for the DDD and ASD cohorts, based on the enrichment of each category compared to healthy controls.

(C) Enrichment and excess of cryptic splice *de novo* mutations in the DDD and ASD cohorts compared to healthy controls at different Δ score thresholds.

(D) List of novel candidate disease genes enriched for *de novo* mutations in the DDD and ASD cohorts (FDR <0.01), when predicted cryptic splice mutations were included together with protein-coding mutations in the enrichment analysis. Phenotypes that were present in multiple individuals are shown.

(E) Three examples of predicted *de novo* cryptic splice mutations in autism patients that validate on RNA-seq, resulting in intron retention, exon skipping, and exon extension, respectively. For each example, RNA-seq coverage and junction counts for the affected individual are shown at the top, and a control individual

(legend continued on next page)

whole-genome sequencing data from 15,496 humans from the Genome Aggregation Database (gnomAD) cohort (Lek et al., 2016) to calculate the observed and expected counts of cryptic splice mutations at common allele frequencies. Overall, we observe a 56% depletion of common cryptic splice mutations (Δ score $\geq$0.8) at a distance >50 nt from an exon-intron boundary (Figure 4D), consistent with greater difficulty in predicting the impact of deep intronic variants, as we had observed in the RNA-seq data.

We next sought to estimate the potential for cryptic splice mutations to contribute to penetrant genetic disease, relative to other types of protein-coding variation, by measuring the number of rare cryptic splice mutations per individual in the gnomAD cohort. Based on the fraction of predicted cryptic splice mutations that are under negative selection (Figure 4A), the average human carries ~5 rare functional cryptic splice mutations (allele frequency <0.1%), compared to ~11 rare protein-truncating variants (Figure 4E). Cryptic splice variants outnumber essential GT or AG splice-disrupting variants roughly 2:1. We caution that a significant fraction of these cryptic splice variants may not fully abrogate gene function, either because they produce in-frame alterations, or because they do not completely shift splicing to the aberrant isoform.

De Novo Cryptic Splice Mutations Are a Major Cause of Rare Genetic Disorders

Large-scale sequencing studies of patients with autism spectrum disorders and severe intellectual disability have demonstrated the central role of *de novo* protein-coding mutations (missense, nonsense, frameshift, and essential splice dinucleotide) that disrupt genes in neurodevelopmental pathways (Fitzgerald et al., 2015; Iossifov et al., 2014; McRae et al., 2017; Neale et al., 2012; De Rubeis et al., 2014; Sanders et al., 2012). To assess the clinical impact of noncoding mutations that act through altered splicing, we applied the neural network to predict the effects of *de novo* mutations in 4,293 individuals with intellectual disability from the Deciphering Developmental Disorders (DDD) cohort (McRae et al., 2017), 3,953 individuals with autism spectrum disorders (ASDs) from the Simons Simplex Collection (De Rubeis et al., 2014; Sanders et al., 2012; Turner et al., 2016) and the Autism Sequencing Consortium, and 2,073 unaffected sibling controls from the Simons Simplex Collection. To control for differences in *de novo* variant ascertainment across studies, we normalized the expected number of *de novo* variants such that the number of synonymous mutations per individual was the same across cohorts.

De novo mutations that are predicted to disrupt splicing are enriched 1.51-fold in intellectual disability ($p = 0.000416$) and 1.30-fold in autism spectrum disorder ($p = 0.0203$) compared to healthy controls (Δ score $\geq$0.1, Figure 5A; Table S3). Splice-disrupting mutations are also significantly enriched in cases versus controls when considering only synonymous and intronic mutations (Figures S5A–S5C), excluding the possibility that the enrichment could be explained solely by mutations with dual protein-coding and splicing effects. Based on the excess of *de novo* mutations in affected versus unaffected individuals, cryptic splice mutations are estimated to comprise about 11% of pathogenic mutations in autism spectrum disorder, and 9% in intellectual disability (Figure 5B), after adjusting for the expected fraction of mutations in regions that lacked sequencing coverage or variant ascertainment in each study. Most *de novo* predicted cryptic splice mutations in affected individuals had Δ scores <0.5 (Figures 5C, S5D, and S5E) and would be expected to produce a mixture of normal and aberrant transcripts based on variants with similar scores in the GTEx RNA-seq dataset.

To estimate the enrichment of cryptic splice mutations in candidate disease genes compared to chance, we calculated the probability of calling a *de novo* cryptic splice mutation for each individual gene using trinucleotide context to adjust for mutation rate (Samocha et al., 2014) (Table S3). Combining both cryptic splice mutations and protein-coding mutations in novel gene discovery yields 5 additional candidate genes associated with intellectual disability and 2 additional genes associated with autism spectrum disorder (Figure 5D; Table S3) that would have been below the discovery threshold (false discovery rate [FDR] <0.01) when considering only protein-coding mutations (Sanders et al., 2015).

Experimental Validation of *De Novo* Cryptic Splice Mutations in Autism Patients

We obtained peripheral blood-derived lymphoblastoid cell lines (LCLs) from 36 individuals from the Simons Simplex Collection, which harbored predicted *de novo* cryptic splice mutations in genes with at least a minimal level of LCL expression (Iossifov et al., 2014; Sanders et al., 2015); each individual represented the only case of autism within their immediate family. As is the case for most rare genetic diseases, the tissue and cell type of relevance (presumably developing brain) was not accessible. Hence, we performed high-depth mRNA sequencing (~350 million × 150-bp single-end reads per sample, roughly 10 times the coverage of GTEx) to compensate for the weak expression of many of these transcripts in LCLs. To ensure that we were validating a representative set of predicted cryptic splice variants, rather than simply the top predictions, we applied relatively permissive thresholds (Δ score >0.1 for splice loss variants and Δ score >0.5 for splice gain variants; STAR Methods) and performed experimental validation on all *de novo* variants meeting these criteria.

After excluding 8 individuals who had insufficient RNA-seq coverage at the gene of interest (Figure S6), we identified unique, aberrant splicing events associated with the predicted *de novo* cryptic splice mutation in 21 out of 28 patients (Figures 5E and S6). These aberrant splicing events were absent from the other 35 individuals for whom deep LCL RNA-seq was obtained, as well as the 149 individuals from the GTEx cohort. Among the

without the mutation is shown at the bottom. Sequences are shown on the sense strand with respect to the transcription of the gene. Blue and gray arrows demarcate the positions of the junctions in the individual with the variant and the control individual, respectively.
(F) Validation status for 36 predicted cryptic splice sites selected for experimental validation by RNA-seq.
See also Figures S4, S5, and S6 and Tables S3 and S4.

21 confirmed *de novo* cryptic splice mutations, we observed 9 cases of novel junction creation (Iossifov et al., 2014; Sanders et al., 2015), 8 cases of exon skipping, and 4 cases of intron retention, as well as more complex splicing aberrations (Figure 5F; Table S4). Seven cases did not show aberrant splicing in LCLs, despite adequate expression of the transcript. Although a subset of these may represent false positive predictions, some cryptic splice mutations may result in tissue-specific alternative splicing that is not observable in LCLs under these experimental conditions.

The high validation rate of predicted cryptic splice mutations in patients with autism spectrum disorder (75%), despite the limitations of the RNA-seq assay, indicates that most predictions are functional. However, the enrichment of *de novo* cryptic splice variants in cases compared to controls (1.5-fold in DDD and 1.3-fold in ASD, Figure 5A) is only 38% of the effect size observed for *de novo* protein-truncating variants (2.5-fold in DDD and 1.7-fold in ASD) (Iossifov et al., 2014; McRae et al., 2017; De Rubeis et al., 2014). This allows us to quantify that functional cryptic splice mutations have roughly 50% of the clinical penetrance of classic forms of protein-truncating mutation (stop-gain, frameshift, and essential splice dinucleotide), on account of many of them only partially disrupting production of the normal transcript. Indeed, some of the most well-characterized cryptic splice mutations in Mendelian diseases, such as c.315-48T > C in *FECH* (Gouya et al., 2002) and c.-32-13T > G in *GAA* (Boerkoel et al., 1995), are hypomorphic alleles associated with milder phenotype or later age of onset. The estimate of clinical penetrance is calculated for all *de novo* variants meeting a relatively permissive threshold (Δ score $\geq$0.1), and variants with stronger prediction scores would be expected to have correspondingly higher penetrance.

Based on the excess of *de novo* mutations in cases versus controls across the ASD and DDD cohorts, 250 cases can be explained by *de novo* cryptic splice mutations compared to 909 cases that can be explained by *de novo* protein-truncating variants (Figure 5B). This is consistent with our earlier estimate of the average number of rare cryptic splice mutations ($\sim$5) compared to rare protein-truncating variants ($\sim$11) per person in the general population (Figure 2E), once the reduced penetrance of cryptic splice mutations is factored in. The widespread distribution of cryptic splice mutations across the genome suggests that the fraction of cases explained by cryptic splice mutations in neurodevelopmental disorders (9%–11%, Figure 5B) is likely to generalize to other rare genetic disorders where the primary disease mechanism is loss of the functional protein. To facilitate the interpretation of splice-altering mutations, we precomputed the Δ score predictions for all possible single nucleotide substitutions genome-wide and provide them as a resource to the scientific community. We believe that this resource will promote understanding of this previously under-appreciated source of genetic variation.

DISCUSSION

Despite the limited diagnostic yield of exome sequencing in patients with severe genetic disorders, clinical sequencing has focused on rare coding mutations, largely disregarding variation in the noncoding genome due to the difficulty of interpretation. Here, we introduce a deep learning network that accurately predicts splicing from the primary nucleotide sequence, thereby identifying noncoding mutations that disrupt the normal patterning of exons and introns with severe consequences on the resulting protein. We show that predicted cryptic splice mutations validate at a high rate by RNA-seq, are strongly deleterious in the human population, and are a major cause of rare genetic disease.

By using the deep learning network as an *in silico* model of the spliceosome, we were able to reconstruct the specificity determinants that enable the spliceosome to achieve its remarkable precision *in vivo*. We reaffirm many of the discoveries that were made over the past four decades of research into splicing mechanisms and show that the spliceosome integrates a large number of short- and long-range specificity determinants in its decisions. In particular, we find that the perceived degeneracy of most splice motifs is explained by the presence of long-range determinants such as exon-intron lengths and nucleosome positioning, which more than compensate and render additional specificity at the motif level unnecessary. Our findings demonstrate the promise of deep learning models for providing biological insights, rather than merely serving as black box classifiers.

Deep learning is a relatively new technique in biology and is not without potential trade-offs. By learning to automatically extract features from a sequence, deep learning models can utilize sequence determinants not well described by human experts, but there is also the risk that the model may incorporate features that do not reflect the true behavior of the spliceosome. These irrelevant features could increase the apparent accuracy of predicting annotated exon-intron boundaries but would reduce the accuracy of predicting the splice-altering effects of arbitrary sequence changes induced by genetic variation. Because accurate prediction of variants provides the strongest evidence that the model can generalize to true biology, we provide validation of predicted splice-altering variants using three fully orthogonal methods: RNA-seq, natural selection in human populations, and enrichment of *de novo* variants in case versus control cohorts. While this does not fully preclude the incorporation of irrelevant features into the model, the resulting model appears faithful enough to the true biology of splicing to be of significant value for practical applications such as identifying cryptic splice mutations in patients with genetic diseases.

Compared to other classes of protein-truncating mutations, a particularly interesting aspect of cryptic splice mutations is the widespread phenomenon of alternative splicing due to incompletely penetrant splice-altering variants, which tend to weaken canonical splice sites relative to alternative splice sites, resulting in the production of a mixture of both aberrant and normal transcripts in the RNA-seq data. The observation that these variants frequently drive tissue-specific alternative splicing highlights the unexpected role played by cryptic splice mutations in generating novel alternative splicing diversity. A potential future direction would be to train deep learning models on splice junction annotations from

RNA-seq of the relevant tissue, thereby obtaining tissue-specific models of alternative splicing. Training the network on annotations derived directly from RNA-seq data also helps to fill gaps in the GENCODE annotations, which improves the performance of the model on variant prediction (Figures S3G and S3H).

Our understanding of how mutations in the noncoding genome lead to human disease remains far from complete. The discovery of penetrant *de novo* cryptic splice mutations in childhood neurodevelopmental disorders demonstrates that improved interpretation of the noncoding genome can directly benefit patients with severe genetic disorders. Cryptic splice mutations also play major roles in cancer (Jung et al., 2015; Supek et al., 2014), and recurrent somatic mutations in splice factors have been shown to produce widespread alterations in splicing specificity (Shirai et al., 2015; Yoshida et al., 2011). Much work remains to be done to understand regulation of splicing in different tissues and cellular contexts, particularly in the event of mutations that directly impact proteins in the spliceosome. In light of recent advances in oligonucleotide therapy that could potentially target splicing defects in a sequence-specific manner (Finkel et al., 2017), greater understanding of the regulatory mechanisms that govern this remarkable process could pave the way for novel candidates for therapeutic intervention.

STAR★METHODS

Detailed methods are provided in the online version of this paper and include the following:

- KEY RESOURCES TABLE
- CONTACT FOR REAGENT AND RESOURCE SHARING
- EXPERIMENTAL MODEL AND SUBJECT DETAILS
- METHOD DETAILS
  - Deep learning for splice prediction
  - Analyses on the GTEx RNA-seq dataset
  - Analyses on the ExAC and gnomAD datasets
  - Analyses on the DDD and ASD datasets
- DATA AND SOFTWARE AVAILABILITY

SUPPLEMENTAL INFORMATION

Supplemental Information includes six figures and four tables and can be found with this article online at https://doi.org/10.1016/j.cell.2018.12.015.

ACKNOWLEDGMENTS

We would like to acknowledge J. K. Pritchard for insightful discussions and support, the Genome Aggregation Database (gnomAD), and the groups that provided exome and genome variant data to this resource. S.J.S. was supported by a grant from the Simons Foundation (SFARI #402281 and #574598).

AUTHOR CONTRIBUTIONS

K.J. performed the deep learning and population depletion analyses with assistance from D.K., Y.I.L., H.G., A.K., and S.B. S.K.P. performed the GTEx analysis with assistance from E.K. and W.C. J.F.M. performed the disease analysis with assistance from J.A.K. S.F.D. performed the RNA-seq validation in autism samples with assistance from J.A., G.B.S., E.D.C., and S.J.S. K.K.-H.F. supervised the analyses.

DECLARATION OF INTERESTS

K.J., S.K.P., J.F.M., J.A.K., W.C., E.K., H.G., A.K., S.B., and K.K.-H.F. were employed by Illumina at the time of this study. The following patents related to this work have been filed: Deep Learning-Based Splice Site Classification, Deep Learning-Based Aberrant Splicing Detection, Aberrant Splicing Detection Using Convolutional Neural Networks (CNNS).

Received: March 29, 2018
Revised: August 31, 2018
Accepted: December 10, 2018
Published: January 17, 2019

REFERENCES

Amit, M., Donyo, M., Hollander, D., Goren, A., Kim, E., Gelfman, S., Lev-Maor, G., Burstein, D., Schwartz, S., Postolsky, B., et al. (2012). Differential GC content between exons and introns establishes distinct strategies of splice-site recognition. Cell Rep. *1*, 543–556.

Berget, S.M. (1995). Exon recognition in vertebrate splicing. J. Biol. Chem. *270*, 2411–2414.

Boerkoel, C.F., Exelbert, R., Nicastri, C., Nichols, R.C., Miller, F.W., Plotz, P.H., and Raben, N. (1995). Leaky splicing mutation in the acid maltase gene is associated with delayed onset of glycogenosis type II. Am. J. Hum. Genet. *56*, 887–897.

Boyd, S., Cortes, C., Mohri, M., and Radovanovic, A. (2012). Accuracy at the top. In Advances in Neural Processing Systems, F. Pereira, C.J.C. Burges, L. Bottou, and K.Q. Weinberger, eds. (NIPS), pp. 953–961.

Close, P., East, P., Dirac-Svejstrup, A.B., Hartmann, H., Heron, M., Maslen, S., Chariot, A., Söding, J., Skehel, M., and Svejstrup, J.Q. (2012). DBIRD complex integrates alternative mRNA splicing with RNA polymerase II transcript elongation. Nature *484*, 386–389.

Cooper, T.A., Wan, L., and Dreyfuss, G. (2009). RNA and disease. Cell *136*, 777–793.

Cummings, B.B., Marshall, J.L., Tukiainen, T., Lek, M., Donkervoort, S., Foley, A.R., Bolduc, V., Waddell, L.B., Sandaradura, S.A., O'Grady, G.L., et al. (2017). Improving genetic diagnosis in Mendelian disease with transcriptome sequencing. Sci. Transl. Med. Published online April 19, 2017. https://doi.org/10.1126/scitranslmed.aal5209.

De Rubeis, S., He, X., Goldberg, A.P., Poultney, C.S., Samocha, K., Cicek, A.E., Kou, Y., Liu, L., Fromer, M., Walker, S., et al.; DDD Study; Homozygosity Mapping Collaborative for Autism; UK10K Consortium (2014). Synaptic, transcriptional and chromatin genes disrupted in autism. Nature *515*, 209–215.

Fairbrother, W.G., Yeh, R.F., Sharp, P.A., and Burge, C.B. (2002). Predictive identification of exonic splicing enhancers in human genes. Science *297*, 1007–1013.

Farh, K.K.H., Marson, A., Zhu, J., Kleinewietfeld, M., Housley, W.J., Beik, S., Shoresh, N., Whitton, H., Ryan, R.J.H., Shishkin, A.A., et al. (2015). Genetic and epigenetic fine mapping of causal autoimmune disease variants. Nature *518*, 337–343.

Finkel, R.S., Mercuri, E., Darras, B.T., Connolly, A.M., Kuntz, N.L., Kirschner, J., Chiriboga, C.A., Saito, K., Servais, L., Tizzano, E., et al.; ENDEAR Study Group (2017). Nusinersen versus sham control in infantile-onset spinal muscular atrophy. N. Engl. J. Med. *377*, 1723–1732.

Fitzgerald, T.W., Gerety, S.S., Jones, W.D., van Kogelenberg, M., King, D.A., McRae, J., Morley, K.I., Parthiban, V., Al-Turki, S., Ambridge, K., et al.; Deciphering Developmental Disorders Study (2015). Large-scale discovery of novel genetic causes of developmental disorders. Nature *519*, 223–228.

Gouya, L., Puy, H., Robreau, A.-M., Bourgeois, M., Lamoril, J., Da Silva, V., Grandchamp, B., and Deybach, J.-C. (2002). The penetrance of dominant erythropoietic protoporphyria is modulated by expression of wildtype FECH. Nat. Genet. *30*, 27–28.

Harrow, J., Frankish, A., Gonzalez, J.M., Tapanari, E., Diekhans, M., Kokocinski, F., Aken, B.L., Barrell, D., Zadissa, A., Searle, S., et al. (2012). GENCODE: The reference human genome annotation for The ENCODE Project. Genome Res. *22*, 1760–1774.

He, K., Zhang, X., Ren, S., and Sun, J. (2016). Deep residual learning for image recognition. In Proceedings of the IEEE Conference on Computer Vision and Pattern Recognition (CVPR), L. O'Conner, ed. (IEEE), pp. 770–778.

Iossifov, I., O'Roak, B.J., Sanders, S.J., Ronemus, M., Krumm, N., Levy, D., Stessman, H.A., Witherspoon, K.T., Vives, L., Patterson, K.E., et al. (2014). The contribution of de novo coding mutations to autism spectrum disorder. Nature *515*, 216–221.

Irimia, M., Weatheritt, R.J., Ellis, J.D., Parikshak, N.N., Gonatopoulos-Pournatzis, T., Babor, M., Quesnel-Vallières, M., Tapial, J., Raj, B., O'Hanlon, D., et al. (2014). A highly conserved program of neuronal microexons is misregulated in autistic brains. Cell *159*, 1511–1523.

Jonkers, I., Kwak, H., and Lis, J.T. (2014). Genome-wide dynamics of Pol II elongation and its interplay with promoter proximal pausing, chromatin, and exons. eLife *3*, e02407.

Jung, H., Lee, D., Lee, J., Park, D., Kim, Y.J., Park, W.-Y., Hong, D., Park, P.J., and Lee, E. (2015). Intron retention is a widespread mechanism of tumor-suppressor inactivation. Nat. Genet. *47*, 1242–1248.

Lee, H., Deignan, J.L., Dorrani, N., Strom, S.P., Kantarci, S., Quintero-Rivera, F., Das, K., Toy, T., Harry, B., Yourshaw, M., et al. (2014). Clinical exome sequencing for genetic identification of rare Mendelian disorders. JAMA *312*, 1880–1887.

Lek, M., Karczewski, K.J., Minikel, E.V., Samocha, K.E., Banks, E., Fennell, T., O'Donnell-Luria, A.H., Ware, J.S., Hill, A.J., Cummings, B.B., et al.; Exome Aggregation Consortium (2016). Analysis of protein-coding genetic variation in 60,706 humans. Nature *536*, 285–291.

Li, Y.I., Knowles, D.A., Humphrey, J., Barbeira, A.N., Dickinson, S.P., Im, H.K., and Pritchard, J.K. (2018). Annotation-free quantification of RNA splicing using LeafCutter. Nat. Genet. *50*, 151–158.

Lonsdale, J., Thomas, J., Salvatore, M., Phillips, R., Lo, E., Shad, S., Hasz, R., Walters, G., Garcia, F., Young, N., et al.; GTEx Consortium (2013). The Genotype-Tissue Expression (GTEx) project. Nat. Genet. *45*, 580–585.

Luco, R.F., Pan, Q., Tominaga, K., Blencowe, B.J., Pereira-Smith, O.M., and Misteli, T. (2010). Regulation of alternative splicing by histone modifications. Science *327*, 996–1000.

Maurano, M.T., Humbert, R., Rynes, E., Thurman, R.E., Haugen, E., Wang, H., Reynolds, A.P., Sandstrom, R., Qu, H., Brody, J., et al. (2012). Systematic localization of common disease-associated variation in regulatory DNA. Science *337*, 1190–1195.

McLaren, W., Gil, L., Hunt, S.E., Riat, H.S., Ritchie, G.R.S., Thormann, A., Flicek, P., and Cunningham, F. (2016). The Ensembl variant effect predictor. Genome Biol. *17*, 122.

McRae, J.F., Clayton, S., Fitzgerald, T.W., Kaplanis, J., Prigmore, E., Rajan, D., Sifrim, A., Aitken, S., Akawi, N., Alvi, M., et al.; Deciphering Developmental Disorders Study (2017). Prevalence and architecture of de novo mutations in developmental disorders. Nature *542*, 433–438.

Neale, B.M., Kou, Y., Liu, L., Ma'ayan, A., Samocha, K.E., Sabo, A., Lin, C.-F., Stevens, C., Wang, L.-S., Makarov, V., et al. (2012). Patterns and rates of exonic de novo mutations in autism spectrum disorders. Nature *485*, 242–245.

Pertea, M., Lin, X., and Salzberg, S.L. (2001). GeneSplicer: A new computational method for splice site prediction. Nucleic Acids Res. *29*, 1185–1190.

Reese, M.G., Eeckman, F.H., Kulp, D., and Haussler, D. (1997). Improved splice site detection in Genie. J. Comput. Biol. *4*, 311–323.

Samocha, K.E., Robinson, E.B., Sanders, S.J., Stevens, C., Sabo, A., McGrath, L.M., Kosmicki, J.A., Rehnström, K., Mallick, S., Kirby, A., et al. (2014). A framework for the interpretation of de novo mutation in human disease. Nat. Genet. *46*, 944–950.

Sanders, S.J., Murtha, M.T., Gupta, A.R., Murdoch, J.D., Raubeson, M.J., Willsey, A.J., Ercan-Sencicek, A.G., DiLullo, N.M., Parikshak, N.N., Stein, J.L., et al. (2012). De novo mutations revealed by whole-exome sequencing are strongly associated with autism. Nature *485*, 237–241.

Sanders, S.J., He, X., Willsey, A.J., Ercan-Sencicek, A.G., Samocha, K.E., Cicek, A.E., Murtha, M.T., Bal, V.H., Bishop, S.L., Dong, S., et al.; Autism Sequencing Consortium (2015). Insights into autism spectrum disorder genomic architecture and biology from 71 risk loci. Neuron *87*, 1215–1233.

Schwartz, S., Meshorer, E., and Ast, G. (2009). Chromatin organization marks exon-intron structure. Nat. Struct. Mol. Biol. *16*, 990–995.

Shirai, C.L., Ley, J.N., White, B.S., Kim, S., Tibbitts, J., Shao, J., Ndonwi, M., Wadugu, B., Duncavage, E.J., Okeyo-Owuor, T., et al. (2015). Mutant U2AF1 expression alters hematopoiesis and Pre-mRNA splicing in vivo. Cancer Cell *27*, 631–643.

Soemedi, R., Cygan, K.J., Rhine, C.L., Wang, J., Bulacan, C., Yang, J., Bayrak-Toydemir, P., McDonald, J., and Fairbrother, W.G. (2017). Pathogenic variants that alter protein code often disrupt splicing. Nat. Genet. *49*, 848–855.

Spies, N., Nielsen, C.B., Padgett, R.A., and Burge, C.B. (2009). Biased chromatin signatures around polyadenylation sites and exons. Mol. Cell *36*, 245–254.

Supek, F., Miñana, B., Valcárcel, J., Gabaldón, T., and Lehner, B. (2014). Synonymous mutations frequently act as driver mutations in human cancers. Cell *156*, 1324–1335.

Tan, T.Y., Dillon, O.J., Stark, Z., Schofield, D., Alam, K., Shrestha, R., Chong, B., Phelan, D., Brett, G.R., Creed, E., et al. (2017). Diagnostic impact and cost-effectiveness of whole-exome sequencing for ambulant children with suspected monogenic conditions. JAMA Pediatr. *171*, 855–862.

Tennessen, J.A., Bigham, A.W., O'Connor, T.D., Fu, W., Kenny, E.E., Gravel, S., McGee, S., Do, R., Liu, X., Jun, G., et al. (2012). Evolution and functional impact of rare coding variation from deep sequencing of human exomes. Science *337*, 64–69.

The GTEx Consortium, Welter, D., MacArthur, J., Morales, J., Burdett, T., Hall, P., Junkins, H., Klemm, A., Flicek, P., Manolio, T., et al. (2015). The Genotype-Tissue Expression (GTEx) pilot analysis: Multitissue gene regulation in humans. Science *348*, 648–660.

Turner, T.N., Hormozdiari, F., Duyzend, M.H., McClymont, S.A., Hook, P.W., Iossifov, I., Raja, A., Baker, C., Hoekzema, K., Stessman, H.A., et al. (2016). Genome sequencing of autism-affected families reveals disruption of putative noncoding regulatory DNA. Am. J. Hum. Genet. *98*, 58–74.

Ule, J., Jensen, K.B., Ruggiu, M., Mele, A., Ule, A., and Darnell, R.B. (2003). CLIP identifies Nova-regulated RNA networks in the brain. Science *302*, 1212–1215.

van den Oord, A., Dieleman, S., Zen, H., Simonyan, K., Vinyals, O., Graves, A., Kalchbrenner, N., Senior, A., and Kavukcuoglu, K. (2016). WaveNet: A generative model for raw audio. ArXiv, ArXiv:1609.03499.

Wang, Z., and Burge, C.B. (2008). Splicing regulation: From a parts list of regulatory elements to an integrated splicing code. RNA *14*, 802–813.

Wang, Z., Rolish, M.E., Yeo, G., Tung, V., Mawson, M., and Burge, C.B. (2004). Systematic identification and analysis of exonic splicing silencers. Cell *119*, 831–845.

Wang, E.T., Sandberg, R., Luo, S., Khrebtukova, I., Zhang, L., Mayr, C., Kingsmore, S.F., Schroth, G.P., and Burge, C.B. (2008). Alternative isoform regulation in human tissue transcriptomes. Nature *456*, 470–476.

Wu, J., Anczuków, O., Krainer, A.R., Zhang, M.Q., and Zhang, C. (2013). OLego: Fast and sensitive mapping of spliced mRNA-seq reads using small seeds. Nucleic Acids Res. *41*, 5149–5163.

Xiong, H.Y., Alipanahi, B., Lee, L.J., Bretschneider, H., Merico, D., Yuen, R.K.C., Hua, Y., Gueroussov, S., Najafabadi, H.S., Hughes, T.R., et al. (2015). The human splicing code reveals new insights into the genetic determinants of disease. Science *347*, 1254806.

Yang, Y., Muzny, D.M., Xia, F., Niu, Z., Person, R., Ding, Y., Ward, P., Braxton, A., Wang, M., Buhay, C., et al. (2014). Molecular findings among patients referred for clinical whole-exome sequencing. JAMA *312*, 1870–1879.

Yeo, G., and Burge, C.B. (2004). Maximum entropy modeling of short sequence motifs with applications to RNA splicing signals. J. Comput. Biol. *11*, 377–394.

Yoshida, K., Sanada, M., Shiraishi, Y., Nowak, D., Nagata, Y., Yamamoto, R., Sato, Y., Sato-Otsubo, A., Kon, A., Nagasaki, M., et al. (2011). Frequent pathway mutations of splicing machinery in myelodysplasia. Nature *478*, 64–69.

Article

Cell

Mammalian Near-Infrared Image Vision through Injectable and Self-Powered Retinal Nanoantennae

Yuqian Ma,[1,5] Jin Bao,[1,2,5,*] Yuanwei Zhang,[3,5] Zhanjun Li,[3] Xiangyu Zhou,[1] Changlin Wan,[1] Ling Huang,[3] Yang Zhao,[3] Gang Han,[3,*] and Tian Xue[1,2,4,6,*]

[1]Hefei National Laboratory for Physical Sciences at the Microscale, Neurodegenerative Disorder Research Center, CAS Key Laboratory of Brain Function and Disease, School of Life Sciences, Division of Life Sciences and Medicine, University of Science and Technology of China, Hefei, Anhui 230026, China

[2]Center for Excellence in Brain Science and Intelligence Technology, Chinese Academy of Sciences, Shanghai 200031, China

[3]Department of Biochemistry and Molecular Pharmacology, University of Massachusetts Medical School, Worcester, MA 01605, USA

[4]Institute for Stem Cell and Regeneration, Chinese Academy of Sciences, Beijing 100101, China

[5]These authors contributed equally

[6]Lead Contact

*Correspondence: baojin@ustc.edu.cn (J.B.), gang.han@umassmed.edu (G.H.), xuetian@ustc.edu.cn (T.X.)

https://doi.org/10.1016/j.cell.2019.01.038

SUMMARY

Mammals cannot see light over 700 nm in wavelength. This limitation is due to the physical thermodynamic properties of the photon-detecting opsins. However, the detection of naturally invisible near-infrared (NIR) light is a desirable ability. To break this limitation, we developed ocular injectable photoreceptor-binding upconversion nanoparticles (pbUCNPs). These nanoparticles anchored on retinal photoreceptors as miniature NIR light transducers to create NIR light image vision with negligible side effects. Based on single-photoreceptor recordings, electroretinograms, cortical recordings, and visual behavioral tests, we demonstrated that mice with these nanoantennae could not only perceive NIR light, but also see NIR light patterns. Excitingly, the injected mice were also able to differentiate sophisticated NIR shape patterns. Moreover, the NIR light pattern vision was ambient-daylight compatible and existed in parallel with native daylight vision. This new method will provide unmatched opportunities for a wide variety of emerging bio-integrated nanodevice designs and applications.

INTRODUCTION

Vision is an essential sensory modality for humans. Our visual system detects light between 400 and 700 nm (Dubois, 2009; Wyszecki and Stiles, 1982; Schnapf et al., 1988), so called visible light. In mammalian photoreceptor cells, light absorbing pigments, consisting of opsins and their covalently linked retinals, are known as intrinsic photon detectors. However, the detection of longer wavelength light, such as near-infrared (NIR) light, though a desirable ability, is a formidable challenge for mammals. This is because detecting longer wavelength light, with lower energy photons, requires opsins (e.g., human red cone opsins) to have much lower energy barriers. Consequently, this results in unendurable high thermal noise, thus making NIR visual pigments impractical (Ala-Laurila et al., 2003; Baylor et al., 1980; Luo et al., 2011; St George, 1952). This physical limitation means that no mammalian photoreceptor can effectively detect NIR light that exceeds 700 nm, and mammals are unable to see NIR light and to project a NIR image to the brain.

To this end, the successful integration of nanoparticles with biological systems has accelerated basic scientific discoveries and their translation into biomedical applications (Desai, 2012; Mitragotri et al., 2015). To develop abilities that do not exist naturally, miniature nanoscale devices and sensors designed to intimately interface with mammals including humans are of growing interest. Here, we report on an ocular injectable, self-powered, built-in NIR light nanoantenna that can extend the mammalian visual spectrum to the NIR range. These retinal photoreceptor-binding upconversion nanoparticles (pbUCNPs) act as miniature energy transducers that can transform mammalian invisible NIR light *in vivo* into short wavelength visible emissions (Liu et al., 2017; Wu et al., 2009). As sub-retinal injections are a commonly used ophthalmological practice in animals and humans (Hauswirth et al., 2008; Peng et al., 2017), our pbUCNPs were dissolved in PBS and then injected into the sub-retinal space in the eyes of mice. These nanoparticles were then anchored and bound to the photoreceptors in the mouse retina.

Through *in vivo* electroretinograms (ERGs) and visually evoked potential (VEP) recordings in the visual cortex, we showed that the retina and visual cortex of the pbUCNP-injected mice were both activated by NIR light. From animal behavioral tests, we further demonstrated that the pbUCNP-injected mice acquired NIR light sensation and unique ambient daylight-compatible NIR light image vision. As a result, the built-in NIR nanoantennae allowed the mammalian visual spectrum to extend into the NIR realm effectively without obvious side effects. Excitingly, we found that pbUCNP-injected animals perceived both NIR and visible light patterns simultaneously. They also differentiated between sophisticated NIR light shape patterns (such as triangles

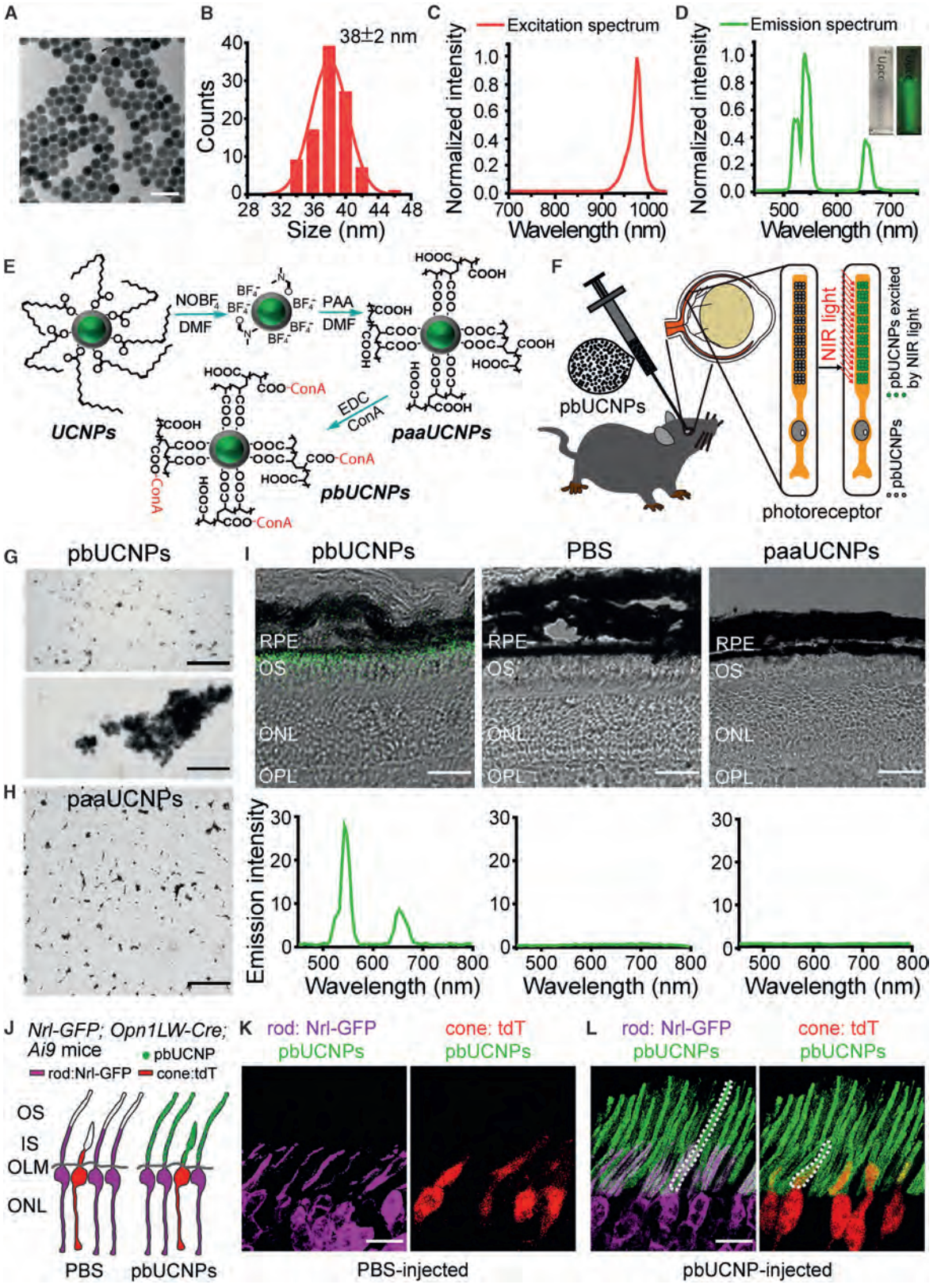

(legend on next page)

and circles). Importantly, this nanoscale device activated the photoreceptors by an exceptionally low power NIR light-emitting diode (LED) light (1.62 mW/cm^2), which was attributed to the proximity between the nanoantennae and photoreceptors in the eye. Moreover, we comprehensively examined the biocompatibility of the pbUCNPs and found negligible side effects.

Therefore, these novel photoreceptor-binding NIR light nanoantennae provide an injectable, self-powered, biocompatible, and NIR-visible light compatible solution to extend the mammalian visual spectrum into the NIR range. This concept-proving research should guide future studies with respect to extending human and non-human vision without the need for any external device or genetic manipulation. Endowing mammals with NIR vision capacity could also pave the way for critical civilian and military applications.

RESULTS

The Design of pbUCNPs

The human eye is most sensitive to visible light at an electromagnetic wavelength of ~550 nm under photopic conditions (Bieber et al., 1995; Boynton, 1996). To convert NIR light to this wavelength, we generated core-shell-structured upconversion nanoparticles (UCNPs) (i.e., 38 ± 2 nm β-$NaYF_4$:20%Yb, 2% Er@β-$NaYF_4$) (Figures 1A and 1B), which exhibited an excitation spectrum peak at 980 nm and emission peak at 535 nm upon 980-nm light irradiation (Mai et al., 2006; Wu et al., 2015) (Figures 1C and 1D). To design water-soluble pbUCNPs, we further conjugated concanavalin A protein (ConA) with poly acrylic acid-coated UCNPs (paaUCNPs) (Figure 1E; STAR Methods). ConA can bind to sugar residue and derivatives of the photoreceptor outer segment, forming glyosidic bonds (Bridges, 1981; Bridges and Fong, 1980; Rutishauser and Sachs, 1975). Successful ConA conjugation on the surface of the UCNPs was suggested by the appearance of N-H bending peaks in the Fourier transform infrared (FT-IR) spectrum (Figure S1A) and by the ~285 nm protein absorption on the ultraviolet-visible spectroscopy (UV/Vis) spectrum (Figure S1B). To confirm the glyosidic bonds between ConA and glycoproteins, we added β-cyclodextrin, which possesses a similar glucosyl unit as that found on the photoreceptor outer segment, to the pbUCNP solution. Characteristic ConA-β-cyclodextrin aggregation thus occurred, as seen in the transmission electron microscope (TEM) images (Figure 1G) and dynamic light scattering (DLS) spectrum (Figure S1C). This result suggests that the pbUCNPs can bind to glycoproteins on the photoreceptor outer segment. In contrast, the paaUCNPs without ConA remained monodispersed when β-cyclodextrin was added (Figures 1H and S1D). After injecting these pbUCNPs into the mouse sub-retinal spaces (Figures 1F and S1E), we observed that, through the glyosidic bond, these pbUCNPs self-anchored and remained tightly bound to the inner and outer segments of both rods and cones (Figures 1J–1L) forming a layer of built-in nanoantennae with the characteristic upconversion spectrum (Figures 1I, left, S1F, and S1G). In contrast, the injected paaUCNPs were loosely bound and easily removed from the photoreceptors with gentle washing (Figure 1I, right).

We then evaluated the biocompatibility and potential side effects of the pbUCNPs *in vivo*. We found that the pbUCNP injection did not cause a higher rate of adverse reactions compared with the control PBS injection. All common minor or transient side effects (e.g., cataracts, corneal opacity) generally associated with sub-retinal injection (Qi et al., 2015; Zhao et al., 2011) disappeared completely 2 weeks after the injections (Table S1). In addition, we evaluated possible retinal degeneration by counting the number of photoreceptors in the retinal outer nuclear layer (ONL), a standard and widely used method in the field of retinal research, as photoreceptors are sensitive and prone to degenerate upon stress (Chen et al., 2006; Namekata et al., 2013; Wang et al., 2013). As a result, we observed that the retinal layer structure and the number of photoreceptor layers in the retinal ONL were not changed, even with 50 μg of pbUCNPs injected into each eye, up to 2 months after the injections (Figures 2A and 2B). This result clearly suggested that there was no obvious retinal degeneration using this standard measure.

Figure 1. Characterzations of pbUCNPs

(A) Transmission electron microscopy (TEM) image of UCNPs (as-synthesized core-shell-structured β-$NaYF_4$:20%Yb, 2%Er@β-$NaYF_4$). Scale bar, 100 nm.

(B) Corresponding size distribution of UCNPs.

(C) Excitation spectrum of UCNPs measured as emission light intensity at 535 nm by 700–1,040 nm excitation.

(D) Emission spectrum of UCNPs upon 980-nm continuous wave (CW) laser irradiation. Inset displays photographs of UCNP solutions with (right) and without (left) 980-nm CW laser excitation.

(E) Schematic illustration of surface modification procedures for ConA-functionalized photoreceptor-binding UCNPs (pbUCNPs).

(F) Left: illustration of sub-retinal injection of pbUCNPs in mice. See also Figure S1. Right: illustration of pbUCNPs binding to the outer segments of photoreceptors and generation of green light upon near-infrared (NIR) light illumination.

(G) TEM images of pbUCNPs before (top) and after (bottom) addition of 200 nM β-cyclodextrin showing characteristic aggregation of pbUCNPs in the presence of β-cyclodextrin. See also Figure S1. Scale bar, 2 μm.

(H) TEM images of UCNPs without ConA-conjugation (paaUCNPs) mixed with 200 nM β-cyclodextrin, showing no obvious aggregation. See also Figure S1. Scale bar, 2 μm.

(I) Top: overlays of transmission and luminescence optical images (green: 980-nm excitation/535-nm emission) of retinal slices from pbUCNP-injected, PBS-injected, and paaUCNP-injected mice. Bottom: emission spectrum recorded from retinal outer segment layers (OS) upon 980-nm light excitation. All retinal slices were washed with PBS during fixation. Only pbUCNPs remained bound to the photoreceptor outer segments. RPE, retinal pigment epithelium; OS, outer segment of photoreceptors; ONL, outer nuclear layer; OPL, outer plexiform layer. Scale bar, 30 μm.

(J) Schematic illustration of distribution of pbUCNPs (green) in the retina. Rods are labeled with Nrl-GFP in pseudo color violet. Cones are labeled with Opn1LW-Cre; Ai9-lsl-tdTomato in pseudo color red. OS, outer segment of photoreceptors; IS, inner segment of photoreceptors; OLM, outer limiting membrane; ONL, outer nuclear layer.

(K and L) Overlaid green (pbUCNPs)/violet (rods) and green (pbUCNPs)/red (cones) channel fluorescence images of retina from PBS-injected mice (K) and pbUCNP-injected mice (L). Examples of continuous inner and outer segments of a rod and a cone are shown in dashed contour lines. Scale bars, 10 μm.

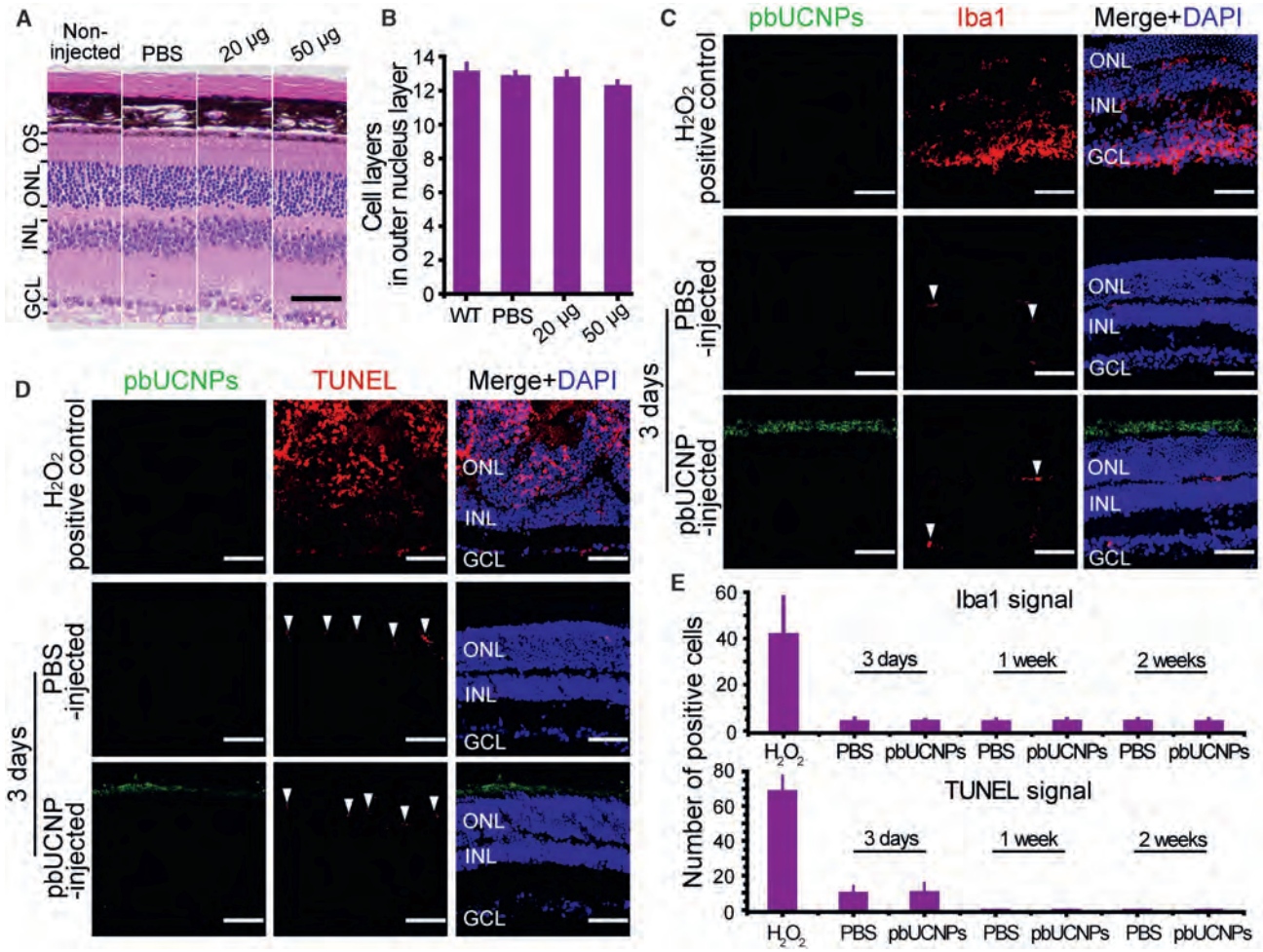

Figure 2. Biocompatibility of pbUCNPs

(A) H&E staining of retinal slices from non-injected, PBS-injected, 20 μg/eye and 50 μg/eye pbUCNP-injected mice. OS, outer segment of photoreceptors; ONL, outer nuclear layer; INL, inner nuclear layer; GCL, ganglion cell layer. Scale bar, 50 μm.

(B) Number of cell layers in outer nuclear layer (ONL) of retinae. Data are mean ± SD (n = 4 retinae).

(C) Microglia marker Iba1 staining of retinal slices 3 days after injection. H_2O_2-injected mice (positive control) showed strong activation of microglia. Few basal Iba1 signals were observed in the pbUCNP-injected retina, similar to that observed in PBS-injected retina (indicated by arrow heads). Red, Iba1; green, pbUCNP emission upon excitation by NIR light; blue, DAPI (4′,6-diamidino-2-phenylindole) signal indicating cell nuclei. Scale bar, 50 μm.

(D) Apoptosis detection by TUNEL staining 3 days after injection. Strong TUNEL signals were observed in the H_2O_2-injected mouse retinae (positive control), but few were observed in PBS-injected or pbUCNP-injected mice (indicated by arrow heads). Red, TUNEL staining; green, pbUCNP emission upon excitation by NIR light; blue, DAPI. Scale bar, 50 μm.

(E) Number of Iba1 and TUNEL stained cells per 0.04 mm^2 averaged from four retinae for each condition. See also Figure S2. Data are mean ± SD (n = 4 retinae). See also Table S1.

Moreover, we examined potential inflammation in the retinal through microglia marker Iba1 staining that is a widely used indicator of microglia accumulation (Krady et al., 2005). From this, we observed negligible retinal inflammation at 3 days or 1, 2, 4, and 10 weeks after pbUCNP injection (Figures 2C, 2E, and S2A). We further examined retinal cell apoptosis after injection via terminal deoxynucleotidyl transferase deoxyuridine triphosphate (dUTP) nick-end labeling (TUNEL). We only found sparse TUNEL signals 3 days after injection in both the PBS and pbUCNP-injected retinae (Figure 2D), with the TUNEL signals being undetectable 1, 2, 4, and 10 weeks after pbUCNP injection (Figures 2E and S2B). These results suggest that the pbUCNP injection did not cause obvious acute or long-term side effects. In addition, the excitation and emission spectra of the pbUCNPs in either fixed or fresh retinae were in good agreement with those measured from pbUCNP solution, indicating that binding with the photoreceptors did not change the characteristics of the pbUCNPs (Figures S2C and S2D).

NIR Light-Mediated Photoreceptor Activation

Based on the biocompatibility noted above, we tested if the photoreceptors could be activated by NIR light with the help of pbUCNPs. We performed single rod suction pipette recordings on acutely dissected retinae from pbUCNP-injected and

non-injected mice (Figure 3A). The action spectra of rods from pbUCNP-injected and non-injected mice were identical in the visible light range, with differences only appearing after 900 nm, where the action spectra of rods from pbUCNP-injected mice matched the excitation spectra of pbUCNPs (Figure S3A). The rods from pbUCNP-injected mice had normal visible light (535 nm)-elicited photocurrents compared with that of non-injected mice (Figures 3B and 3D). The 980-nm light flash elicited rod photocurrents from pbUCNP-injected mice (Figure 3E), whereas the rods from non-injected mice exhibited no responses (Figure 3C). The amplitude and kinetics of the 980-nm light-elicited photocurrents were identical to those activated by 535-nm visible light (Figures 3F–3H). The similar time-to-peak values suggest that, compared to the visible light stimulation, there was no delay in the activation of the rods by NIR light. Furthermore, the pbUCNPs did not alter the light adaptation or dark noise characteristics of the rods, and rods adapted to visible and NIR light in the same manner following the Weber-Fechner relationship (Baylor et al., 1980; Morshedian et al., 2018; Fu et al., 2008) (Figure S4). To determine whether the pbUCNPs can serve as NIR nanosensors *in vivo*, we recorded the population response of photoreceptors activated by light via ERGs (Dalke et al., 2004) (Figure 3I). Upon 980-nm NIR light illumination to the eye, the ERG from pbUCNP-injected mice resembled that of visible light-induced responses, whereas no such signal could be detected from the non-injected control mice. Furthermore, we performed ERG recordings on pbUCNP-injected rod-functionless mice (*Gnat1*$^{-/-}$) and demonstrated that, through the pbUCNPs, 980-nm NIR light indeed activated cones *in vivo* (Figure S3B).

NIR Light Sensation of pbUCNP-Injected Mice

To reveal whether pbUCNP-injected mice could see NIR light, we first performed pupillary light reflex (PLR) experiments (Xue et al., 2011). The pupils of the pbUCNP-injected mice showed strong constrictions upon 980-nm light illumination, whereas the non-injected control mice did not exhibit PLR with the same NIR illumination (Figure 4A). Moreover, we discovered that the PLR of the pbUCNP-injected mice was two orders of magnitude more sensitive to NIR light than that of the non-photoreceptor-binding paaUCNP-injected mice (Figure 4B). This was attributed to the proximity between the pbUCNPs and the bound photoreceptors. Photon upconversion was measured (Figure S5A) and showed a non-linear light intensity relationship plotted at the log-log scale (Figure S5B). We fitted the power relationship between emitted 535-nm light and 980-nm excitation light and determined the power to be 1.6. Interestingly, we found that this non-linearity was also shown in the NIR light-induced behavior. The light dose-response curves of the PLR (normalized pupil area versus light intensity) were fitted to the Hill function. The NIR light-induced PLR dose-response curve was steeper than that of visible light, and the Hill coefficients for the NIR and visible light PLR dose-responses were 1.10 and 0.78, respectively (Figure S5C). To obtain the theoretical NIR light PLR dose-response curve, the fitted upconversion function was applied to the visible light PLR dose-response Hill function. This theoretical NIR light PLR dose-response curve agreed well with the experimental NIR light PLR response (Figure S5C). Therefore, the non-linearity shown in the NIR light-induced behavior was attributed to the non-linearity of the upconversion process.

In addition to the above sub-conscious light sensation PLR behavior, we also explored whether pbUCNP-injected mice could consciously perceive NIR light. In this regard, we performed light-dark box experiments with visible and NIR light (Figures 4C and 4D) as well as light-induced fear-conditioning experiments (Figures 4E and 4F). In the conventional light-dark box experiments with visible light, mice instinctively preferred the dark box to the light box illuminated with visible light. In our study, we replaced conventionally used visible light with 980-nm LED light, which delivered 8.1×10^7 photons $\times\ \mu m^{-2} \times s^{-1}$ at the center of the light box, equal to a power density of 1.62 mW/cm^2. The pbUCNP-injected mice exhibited a significant preference for the dark box, whereas the non-injected control mice could not distinguish between the NIR light (980 nm)-illuminated and dark boxes (Figure 4D; Video S1). This suggests that mice with injected nanoantennae perceived NIR light and exhibited innate light-sensing behavior. To exclude the possibility of any visible light emission from the NIR LEDs, the emission spectra of the 980-nm LEDs were measured and no light emission below 900 nm was detected (Figures S5D and S5E).

We then tested whether such NIR light perception can serve as a visual cue for learned behavior. Mice were trained to pair a 20-s 535-nm light pulse to a 2-s foot shock (Figure 4E) in order to acquire a conditioned freezing behavior. After acquisition of such conditioning, mice received either NIR light at 980 nm or visible light at 535 nm as conditional stimuli (CS) in the test trials. The pbUCNP-injected mice showed significant freezing behavior in response to both wavelengths, whereas the non-injected control mice exhibited freezing behavior only to visible light stimuli (Figure 4F; Video S2). These results clearly demonstrated that mice acquired NIR light sensation and were able to "see" NIR light with our ocular injectable photoreceptor targeting nanoantennae.

NIR Light-Activated Imaging Visual Pathway of pbUCNP-Injected Mice

In addition to the NIR light sensation, we were curious whether pbUCNP-injected mice had acquired NIR light image visual ability. In general, visual image perception is associated with activation of the visual cortex. In order to record visually evoked potential (VEPs), we placed recording electrodes in six different locations of the visual cortex (No. 1, 2, 3, and 5 in the monocular areas and No. 4 and 6 in the binocular areas) during contralateral eye illumination (Cooke et al., 2015; Smith and Trachtenberg, 2007) (Figure 5A). When the visible 535-nm light pulse was applied, VEPs were detected at all locations in both the non-injected controls and pbUCNP-injected mice (Figures 5B and 5D). In contrast, under 980-nm NIR light illumination, no VEPs were observed in the control mice, but were detected from the binocular visual cortical areas in pbUCNP-injected mice (Figures 5C and 5E). This is topologically consistent with the pbUCNP injection site (temporal side, binocular projection area) in the retina.

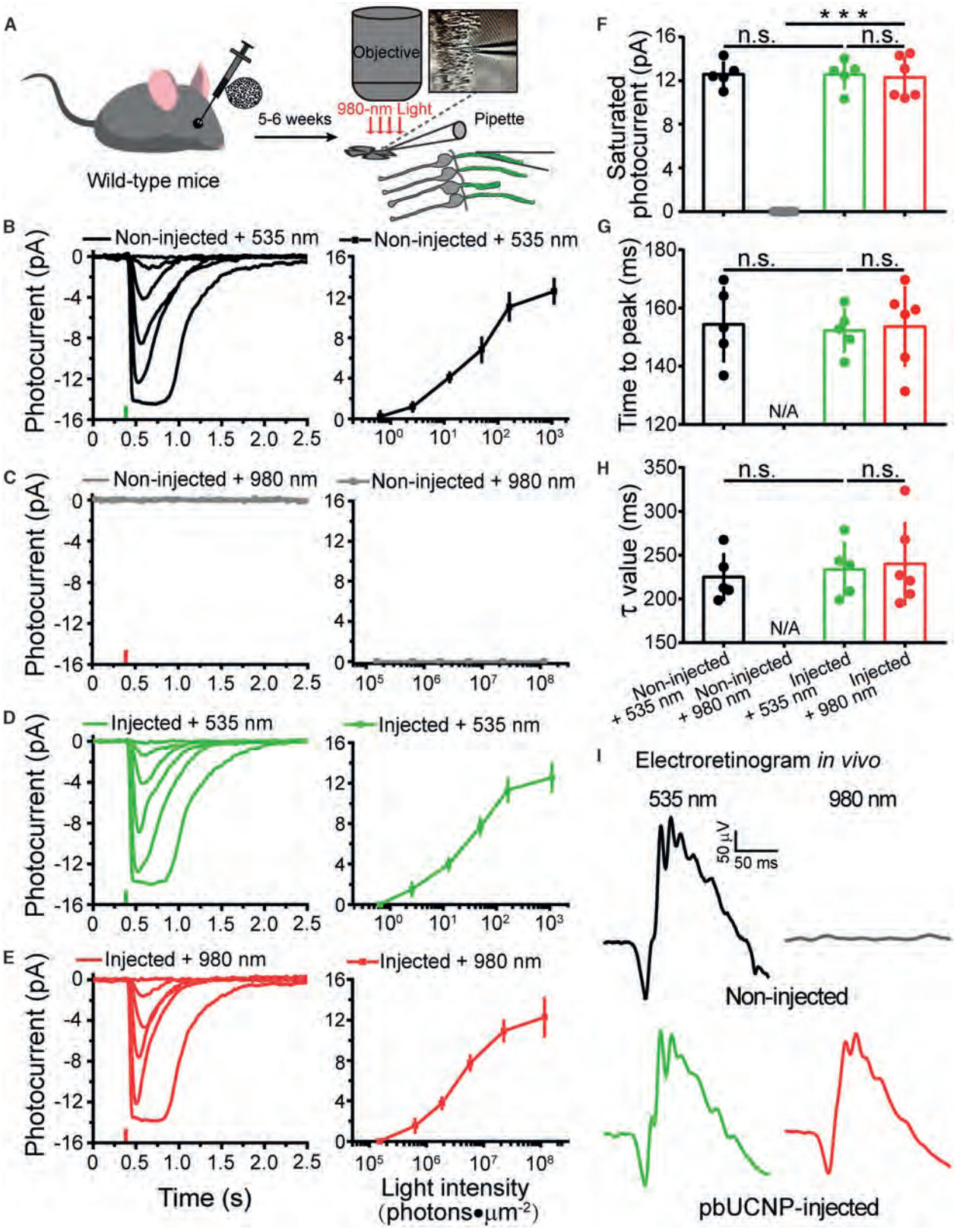

(legend on next page)

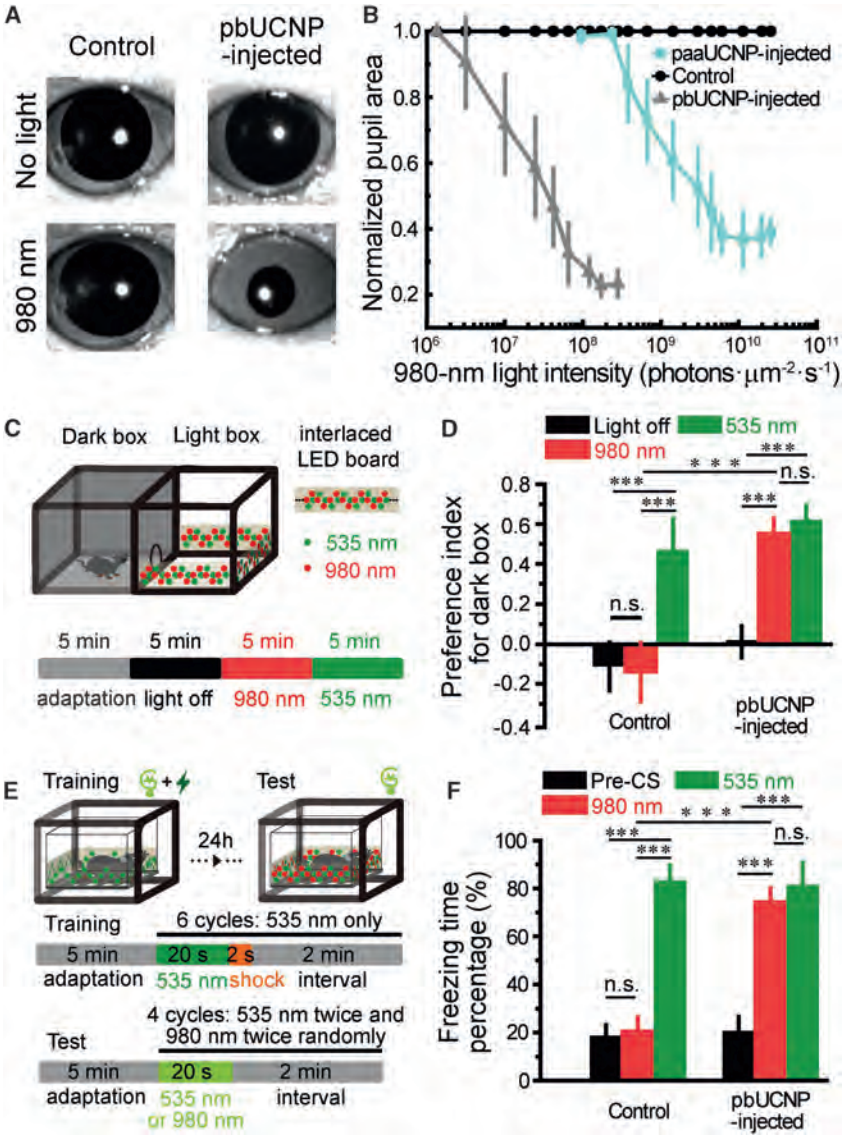

Figure 4. NIR Light Sensation of pbUCNP-Injected Mice

(A) Images showing pupil constriction from non-injected control and pbUCNP-injected mice under 980-nm light stimulation (40 s). Intensity of 980-nm light: 1.21 × 10^8 photons × μm^{-2} × s^{-1}.

(B) Dose-response curves of normalized pupil constriction with 980-nm light stimulation (paaUCNP-injected mice, n = 4; pbUCNP-injected mice, n = 5; control mice, n = 4; data are mean ± SD).

(C) Light-dark box experiment diagram. Light box was illuminated with an array of LED lights interlaced by 980-nm and 535-nm LEDs. Illumination protocol is shown at the bottom. Each section contained four episodes and each episode was 5 min long. The first 5-min episode was adaptation in the light-dark box with ambient light followed by a 5-min episode in complete darkness. The 980-nm and 535-nm LEDs were then lit consecutively for the light box for 5 min each.

(D) Preference index for dark box under three different light box conditions (light off, 980 nm, and 535 nm). Preference index = (time spent in dark box − in light box) / (time spent in dark box + in light box). Intensities of the 980-nm and 535-nm lights at the center of the box were 8.1 × 10^7 and 9.1 × 10^2 photons × μm^{-2} × s^{-1}, respectively (Control: n = 5, pbUCNP-injected: n = 6; data are mean ± SD, two-sided t test, ***p < 0.001; n.s., not significant).

(E) Fear-conditioning experiment diagram and protocol. A 535-nm light pulse was paired with a foot-shock to form conditioning during training. Tests were then carried out 24 h later with a 980-nm or 535-nm light pulse alone.

(F) Percentages of freezing time during 20 s "Pre-CS," 980-nm, and 535-nm light stimulation ("Pre-CS": before conditional stimulation, a 20-s period of adaptation right before light stimulation onset). Intensities of the 980-nm and 535-nm lights at the center of the box were 1.07 × 10^8 and 1.47 × 10^3 photons × μm^{-2} × s^{-1}, respectively. Data are mean ± SD (control: n = 6, pbUCNP-injected: n = 7; two-sided t test; n.s., not significant; ***p < 0.001).

See also Figure S5 and Videos S1 and S2.

NIR Light Pattern Vision

We next examined whether mice obtained NIR light pattern vision. Accordingly, Y-shaped water maze behavioral experiments were conducted to determine whether mice could discriminate between different light patterns (Prusky et al., 2000) (Figure 6A). The mice were trained to find a hidden platform that was associated with one of two patterns. We designed five different tasks to examine their NIR pattern vision ability

Figure 3. NIR Light-Mediated Photoreceptor Activation through pbUCNPs

(A) Illustration of rod outer segment suction pipette recordings from freshly isolated retinae. Stimulation light was either 980-nm or 535-nm through the imaging objective.

(B–E) Photocurrents and intensity-response curves of rods from non-injected mice with 535-nm (B) (n = 5) or 980-nm (C) (n = 6) light stimulations and pbUCNP-injected mice with 535-nm (D) (n = 5) or 980-nm (E) (n = 6) light stimulations. Tiny colored vertical bars on the x axis indicate time of light flashes. Photocurrent traces were averaged from 5–7 sweeps. Intensity-response data are mean ± SD.

(F) Saturated photocurrent in (B)–(E).

(G) Time-to-peak, time from light stimulation to peak amplitude of dim light photocurrents in (B)–(E).

(H) Decay time constant of dim light photocurrent in (B)–(E). Data are mean ± SD; n.s., not significant; ***p < 0.001.

(I) Electroretinograms (ERGs) recorded from mice under 535-nm or 980-nm light stimulation. No response was observed in non-injected control mice under 980-nm light stimulation (gray). Light intensities: 535 nm, 8.26 × 10^3 photons × μm^{-2}; 980 nm, 9.83 × 10^8 photons × μm^{-2}.

See also Figures S3 and S4.

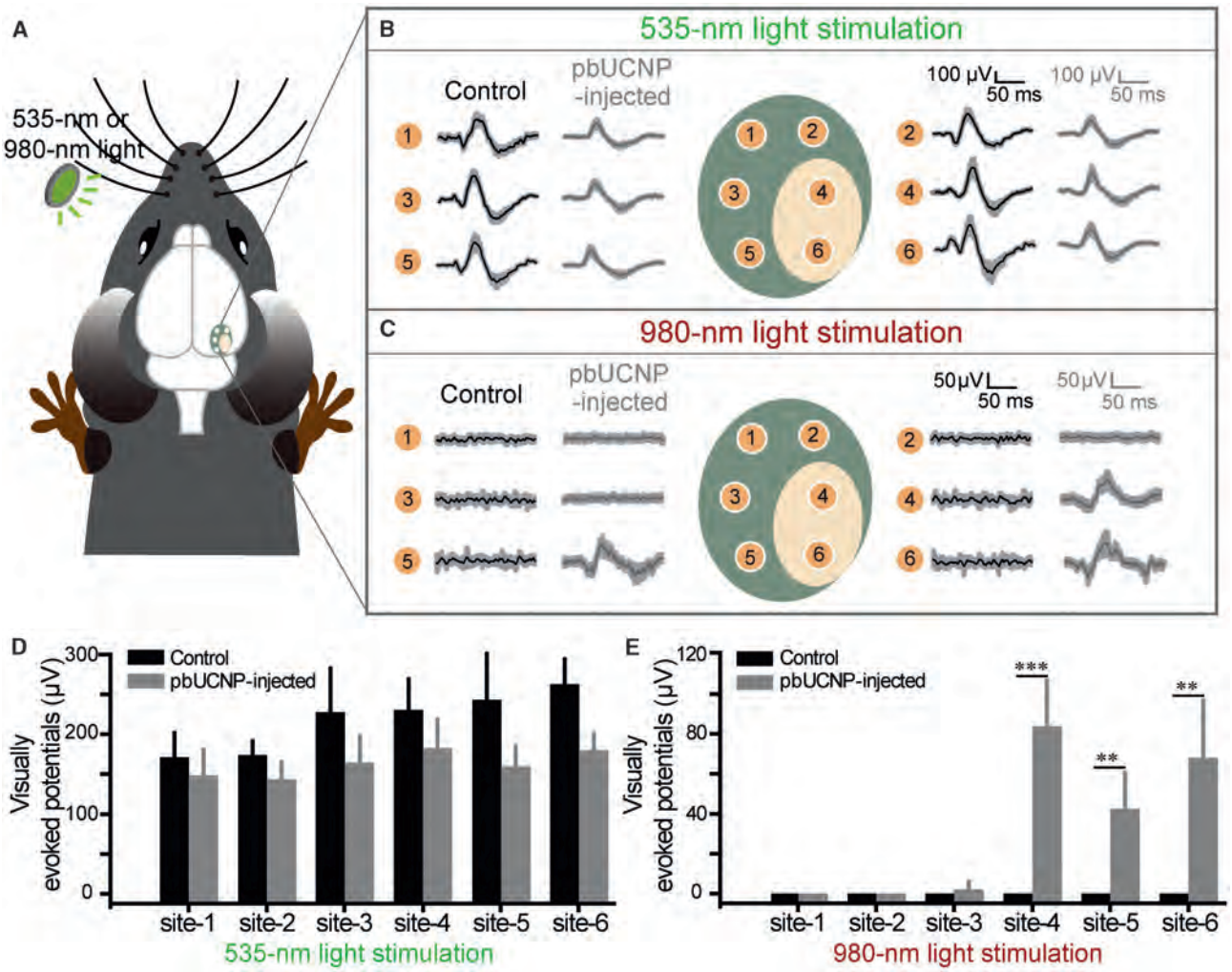

Figure 5. NIR Light Activated the Imaging Visual Pathway of pbUCNP-Injected Mice

(A) Diagram of six recording sites for visually evoked potentials (VEPs) in the mouse visual cortex.

(B and C) VEPs of non-injected control (black traces) and pbUCNP-injected mice (gray traces) under 535-nm (B) and 980-nm (C) light illumination. Intensities of the 535-nm and 980-nm lights were 3.37×10^3 and 7.07×10^8 photons $\times$ $\mu m^{-2} \times s^{-1}$, respectively. Recording sites 1, 2, 3, and 5 were monocular areas; 4 and 6 were binocular areas. Traces were averaged from six sweeps and presented as mean ± SD (shaded area).

(D and E) Peak VEPs triggered by 535-nm (D) or 980-nm (E) light at each recording site (mean ± SD, n = 4 for both, two-sided t test, $^{**}p < 0.01$, $^{***}p < 0.001$).

regarding different pattern stimuli and various background light conditions. Task 1 used light gratings as pattern stimuli (Figures 6B and S6A). After training with 980-nm light gratings, the pbUCNP-injected mice were able to discriminate between the two orientations (vertical or horizontal) of the NIR light gratings, whereas the non-injected control mice made such choices in a random manner (Figure 6C; Video S3). In the parallel control testing, when the mice were trained and tested with visible light gratings, both the pbUCNP-injected and non-injected mice were able to find the associated platform (Figures 6C, S6B, and S6C). We then measured the spatial resolution of the NIR image perception. The pbUCNP-injected mice detected the visible light gratings with a maximum spatial frequency of 0.31 ± 0.04 cycles/degree, which did not significantly differ from that of the non-injected control mice (0.35 ± 0.02 cycles/degree). This indicates that the sub-retinal injection of pbUCNPs did not interfere with visible light vision. With respect to NIR light gratings, the pbUCNP-injected mice detected a maximum of 0.14 ± 0.06 cycles/degree. This decrease in spatial resolution in NIR light vision may be due to the isotropic radiation and scattering of the *in situ* transduced visible light from the NIR light-excited pbUCNPs (Figures 6D and S6D).

In addition, to confirm if visible light background interfered with the NIR light pattern perception, we designed Task 2 using two LED boards with visible (535 nm) and NIR (980 nm) LED arrays arranged in a perpendicular manner on each board. These two boards appeared identical under an ambient visible light background when all LEDs (visible and NIR) were turned off. The orientations for the 535-nm and 980-nm LED stripes between the two boards were 90° rotated respectively (Figure 6E).

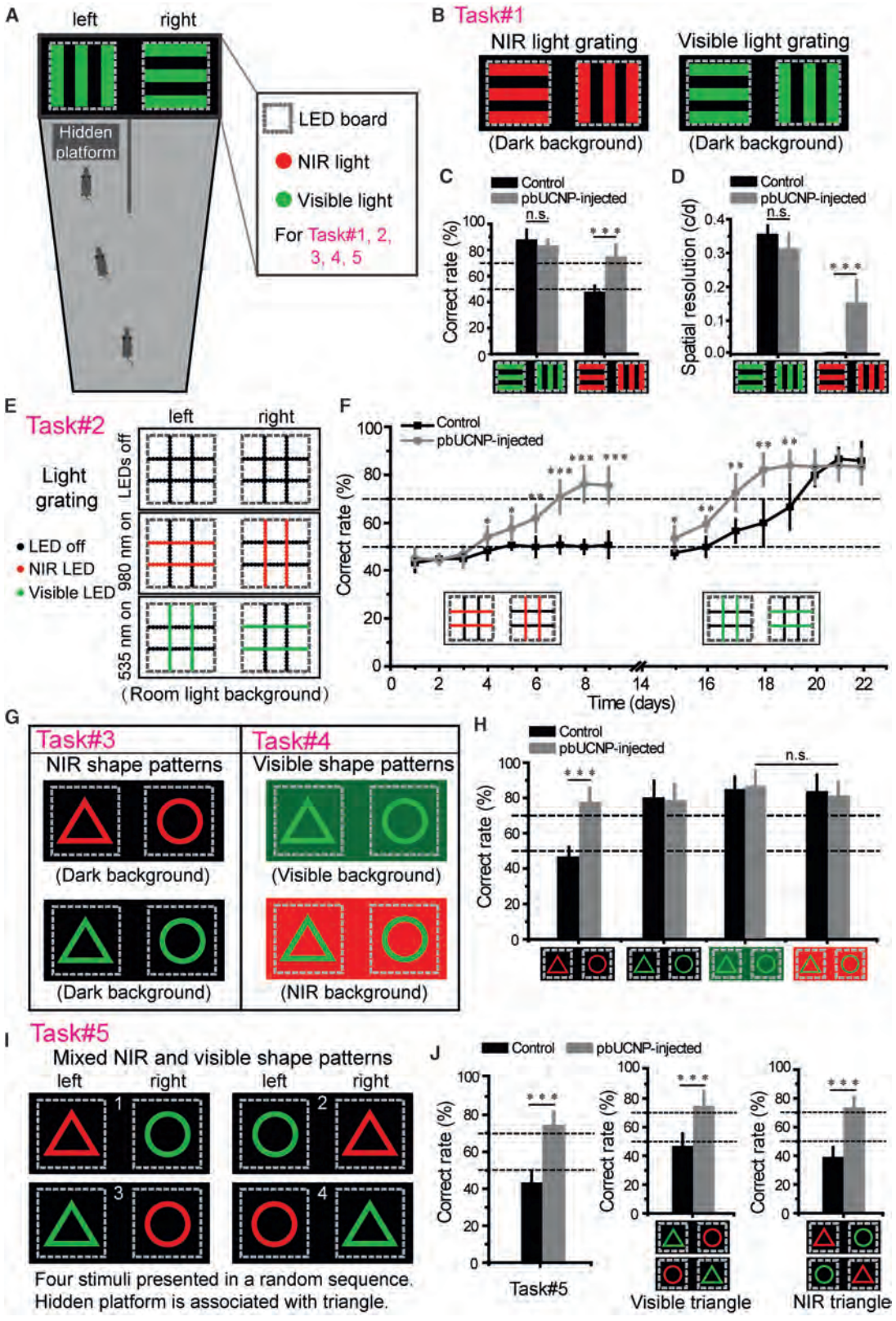

(legend on next page)

Trainings were carried out under visible room light (196 lux) and with only the 980-nm LEDs on. In the tests, only pbUCNP-injected mice learnt to locate the platform (Figure 6F), indicating that NIR light pattern vision persisted in the visible light-illuminated environment. Interestingly, we subsequently tested these mice with the 535-nm LEDs on and 980-nm LEDs off. Both pbUCNP-injected and control mice could discriminate the visible light gratings, again indicating that pbUCNP injection did not affect normal visible light vision. Additionally, pbUCNP-injected mice could discriminate the visible light gratings from the beginning of the test, suggesting that pbUCNP-injected mice were able to implement the rule learnt from the NIR light pattern to visible light pattern discrimination, indicating that NIR light patterns did not differ perceptually from visible light patterns for pbUCNP-injected mice (Figure 6F; Video S4).

To test more sophisticated pattern vision, we further prompted animals to discriminate triangular and circular patterns in Task 3 (Figure 6G). We found that pbUCNP-injected mice were able to discriminate NIR and visible light patterns in the dark environment, whereas non-injected control mice could only detect the visible light pattern (Figures 6H, S6E, and S6F; Video S5), indicating that pbUCNP-injected mice could perceive sophisticated NIR light patterns. We subsequently speculated whether background NIR light would interfere with the visible light pattern vision of pbUCNP-injected mice. Thus, in Task 4, mice were tested to discriminate between visible light triangles and circles under a visible or NIR light background (Figure 6G). Same as control mice, the pbUCNP-injected mice did not behave differently regarding their ability to discriminate visible light patterns under dark, visible, or NIR light backgrounds (Figures 6H and S6F–S6H; Video S5). These results clearly suggest that background NIR light does not interfere with visible light pattern perception.

Task 5 was designed to test whether pbUCNP-injected mice could see NIR and visible light patterns simultaneously. In general, saturation by visible light is a common problem for conventionally used tools, such as optoelectronic night vision devices or IR cameras, as it prevents smooth detection between visible and NIR light objects. To test if our built-in NIR light vision could overcome this problem and coexist with visible light vision, we designed the following experiments. Mice were first trained in a Y-shaped water maze with visible light triangles and circles to learn that the platform was associated with triangles only. During the test trials, we presented one visible (535 nm) and one NIR (980 nm) light in a triangular-circular pattern at the left-right ends of the water maze, shuffled in a random sequence (Figure 6I). Only the pbUCNP-injected mice were able to discriminate between the two patterns with different shapes and wavelengths (Figures 6J, left, and S6I). To exclude the possibility that mice simply used either visible or NIR light patterns to guide decision-making rather than seeing them simultaneously, we calculated the correct choice rates separately for the visible and NIR light triangle patterns. In the subset of stimuli where the triangular patterns was in visible light (Figure 6J, middle), control mice selected both sides randomly, indicating they did not simply use the visible triangle to make decisions. When the circular pattern was in visible light, control mice still picked the side randomly, indicating that the mice did not use the strategy of avoiding circles to make decisions (Figure 6J, right). In contrast, pbUCNP-injected mice made correct choices in both cases (Video S5), suggesting they used visible and NIR light patterns together to guide behavior. These results clearly indicate that the built-in nanoantennae enabled mice to see visible and NIR light patterns simultaneously.

DISCUSSION

In this study, we demonstrated the successful application of UCNPs as ocular injectable NIR light transducers, which extended mammalian vision into the NIR realm. These implanted nanoantennae were proven to be biocompatible and did not interfere with normal visible light vision. Importantly, animals were able to detect NIR and visible light images simultaneously.

Extension of the Visual Spectrum into the NIR Range

One way to obtain NIR light vision is to implement new machinery for NIR photon transduction, such as the thermal detection of snakes (Gracheva et al., 2010). However, a more plausible method to achieve such NIR photon detection is the use of the endogenous visual system. The method we developed here utilized the very first step of the visual image perception process through photoreceptor outer-segment binding NIR nanoantennae. The NIR light image was projected to the retina through the optical part of the eyes, cornea, and lens, after which the pbUCNPs upconverted NIR light into visible light and then activated the bound photoreceptors. Subsequently, the retinal

Figure 6. NIR Light Pattern Vision of pbUCNP-Injected Mice

(A) Diagram of Y-shaped water maze for Tasks 1–5.

(B) Stimuli of Task 1. Experiments were under dark background. See also Figure S6.

(C) Correct rates of Task 1 for light grating discrimination (pbUCNP-injected mice: n = 7; non-injected control mice: n = 6).

(D) Visual spatial resolutions of pbUCNP-injected and control mice for 535-nm and 980-nm light gratings.

(E) Diagram of visual stimuli in Task 2. Light grating stimulations were LED arrays with ambient room light as background.

(F) Correct rates of Task 2 with respect to discrimination of 980-nm (days 1–9) and 535-nm (days 15–22) light LED gratings under room light background (pbUCNP-injected mice: n = 7 and control mice: n = 5).

(G) Visual stimuli of Tasks 3 and 4. Triangular and circular patterns were made of LEDs and presented at the end of the water maze.

(H) Correct rates of Tasks 3 and 4 in discriminating triangular and circular patterns under dark, visible light, or NIR light background (pbUCNP-injected: n = 5 and control: n = 6).

(I) Diagram of four stimuli in Task 5. Four stimuli were mixed and shuffled randomly in position.

(J) Correct rates of Task 5 in discriminating NIR and visible light shape patterns simultaneously (left), with triangular pattern in visible light (middle) and in NIR light (right) (pbUCNP-injected: n = 5 and Control: n = 6). All data are mean ± SD (two-sided t test, $^{**}p < 0.01$, $^{***}p < 0.001$; n.s., not significant).

See also Videos S3, S4, and S5.

circuit and cortical visual system generated perception of the NIR image. It is important to note that these injected nanoantennae did not interfere with natural visible light vision. The ability to simultaneously detect visible and NIR light patterns suggests enhanced mammalian visual performance by extending the native visual spectrum without genetic modification and avoiding the need for bulky external devices. This approach offers several advantages over the currently used optoelectronic devices, such as no need for any external energy supply, and is compatible with other human activities.

Improved Efficiency through ConA Modification of UCNPs

Regarding the practical applications of UCNPs, higher visual sensitivity and resolution are desirable. We modified the UCNPs and generated photoreceptor-binding nanoparticles to increase the proximity between the nanoparticles and photoreceptors. Thus, sensitivity to NIR light with respect to generating light-induced behaviors was improved by two orders of magnitude. Therefore, it is now possible to use biocompatible low-power NIR LEDs to elicit visual behavior in animals, rather than the more invasive high-power NIR lasers inevitably used in conventional UCNP biomedical applications (Chen et al., 2018; He et al., 2015). In the Y-shaped water maze experiment, we estimated that the 980-nm LED light was transduced to 535-nm light by the pbUCNPs at 293 photons × μm^{-2} × s^{-1} intensity at the retina. The rod and cone-mediated visual behavior thresholds of mice are 0.012 and 200 photons × μm^{-2} × s^{-1} at the cornea, respectively (Sampath et al., 2005), equal to 0.003 and 50 photons × μm^{-2} × s^{-1} at the retina (Do et al., 2009). Therefore, in our system, the 293 photons × μm^{-2} × s^{-1} at the retina was adequate to activate both rod and cone photoreceptors, and in practice, this NIR visual system was able to detect NIR light that was of several magnitudes lower intensity than currently applied. Compared to rods, cones encode several orders of magnitude higher intensity light and are more important for human high acuity vision. Thus, pbUCNP-bound cones may mediate high-resolution NIR image pattern vision. Retinae also possess intrinsic photosensitive retinal ganglion cells (ipRGCs), which mediate non-image forming visual functions, such as photoentrainment of the circadian rhythm (Do and Yau, 2010). Under the intensity used in our behavioral experiment, NIR light did not activate ipRGCs (Figure S5F), which was likely due to the longer distance of ipRGCs to pbUCNPs and their low sensitivity (Do et al., 2009). With respect to NIR image spatial resolution, pbUCNP-injected mice had good NIR eye sight (0.14 ± 0.06 cycles/degree, half of the visible image resolution), allowing them to see sophisticated NIR light patterns.

Biocompatible NIR Nanoantennae

Sub-retinal injection in humans is a common practice in ophthalmological treatment (Hauswirth et al., 2008; Peng et al., 2017). The implantation of microscale sub-retinal devices is a potential method of repairing vision following retinal photoreceptor degeneration, though current devices can lead to biocompatibility issues, such as retinal detachment, fibrosis, and inflammation (Zrenner, 2013). Yet, this did not occur in our system, as the intimate contact between the pbUCNPs and photoreceptors did not cause any separation between the photoreceptors and retinal pigment epithelium, the latter of which is the supporting layer for photoreceptors. As a result, neither inflammation nor apoptosis occurred, which is in line with that of another reported retinal application of rare earth nanoparticles (Chen et al., 2006). The stability and compatibility of the pbUCNPs were also demonstrated by successful detection of NIR light images, even after 10 weeks without any repeated injections.

Further Development of pbUCNPs

In the present study, we created NIR light vision while overcoming several key drawbacks that yet exist in currently used man-made systems. It may also be possible to design NIR color vision through multicolor NIR light-sensitive UCNPs that have multiple NIR light absorption peak wavelengths and corresponding multicolor visible light emissions. Further applications using our strategy for visual repair and enhancement could also be achieved by similar nanoparticles with tailored light absorptions. In addition, combined with a drug delivery system, these photoreceptor-binding nanoparticles could be modified to release small molecules locally upon light stimulation.

In summary, these nanoparticles not only provide the potential for close integration within the human body to extend the visual spectrum, but also open new opportunities to explore a wide variety of animal vision-related behaviors. Furthermore, they exhibit considerable potential with respect to the development of bio-integrated nanodevices in civilian encryption, security, military operations, and human-machine interfaces, which require NIR light image detection that goes beyond the normal functions of mammals, including human beings. Moreover, in addition to visual ability enhancement, this nanodevice can serve as an integrated and light-controlled system in medicine, which could be useful in the repair of visual function as well as in drug delivery for ocular diseases.

STAR★METHODS

Detailed methods are provided in the online version of this paper and include the following:

- KEY RESOURCES TABLE
- CONTACT FOR REAGENT AND RESOURCE SHARING
- EXPERIMENTAL MODEL AND SUBJECT DETAILS
  - Mice
- METHOD DETAILS
  - Synthesis of pbUCNPs
  - Sub-retinal injection
  - Distribution and spectrum analysis
  - Retinal histology
  - TUNEL Apoptosis detection
  - Microglia staining
  - Single cell electrophysiology
  - Electroretinography
  - Pupillary light reflex
  - Light-dark box
  - Light induced fear conditioning
  - Visually evoked potential
  - Y shaped water maze

- QUANTIFICATION AND STATISTICAL ANALYSIS
  - Imaging quantifications
  - Statistics
  - Fitting procedures

SUPPLEMENTAL INFORMATION

Supplemental Information can be found with this article online at https://doi.org/10.1016/j.cell.2019.01.038.

A video abstract is available at https://doi.org/10.1016/j.cell.2019.01.038#mmc7.

ACKNOWLEDGMENTS

We thank members of the Neuroscience Pioneer Club for valuable discussions. We thank Drs. Dangsheng Li and Zilong Qiu for reading this manuscript and providing helpful comments. We thank Dr. Yang Xiang from University of Massachusetts Medical School for helpful discussion. We thank Min Wei and Shouzhen Li for helpful discussions and Jiawei Shen and Dr. Huan Zhao for helping illustration drawing and videos clipping. We thank Dr. Kai Huang and Mr. Nuo Yu for helping characterizing nanoparticles. We thank Dr. Qiuping Wang and Xiaokang Ding from National Synchrotron Radiation Laboratory for helping with the measurement of various spectra of light sources. We thank Dr. Yuen Wu and Xing Wang from School of Chemistry and Materials Science (USTC) for helping with the measurement of the absorption spectrum of pbUCNPs. We acknowledge support from the National Key Research and Development Program of China (2016YFA0400900), the Strategic Priority Research Program of the Chinese Academy of Science (XDA16020603, XDPB10, XDB02010000), the National Young Scientists 973 Program of China (2013CB967700), the National Natural Science Foundation of China (81790644, 61890953, 31322024, 81371066, 91432104, 31571073, 81401025, 61727811, 91748212), the NIH (R01MH103133 to G.H.), a UMass OTCV award, a Worcester Foundation Mel Cutler Award to G.H., and the Human Frontier Science Program (RGY-0090/2014).

AUTHOR CONTRIBUTIONS

Conceptualization, T.X. and G.H.; Methodology, Y.M., J.B., G.H., and T.X.; Investigation, Y.M., J.B., Y. Zhang, Z.L., L.H., Y. Zhao, X.Z., C.W., G.H., and T.X.; Validation, J.B., G.H., and T.X.; Formal Analysis, Y.M. and J.B.; Writing – Original Draft, J.B., Y.M., Y. Zhang, G.H., and T.X.; Writing – Review & Editing, J.B., Y.M., G.H., and T.X.; Funding Acquisition, J.B., G.H., and T.X.; Supervision, J.B., G.H., and T.X.

DECLARATION OF INTERESTS

T.X. and G.H. have a patent application related to this work.

Received: June 6, 2018
Revised: November 9, 2018
Accepted: January 24, 2019
Published: February 28, 2019

REFERENCES

Ala-Laurila, P., Albert, R.J., Saarinen, P., Koskelainen, A., and Donner, K. (2003). The thermal contribution to photoactivation in A2 visual pigments studied by temperature effects on spectral properties. Vis. Neurosci. *20*, 411–419.

Baylor, D.A., Matthews, G., and Yau, K.W. (1980). Two components of electrical dark noise in toad retinal rod outer segments. J. Physiol. *309*, 591–621.

Bieber, M.L., Volbrecht, V.J., and Werner, J.S. (1995). Spectral efficiency measured by heterochromatic flicker photometry is similar in human infants and adults. Vision Res. *35*, 1385–1392.

Bourin, M., and Hascoët, M. (2003). The mouse light/dark box test. Eur. J. Pharmacol. *463*, 55–65.

Boynton, R.M. (1996). Frederic Ives Medal paper. History and current status of a physiologically based system of photometry and colorimetry. J. Opt. Soc. Am. A Opt. Image Sci. Vis. *13*, 1609–1621.

Bridges, C.D.B. (1981). Lectin receptors of rods and cones. Visualization by fluorescent label. Invest. Ophthalmol. Vis. Sci. *20*, 8–16.

Bridges, C.D.B., and Fong, S.L. (1980). Lectin receptors on rod and cone membranes. Photochem. Photobiol. *32*, 481–486.

Burstyn-Cohen, T., Lew, E.D., Través, P.G., Burrola, P.G., Hash, J.C., and Lemke, G. (2012). Genetic dissection of TAM receptor-ligand interaction in retinal pigment epithelial cell phagocytosis. Neuron *76*, 1123–1132.

Calvert, P.D., Krasnoperova, N.V., Lyubarsky, A.L., Isayama, T., Nicoló, M., Kosaras, B., Wong, G., Gannon, K.S., Margolskee, R.F., Sidman, R.L., et al. (2000). Phototransduction in transgenic mice after targeted deletion of the rod transducin alpha -subunit. Proc. Natl. Acad. Sci. USA *97*, 13913–13918.

Chen, J., Patil, S., Seal, S., and McGinnis, J.F. (2006). Rare earth nanoparticles prevent retinal degeneration induced by intracellular peroxides. Nat. Nanotechnol. *1*, 142–150.

Chen, S., Weitemier, A.Z., Zeng, X., He, L., Wang, X., Tao, Y., Huang, A.J.Y., Hashimotodani, Y., Kano, M., Iwasaki, H., et al. (2018). Near-infrared deep brain stimulation via upconversion nanoparticle-mediated optogenetics. Science *359*, 679–684.

Cooke, S.F., and Bear, M.F. (2013). How the mechanisms of long-term synaptic potentiation and depression serve experience-dependent plasticity in primary visual cortex. Philos. Trans. R. Soc. Lond. B Biol. Sci. *369*, 20130284.

Cooke, S.F., Komorowski, R.W., Kaplan, E.S., Gavornik, J.P., and Bear, M.F. (2015). Erratum: Visual recognition memory, manifested as long-term habituation, requires synaptic plasticity in V1. Nat. Neurosci. *18*, 926.

Cui, Z.Z., Feng, R.B., Jacobs, S., Duan, Y.H., Wang, H.M., Cao, X.H., and Tsien, J.Z. (2013). Increased NR2A: NR2B ratio compresses long-term depression range and constrains long-term memory. Sci. Rep. *3*, 1036.

Dalke, C., Löster, J., Fuchs, H., Gailus-Durner, V., Soewarto, D., Favor, J., Neuhäuser-Klaus, A., Pretsch, W., Gekeler, F., Shinoda, K., et al. (2004). Electroretinography as a screening method for mutations causing retinal dysfunction in mice. Invest. Ophthalmol. Vis. Sci. *45*, 601–609.

Desai, N. (2012). Challenges in development of nanoparticle-based therapeutics. AAPS J. *14*, 282–295.

Do, M.T.H., and Yau, K.W. (2010). Intrinsically photosensitive retinal ganglion cells. Physiol. Rev. *90*, 1547–1581.

Do, M.T., Kang, S.H., Xue, T., Zhong, H., Liao, H.W., Bergles, D.E., and Yau, K.W. (2009). Photon capture and signalling by melanopsin retinal ganglion cells. Nature *457*, 281–287.

Dong, A., Ye, X., Chen, J., Kang, Y., Gordon, T., Kikkawa, J.M., and Murray, C.B. (2011). A generalized ligand-exchange strategy enabling sequential surface functionalization of colloidal nanocrystals. J. Am. Chem. Soc. *133*, 998–1006.

Dubois, E. (2009). The Structure and Properties of Color Spaces and the Representation of Color Images (Morgan & Claypool Publishers).

Fu, Y., Kefalov, V., Luo, D.G., Xue, T., and Yau, K.W. (2008). Quantal noise from human red cone pigment. Nat. Neurosci. *11*, 565–571.

Govardovskii, V.I., Fyhrquist, N., Reuter, T., Kuzmin, D.G., and Donner, K. (2000). In search of the visual pigment template. Vis. Neurosci. *17*, 509–528.

Gracheva, E.O., Ingolia, N.T., Kelly, Y.M., Cordero-Morales, J.F., Hollopeter, G., Chesler, A.T., Sánchez, E.E., Perez, J.C., Weissman, J.S., and Julius, D. (2010). Molecular basis of infrared detection by snakes. Nature *464*, 1006–1011.

Hauswirth, W.W., Aleman, T.S., Kaushal, S., Cideciyan, A.V., Schwartz, S.B., Wang, L., Conlon, T.J., Boye, S.L., Flotte, T.R., Byrne, B.J., and Jacobson, S.G. (2008). Treatment of leber congenital amaurosis due to RPE65 mutations by ocular subretinal injection of adeno-associated virus gene vector: short-term results of a phase I trial. Hum. Gene Ther. *19*, 979–990.

He, S., Krippes, K., Ritz, S., Chen, Z., Best, A., Butt, H.J., Mailänder, V., and Wu, S. (2015). Ultralow-intensity near-infrared light induces drug delivery by upconverting nanoparticles. Chem. Commun. (Camb.) *51*, 431–434.

Karnas, D., Hicks, D., Mordel, J., Pévet, P., and Meissl, H. (2013). Intrinsic photosensitive retinal ganglion cells in the diurnal rodent, Arvicanthis ansorgei. PLoS ONE *8*, e73343.

Krady, J.K., Basu, A., Allen, C.M., Xu, Y., LaNoue, K.F., Gardner, T.W., and Levison, S.W. (2005). Minocycline reduces proinflammatory cytokine expression, microglial activation, and caspase-3 activation in a rodent model of diabetic retinopathy. Diabetes *54*, 1559–1565.

Le, Y.Z., Ash, J.D., Al-Ubaidi, M.R., Chen, Y., Ma, J.X., and Anderson, R.E. (2004). Targeted expression of Cre recombinase to cone photoreceptors in transgenic mice. Mol. Vis. *10*, 1011–1018.

Liu, Y., Lu, Y., Yang, X., Zheng, X., Wen, S., Wang, F., Vidal, X., Zhao, J., Liu, D., Zhou, Z., et al. (2017). Amplified stimulated emission in upconversion nanoparticles for super-resolution nanoscopy. Nature *543*, 229–233.

Luo, D.G., Yue, W.W.S., Ala-Laurila, P., and Yau, K.W. (2011). Activation of visual pigments by light and heat. Science *332*, 1307–1312.

Mai, H.X., Zhang, Y.W., Si, R., Yan, Z.G., Sun, L.D., You, L.P., and Yan, C.H. (2006). High-quality sodium rare-earth fluoride nanocrystals: controlled synthesis and optical properties. J. Am. Chem. Soc. *128*, 6426–6436.

Mitragotri, S., Anderson, D.G., Chen, X., Chow, E.K., Ho, D., Kabanov, A.V., Karp, J.M., Kataoka, K., Mirkin, C.A., Petrosko, S.H., et al. (2015). Accelerating the translation of nanomaterials in biomedicine. ACS Nano *9*, 6644–6654.

Morshedian, A., Woodruff, M.L., and Fain, G.L. (2018). Role of recoverin in rod photoreceptor light adaptation. J Physiol *596*, 1513–1526.

Namekata, K., Kimura, A., Kawamura, K., Guo, X., Harada, C., Tanaka, K., and Harada, T. (2013). Dock3 attenuates neural cell death due to NMDA neurotoxicity and oxidative stress in a mouse model of normal tension glaucoma. Cell Death Differ. *20*, 1250–1256.

Peng, Y., Tang, L., and Zhou, Y. (2017). Subretinal injection: a review on the novel route of therapeutic delivery for vitreoretinal diseases. Ophthalmic Res. *58*, 217–226.

Pittler, S.J., and Baehr, W. (1991). Identification of a nonsense mutation in the rod photoreceptor cGMP phosphodiesterase beta-subunit gene of the rd mouse. Proc. Natl. Acad. Sci. USA *88*, 8322–8326.

Prusky, G.T., West, P.W.R., and Douglas, R.M. (2000). Behavioral assessment of visual acuity in mice and rats. Vision Res. *40*, 2201–2209.

Qi, Y., Dai, X., Zhang, H., He, Y., Zhang, Y., Han, J., Zhu, P., Zhang, Y., Zheng, Q., Li, X., et al. (2015). Trans-corneal subretinal injection in mice and its effect on the function and morphology of the retina. PLoS ONE *10*, e0136523.

Roberts, J.E. (1961). Lanthanum and neodymium salts of trifluoroacetic acid. J. Am. Chem. Soc. *83*, 1087–1088.

Rutishauser, U., and Sachs, L. (1975). Cell-to-cell binding induced by different lectins. J. Cell Biol. *65*, 247–257.

Sampath, A.P., Strissel, K.J., Elias, R., Arshavsky, V.Y., McGinnis, J.F., Chen, J., Kawamura, S., Rieke, F., and Hurley, J.B. (2005). Recoverin improves rod-mediated vision by enhancing signal transmission in the mouse retina. Neuron *46*, 413–420.

Schmidt, T.M., and Kofuji, P. (2010). Differential cone pathway influence on intrinsically photosensitive retinal ganglion cell subtypes. J. Neurosci. *30*, 16262–16271.

Schnapf, J.L., Kraft, T.W., Nunn, B.J., and Baylor, D.A. (1988). Spectral sensitivity of primate photoreceptors. Vis. Neurosci. *1*, 255–261.

Smith, S.L., and Trachtenberg, J.T. (2007). Experience-dependent binocular competition in the visual cortex begins at eye opening. Nat. Neurosci. *10*, 370–375.

Soucy, E., Wang, Y., Nirenberg, S., Nathans, J., and Meister, M. (1998). A novel signaling pathway from rod photoreceptors to ganglion cells in mammalian retina. Neuron *21*, 481–493.

St George, R.C.C. (1952). The interplay o light and heat in bleaching rhodopsin. J. Gen. Physiol. *35*, 495–517.

Wang, D., Li, Y., Wang, Z., Sun, G.Y., and Zhang, Q.H. (2013). Nimodipine rescues N-methyl-N-nitrosourea-induced retinal degeneration in rats. Pharmacogn. Mag. *9*, 149–154.

Wu, S., Han, G., Milliron, D.J., Aloni, S., Altoe, V., Talapin, D.V., Cohen, B.E., and Schuck, P.J. (2009). Non-blinking and photostable upconverted luminescence from single lanthanide-doped nanocrystals. Proc. Natl. Acad. Sci. USA *106*, 10917–10921.

Wu, X., Chen, G., Shen, J., Li, Z., Zhang, Y., and Han, G. (2015). Upconversion nanoparticles: a versatile solution to multiscale biological imaging. Bioconjug. Chem. *26*, 166–175.

Wyszecki, G., and Stiles, W.S. (1982). Color Science: Concepts and Methods, Quantitative Data and Formulae, Second edition (John Wiley and Sons).

Xue, T., Do, M.T.H., Riccio, A., Jiang, Z., Hsieh, J., Wang, H.C., Merbs, S.L., Welsbie, D.S., Yoshioka, T., Weissgerber, P., et al. (2011). Melanopsin signalling in mammalian iris and retina. Nature *479*, 67–73.

Zhao, L., Ma, W., Fariss, R.N., and Wong, W.T. (2011). Minocycline attenuates photoreceptor degeneration in a mouse model of subretinal hemorrhage microglial: inhibition as a potential therapeutic strategy. Am. J. Pathol. *179*, 1265–1277.

Zrenner, E. (2013). Fighting blindness with microelectronics. Sci. Transl. Med. *5*, 210ps16.

Cell

Article

Transcription Factors Activate Genes through the Phase-Separation Capacity of Their Activation Domains

Ann Boija,[1,7] Isaac A. Klein,[1,2,7] Benjamin R. Sabari,[1] Alessandra Dall'Agnese,[1] Eliot L. Coffey,[1,3] Alicia V. Zamudio,[1,3] Charles H. Li,[1,3] Krishna Shrinivas,[4,5] John C. Manteiga,[1,3] Nancy M. Hannett,[1] Brian J. Abraham,[1] Lena K. Afeyan,[1,3] Yang E. Guo,[1] Jenna K. Rimel,[6] Charli B. Fant,[6] Jurian Schuijers,[1] Tong Ihn Lee,[1] Dylan J. Taatjes,[6,8] and Richard A. Young[1,3,8,9,*]

[1]Whitehead Institute for Biomedical Research, Cambridge, MA 02142, USA
[2]Department of Medical Oncology, Dana-Farber Cancer Institute, Harvard Medical School, Boston, MA 02215, USA
[3]Department of Biology, Massachusetts Institute of Technology, Cambridge, MA 02139, USA
[4]Department of Chemical Engineering, Massachusetts Institute of Technology, Cambridge, MA 02139, USA
[5]Institute of Medical Engineering and Science, Massachusetts Institute of Technology, Cambridge, MA 02139, USA
[6]Department of Biochemistry, University of Colorado, Boulder, CO 80303, USA
[7]These authors contributed equally
[8]Senior author
[9]Lead Contact
*Correspondence: young@wi.mit.edu
https://doi.org/10.1016/j.cell.2018.10.042

SUMMARY

Gene expression is controlled by transcription factors (TFs) that consist of DNA-binding domains (DBDs) and activation domains (ADs). The DBDs have been well characterized, but little is known about the mechanisms by which ADs effect gene activation. Here, we report that diverse ADs form phase-separated condensates with the Mediator coactivator. For the OCT4 and GCN4 TFs, we show that the ability to form phase-separated droplets with Mediator *in vitro* and the ability to activate genes *in vivo* are dependent on the same amino acid residues. For the estrogen receptor (ER), a ligand-dependent activator, we show that estrogen enhances phase separation with Mediator, again linking phase separation with gene activation. These results suggest that diverse TFs can interact with Mediator through the phase-separating capacity of their ADs and that formation of condensates with Mediator is involved in gene activation.

INTRODUCTION

Regulation of gene expression requires that the transcription apparatus be efficiently assembled at specific genomic sites. DNA-binding transcription factors (TFs) ensure this specificity by occupying specific DNA sequences at enhancers and promoter-proximal elements. TFs typically consist of one or more DNA-binding domains (DBDs) and one or more separate activation domains (ADs) (Brent and Ptashne, 1985; Keegan et al., 1986). While the structure and function of TF DBDs are well documented, comparatively little is understood about the structure of ADs and how these interact with coactivators to drive gene expression.

The structure of TF DBDs and their interaction with cognate DNA sequences has been described at atomic resolution for many TFs, and TFs are generally classified according to the structural features of their DBDs (Fulton et al., 2009; Vaquerizas et al., 2009). For example, DBDs can be composed of zinc-coordinating, basic helix-loop-helix, basic-leucine zipper, or helix-turn-helix DNA-binding structures. These DBDs selectively bind specific DNA sequences that range from 4 to 12 bp, and the DNA binding sequences favored by hundreds of TFs have been described (Hume et al., 2015; Jolma et al., 2013; Khan et al., 2018). Multiple TF molecules typically bind together at any one enhancer or promoter-proximal element. For example, at least eight different TF molecules bind a 50-bp core component of the interferon (IFN)-β enhancer (Panne et al., 2007).

Anchored in place by the DBD, the AD interacts with coactivators, which integrate signals from multiple TFs to regulate transcriptional output (Allen and Taatjes, 2015; Juven-Gershon and Kadonaga, 2010; Malik and Roeder, 2010; Plaschka et al., 2016; Reiter et al., 2017; Soutourina, 2018; Taatjes, 2010). In contrast to the structured DBD, the ADs of most TFs are low-complexity amino acid sequences not amenable to crystallography. These intrinsically disordered regions (IDRs) have therefore been classified by their amino acid profile as acidic, proline, serine/threonine, or glutamine rich or by their hypothetical shape as acid blobs, negative noodles, or peptide lassos (Mitchell and Tjian, 1989; Roberts, 2000; Sigler, 1988; Staby et al., 2017; Triezenberg, 1995). Remarkably, hundreds of TFs are thought to interact with the same small set of coactivator complexes, which include Mediator and p300 (Allen and Taatjes, 2015; Avantaggiati et al., 1996; Dai and Markham, 2001; Eckner et al., 1996; Green, 2005; Merika et al., 1998; Oliner et al., 1996; Yin and Wang, 2014; Yuan et al., 1996). ADs that share little

sequence homology are functionally interchangeable among TFs (Godowski et al., 1988; Hope and Struhl, 1986; Jin et al., 2016; Lech et al., 1988; Ransone et al., 1990; Sadowski et al., 1988; Struhl, 1988; Tora et al., 1989); this interchangeability is not readily explained by traditional lock-and-key models of protein-protein interaction. Thus, how the diverse ADs of hundreds of different TFs interact with a similar small set of coactivators remains a conundrum.

Recent studies have shown that the AD of the yeast TF GCN4 binds to the Mediator subunit MED15 at multiple sites and in multiple orientations and conformations (Brzovic et al., 2011; Jedidi et al., 2010; Tuttle et al., 2018; Warfield et al., 2014). The products of this type of protein-protein interaction, where the interaction interface cannot be described by a single conformation, have been termed ''fuzzy complexes'' (Tompa and Fuxreiter, 2008). These dynamic interactions are also typical of the IDR-IDR interactions that facilitate formation of phase-separated biomolecular condensates (Alberti, 2017; Banani et al., 2017; Hyman et al., 2014; Shin and Brangwynne, 2017; Wheeler and Hyman, 2018).

We recently proposed that transcriptional control may be driven by the formation of phase-separated condensates (Hnisz et al., 2017) and demonstrated that the coactivator proteins MED1 and BRD4 form phase-separated condensates at super-enhancers (SEs) (Sabari et al., 2018). Here, we report that diverse TF ADs phase separate with the Mediator coactivator. We show that the embryonic stem cell (ESC) pluripotency TF OCT4, the estrogen receptor (ER), and the yeast TF GCN4 form phase-separated condensates with Mediator and require the same amino acids or ligands for both activation and phase separation. We propose that IDR-mediated phase separation with coactivators is a mechanism by which TF ADs activate genes.

RESULTS

Mediator Condensates at ESC SEs Depend on OCT4

OCT4 is a master TF essential for the pluripotent state of ESCs and is a defining TF at ESC SEs (Whyte et al., 2013). The Mediator coactivator, which forms condensates at ESC SEs (Sabari et al., 2018), is thought to interact with OCT4 via the MED1 subunit (Table S1) (Apostolou et al., 2013). If OCT4 contributes to the formation of Mediator condensates, then OCT4 puncta should be present at the SEs where MED1 puncta have been observed. Indeed, immunofluorescence (IF) microscopy with concurrent nascent RNA fluorescence in situ hybridization (FISH) revealed discrete OCT4 puncta at the SEs of the key pluripotency genes *Esrrb*, *Nanog*, *Trim28*, and *Mir290* (Figure 1). Average image analysis confirmed that OCT4 IF was enriched at center of RNA FISH foci. This enrichment was not seen using a randomly selected nuclear position (Figure S1). These results confirm that OCT4 occurs in puncta at the same SEs where Mediator forms condensates (Sabari et al., 2018) and where chromatin immunoprecipitation sequencing (ChIP-seq) shows co-occupancy of OCT4 and MED1 (Figure 1).

We investigated whether the Mediator condensates present at SEs are dependent on OCT4 using a degradation strategy (Nabet et al., 2018). Degradation of OCT4 in an ESC line bearing endogenous knockin of DNA encoding the FKBP protein fused to OCT4 was induced by addition of dTag for 24 hr (Weintraub et al., 2017) (Figures 2A and S2A). Induction of OCT4 degradation reduced OCT4 protein levels but did not affect MED1 levels (Figure S2B). ChIP-seq analysis showed a reduction of OCT4 and MED1 occupancy at enhancers, with the most profound effects occurring at SEs, as compared to typical enhancers (TEs) (Figure 2B). RNA sequencing (RNA-seq) revealed that expression of SE-driven genes was concomitantly decreased (Figure 2B). For example, OCT4 and MED1 occupancy was reduced by approximately 90% at the *Nanog* SE (Figure 2C), associated with a 60% reduction in *Nanog* mRNA levels (Figure 2D). IF microscopy with concurrent DNA FISH showed that OCT4 degradation caused a reduction in MED1 condensates at *Nanog* (Figures 2E and S2C). These results indicate that the presence of Mediator condensates at an ESC SE is dependent on OCT4.

ESC differentiation causes a loss of OCT4 binding at certain ESC SEs, which leads to a loss of these OCT4-dependent SEs, and thus should cause a loss of Mediator condensates at these sites. To test this idea, we differentiated ESCs by leukemia inhibitory factor (LIF) withdrawal. In the differentiated cell population, we observed reduced OCT4 and MED1 occupancy at the *Mir290* SE (Figures 2F, 2G, and S2D) and reduced levels of *Mir290* miRNA (Figure 2H), despite continued expression of MED1 protein (Figure S2E). Correspondingly, MED1 condensates were reduced at *Mir290* (Figures 2I and S2F) in the differentiated cell population. These results are consistent with those obtained with the OCT4 degron experiment and support the idea that Mediator condensates at these ESC SEs are dependent on occupancy of the enhancer elements by OCT4.

OCT4 Is Incorporated into MED1 Liquid Droplets

OCT4 has two intrinsically disordered ADs responsible for gene activation, which flank a structured DBD (Figure 3A) (Brehm et al., 1997). Since IDRs are capable of forming dynamic networks of weak interactions, and the purified IDRs of proteins involved in condensate formation can form phase-separated droplets (Burke et al., 2015; Lin et al., 2015; Nott et al., 2015), we next investigated whether OCT4 is capable of forming droplets *in vitro*, with and without the IDR of the MED1 subunit of Mediator.

Recombinant OCT4-GFP fusion protein was purified and added to droplet formation buffers containing a crowding agent (10% PEG-8000) to simulate the densely crowded environment of the nucleus. Fluorescent microscopy of the droplet mixture revealed that OCT4 alone did not form droplets throughout the range of concentrations tested (Figure 3B). In contrast, purified recombinant MED1-IDR-GFP fusion protein exhibited concentration-dependent liquid-liquid phase separation (Figure 3B), as described previously (Sabari et al., 2018).

We then mixed the two proteins and found that droplets of MED1-IDR incorporate and concentrate purified OCT4-GFP to form heterotypic droplets (Figure 3C). In contrast, purified GFP was not concentrated into MED1-IDR droplets (Figures 3C and S3A). OCT4-MED1-IDR droplets were near micrometer sized (Figure S3B), exhibited fast recovery after photobleaching (Figure 3D), had a spherical shape (Figure S3C), and were salt

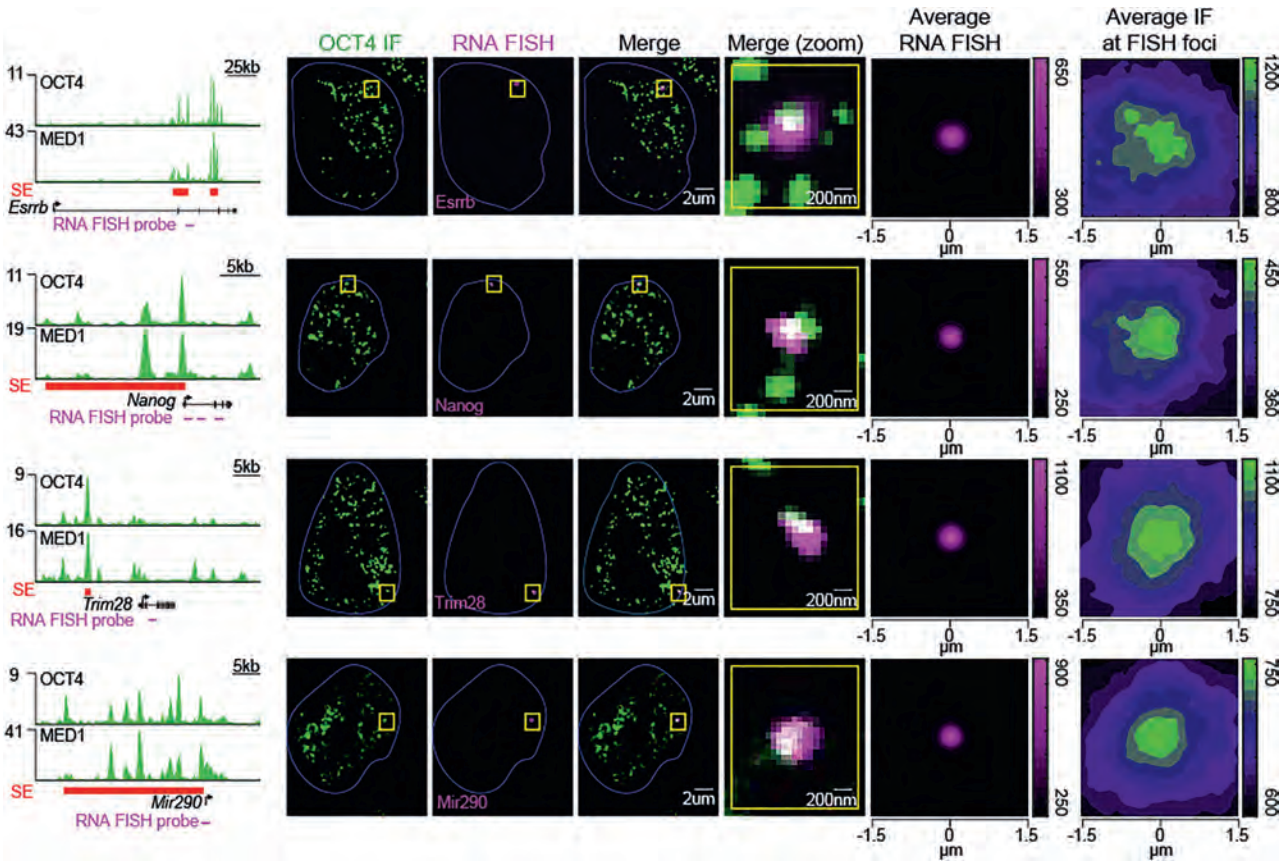

Figure 1. OCT4 and Mediator Occupy SEs *In Vivo*

ChIP-seq tracks of OCT4 and MED1 in ESCs at SEs (left column) and OCT4 IF with concurrent RNA-FISH demonstrating occupancy of OCT4 at *Esrrb*, *Nanog*, *Trim28*, and *Mir290*. Hoechst staining was used to determine the nuclear periphery, highlighted with a blue line. The two rightmost columns show average RNA FISH signal and average OCT4 IF signal centered on the RNA-FISH focus from at least 11 images. Average OCT4 IF signal at a randomly selected nuclear position is displayed in Figure S1.

See also Figure S1 and Tables S1, S2, and S4.

sensitive (Figures 3E and S3D). Thus, they exhibited characteristics associated with phase-separated liquid condensates (Banani et al., 2017; Shin and Brangwynne, 2017). Furthermore, we found that OCT4-MED1-IDR droplets could form in the absence of any crowding agent (Figures S3E and S3F).

Residues Required for OCT4-MED1-IDR Droplet Formation and Gene Activation

We next investigated whether specific OCT4 amino acid residues are required for the formation of OCT4-MED1-IDR phase-separated droplets, as multiple categories of amino acid interaction have been implicated in forming condensates. For example, serine residues are required for MED1 phase separation (Sabari et al., 2018). We asked whether amino acid enrichments in the OCT4 ADs might point to a mechanism for interaction. An analysis of amino acid frequency and charge bias showed that the OCT4 IDRs are enriched in proline and glycine and have an overall acidic charge (Figure 4A). ADs are known to be enriched in acidic amino acids and proline and have historically been classified on this basis (Frietze and Farnham, 2011), but the mechanism by which these enrichments might cause gene activation is not known. We hypothesized that proline or acidic amino acids in the ADs might facilitate interaction with the phase-separated MED1-IDR droplet. To test this, we designed fluorescently labeled proline and glutamic acid decapeptides and investigated whether these peptides can be concentrated in MED1-IDR droplets. When added to droplet formation buffer alone, these peptides remained in solution (Figure S4A). When mixed with MED1-IDR-GFP, however, proline peptides were not incorporated into MED1-IDR droplets, while the glutamic acid peptides were concentrated within (Figures 4B and S4B). These results show that peptides with acidic residues are amenable to incorporation within MED1 phase-separated droplets.

Based on these results, we deduced that an OCT4 protein lacking acidic amino acids in its ADs might be defective in its ability to phase separate with MED1-IDR. Such a dependence on acidic residues would be consistent with our observation that OCT4-MED1-IDR droplets are highly salt sensitive. To test this idea, we generated a mutant OCT4 in which all acidic residues in the ADs were replaced with alanine (thus changing 17 AAs in the N-terminal AD and 6 in the C-terminal AD) (Figure 4C). When this GFP-fused OCT4 mutant was mixed with purified

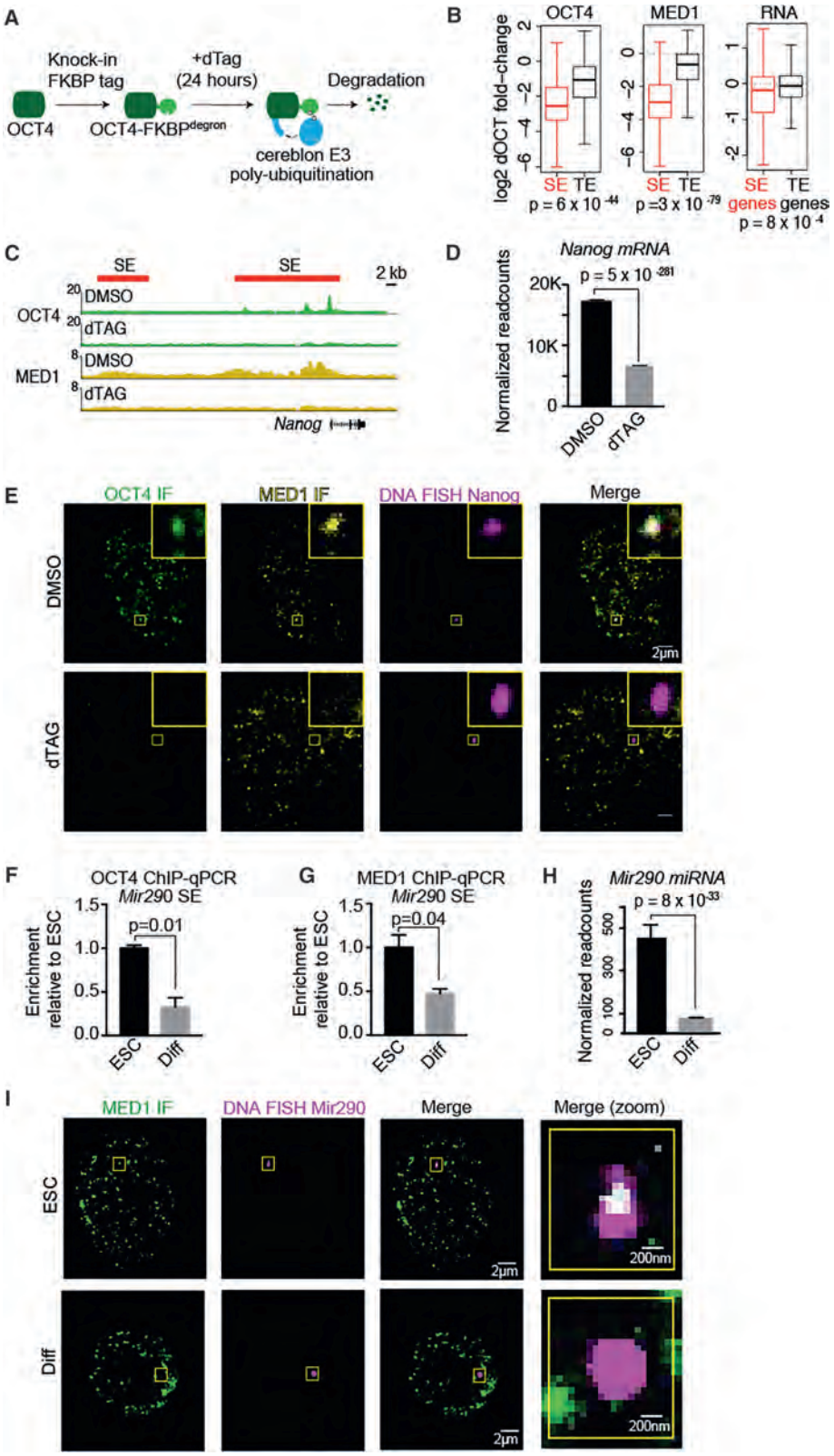

(legend on next page)

MED1-IDR, entry into droplets was highly attenuated (Figures 4C and S4C). To test whether this effect was specific for acidic residues, we generated a mutant of OCT4 in which all the aromatic amino acids within the ADs were changed to alanine. We found that this mutant was still incorporated into MED1-IDR droplets (Figures S4C and S4D). These results indicate that the ability of OCT4 to phase separate with MED1-IDR is dependent on acidic residues in the OCT4 IDRs.

To ensure that these results were not specific to the MED1-IDR, we explored whether purified Mediator complexes would form droplets *in vitro* and incorporate OCT4. The human Mediator complex was purified as previously described (Meyer et al., 2008) and then concentrated for use in the droplet formation assay (Figure S4E). Because purified endogenous Mediator does not contain a fluorescent tag, we monitored droplet formation by differential interference contrast (DIC) microscopy and found it to form droplets alone at ~200–400 nM (Figure 4D). Consistent with the results for MED1-IDR droplets, OCT4 was incorporated within human Mediator complex droplets, but incorporation of the OCT4 acidic mutant was attenuated. These results indicate that the MED1-IDR and the complete Mediator complex each exhibit phase-separating behaviors and suggest that they both incorporate OCT4 in a manner that is dependent on electrostatic interactions provided by acidic amino acids.

To test whether the OCT4 AD acidic mutations affect the ability of the factor to activate transcription *in vivo*, we utilized a GAL4 transactivation assay (Figure 4E). In this system, ADs or their mutant counterparts are fused to the GAL4 DBD and expressed in cells carrying a luciferase reporter plasmid. We found that the wild-type OCT4-AD fused to the GAL4-DBD was able to activate transcription, while the acidic mutant lost this function (Figure 4E). These results indicate that the acidic residues of the OCT4 ADs are necessary for both incorporation into MED1 phase-separated droplets *in vitro* and for gene activation *in vivo*.

Multiple TFs Phase Separate with Mediator Subunit Droplets

TFs with diverse types of ADs have been shown to interact with Mediator subunits, and MED1 is among the subunits that is most targeted by TFs (Table S1). An analysis of mammalian TFs confirmed that TFs and their putative ADs are enriched in IDRs, as previous analyses have shown (Liu et al., 2006; Staby et al., 2017) (Figure 5A). We reasoned that many different TFs might interact with the MED1-IDR to generate liquid droplets and therefore be incorporated into MED1 condensates. To assess whether diverse MED1-interacting TFs can phase separate with MED1, we prepared purified recombinant, mEGFP-tagged, full-length MYC, p53, NANOG, SOX2, RARa, GATA2, and ER (Table S3). When added to droplet formation buffers, most TFs formed droplets alone (Figure 5B). When added to droplet formation buffers with MED1-IDR, all 7 of these TFs concentrated into MED1-IDR droplets (Figures 5C and S5A). We selected p53 droplets for fluorescence recovery after photobleaching (FRAP) analysis; they exhibited rapid and dynamic internal reorganization (Figure S5B), supporting the notion that they are liquid condensates. These results indicate that TFs previously shown to interact with the MED1 subunit of Mediator can do so by forming phase-separated condensates with MED1.

Estrogen Stimulates Phase Separation of ER with MED1

ER is a well-studied example of a ligand-dependent TF. ER consists of an N-terminal ligand-independent AD, a central DBD, and a C-terminal ligand-dependent AD (also called the ligand binding domain [LBD]) (Figure 6A). Estrogen facilitates the interaction of ER with MED1 by binding the LBD of ER, which exposes a binding pocket for LXXLL motifs within the MED1-IDR (Figures 6A and 6B) (Manavathi et al., 2014). We noted that ER can form heterotypic droplets with the MED1-IDR recombinant protein used thus far in these studies (Figure 5C), which lacks the LXXLL motifs. This led us to investigate whether ER-MED1 droplet formation is responsive to estrogen and whether this involves the MED1 LXXLL motifs.

We performed droplet formation assays using a MED1-IDR recombinant protein containing LXXLL motifs (MED1-IDRXL-mCherry) and found that, similar to MED1-IDR and complete Mediator, it had the ability to form droplets alone (Figure 6C). We then tested the ability of ER to phase separate with MED1-IDRXL-mCherry and MED1-IDR-mCherry droplets.

Figure 2. MED1 Condensates Are Dependent on OCT4 Binding *In Vivo*

(A) Schematic of OCT4 degradation. The C terminus of OCT4 is endogenously biallelically tagged with the FKBP protein; when exposed to the small molecule dTag, OCT4 is ubiquitylated and rapidly degraded.

(B) Boxplot representation of log2 fold change in OCT4 and MED1 ChIP-seq reads and RNA-seq reads of super-enhancer (SE)- or typical enhancer (TE)-driven genes, in ESCs carrying the OCT4 FKBP tag, treated with DMSO, or dTAG for 24 hr. The box represents the interquartile; whiskers are 1.5× the interquartile range.

(C) Genome browser view of OCT4 (green) and MED1 (yellow) ChIP-seq data at the *Nanog* locus. The *Nanog* SE (red) shows a 90% reduction of OCT4 and MED1 binding after OCT4 degradation.

(D) Normalized RNA-seq read counts of *Nanog* mRNA shows a 60% reduction upon OCT4 degradation. Error bars represent SEM.

(E) Confocal microscopy images OCT4 and MED1 IF with DNA FISH to the *Nanog* locus in ESCs carrying the OCT4 FKBP tag, treated with DMSO or dTAG. Inset represents a zoomed in view of the yellow box. The merge view displays all three channels (OCT4 IF, MED1 IF, and *Nanog* DNA FISH) together.

(F) OCT4 ChIP-qPCR to the *Mir290* SE in ESCs and differentiated cells (Diff) presented as enrichment over control, relative to signal in ESCs. Error bars represent the SEM from two biological replicates.

(G) MED1 ChIP-qPCR to the *Mir290* SE in ESCs and differentiated cells (Diff) presented as enrichment over control, relative to signal in ESCs. Error bars represent the SEM from two biological replicates.

(H) Normalized RNA-seq read counts of *Mir290* miRNA in ESCs or differentiated cells (Diff). Error bars represents the SEM from two biological replicates.

(I) Confocal microscopy images of MED1 IF and DNA FISH to the *Mir290* genomic locus in ESCs and differentiated cells. Merge (zoom) represents a zoomed-in view of the yellow box in the merged channel.

See also Figure S2 and Tables S2 and S4.

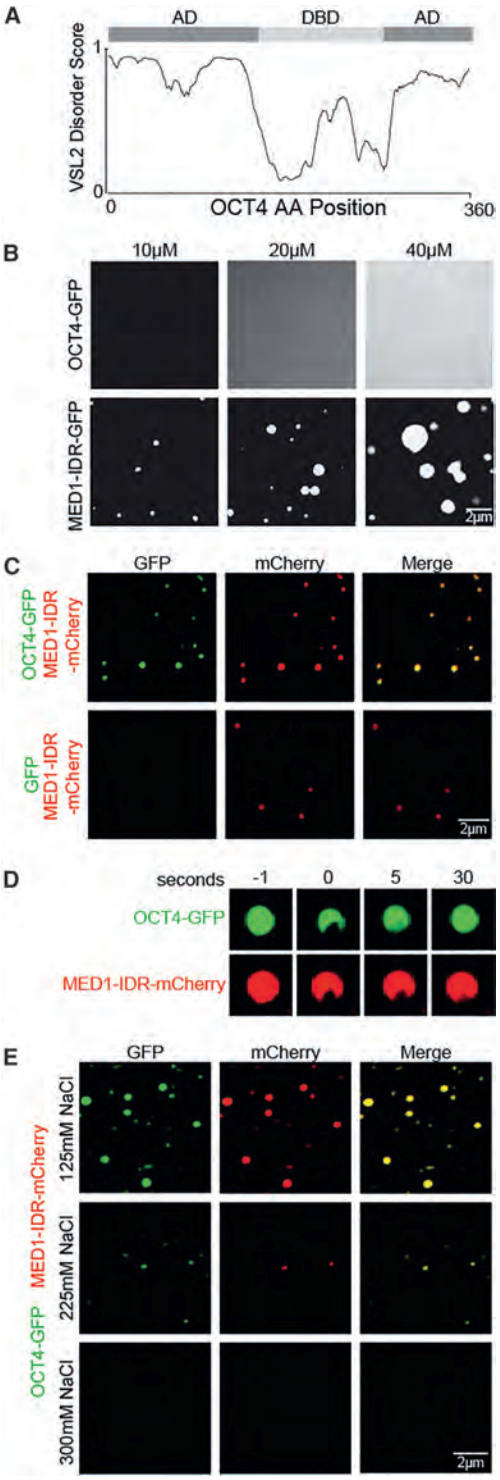

Figure 3. OCT4 Forms Liquid Droplets with MED1 *In Vitro*

(A) Graph of intrinsic disorder of OCT4 as calculated by the VSL2 algorithm (http://www.pondr.com/). The DNA binding domain (DBD) and activation domains (ADs) are indicated above the disorder score graph (Brehm et al., 1997).

(B) Representative images of droplet formation of OCT4-GFP (top row) and MED1-IDR-GFP (bottom row) at the indicated concentration in droplet formation buffer with 125 mM NaCl and 10% PEG-8000.

(C) Representative images of droplet formation of MED1-IDR-mCherry mixed with GFP or OCT4-GFP at 10 μM each in droplet formation buffer with 125 mM NaCl and 10% PEG-8000.

(D) FRAP of heterotypic droplets of OCT4-GFP and MED1-IDR-mCherry. Confocal images were taken at indicated time points relative to photobleaching (0).

(E) Representative images of droplet formation of 10 μM MED1-IDR-mCherry and OCT4-GFP in droplet formation buffer with varying concentrations of salt and 10% PEG-8000.

See also Figure S3 and Table S3.

Some recombinant ER was incorporated and concentrated into MED1-IDRXL-mCherry droplets, but the addition of estrogen considerably enhanced heterotypic droplet formation (Figures 6D and 6E). In contrast, the addition of estrogen had little effect on droplet formation when the experiment was conducted with MED1-IDR-mCherry, which lacks the LXXLL motifs (Figure S6). These results show that estrogen, which stimulates ER-mediated transcription *in vivo*, also stimulates incorporation of ER into MED1-IDR droplets *in vitro*. Thus, OCT4 and ER both require the same amino acids/ligands for both phase separation and activation. Furthermore, since the LBD is a structured domain that undergoes a conformation shift upon estrogen binding to interact with MED1, it appears that structured interactions may contribute to transcriptional condensate formation.

GCN4 and MED15 Phase Separation Is Dependent on Residues Required for Activation

Among the best-studied TF-coactivator systems is the yeast TF GCN4 and its interaction with the MED15 subunit of Mediator (Brzovic et al., 2011; Herbig et al., 2010; Jedidi et al., 2010). The GCN4 AD has been dissected genetically, the amino acids that contribute to activation have been identified (Drysdale et al., 1995; Staller et al., 2018), and recent studies have shown that the GCN4 AD interacts with MED15 in multiple orientations and conformations to form a "fuzzy complex" (Tuttle et al., 2018). Weak interactions that form fuzzy complexes have features of the IDR-IDR interactions that are thought to produce phase-separated condensates.

To test whether GCN4 and MED15 can form phase-separated droplets, we purified recombinant yeast GCN4-GFP and the N-terminal portion of yeast MED15-mCherry containing residues 6–651 (hereafter called MED15), which are responsible for the interaction with GCN4. When added separately to droplet formation buffer, GCN4 formed micrometer-sized droplets only at quite high concentrations (40 μM), and MED15 formed only small droplets at this high concentration (Figure 7A). When mixed together, however, the GCN4 and MED15 recombinant proteins formed double-positive, micrometer-sized, spherical droplets at lower concentrations (Figures 7B and S7A). These GCN4-MED15 droplets exhibited rapid FRAP kinetics (Figure S7B), consistent with liquid-like behavior. We generated a phase diagram of these two proteins and found that they formed droplets together at low concentration (Figures S7C and S7D). This suggests that interaction between the two is required for phase separation at low concentration.

The ability of GCN4 to interact with MED15 and activate gene expression has been attributed to specific hydrophobic patches

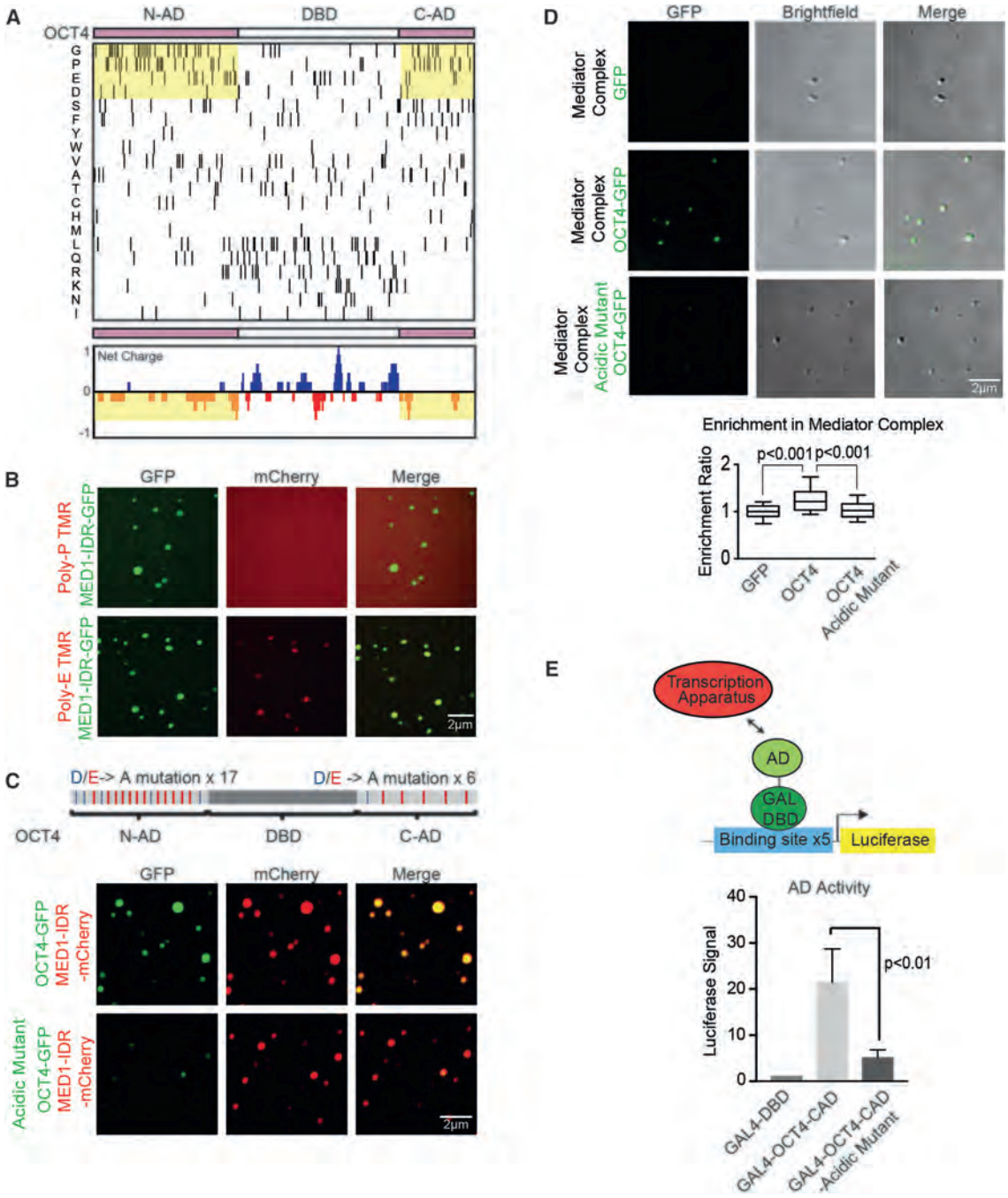

Figure 4. OCT4 Phase Separation with MED1 Is Dependent on Specific Interactions

(A) Amino acid enrichment analysis ordered by frequency of amino acid in the ADs (top). Net charge per amino acid residue analysis of OCT4 (bottom).

(B) Representative images of droplet formation showing that Poly-E peptides are incorporated into MED1-IDR droplets. MED1-GFP and a tetramethylrhodamine (TMR)-labeled proline or glutamic acid decapeptide (Poly-P and Poly-E, respectively) were added to droplet formation buffers at 10 μM each with 125 mM NaCl and 10% PEG-8000.

(C) Top: schematic of OCT4 protein, horizontal lines in the AD mark acidic D residues (blue) and acidic E residues (red). All 17 acidic residues in the N-AD and 6 acidic residues in the C-AD were mutated to alanine to generate an OCT4-acidic mutant. Bottom: representative confocal images of droplet formation showing that the OCT4 acidic mutant has an attenuated ability to concentrate into MED1-IDR droplets. 10 μM MED1-IDR-mCherry and OCT4-GFP or OCT4-acidic mutant-GFP was added to droplet formation buffers with 125 mM NaCl and 10% PEG-8000.

(D) Top: representative images of droplet formation showing that OCT4 but not the OCT4 acidic mutant is incorporated into Mediator complex droplets. Purified Mediator complex was mixed with 10 μM GFP, OCT4-GFP, or OCT4-acidic mutant-GFP in droplet formation buffers with 140 mM NaCl and 10% PEG-8000.

(legend continued on next page)

and aromatic residues in the GCN4 AD (Drysdale et al., 1995; Staller et al., 2018; Tuttle et al., 2018). We created a mutant of GCN4 in which the 11 aromatic residues contained in these hydrophobic patches were changed to alanine (Figure 7C). When added to droplet formation buffers, the ability of the mutant protein to form droplets alone was attenuated (Figure S7E). Next, we tested whether droplet formation with MED15 was affected; indeed, the mutated protein has a compromised ability to form droplets with MED15 (Figures 7C and S7F). Similar results were obtained when GCN4 and the aromatic mutant of GCN4 was added to droplet formation buffers with the complete Mediator complex; while GCN4 was incorporated into Mediator droplets, the incorporation of the GCN4 mutant into Mediator droplets was attenuated (Figures 7D and S7G). These results demonstrate that multivalent, weak interactions between the AD of GCN4 and MED15 promote phase separation into liquid-like droplets.

The ADs of yeast TFs can function in mammalian cells and can do so by interacting with human Mediator (Oliviero et al., 1992). To investigate whether the aromatic mutant of GCN4 AD is impaired in its ability to recruit Mediator *in vivo*, the GCN4 AD and the GCN4 mutant AD were tethered to a Lac array in U2OS cells (Figure 7E) (Janicki et al., 2004). While the tethered GCN4 AD caused robust Mediator recruitment, the GCN4 aromatic mutant did not (Figure 7E). We used the GAL4 transactivation assay described previously to confirm that the GCN4 AD was capable of transcriptional activation *in vivo*, whereas the GCN4 aromatic mutant had lost that property (Figure 7F). These results provide further support for the idea that TF AD amino acids that are essential for phase separation with Mediator are required for gene activation.

DISCUSSION

The results described here support a model whereby TFs interact with Mediator and activate genes by the capacity of their ADs to form phase-separated condensates with this coactivator. For both the mammalian ESC pluripotency TF OCT4 and the yeast TF GCN4, we found that the AD amino acids required for phase separation with Mediator condensates were also required for gene activation *in vivo*. For ER, we found that estrogen stimulates the formation of phase-separated ER-MED1 droplets. ADs and coactivators generally consist of low-complexity amino acid sequences that have been classified as IDRs, and IDR-IDR interactions have been implicated in facilitating the formation of phase-separated condensates. We propose that IDR-mediated phase separation with Mediator is a general mechanism by which TF ADs effect gene expression and provide evidence that this occurs *in vivo* at SEs. We suggest that the ability to phase separate with Mediator, which would employ the features of high valency and low-affinity characteristic of liquid-liquid phase-separated condensates, operates alongside an ability of some TFs to form high-affinity interactions with Mediator (Figure 7G) (Taatjes, 2017).

The model that TF ADs function by forming phase-separated condensates with coactivators explains several observations that are difficult to reconcile with classical lock-and-key models of protein-protein interaction. The mammalian genome encodes many hundreds of TFs with diverse ADs that must interact with a small number of coactivators (Allen and Taatjes, 2015; Arany et al., 1995; Avantaggiati et al., 1996; Dai and Markham, 2001; Eckner et al., 1996; Gelman et al., 1999; Green, 2005; Liu et al., 2009; Merika et al., 1998; Oliner et al., 1996; Yin and Wang, 2014; Yuan et al., 1996), and ADs that share little sequence homology are functionally interchangeable among TFs (Godowski et al., 1988; Hope and Struhl, 1986; Jin et al., 2016; Lech et al., 1988; Ransone et al., 1990; Sadowski et al., 1988; Struhl, 1988; Tora et al., 1989). The common feature of ADs—the possession of low-complexity IDRs—is also a feature that is pronounced in coactivators. The model of coactivator interaction and gene activation by phase-separated condensate formation thus more readily explains how many hundreds of mammalian TFs interact with these coactivators.

Previous studies have provided important insights that prompted us to investigate the possibility that TF ADs function by forming phase-separated condensates. TF ADs have been classified by their amino acid profile as acidic, proline rich, serine/threonine rich, glutamine rich, or by their hypothetical shape as acid blobs, negative noodles, or peptide lassos (Sigler, 1988). Many of these features have been described for IDRs that are capable of forming phase-separated condensates (Babu, 2016; Darling et al., 2018; Das et al., 2015; Dunker et al., 2015; Habchi et al., 2014; van der Lee et al., 2014; Oldfield and Dunker, 2014; Uversky, 2017; Wright and Dyson, 2015). Evidence that the GCN4 AD interacts with MED15 in multiple orientations and conformations to form a "fuzzy complex" (Tuttle et al., 2018) is consistent with the notion of dynamic low-affinity interactions characteristic of phase-separated condensates. Likewise, the low complexity domains of the FET (FUS/EWS/TAF15) RNA-binding proteins (Andersson et al., 2008) can form phase-separated hydrogels and interact with the RNA polymerase II C-terminal domain (CTD) in a CTD phosphorylation-dependent manner (Kwon et al., 2013); this may explain the mechanism by which RNA polymerase II is recruited to active genes in its unphosphorylated state and released for elongation following phosphorylation of the CTD.

The model we describe here for TF AD function may explain the function of a class of heretofore poorly understood fusion oncoproteins. Many malignancies bear fusion-protein translocations involving portions of TFs (Bradner et al., 2017; Kim et al., 2017; Latysheva et al., 2016). These abnormal gene

Bottom: enrichment ratio of GFP, OCT4-GFP, or OCT4-acidic mutant-GFP in Mediator complex droplets. n > 20; error bars represent the distribution between the 10th and 90th percentiles.

(E) Top: GAL4 activation assay schematic. The GAL4 luciferase reporter plasmid was transfected into mouse ESCs with an expression vector for the GAL4-DBD fusion protein. Bottom: the AD activity was measured by luciferase activity of mouse ESCs transfected with GAL4-DBD, GAL4-OCT4-CAD, or GAL4-OCT4-CAD-acidic mutant. Error bars represent SEM.

See also Figure S4 and Table S3.

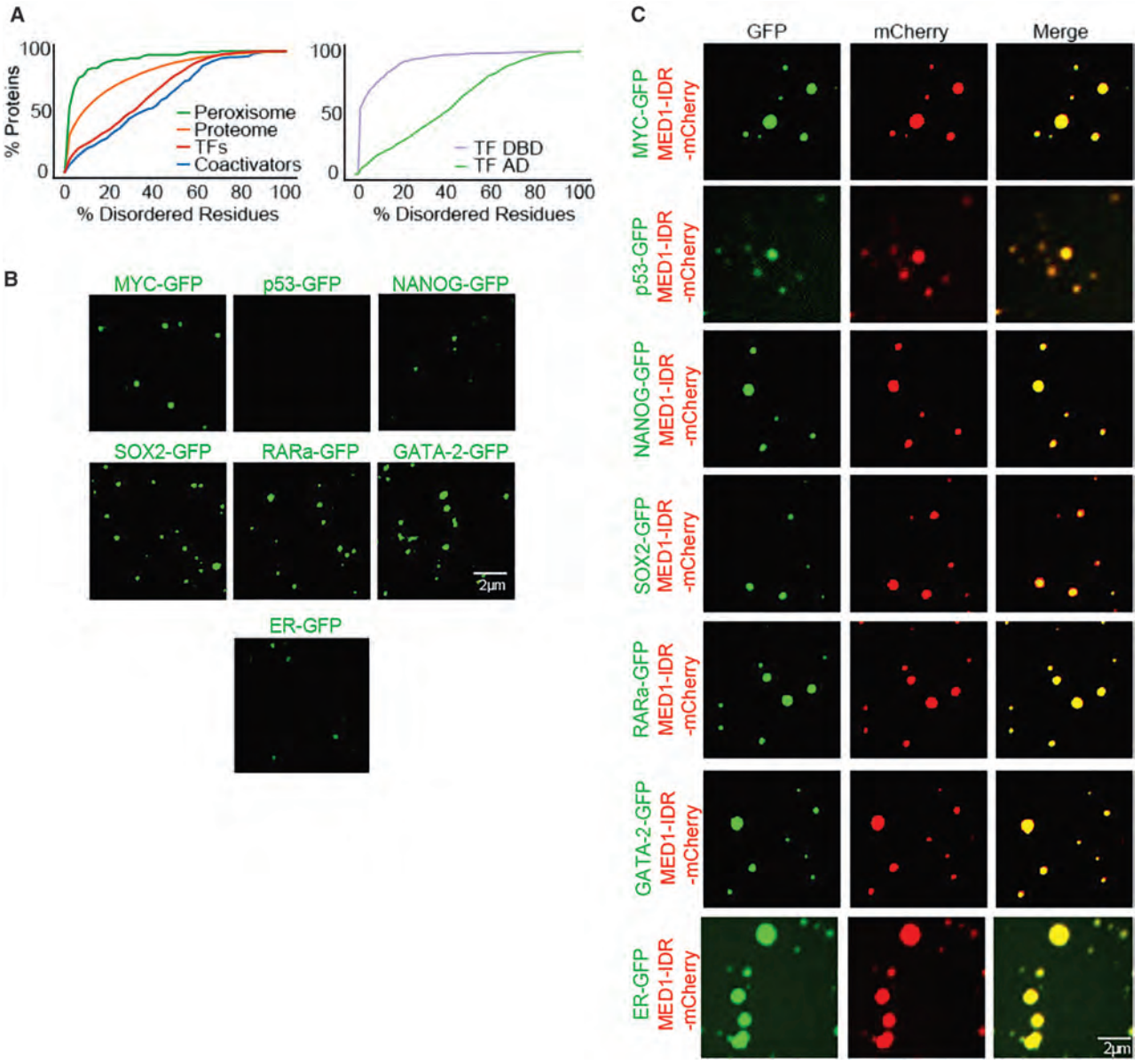

Figure 5. Multiple TFs Phase Separate with Mediator Droplets

(A) Left: percentage of disorder of various protein classes (x axis) plotted against the cumulative fraction of disordered proteins of that class (y axis). Right: disorder content of transcription factor (TF) DNA-binding domains (DBD) and putative activation domains (ADs).

(B) Representative images of droplet formation assaying homotypic droplet formation of indicated TFs. Recombinant MYC-GFP (12 μM), p53-GFP (40 μM), NANOG-GFP (10 μM), SOX2-GFP (40 μM), RARa-GFP (40 μM), GATA-2-GFP (40 μM), and ER-GFP (40 μM) was added to droplet formation buffers with 125 mM NaCl and 10% PEG-8000.

(C) Representative images of droplet formation showing that all tested TFs were incorporated into MED1-IDR droplets. 10 μM of MED1-IDRmCherry and 10 μM of MYC-GFP, p53-GFP, NANOG-GFP, SOX2-GFP, RARa-GFP, GATA-2-GFP, or ER-GFP were added to droplet formation buffers with 125 mM NaCl and 10% PEG-8000.

See also Figure S5 and Table S3.

products often fuse a DNA- or chromatin-binding domain to a wide array of partners, many of which are IDRs. For example, MLL may be fused to 80 different partner genes in AML (Winters and Bernt, 2017), the EWS-FLI rearrangement in Ewing's sarcoma causes malignant transformation by recruitment of a disordered domain to oncogenes (Boulay et al., 2017; Chong et al., 2017), and the disordered phase-separating protein FUS is found fused to a DBD in certain sarcomas (Crozat et al., 1993; Patel et al., 2015). Phase separation provides a mechanism by which such gene products result in aberrant

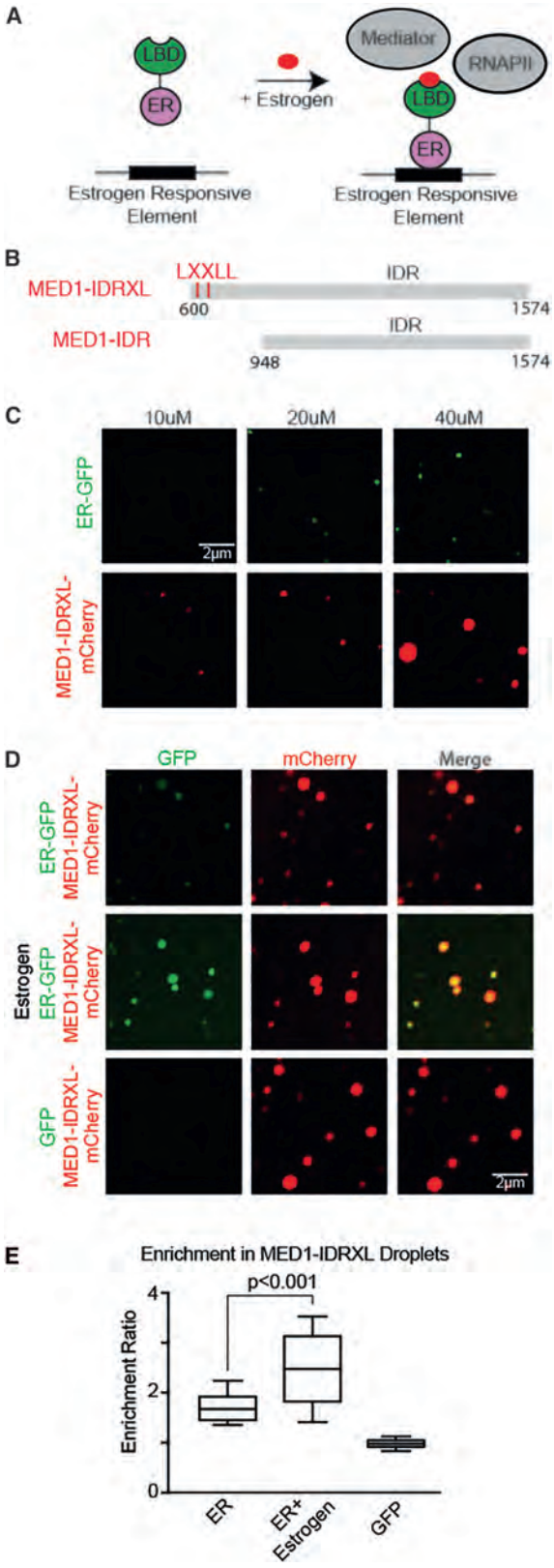

Figure 6. Estrogen Stimulates Phase Separation of ER with MED1

(A) Schematic of estrogen stimulated gene activation. Estrogen facilitates the interaction of ER with Mediator and RNAPII by binding the ligand binding domain (LBD) of ER, which exposes a binding pocket for LXXLL motifs within the MED1-IDR.

(B) Schematic view of MED1-IDRXL and MED1-IDR used for recombinant protein production.

(C) Representative images of droplet formation, assaying homotypic droplet formation of ER-GFP, and MED1-IDRXL-mCherry performed with the indicated protein concentration in droplet formation buffers with 125 mM NaCl and 10% PEG-8000.

(D) Representative confocal images of droplet formation showing that ER is incorporated into MED1-IDRXL droplets and the addition of estrogen enhanced heterotypic droplet formation. ER-GFP, ER-GFP in the presence of estrogen, or GFP is mixed with MED1-IDRXL. 10 μM of each indicated protein was added to droplet formation buffers with 125 mM NaCl and 10% PEG-8000.

(E) Enrichment ratio in MED1-IDRXL droplets of ER-GFP, ER-GFP in the presence of estrogen, or GFP. n > 20; error bars represent the distribution between the 10th and 90th percentiles.

See also Figure S6 and Table S3.

gene expression programs; by recruiting a disordered protein to the chromatin, diverse coactivators may form phase-separated condensates to drive oncogene expression. Understanding the interactions that compose these aberrant transcriptional condensates, their structures, and behaviors may open new therapeutic avenues.

STAR★METHODS

Detailed methods are provided in the online version of this paper and include the following:

- KEY RESOURCES TABLE
- CONTACT FOR REAGENT AND RESOURCE SHARING
- EXPERIMENTAL MODEL AND SUBJECT DETAILS
  - Cells
  - Cell culture conditions
- METHOD DETAILS
  - Immunofluorescence with RNA FISH
  - Immunofluorescence with DNA FISH
  - Tissue culture
  - Western blot
  - Chromatin immunoprecipitation (ChIP) qPCR and sequencing
  - RNA-Seq
  - Protein purification
  - *In vitro* droplet assay
  - Genome editing and protein degradation
  - GAL4 transcription assay
  - Lac binding assay
  - Purification of CDK8-Mediator
- QUANTIFICATION AND STATISTICAL ANALYSIS
  - Experimental design
  - Average image and radial distribution analysis
  - Chromatin immunoprecipitation PCR and sequencing (ChIP) analysis
  - Super-enhancer identification
  - RNA-Seq analysis
  - Enrichment and charge analysis of OCT4

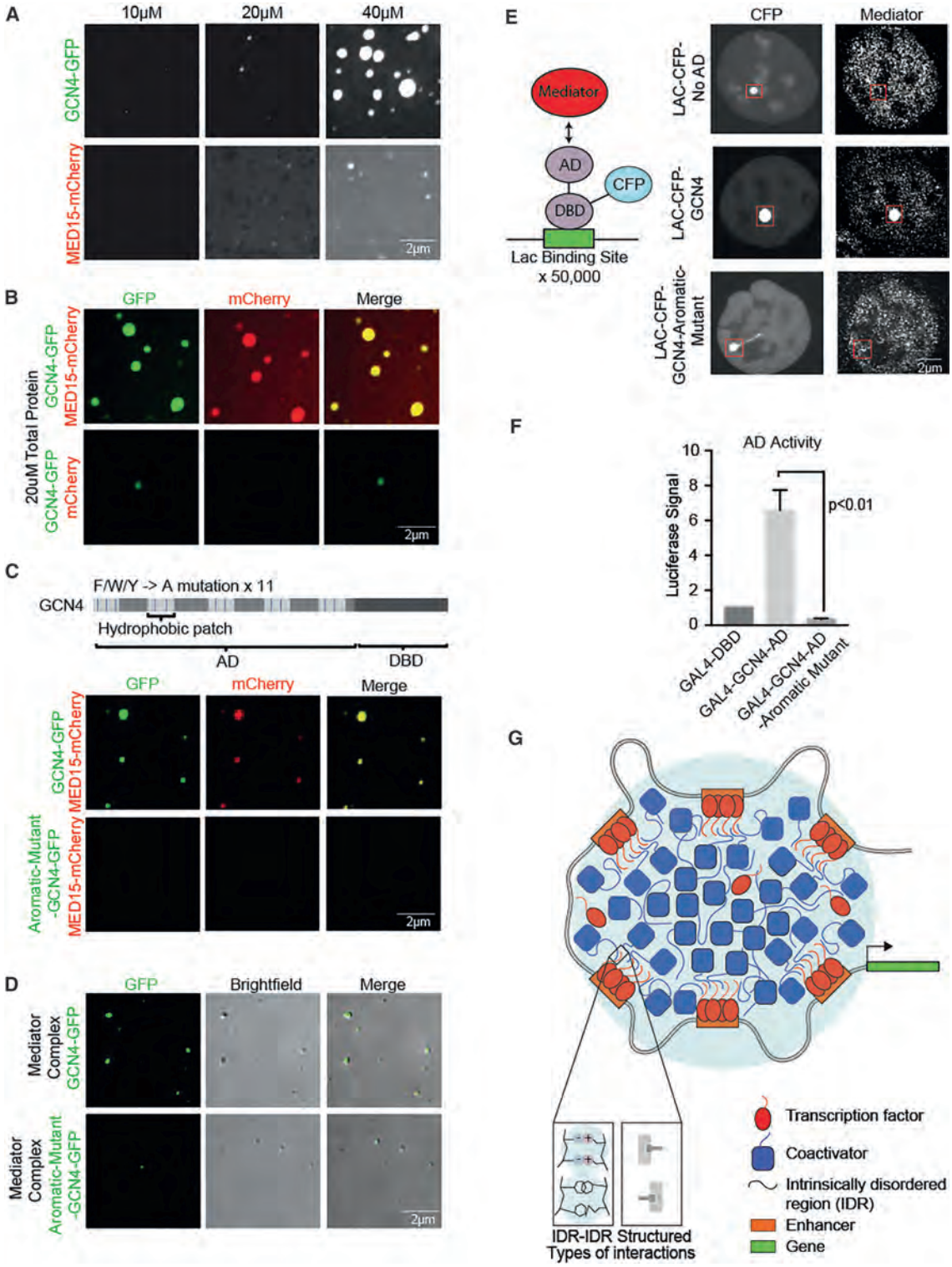

Figure 7. TF-Coactivator Phase Separation Is Dependent on Residues Required for Transactivation

(A) Representative confocal images of droplet formation of GCN4-GFP or MED15-mCherry were added to droplet formation buffers with 125 mM NaCl and 10% PEG-8000.

(B) Representative images of droplet formation showing that GCN4 forms droplets with MED15. GCN4-GFP and mCherry or GCN4-GFP and MED15-mCherry were added to droplet formation buffers at 10 μM with 125 mM NaCl and 10% PEG-8000 and imaged on a fluorescent microscope with the indicated filters.

(legend continued on next page)

- Disorder enrichment analysis
- Imaging analysis of *in vitro* droplets

- DATA AND SOFTWARE AVAILABILITY
  - Datasets

SUPPLEMENTAL INFORMATION

Supplemental Information includes seven figures and four tables and can be found with this article online at https://doi.org/10.1016/j.cell.2018.10.042.

ACKNOWLEDGMENTS

We thank Wendy Salmon of the W.M. Keck Microscopy Facility, the Whitehead Genomics Core, Arup Chakraborty, and Philip A. Sharp. The work was supported by NIH grant GM123511 and NSF grant PHY1743900 (R.A.Y.), NIH grant GM117370 (D.J.T.), Swedish Research Council Postdoctoral Fellowship (VR 2017-00372) (A.B.), NIH grant T32CA009172 (I.A.K.), a Damon Runyon Cancer Research Foundation Fellowship (2309-17) (B.R.S.), a NSF Graduate Research Fellowship (A.V.Z.), a Hope Funds for Cancer Research fellowship (B.J.A.), a Cancer Research Institute Irvington Fellowship (Y.E.G.), NIH grant T32GM08759 (C.B.F.), and a NWO Rubicon Fellowship (J.S.).

AUTHOR CONTRIBUTIONS

Conceptualization, A.B., I.A.K., and R.A.Y.; Methodology, A.B., I.A.K., B.R.S., A.D., and E.L.C.; Software, K.S. and B.J.A.; Formal Analysis, A.B., I.A.K., C.H.L., K.S., and B.J.A.; Investigation, A.B., I.A.K., B.R.S., A.D., E.L.C., A.V.Z., C.H.L., J.C.M., N.M.H., L.K.A., Y.E.G., J.K.R., C.B.F., and J.S.; Resources, D.J.T. and R.A.Y.; Data Curation, B.J.A.; Writing – Original Draft, A.B., I.A.K., and R.A.Y.; Writing – Reviewing and Editing, all authors; Visualization, A.B., I.A.K., B.R.S., A.D., C.H.L., K.S., B.J.A., and J.S.; Supervision, T.I.L., D.J.T., and R.A.Y.; Project Administration, A.B., I.A.K., and R.A.Y.; Funding Acquisition, D.J.T. and R.A.Y.

DECLARATION OF INTERESTS

The Whitehead Institute filed a patent application based in part on this paper. R.A.Y. is a founder and shareholder of Syros Pharmaceuticals, Camp4 Therapeutics, and Omega Therapeutics. I.A.K. is a consultant to InfiniteMD, Best Doctors, and Foundation Medicine and is a shareholder of InfiniteMD. B.J.A. and T.I.L. are shareholders of Syros Pharmaceuticals. T.I.L. is a consultant to Camp4 Therapeutics.

Received: June 12, 2018
Revised: August 20, 2018
Accepted: October 16, 2018
Published: November 15, 2018

REFERENCES

Alberti, S. (2017). The wisdom of crowds: Regulating cell function through condensed states of living matter. J. Cell Sci. *130*, 2789–2796.

Allen, B.L., and Taatjes, D.J. (2015). The Mediator complex: A central integrator of transcription. Nat. Rev. Mol. Cell Biol. *16*, 155–166.

Andersson, M.K., Ståhlberg, A., Arvidsson, Y., Olofsson, A., Semb, H., Stenman, G., Nilsson, O., and Åman, P. (2008). The multifunctional FUS, EWS and TAF15 proto-oncoproteins show cell type-specific expression patterns and involvement in cell spreading and stress response. BMC Cell Biol. *9*, 37.

Apostolou, E., Ferrari, F., Walsh, R.M., Bar-Nur, O., Stadtfeld, M., Cheloufi, S., Stuart, H.T., Polo, J.M., Ohsumi, T.K., Borowsky, M.L., et al. (2013). Genome-wide chromatin interactions of the Nanog locus in pluripotency, differentiation, and reprogramming. Cell Stem Cell *12*, 699–712.

Arany, Z., Newsome, D., Oldread, E., Livingston, D.M., and Eckner, R. (1995). A family of transcriptional adaptor proteins targeted by the E1A oncoprotein. Nature *374*, 81–84.

Avantaggiati, M.L., Carbone, M., Graessmann, A., Nakatani, Y., Howard, B., and Levine, A.S. (1996). The SV40 large T antigen and adenovirus E1a oncoproteins interact with distinct isoforms of the transcriptional co-activator, p300. EMBO J. *15*, 2236–2248.

Babu, M.M. (2016). The contribution of intrinsically disordered regions to protein function, cellular complexity, and human disease. Biochem. Soc. Trans. *44*, 1185–1200.

Banani, S.F., Lee, H.O., Hyman, A.A., and Rosen, M.K. (2017). Biomolecular condensates: Organizers of cellular biochemistry. Nat. Rev. Mol. Cell Biol. *18*, 285–298.

Boulay, G., Sandoval, G.J., Riggi, N., Iyer, S., Buisson, R., Naigles, B., Awad, M.E., Rengarajan, S., Volorio, A., McBride, M.J., et al. (2017). Cancer-specific retargeting of BAF complexes by a prion-like domain. Cell *171*, 163–178.

Bradner, J.E., Hnisz, D., and Young, R.A. (2017). Transcriptional addiction in cancer. Cell *9*, 629–643.

Brehm, A., Ohbo, K., and Schöler, H. (1997). The carboxy-terminal transactivation domain of Oct-4 acquires cell specificity through the POU domain. Mol. Cell. Biol. *17*, 154–162.

Brent, R., and Ptashne, M. (1985). A eukaryotic transcriptional activator bearing the DNA specificity of a prokaryotic repressor. Cell *43*, 729–736.

Brzovic, P.S., Heikaus, C.C., Kisselev, L., Vernon, R., Herbig, E., Pacheco, D., Warfield, L., Littlefield, P., Baker, D., Klevit, R.E., and Hahn, S. (2011). The acidic transcription activator Gcn4 binds the mediator subunit Gal11/Med15 using a simple protein interface forming a fuzzy complex. Mol. Cell *44*, 942–953.

Burke, K.A., Janke, A.M., Rhine, C.L., and Fawzi, N.L. (2015). Residue-by-residue view of in vitro FUS granules that bind the C-terminal domain of RNA polymerase II. Mol. Cell *60*, 231–241.

(C) Top: schematic of GCN4 protein composed of an activation domain (AD) and DNA-binding domain (DBD). Aromatic residues in the hydrophobic patches of the AD are marked by blue lines. All 11 aromatic residues in the hydrophobic patches were mutated to alanine to generate a GCN4-aromatic mutant. Bottom: representative images of droplet formation showing that the ability of GCN4 aromatic mutant to form droplets with MED15 is attenuated. GCN4-GFP or GCN4-Aromatic mutant-GFP and MED15-mCherry were added to droplet formation at 10 μM each with 125 mM NaCl and 10% PEG-8000.
(D) Representative images of droplet formation showing that GCN4 wild-type but not GCN4 aromatic mutant are incorporated into Mediator complex droplets. 10 μM of GCN4-GFP or GCN4-Aromatic mutant-GFP was mixed with purified Mediator complex in droplet formation buffer with 125 mM NaCl and 10% PEG-8000.
(E) Left: schematic of the Lac assay. A U2OS cell bearing 50,000 repeats of the Lac operon is transfected with a Lac binding domain-CFP-AD fusion protein. Right: IF of MED1 in Lac-U2OS cells transfected with the indicated Lac binding protein construct.
(F) GAL4 activation assay. Transcriptional output as measured by luciferase activity in 293T cells, of the indicated activation domain fused to the GAL4 DBD. Error bars represent SEM.
(G) Model showing TFs and coactivators forming phase-separated condensates at SEs to drive gene activation. In this model, transcriptional condensates incorporate both dynamic and structured interactions.
See also Figure S7 and Table S3.

Chong, S., Dugast-darzacq, C., Liu, Z., Dong, P., and Dailey, G.M. (2017). Dynamic and selective low-complexity domain interactions revealed by live-cell single-molecule imaging. bioRxiv. https://doi.org/10.1101/208710.

Crozat, A., Åman, P., Mandahl, N., and Ron, D. (1993). Fusion of CHOP to a novel RNA-binding protein in human myxoid liposarcoma. Nature *363*, 640–644.

Dai, Y.S., and Markham, B.E. (2001). p300 Functions as a coactivator of transcription factor GATA-4. J. Biol. Chem. *276*, 37178–37185.

Darling, A.L., Liu, Y., Oldfield, C.J., and Uversky, V.N. (2018). Intrinsically disordered proteome of human membrane-less organelles. Proteomics *18*, e1700193.

Das, R.K., Ruff, K.M., and Pappu, R.V. (2015). Relating sequence encoded information to form and function of intrinsically disordered proteins. Curr. Opin. Struct. Biol. *32*, 102–112.

Drysdale, C.M., Dueñas, E., Jackson, B.M., Reusser, U., Braus, G.H., and Hinnebusch, A.G. (1995). The transcriptional activator GCN4 contains multiple activation domains that are critically dependent on hydrophobic amino acids. Mol. Cell. Biol. *15*, 1220–1233.

Dunker, A.K., Bondos, S.E., Huang, F., and Oldfield, C.J. (2015). Intrinsically disordered proteins and multicellular organisms. Semin. Cell Dev. Biol. *37*, 44–55.

Eckner, R., Yao, T.P., Oldread, E., and Livingston, D.M. (1996). Interaction and functional collaboration of p300/CBP and bHLH proteins in muscle and B-cell differentiation. Genes Dev. *10*, 2478–2490.

Frietze, S., and Farnham, P.J. (2011). Transcription factor effector domains. Subcell. Biochem. *52*, 261–277.

Fulton, D.L., Sundararajan, S., Badis, G., Hughes, T.R., Wasserman, W.W., Roach, J.C., and Sladek, R. (2009). TFCat: The curated catalog of mouse and human transcription factors. Genome Biol. *10*, R29.

Gelman, L., Zhou, G., Fajas, L., Raspé, E., Fruchart, J.C., and Auwerx, J. (1999). p300 interacts with the N- and C-terminal part of PPARgamma2 in a ligand-independent and -dependent manner, respectively. J. Biol. Chem. *274*, 7681–7688.

Godowski, P.J., Picard, D., and Yamamoto, K.R. (1988). Signal transduction and transcriptional regulation by glucocorticoid receptor-LexA fusion proteins. Science *241*, 812–816.

Green, M.R. (2005). Eukaryotic transcription activation: Right on target. Mol. Cell *18*, 399–402.

Habchi, J., Tompa, P., Longhi, S., and Uversky, V.N. (2014). Introducing protein intrinsic disorder. Chem. Rev. *114*, 6561–6588.

Herbig, E., Warfield, L., Fish, L., Fishburn, J., Knutson, B.A., Moorefield, B., Pacheco, D., and Hahn, S. (2010). Mechanism of Mediator recruitment by tandem Gcn4 activation domains and three Gal11 activator-binding domains. Mol. Cell. Biol. *30*, 2376–2390.

Hnisz, D., Shrinivas, K., Young, R.A., Chakraborty, A.K., and Sharp, P.A. (2017). A phase separation model for transcriptional control. Cell *169*, 13–23.

Holehouse, A.S., Das, R.K., Ahad, J.N., Richardson, M.O.G., and Pappu, R.V. (2017). CIDER: Resources to analyze sequence-ensemble relationships of intrinsically disordered proteins. Biophys. J. *112*, 16–21.

Hope, I.A., and Struhl, K. (1986). Functional dissection of a eukaryotic transcriptional activator protein, GCN4 of yeast. Cell *46*, 885–894.

Hume, M.A., Barrera, L.A., Gisselbrecht, S.S., and Bulyk, M.L. (2015). UniPROBE, update 2015: New tools and content for the online database of protein-binding microarray data on protein-DNA interactions. Nucleic Acids Res. *43*, D117–D122.

Hyman, A.A., Weber, C.A., and Jülicher, F. (2014). Liquid-liquid phase separation in biology. Annu. Rev. Cell Dev. Biol. *30*, 39–58.

Janicki, S.M., Tsukamoto, T., Salghetti, S.E., Tansey, W.P., Sachidanandam, R., Prasanth, K.V., Ried, T., Shav-Tal, Y., Bertrand, E., Singer, R.H., and Spector, D.L. (2004). From silencing to gene expression: Real-time analysis in single cells. Cell *116*, 683–698.

Jedidi, I., Zhang, F., Qiu, H., Stahl, S.J., Palmer, I., Kaufman, J.D., Nadaud, P.S., Mukherjee, S., Wingfield, P.T., Jaroniec, C.P., and Hinnebusch, A.G. (2010). Activator Gcn4 employs multiple segments of Med15/Gal11, including the KIX domain, to recruit mediator to target genes in vivo. J. Biol. Chem. *285*, 2438–2455.

Jin, W., Wang, L., Zhu, F., Tan, W., Lin, W., Chen, D., Sun, Q., and Xia, Z. (2016). Critical POU domain residues confer Oct4 uniqueness in somatic cell reprogramming. Sci. Rep. *6*, 20818.

Jolma, A., Yan, J., Whitington, T., Toivonen, J., Nitta, K.R., Rastas, P., Morgunova, E., Enge, M., Taipale, M., Wei, G., et al. (2013). DNA-binding specificities of human transcription factors. Cell *152*, 327–339.

Juven-Gershon, T., and Kadonaga, J.T. (2010). Regulation of gene expression via the core promoter and the basal transcriptional machinery. Dev. Biol. *339*, 225–229.

Keegan, L., Gill, G., and Ptashne, M. (1986). Separation of DNA binding from the transcription-activating function of a eukaryotic regulatory protein. Science *231*, 699–704.

Khan, A., Fornes, O., Stigliani, A., Gheorghe, M., Castro-Mondragon, J.A., van der Lee, R., Bessy, A., Chèneby, J., Kulkarni, S.R., Tan, G., et al. (2018). JASPAR 2018: Update of the open-access database of transcription factor binding profiles and its web framework. Nucleic Acids Res. *46* (D1), D260–D266.

Kim, P., Ballester, L.Y., and Zhao, Z. (2017). Domain retention in transcription factor fusion genes and its biological and clinical implications: A pan-cancer study. Oncotarget *8*, 110103–110117.

Kwon, I., Kato, M., Xiang, S., Wu, L., Theodoropoulos, P., Mirzaei, H., Han, T., Xie, S., Corden, J.L., and McKnight, S.L. (2013). Phosphorylation-Regulated Binding of RNA Polymerase II to Fibrous Polymers of Low-Complexity Domains. Cell *155*, 1049–1060.

Latysheva, N.S., Oates, M.E., Maddox, L., Flock, T., Gough, J., Buljan, M., Weatheritt, R.J., and Babu, M.M. (2016). Molecular principles of gene fusion mediated rewiring of protein interaction networks in cancer. Mol. Cell *63*, 579–592.

Lech, K., Anderson, K., and Brent, R. (1988). DNA-bound Fos proteins activate transcription in yeast. Cell *52*, 179–184.

Lin, Y., Protter, D.S.W., Rosen, M.K., and Parker, R. (2015). Formation and maturation of phase-separated liquid droplets by RNA-binding proteins. Mol. Cell *60*, 208–219.

Liu, J., Perumal, N.B., Oldfield, C.J., Su, E.W., Uversky, V.N., and Dunker, A.K. (2006). Intrinsic disorder in transcription factors. Biochemistry *45*, 6873–6888.

Liu, W.-L., Coleman, R.A., Ma, E., Grob, P., Yang, J.L., Zhang, Y., Dailey, G., Nogales, E., and Tjian, R. (2009). Structures of three distinct activator-TFIID complexes. Genes Dev. *23*, 1510–1521.

Malik, S., and Roeder, R.G. (2010). The metazoan Mediator co-activator complex as an integrative hub for transcriptional regulation. Nat. Rev. Genet. *11*, 761–772.

Manavathi, B., Samanthapudi, V.S.K., and Gajulapalli, V.N.R. (2014). Estrogen receptor coregulators and pioneer factors: The orchestrators of mammary gland cell fate and development. Front. Cell Dev. Biol. *2*, 34.

Merika, M., Williams, A.J., Chen, G., Collins, T., and Thanos, D. (1998). Recruitment of CBP/p300 by the IFN beta enhanceosome is required for synergistic activation of transcription. Mol. Cell *1*, 277–287.

Meyer, K.D., Donner, A.J., Knuesel, M.T., York, A.G., Espinosa, J.M., and Taatjes, D.J. (2008). Cooperative activity of cdk8 and GCN5L within Mediator directs tandem phosphoacetylation of histone H3. EMBO J. *27*, 1447–1457.

Mitchell, P.J., and Tjian, R. (1989). Transcriptional regulation in mammalian cells by sequence-specific DNA binding proteins. Science *245*, 371–378.

Nabet, B., Roberts, J.M., Buckley, D.L., Paulk, J., Dastjerdi, S., Yang, A., Leggett, A.L., Erb, M.A., Lawlor, M.A., Souza, A., et al. (2018). The dTAG system for immediate and target-specific protein degradation. Nat. Chem. Biol. *14*, 431–441.

Nott, T.J., Petsalaki, E., Farber, P., Jervis, D., Fussner, E., Plochowietz, A., Craggs, T.D., Bazett-Jones, D.P., Pawson, T., Forman-Kay, J.D., and Baldwin,

A.J. (2015). Phase transition of a disordered nuage protein generates environmentally responsive membraneless organelles. Mol. Cell *57*, 936–947.

Oates, M.E., Romero, P., Ishida, T., Ghalwash, M., Mizianty, M.J., Xue, B., Dosztányi, Z., Uversky, V.N., Obradovic, Z., Kurgan, L., et al. (2013). D^2P^2: Database of disordered protein predictions. Nucleic Acids Res. *41*, D508–D516.

Oldfield, C.J., and Dunker, A.K. (2014). Intrinsically disordered proteins and intrinsically disordered protein regions. Annu. Rev. Biochem. *83*, 553–584.

Oliner, J.D., Andresen, J.M., Hansen, S.K., Zhou, S., and Tjian, R. (1996). SREBP transcriptional activity is mediated through an interaction with the CREB-binding protein. Genes Dev. *10*, 2903–2911.

Oliviero, S., Robinson, G.S., Struhl, K., and Spiegelman, B.M. (1992). Yeast GCN4 as a probe for oncogenesis by AP-1 transcription factors: Transcriptional activation through AP-1 sites is not sufficient for cellular transformation. Genes Dev. *6*, 1799–1809.

Panne, D., Maniatis, T., and Harrison, S.C. (2007). An atomic model of the interferon-β enhanceosome. Cell *129*, 1111–1123.

Patel, A., Lee, H.O., Jawerth, L., Maharana, S., Jahnel, M., Hein, M.Y., Stoynov, S., Mahamid, J., Saha, S., Franzmann, T.M., et al. (2015). A liquid-to-solid phase transition of the ALS protein FUS accelerated by disease mutation. Cell *162*, 1066–1077.

Plaschka, C., Nozawa, K., and Cramer, P. (2016). Mediator architecture and RNA polymerase II interaction. J. Mol. Biol. *428*, 2569–2574.

Ransone, L.J., Wamsley, P., Morley, K.L., and Verma, I.M. (1990). Domain swapping reveals the modular nature of Fos, Jun, and CREB proteins. Mol. Cell. Biol. *10*, 4565–4573.

Reiter, F., Wienerroither, S., and Stark, A. (2017). Combinatorial function of transcription factors and cofactors. Curr. Opin. Genet. Dev. *43*, 73–81.

Roberts, S.G. (2000). Mechanisms of action of transcription activation and repression domains. Cell. Mol. Life Sci. *57*, 1149–1160.

Sabari, B.R., Dall'Agnese, A., Boija, A., Klein, I.A., Coffey, E.L., Shrinivas, K., Abraham, B.J., Hannett, N.M., Zamudio, A.V., Manteiga, J.C., et al. (2018). Coactivator condensation at super-enhancers links phase separation and gene control. Science *361*, 80.

Sadowski, I., Ma, J., Triezenberg, S., and Ptashne, M. (1988). GAL4-VP16 is an unusually potent transcriptional activator. Nature *335*, 563–564.

Saint-andré, V., Federation, A.J., Lin, C.Y., Abraham, B.J., Reddy, J., Lee, T.I., Bradner, J.E., and Young, R.A. (2016). Models of human core transcriptional regulatory circuitries. Genome Res. *26*, 385–396.

Schindelin, J., Arganda-Carreras, I., Frise, E., Kaynig, V., Longair, M., Pietzsch, T., Preibisch, S., Rueden, C., Saalfeld, S., Schmid, B., et al. (2012). Fiji: an open-source platform for biological-image analysis. Nat. Methods *9*, 676–682.

Shin, Y., and Brangwynne, C.P. (2017). Liquid phase condensation in cell physiology and disease. Science. Published online September 22, 2017. https://doi.org/10.1126/science.aaf4382.

Sigler, P.B. (1988). Transcriptional activation. Acid blobs and negative noodles. Nature *333*, 210–212.

Soutourina, J. (2018). Transcription regulation by the Mediator complex. Nat. Rev. Mol. Cell Biol. *19*, 262–274.

Staby, L., O'Shea, C., Willemoës, M., Theisen, F., Kragelund, B.B., and Skriver, K. (2017). Eukaryotic transcription factors: Paradigms of protein intrinsic disorder. Biochem. J. *474*, 2509–2532.

Staller, M.V., Holehouse, A.S., Swain-Lenz, D., Das, R.K., Pappu, R.V., and Cohen, B.A. (2018). A high-throughput mutational scan of an intrinsically disordered acidic transcriptional activation domain. Cell Syst. *6*, 444–455.

Struhl, K. (1988). The JUN oncoprotein, a vertebrate transcription factor, activates transcription in yeast. Nature *332*, 649–650.

Taatjes, D.J. (2010). The human Mediator complex: A versatile, genome-wide regulator of transcription. Trends Biochem. Sci. *35*, 315–322.

Taatjes, D.J. (2017). Transcription factor-mediator interfaces: Multiple and multi-valent. J. Mol. Biol. *429*, 2996–2998.

Tompa, P., and Fuxreiter, M. (2008). Fuzzy complexes: Polymorphism and structural disorder in protein-protein interactions. Trends Biochem. Sci. *33*, 2–8.

Tora, L., White, J., Brou, C., Tasset, D., Webster, N., Scheer, E., and Chambon, P. (1989). The human estrogen receptor has two independent nonacidic transcriptional activation functions. Cell *59*, 477–487.

Triezenberg, S.J. (1995). Structure and function of transcriptional activation domains. Curr. Opin. Genet. Dev. *5*, 190–196.

Tuttle, L.M., Pacheco, D., Warfield, L., Luo, J., Ranish, J., Hahn, S., and Klevit, R.E. (2018). Gcn4-mediator specificity is mediated by a large and dynamic fuzzy protein-protein complex. Cell Rep. *22*, 3251–3264.

Uversky, V.N. (2017). Intrinsically disordered proteins in overcrowded milieu: Membrane-less organelles, phase separation, and intrinsic disorder. Curr. Opin. Struct. Biol. *44*, 18–30.

van der Lee, R., Buljan, M., Lang, B., Weatheritt, R.J., Daughdrill, G.W., Dunker, A.K., Fuxreiter, M., Gough, J., Gsponer, J., Jones, D.T., et al. (2014). Classification of intrinsically disordered regions and proteins. Chem. Rev. *114*, 6589–6631.

Vaquerizas, J.M., Kummerfeld, S.K., Teichmann, S.A., and Luscombe, N.M. (2009). A census of human transcription factors: Function, expression and evolution. Nat. Rev. Genet. *10*, 252–263.

Warfield, L., Tuttle, L.M., Pacheco, D., Klevit, R.E., and Hahn, S. (2014). A sequence-specific transcription activator motif and powerful synthetic variants that bind Mediator using a fuzzy protein interface. Proc. Natl. Acad. Sci. USA *111*, E3506–E3513.

Weintraub, A.S., Li, C.H., Zamudio, A.V., Sigova, A.A., Hannett, N.M., Day, D.S., Abraham, B.J., Cohen, M.A., Nabet, B., Buckley, D.L., et al. (2017). YY1 Is a structural regulator of enhancer-promoter loops. Cell *171*, 1573–1588.

Wheeler, R.J., and Hyman, A.A. (2018). Controlling compartmentalization by non-membrane-bound organelles. Philos. Trans. R. Soc. Lond. B Biol. Sci. *26*, 373.

Whyte, W.A., Orlando, D.A., Hnisz, D., Abraham, B.J., Lin, C.Y., Kagey, M.H., Rahl, P.B., Lee, T.I., and Young, R.A. (2013). Master transcription factors and mediator establish super-enhancers at key cell identity genes. Cell *153*, 307–319.

Winters, A.C., and Bernt, K.M. (2017). MLL-rearranged leukemias—An update on science and clinical approaches. Front Pediatr. *5*, 4.

Wright, P.E., and Dyson, H.J. (2015). Intrinsically disordered proteins in cellular signalling and regulation. Nat. Rev. Mol. Cell Biol. *16*, 18–29.

Yin, J.W., and Wang, G. (2014). The Mediator complex: A master coordinator of transcription and cell lineage development. Development *141*, 977–987.

Yuan, W., Condorelli, G., Caruso, M., Felsani, A., and Giordano, A. (1996). Human p300 protein is a coactivator for the transcription factor MyoD. J. Biol. Chem. *271*, 9009–9013.

AACR American Association for Cancer Research

ANNUAL MEETING 2020 • SAN DIEGO

APRIL 24-29

TURNING SCIENCE INTO LIFESAVING CARE

Join us in San Diego for the latest innovative and inspiring cancer research from around the world...**the AACR ANNUAL MEETING 2020!**

Late-Breaking Abstracts and Clinical Trials Abstract Submission Deadline: Thursday, January 30, 2020

Advance Registration Deadline: Friday, February 21, 2020

Become a Member!
Join the AACR and receive a discount on registration.

ABIM CME MOC ACCREDITED — Continuing Medical Education Activity - *AMA PRA Category 1 Credits™* available

The AACR Annual Meeting highlights the work of the greatest minds in cancer science and medicine from institutions all over the world. This meeting presents the many scientific discoveries across the breadth of cancer research—from prevention, early detection, and interception; to cancer biology, translational, and clinical studies; to survivorship, population science, and advocacy. This year's program, with the theme of "Turning Science into Lifesaving Care," will be a comprehensive, cutting-edge scientific event that you will not want to miss!

We look forward to seeing you!

AACR.ORG • #AACR20

1901031N

Resource

Cell

Extensive Unexplored Human Microbiome Diversity Revealed by Over 150,000 Genomes from Metagenomes Spanning Age, Geography, and Lifestyle

Edoardo Pasolli,[1] Francesco Asnicar,[1,8] Serena Manara,[1,8] Moreno Zolfo,[1,8] Nicolai Karcher,[1] Federica Armanini,[1] Francesco Beghini,[1] Paolo Manghi,[1] Adrian Tett,[1] Paolo Ghensi,[1] Maria Carmen Collado,[2] Benjamin L. Rice,[3] Casey DuLong,[4] Xochitl C. Morgan,[5] Christopher D. Golden,[4] Christopher Quince,[6] Curtis Huttenhower,[4,7] and Nicola Segata[1,9,*]

[1]CIBIO Department, University of Trento, Trento, Italy
[2]Institute of Agrochemistry and Food Technology-National Research Council, Valencia, Spain
[3]Harvard University, Cambridge, MA, USA
[4]Harvard T.H. Chan School of Public Health, Boston, MA, USA
[5]University of Otago, Otago, New Zealand
[6]Warwick Medical School, University of Warwick, Warwick, UK
[7]The Broad Institute, Cambridge, MA, USA
[8]These authors contributed equally
[9]Lead Contact
*Correspondence: nicola.segata@unitn.it
https://doi.org/10.1016/j.cell.2019.01.001

SUMMARY

The body-wide human microbiome plays a role in health, but its full diversity remains uncharacterized, particularly outside of the gut and in international populations. We leveraged 9,428 metagenomes to reconstruct 154,723 microbial genomes (45% of high quality) spanning body sites, ages, countries, and lifestyles. We recapitulated 4,930 species-level genome bins (SGBs), 77% without genomes in public repositories (unknown SGBs [uSGBs]). uSGBs are prevalent (in 93% of well-assembled samples), expand underrepresented phyla, and are enriched in non-Westernized populations (40% of the total SGBs). We annotated 2.85 M genes in SGBs, many associated with conditions including infant development (94,000) or Westernization (106,000). SGBs and uSGBs permit deeper microbiome analyses and increase the average mappability of metagenomic reads from 67.76% to 87.51% in the gut (median 94.26%) and 65.14% to 82.34% in the mouth. We thus identify thousands of microbial genomes from yet-to-be-named species, expand the pangenomes of human-associated microbes, and allow better exploitation of metagenomic technologies.

INTRODUCTION

Despite extensive recent studies of the human microbiome using a variety of culture-independent molecular technologies (Human Microbiome Project Consortium, 2012; Qin et al., 2010; Quince et al., 2017a; Rinke et al., 2013), most characterization of these ecosystems is still focused on microbes that are easily cultivable, particularly when those with sequenced isolate genomes are considered. Since physiological characterization of diverse, uncharacterized human-associated microbes by cultivation can be difficult in high throughput (Browne et al., 2016), additional approaches are needed that scale with the extent of populations that can now be surveyed using metagenomic sequencing. Culture-independent genomic approaches that are scalable to large cohorts (Human Microbiome Project Consortium, 2012; Qin et al., 2010; Quince et al., 2017a) have facilitated access to an expanded set of isolation-recalcitrant members of the microbiome, but they also suggested the presence of a large fraction of still unexplored diversity (Nielsen et al., 2014; Rinke et al., 2013).

Here, we present a set of 154,723 microbial genomes that are often prevalent, population specific, and/or geographically specific that we reconstructed via single-sample assembly from a total of 9,428 global, body-wide metagenomes. Other studies have also succeeded in reconstructing microbial genomes by metagenomic assembly on single human cohorts (Bäckhed et al., 2015; Brooks et al., 2017; Ferretti et al., 2018; Human Microbiome Project Consortium, 2012; Raveh-Sadka et al., 2015; Sharon et al., 2013), but systematic cross-study cataloging of metagenomically assembled genomes focused so far on non-human environments (Oyama et al., 2017; Parks et al., 2017). Complementary techniques, such as co-abundance of gene groups (Nielsen et al., 2014), can identify genomic bins without reference, but these techniques do not account for sample-specific strains and strain-level differences in the sequence reconstruction and thus require downstream single-nucleotide variation analysis on specific genomic regions to uncover strain variability (Quince et al., 2017b; Truong et al., 2017).

Using large-scale single-sample metagenomic assembly supported by strict quality control (including filtering based on nucleotide polymorphisms), we identified 3,796 species-level clades (comprising 34,205 genomes) without previous whole-genome

information. This identified several taxa prevalent but previously unobserved even in well-profiled populations (e.g., a genus-level Ruminococcaceae clade phylogenetically close to *Faecalibacterium*), extensive taxonomically uncharacterized species associated with non-Western populations, and the presence of several taxa from undersampled phyla (e.g., Saccharibacteria and Elusimicrobia) in oral and gut microbiomes. The resulting genome set can thus serve as the basis for future strain-specific comparative genomics to associate variants in the human microbiome with environmental exposures and health outcomes across the globe.

RESULTS

Recovering Over 150,000 Microbial Genomes from ~10,000 Human Metagenomes

We employed a very large-scale metagenomic assembly approach to reconstruct bacterial and archaeal genomes populating the human microbiome (see STAR Methods). From a total of 9,316 metagenomes spanning 46 datasets from multiple populations, body sites, and host ages (Table S1), and an additional cohort from Madagascar (Golden et al., 2017) (STAR Methods; Table S1), we reconstructed a total of 154,723 genomes (each made up of a group of clustered contigs; see STAR Methods) using a single-sample assembly strategy tailored at maximizing the quality rather than the quantity of genomes reconstructed from each sample. The resulting catalog greatly expands the set of ~150,000 microbial genomes publicly available (see STAR Methods). All assembled genomes passed strict quality control including estimation of completeness, contamination, and a measure of strain heterogeneity (see STAR Methods), and they exceed the thresholds to be defined medium quality (MQ) according to recent guidelines (Bowers et al., 2017) (completeness >50%, contamination <5%). The quality of these genomes was comparable with that of isolate sequencing (STAR Methods; Table S2) and in line also with the quality achievable by manually curated metagenomic approaches (Table S2) and time-series or cross-sectional metagenomic co-binning (see STAR Methods; Table S2). Genomes may include contigs from plasmids (see STAR Methods), and stricter quality control reduced the set of near-complete, high-quality (HQ) genomes to 70,178 with completeness higher than 90% and reduced probability of intra-sample strain heterogeneity (<0.5% polymorphic positions, see STAR Methods). The main characteristics of HQ genomes are in line and in some cases better than those from the compendium of reference genomes available in public repositories, although MQ genomes also had similar quality scores compared to HQ genomes (modulo completeness; STAR Methods). The set of genomes we reconstructed (Table S3; Data and Software Availability) and the associated 2.85 million (M) total functional annotations (STAR Methods; Figure S1) are thus appropriate as a basis for more in-depth microbial community analyses.

Human Microbiome Genomes Belong to ~5,000 Functionally Annotated SGBs

To organize the 154,723 genomes into species-level genome bins (SGBs), we employed an all-versus-all genetic distance quantification followed by clustering and identification of genome bins spanning a 5% genetic diversity, which is consistent with the definition of known species (see STAR Methods) and with other reports (Jain et al., 2018). We obtained 4,930 SGBs from 22 known phyla (Figure 1A; Table S4). This is likely an underestimate of the total phylum-level diversity, because some SGBs are very divergent from all previously available reference genomes and cannot be confidently assigned to a taxonomic family (Table S4): 345 SGBs (58% of which with HQ or multiple reconstructed genomes) display more than 30% Mash-estimated genetic distance (Ondov et al., 2016) from the closest isolate with a phylum assignment (Figure S2A). The SGB genomic catalog spans on average 3.0%, SD 1.8% intra-SGB nucleotide genetic variability, and each SGB contains up to 3,457 genomes from different individuals (average 31.4, SD 147.6; Figures 1C and S2B).

Functional annotation of all the reconstructed genomes assigned a UniRef90 (The UniProt Consortium, 2017) label to 230 M genes and a UniRef50 to 268 M genes (72.7% and 84.8% of the total of 316 M genes, respectively). Additional EggNOG (Huerta-Cepas et al., 2017) labels were assigned to 80.8% of the 4,930 SGBs' genome representatives. The functional potential profiles of the genomes had, as expected, clear phylogenetic differentiation (Figure S1), and the rate of annotation varied greatly in SGBs (e.g., >90% genes annotated for well-studies species such as *Escherichia coli* or *Bacteroides fragilis* versus 22% for ID 15286, which is the largest SGB without reference genomes). Each of the body sites considered had a clear distinctive set of annotations with the adult fecal microbiome enriched for 101,056 gene families (Table S5, Bonferroni-corrected Fisher's test $p < 0.01$), representative of anaerobe-specific functions such as formate oxidation and methanogenesis and a strong representation of biofilm formation functions in the oral cavity and on the skin. Genomes from the stool microbiome of newborns had 94,562 enriched gene families (Table S5, Bonferroni-corrected Fisher's test $p < 0.01$) comprising a variety of functions such as folate biosynthesis and lactose, oligosaccharides, and mucin degradation that are typical of the niche and nutritional regime of unweaned infants (Asnicar et al., 2017; Marcobal et al., 2011; Yatsunenko et al., 2012). Age-specific functions (Table S5) are characterized by the later host developmental stages of children (17,121 specific functions) and school-age individuals (349 specific functions). The Westernization process has also a strong influence on the functions encoded in the stool microbiome, with a total of 106,872 differential families (Table S5, Bonferroni-corrected Fisher's test $p < 0.01$) spanning enzymes involved in the metabolism of complex carbohydrates, such as xylose and cellulose, and in specific cobalamin biosynthesis pathways; these are likely reflecting dietary habits, among other environmental differences. The organization of the reconstructed genomes in SGBs and their functional profiling will be the basis for comprehensive future metagenomic characterizations.

The Reconstructed Genomes and SGBs Increase the Diversity and Mappability of the Human Microbiome

We identified 3,796 SGBs (i.e., 77.0% of the total) covering unexplored microbial diversity as they represent species without any publicly available genomes from isolate sequencing or previous metagenomic assemblies (Figures 1B and S3A). These SGBs, that we named unknown SGBs (uSGBs), include on average

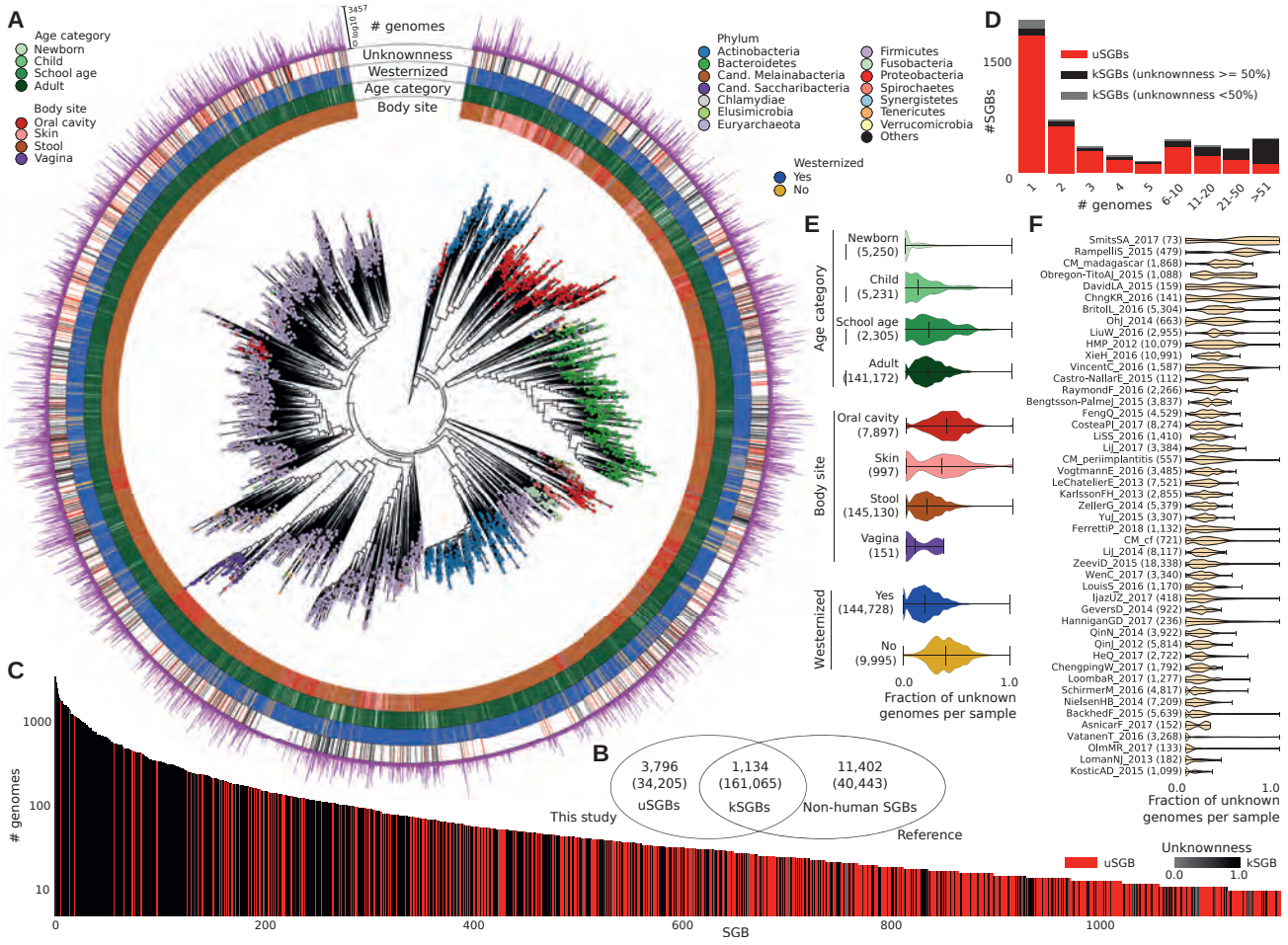

Figure 1. 4,930 SGBs Assembled from 9,428 Meta-analyzed Body-wide Metagenomes

(A) A human-associated microbial phylogeny of representative genomes from each species-level genome bin (SGB). Figure S3A reports the same phylogeny but including isolate genomes not found in the human-associated metagenomes.

(B) Overlap of SGBs containing both existing microbial genomes (including other metagenomic assemblies) and genomes reconstructed here (kSGBs), SGBs with only genomes reconstructed here and without existing isolate or metagenomically assembled genomes (uSGBs), and SGBs with only existing genomes and no genomes from our metagenomic assembly of human microbiomes (non-human SGBs).

(C) Many SGBs contain no genomes from sequenced isolates or publicly available metagenomic assemblies (uSGBs). Only SGBs containing >10 genomes are shown.

(D) Fraction of uSGBs and kSGBs as a function of the size of the SGBs (i.e., number of genomes in the SGB).

(E) Distribution of the fraction of uSGBs in each sample by age category, body site, and lifestyle.

(F) Distribution of the fraction of uSGBs in each study.

9.0, SD 45.4 reconstructed genomes, and 1,693 of them (45%) had at least one HQ genome. Recursive clustering of SGBs' representatives at genus- and family-level genetic divergence (see STAR Methods) provided taxonomic context for 75.2% of the uSGBs with 1,472 assignments to genera and 1,383 more to families (Table S4). The 941 uSGBs that were left unplaced at family level remained unassigned for limitations of whole-genome similarity estimates, but we report the similarity and taxonomy of the closest matching strain (Table S4).

Only 1,134 of the 4,930 SGBs represent at least partially known SGBs (kSGBs) that include one or more genomes in public databases. This number of kSGBs is consistent with the 1,266 species we found at least once in the same set of metagenomes (Pasolli et al., 2017) at >0.01% abundance using reference-based taxonomic profiling (Truong et al., 2015). Most uSGBs represent instead relatively rare human-associated microbes (46.7% of uSGBs comprise one reconstructed genome only, Table S4, and 46.1% genomes in uSGBs are at <0.5% relative abundance, STAR Methods and Table S4), but some uSGBs are highly prevalent, with 10 uSGBs in the set of the 100 SGBs with the largest number of reconstructed genomes (Figures 1C, 1D, and S2B) and 368 genomes in uSGBs accounting for >10% of reads. Because many uSGBs are associated with specific sample types (e.g., oral cavity or non-Westernized samples, Figure 1E), the actual number of possibly redundant genomes they contain is likely underestimated for those sample

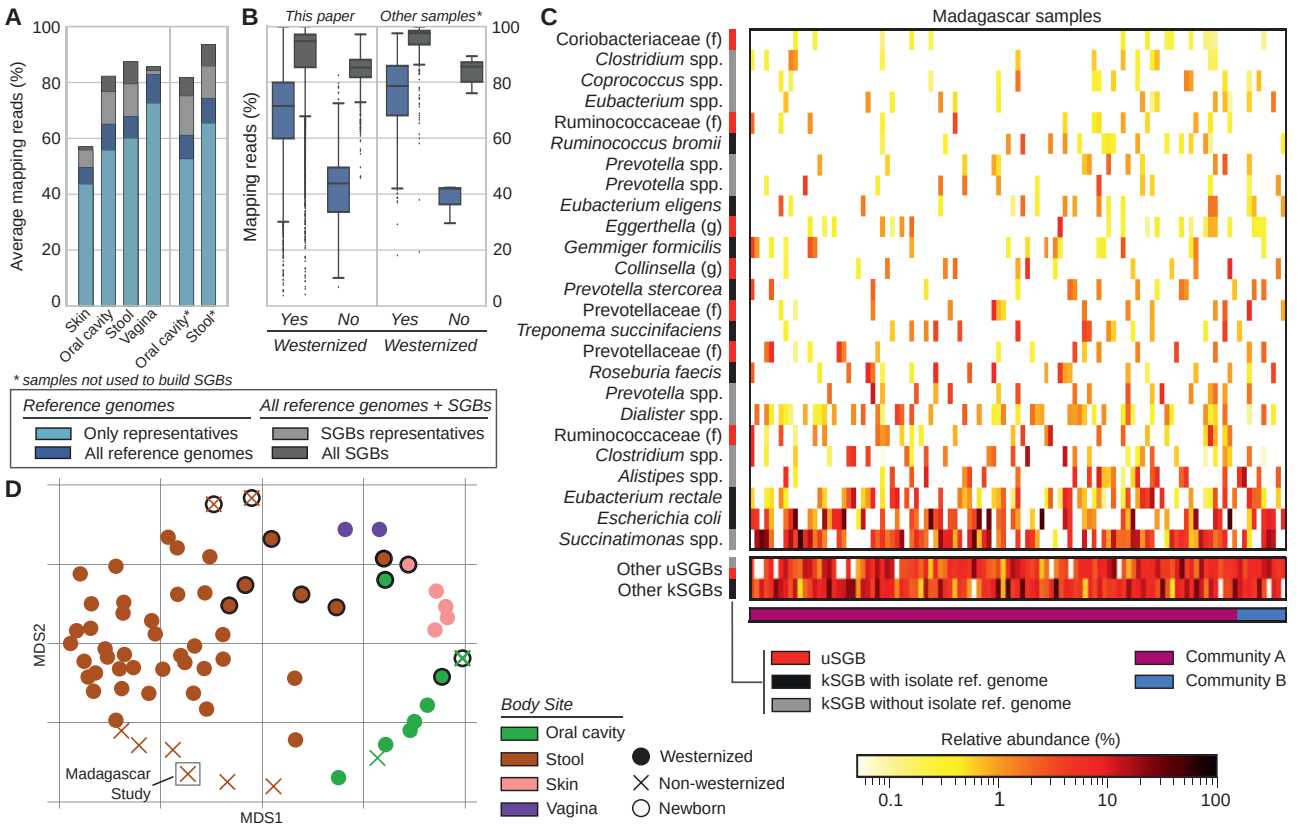

Figure 2. The Expanded Genome Set Substantially Increases the Mappability of Human Metagenomes

(A) We mapped the subsampled original 9,428 metagenomes and 389 additional samples not considered for building the SGBs against the 154,723 reconstructed genomes and 80,990 previously available genomes. Raw-read mappability increased significantly (Mann-Whitney U test, $p < 1e{-}50$), e.g., from an average of 67.76% to 87.51% in the gut. Representative genomes refer to the highest-quality genomes selected from the 4,930 human SGBs and the 11,402 non-human SGBs. Extended statistics are in Figure S4.

(B) Metagenomic read mappability increases more in non-Westernized than Westernized gut microbiomes (Welch's t test, $p < 1e{-}50$), both when considering samples used for SGBs' reconstruction (26.50% average increase in 7,059 Westernized samples versus 96.56% in 454 non-Westernized samples) and when considering 264 additional samples not used for SGBs' reconstruction (25.16% versus 117.40% average increase, respectively).

(C) The gut microbiomes from Madagascar we sequenced here showed several highly abundant uSGBs and a large set of SGBs reconstructed in only subsets of the samples. Many kSGBs in this dataset do not contain isolate genomes but only previous metagenomic assemblies. The 25 most abundant SGBs are reported and ordered according to their average relative abundance.

(D) Multidimensional scaling on datasets using the Bray-Curtis distance on per-dataset SGB prevalences highlights distinct microbial communities between Westernized and non-Westernized populations within and between body sites and age categories.

types with comparably fewer metagenomes available. Functional annotation of uSGB genomes assigned a UniRef90 cluster to only 31.9% of the genes, while the annotation rate increased to 81.0% for kSGB genomes.

The expanded human microbiome diversity induced by the uSGBs (200% increase in the reconstructed phylogenetic branch length, 50% considering only uSGBs with >10 genomes, Figure 1A) can be crucial as a genomic reference in the characterization ("mappability") of the sequence information in a metagenome. Genomes in uSGBs are indeed responsible for a substantial decrease of the metagenomic reads that do not match any microbial reference (Figures 2A and S4). This is due both to uSGBs representing target microbes without assigned species (16.76% average increase using only representative genomes of uSGBs, Figure 2A) and to the expansion of pangenomes of kSGBs and uSGBs (27.84% increase when considering all genomes instead of only SGB representatives). On average, the read mappability for stool samples reached 87.51% (29.14% increase, Figure 2A) and 82.34% in the oral cavity (26.40% increase, Figure 2A). Some outlier samples decreased the averages as the median final mappabilities were higher, reaching 94.26% for the stool microbiome and 90.13% for the oral microbiome in Westernized populations. The mappability of the skin microbiome was also increased (15.17% increase) but reached a lower overall value (57.07%) because fewer skin samples were available and non-bacterial organisms such as the molluscum contagiosum virus (Oh et al., 2014) and fungi from the *Malassezia* genus (Tett et al., 2017) also populate the skin. Mappability in the vaginal microbiomes was instead already high (82.77%) due to a reduced panel of known species dominating the large majority of these communities, but the set of 4,930 reconstructed SGBs still increased the mappability by

3.42%. The mappability increase is dramatic for the gut microbiomes of non-Westernized populations that are very poorly represented by available reference genomes (42.33% mappability) and can now reach a mappability of 83.20%, which is comparable with that of Westernized populations (Figure 2B). These substantial gains in read mappability when using our genome catalog are achieved also for stool and oral samples not used to construct the resource (STAR Methods; Figures 2A and 2B), confirming its relevance as reference for future studies.

SGBs without publicly available genomes (uSGBs) represent 34,205 reconstructed genomes (Figure 1B), belonging to metagenomes in different body sites, ages, and general lifestyles (Figures 1E and 1F). Microbiomes with lower diversity, such as those from infants or the female urogenital tract, carried a generally lower fraction of uSGBs. Populations with non-Westernized lifestyles—including the Madagascar cohort we sequenced (Figures 2C and 2D)—conversely yielded a fraction of genomes in uSGBs nearly double that of Western-style populations (average 40% and 21%, respectively, $p < 1e{-}50$, Figure 1E). Most of the abundant kSGBs in the Madagascar cohort do not include isolate genomes but only sequences from previous metagenomic assemblies (Figure 2C), and these uSGBs and poorly characterized kSGBs are contributing to the clear distinction of the gut microbiome with respect to general lifestyles (Figure 2D). The higher rate of uSGB recovery in non-Westernized populations is likely the consequence of comparatively fewer studies profiling these populations and their more diverse gut microbiomes.

The Diversity of Human-Associated Archaea and Bacterial Phyla Is Expanded by uSGBs

Many clades, including some phyla, were greatly expanded by reconstructed genomes belonging to species that do not have deposited genome sequences or taxonomic labels (uSGBs). For example, the candidate phylum Saccharibacteria (previously named TM7) contains members of the oral microbiome that are particularly difficult to cultivate (He et al., 2015; Solden et al., 2016). For this clade, we reconstructed 387 genomes from 108 SGBs (Figure 1A), some representing members observed only using 16S rRNA gene sequencing (Brinig et al., 2003; Segata et al., 2012a). An isolate reference genome was only available for a single SGB within this clade (ID 19849); the other 16 reference genomes for this phylum were undetected in oral cavity metagenomes (Figure S3B). The 107 Saccharibacteria uSGBs thus suggest a substantially undersampled diversity of human-associated members of this phylum. Its importance is also confirmed by the occurrence of at least one genome from these 108 SGBs in 33% of oral cavity samples, where they can reach average abundances above 3% (Table S4) and maximum abundances exceeding 10%.

We further recovered 675 genomes of Archaea (526 from 6 kSGBs and 149 from 13 uSGBs, Figure 1A) and reconstructed its phylogeny (Figure S3C). More than half of these genomes (n = 487) belonged to the *Methanobrevibacter smithii* kSGB (ID 714), which was present at relatively low abundance (average 1.06%, SD 1.26%). A related but diverged SGB including 94 genomes was identified (ID 713, 5.6% nucleotide divergence from the *M. smithii* isolate genome) at comparable abundance (average 0.92%, SD 2.02%), but it notably accounted for up to 20% of all reads in some gut samples. Among uSGBs, we also reconstructed genomes assigned to *Thermoplasmatales* (ID 376, 378, 380, 381), Candidatus *Methanomethylophilus* (ID 372, 382, 384), *Methanomassiliicoccus* (ID 362, 364), and *Methanosphaera* (ID 697), all very distant from their nearest reference genomes (average 22.4%, SD 4.0% nucleotide distance). This expanded human-associated archaeal diversity suggests the presence of several as-yet-uncharacterized archaea of potentially unique functional relevance in this ecosystem.

Several Prevalent Uncharacterized Intestinal Clostridiales Clades Occur Phylogenetically between Ruminococcus and Faecalibacterium

Some of the uSGBs with the largest number of reconstructed genomes are also highly abundant in the gut microbiome, with 1,153 uSGBs totaling >13,000 genomes each present in the sample where it has been reconstructed at an average abundance >1% (and 172 uSGBs at >5% average abundance). Among them, uSGB ID 15286, that we named "*Candidatus* Cibiobacter qucibialis", is the most prevalent uSGB, comprising 1,813 reconstructed genomes. This species is phylogenetically placed between *Faecalibacterium* and *Ruminococcus* (Figures 3A and S5A), key members of the gut microbiome that are typically present at comparably lower abundances (1.84% *Faecalibacterium* kSGB and 1.29% *Ruminococcus* kSBG in contrast to 2.47% *Ca.* Cibiobacter qucibialis). Six other prevalent (1,563 total genomes) and abundant (1.14% average abundance) SGBs occurred monophyletically in the same subtree between faecalibacteria and ruminococci (Figure 3A). Only one of these seven total SGBs contains an isolate genome, which is the recently sequenced *Gemmiger formicilis* genome (Gossling and Moore, 1975) included in kSGB ID 15300 (1,212 genomes, Figures 3A and 3B). A genome from the *Subdoligranulum variabile* species, itself not found in any of the study's assemblies, was the only other reference phylogenetically close to this clade, explaining the previous identification of an unknown *Subdoligranulum* ("*Subdoligranulum* unclassified") as the most prevalent single taxon in reference-based profiles of the gut microbiome (Pasolli et al., 2017). This prevalent 7-SGBs clade comprising 3,370 reconstructed genomes that can be very abundant (>5% relative abundance in >200 samples) is thus an important but so far neglected genus-level lineage in the human microbiome.

In an estimated maximum-likelihood whole-genome phylogeny of the 1,813 genomes belonging to *Ca.* Cibiobacter qucibialis (Figure 3C), genomes of non-Westernized populations were placed together in a monophyletic subtree (Figure 3C). This subtree included 26 strains from the Madagascar microbiomes we sequenced in this work, in addition to strains from three other populations with traditional lifestyles but differing geographic locations (Figure 3D). Although the non-Westernized subtree includes few genomes (2% of the total), this is a consequence of limited sampling from these population types because the prevalence of this SGB in Westernized populations is comparable (23% against 15% in non-Westernized populations). No clear internal clustering was evident for Westernized samples (Figure 3C), except for a large set of 222 samples retrieved from

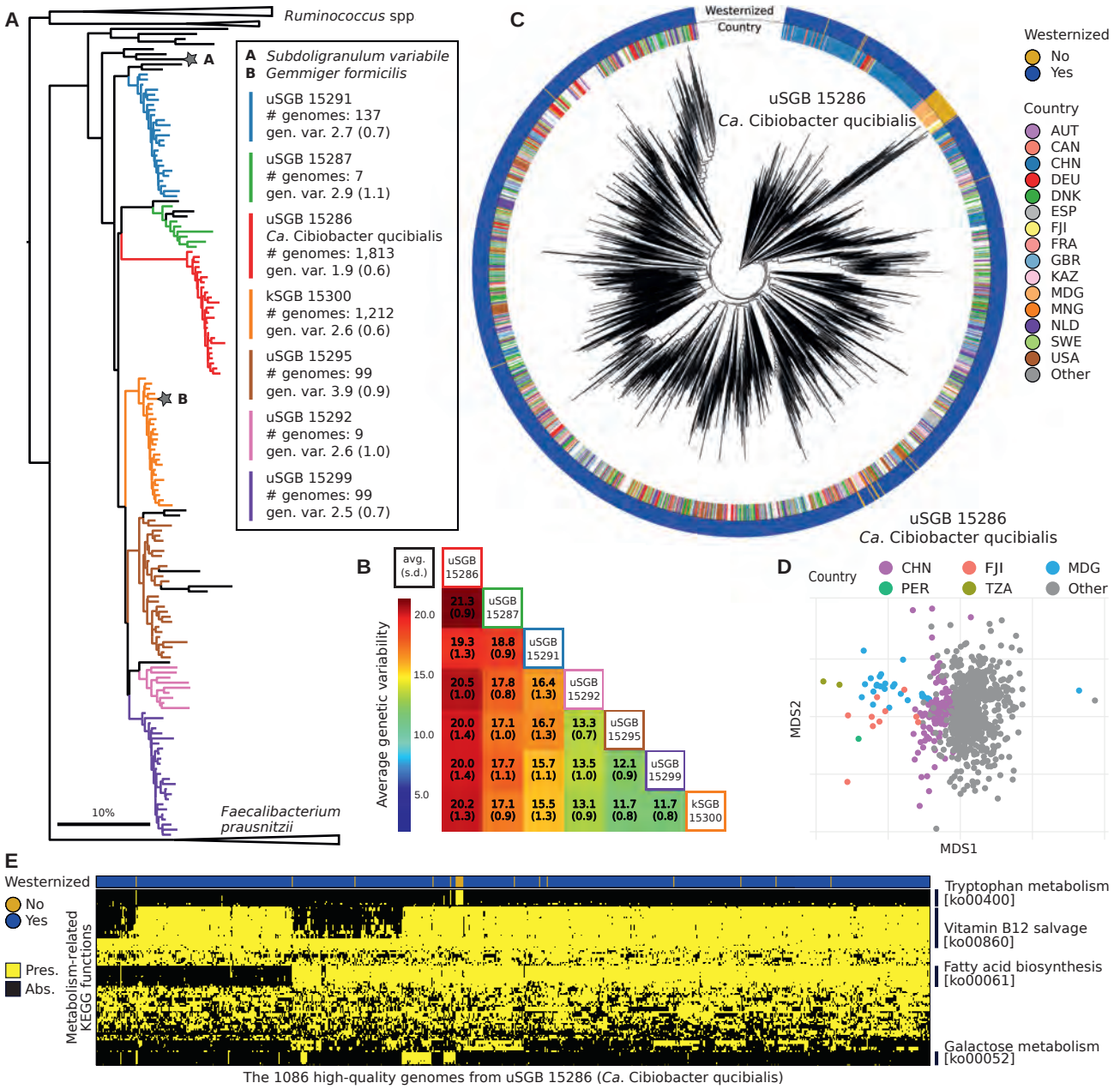

Figure 3. Several Prevalent Intestinal uSGBs Are Found within the Clostridiales Order Related to *Ruminococcus* and *Faecalibacterium*

(A) All SGBs in the assembled phylogeny (Figure 1A) placed between reference genomes for *Ruminococcus* and *Faecalibacterium* species that are reported as collapsed trees. A maximum of 25 HQ genomes from each SGB are displayed, and SGBs with <3 genomes are left black.

(B) The monophyletic clade with the six uSGBs and the kSGB containing *Gemmiger formicilis* represent clearly divergent species with inter-species genetic distance typical of genus-level divergence (average 16.6%, SD 3.1% nucleotide distance).

(C) A whole-genome phylogeny for the 1,806 genomes in *Ca.* Cibiobacter qucibialis (STAR Methods). Some subtrees associate with geography and non-Westernized populations, while others seems to be geography- and lifestyle-independent (see text).

(D) Multidimensional scaling of genetic distances among genomes of *Ca.* Cibiobacter qucibialis highlights the divergence of strains carried by non-Westernized populations, with Chinese populations subclustering within the large cluster of Westernized populations.

(E) Madagascar-associated strains of *Ca.* Cibiobacter qucibialis (uSGB 15286) uniquely possess the *trp* operon for tryptophan metabolism (Table S7). Other functional clusters in Westernized strains from geographically heterogeneous populations include vitamin B12 and fatty acid biosynthesis and galactose metabolism. The KEGG functions present in >80% or in <20% of the samples were discarded except for significant associations with lifestyle.

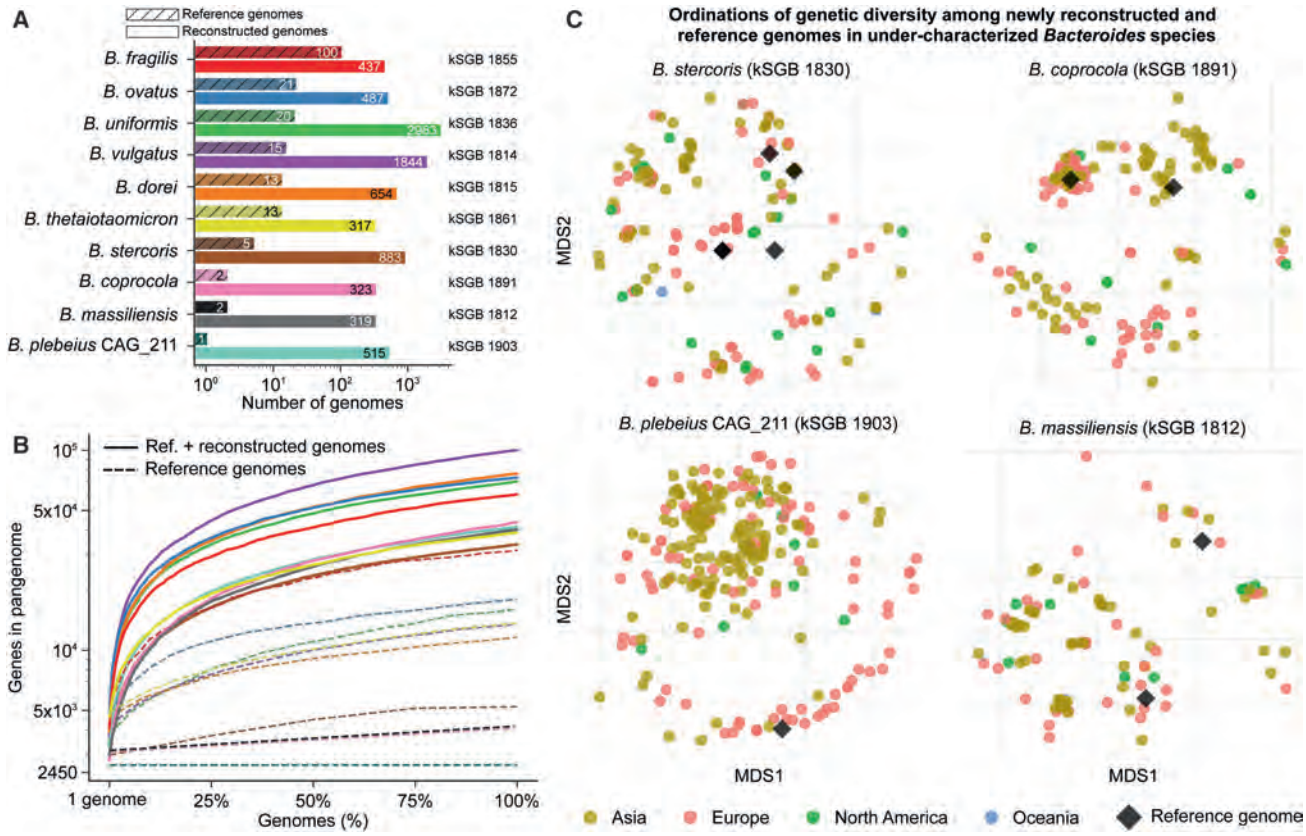

Figure 4. The Metagenomically Reconstructed Genomes Greatly Expand the Genetic and Functional Diversity of the Ten *Bacteroides* Species Most Prevalent in the Human Gut

(A) Additional *Bacteroides* genomes we assembled from metagenomes increase the size of the ten most prevalent *Bacteroides* kSGBs from 4 to >500 times.

(B) The expanded *Bacteroides* kSGBs account for much larger pangenomes that capture a greater functional potential.

(C) Ordinations on intra-SGB genetic distances (fractions of nucleotide mutations in the core genome) highlight the genetic structure of *Bacteroides* species and that reference genomes were available only for a reduced subset of subspecies structures (additional ordinations are in Figure S6A).

the seven Chinese cohorts that are monophyletically placed in the same subtree despite widely different pre-sequencing protocols (Table S6) and resemble non-Westernized genomes (Figures 3C and 3D). This suggests a complex process of gut microbial ecological establishment in which both host lifestyle and biogeography play roles with comparable effect sizes.

Functional potential profiling of SGBs can suggest metabolic features that distinguish each clade, and for *Ca.* Cibiobacter qucibialis, we found functional modules specific to only some of the constituent strains (Figure 3E; Table S7). These include the pathway for the biosynthesis of vitamin B12 from precorrin-2, lacking in some Westernized strains that instead use other pathways for vitamin B12 production, as well as gene clusters devoted to fatty acid biosynthesis and galactose metabolism (Figure 3E). A strong lifestyle-associated difference characterized the non-Westernized strains in *Ca.* Cibiobacter qucibialis (uSGB 15286), as they were the only strains in this SGB with the whole set of genes in the *trp* operon for tryptophan metabolism. The Trp biosynthetic pathway can be organized as whole-pathway operon or as dispersed genes in different bacterial species (Merino et al., 2008), as a result of organismal divergence, adjustment to environmental availability of key molecules, and lateral gene transfer events (Xie et al., 2003). We speculate that the presence of the whole operon in the non-Westernized strains may be indicative of divergent evolution in the Westernized strains of *Ca.* Cibiobacter qucibialis, potentially as a consequence of a loss-of-operon event.

Sample-Specific Strain Recovery Greatly Enlarges the Pangenomes of Key Intestinal Microbes

Bacteroides are among the most studied intestinal species (Marcobal et al., 2011) and are core in European and American populations (Human Microbiome Project Consortium, 2012; Nielsen et al., 2014), but our analysis still recovered unsampled intra-species diversity. Among the ten largest SGBs, the number of available isolate genomes ranges from 1 (*Bacteroides plebeius*) to 100 (*Bacteroides fragilis*), whereas we added from 317 to 2,983 individual representatives (Figure 4A). These expanded genome sets provide much larger collections of distinct genes that can be present in strains of each species, i.e., pangenomes, which spanned ~30,000 to >70,000 genes per *Bacteroides* species, capturing a substantially wider functional potential

compared to isolate genomes (Figure 4B). The number of genomes in a species bin did not correlate well with the size of the associated pangenome (Pearson correlation 0.48, p = 0.16), indicating that pangenome recovery is not simply a function of the amount of associated sequence. No *Bacteroides* pangenomes approached saturation even given the amount of sequence included in this study (average of 276, SD 93 additional pan-genes when moving from the 99th percentile to the whole set of reconstructed genomes), suggesting that even for common, well-studied organisms, a surprising amount of intra-species genomic diversity (and associated biochemical function) remains to be captured.

Most of the *Bacteroides* SGBs contained distinct subspecies clusters, and many of these subspecies include only genomes we reconstructed in this work (Figures 4C and S6A). Some of the most abundant *Bacteroides* species (including *B. stercoris* and *B. plebeius*) were only partially captured by isolate genomes, and the additional reconstructed genomes accounted for an average of 95.8%, SD 5.0% total branch length in the ten core-genome phylogenies. Considering that genetic sub-speciation is highly correlated with functional diversification (correlations > 0.8, p < 1e−50, Figure S6B), the reconstructed genomes thus uncover not only genetic diversity but also relevant functional diversity included in otherwise inaccessible *Bacteroides* subspecies.

Some uSGBs and Subspecies Are Strongly Associated with Non-Westernized Populations

To further assess the specificity of the unexplored uSGBs among global populations, we profiled the gut microbiomes of two rural communities with non-Western lifestyles from northeastern Madagascar (STAR Methods). The SGB profiles of the Madagascar population were profoundly different from that of Western-style populations (Figures 2C and 2D), with 49 of the 941 large (>10 genomes) SGBs highly enriched in this east-African population and 8 SGBs uniformly absent (20 total depleted SGBs, Fisher's test Bonferroni-corrected p < 0.05, Figure 5A, Table S6). An SGB that contains a previously co-assembled *Succinatimonas* sp. but no isolate genomes was the strongest association with the Madagascar population (Fisher's Bonferroni-corrected p = 8.2e−99), as well as with non-Westernized populations generally (p = 4.3e−244), across which it was successfully assembled in 55.9% of the samples (4.55% average and 56% maximum relative abundance) compared to only 1.6% in Westernized samples (3.34% average and 20.13% maximum relative abundance). The type strain of this genus (*Succinatimonas hippei*) was isolated from the gut of a healthy Japanese individual in 2010 (Morotomi et al., 2010) and is phylogenetically similar to isolates from poultry. The ability to degrade D-xylose is characteristic of the clade, a plant-sugar whose metabolism was previously reported as enriched in rural microbiomes (De Filippo et al., 2010). The phylogenetic structure of *Succinatimonas* SGB 3677 also suggests further specialization to specific host lifestyles at the subspecies level, with 99 of the 117 genomes from Westernized populations tightly clustering together and well separated from all 246 genomes from the five non-Westernized populations (Figures 5C and S5B). This SGB in the *Succinatimonas* genus shows a geographically consistent pattern of lifestyle association, resulting in dramatically different prevalences across the globe (p = 4.3e−244) as well as intra-species geographically specific genetic diversification.

The non-Westernized gut microbiome is overall enriched for uSGBs rather than kSGBs (Figures 5A and 5B), which was consistent despite the different protocols used in the considered studies (Table S6). These include several uSGBs in the Firmicutes and Actinobacteria phyla but also in less typically human-associated phyla such as the Elusimicrobia phylum. Two Elusimicrobia uSGBs were associated with the Madagascar (ID 19692 and ID 19694, Fisher's test p = 4.64e−11 and 9.76e−05, respectively) and non-Westernized gut microbiome (ID 19694, p = 1.52e−53) but showed 22% nucleotide divergence from the closest isolate genome (Figures 5D and S5A). 22 isolate genomes are available for this phylum, but they were typically recovered from termites and other insects (Herlemann et al., 2007) and were even more genetically distant from those we identified in humans (>30% nucleotide distance). While these divergent Elusimicrobia uSGBs populate the non-Westernized gut microbiome with some frequency (15.4% prevalence, 0.73% average relative abundance, Figure 5D), they are rarely found in Westernized individuals (0.31% prevalence).

Bacteroides uniformis was the strongest Westernized-lifestyle-associated bacterium (Figure 5B; Table S6), and 13 other *Bacteroides* species with a combined total of 10,992 genomes also showed the same trend (2.66% versus 0.86% prevalence and 5.77% Westernized versus 1.69% non-Westernized average abundance). With the exception of four unnamed low-prevalence *Bacteroides* SGBs (434 genomes in total), no species of this clade was significantly enriched in non-Westernized populations; instead, these were highly enriched in *Prevotella* species (12 kSGBs against no significant *Prevotella* kSGB in Westernized populations), as expected (De Filippo et al., 2010; Obregon-Tito et al., 2015). Several other known and relatively well-characterized species (including *Alistipes putredinis*, *Parabacteroides distasonis*, and *Akkermansia muciniphila*) were significantly associated with Westernized populations, in total accounting for >23 times more kSGBs than uSGBs. Conversely, among SGBs enriched in non-Westernized populations, uSGBs greatly outnumbered kSGBs (144 versus 63, Fisher's test p = 1.0e−23). This further confirms that populations with non-urbanized and traditional lifestyles have a more uncharacterized gut microbiome that is made more accessible to future characterization by these results.

Microbiome differentiation between lifestyles was also reflected at the functional level (Figure 5E; Tables S5 and S6). Sulfur energy metabolism (ko00920), vitamin B12 salvage (ko00860), and the sodium-ion-specific ATP synthase operon *ntp* (ko00190) were among the KEGG functional modules significantly enriched in Westernized microbiomes (Figure 5E). Other functions were present in both lifestyles but encoded by different enzymes and pathways. For example, both groups' microbiomes encoded extensive antibiotic biosynthesis genes (Figure 5E), but while Westernized-enriched SGBs encoded the pathway for penicillin and cephalosporin biosynthesis (ko00311), non-Westernized-enriched SGBs more often carried genes for macrolide biosynthesis (ko00523). Similarly, genes for tryptophan metabolism were differently present in the two groups, with parts of

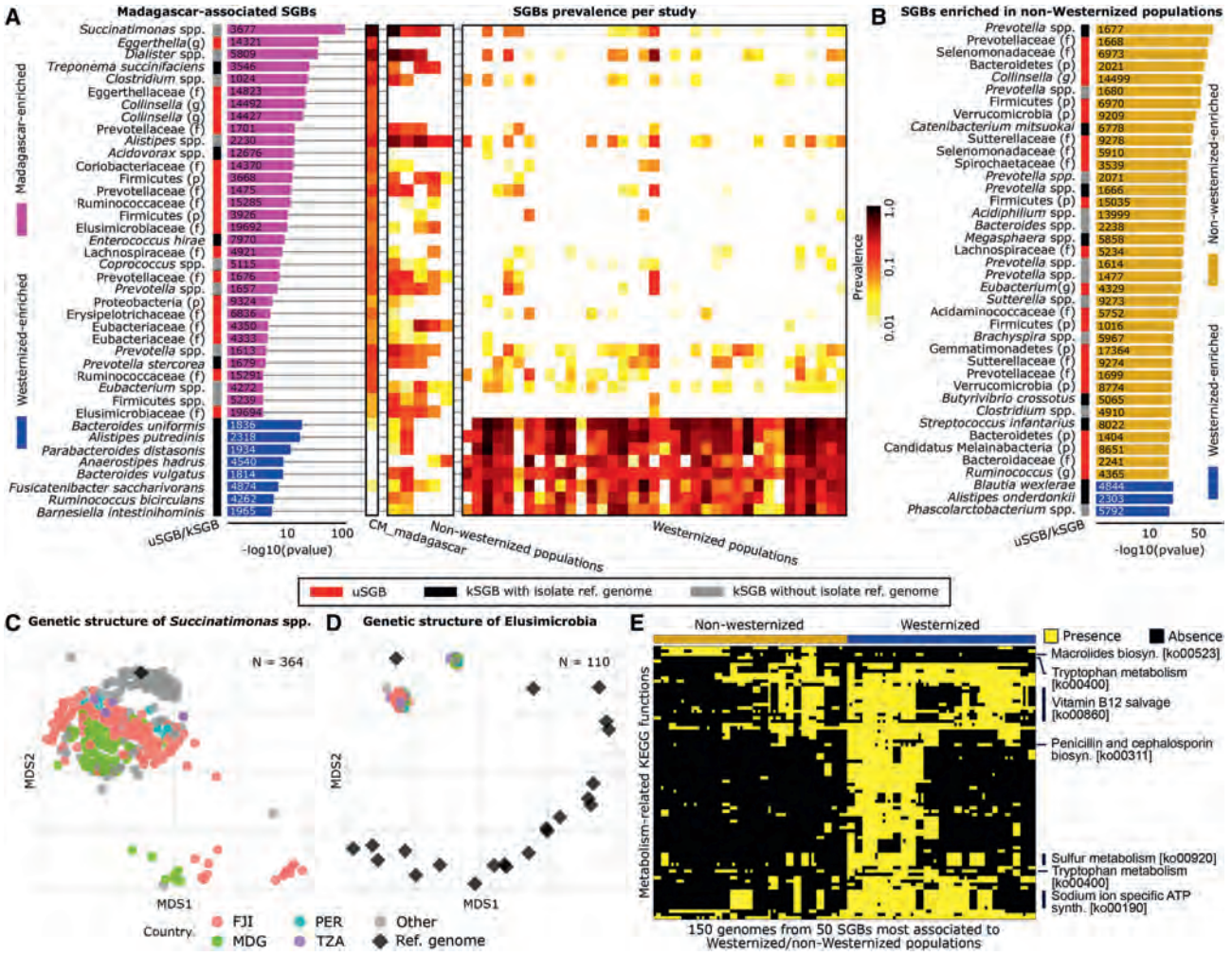

Figure 5. SGBs and Single Reconstructed Genomes Associated with Westernized and Non-Westernized Lifestyles

(A) 49 total large (>10 genomes) SGBs were significantly enriched (Fisher's test) in the set of 112 Madagascar gut metagenomes sequenced for this study, and 20 were significantly depleted (Fisher's test) relative to Western gut microbiomes (complete results in Table S6). Most Madagascar-enriched SGBs are uSGBs or contain only isolate sequences that were themselves assembled from other metagenomes in other studies.

(B) 232 total SGBs were differentially present with respect to the total set of non-Westernized populations, again with the 40 most significant—excluding those already reported in (A)—shown here (Fisher's test, complete results in Table S6).

(C) The intra-SGB genetic structure of *Succinatimonas* spp., the bacterium most associated with non-Westernized lifestyles (multidimensional scaling [MDS] on percentage nucleotide distances between genomes). The few genomes assembled from Westernized countries are tightly clustering together, while strains from non-Westernized populations are distinct and not well represented by the only available co-assembled (but not cultivated) strain.

(D) MDS of the two uSGBs (ID 19692 and ID 19694) enriched in the Madagascar cohort and available isolate genomes for the containing Elusimicrobia phylum (phylogeny in Figure S5A). The metagenomically assembled genomes in Elusimicrobia SGBs greatly diverge from the non-human-associated isolate genomes in the phylum.

(E) Significant differences in functional potential between the 25 SGBs most strongly associated with Westernized and non-Westernized populations. We report the differential KEGG pathways (Fisher's test Bonferroni-corrected $p < 0.05$, full list in Table S6) whose components are found in the set of representative genomes for the 50 species (only three genomes per SGB).

the same pathway (ko00400) differentially present in Westernized and non-Westernized communities (Figure 5E). UniRef50 annotations of all genomes highlighted many additional differences (82,563 with Bonferroni-corrected $p < 0.01$, Table S5), spanning also fimbrial functions and degradation of complex pectins enriched in the non-Westernized microbiomes. These associations of microbial functional potential with population capture a wide range of potential diet, metabolic, genetic, and exposure differences (De Filippo et al., 2010; Yatsunenko et al., 2012) and suggest that there are multiple ways in which the gut microbiome adapts to the diversity of human hosts.

DISCUSSION

This work expands the collection of microbial genomes associated with the human microbiome by more than doubling the

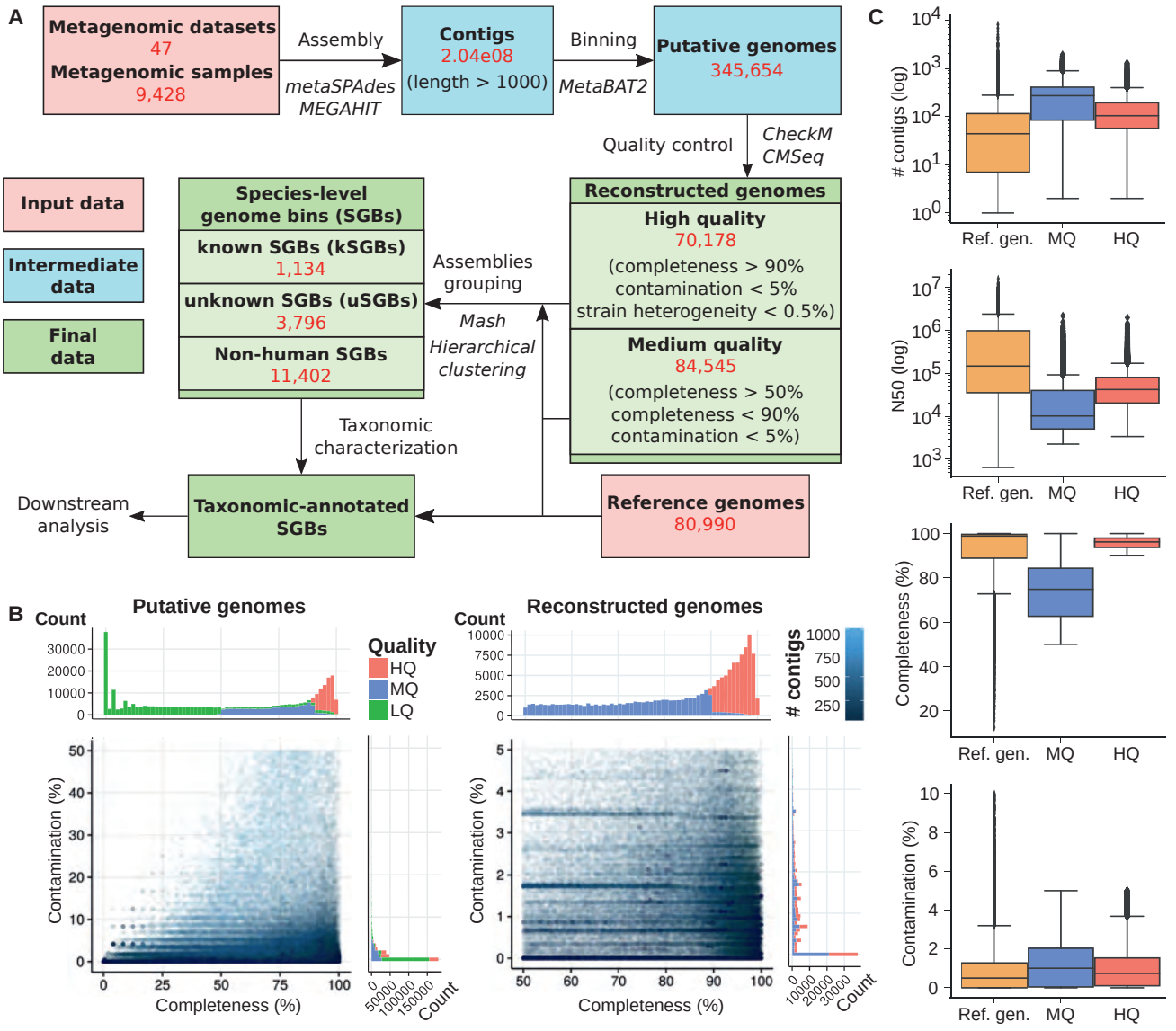

Figure 6. Methodology Overview and Quality Characteristics for the 154,723 Reconstructed Genomes

(A) Overview of the overall strategy and datasets employed for the reconstruction of microbial genomes and their organizations in SGBs.

(B) Completeness and contamination values estimated by CheckM are reported for LQ (low quality, completeness <50% or contamination >5%), MQ (completeness in the range [50%, 90%] and contamination <5%), and HQ (completeness >90%, contamination <5%, CMSeq strain heterogeneity <0.5%) genomes. LQ genomes are excluded from the rest of the analysis.

(C) Comparisons between the genomes from UniRef/NCBI used as references and our reconstructed genomes.

current collections with over 150,000 newly reconstructed genomes, in the process recovering hidden functional and phylogenetic diversity associated with global populations (particularly those that are undersampled from non-Western lifestyles and non-gut areas, Figure 1E). More than 94% of metagenomic reads can now be mapped to the expanded genome catalog for half of the gut microbiomes, enabling a much more comprehensive profiling of these communities. The metagenomic-assembly strategies employed here (Li et al., 2015; Nurk et al., 2017) represent a scalable methodology for very large-scale integration of metagenomes (Figure 6) that we extensively validated (STAR Methods; Figures 7 and S7) and could be fruitfully applied to additional or non-human-associated metagenomes. The methods are also compatible with emerging technologies such as synthetic (Kuleshov et al., 2016) or single-molecule (Brown et al., 2017) long-read sequencing, which will further add to the diversity of microbial genomes. Finally, the study's results themselves emphasize the phylogenetic and functional diversity that remains to be captured from rare organisms, especially for sample types other than stool, global human populations, and varied lifestyles for the human microbiome.

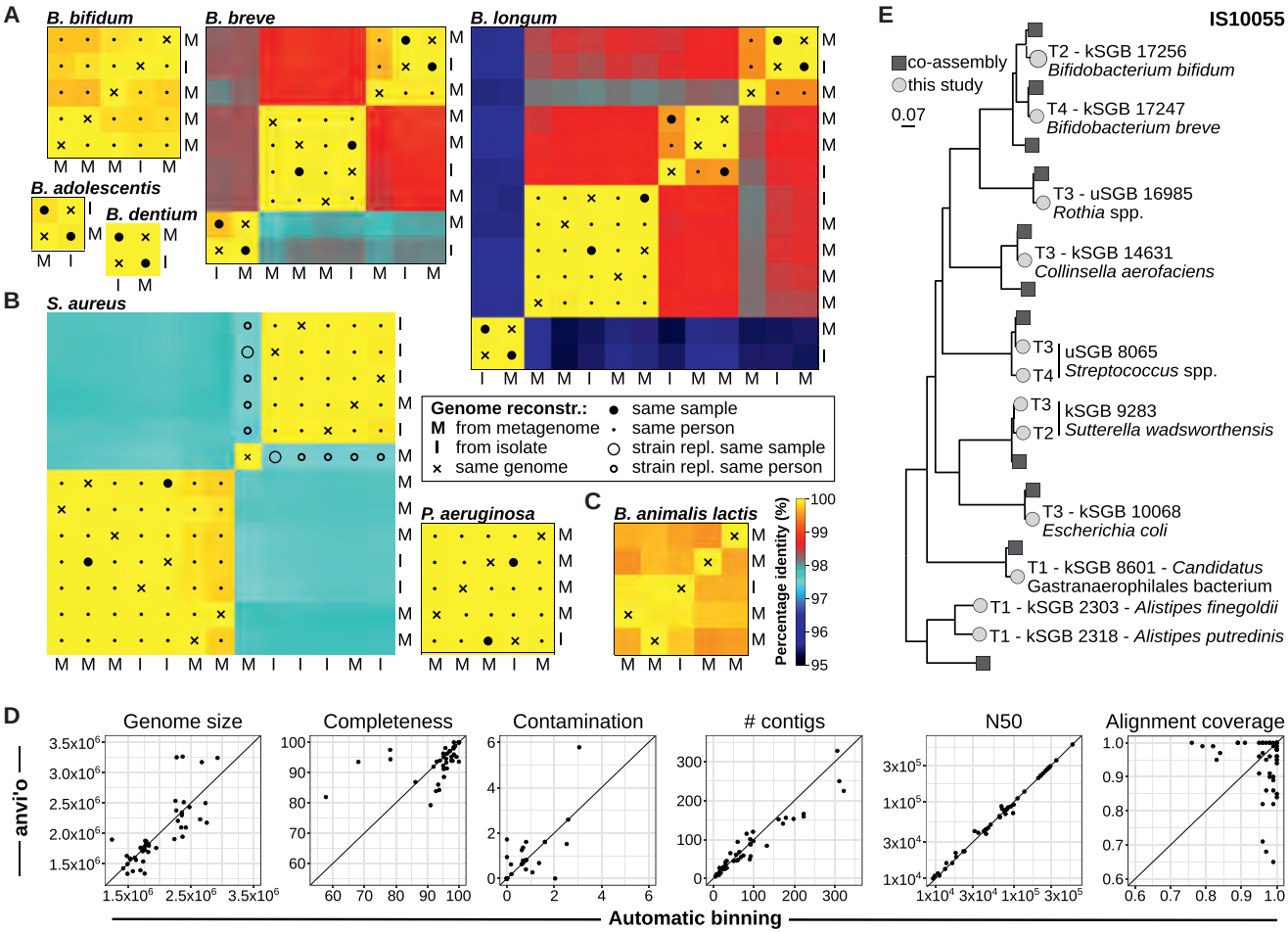

Figure 7. Quality of the Single-Sample Assembled Genomes against Multiple Alternative Genome Reconstruction Approaches

(A) Percentage identity between genomes from isolates (I) and genomes we reconstructed from metagenomes (M) for five *Bifidobacterium* species from the FerrettiP_2018 dataset (Ferretti et al., 2018). We mark isolates and metagenomes coming from the same specimen (big filled circles) and coming from specimens of the same mother-infant pair (small filled circles). In all cases, our automatic pipeline reconstructs genomes from metagenomes that are almost identical to the genomes of the expected isolated strains.

(B) The strains of *S. aureus* and *P. aeruginosa* isolated from three patients are almost perfectly matching the genomes reconstructed from sputum metagenomes sequenced at multiple time points. In the only case in which a *S. aureus* genome from a metagenome is not matching the strain isolated from a previous time point in the same patient, we verified with MLST typing that a clinical event of strain-replacement from ST45 to ST273 occurred.

(C) In the dataset by Nielsen et al. (2014), we successfully recover at >99.5% identity the strain of a *B. animalis* subspecies lactis present in a commercial probiotic product that was consumed by the enrolled subjects, even if the probiotic strain was at low relative abundance in the stool microbiome (<0.3% on average [Nielsen et al., 2014]).

(D) Comparison of the 46 manually curated genomes (using anvi'o) with automatically assembled (using metaSPAdes) and binned (using MetaBAT2) genomes.

(E) Example comparison between the set of single-sample assembled genomes and co-assembled genomes for a time series (n = 5) of gut metagenomes from a newborn. Several genomes reconstructed with the two approaches have the same phylogenetic placement, with single-sample assembly retrieving the same (or a very closely related) genome at multiple time points, and both methods retrieving some unique genomes. This is an example of the comprehensive comparison performed in the STAR Methods and reported in Table S2 and Figure S7B.

Even within the current data collection, a variety of results remain to be explored. Part of the metagenomic reads that could not be mapped against our extended bacterial and archaeal resource are likely coming from viral and eukaryotic genomes. For example, we found substantial amounts of viruses (>0.5% relative read depth in 101 samples for bacteriophages never found as prophages in reference bacterial genomes), of the intestinal eukaryotic parasite *Blastocystis* (>0.5% in 158 samples), and of the skin fungus *Malassezia* (>0.5% in 297 samples). Considering that *de novo* discovery of non-bacterial genomes is very challenging and should receive more attention in the future, eukaryotic microorganisms and viruses may thus account for some of the remaining unmappable sequences in these data (Figure 2). These results help to pinpoint microbes unique to a particular population, environment, or exposure, and most importantly, future work may then be able to more easily capture

specific strains or microbial molecular mechanisms that are causal in microbiome-associated human health conditions.

STAR★METHODS

Detailed methods are provided in the online version of this paper and include the following:

- KEY RESOURCES TABLE
- CONTACT FOR REAGENT AND RESOURCE SHARING
- EXPERIMENTAL MODEL AND SUBJECT DETAILS
- METHOD DETAILS
  - Overview of the approach
  - Meta-analyzed publicly available metagenomic datasets
  - Enrollment of participants from non-Westernized populations from Madagascar and Ethiopia
  - Sample collection of non-Westernized cohorts
  - DNA extraction and sequencing
  - Description of the non-Westernized cohorts
  - Isolate genomes and available metagenomic assemblies used as references
  - Metagenomic assembly and contig binning
  - Quality control of metagenomic assemblies
  - Validation of the pipeline for genome reconstruction from metagenomics using isolate sequencing and manually curated genomes
  - Evaluation of single-sample assemblies against co-assembly and co-binning methods
  - Grouping of metagenomic assemblies into species-level genome bins
  - Reconstruction of the human-microbiome phylogenetic structure
  - Quantification of the fraction of reads that can be mapped against SGBs
  - Pangenome, phylogenetic, and functional analysis of kSGB and uSGBs
- QUANTIFICATION AND STATISTICAL ANALYSIS
- DATA AND SOFTWARE AVAILABILITY

SUPPLEMENTAL INFORMATION

Supplemental Information includes seven figures and seven tables and can be found with this article online at https://doi.org/10.1016/j.cell.2019.01.001.

ACKNOWLEDGMENTS

We thank the MAHERY team, particularly Anjaranirina Evelyn Jean Gasta, Hervet Randriamady, and Miadana Vonona Arisoa, and the GeNaPi Project Team, particularly Mari Olcina, Lourdes Larruy, Carla Muñoz, and Cristina Alcántara. We thank Levi Waldron and all the members of the Segata and Huttenhower laboratories for fruitful discussions, the students of the Computational Microbial Genomics master course at University of Trento for help with the manual curation of assemblies, and the HPC and NGS facilities at University of Trento. This work was supported by EU-H2020 (DiMeTrack-707345) to E.P.; by NIH NHGRI (R01HG005220), NIDDK (R24DK110499), NIDDK (U54DE023798), CMIT (6935956) to C.H.; and by ERC (MetaPG-716575), MIUR (RBFR13EWWI), EU-FP7 (PCIG13-GA-2013-618833), CARITRO (2013.0239), and LEO Pharma Foundation to N.S. Madagascar data and sample collection was supported by the Rockefeller Foundation to C.D.G.

AUTHOR CONTRIBUTIONS

Conception and design, E.P. and N.S.; Methodology and analysis; E.P., F. Asnicar, S.M., M.Z., N.K., F.B., C.Q., and N.S.; Sample collection, processing, and data generation, F. Armanini, P.G., M.C.C., B.L.R., C.D., X.C.M., C.D.G., and C.H.; Public data collection and curation, E.P., N.K., F.B., P.M., and A.T.; Data interpretation, E.P., F. Asnicar, S.M., M.Z., C.H., and N.S.; Manuscript preparation: E.P., F. Asnicar, S.M., M.Z., N.K., C.H., and N.S.

DECLARATION OF INTERESTS

The authors declare no competing interests.

Received: August 29, 2018
Revised: November 15, 2018
Accepted: December 28, 2018
Published: January 17, 2019

REFERENCES

Alneberg, J., Bjarnason, B.S., de Bruijn, I., Schirmer, M., Quick, J., Ijaz, U.Z., Lahti, L., Loman, N.J., Andersson, A.F., and Quince, C. (2014). Binning metagenomic contigs by coverage and composition. Nat. Methods *11*, 1144–1146.

Altschul, S.F., Gish, W., Miller, W., Myers, E.W., and Lipman, D.J. (1990). Basic local alignment search tool. J. Mol. Biol. *215*, 403–410.

Asnicar, F., Weingart, G., Tickle, T.L., Huttenhower, C., and Segata, N. (2015). Compact graphical representation of phylogenetic data and metadata with GraPhlAn. PeerJ *3*, e1029.

Asnicar, F., Manara, S., Zolfo, M., Truong, D.T., Scholz, M., Armanini, F., Ferretti, P., Gorfer, V., Pedrotti, A., Tett, A., et al. (2017). Studying Vertical Microbiome Transmission from Mothers to Infants by Strain-Level Metagenomic Profiling. mSystems 2. https://doi.org/10.1128/mSystems.00164-16.

Bäckhed, F., Roswall, J., Peng, Y., Feng, Q., Jia, H., Kovatcheva-Datchary, P., Li, Y., Xia, Y., Xie, H., Zhong, H., et al. (2015). Dynamics and Stabilization of the Human Gut Microbiome during the First Year of Life. Cell Host Microbe *17*, 852.

Beghini, F., Pasolli, E., Truong, T.D., Putignani, L., Cacciò, S.M., and Segata, N. (2017). Large-scale comparative metagenomics of Blastocystis, a common member of the human gut microbiome. ISME J. *11*, 2848–2863.

Bowers, R.M., Kyrpides, N.C., Stepanauskas, R., Harmon-Smith, M., Doud, D., Reddy, T.B.K., Schulz, F., Jarett, J., Rivers, A.R., Eloe-Fadrosh, E.A., et al.; Genome Standards Consortium (2017). Minimum information about a single amplified genome (MISAG) and a metagenome-assembled genome (MIMAG) of bacteria and archaea. Nat. Biotechnol. *35*, 725–731.

Brinig, M.M., Lepp, P.W., Ouverney, C.C., Armitage, G.C., and Relman, D.A. (2003). Prevalence of bacteria of division TM7 in human subgingival plaque and their association with disease. Appl. Environ. Microbiol. *69*, 1687–1694.

Brister, J.R., Ako-Adjei, D., Bao, Y., and Blinkova, O. (2015). NCBI viral genomes resource. Nucleic Acids Res. *43*, D571–D577.

Brito, I.L., Yilmaz, S., Huang, K., Xu, L., Jupiter, S.D., Jenkins, A.P., Naisilisili, W., Tamminen, M., Smillie, C.S., Wortman, J.R., et al. (2016). Mobile genes in the human microbiome are structured from global to individual scales. Nature *535*, 435–439.

Brooks, B., Olm, M.R., Firek, B.A., Baker, R., Thomas, B.C., Morowitz, M.J., and Banfield, J.F. (2017). Strain-resolved analysis of hospital rooms and infants reveals overlap between the human and room microbiome. Nat. Commun. *8*, 1814.

Brown, B.L., Watson, M., Minot, S.S., Rivera, M.C., and Franklin, R.B. (2017). MinION™ nanopore sequencing of environmental metagenomes: a synthetic approach. Gigascience *6*, 1–10.

Browne, H.P., Forster, S.C., Anonye, B.O., Kumar, N., Neville, B.A., Stares, M.D., Goulding, D., and Lawley, T.D. (2016). Culturing of 'unculturable' human microbiota reveals novel taxa and extensive sporulation. Nature *533*, 543–546.

Buchfink, B., Xie, C., and Huson, D.H. (2015). Fast and sensitive protein alignment using DIAMOND. Nat. Methods *12*, 59–60.

Capella-Gutiérrez, S., Silla-Martínez, J.M., and Gabaldón, T. (2009). trimAl: a tool for automated alignment trimming in large-scale phylogenetic analyses. Bioinformatics *25*, 1972–1973.

Cole, J.R., Wang, Q., Fish, J.A., Chai, B., McGarrell, D.M., Sun, Y., Brown, C.T., Porras-Alfaro, A., Kuske, C.R., and Tiedje, J.M. (2014). Ribosomal Database Project: data and tools for high throughput rRNA analysis. Nucleic Acids Res. *42*, D633–D642.

Costea, P.I., Coelho, L.P., Sunagawa, S., Munch, R., Huerta-Cepas, J., Forslund, K., Hildebrand, F., Kushugulova, A., Zeller, G., and Bork, P. (2017). Subspecies in the global human gut microbiome. Mol. Syst. Biol. *13*, 960.

De Filippo, C., Cavalieri, D., Di Paola, M., Ramazzotti, M., Poullet, J.B., Massart, S., Collini, S., Pieraccini, G., and Lionetti, P. (2010). Impact of diet in shaping gut microbiota revealed by a comparative study in children from Europe and rural Africa. Proc. Natl. Acad. Sci. USA *107*, 14691–14696.

Eddy, S.R. (2011). Accelerated Profile HMM Searchese1002195. PLoS Comput Biol *7*.

Eren, A.M., Esen, Ö.C., Quince, C., Vineis, J.H., Morrison, H.G., Sogin, M.L., and Delmont, T.O. (2015). Anvi'o: an advanced analysis and visualization platform for 'omics data. PeerJ *3*, e1319.

Ferretti, P., Pasolli, E., Tett, A., Asnicar, F., Gorfer, V., Fedi, S., Armanini, F., Truong, D.T., Manara, S., Zolfo, M., et al. (2018). Mother-to-Infant Microbial Transmission from Different Body Sites Shapes the Developing Infant Gut Microbiome. Cell Host Microbe *24*, 133–145.e5.

Forouzan, E., Shariati, P., Mousavi Maleki, M.S., Karkhane, A.A., and Yakhchali, B. (2018). Practical evaluation of 11 de novo assemblers in metagenome assembly. J. Microbiol. Methods *151*, 99–105.

Franzosa, E.A., McIver, L.J., Rahnavard, G., Thompson, L.R., Schirmer, M., Weingart, G., Schwarzberg Lipson, L., Knight, R., Caporaso, G., Segata, N., et al. (2018). Species-level functional profiling of metagenomes and metatranscriptomes. Nat. Methods *15*, 962–968.

Golden, C.D., Anjaranirina, E.J.G., Fernald, L.C.H., Hartl, D.L., Kremen, C., Milner, D.A., Jr., Ralalason, D.H., Ramihantaniarivo, H., Randriamady, H., Rice, B.L., et al. (2017). Cohort Profile: The Madagascar Health and Environmental Research (MAHERY) study in north-eastern Madagascar. Int. J. Epidemiol. *46*, 1747–1748d.

Goslee, S.C., and Urban, D.L. (2007). The ecodist package for dissimilarity-based analysis of ecological data. J. Stat. Softw. *22*. https://doi.org/10.18637/jss.v022.i07.

Gossling, J., and Moore, W.E.C. (1975). Gemmiger formicilis, n.gen., n.sp., an Anaerobic Budding Bacterium from Intestines. Int. J. Syst. Evol. Microbiol. *25*, 202–207.

He, X., McLean, J.S., Edlund, A., Yooseph, S., Hall, A.P., Liu, S.-Y., Dorrestein, P.C., Esquenazi, E., Hunter, R.C., Cheng, G., et al. (2015). Cultivation of a human-associated TM7 phylotype reveals a reduced genome and epibiotic parasitic lifestyle. Proc. Natl. Acad. Sci. USA *112*, 244–249.

Herlemann, D.P.R., Geissinger, O., and Brune, A. (2007). The termite group I phylum is highly diverse and widespread in the environment. Appl. Environ. Microbiol. *73*, 6682–6685.

Huerta-Cepas, J., Szklarczyk, D., Forslund, K., Cook, H., Heller, D., Walter, M.C., Rattei, T., Mende, D.R., Sunagawa, S., Kuhn, M., et al. (2016). eggNOG 4.5: a hierarchical orthology framework with improved functional annotations for eukaryotic, prokaryotic and viral sequences. Nucleic Acids Res. *44* (D1), D286–D293.

Huerta-Cepas, J., Forslund, K., Coelho, L.P., Szklarczyk, D., Jensen, L.J., von Mering, C., and Bork, P. (2017). Fast Genome-Wide Functional Annotation through Orthology Assignment by eggNOG-Mapper. Mol. Biol. Evol. *34*, 2115–2122.

Human Microbiome Project Consortium (2012). Structure, function and diversity of the healthy human microbiome. Nature *486*, 207–214.

Jain, C., Rodriguez-R, L.M., Phillippy, A.M., Konstantinidis, K.T., and Aluru, S. (2018). High throughput ANI analysis of 90K prokaryotic genomes reveals clear species boundaries. Nat. Commun. *9*, 5114.

Kang, D.D., Froula, J., Egan, R., and Wang, Z. (2015). MetaBAT, an efficient tool for accurately reconstructing single genomes from complex microbial communities. PeerJ *3*, e1165.

Katoh, K., and Standley, D.M. (2013). MAFFT multiple sequence alignment software version 7: improvements in performance and usability. Mol. Biol. Evol. *30*, 772–780.

Kuleshov, V., Jiang, C., Zhou, W., Jahanbani, F., Batzoglou, S., and Snyder, M. (2016). Synthetic long-read sequencing reveals intraspecies diversity in the human microbiome. Nat. Biotechnol. *34*, 64–69.

Langmead, B., and Salzberg, S.L. (2012). Fast gapped-read alignment with Bowtie 2. Nat. Methods *9*, 357–359.

Li, H., and Durbin, R. (2009). Fast and accurate short read alignment with Burrows-Wheeler transform. Bioinformatics *25*, 1754–1760.

Li, D., Liu, C.-M., Luo, R., Sadakane, K., and Lam, T.-W. (2015). MEGAHIT: an ultra-fast single-node solution for large and complex metagenomics assembly via succinct de Bruijn graph. Bioinformatics *31*, 1674–1676.

Liu, W., Zhang, J., Wu, C., Cai, S., Huang, W., Chen, J., Xi, X., Liang, Z., Hou, Q., Zhou, B., et al. (2016). Unique Features of Ethnic Mongolian Gut Microbiome revealed by metagenomic analysis. Sci. Rep. *6*, 34826.

Manara, S., Pasolli, E., Dolce, D., Ravenni, N., Campana, S., Armanini, F., Asnicar, F., Mengoni, A., Galli, L., Montagnani, C., et al. (2018). Whole-genome epidemiology, characterisation, and phylogenetic reconstruction of Staphylococcus aureus strains in a paediatric hospital. Genome Med. *10*, 82.

Marchler-Bauer, A., Anderson, J.B., DeWeese-Scott, C., Fedorova, N.D., Geer, L.Y., He, S., Hurwitz, D.I., Jackson, J.D., Jacobs, A.R., Lanczycki, C.J., et al. (2003). CDD: a curated Entrez database of conserved domain alignments. Nucleic Acids Red *31*, 383–387.

Marcobal, A., Barboza, M., Sonnenburg, E.D., Pudlo, N., Martens, E.C., Desai, P., Lebrilla, C.B., Weimer, B.C., Mills, D.A., German, J.B., and Sonnenburg, J.L. (2011). Bacteroides in the infant gut consume milk oligosaccharides via mucus-utilization pathways. Cell Host Microbe *10*, 507–514.

Merino, E., Jensen, R.A., and Yanofsky, C. (2008). Evolution of bacterial trp operons and their regulation. Curr. Opin. Microbiol. *11*, 78–86.

Meyer, F., Hofmann, P., Belmann, P., Garrido-Oter, R., Fritz, A., Sczyrba, A., and McHardy, A.C. (2018). AMBER: Assessment of Metagenome BinnERs. GigaScience *7*.. https://doi.org/10.1093/gigascience/giy069.

Morotomi, M., Nagai, F., Watanabe, Y., and Tanaka, R. (2010). Succinatimonas hippei gen. nov., sp. nov., isolated from human faeces. Int. J. Syst. Evol. Microbiol. *60*, 1788–1793.

NCBI Resource Coordinators (2013). Database resources of the National Center for Biotechnology Information. Nucleic Acids Res. *41*, D8–D20.

Nguyen, L.-T., Schmidt, H.A., von Haeseler, A., and Minh, B.Q. (2015). IQ-TREE: a fast and effective stochastic algorithm for estimating maximum-likelihood phylogenies. Mol. Biol. Evol. *32*, 268–274.

Nielsen, H.B., Almeida, M., Juncker, A.S., Rasmussen, S., Li, J., Sunagawa, S., Plichta, D.R., Gautier, L., Pedersen, A.G., Le Chatelier, E., et al.; MetaHIT Consortium; MetaHIT Consortium (2014). Identification and assembly of genomes and genetic elements in complex metagenomic samples without using reference genomes. Nat. Biotechnol. *32*, 822–828.

Nikolenko, S.I., Korobeynikov, A.I., and Alekseyev, M.A. (2013). BayesHammer: Bayesian clustering for error correction in single-cell sequencing. BMC Genomics *14* (*Suppl 1*), S7.

Nurk, S., Meleshko, D., Korobeynikov, A., and Pevzner, P.A. (2017). metaSPAdes: a new versatile metagenomic assembler. Genome Res. *27*, 824–834.

Obregon-Tito, A.J., Tito, R.Y., Metcalf, J., Sankaranarayanan, K., Clemente, J.C., Ursell, L.K., Zech Xu, Z., Van Treuren, W., Knight, R., Gaffney, P.M., et al. (2015). Subsistence strategies in traditional societies distinguish gut microbiomes. Nat. Commun. *6*, 6505.

Oh, J., Byrd, A.L., Deming, C., Conlan, S., Kong, H.H., and Segre, J.A.; NISC Comparative Sequencing Program (2014). Biogeography and individuality shape function in the human skin metagenome. Nature *514*, 59–64.

O'Leary, N.A., Wright, M.W., Brister, J.R., Ciufo, S., Haddad, D., McVeigh, R., Rajput, B., Robbertse, B., Smith-White, B., Ako-Adjei, D., et al. (2016). Reference sequence (RefSeq) database at NCBI: current status, taxonomic expansion, and functional annotation. Nucleic Acids Res. *44* (D1), D733–D745.

Ondov, B.D., Treangen, T.J., Melsted, P., Mallonee, A.B., Bergman, N.H., Koren, S., and Phillippy, A.M. (2016). Mash: fast genome and metagenome distance estimation using MinHash. Genome Biol. *17*, 132.

Oyama, L.B., Girdwood, S.E., Cookson, A.R., Fernandez-Fuentes, N., Privé, F., Vallin, H.E., Wilkinson, T.J., Golyshin, P.N., Golyshina, O.V., Mikut, R., et al. (2017). The rumen microbiome: an underexplored resource for novel antimicrobial discovery. NPJ Biofilms Microbiomes *3*, 33.

Page, A.J., Cummins, C.A., Hunt, M., Wong, V.K., Reuter, S., Holden, M.T., Fookes, M., Falush, D., Keane, J.A., and Parkhill, J. (2015). Roary: rapid large-scale prokaryote pan genome analysis. Bioinformatics *31*, 3691–3693.

Parks, D.H., Imelfort, M., Skennerton, C.T., Hugenholtz, P., and Tyson, G.W. (2015). CheckM: assessing the quality of microbial genomes recovered from isolates, single cells, and metagenomes. Genome Res. *25*, 1043–1055.

Parks, D.H., Rinke, C., Chuvochina, M., Chaumeil, P.-A., Woodcroft, B.J., Evans, P.N., Hugenholtz, P., and Tyson, G.W. (2017). Recovery of nearly 8,000 metagenome-assembled genomes substantially expands the tree of life. Nat. Microbiol. *2*, 1533–1542.

Pasolli, E., Schiffer, L., Manghi, P., Renson, A., Obenchain, V., Truong, D.T., Beghini, F., Malik, F., Ramos, M., Dowd, J.B., et al. (2017). Accessible, curated metagenomic data through ExperimentHub. Nat. Methods *14*, 1023–1024.

Price, M.N., Dehal, P.S., and Arkin, A.P. (2010). FastTree 2–approximately maximum-likelihood trees for large alignments. PLoS ONE *5*, e9490.

Pritchard, L., Glover, R.H., Humphris, S., Elphinstone, J.G., and Toth, I.K. (2016). Genomics and taxonomy in diagnostics for food security: soft-rotting enterobacterial plant pathogens. Anal. Methods *8*, 12–24.

Qin, J., Li, R., Raes, J., Arumugam, M., Burgdorf, K.S., Manichanh, C., Nielsen, T., Pons, N., Levenez, F., Yamada, T., et al.; MetaHIT Consortium (2010). A human gut microbial gene catalogue established by metagenomic sequencing. Nature *464*, 59–65.

Quince, C., Walker, A.W., Simpson, J.T., Loman, N.J., and Segata, N. (2017a). Shotgun metagenomics, from sampling to analysis. Nat. Biotechnol. *35*, 833–844.

Quince, C., Delmont, T.O., Raguideau, S., Alneberg, J., Darling, A.E., Collins, G., and Eren, A.M. (2017b). DESMAN: a new tool for de novo extraction of strains from metagenomes. Genome Biol. *18*, 181.

Rampelli, S., Schnorr, S.L., Consolandi, C., Turroni, S., Severgnini, M., Peano, C., Brigidi, P., Crittenden, A.N., Henry, A.G., and Candela, M. (2015). Metagenome Sequencing of the Hadza Hunter-Gatherer Gut Microbiota. Curr. Biol. *25*, 1682–1693.

Raveh-Sadka, T., Thomas, B.C., Singh, A., Firek, B., Brooks, B., Castelle, C.J., Sharon, I., Baker, R., Good, M., Morowitz, M.J., and Banfield, J.F. (2015). Gut bacteria are rarely shared by co-hospitalized premature infants, regardless of necrotizing enterocolitis development. eLife *4*, e05477.

Rinke, C., Schwientek, P., Sczyrba, A., Ivanova, N.N., Anderson, I.J., Cheng, J.-F., Darling, A., Malfatti, S., Swan, B.K., Gies, E.A., et al. (2013). Insights into the phylogeny and coding potential of microbial dark matter. Nature *499*, 431–437.

Seemann, T. (2014). Prokka: rapid prokaryotic genome annotation. Bioinformatics *30*, 2068–2069.

Segata, N., Haake, S.K., Mannon, P., Lemon, K.P., Waldron, L., Gevers, D., Huttenhower, C., and Izard, J. (2012a). Composition of the adult digestive tract bacterial microbiome based on seven mouth surfaces, tonsils, throat and stool samples. Genome Biol. *13*, R42.

Segata, N., Waldron, L., Ballarini, A., Narasimhan, V., Jousson, O., and Huttenhower, C. (2012b). Metagenomic microbial community profiling using unique clade-specific marker genes. Nat. Methods *9*, 811–814.

Segata, N., Börnigen, D., Morgan, X.C., and Huttenhower, C. (2013). PhyloPhlAn is a new method for improved phylogenetic and taxonomic placement of microbes. Nat. Commun. *4*, 2304.

Sharon, I., Morowitz, M.J., Thomas, B.C., Costello, E.K., Relman, D.A., and Banfield, J.F. (2013). Time series community genomics analysis reveals rapid shifts in bacterial species, strains, and phage during infant gut colonization. Genome Res. *23*, 111–120.

Smits, S.A., Leach, J., Sonnenburg, E.D., Gonzalez, C.G., Lichtman, J.S., Reid, G., Knight, R., Manjurano, A., Changalucha, J., Elias, J.E., et al. (2017). Seasonal cycling in the gut microbiome of the Hadza hunter-gatherers of Tanzania. Science *357*, 802–806.

Solden, L., Lloyd, K., and Wrighton, K. (2016). The bright side of microbial dark matter: lessons learned from the uncultivated majority. Curr. Opin. Microbiol. *31*, 217–226.

Stamatakis, A. (2014). RAxML version 8: a tool for phylogenetic analysis and post-analysis of large phylogenies. Bioinformatics *30*, 1312–1313.

Tatusov, R.L., Fedorova, N.D., Jackson, J.D., Jacobs, A.R., Kiryutin, B., Koonin, E.V., Krylov, D.M., Mazumder, R., Mekhedov, S.L., Nikolskaya, A.N., et al. (2003). The COG database: an updated version includes eukaryotes. BMC Bioinformatics *4*, 41.

Tett, A., Pasolli, E., Farina, S., Truong, D.T., Asnicar, F., Zolfo, M., Beghini, F., Armanini, F., Jousson, O., De Sanctis, V., et al. (2017). Unexplored diversity and strain-level structure of the skin microbiome associated with psoriasis. NPJ Biofilms Microbiomes *3*, 14.

The UniProt Consortium (2017). UniProt: the universal protein knowledgebase. Nucleic Acids Res. *45* (D1), D158–D169.

Truong, D.T., Franzosa, E.A., Tickle, T.L., Scholz, M., Weingart, G., Pasolli, E., Tett, A., Huttenhower, C., and Segata, N. (2015). MetaPhlAn2 for enhanced metagenomic taxonomic profiling. Nat. Methods *12*, 902–903.

Truong, D.T., Tett, A., Pasolli, E., Huttenhower, C., and Segata, N. (2017). Microbial strain-level population structure and genetic diversity from metagenomes. Genome Res. *27*, 626–638.

Uritskiy, G.V., DiRuggiero, J., and Taylor, J. (2018). MetaWRAP-a flexible pipeline for genome-resolved metagenomic data analysis. Microbiome *6*, 158.

van der Walt, A.J., van Goethem, M.W., Ramond, J.-B., Makhalanyane, T.P., Reva, O., and Cowan, D.A. (2017). Assembling metagenomes, one community at a time. BMC Genomics *18*, 521.

Wang, Q., Garrity, G.M., Tiedje, J.M., and Cole, J.R. (2007). Naive Bayesian classifier for rapid assignment of rRNA sequences into the new bacterial taxonomy. Appl. Environ. Microbiol. *73*, 5261–5267.

Xie, G., Bonner, C.A., Brettin, T., Gottardo, R., Keyhani, N.O., and Jensen, R.A. (2003). Lateral gene transfer and ancient paralogy of operons containing redundant copies of tryptophan-pathway genes in Xylella species and in heterocystous cyanobacteria. Genome Biol. *4*, R14.

Yatsunenko, T., Rey, F.E., Manary, M.J., Trehan, I., Dominguez-Bello, M.G., Contreras, M., Magris, M., Hidalgo, G., Baldassano, R.N., Anokhin, A.P., et al. (2012). Human gut microbiome viewed across age and geography. Nature *486*, 222–227.

Cell

Anti-NKG2A mAb Is a Checkpoint Inhibitor that Promotes Anti-tumor Immunity by Unleashing Both T and NK Cells

Pascale André,[1,*] Caroline Denis,[1] Caroline Soulas,[1] Clarisse Bourbon-Caillet,[1] Julie Lopez,[1] Thomas Arnoux,[1] Mathieu Bléry,[1] Cécile Bonnafous,[1] Laurent Gauthier,[1] Ariane Morel,[1] Benjamin Rossi,[1] Romain Remark,[1] Violette Breso,[1] Elodie Bonnet,[1] Guillaume Habif,[1] Sophie Guia,[2] Ana Ines Lalanne,[3] Caroline Hoffmann,[3,4] Olivier Lantz,[3] Jérôme Fayette,[5] Agnès Boyer-Chammard,[1] Robert Zerbib,[1] Pierre Dodion,[1] Hormas Ghadially,[6] Maria Jure-Kunkel,[7] Yannis Morel,[1] Ronald Herbst,[7] Emilie Narni-Mancinelli,[2] Roger B. Cohen,[8] and Eric Vivier[1,2,9,10,*]

[1]Innate Pharma, 117 Avenue de Luminy, 13009 Marseille, France
[2]Aix Marseille Université, INSERM, CNRS, Centre d'Immunologie de Marseille-Luminy, 13009 Marseille, France
[3]Unité INSERM U932, Immunité et Cancer, Institut Curie, 75248 Paris Cedex 5, France
[4]Service ORL et Chirurgie cervico-faciale, Institut Curie, 75248 Paris Cedex 5, France
[5]Centre Léon Bérard, 69008 Lyon, France
[6]MedImmune, Ltd., Aaron Klug Building, Granta Park, Cambridge, CB21 6GH, UK
[7]MedImmune, LLC, One MedImmune Way, Gaithersburg, MD 20878, USA
[8]Abramson Cancer Center, 3400 Civic Center Boulevard West Pavilion, Philadelphia, PA, USA
[9]Service d'Immunologie, Marseille Immunopole, Hôpital de la Timone, Assistance Publique-Hôpitaux de Marseille, 13005 Marseille, France
[10]Lead Contact
*Correspondence: pascale.andre@innate-pharma.fr (P.A.), vivier@ciml.univ-mrs.fr (E.V.)
https://doi.org/10.1016/j.cell.2018.10.014

SUMMARY

Checkpoint inhibitors have revolutionized cancer treatment. However, only a minority of patients respond to these immunotherapies. Here, we report that blocking the inhibitory NKG2A receptor enhances tumor immunity by promoting both natural killer (NK) and $CD8^+$ T cell effector functions in mice and humans. Monalizumab, a humanized anti-NKG2A antibody, enhanced NK cell activity against various tumor cells and rescued $CD8^+$ T cell function in combination with PD-x axis blockade. Monalizumab also stimulated NK cell activity against antibody-coated target cells. Interim results of a phase II trial of monalizumab plus cetuximab in previously treated squamous cell carcinoma of the head and neck showed a 31% objective response rate. Most common adverse events were fatigue (17%), pyrexia (13%), and headache (10%). NKG2A targeting with monalizumab is thus a novel checkpoint inhibitory mechanism promoting anti-tumor immunity by enhancing the activity of both T and NK cells, which may complement first-generation immunotherapies against cancer.

INTRODUCTION

Immuno-oncology has revolutionized cancer treatment (Okazaki and Honjo, 2007; Okazaki et al., 2013; Baumeister et al., 2016; Schumacher and Schreiber, 2015; Sharma and Allison, 2015a, 2015b). Unprecedented improvements in tumor control have been achieved using therapeutic monoclonal antibodies (mAbs) that block immune inhibitory "checkpoint" receptors. In particular, mAbs directed against the PD-1 (programmed-cell death protein 1)/PD-L1 (programmed -cell death ligand 1) axis (PDx) in monotherapy or combination therapy have been approved for the treatment of several indications, including metastatic melanoma, non-small-cell lung cancer, kidney cancer, bladder cancer, Hodgkin lymphoma, and solid tumors that are microsatellite instability-high or mismatched repair-deficient (Okazaki and Honjo, 2007; Okazaki et al., 2013; Baumeister et al., 2016; Schumacher and Schreiber, 2015; Sharma and Allison, 2015a, 2015b). Such treatment often yields durable benefits, and, in most patients, toxicity can be controlled. However, only a subset of the patients treated with antibodies specific for PD-1 or PD-L1 display a strong response, and the cancers of a substantial fraction of patients are resistant to these immune checkpoint inhibitors (ICI). Therefore, one of the major challenges in immuno-oncology is understanding the mechanisms of resistance to ICI, to increase the proportion of patients benefiting from such treatment and to control treatment toxicity. One approach that could be used is to identify novel molecular targets, the modulation of which boosts anti-tumor immunity. Blocking other inhibitory pathways of effector lymphocytes, such as T cells and NK cells, is attracting considerable research interest in this context.

Cell surface receptors harboring intracytoplasmic tyrosine-based inhibitory motifs (ITIMs) are particularly relevant in this respect. These motifs are phosphorylated and recruit the phosphatases (SHP-1/2 or SHIP) responsible for transmitting the inhibition signal to immune effector cells (Daëron et al., 2008). Bioinformatics analyses of the human genome have predicted the presence of more than 300 type I and type II integral membrane proteins containing at least one ITIM domain (Daëron et al., 2008), but only a few of these receptors are currently targeted in therapeutic approaches.

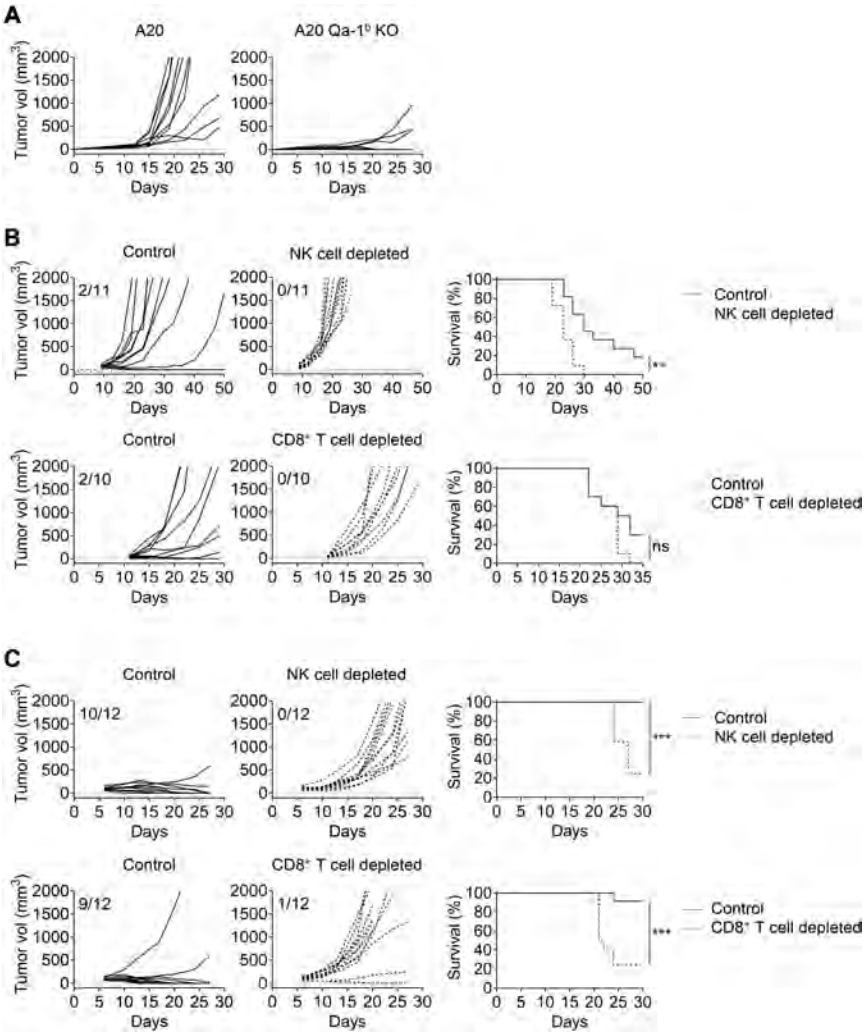

Figure 1. NKG2A Is an Inhibitory Receptor that Blocks the Anti-tumor Efficacy of NK and CD8$^+$ T Cells

(A) Qa-1^b-sufficient or -deficient A20 tumor cells were engrafted subcutaneously (s.c.) in BALB/c mice.

(B) BALB/c mice were treated with an anti-aGM1 pAbs or with control rabbit serum, an anti-CD8α mAb, or rat IgG2b isotype control and then subcutaneously engrafted with A20 tumor cells. Graphs show tumor growth in each individual mouse and combined survival curves. Complete regressions are indicated. log rank test, **p = 0.0020; ns, no significant.

(C) Experiment similar to that in (B), but with Qa-1^b KO A20 tumor cells. Complete regressions are indicated. log rank test, ***p = 0.0002 (NK cell depletion) and ***p = 0.0006 (CD8$^+$ T cell depletion). See also Figure S1.

NKG2A is an ITIM-bearing receptor expressed on both T and NK cells. Approximately half of peripheral blood NK cells express NKG2A (André et al., 1999; Mahapatra et al., 2017; Manser and Uhrberg, 2016) and its expression on NK cells can be upregulated upon stimulation with cytokines, such as interleukin-15 (IL-15) (Brady et al., 2004; Mori et al., 1998). In healthy individuals, around 5% of human peripheral blood CD8$^+$ T cells express cell-surface NKG2A at steady state, but this expression can be upregulated by chronic antigenic stimulation (Bertone et al., 1999; McMahon et al., 2002; Mingari et al., 1998; Sheu et al., 2005). NKG2A is expressed at the cell surface as a heterodimer with CD94 in humans and mice and recognizes the non-classical class I major histocompatibility complex (MHC-I) molecules human leukocyte antigen (HLA)-E in humans and Qa-1^b in mice. Binding of NKG2A/CD94 to its cognate ligand inhibits T and NK cell effector functions (Le Dréan et al., 1998; Rapaport et al., 2015). This inhibition is dependent on the recruitment of the SHP-1 tyrosine phosphatase to the tyrosine-phosphorylated form of the ITIM in NKG2A (Viant et al., 2014).

Here, we show that NKG2A blockade enhances the anti-tumor immunity mediated by NK and CD8$^+$ T cells. We developed a humanized anti-NKG2A immunoglobulin G (IgG) 4-blocking mAb (monalizumab), and we describe its anti-tumor efficacy *in vitro* and *in vivo* when used as a single agent or in combination with other therapeutic antibodies, such as durvalumab, blocking PD-L1, or cetuximab, directed against the epidermal growth factor receptor (EGFR), which is expressed by tumor cells.

RESULTS

NKG2A Blockade Promotes Anti-tumor Immunity

We assessed the impact of NKG2A on cytotoxic lymphocyte activity by using BALB/c B cell lymphoma A20 cells, which express the non-classical MHC-I Qa-1^b molecule, the mouse homolog of HLA-E, and generating the corresponding Qa-1^b-knockout cells (Figure S1A). The growth rates of parental and Qa-1^b-deficient A20 cells were similar *in vitro* (data not shown). As expected, the frequency of activated NKG2A$^+$ NK cells—assessed based on the expression of CD107a, a degranulation marker—was higher in cocultures with Qa-1^b-deficient A20 cells than in cocultures with parental cells (data not shown). Following their subcutaneous injection into syngeneic BALB/c mice, wild-type A20 B cell lymphoma cells progressively grew in all mice (Figure 1A, left panel). By contrast, 70% of the mice into which genetically engineered Qa-1^b-deficient A20 cells were injected did not display tumor growth (Figure 1A, right panel). Both NK cells and CD8$^+$ T cells were required to control tumor growth, because the administration of anti-asialo-GM1 and anti-CD8α mAbs, respectively, into tumor-bearing mice abolished the control of parental and Qa-1^b-deficient tumor growth and led to premature death (Figures 1B and 1C). These results validate Qa-1^b as a potentially useful target.

We then dissected the immune response to A20 in the tumor bed by analyzing tumor-infiltrating lymphocytes (TILs). A20

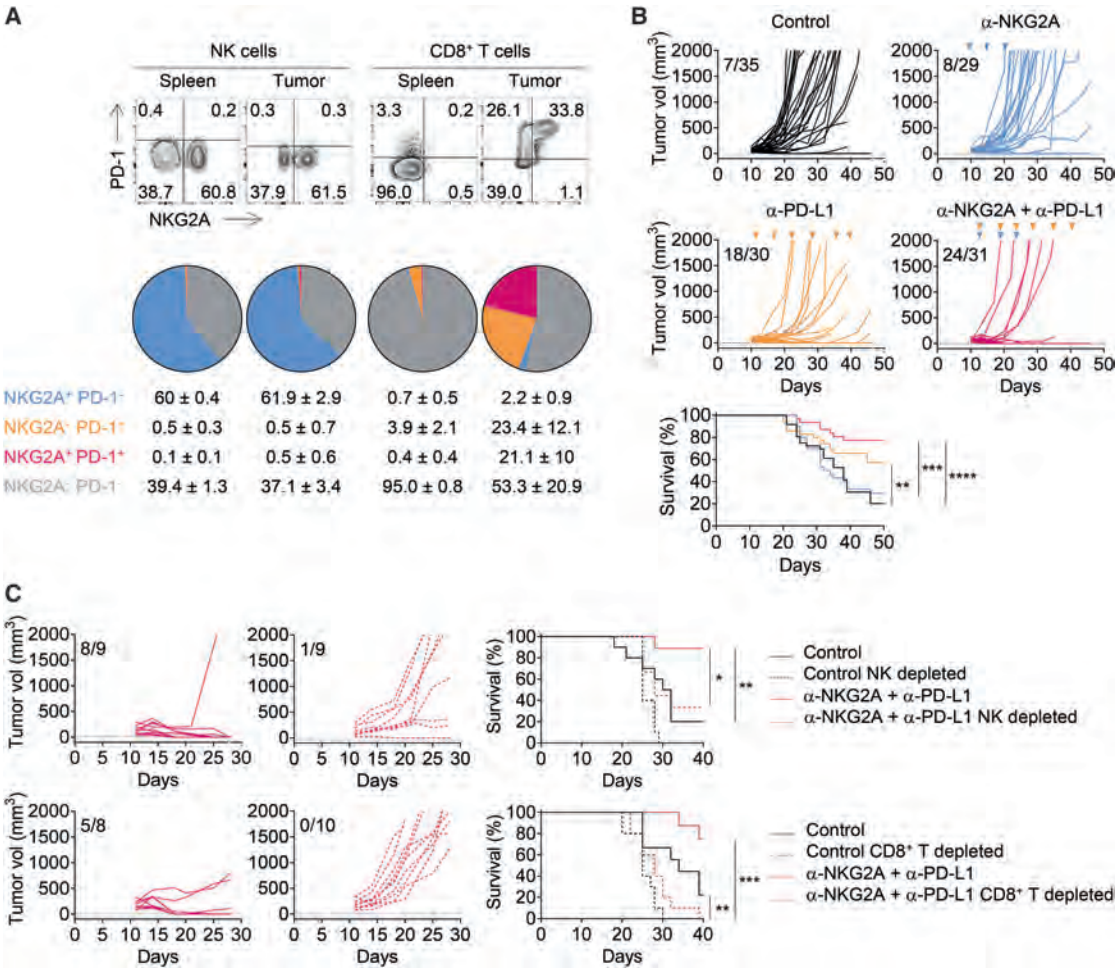

Figure 2. Combined Blockade of NKG2A and PD-1/PD-L1 Promotes Anti-tumor Immunity in A20 Tumor-Bearing BALB/c Mice

(A) Flow cytometry characterization of NK and CD8$^+$ TILs 19 days after A20 tumor cells engraftment. The spleen was used as control. Upper panels: representative fluorescence-activated cell sorting (FACS) profiles of PD-1 and NKG2A expression on NK and CD8$^+$ T cells in the spleen and the tumor bed. Lower panels: pie chart analysis (mean ± SD). The data presented are the pooled results of three independent experiments (n = 12).

(B) A20 tumor cells were engrafted in BALB/c mice. Tumor-bearing mice were then treated at 3- to 4-day intervals with an isotype control (IC), anti-NKG2A, anti-PD-L1, or a combination of these last two mAbs. Graphs show tumor growth in each individual mouse and combined survival curves. The data presented are the pooled results of three independent experiments. Complete regression are indicated. log rank test, **p = 0.0087; ***p = 0.0001; ****p < 0.0001.

(C) Experiment similar to that described in (B) but with treatment of the mice with an anti-asialo-GM1 pAbs or an anti-CD8α mAb 1 day before the initiation of immunotherapy with the combination of anti-NKG2A and anti-PD-L1 mAbs. Graphs show tumor growth in each individual and combined survival curves. Complete regression are indicated. log rank test, *p < 0.0016; **p < 0.01; ***p = 0.0001.

See also Figure S2.

tumors were found to be infiltrated by NK and CD8$^+$ T cells. ~60% of tumor-infiltrating NK cells expressed the NKG2A receptor (Figure 2A). We also monitored PD-1 expression, because the immune control of A20 tumors has been reported to be partially dependent on PD-1 (Sagiv-Barfi et al., 2015). The expression of PD-1, either alone or together with NKG2A, was barely detectable on the surface of tumor-infiltrating NK cells. We did not observe NKG2A expression on the surface of CD8$^+$ T cells from the spleen, and few cells expressed PD-1 (~0.5%) (Figure 2A). However, PD-1$^+$ CD8$^+$ T cells accounted for ~45% of TILs. Importantly, NKG2A was also expressed on the surface of around half the PD-1$^+$ CD8$^+$ TILs. In this model, we also observed that double-positive PD-1$^+$ NKG2A$^+$ CD8$^+$ TILs displayed higher levels of PD-1 and NKG2A expression at their surface than cells positive only for PD-1 or for NKG2A (Figure 2A). Very few CD8$^+$ TILs (~2%) expressed NKG2A without PD-1.

We then investigated whether NKG2A blockade could promote anti-tumor immunity. We generated a recombinant mouse version of the rat anti-mouse NKG2A antibody 20d5 (Vance et al., 1999). We confirmed that the blockade of NKG2A *in vitro* promoted the expression of CD107a by NK cells cocultured with Qa-1B$^+$ A20 tumors, but not with Qa-1B$^-$ YAC-1 target cells (Figure S1B). When used as single agents *in vitro*, anti-NKG2A and anti-PD-L1 mAbs only modestly improved *ex vivo* tumor-infiltrating CD8$^+$ T cell effector activities after restimulation with

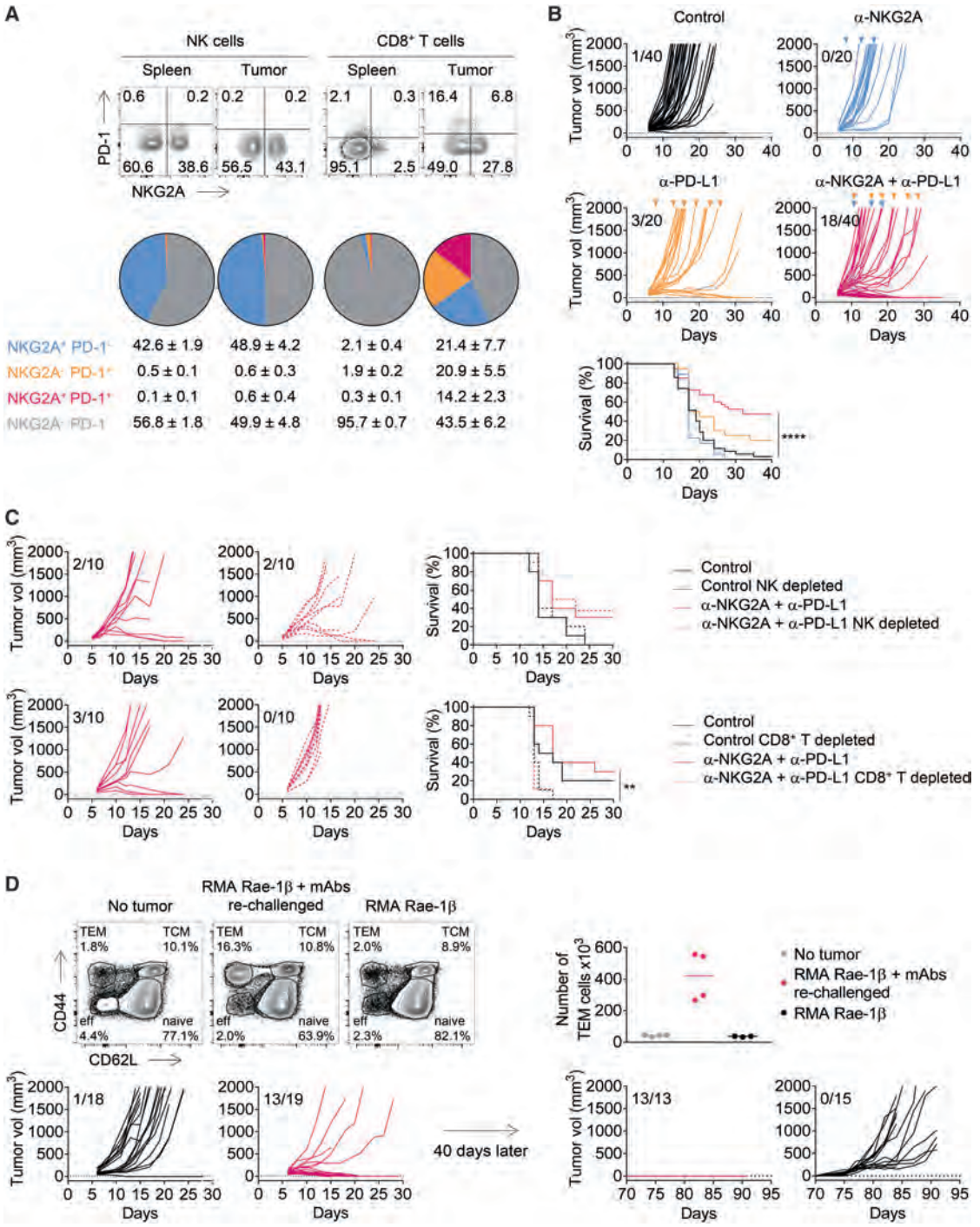

Figure 3. Combined Blockade of NKG2A and PD-1/PD-L1 Promotes Anti-Tumor Immunity in RMA Rae-1β Tumor-Bearing C57BL/6J Mice

(A) RMA Rae-1β tumor cells were injected subcutaneously into C57BL/6J mice. Flow cytometry characterization of NK and CD8$^+$ TILs 12 days post-injection, with the spleen used as the standard. Upper panels: representative FACS profiles of PD-1 and NKG2A expression at the surface of NK and CD8$^+$ T cells in the spleen and the tumor bed. Lower panels: pie chart analysis (mean ± SD). The data presented are the pooled results of two independent experiments (n = 8 mice).

(B) RMA Rae-1β tumor-bearing C57BL/6J mice were treated with IC antibodies, anti-NKG2A, anti-PD-L1, or a combination of these last two mAbs. Graphs show tumor growth in each individual mouse and combined survival curves. The data presented are the pooled results of four independent experiments. Complete regressions are indicated. log rank test, ****$p < 0.0001$.

(C) Experiment similar to that in (B), except that the mice were treated with anti-NK1.1 mAb or anti-aCD8α mAb 1 day before the initiation of immunotherapy with the combination of anti-NKG2A and anti-PD-L1 mAbs. Graphs show tumor growth in each individual mouse and combined survival curves. Complete regressions are indicated. log rank test, **$p = 0.0024$.

(legend continued on next page)

A20 cells (Figure S1C). By contrast, the use of anti-NKG2A and anti-PD-L1 mAbs in combination increased the frequency of CD107a-expressing NKG2A$^+$ PD-1$^+$ CD8$^+$ TILs.

We further investigated the effects of immunotherapy with anti-NKG2A and anti-PD-L1 mAbs by treating A20 tumor-bearing mice with anti-NKG2A mAb, anti-PD-L1 mAb, or a combination of both blocking reagents (Figure 2B). In this experimental setting, anti-NKG2A mAb did not rescue mice from death when used as a single agent when compared to control group. By contrast, anti-PD-L1 mAb rescued ~40% of tumor-bearing mice from death, as shown by comparison with untreated mice. Interestingly, a combination of anti-NKG2A and anti-PD-L1 mAbs had a synergistic effect, improving the control of tumor growth and rescuing ~75% of the mice from death (Figure 2B). The results obtained for mice treated with anti-asialo-GM1 or anti-CD8α antibodies also demonstrated that the anti-tumor effect of the anti-NKG2A/PD-L1 mAbs combination therapy was dependent on both NK and CD8$^+$ T cells (Figure 2C). Thus, the combination of a blocking anti-NKG2A mAb with a blocking anti-PD-L1 mAb had a therapeutic anti-tumor effect, because it unleashed NK cells and CD8$^+$ T cells in the A20 model. Similar results were obtained with a combination of anti-NKG2A/PD-1 mAbs (Figure S2).

Combined Blockade of NKG2A and PD-L1 Promotes the Generation of Protective Anti-tumor Memory

We investigated the anti-tumor therapeutic properties of the anti-NKG2A mAb further by using this antibody to treat C57BL/6 mice bearing another tumor, i.e., the subcutaneously injected RMA-Rae-1β T lymphoma. Like A20 cells, RMA-Rae-1β tumor cells express Qa-1^b and PD-L1 (Figure S3). The frequency of NKG2A$^+$ NK cells in the tumor was higher than that in the spleen, but tumor-infiltrating NK cells did not express PD-1, as observed in the A20 model (Figure 3A). We found that ~20% of total CD8$^+$ TILs expressed NKG2A, but not PD-1; ~15% expressed both these molecules; and ~20% expressed PD-1, but not NKG2A (Figure 3A). Neither anti-NKG2A mAb nor anti-PD-L1 monotherapy was effective in RMA-Rae-1β tumor-bearing mice (Figure 3B). However, treatment with a combination of mAbs against NKG2A and PD-L1 resulted in tumor growth control in 45% of the tumor-bearing mice, which were rescued from death. The combination therapy acted through the release of a CD8$^+$ T cell, but not an NK cell inhibition, as the injection of a depleting anti-CD8α mAb, but not anti-NK1.1 mAbs, abolished tumor growth control and impaired mouse survival (Figure 3C).

We observed the generation of CD62L$^-$ CD44$^+$ effector memory CD8$^+$ T cells in the spleens of mice in which RMA-Rae-1β tumors were implanted and then cured by immunotherapy, but not in the spleens of untreated mice (Figure 3D). Accordingly, RMA-Rae-1β tumor cells were completely rejected when injected into mice that had already been injected with the tumor and cured by treatment with anti-NKG2A and anti-PD-L1 mAbs, whereas the injection of these cells led to unchecked tumor growth in untreated mice (Figure 3D). Therefore, in addition to curing mice of their implanted tumors, blocking NKG2A in combination with another ICI can promote durable protective anti-tumor CD8$^+$ T cell memory response in a preclinical mouse model.

HLA-E and NKG2A Expression in Human Tumors

We then monitored the expression of NKG2A and HLA-E at the surface of several human tumors, to identify the indications for which anti-NKG2A therapeutic blocking mAbs might promote anti-tumor immunity in cancer patients. HLA-E was found to be widely expressed on the surfaces of several human tumors. We observed HLA-E expression in lung, pancreas, stomach, colon, head and neck, and liver tumor tissues (Figure 4; Table S1). By contrast, PD-L1 expression was restricted to a fraction of lung, stomach, and colon tumors (Figure S4). HLA-E was strongly expressed by squamous cell carcinoma of the head and neck (SCCHN) and colorectal carcinoma (CRC) (Figures 4A–4C), in which we also detected NKG2A-positive cells. NKG2A-positive cells and HLA-E expression were also found in ovarian, endometrial, CRC, and cervical cancer (Figure 4C). NKp46$^+$ NK and CD8$^+$ TILs were also present in all these tumors. We investigated SCCHN more closely by flow cytometry and detected high frequencies of CD8$^+$ TILs expressing PD-1 and co-expressing both PD-1 and NKG2A in the tumor (Figure 4D). NKG2A-expressing NK cells were also present at high frequency, and some of these cells had a PD-1$^+$ NKG2A$^+$ phenotype. Similar results were obtained for CRC and lung tumors (data not shown). Thus, several tumors expressed HLA-E and were infiltrated with NK and CD8$^+$ TILs expressing NKG2A. Therefore, we reasoned that NKG2A blockade, either alone or together with the use of other checkpoint inhibitors, such as anti-PD-1/PD-L1 antibodies, might improve the anti-tumor efficacy of NK and CD8$^+$ TILs in cancer patients.

Generation and Characterization of a Chimeric Blocking mAb Directed against Human NKG2A

A murine anti-human NKG2A IgG1 mAb clone, Z270, was generated in a previous study (Sivori et al., 1996). We humanized this antibody by fusion with an IgG_4 with a single point mutation in the Fc heavy chain to prevent the formation of half-antibodies and screened the selected humanized clones for binding to CD94-NKG2A with an affinity similar to that of the original murine mAb. The selected humanized clone was named monalizumab (IPH2201/NNC141-0100). Importantly, unlike other anti-NKG2A

(D) Upper left panels: FACS profiles of CD44 and CD62L expression on CD8$^+$ T cells in the spleen of naive (no tumor) mice, mice receiving their first injection of RMA Rae-1β tumor cells (RMA Rae-1β), and mice previously injected with RMA Rae-1β tumors, cured by immunotherapy and rechallenged (RMA Rae-1β + mAbs rechallenged). Percentages of naive (CD44$^-$CD62L$^+$), central memory (TCM, CD44$^+$CD62L$^+$), effector memory (TEM, CD44$^+$CD62L$^-$) and effector CD8$^+$ T cells (eff, CD44$^-$CD62L$^-$) are indicated. Upper right panel: absolute numbers of effector memory CD8$^+$ T cells in the spleen are shown. Lines represent medians. Lower panels: RMA Rae-1β tumor-bearing C57BL/6J mice were treated with IC antibody or with a combination of anti-NKG2A and anti-PD-L1 mAbs. Mice cured by immunotherapy (n = 13) were rechallenged subcutaneously with RMA-Rae-1β tumor cells after 70 days. Untreated C57BL/6J mice (n = 15) also received injections of RMA-Rae-1β cells as a control. The graphs show tumor growth in each individual mouse. The data presented are the pooled results of two independent experiments.

See also Figure S3.

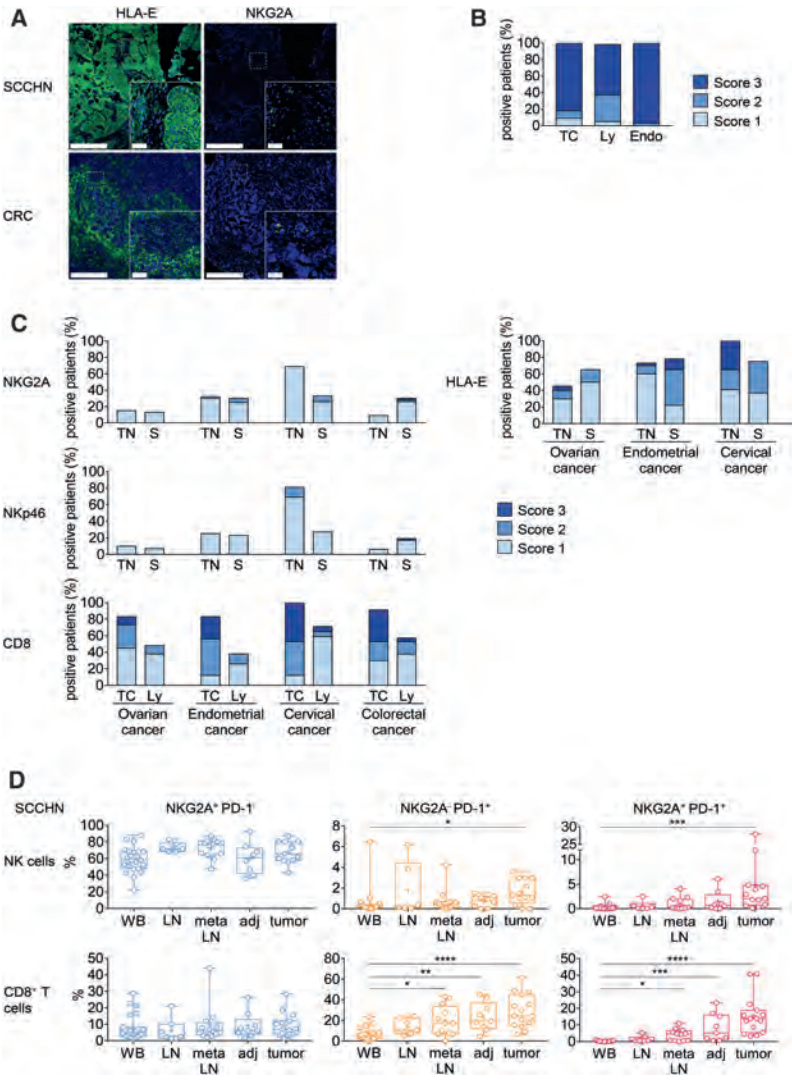

Figure 4. CD8$^+$, NKp46$^+$ and NKG2A$^+$ Immune Cells Are Present in Several Types of HLA-E-Expressing Solid Cancers

(A) Representative example of HLA-E and NKG2A expression on frozen sections from SCCHN and CRC cancer samples. Bright-field images were inverted, and RGB channel splitting was performed. Pseudocolors were attributed to each marker (blue for hematoxylin and green for HLA-E or NKG2A). Scale bars represent 500 μm for low magnification or 50 μm for right inserts.

(B) Semiquantitative analysis of HLA-E expression on formalin-fixed paraffin-embedded (FFPE) SCCHN samples (n = 65). HLA-E expression was assessed on tumor cells (TC), lymphocytes (Ly), and endothelial cells (Endo). Score 1 = 1%–33%; score 2 = 34%–66%; score 3 ≥ 66% of positive cell.

(C) Semiquantitative analysis of NKG2A-, NKp46-, and CD8-positive cells and of HLA-E expression on colorectal cancer (n = 48), ovarian cancer (n = 40), endometrial cancer (n = 40) and cervical cancer (n = 17). CD8, NKp46 and NKG2A cells were quantified in the tumor nest (TN) and stroma (S). HLA-E expression was assessed separately on tumor cells (TC) and lymphocytes (Ly.). Score 1 = 1%–33%; Score 2 = 34%–66%; Score 3 ≥ 66% of positive cells.

(D) Percentages of NK cells (upper panels) and CD8$^+$ T cells (lower panels) expressing NKG2A and PD-1 in SCCHN cancer samples. Cells from WB (whole blood, n = 23), LN (normal lymph node, n = 6), meta LN (metastatic lymph node, n = 12), adj (healthy tissue adjacent to the tumor, n = 8), and tumor (n = 13) were analyzed by flow cytometry. Box and whiskers plot, in which the means are indicated by crosses. Kruskal-Wallis analysis followed by Dunn's multiple comparisons test. *$p < 0.05$; **$p \leq 0.01$; ***$p \leq 0.001$; ****$p < 0.0001$.

See also Figure S4 and Table S1.

mAbs described to date, monalizumab is specific for human NKG2A, as it bound human NKG2A$^+$ cells, but not Ba/F3-transfected cells expressing human NKG2C, the activating isoform of NKG2A (Figure S5A). The EC_{50} calculated by whole blood titration was 4.5 ng/mL for NKG2A$^+$ NK cells and 11.4 ng/mL for NKG2A$^+$ CD8$^+$ T cells (Figure S5B). Finally, another critical feature of monalizumab resides in its capacity to inhibit the binding of HLA-E tetramers to human NK cells expressing NKG2A (Figure S5C).

Monalizumab Promotes the Anti-tumor Cell Activities of Human NK Cells and CD8$^+$ T Cells

We then sought to assess the blocking activity of monalizumab on effector cells by monitoring the cell surface expression of CD107 by NKG2A$^+$ NK cells cocultured with K562 tumor target cells expressing HLA-E (Figures 5A and 5B). The prototypic K562 cells, which lack HLA-E, activated NK cells, but forced HLA-E expression on K562 cells decreased the frequency of CD107$^+$ NKG2A$^+$ NK cells. The addition of monalizumab to the assay restored the production of CD107 by NKG2A$^+$ NK cells to the levels observed with parental K562 targets (Figure 5A). In addition, monalizumab treatment led to increased frequencies of CD107 expression and IFN-γ production when IL-2-activated NK cells were co-cultured with K562-HLA-E$^+$ targets (Figure 5B). We then assessed the anti-tumor efficacy of monalizumab in co-cultures of NK cells with tumor cell lines with different levels of HLA-E expression (Figure S6). Monalizumab increased the frequency of activated NKG2A$^+$ NK cells, as assessed by measuring the cell-surface induction of CD107 and CD137 (4-1BB), an activation-induced costimulatory molecule, in co-cultures with three different SCCHN cell lines and three different ovarian tumor cell lines, although this stimulation was weaker for the CAL-27 and Caov-2 cell lines (Figure S6).

The anti-NKG2A mAb and the anti-PD-L1 mAb had synergistic effects in our preclinical mouse tumor models. We therefore assessed the effects of a combination of monalizumab and durvalumab on NK cell activity against K562 cells co-expressing HLA-E and PD-L1 *in vitro*. NKG2A$^+$ PD-1$^+$ NK cells were generated by chronically stimulating various donor PBMCs with IL-15

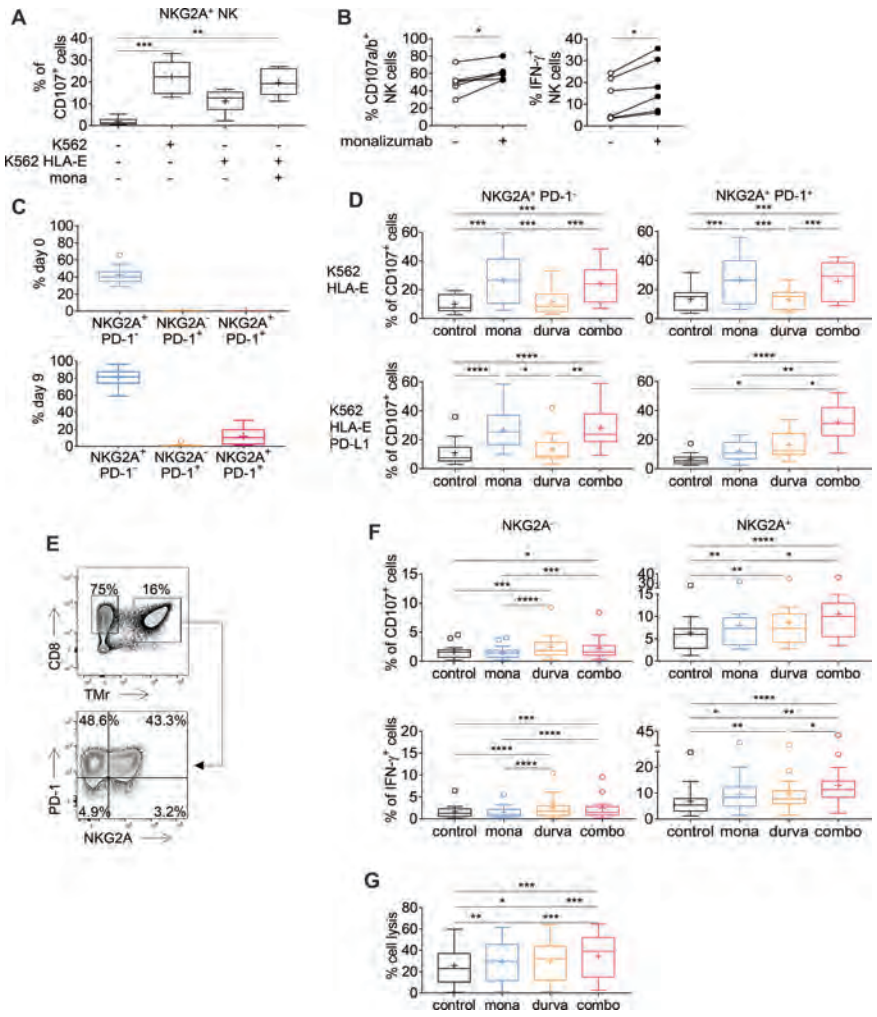

Figure 5. Monalizumab and Durvalumab Unleash NK and CD8$^+$ T Cell Function *In Vitro*

(A) NK cells were co-cultured with K562 or K562 cells expressing HLA-E in the presence or absence of monalizumab. The frequencies of CD107-positive NK cells are shown. Box and whiskers plot, with the means indicated by crosses. N = 8. The whiskers are drawn down to the 25th percentile minus 1.5 times IQR (interquartile range) and up to the 75th percentile plus 1.5 times IQR. Friedman analysis followed by Dunn's multiple comparisons test. **p = 0.006; ***p = 0.0001.

(B) Purified 7 days IL-2-activated NK cells were co-cultured or K562 cells expressing HLA-E in the presence or absence of monalizumab. The frequencies of CD107 and IFN-γ-positive NK cells are shown. Non-parametric Wilcoxon matched-pairs rank test. N = 6; *p = 0.0313.

(C) NK cells were stimulated *in vitro* with IL-15 for 9 days. The data shown are the frequencies of NK cells expressing NKG2A or PD-1 before (day 0) and after (day 9) culture.

(D) The NK cells generated in (C) were co-cultured with K562 cells expressing HLA-E or co-expressing HLA-E and PD-L1 without (control) or with monalizumab (mona), durvalumab (durva), or both these antibodies (combo). The data shown are the frequencies of CD107-expressing NKG2A$^+$ PD-1$^+$or PD-1$^-$ NK cells. Box and whiskers plot, with the means indicated by crosses like in Figure 5A. N = 13 donors. *p < 0.05; **p < 0.01; ***p < 0.001; ****p < 0.0001.

(E) CD8$^+$ T cells were co-cultured *in vitro* with monocytes in the presence of IL-15 and Flu peptide for 9 days. Top panel: one representative dot plot showing the frequency of Flu tetramer positive (TMr$^+$) CD8$^+$ T cells after culture (n = 14). Bottom panel: frequencies of NKG2A$^+$ and/or PD-1$^+$ cells after gating on TMr$^+$ CD8$^+$ T cells (n = 14).

(F) The CD8$^+$ T cells generated in (E) were co-cultured with Flu peptide-pulsed K562 cells expressing PD-L1, HLA-E and HLA-A2 without (control) or with monalizumab (mona), durvalumab (durva), or both antibodies (combo). The data shown are the frequencies of CD107-expressing (upper panels) and IFN-γ-secreting (lower panels) NKG2A$^+$ or NKG2A$^-$ CD8$^+$ T cells (n = 17). The whiskers are drawn like in Figure 5A. *p ≤ 0.05; **p < 0.01; ***p < 0.001; ****p < 0.0001.

(G) The CD8$^+$ T cells generated in (E) were co-cultured with Flu peptide-pulsed K562 cells expressing PD-L1, HLA-E, and HLA-A2 loaded with Cr51 without (control) or with monalizumab (mona), durvalumab (durva), or both antibodies (combo). The data shown are the frequencies of K562 target cell lysis. N = 14 donors. The whiskers are drawn like in Figure 5A. *p < 0.05; **p < 0.01; ***p < 0.001.

See also Figures S5 and S6.

(Figure 5C). The anti-NKG2A monalizumab, used as a single agent, increased the frequencies of CD107$^+$ NKG2A$^+$ PD-1$^-$ NK cells in cocultures with K562-HLA-E or K562-HLA-E-PD-L1 cells (Figure 5D). Addition of durvalumab did not improve NK cell reactivity in this assay. When used as a single agent, monalizumab also improved CD107 expression by NKG2A$^+$ PD-1$^+$ NK cells cocultured with K562-HLA-E targets. The use of monalizumab or durvalumab as single agents only modestly increased the reactivity of NKG2A$^+$ PD-1$^+$ NK cells cocultured with K562-HLA-E-PD-L1 cells, whereas these two antibodies had additive effects when used in combination. Thus, monalizumab efficiently released the inhibition conferred by the engagement of the inhibitory receptor NKG2A. In combination with other ICI, monalizumab has additive effects, promoting NK-cell effector functions.

We assessed the boosting effect of monalizumab on CD8$^+$ T cell functions in more detail because, in our preclinical model, many CD8$^+$ TILs expressed NKG2A (Figures 2A and 3A). We aimed to generate antigen-specific NKG2A$^+$ CD8$^+$ T cells *in vitro* through chronic stimulation with IL-15, monocytes and antigenic peptides derived from human influenza virus (Flu) (Figure 5E). The Flu-specific CD8$^+$ T cells obtained after nine days of culture harbored different phenotypes. In addition to PD-1$^+$ NKG2A$^-$ Flu-specific CD8$^+$ T cells, a substantial fraction of the Flu-specific CD8$^+$ T cells co-expressed PD-1 and NKG2A (Figure 5E). Cells were then cocultured with Flu peptide-pulsed K562-HLA-A2 cells expressing or not expressing the inhibitory ligands HLA-E and PD-L1. The addition of monalizumab or durvalumab modestly increased the frequency of CD107$^+$NKG2A$^+$ Flu-specific-CD8$^+$ T cells (Figure 5F). However, the combination of monalizumab

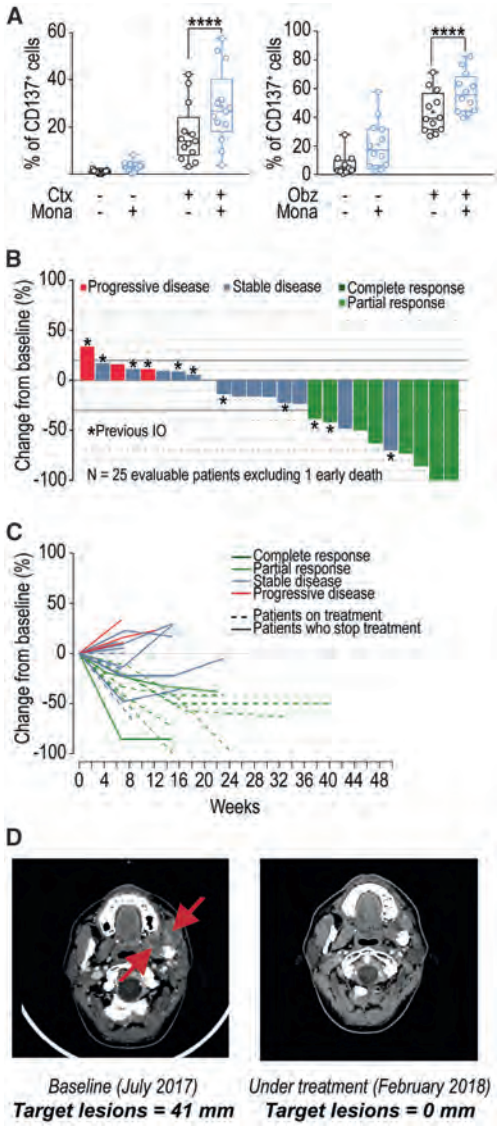

Figure 6. Monalizumab Enhances Human NK Cell-Mediated ADCC and Anti-tumor Activity of Monalizumab and Cetuximab

(A) Left panel: NK cells from healthy donors were co-cultured with the CAL-27 SCCHN cell line in the presence or absence of monalizumab (Mona) or cetuximab (Ctx). The data shown are the frequencies of CD137-expressing NKG2A$^+$ NK cells after 24 hr. N = 13. Student t test comparing the Mona + Cetux combination with Ctx as single agent ****$p < 0.0001$. Right panel: NK cells from healthy donors were co-cultured with 721.221 cells expressing HLA-Cw3 and HLA-Cw4 in the presence or absence of monalizumab (Mona) or obinutuzumab (Obz). The data shown are the frequencies of CD137-expressing NKG2A$^+$ NK cells after 24 hr. N = 12. Student's t test comparing the Mona + Obz combination with Obz as a single agent. ****$p < 0.0001$.

(B) Waterfall plot of the largest change in target lesion relative to the baseline.

(C) Spider plot of the largest change in target lesion relative to the baseline. The patient who died early, due to disease progression, before the first assessment is not represented in these graphs. In accordance with RECIST 1.1, a confirmation of response was required.

(D) Example of a partial response after treatment with the Mona + Cetux combination in a patient with recurrent oral cavity cancer (left masticator space) previously treated by surgery, chemotherapy (cisplatin), and radiation therapy. See also Table 1.

with durvalumab improved CD8$^+$ T cell activity as assessed by CD107 expression and IFN-γ production, and by the killing of target cells in a chromium release assay (Figures 5F and 5G). Thus, monalizumab can promote activation and effector functions of both NK cells and CD8$^+$ T cells, and this effect is more marked when it is used in combination with durvalumab.

Monalizumab Promotes Human NK Cell Antibody-Dependent Cell-Mediated Cytotoxicity

We then evaluated the potential of monalizumab to promote NK-cell effector functions when combined with other commonly used anti-tumor reagents, such as those promoting antibody-dependent cell-mediated cytotoxicity (ADCC). The anti-EGFR mAb cetuximab is used to treat advanced and recurrent and/or metastatic SCCHN and metastatic CRC. Cetuximab mobilizes adaptive and innate immunity against tumor cells, partly by promoting ADCC (Ferris et al., 2018). HLA-E membrane expression in CRC could inhibit cetuximab-mediated cellular cytotoxicity (Levy et al., 2009). We used a combination of monalizumab and cetuximab to stimulate NK cells against an SCCHN cell line *in vitro* (Figure 6A, left panel), and monitored the induction of CD137 as a marker of NK cell activation including ADCC. This combination of mAbs amplified the activation of NK cells, as shown by the higher frequencies of CD137$^+$ NK cells. Monalizumab also enhanced the NK cell-mediated ADCC by the anti-CD20 mAb obinutuzumab in cocultures with B cell lines expressing MHC class I (Figure 6A, right panel). Thus, the anti-NKG2A mAb monalizumab can amplify the beneficial effects of other IO treatments, such as those promoting ADCC.

Tumor Control by a Combination of Monalizumab and Cetuximab in Patients with SCCHN

We found that combinations of NKG2A-blocking mAbs with other IO treatments, such as anti-PD-1 mAbs, anti-PD-L1 mAbs or cetuximab, had additive effects on anti-tumor immunity in preclinical experimental settings *in vitro* and *in vivo*. These results provide a scientific rationale for evaluations of the efficacy and safety of monalizumab in cancer patients. SCCHN tumors were strongly positive for HLA-E and were infiltrated with CD8$^+$ T cells and NK cells, which may express NKG2A (Figures 4A, 4B, and 4D). Cetuximab is used in the standard care regimen for SCCHN (Vermorken et al., 2007). We therefore assessed the safety and efficacy of the combination of monalizumab and cetuximab in patients with previously treated recurrent or metastatic (R/M) SCCHN in a phase II clinical trial (NCT02643550). We evaluated five doses of monalizumab (0.4, 1, 2, 4, 10 mg/kg every 2 weeks) in combination with the approved dose of cetuximab (400 mg/m^2 loading dose and then 250 mg/m^2 weekly). The maximum tolerated dose was not reached and the highest dose of monalizumab tested (10 mg/kg) was used for expansion of the phase II cohort. We used a one-stage Fleming design with futility analysis after the first 11 patients; the overall phase II study will include 40 patients. The characteristics of the patients are shown in Table 1. As of March 9, 2018, 31 patients with R/M SCCHN were treated and evaluable for safety, of which 26 patients were evaluable for efficacy while the remaining patients were studied too early for assessment. All 31 patients had been

Table 1. Characteristics of Patients with Recurrent or Metastatic SCCHN, Enrolled in the NCT02643550 Phase II Clinical Trial

Patient Characteristics, N = 31		N (%)
Age, median [range]		64 [34–76]
Sex	female	10 (32)
	male	21 (68)
ECOG	0	12 (39)
	1	19 (61)
HPV status	positive	4 (13)
	negative	15 (48)
	to be determined	12 (39)
Tobacco	never	6 (19)
	former	20 (65)
	current	5 (16)
Tumor site	oral cavity	14 (45)
	oropharynx	10 (32)
	larynx	4 (13)
	hypopharynx	2 (6)
	nasopharynx	1 (3)
Type of recurrence	local	18 (58)
	distant	13 (42)
Prior lines of systemic therapy (overall)	Number of Previous Lines	
	1	16 (52)
	2	10 (32)
	3	5 (16)
	prior platinum	31 (100)
	prior IO	14 (45)
	prior cetuximab	3 (10)

previously treated with platinum-based chemotherapy, and 24 patients received one or two systemic treatment regimens. Fourteen patients had already received immunotherapies, and three had been already treated with cetuximab for locally advanced disease and had been free from progressive disease for at least 4 months. Safety was the primary endpoint of part I and objective response rate (ORR) of part II. The combination was well tolerated. Most of the adverse events (AE) observed (93%) were of grades 1–2 severity, rapidly reversible and easily manageable. The most common monalizumab-related AEs were fatigue (17%), pyrexia (13%), and headache (10%). Other monalizumab-related AEs (interstitial lung disease, colitis and hypophosphatemia) were reported in 1 patient each. The most frequent AEs reported for cetuximab in previous studies (Vermorken et al., 2007) were skin disorders (rash, 49%; acne, 26%; nail disorders, 16%; dry skin, 14%), and these effects were not exacerbated by monalizumab. No infusion-related reactions were observed (patients received premedication for cetuximab as specified on the label). No treatment-related death was reported. No new or unusual signs suggestive of poor safety were observed with the combination of monalizumab and cetuximab. We thus concluded that the safety profile of the combination was similar to that for the two single agents.

Interim treatment efficacy results for the phase II trial showed that treatment with the monalizumab and cetuximab combination resulted in a confirmed RECIST partial response in 8 of 26 patients (31%), stable disease (SD) in 14 of 26 (54%) and progressive disease (PD) in 3 of 26 (11%) patients and one patient died from progressive disease at week 8 without post-baseline imaging (Figures 6B–6D). The lesion disappeared in one patient, as shown in Figure 6D. Assuming an ORR of 25%, using 10% as the cutoff for inactivity, $\alpha = 0.05$, and a power of 0.76, the predefined number of eight responses required to declare a positive result for the trial already was reached. Two of the eight patients with confirmed responses had previously received immunotherapy. At the time of the analysis, the median response duration was not reached; six responding patients were still on treatment. Median follow-up time was 129 days: 17 patients (55%) were still on treatment, 14 patients (45%) had stopped treatment, because of progressive disease in 12 (38%), and adverse event in one and on the decision of the investigator in the final case. The activity of single agent cetuximab in recurrent and/or metastatic SCCHN is limited with a 13% ORR, a median duration of response (DoR) of 4 months, a median progression-free survival (PFS) of 2.3 months, and a median overall survival (OS) of 5.6 months (Vermorken et al., 2007, 2008). Even if no formal comparison can be made, the activity of monalizumab combined to cetuximab appears higher than historical data for cetuximab alone, although cross-trial comparisons of this kind should be interpreted with caution due to the small number of patients involved and possible differences in patient population and trial methodology. Overall, these data showed that the combination therapy of monalizumab with cetuximab has promise for the treatment of patients with SCCHN with expected toxicity profile of either agent alone.

DISCUSSION

Immune checkpoint inhibitors have greatly improved the control of several types of cancer, but the efficacy of these treatments needs to be further improved, as does the ability to control their toxicity. One way of achieving this goal would be to identify critical immune checkpoints other than PD-1 and CTLA-4 for targeting by therapeutic antibodies to promote effective immune responses to cancers. Most immunomodulatory strategies to date have focused on enhancing T cell responses, but there has been a recent surge of interest in harnessing the relatively underexplored NK cell compartment for therapeutic interventions (Cerwenka and Lanier, 2018; Guillerey and Smyth, 2016; Rautela et al., 2018; Vivier et al., 2012; Chiossone et al., 2018). The manipulation of NK cells in cancer is designed to initiate a multilayered immune response culminating in protective and long-lasting immunity to tumors based on a number of different cell types, including T cells.

Here, we focus on the NKG2A receptor, a well-known ITIM-bearing inhibitory receptor expressed on both T and NK cells (López-Botet et al., 2000; Moretta et al., 2001), emitting inhibitory signals transduced via the protein tyrosine phosphatase SHP-1 (Viant et al., 2014). The abundance of $NKG2A^+CD8^+$ T cells is low in human blood, but NKG2A expression can be induced at the surface of $CD8^+$ T cells upon activation (Braud et al., 2003). The targeting of NKG2A with a blocking antibody would therefore have the unique advantage of enhancing

T and NK cell responses. Another advantage of targeting NKG2A is the safety of this approach, as no abnormalities have been reported in mouse strains lacking CD94 (Vance et al., 1999; Orr et al., 2010), which forms a heterodimer with NKG2A. These mice therefore lack cell-surface NKG2A expression.

One critical point for such an approach is the expression of NKG2A and HLA-E during cancer. We have shown that the NKG2A receptor is expressed on NK and T cells in the tumor bed in many human cancers and we have also shown that its ligand, HLA-E, is frequently overexpressed in tumors. By contrast, classical MHC-I expression is often weak on tumor cells, and this downregulation has been recognized as a major mechanism by which tumor cells escape T cell control (Garrido et al., 2017; Sharma et al., 2017). Unlike classical HLA class I molecules, HLA-E continues to be expressed on the surface of tumor cells, often even more strongly than on healthy cells, in patients with solid tumors or leukemia/lymphoma (Benson et al., 2012; Mamessier et al., 2011; Platonova et al., 2011; Talebian Yazdi et al., 2016). This conservation of expression likely results from the dependence of cell-surface HLA-E expression on many distinct peptides, including the leader peptides of HLA-A, -B, or -C. Downregulation of HLA-E expression therefore would require at least the elimination of three types of HLA molecules. Our data for NKG2A expression are consistent with earlier reports on tumor-infiltrating NK and T cells in melanoma and breast and cervical cancers (Mamessier et al., 2011; Sheu et al., 2005). A complementary study showed in several tumor mouse models that expression of NKG2A is associated with worse clinical outcome (van Montfoort et al., 2018).

One of the key findings of our studies is the demonstration that NKG2A is often co-expressed with PD-1 on $CD8^+$ T cells. PD-1 expression is a hallmark of exhausted $CD8^+$ T cells (Hashimoto et al., 2018). This result therefore suggested that NKG2A expression might constitute an additional brake to release for reversing $CD8^+$ T cell exhaustion. The regulation of NKG2A expression on both NK and $CD8^+$ T cells remains to be dissected in detail. Nevertheless, unlike PD-1 expression, which can be observed on the surface of $CD8^+$ T cells from whole blood or lymph nodes from cancer patients, the number of NKG2A-expressing $CD8^+$ T cells was selectively increased at the tumor bed or adjacent tissue. These results suggest that signals derived specifically from the tumor would be required to induce, or to sustain NKG2A expression.

We also found that HLA-E was more frequently expressed than PD-L1 in several types of cancer. This finding is consistent with previous suggestions that HLA-E expression may account for some of the lack of responsiveness to anti-PD-x observed in Merkel cell carcinoma (Paulson et al., 2018) and in an *in vivo* CRISPR screening program that identified $Qa\text{-}1^b$ (the mouse HLA-E ortholog) as a cancer immunotherapy target, because $Qa\text{-}1^b$ loss-of-function increased the efficacy of immunotherapy by PD-1 blockade (Manguso et al., 2017). These data support the use of a combination of mAbs blocking the PD-x and NKG2A/HLA-E inhibitory pathways. Our results in mice indicate that NKG2A pathway blockade does indeed improve tumor control when combined with a blockade of the PD-1/PD-L1 inhibitory pathway. We also demonstrated the generation of protective memory $CD8^+$ T cells in mice into which RMA-Rae-1β tumors were implanted and then cured by combined PD-L1 and NKG2A blockade. Thus, our preclinical results provide a rationale for combining monalizumab and durvalumab into a novel immunotherapy for cancer patients. Importantly, such a clinical trial is ongoing (NCT02671435) and very recently preliminary safety and efficacy data were reported (Segal et al., 2018). Briefly, the dose escalation part of the study demonstrated the feasibility of combining the two agents with no new safety signals noted beyond the known safety profile for each individual agent. The initial clinical activity data from a cohort expansion in pretreated (median of three previous lines of systemic therapy) microsatellite stable colorectal cancer (MSS CRC; n = 39) demonstrated an ORR of 8% (median duration of response of 16.1 weeks) and a disease control rate (DCR) at 16 weeks of 31% (Segal et al., 2018). Although these results are very preliminary, they are an example of potential therapeutic opportunities for immunotherapy in MSS CRC, a setting in which immune checkpoint-based therapy has, so far, failed to demonstrate any consistent and meaningful clinical benefit.

Combining a blockade of inhibitory signals with the delivery of activating signals should improve the efficacy of immunotherapies. Many possible approaches of this type are being tested, including the triggering of innate immunity via the delivery of TLR ligands (Du et al., 2016), activation of the STING pathway at the tumor bed (Corrales et al., 2016), treatment with antibodies targeting activating cell surface receptors (Callahan et al., 2016; Muntasell et al., 2017), and the use of engineered forms of cytokines, such pegylated IL-2 (Charych et al., 2017; Charych et al., 2016) and IL-2 variants (Sockolosky et al., 2018). Antibodies directed against tumor cells also could be used to stimulate the immune response to tumor cells, thereby helping to eliminate cancer. The mode of action of these treatments differs between antibodies, but efficacy is partly dependent on ADCC, as for rituximab, an anti–CD20 mAb used to treat non-Hodgkin lymphoma and chronic lymphocytic leukemia (Cartron and Watier, 2017). Other antibodies are also used to stimulate the immune system via ADCC. One such antibody is cetuximab, which is used in metastatic CRC and SCCHN. We showed *in vitro* that NKG2A blockade with monalizumab boosts NK cell-mediated ADCC against cetuximab-coated SCCHN tumor cells. Consistent with these data, treatment with a combination of monalizumab and cetuximab was found to be effective in the NCT02643550 phase II clinical trial for SCCHN. Importantly, little, if any, toxicity was associated with blocking NKG2A and especially no signs of auto-immunity. The encouraging results obtained for SCCHN in NCT02643550 and for MSS CRC in NCT02671435 require consolidation in further clinical trials, but they constitute a key step toward the use of monalizumab in combination treatments against cancer. Once the samples from all the patients enrolled in the monalizumab clinical trials will be accessible, translational studies will be performed. In particular, it will be addressed whether the expression of HLA-E at the tumor bed is linked to the HLA types of the patients (Horowitz et al., 2016; Ramsuran et al., 2018) and to the clinical outcome.

In conclusion, we report here the full characterization of a first-in-class immune checkpoint inhibitor, monalizumab. This

therapeutic antibody has several key features. First, it enhances the antitumor activities of both T and NK cells, by blocking the inhibitory function of NKG2A. Second, the ligand of NKG2A is the non-classical MHC class I molecule HLA-E, which is frequently overexpressed on human tumors, providing a mechanism of resistance to lymphocyte activation at the tumor bed. Third, monalizumab is well tolerated in humans and has yielded encouraging efficacy results in clinical trials assessing its use in combination with cetuximab in SCCHN, and in combination with durvalumab in MSS CRC, two clinical conditions with low ORRs, for which therapeutic options are very limited. Therefore, anti-NKG2A mAb is a promising checkpoint inhibitor that promotes antitumor immunity by enhancing the activities of both T and NK cells. Interestingly, NKG2A has been shown to contribute to the inhibition HIV-infected target cell clearance by NK cells (Ramsuran et al., 2018). Thus, beyond cancer, the therapeutic blockade of NKG2A/HLA-E interaction by monalizumab may be beneficial in patients with HIV disease, and in other conditions that remain to be explored.

STAR★METHODS

Detailed methods are provided in the online version of this paper and include the following:

- KEY RESOURCES TABLE
- CONTACT FOR REAGENT AND RESOURCE SHARING
- EXPERIMENTAL MODEL AND SUBJECT DETAILS
  - Mice
  - Cell lines
  - Human primary cells
  - Human trial information
- METHOD DETAILS
  - Monoclonal anti-mouse NKG2A antibody
  - *In vivo* murine tumor experiments
  - Flow cytometry analysis of splenic and tumor-infiltrating mouse lymphocytes (TILs)
  - Functional assays with BALB/c splenocytes and A20 TILs
  - Immunohistochemistry
  - Monocyte-CD8 T cell cocultures
  - Long-term culture of PBMCs with IL-15 for the generation of PD-1$^+$ NK cells
  - Flu-specific CD8$^+$ T cell staining
  - Functional assay with CD8$^+$ T cells (expression of CD107/IFN-γ)
  - Preparation of human TILs
  - Functional assay with CD8$^+$ T cells (cytotoxic assay)
  - Phenotypic analysis of NK cells in day 9 cultures
  - Functional assays with peripheral human NK cells
  - Inhibition of HLA-E tetramers binding
  - Trial design
- QUANTIFICATION AND STATISTICAL ANALYSIS

SUPPLEMENTAL INFORMATION

Supplemental Information includes six figures and one table and can be found with this article online at https://doi.org/10.1016/j.cell.2018.10.014.

ACKNOWLEDGMENTS

We thank Mohammed Dar (Mediumme) for critically reviewing the manuscript; François Romagné (MI-mAbs), Fabien Chanuc, Nicolas Fuseri, and Flavien Caraguel (Innate Pharma) for help and advice during these studies. The E.V. lab was supported by funding from the European Research Council (ERC) under the European Union's Horizon 2020 research and innovation program (TILC, grant agreement no. 694502), the Agence Nationale de la Recherche, Equipe Labellisée "La Ligue," Ligue Nationale contre le Cancer, MSDAvenir, Innate Pharma, and institutional grants to the CIML (INSERM, CNRS, and Aix-Marseille University) and Marseille Immunopole.

AUTHOR CONTRIBUTIONS

P.A., R.Z., and E.V. conceived the project. P.A., C.D., C.S., M.B., C.B., L.G., and O.L. conceived the experiments. J.F., A.B.-C., P.D., and R.B.C. conceived the clinical study. C.H. and O.L. provided access to the human samples. C.B.-C., E.B., J.L., S.G., A.M., B.R., T.A., V.B., and A.I.L. performed the experiments. P.A., C.D., C.S., C.B.-C., G.H., R.R., A.M., H.G., M.J.-K., Y.M., R.H., A.B.-C., P.D., E.N.-M. and E.V. analyzed the data. P.A, E.N.-M. and E.V. wrote the manuscript.

DECLARATION OF INTERESTS

P.A., C.D., C.S., C.B.-C., J.L., T.A., M.B., C.B., L.G., A.M., B.R., R.R., V.B., E.B., A.B-C., R.Z., P.D., Y.M, and E.V. are employees of Innate Pharma. H.G. M.J.-K., and R.H. are employees of MedImmune. P.A., C.D., M.B. have a patent related to this work.

Received: June 13, 2018
Revised: August 3, 2018
Accepted: October 2, 2018
Published: November 29, 2018

REFERENCES

André, P., Brunet, C., Guia, S., Gallais, H., Sampol, J., Vivier, E., and Dignat-George, F. (1999). Differential regulation of killer cell Ig-like receptors and CD94 lectin-like dimers on NK and T lymphocytes from HIV-1-infected individuals. Eur. J. Immunol. *29*, 1076–1085.

Baumeister, S.H., Freeman, G.J., Dranoff, G., and Sharpe, A.H. (2016). Coinhibitory pathways in immunotherapy for cancer. Annu. Rev. Immunol. *34*, 539–573.

Benson, D.M., Jr., Hofmeister, C.C., Padmanabhan, S., Suvannasankha, A., Jagannath, S., Abonour, R., Bakan, C., Andre, P., Efebera, Y., Tiollier, J., et al. (2012). A phase 1 trial of the anti-KIR antibody IPH2101 in patients with relapsed/refractory multiple myeloma. Blood *120*, 4324–4333.

Bertone, S., Schiavetti, F., Bellomo, R., Vitale, C., Ponte, M., Moretta, L., and Mingari, M.C. (1999). Transforming growth factor-beta-induced expression of CD94/NKG2A inhibitory receptors in human T lymphocytes. Eur. J. Immunol. *29*, 23–29.

Brady, J., Hayakawa, Y., Smyth, M.J., and Nutt, S.L. (2004). IL-21 induces the functional maturation of murine NK cells. J. Immunol. *172*, 2048–2058.

Braud, V.M., Aldemir, H., Breart, B., and Ferlin, W.G. (2003). Expression of CD94-NKG2A inhibitory receptor is restricted to a subset of CD8+ T cells. Trends Immunol. *24*, 162–164.

Callahan, M.K., Postow, M.A., and Wolchok, J.D. (2016). Targeting T cell co-receptors for cancer therapy. Immunity *44*, 1069–1078.

Cartron, G., and Watier, H. (2017). Obinutuzumab: what is there to learn from clinical trials? Blood *130*, 581–589.

Cerwenka, A., and Lanier, L.L. (2018). Natural killers join the fight against cancer. Science *359*, 1460–1461.

Charych, D.H., Hoch, U., Langowski, J.L., Lee, S.R., Addepalli, M.K., Kirk, P.B., Sheng, D., Liu, X., Sims, P.W., VanderVeen, L.A., et al. (2016). NKTR-214, an engineered cytokine with biased IL2 receptor binding, increased tumor

exposure, and marked efficacy in mouse tumor models. Clin. Cancer Res. *22*, 680–690.

Charych, D., Khalili, S., Dixit, V., Kirk, P., Chang, T., Langowski, J., Rubas, W., Doberstein, S.K., Eldon, M., Hoch, U., and Zalevsky, J. (2017). Modeling the receptor pharmacology, pharmacokinetics, and pharmacodynamics of NKTR-214, a kinetically-controlled interleukin-2 (IL2) receptor agonist for cancer immunotherapy. PLoS ONE *12*, e0179431.

Chiossone, L., Dumas, P.-Y., Vienne, M., and Vivier, E. (2018). Natural killer cells and other innate lymphoid cells in cancer. Nat. Rev. Immunol. *18*, 671–688.

Corrales, L., McWhirter, S.M., Dubensky, T.W., Jr., and Gajewski, T.F. (2016). The host STING pathway at the interface of cancer and immunity. J. Clin. Invest. *126*, 2404–2411.

Daëron, M., Jaeger, S., Du Pasquier, L., and Vivier, E. (2008). Immunoreceptor tyrosine-based inhibition motifs: a quest in the past and future. Immunol. Rev. *224*, 11–43.

Du, B., Jiang, Q.-L., Cleveland, J., Liu, B.-R., and Zhang, D. (2016). Targeting Toll-like receptors against cancer. J. Cancer Metastasis Treat. *2*, 463–470.

Ferris, R.L., Lenz, H.J., Trotta, A.M., García-Foncillas, J., Schulten, J., Audhuy, F., Merlano, M., and Milano, G. (2018). Rationale for combination of therapeutic antibodies targeting tumor cells and immune checkpoint receptors: Harnessing innate and adaptive immunity through IgG1 isotype immune effector stimulation. Cancer Treat. Rev. *63*, 48–60.

Garrido, F., Ruiz-Cabello, F., and Aptsiauri, N. (2017). Rejection versus escape: the tumor MHC dilemma. Cancer Immunol. Immunother. *66*, 259–271.

Guillerey, C., and Smyth, M.J. (2016). NK cells and cancer immunoediting. Curr. Top. Microbiol. Immunol. *395*, 115–145.

Hashimoto, M., Kamphorst, A.O., Im, S.J., Kissick, H.T., Pillai, R.N., Ramalingam, S.S., Araki, K., and Ahmed, R. (2018). CD8 T cell exhaustion in chronic infection and cancer: opportunities for interventions. Annu. Rev. Med. *69*, 301–318.

Horowitz, A., Djaoud, Z., Nemat-Gorgani, N., Blokhuis, J., Hilton, H.G., Beziat, V., Malmberg, K.J., Norman, P.J., Guethlein, L.A., and Parham, P. (2016). Class I HLA haplotypes form two schools that educate NK cells in different ways. Sci. Immunol. *3*, pii: eaag1672.

Le Dréan, E., Vély, F., Olcese, L., Cambiaggi, A., Guia, S., Krystal, G., Gervois, N., Moretta, A., Jotereau, F., and Vivier, E. (1998). Inhibition of antigen-induced T cell response and antibody-induced NK cell cytotoxicity by NKG2A: association of NKG2A with SHP-1 and SHP-2 protein-tyrosine phosphatases. Eur. J. Immunol. *28*, 264–276.

Levy, E.M., Sycz, G., Arriaga, J.M., Barrio, M.M., von Euw, E.M., Morales, S.B., González, M., Mordoh, J., and Bianchini, M. (2009). Cetuximab-mediated cellular cytotoxicity is inhibited by HLA-E membrane expression in colon cancer cells. Innate Immun. *15*, 91–100.

López-Botet, M., Llano, M., Navarro, F., and Bellón, T. (2000). NK cell recognition of non-classical HLA class I molecules. Semin. Immunol. *12*, 109–119.

Mahapatra, S., Mace, E.M., Minard, C.G., Forbes, L.R., Vargas-Hernandez, A., Duryea, T.K., Makedonas, G., Banerjee, P.P., Shearer, W.T., and Orange, J.S. (2017). High-resolution phenotyping identifies NK cell subsets that distinguish healthy children from adults. PloS ONE *12*, e0181134.

Mamessier, E., Sylvain, A., Thibult, M.L., Houvenaeghel, G., Jacquemier, J., Castellano, R., Gonçalves, A., André, P., Romagné, F., Thibault, G., et al. (2011). Human breast cancer cells enhance self tolerance by promoting evasion from NK cell antitumor immunity. J. Clin. Invest. *121*, 3609–3622.

Manguso, R.T., Pope, H.W., Zimmer, M.D., Brown, F.D., Yates, K.B., Miller, B.C., Collins, N.B., Bi, K., LaFleur, M.W., Juneja, V.R., et al. (2017). In vivo CRISPR screening identifies Ptpn2 as a cancer immunotherapy target. Nature *547*, 413–418.

Manser, A.R., and Uhrberg, M. (2016). Age-related changes in natural killer cell repertoires: impact on NK cell function and immune surveillance. Cancer Immunol. Immunother. *65*, 417–426.

McMahon, C.W., Zajac, A.J., Jamieson, A.M., Corral, L., Hammer, G.E., Ahmed, R., and Raulet, D.H. (2002). Viral and bacterial infections induce expression of multiple NK cell receptors in responding CD8(+) T cells. J. Immunol. *169*, 1444–1452.

Mingari, M.C., Ponte, M., Bertone, S., Schiavetti, F., Vitale, C., Bellomo, R., Moretta, A., and Moretta, L. (1998). HLA class I-specific inhibitory receptors in human T lymphocytes: interleukin 15-induced expression of CD94/NKG2A in superantigen- or alloantigen-activated CD8+ T cells. Proc. Natl. Acad. Sci. USA *95*, 1172–1177.

Moretta, A., Bottino, C., Vitale, M., Pende, D., Cantoni, C., Mingari, M.C., Biassoni, R., and Moretta, L. (2001). Activating receptors and coreceptors involved in human natural killer cell-mediated cytolysis. Annu. Rev. Immunol. *19*, 197–223.

Mori, S., Jewett, A., Cavalcanti, M., Murakami-Mori, K., Nakamura, S., and Bonavida, B. (1998). Differential regulation of human NK cell-associated gene expression following activation by IL-2, IFN-alpha and PMA/ionomycin. Int. J. Oncol. *12*, 1165–1170.

Muntasell, A., Ochoa, M.C., Cordeiro, L., Berraondo, P., López-Díaz de Cerio, A., Cabo, M., López-Botet, M., and Melero, I. (2017). Targeting NK-cell checkpoints for cancer immunotherapy. Curr. Opin. Immunol. *45*, 73–81.

Okazaki, T., Chikuma, S., Iwai, Y., Fagarasan, S., and Honjo, T. (2013). A rheostat for immune responses: the unique properties of PD-1 and their advantages for clinical application. Nat. Immunol. *14*, 1212–1218.

Okazaki, T., and Honjo, T. (2007). PD-1 and PD-1 ligands: from discovery to clinical application. Int. Immunol. *19*, 813–824.

Orr, M.T., Wu, J., Fang, M., Sigal, L.J., Spee, P., Egebjerg, T., Dissen, E., Fossum, S., Phillips, J.H., and Lanier, L.L. (2010). Development and function of CD94-deficient natural killer cells. PLoS One *5*, e15184.

Paulson, K.G., Park, S.Y., Vandeven, N.A., Lachance, K., Thomas, H., Chapuis, A.G., Harms, K.L., Thompson, J.A., Bhatia, S., Stang, A., et al. (2018). Merkel cell carcinoma: current US incidence and projected increases based on changing demographics. J. Am. Acad. Dermatol. *78*, 457–463.e2.

Platonova, S., Cherfils-Vicini, J., Damotte, D., Crozet, L., Vieillard, V., Validire, P., André, P., Dieu-Nosjean, M.C., Alifano, M., Régnard, J.F., et al. (2011). Profound coordinated alterations of intratumoral NK cell phenotype and function in lung carcinoma. Cancer Res. *71*, 5412–5422.

Ramsuran, V., Naranbhai, V., Horowitz, A., Qi, Y., Martin, M.P., Yuki, Y., Gao, X., Walker-Sperling, V., Del Prete, G.Q., Schneider, D.K., et al. (2018). Elevated *HLA-A* expression impairs HIV control through inhibition of NKG2A-expressing cells. Science *359*, 86–90.

Rapaport, A.S., Schriewer, J., Gilfillan, S., Hembrador, E., Crump, R., Plougastel, B.F., Wang, Y., Le Friec, G., Gao, J., Cella, M., et al. (2015). The inhibitory receptor NKG2A sustains virus-specific $CD8^+$ T cells in response to a lethal poxvirus infection. Immunity *43*, 1112–1124.

Rautela, J., Souza-Fonseca-Guimaraes, F., Hediyeh-Zadeh, S., Delconte, R.B., Davis, M.J., and Huntington, N.D. (2018). Molecular insight into targeting the NK cell immune response to cancer. Immunol. Cell Biol. *96*, 477–484.

Sagiv-Barfi, I., Kohrt, H.E., Czerwinski, D.K., Ng, P.P., Chang, B.Y., and Levy, R. (2015). Therapeutic antitumor immunity by checkpoint blockade is enhanced by ibrutinib, an inhibitor of both BTK and ITK. Proc. Natl. Acad. Sci. USA *112*, E966–E972.

Schumacher, T.N., and Schreiber, R.D. (2015). Neoantigens in cancer immunotherapy. Science *348*, 69–74.

Segal, N.H., Naidoo, J., Curigliano, G., Patel, S., Sahebjam, S., Papadopoulos, K.P., Gordon, M.S., Wang, D., Rueda, A.G., Song, X., et al. (2018). First-in-human dose escalation of monalizumab plus durvalumab, with expansion in patients with metastatic microsatellite-stable colorectal cancer. J. Clin. Oncol. *36* (*Suppl 15*), 3540–3540.

Sharma, P., and Allison, J.P. (2015a). The future of immune checkpoint therapy. Science *348*, 56–61.

Sharma, P., and Allison, J.P. (2015b). Immune checkpoint targeting in cancer therapy: toward combination strategies with curative potential. Cell *161*, 205–214.

Sharma, P., Hu-Lieskovan, S., Wargo, J.A., and Ribas, A. (2017). Primary, adaptive, and acquired resistance to cancer immunotherapy. Cell *168*, 707–723.

Sheu, B.C., Chiou, S.H., Lin, H.H., Chow, S.N., Huang, S.C., Ho, H.N., and Hsu, S.M. (2005). Up-regulation of inhibitory natural killer receptors CD94/NKG2A with suppressed intracellular perforin expression of tumor-infiltrating CD8+ T lymphocytes in human cervical carcinoma. Cancer Res. *65*, 2921–2929.

Sivori, S., Vitale, M., Bottino, C., Marcenaro, E., Sanseverino, L., Parolini, S., Moretta, L., and Moretta, A. (1996). CD94 functions as a natural killer cell inhibitory receptor for different HLA class I alleles: identification of the inhibitory form of CD94 by the use of novel monoclonal antibodies. Eur. J. Immunol. *26*, 2487–2492.

Sockolosky, J.T., Trotta, E., Parisi, G., Picton, L., Su, L.L., Le, A.C., Chhabra, A., Silveria, S.L., George, B.M., King, I.C., et al. (2018). Selective targeting of engineered T cells using orthogonal IL-2 cytokine-receptor complexes. Science *359*, 1037–1042.

Talebian Yazdi, M., van Riet, S., van Schadewijk, A., Fiocco, M., van Hall, T., Taube, C., Hiemstra, P.S., and van der Burg, S.H. (2016). The positive prognostic effect of stromal CD8+ tumor-infiltrating T cells is restrained by the expression of HLA-E in non-small cell lung carcinoma. Oncotarget *7*, 3477–3488.

van Montfoort, N., Borst, L., Korrer, M.J., Sluijter, M., Marijt, K., Santegoets, S., van Ham, V., Ehrsan, I., Pornpimol-Charoenteng, K., Zervakis, G., et al. (2018). NKG2A blockade potentiates CD8 T-cell immunity induced by cancer vaccines. Cell *175*. Published online November 29, 2018. https://doi.org/10.1016/j.cell.2018.10.028.

Vance, R.E., Jamieson, A.M., and Raulet, D.H. (1999). Recognition of the class Ib molecule Qa-1(b) by putative activating receptors CD94/NKG2C and CD94/NKG2E on mouse natural killer cells. J. Exp. Med. *190*, 1801–1812.

Vermorken, J.B., Trigo, J., Hitt, R., Koralewski, P., Diaz-Rubio, E., Rolland, F., Knecht, R., Amellal, N., Schueler, A., and Baselga, J. (2007). Open-label, uncontrolled, multicenter phase II study to evaluate the efficacy and toxicity of cetuximab as a single agent in patients with recurrent and/or metastatic squamous cell carcinoma of the head and neck who failed to respond to platinum-based therapy. J. Clin. Oncol. *25*, 2171–2177.

Vermorken, J.B., Herbst, R.S., Leon, X., Amellal, N., and Baselga, J. (2008). Overview of the efficacy of cetuximab in recurrent and/or metastatic squamous cell carcinoma of the head and neck in patients who previously failed platinum-based therapies. Cancer *112*, 2710–2719.

Viant, C., Fenis, A., Chicanne, G., Payrastre, B., Ugolini, S., and Vivier, E. (2014). SHP-1-mediated inhibitory signals promote responsiveness and anti-tumour functions of natural killer cells. Nat. Commun. *5*, 5108.

Vivier, E., Ugolini, S., Blaise, D., Chabannon, C., and Brossay, L. (2012). Targeting natural killer cells and natural killer T cells in cancer. Nat. Rev. Immunol. *12*, 239–252.

With the Rio, You Get it All

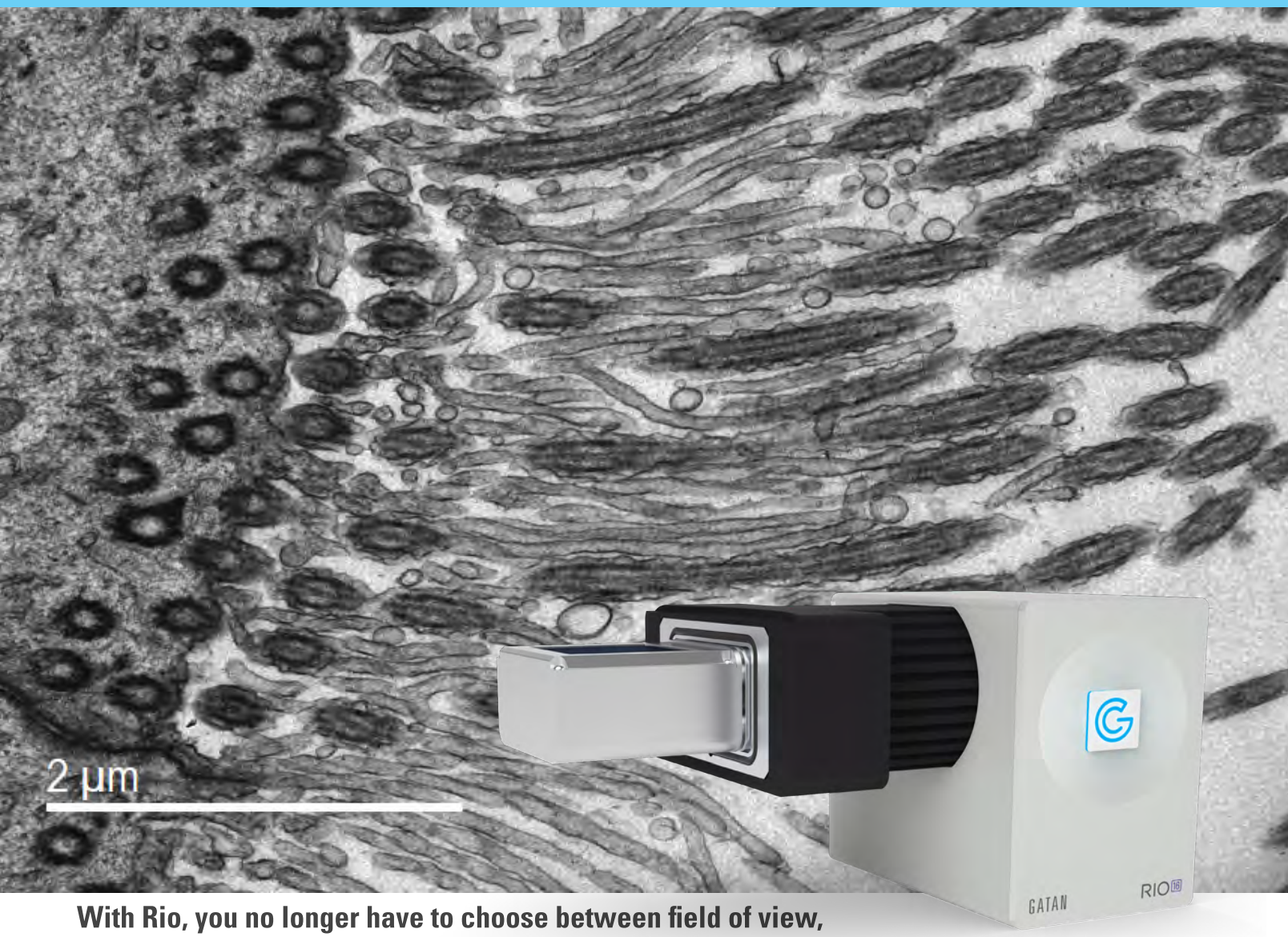

With Rio, you no longer have to choose between field of view, resolution, speed, and sensitivity for electron microscopy.

With Rio, you get it all.

- **High sensitivity:** Newly optimized scintillator and 1:1 fiber optic coupling
  Gpixel CMOS sensor with 100% duty cycle and ultra-low readout noise
- **High resolution:** 9 µm pixel, optimal for 30 – 200 kV operation
- **Large field of view:** Up to 16 megapixels (4k x 4k)
- **High speed:** Up to 20 4k x 4k resolution frames per second and 160 1k x 1k frames per second

Rio – The clear new performance benchmark for scintillator cameras up to 200 kV operation.

GATAN

Cilia sample courtesy of Hitachi.

Cell

DNA Microscopy: Optics-free Spatio-genetic Imaging by a Stand-Alone Chemical Reaction

Joshua A. Weinstein,[1,8,*] Aviv Regev,[1,2,3,4,*] and Feng Zhang[1,3,5,6,7,*]
[1]Broad Institute of MIT and Harvard, Cambridge, MA 02142, USA
[2]Department of Biology, Koch Institute for Integrative Cancer Research, Massachusetts Institute of Technology, Cambridge, MA 02140, USA
[3]Howard Hughes Medical Institute, MIT, Cambridge, MA 02139, USA
[4]Klarman Cell Observatory, Broad Institute of MIT and Harvard, Cambridge, MA 02142, USA
[5]McGovern Institute for Brain Research at MIT, Cambridge, MA 02139, USA
[6]Department of Brain and Cognitive Science, Massachusetts Institute of Technology, Cambridge, MA 02139, USA
[7]Department of Biological Engineering, Massachusetts Institute of Technology, Cambridge, MA 02139, USA
[8]Lead Contact
*Correspondence: jwein@broadinstitute.org (J.A.W.), aregev@broadinstitute.org (A.R.), zhang@broadinstitute.org (F.Z.)
https://doi.org/10.1016/j.cell.2019.05.019

SUMMARY

Analyzing the spatial organization of molecules in cells and tissues is a cornerstone of biological research and clinical practice. However, despite enormous progress in molecular profiling of cellular constituents, spatially mapping them remains a disjointed and specialized machinery-intensive process, relying on either light microscopy or direct physical registration. Here, we demonstrate DNA microscopy, a distinct imaging modality for scalable, optics-free mapping of relative biomolecule positions. In DNA microscopy of transcripts, transcript molecules are tagged *in situ* with randomized nucleotides, labeling each molecule uniquely. A second *in situ* reaction then amplifies the tagged molecules, concatenates the resulting copies, and adds new randomized nucleotides to uniquely label each concatenation event. An algorithm decodes molecular proximities from these concatenated sequences and infers physical images of the original transcripts at cellular resolution with precise sequence information. Because its imaging power derives entirely from diffusive molecular dynamics, DNA microscopy constitutes a chemically encoded microscopy system.

INTRODUCTION

The spatial organization of cells with unique gene expression patterns within tissues is essential to their function and is at the foundation of differentiation, specialization, and physiology in higher organisms. For example, neurons of the CNS express protocadherins and neurexins in highly diverse spatial patterns across neural tissue that govern cells' intrinsic states, morphology, and synaptic connectivity (Lefebvre et al., 2012; Schreiner et al., 2014). Spatial co-localization of B- and T-lymphocytes in the immune system that express diverse immune receptors—genetically distinct due to somatic mutations—permits signaling feedback critical for immune clonal selection (Victora and Nussenzweig, 2012). In the gut, epithelial, immune, endocrine, and neural cells are spatially distributed in specific ways that impact how we sense and respond to the environment, with implications for autoimmune disease, food allergies, and cancer. In the tissue context of disease, cell microenvironments may be critical for tumorigenesis (Herishanu et al., 2011; Joyce and Fearon, 2015), immune surveillance and dysfunction, invasion, and metastasis. In tumors in particular, genes with different mutations are expressed in distinct cells, impacting tumorigenesis and leading to neoantigens presented to the immune system (Schumacher and Schreiber, 2015).

Although imaging of cells and tissues has been a cornerstone of biology ever since cells were discovered under the light microscope centuries ago, advances in microscopy have to date largely not incorporated the growing capability to make precise measurements of genomic sequences. While microscopy illuminates spatial detail, it does not capture genetic information unless it is performed in tandem with separate genetic assays. Conversely, genomic and transcriptomic sequencing do not inherently capture spatial details.

One strategy to bridge this gap by spatially quantifying genes of known sequence is hybridization methods (Lubeck et al., 2014; Chen et al., 2015; Moffitt et al., 2016). However, somatic mutation, stochastic gene splicing, and other forms of single-nucleotide variation that is not known *a priori* play a central role in the function and pathology of spatially complex systems (such as the nervous, immune, gastrointestinal, and tumor examples above). As a result, single-nucleotide sequencing and microscopy must be fully integrated to ultimately understand these systems. Recent approaches to do so rely on optical readouts that require elaborate experimental systems (Lee et al., 2014), physical registration and capture of molecules on grids (Junker et al., 2014; Ståhl et al., 2016), or an assumption of similarity among multiple samples so that distinct experiments performed on distinct specimens may be correlated (Satija et al., 2015; Achim et al., 2015). These approaches closely mirror the two ways in which microscopic images have been acquired to date: either (1) detecting electromagnetic radiation (e.g.,

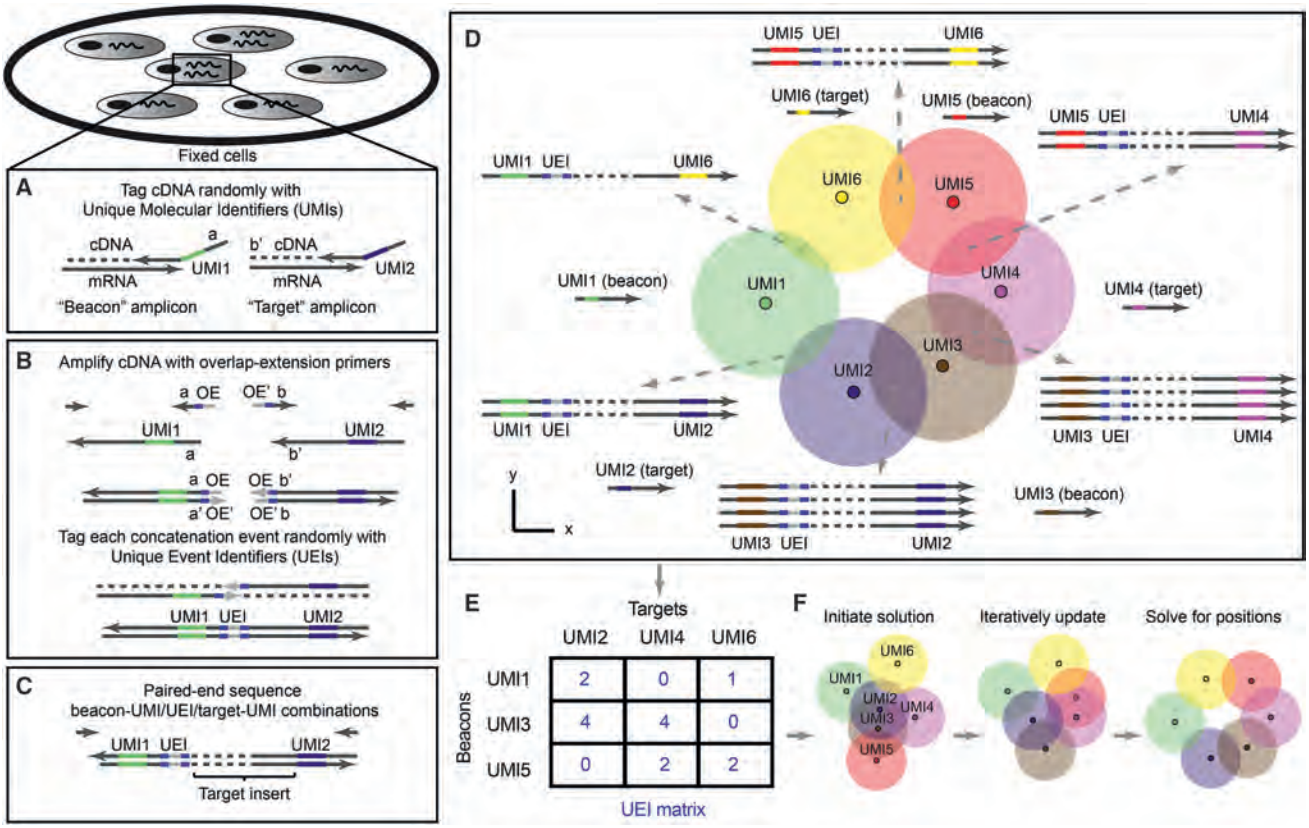

Figure 1. DNA Microscopy

(A and B) Method steps. Cells are fixed and cDNA is synthesized for beacon and target transcripts with randomized nucleotides (UMIs), labeling each molecule uniquely (A). *In situ* amplification of UMI-tagged cDNA directs the formation of concatemer products between beacon and target copies (B). The overhang-primers responsible for concatenation further label each concatenation event uniquely with randomized nucleotides, generating unique event identifiers (UEIs).

(C and D) Paired-end sequencing generates readouts including a beacon-UMI, a target-UMI, the UEI that associates them, and the target gene insert (C). A bird's-eye view of the experiment (D) shows the manner in which the DNA microscopy reaction encodes spatial location. Diffusing and amplifying clouds of UMI-tagged DNA overlap to extents that are determined by the proximity of their centers.

(E and F) UEIs between pairs of UMIs occur at frequencies determined by the degree of diffusion cloud overlap. These frequencies are read out by DNA sequencing, and inserted into a UEI matrix (E) that is then used to infer original UMI positions (F).

See also Figures S1 and S2.

photons or electrons) that has interacted with or been emitted by a sample, or (2) interrogating known locations by physical contact or ablation (e.g., dissection).

Here, we propose a distinct third modality for microscopy which requires neither optics nor physical capture from known coordinates but rather relies on image reconstruction from the relative physical proximity of individual molecules (Figure 1) and focuses on obtaining precise genetic information at high spatial resolution. This principle, of determining coordinates not in relation to an absolute coordinate system but instead in relation to one another, has previously been used in other contexts. For example, in the theory of sensor localization distances between points are explicitly measured and then their relative positions are estimated from these distances (Aspnes et al., 2006). Numerical work has further shown that such estimates can be made using sparse and noisy measurements (Singer, 2008). Here, we build on and adapt the same theoretical concept of "point-to-point communication" through biochemistry to allow position reconstruction from co-localization data of biomolecules to demonstrate a novel form of microscopy, called DNA microscopy. DNA microscopy reconstructs the positions of molecules from the stochastic output of a stand-alone chemical reaction. We confirm that DNA microscopy is able to resolve the 2D physical dimensionality of a specimen, and then demonstrate that it is able to accurately reconstruct a multicellular ensemble *de novo* without optics or any prior knowledge of how biological specimens are organized. Finally, we demonstrate the ability of DNA microscopy to resolve and segment individual cells for transcriptional analysis.

RESULTS

Principle of DNA Microscopy for Spatio-genetic Imaging

DNA microscopy generates images by first randomly tagging individual DNA or RNA molecules with DNA-molecular identifiers. Each deposited DNA-molecular identifier then "communicates"

with its neighbors through two parallel processes. The first process broadcasts amplifying copies of DNA-molecular identifiers to neighbors in its vicinity via diffusion. The second process encodes the proximity between the centers of overlapping molecular diffusion clouds: DNA-molecular identifiers undergo concatenation if they belong to diffusion clouds that overlap. Finally, an algorithm infers from these association rates the relative positions of all original molecules.

DNA microscopy is premised on the notion that DNA can function as an imaging medium in a manner equivalent to light. In the same way that light microscopy images molecules that interact with photons (either due to diffraction or scattering or because these molecules emit photons themselves) and encodes these images in the wavelengths and directions of these photons, DNA microscopy images molecules that interact with DNA (including DNA, RNA, or molecules that have been tagged with either DNA or RNA) and encodes these images in the DNA sequence products of a chemical reaction.

With this analogy in mind, we can imagine superposing two distinct physical processes: a fluorophore radially emitting photons at a specific fluorescence wavelength, and a DNA molecule with a specific sequence undergoing PCR amplification, and its copies diffusing radially. Optical microscopes use lenses to ensure that photons hitting a detector or the human eye will retain some information regarding their point of origin, based on where they hit. However, the ''soup'' of DNA molecules generated in a DNA microscopy reaction does not afford this luxury. We therefore need a different way to distinguish the identities of point sources so that all data are encoded into the DNA itself.

To molecularly distinguish point sources we rely on unique molecular identifiers, or UMIs (Kinde et al., 2011), consisting of randomized bases that tag a molecule before any copy of it has been made (Figure 1A). Because the diversity of UMIs scales exponentially with their length, we have high confidence that when one long UMI tags a molecule, no other molecule in the rest of that sample has been tagged with that same long UMI. We can now use overlap extension PCR to concatenate the diffusing and amplifying copies of these UMIs (with any biological DNA sequences they tag simply carried along). The rate at which they concatenate will reflect the distance between their points of origin.

However, once we sequence the final DNA products, we are still left with the problem of how to quantitatively read out these concatenation rates from DNA sequence alone. Using read-abundances belonging to concatenated DNA products carries serious drawbacks. For example, trace cross-contamination between samples could easily introduce artifactual UMI-UMI associations, and biases in downstream DNA library preparation could heavily distort association frequencies. Most serious, however, is PCR chimerization: any *ex situ* amplification of the DNA library would necessarily introduce template-switching at some rate that would corrupt the data.

We reasoned that if the overlap extension primers contained randomized bases that did not participate in priming themselves, then although each priming event would result in replacement of this randomized sequence, each overlap extension event would fix the new bases in between the now-concatenated sequences (Figure 1B). The concatenated sequences would then carry these randomized bases forward, intact, as they amplified. These bases would from then on be a unique record of that individual concatenation event. We called these new concatenated randomized sequences unique event identifiers, or UEIs, and used them to encode molecular positions into the DNA microscopy reaction.

Experimental Assay for DNA Microscopy to Encode Relative Positions of Molecules in Cells

To demonstrate DNA microscopy, we aimed to image transcripts belonging to a mixed population of two co-cultured human cell lines, GFP-expressing MDA-MB-231 cells and RFP-expressing BT-549 cells. As an initial proof of concept, we aimed to recover images that appear cell-like and where GFP and RFP transcripts are positioned in mutually exclusive cells, whereas GAPDH and ACTB, expressed in both cell lines, are ubiquitous.

In the first step of the experiment, we tag cDNA synthesized *in situ* with UMIs. We designed reaction chambers to both grow cells and perform all reactions (Figures S1A–S1C; STAR Methods). We cultured the cells, and, following fixation and permeabilization, synthesized cDNA by reverse transcription from GFP, RFP, GAPDH, and ACTB gene transcripts (Tables S1 and S2), with primers tagged with 29-nt long UMIs (Figures 1A and S1D). Notably, we designed the reaction to distinguish two types of UMI-tagged cDNA molecules: ''beacons,'' synthesized from ACTB (chosen as a universally expressed gene whose sequence would not be analyzed in later stages), and ''targets'' (everything else). We achieved this distinction between beacon and target amplicons by the artificial sequence-adapters assigned to the primers annealing to each.

In the second step of the experiment, we allow beacon-cDNA and target-cDNA molecules, along with the UMIs that tag them, to amplify, diffuse, and concatenate *in situ* in a manner that generates a new UEI distinct for each concatenation event (Figures 1B and S1D) through overlap-extension PCR (Turchaninova et al., 2013). By design, target amplicon-products will only concatenate to beacon amplicon-products, thereby preventing self-reaction. The middle of each overlap-extension primer includes 10 randomized nucleotides, such that each new concatenation event generates a new 20-nt UEI. Paired-end sequencing of the final concatenated products generates reads each containing a beacon UMI, a target UMI, and a UEI associating them (Figure 1C).

The key to DNA microscopy is that because UEI formation is a second order reaction involving two UMI-tagged PCR amplicons, UEI counts are driven by the co-localization of UMI concentrations, and thus contain information on the proximity between the physical points at which each UMI began to amplify (Figure 1D). In particular, as UMI-tagged cDNA amplifies and diffuses in the form of clouds of clonal sequences that overlap to varying extents, the degree of overlap (Figure 1D, circle intersection)—and thus the probability of concatenation and UEI formation—depends on the proximity of the original (un-amplified) cDNA molecules (Figure 1D, small dark circles). UMI-diffusion clouds with greater overlap generate more concatemers or UEIs, whereas those clouds with less overlap generate fewer UEIs. Although individual diffusion clouds may differ in form, their

collective statistical properties will nevertheless allow for original UMI coordinates to be inferred by consensus, given the constraint that positions must occupy the low (two- or three-) dimensionality of physical space.

To obtain reliable estimates of UEIs between every pair of UMIs, we must address sources of noise, such as sequencing error. We cluster beacon-UMIs, target-UMIs, and UEIs by separately identifying "peaks" in read-abundances using a log-linear time clustering algorithm (Figure S2A; STAR Methods) in a manner analogous to watershed image segmentation, but in the space of sequences. For target UMIs, this allows us to aggregate biological gene sequences originating from *single* target molecules and achieve low error rates (0.1%–0.3%/bp across ~100 bp) by taking a consensus of the associated reads (Figure S2B). We then assign each identified UEI a single consensus beacon-UMI/target-UMI pair based on read-number plurality, and prune the data (by eliminating UMIs associating with only one UEI) to form a sparse matrix whose elements contain integer counts of UEIs pairing each beacon-UMI (matrix rows) and each target-UMI (matrix columns) (Figure 1E; STAR Methods). The resulting UEI matrices, containing on the order of 10^5–10^6 total UMIs among which we estimate <1/1,000 false-positives, have on average ~10 UEIs per UMI (Figure S3; Tables S3 and S4) and form the datasets upon which we built an engine for image inference.

A Two-Part Computational Strategy to Infer DNA Microscopy Images

Next, we developed an algorithmic approach to use UEI prevalence to infer UMI proximity and reconstruct an image of the original sample and its transcripts (Figure 1F). We follow a two-step approach. We first partitioned the data into smaller subsets to gauge how well local information between UMIs had been encoded into the UEI matrix. This entailed applying spectral graph theory (in a manner agnostic to the physics of the experiment) to the problem of cutting the data matrix into highly connected submatrices, allowing us to both analyze and visualize local structure and dimensionality. We then devise a more general solution to achieve DNA microscopy inference over large length scales. To do this, we constructed a physical model that used our preliminary linear analysis of the data matrix to constrain a nonlinear maximization of the probability of observing the DNA microscopy data given underlying molecular coordinates.

A "Zoom" Function Infers Local Spatial Encodings from UEI Matrices

We first appreciate that if the UEI matrix had successfully encoded relative UMI coordinates, these coordinates would be reflected in the rows and columns of the matrix. The matrix rows and columns would span a space having a dimensionality scaling with the total number of UMIs. However, if they encoded UMI coordinates within a sample, they would collectively sweep out a curve of far smaller dimensionality, only equal to the physical dimensionality of the sample.

As a toy example, consider a comparison between three systems in which a single target UMI ("2") is in each of three positions in one dimension relative to two beacon UMIs ("1" and "3") with which it forms UEIs (Figure 2A). The target UMI begins closest to one of the two beacon UMIs, and as a result, its diffusion cloud overlaps most with that beacon UMI's diffusion cloud. Thus, its reaction rate with that beacon UMI is relatively higher (Figure 2B) and results in a correspondingly larger number of UEIs (Figure 2C). If the target UMI is further away, the balance of overlaps between diffusion clouds changes. Indeed, plotting expected UEI matrix elements for the target UMI on two axes, we see that its trajectory remains one-dimensional (Figure 2D).

Extending to a large population of target UMIs across many positions, these new target UMIs, just like the target UMI in the toy example, also interact with the same two beacon UMIs. Therefore, we can also plot them on the same two axes, and wherever they land, we could expect them to scatter around the same one-dimensional manifold followed by the target UMI of the original example. It is important to note that although the variation of points across these axes may in fact all be equivalent, inspection of their axial projections allows visualization of their underlying dimensionality.

In any real dataset, UEI count is affected not only by position but also by additional variables (such as amplification biases and diffusion rates), each potentially adding to the data's total dimensionality. However, these sources of variation would be suppressed along the principal dimensions of a UEI matrix so long as their effect on neighboring UMIs is not systematically correlated.

To identify the principal dimensions of the UEI matrix, we can analyze the graph of UMI vertices and weighted UEI count edges by constructing a Graph Laplacian matrix from the raw UEI matrix (with its diagonal elements set so that each row sums to zero). The Graph Laplacian eigenvectors with the smallest-magnitude eigenvalues would visualize the most systematic forms of variation in the DNA microscopy data (STAR Methods) and illuminate the low-dimensional manifold, if any, it occupied. However, even a low-dimensional manifold could be folded in complex ways in the high-dimensional space formed by a full UEI matrix, making it difficult to analyze the manifold's shape over large distances, especially in areas of the manifold that are sparsely populated. Analyzing the UEI matrix manifold therefore first requires analyzing UMI subsets corresponding to *local* regions of the original sample. We return to global relations in subsequent sections.

To perform this local investigation, we developed a "zoom" function for DNA microscopy data by applying a recursive graph-cut algorithm, identifying putative cuts by using the spectral approximation to the cut of minimum-conductance (Shi and Malik, 2000) (STAR Methods). This criterion separates sub-sets of UMIs exhibiting small UEI-flux relative to the number of UMIs they comprised. The algorithm first finds the sparsest cut to the entire dataset, then the sparsest cuts to the resulting halves, and so on until a further sparse cut cannot be made (STAR Methods). We then visualize each of these sub-regions by the eigenvectors corresponding to the smallest-magnitude eigenvalues of their UEI-Graph Laplacian sub-matrix.

Successful Inference of Local Structure Identifies Cell-like Structures with Specific Marker Expression

Strikingly, and consistent with our theoretical reasoning, although the UMIs in these sub-sets fully spanned at least all

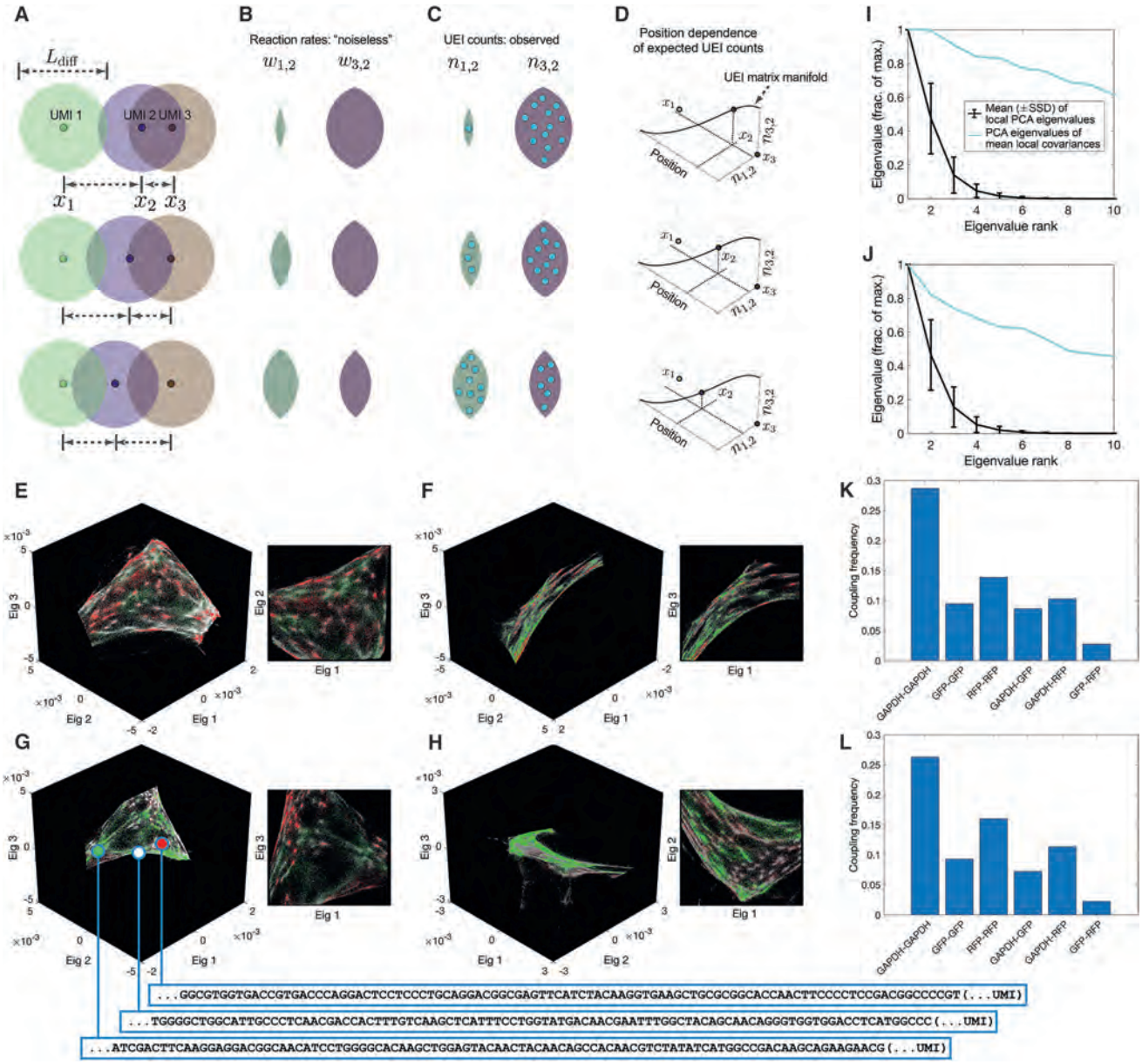

Figure 2. Encoding and Decoding Molecular Localization with DNA Microscopy

(A–D) Expected behavior of UEI counts. Diffusion profiles with length scale L_{diff} belonging to different amplifying UMIs overlap to degrees that depend on the distance between their points of origin (A). Greater overlaps between diffusion profiles result in larger reaction rates (B), which in turn result in higher UEI formation frequencies (C). Because UEI counts are therefore proper functions of position, as a UMI relocates, it sweeps out a curve along the UEI count axes equal to the dimensionality of space it occupies (D).

(E–H) Data segmentation permits individual sets of 10^4 strongly interacting UMIs to be visualized independently. The top three non-trivial eigenvectors for the largest data segments of samples 1 (E and F) and 2 (G and H) are shown, along with a different, magnified view of the same plot. Transcripts are colored by sequence identity: gray, ACTB (beacons); white, GAPDH; green, GFP; red, RFP.

(I and J) Quantitative assessment of manifold dimensionality. PCA spectra from local (black) or averaged-local (cyan) covariance matrices formed from the global UEI matrix eigenvector-coordinates of UMIs in samples 1 (I) and 2 (J). Covariance matrices were constructed for each UMI forming UEIs with at least 100 other UMIs, using the first 100 eigenvector coordinates belonging to these associating UMIs alone.

(K and L) Average coupling frequencies for each beacon with different target amplicons in samples 1 (K) and 2 (L). A coupling frequency between amplicon types k and l is defined as the average across all beacon UMIs i of the product $p_{ik}p_{il}$, where $p_{ik} = \sum_{j \in S_{ik}} n_{ij} / \sum_{i'} n_{i'j}$. Here, n_{ij} is the number of UEIs associating beacon UMI i with target UMI j, and S_{ik} is the set of all target UMIs of amplicon type k associating with beacon UMI i.

See also Figure S3 and Tables S1, S3, and S4.

three eigenvector dimensions, the manifolds swept out by the UMIs appeared only two-dimensional when represented in three-dimensional scatterplots (Figures 2E–2H). We further quantified the UEI data manifold's local dimensionality by performing principal-component analysis (PCA) on the spread of UMIs forming UEIs with each individual UMI (Figures 2I and 2J; STAR Methods). When highly connected UMIs (associating with at least 100 other UMIs) were analyzed individually over the first 100 eigenvectors of the UEI-Graph Laplacian matrix, their coordinate-covariance matrix eigenvalues decayed quickly. However, when their covariance matrices were averaged, the eigenvalues of the resulting matrix decayed slowly. These observations confirmed a low dimensionality of the UEI data manifold, consistent with neighborhoods of UMIs with low spatial dimensionality having been successfully encoded into the UEI data matrix.

The two-dimensional manifolds exhibited clusters of UMIs with indications of cellular resolution, by recapitulating the genetic composition of the cell lines used in the experiment: a pervasive distribution of the constitutively expressed *ACTB* and *GAPDH* sequences, but a mutual exclusion between GFP and RFP (Figures 2E–2H). Even on average across the dataset, UEIs formed 3 to 5 times more frequently via an intermediary beacon UMI between two GFP or RFP target UMIs and GAPDH target UMIs than between GFP and RFP (Figures 2K and 2L). Thus, an observer unaware of the spatial dimensionality of the specimen or that cells even existed could discover both by analyzing the DNA microscopy sequencing data alone. Together, these two observations confirmed both cellular and local supra-cellular resolution in DNA microscopy.

Inference of Global Molecular Positions from DNA Microscopy Data

Next, we expanded our inference beyond the local scope of a few thousands of proximal transcript molecules, by developing a framework for evaluating the likelihood of a global position-estimate solution.

We reasoned that each UEI's occurrence is analogous to a ''coin-toss'' experiment performed on every UMI-pair, with each pair's ''occurrence'' probability proportional to the corresponding reaction rate (Figure 3A; STAR Methods). We modeled the reaction rate between a beacon UMI and a target UMI as an isotropic Gaussian function of the distance separating them. Because, like in a coin-toss experiment, the probability of observing a given dataset is contingent on the probabilities of all possible outcomes together, our diffusion model of a Gaussian ''point-spread function'' imposed constraints on the probabilities of UMIs in aggregate, not on each UMI individually.

In this probability function, UEIs in DNA microscopy act in the same manner as photons do in optical super-resolution localization microscopy (Hell, 2009): both narrow a point-spread function governed by a physical length scale (wavelength in the case of light, diffusion distance in the case of DNA) as they accrue by dividing that length scale by the square-root of their total number (Figures 3B and 3C; STAR Methods). In real datasets, UEIs increase progressively with increasing read depth, whereas UMIs saturate more quickly (Figures 3D and 3E). In this way, read depth in DNA microscopy constitutes a dial to increase the number of UEIs per UMI, enhancing an image's resolution.

Unlike its optical counterpart, however, DNA microscopy resolves a molecule's position by orienting it relative to other molecules, and its uncertainty is therefore a function of these relationships. A relationship between two UMIs may come in two forms: those that are direct and involve UEIs linking them, and indirect relationships that occur via intermediaries. The latter emerges in the structure of the data, but will not strongly influence UMI positions if these positions are optimized independently. This may be seen in the logarithm of the UEI-count probability function (Figure 3F). This log-probability is the sum of two components (Figure 3F, top): (1) a sum of squared-differences between positions, weighted by individual UEI counts, and (2) a function of total UEI counts and total expected reaction rates (that are themselves functions of UMI positions) across the entire dataset. In order to still calculate the log-probability as a whole in a way that scales linearly with data size, we implemented the fast Gauss Transform (Greengard and Strain, 1991) (Figures S4A and S4B).

If each UMI's position is updated independently to maximize this log-probability function, it will experience two forces, corresponding to the function's two added components: the first pulls together UMIs that have directly formed UEIs between them, and the second repels all UMIs from all other UMIs. The likelihood of the position-solution is maximized when these two forces balance. During the maximization's update-process, the only way in which an indirect relationship between UMIs will influence their position-solution is if intermediary UMIs that directly form UEIs with them separately have already changed position.

To ensure that large length scale optimization captures these indirect UMI relationships encoded in the data, we developed a new maximum likelihood framework, which we called spectral maximum likelihood estimation or sMLE, to generate global representations of the DNA microscopy data. First, we note that because maximizing the first component of the log-probability entails minimizing the magnitude of the sum of squared-differences, it can be individually solved by identifying the smallest-magnitude eigenvalue/eigenvector pairs of the UEI Graph Laplacian introduced earlier (Figure 3F, bottom; STAR Methods). Each eigenvector represents a distinct way in which UMIs can be globally rearranged to suit orientation requirements expressed by the sum of squared-differences between local points. The eigenvector with the smallest-magnitude eigenvalue represents the best arrangement, the second smallest-magnitude eigenvalue the second best, and so on. Critically, these eigenvectors are not themselves solutions to the global maximum likelihood problem for a DNA microscopy dataset: they are local and linear solutions, and will individually exhibit all of the distortions observed in Figures 2E–2H.

However, we reasoned that because sums of eigenvector solutions to the local linear problem would produce solutions that would also satisfy local constraints, sum-coefficients of these eigenvectors could act as variables in a larger-scale non-linear likelihood maximization. By seeding a solution with the two eigenvectors corresponding to the smallest-magnitude eigenvalues, optimizing their coefficients, then incorporating successive eigenvectors and repeating, we could find global solutions that were also well-constrained locally. These sMLE

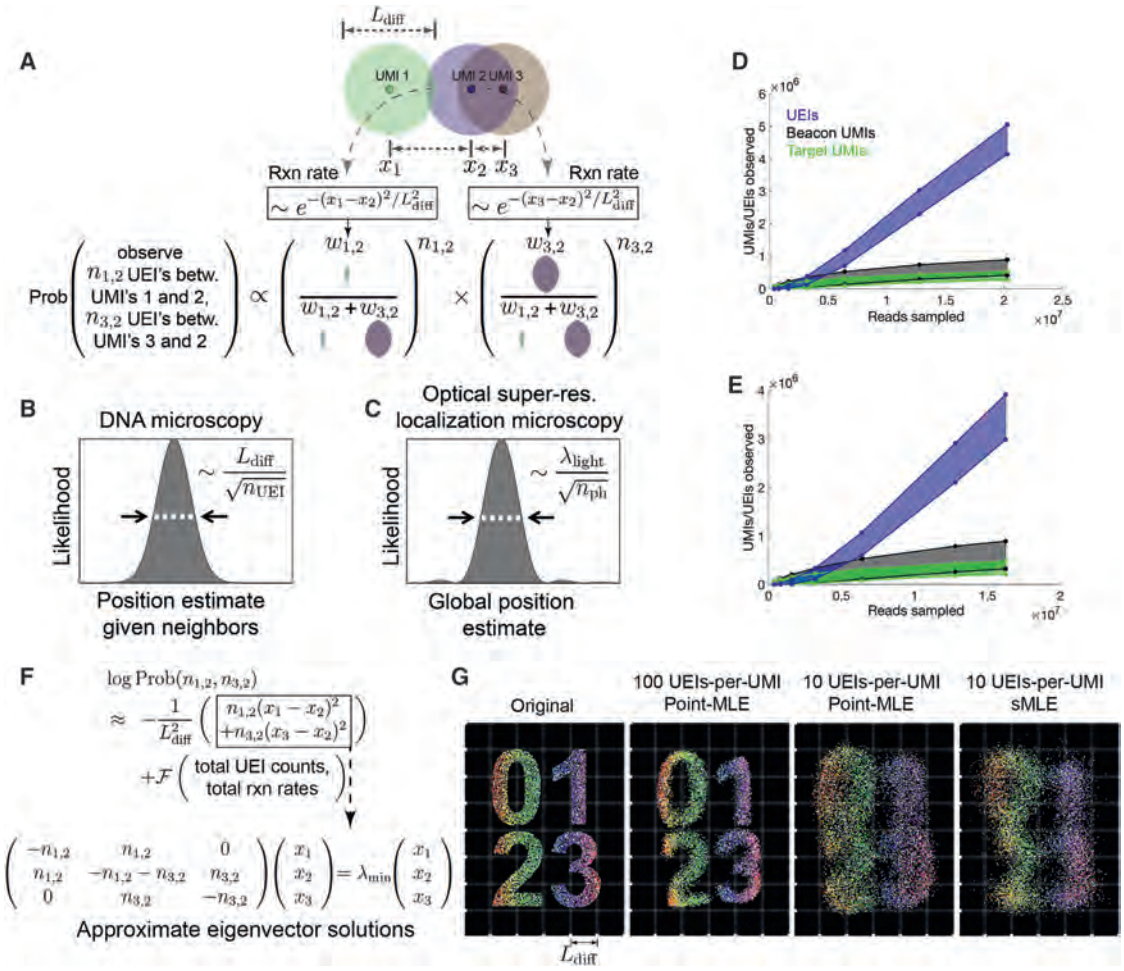

Figure 3. Image Inference from DNA Microscopy Data

(A) Modeling diffusion of amplifying UMIs as isotropic across length scale L_{diff} allows the likelihood of a UMI-position solution to be evaluated given observed UEI counts.

(B and C) Uncertainty in DNA (B) versus optical super-resolution (C) microscopy. Given its reacting partners' positions, DNA microscopy (left) defines a UMI's uncertainty as a physical length scale (DNA diffusion distance, L_{diff}) divided by the square-root of the number of individual quanta measured (UEIs) in a manner analogous to quanta (photons) in super-resolution microscopy (right).

(D and E) Rarefaction of UMI and UEI data. Shown are curves with an upper-bound, indicating total UMI/UEI counts, and a lower-bound, indicating those from the final pruned UEI matrix, for samples 1 (D) and 2 (E).

(F) The sMLE algorithm uses eigenvector solutions to part of the position-probability function to identify a linear basis for the solution to the full likelihood function.

(G) sMLE enhances performance in free-diffusion simulation tests. From left: original image, results from point-MLE on simulated images with 100 or 10 UEIs/UMI, and from sMLE with 10 UEIs/UMI.

See also Figures S3 and S4.

solutions showed strong advantages in simple simulations over maximizing the likelihood while treating every UMI independently, especially when UEI counts were limiting (Figure 3G). This effect remained present even when the simulated the form of the diffusion profiles deviated from our Gaussian model (Figure S4C).

DNA Microscopy Correctly Recapitulates Optical Microscopy Data

We next sought to apply the sMLE inference framework to determine whether DNA microscopy could resolve supra-cellular coordinates compared to optical microscopy. To this end, we constructed reaction chambers with glass slides (Figures S1B and S1C) and plated GFP- and RFP-expressing cells in a highly localized pattern within the chamber (Figure S1C). We then imaged GFP- and RFP-expression in cells across the entire area of the reaction chamber using an epifluorescence microscope before the DNA microscopy reaction (Figures 4A and 4B), sequenced the resulting DNA library to saturation (Figure 4C), and applied the sMLE inference algorithm.

Strikingly, the resulting image recapitulates optical microscopy data without systematic distortion (Figure 4D), and recapitulates both the shape of the cell population boundary as well as the distribution of GFP- and RFP-expressing cells within

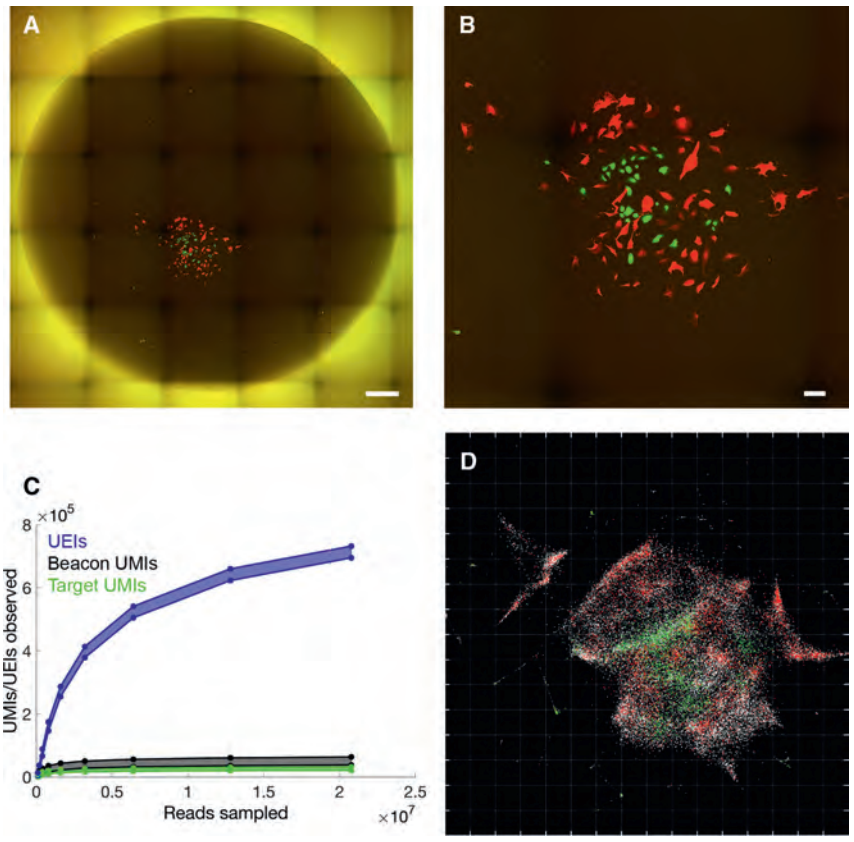

Figure 4. Accurate Reconstruction by DNA Microscopy of Fluorescence Microscopy Data

(A and B) Optical imaging of co-cultured cells.

(A) Full reaction chamber view of co-cultured GFP- and RFP-expressing cells (scale bar, 500 um).

(B) Zoomed view of the same cell population (scale bar, 100 um).

(C and D) DNA microscopy of co-cultured cells.

(C) Rarefaction of UMIs and UEIs with increasing read-sampling depth.

(D) sMLE inference applied to DNA microscopy data, reflected/rotated and rescaled for visual comparison with photograph. Transcripts, sequenced to 98 bp, are colored by sequence identity: gray, ACTB (beacons); white, GAPDH; green, GFP; red, RFP. Grid-line spacings: diffusion length scales (L_{diff}), emerging directly from the optimization (STAR Methods).

See also Figure S4 and Tables S1, S2, S3, and S4.

it. Importantly, the inferred image preserves the correct aspect ratio: the individual axes only needed to be rotated and reflected, but did not need to be independently re-scaled. This demonstrated that DNA microscopy is capable of generating accurate physical images of cell populations.

Large-Length-Scale Optimization and the Folded Manifold Problem

We applied DNA microscopy to optimization at larger length scales. Applying sMLE inference to the original data from several hundred cells used to generate the original eigenvector representations (Figure 2) gave images that reproduced the individual cell compositions of the earlier visualizations (Figure 5). These large-scale optimizations were also robust to data down-sampling (Figure S5).

However, the reconstructed images exhibited ''folding'' that indicated how the process of projecting large and curved high-dimensional manifolds onto two-dimensional planes was vulnerable to distortions. The causes for this ''manifold folding'' problem are illustrated by how low-dimensional manifolds come into being within a high-dimensional UEI data matrix (Figures 2A–2D). The eigenvector calculation (Figure 3F) involves identifying hyperplanes that can be drawn through these low-dimensional manifolds that maximally account for variation in the UEI data. It does this in a manner similar to linear regression, balancing the advantage of fitting certain parts of the data with the costs of not fitting other parts of the data.

This balancing can yield errors in several ways. If a large number of UMIs in one part of the dataset rotate the top calculated eigenvectors (with the smallest-magnitude eigenvalues) away from UMIs in a different part of the dataset, then projecting the global dataset onto these eigenvectors will cause these neglected UMIs to fold on top of one another. This will produce the type of ''folding'' artifact observed for large-scale optimization (Figure 5). If we avoid eigenvector calculation entirely and optimize each UMI's position independently (Figures S6A and S6B) we avoid such defects, but obtain close-packed images, as predicted by simulation (Figure 3G), that do not preserve empty space. This highlights the distinct nature of DNA microscopy's imaging capabilities compared to light microscopy's: while in light microscopy density is the key challenge, in DNA microscopy it is sparsity that can be challenging.

Cell Segmentation Can Be Performed on the UEI Matrix Based on Diffusion Distance

We next analyzed the degree to which the UEI matrix could be used to segment cells and analyze single-cell gene expression. Importantly, up to this point, no step in the process—experimental or computational—had knowledge that cells even exist. To perform segmentation, we applied the same recursive graph cut algorithm as used earlier (Figures 2E–2H) to generate local eigenvector visualizations of the data. By increasing the conductance-threshold dictating whether segments of the data should be left intact, we assigned transcripts to putative cells (Figures 6A, 6B, S6C, and S6D), again without regard to transcript identity (i.e., GFP versus RFP). To quantify segmentation quality, we calculated the probability that, within each putative cell, the minority fluorescent gene transcript would occur at or lower than its current value, given its prevalence in the dataset. We found the median p value decayed rapidly, over a range of conductance thresholds, to $<10^{-10}$, with

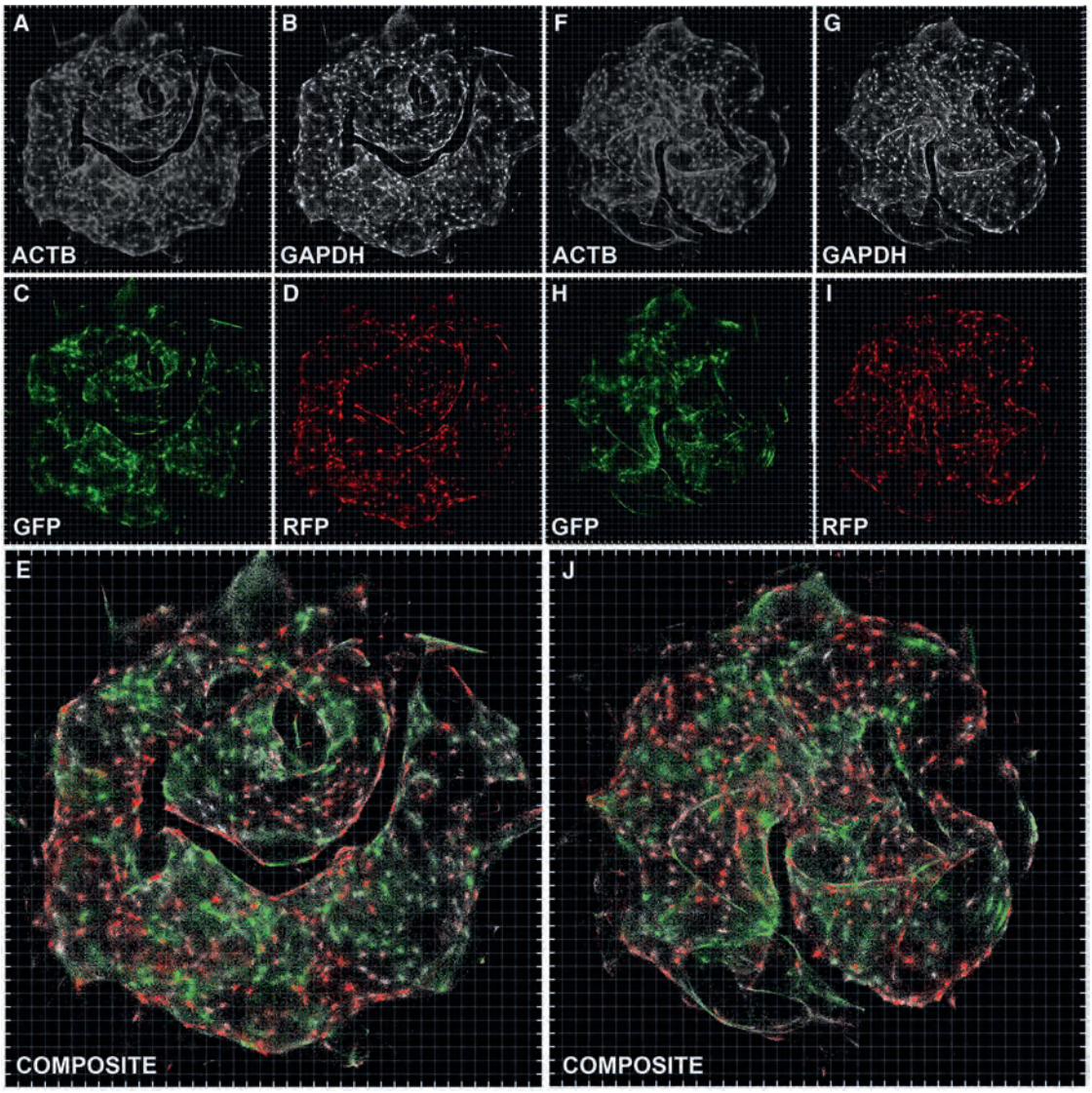

Figure 5. Inferred Large-Scale DNA Microscopy Images Preserve Cellular Resolution

(A–J) Inference using the sMLE global inference approach for sample 1 (A–E) and sample 2 (F–J), with each transcript type shown separately (A–D and F–I) or together (E and J) (although inferences are performed on all transcripts simultaneously and are blinded to transcript identity). Grid-line spacings: diffusion length scales (L_{diff}), emerging directly from the optimization (STAR Methods).

See also Figures S4, S5, and S6 and Tables S1, S2, S3, S4, S5, and S6.

increased numbers of reads and of resolved cells analyzed (Figures 6C and 6D).

This analysis remained agnostic to inferred molecular positions and demonstrated that modularity within the raw UEI data matrix was sufficient to perform rough segmentation of individual cells. In order to observe the degree to which inferred molecular positions could help improve cell segmentation, we quantified, for each UEI-connected UMI pair belonging to the same spectrally segmented cell, the fraction of their respective position uncertainties that overlapped (STAR Methods). We assigned this UMI overlap-fraction the symbol g, which could vary between 0 and 1. We then separated sub-sets of UMIs into distinct cells if no pair of UMIs connecting these sets had a value of g of at least a specified threshold. We analyzed GFP and RFP sequestration across cells with either the initial position-independent segmentation ($g = 0$), or with fraction-overlap threshold $g = 0.75$ or 0.9 (Figures 6E and 6F) using sMLE-inferred UMI coordinates. Increasing the threshold g enhanced the sequestration between GFP and RFP transcripts among cells, demonstrating the usefulness of applying inferred positions to the task of *de novo* cell segmentation.

Imaging Large Numbers of Different Transcripts in DNA Microscopy

To demonstrate that DNA microscopy and its associated cell segmentation could be extended to larger numbers of genes,

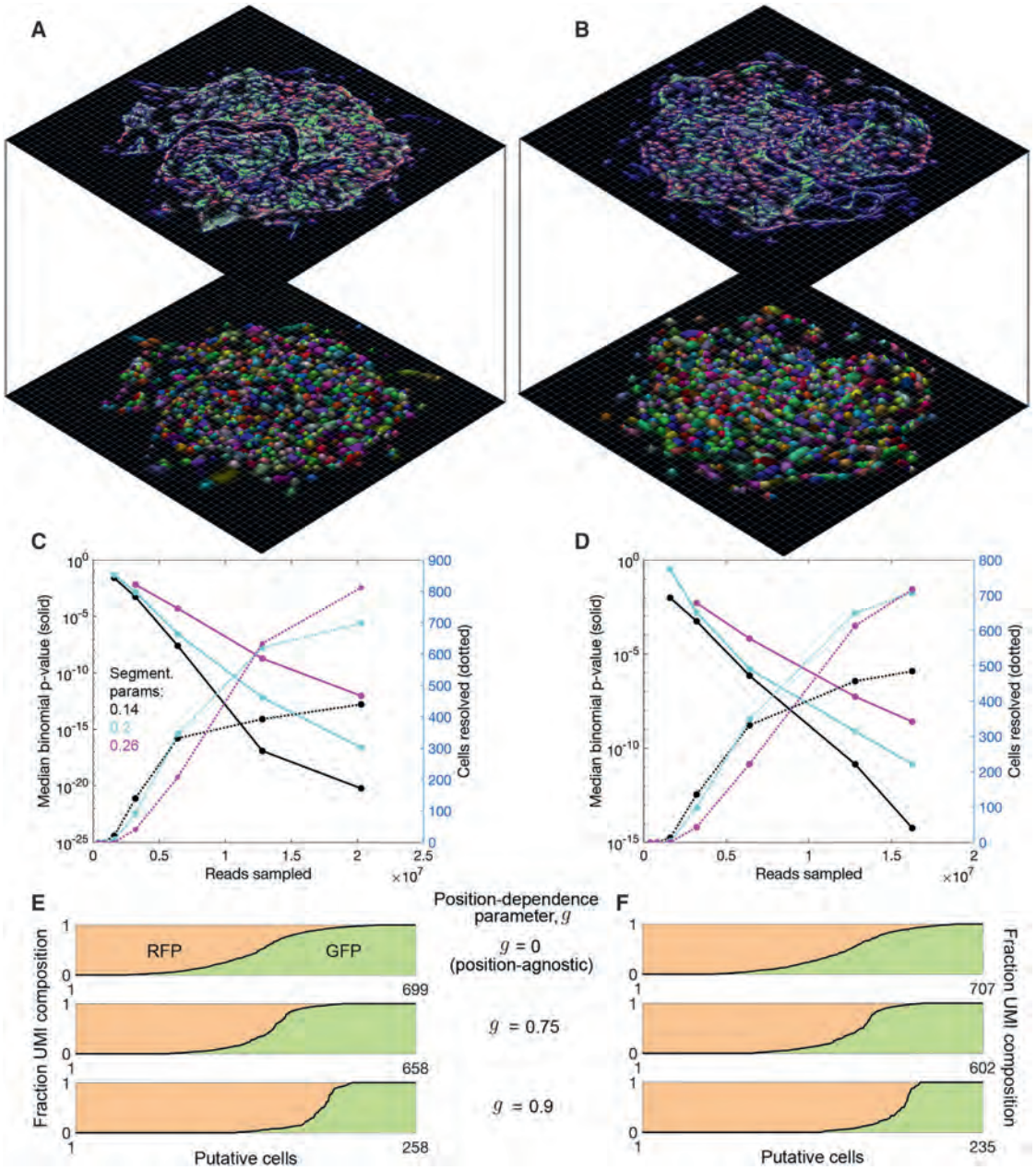

Figure 6. Segmentation of DNA Microscopy Data Recovers Cells *De Novo*

(A and B) Data segmentation recovers putative cells without *a priori* knowledge. Cell segmentation for samples 1 (A) and 2 (B) by recursive graph-cutting of the UEI matrix is shown with a random color assigned to each inferred cell, qualifying if it contained at least 50 UMIs and had at least one transcript each of ACTB and GAPDH. The minimum conductance threshold was set to 0.2. Surface height and color opacity scale with likelihood density, normalized to the maximum value within each putative cell.

(C and D) Segmentation performance. The effects of cell segmentation for samples 1 (C) and 2 (D) with minimum conductance thresholds 0.14 (black), 0.2 (cyan), and 0.26 (magenta) are shown on binomial p values quantifying segmentation fidelity (solid lines) and putative cell count (dotted lines).

(E and F) Inclusion of position information from sMLE inferences improves performance. Shown is the separation of fluorescent protein transgenes among decreasing numbers of identifiable cells for samples 1 (E) and 2 (F), with GFP UMI fraction and RFP UMI fraction shown in green and red shades, respectively. See also Figures S4 and S6 and Tables S1, S2, S3, and S4.

we synthesized cDNA by reverse transcription from up to 20 additional genes that have been previously shown to be differentially enriched (although not exclusively expressed) in MDA-MB-231 and BT-549 cell lines (Klijn et al., 2015) (Tables S5 and S6; STAR Methods). We performed global image inference (Figures S6E and S6F) and applied our recursive graph-cutting cell

segmentation algorithm (Figures S6G and S6H). Rarefaction analysis demonstrated rapid saturation of UMI and UEI counts (Figures S6I and S6J). Pearson correlations between the GFP-fraction per spectrally segmented cell (out of total transgene transcripts per cell) and fraction of endogenous genes expected to be enriched in the GFP cell line (out of total endogenous gene transcripts enriched in either cell line) gave $r = 0.29–0.41$ ($n = 764$ and 265) for two experiments, respectively (p value $<10^{-6}$, permutation test). This demonstrated that the transgenes labeling these cell types retained information about cell-type-specific endogenous expression, and that this information could be read out from DNA microscopy data. Moreover, because DNA microscopy measures full amplicon sequences, it can readily distinguish transcript variants for example from two different alleles, such that each localized transcript is assigned to a specific allele, without the need for any *a priori* known allele-specific primers (Figures S6K and S6L).

To more directly compare between the DNA microscopy data and bulk RNA profiling data for these genes, we classified each putative cell in our dataset as MDA-MB-231 if it had more GFP UMIs than RFP UMIs, and as BT-549 otherwise, and then compared these cell's profiles to previously measured ones. We found a good correlation between UMI counts and read counts among endogenous genes for each putative cell type individually (Spearman $r_s = 0.54–0.64$, Figures S6M and S6N), further matching DNA microscopy quantitation with bulk RNA sequencing (RNA-seq) data. The data further provided the opportunity to analyze the contribution of gene insert size to average UEI formation distance. In the context of the DNA microscopy experiment and over the range of gene insert sizes measured (200–300 bp), we observed this effect to be minimal (Figures S6O–S6R).

DISCUSSION

The fundamental advance of DNA microscopy is to physically image biological specimens using an unstructured and standalone chemical reaction without optical information, making it a distinct microscopic imaging modality. We have drawn a close technological analogy between DNA microscopy and optical super-resolution microscopy: both take advantage of stochastic physics to reduce measurement uncertainty beyond what may seem superficially to be a physically imposed limit.

However, the two differ in several fundamental ways and as a result are highly complementary. Optical super-resolution microscopy relies on the quantum mechanics of fluorescent energy decay. DNA microscopy, however, relies entirely on thermodynamic entropy. The moment we tag biomolecules with UMIs in the DNA microscopy protocol, the sample gains spatially stratified and chemically distinguishable DNA point sources. This tagging process thereby introduces a spatial chemical gradient across the sample that did not previously exist. Once these point sources begin to amplify by PCR and diffuse, this spatial gradient begins to disappear. This entropic homogenization of the sample is what enables different UMI diffusion clouds to interact and UEIs to form. It is therefore this increase in the system's entropy that most directly drives the DNA microscopy reaction to record meaningful information about a specimen, including both the UMI coordinates and differences in spatial impedances that each UMI diffusion cloud experiences as it evolves.

Detection of these spatial barriers, achieved by comparing UEI formation rates at different length scales, is central to cell segmentation in DNA microscopy and offers an important distinct tool for analyzing biological morphology. The use of a low-pass spectral filter to perform cellular segmentation from UEI data matrices further clarifies the parallels between DNA microscopy and light microscopy, in which low-pass filters permit morphology to be inferred from high-variance pixel intensities.

However, one key weakness of DNA microscopy remains the resolution of empty space, and future work will be needed to eliminate this obstacle to produce high-quality reconstructions of samples over large lengths where there are gaps in molecular density. There are two potential solutions to this problem: an experimental one and an analytical one. First, a "landmark"-based experimental approach, in which specific DNA sequences are deposited at known physical locations to assist in the image reconstruction process, may ultimately prove the most cost-effective way to achieve this. Second, better analytical techniques to correct for large length scale distortions may prove equally effective, without complicating the experiment itself.

DNA microscopy offers a distinct form of optics-free imaging that leverages the large economies of scale in DNA sequencing. The technology does not require sacrificing spatial resolution for sequence accuracy, because it benefits, rather than suffers, from high signal density and it does not hinge on optical resolution of diffraction-limited "spots" *in situ*. By using chemistry itself as its means of image acquisition, DNA microscopy decouples spatial resolution from specimen penetration depth (otherwise linked by the properties of electromagnetic radiation) and thereby sidesteps a tradeoff imposed by the physics of wave propagation. Furthermore, by virtue of capturing an image of a sample through a volumetric chemical reaction, DNA microscopy may provide an ideal avenue for three-dimensional imaging of intact whole mount specimens.

Because DNA microscopy does not rely on specialized equipment and can be performed in a multi-well format with normal lab pipettes, it is highly scalable, such that a large number of samples can be processed in parallel. It is fully multiplex-compatible (imaging any PCR template) and uses sequencing-depth as a dial to enhance genetic detail, through the accrual of UMIs (including those belonging to low-abundance transcripts, in a manner equivalent to any traditional sequencing assay) and spatial detail through the accrual of UEIs.

Moreover, because DNA microscopy reads out single-nucleotide variation in the biological DNA or RNA sequences it targets, it spatially resolves the astronomically large potential variation that exists in somatic mutations, stochastic RNA splicing, RNA editing, and similar forms of genetic diversity in cell populations. We demonstrated that DNA microscopy achieves this at high sequencing accuracy (99.7%–99.9%/bp) over long read lengths (~100 bp) (Figures S2 and S6), such that transcripts from different alleles are uniquely positioned, without the need to know *a priori* the extent of genetic diversity. In this way, DNA microscopy is a compelling approach to study the tissue organization of cells such as lymphocytes, neurons,

or mutated cancer cells, where somatic mutation, recombined gene segments, and other sources of nucleotide-level variation endow unique molecular identities with important physical consequences.

Our development of a chemically encoded microscopy system lays the foundation for new theoretical and experimental applications and extensions of the technology. Future experimental and computational enhancements should better resolve large length scales that include large spatial gaps between groups of molecules. Furthermore, the UEI, by effectively functioning in these experiments as a DNA analog of the photon, has illuminated a wider potential role for DNA as a medium for artificial precise biological recordings of chemical kinetics. Most directly, the principle of DNA microscopy can be applied beyond the transcriptome, for example directly to DNA sequences or to proteins detected with DNA-labeled antibodies. Looking to the future, a full exploration of individual and idiosyncratic biological spatial structures by encoding them into DNA bases, instead of pixels, as demonstrated here, may complement existing grid-capture and wave-based imaging methods and reveal new and previously inaccessible layers of information.

STAR★METHODS

Detailed methods are provided in the online version of this paper and include the following:

- KEY RESOURCES TABLE
- CONTACT FOR REAGENT AND RESOURCE SHARING
- EXPERIMENTAL MODEL AND SUBJECT DETAILS
- METHOD DETAILS
  - Bead-plate reaction chambers
  - Glass-slide reaction chambers
  - Cell seeding
  - In situ preparation
  - Sequencing
  - UMI/UEI design
  - Remark on reagent quality control
- QUANTIFICATION AND STATISTICAL ANALYSIS
  - Read parsing
  - UMI/UEI clustering
  - UEI-UMI pairing
  - Estimating a false positive rate
  - Image inference
  - Local linearization of the image inference problem
  - Curating spectral segmentation using inferred UMI positions
  - Global likelihood maximization
  - Point-MLE solution
  - Spectral MLE (sMLE) solution
  - Resolution and UEI count
  - Simulation
- DATA AND SOFTWARE AVAILABILITY

SUPPLEMENTAL INFORMATION

Supplemental Information can be found online at https://doi.org/10.1016/j.cell.2019.05.019.

ACKNOWLEDGMENTS

We thank Andrew Piacitelli for his help sustaining experimental progress while this paper was being written. We thank Paul Blainey and his lab for their generosity and provision of their clean room for PDMS work, and for particularly helpful discussions with David Feldman and Lily Xu. We thank Jennifer Rood and Rhiannon Macrae for valuable feedback on this manuscript. This work was supported by NIH (R01HG009276), the Simons Foundation LSRF Fellowship (to J.A.W.), and the Klarman Cell Observatory. F.Z. is a New York Stem Cell Foundation-Robertson Investigator. F.Z. is supported by NIH (1R01-HG009761, 1R01-MH110049, and 1DP1-HL141201), the New York Stem Cell Foundation, the G. Harold and Leila Mathers Foundation, the Poitras Center for Affective Disorders Research at MIT, the Hock E. Tan and K. Lisa Yang Center for Autism Research at MIT, J. and P. Poitras, and R. Metcalfe. A.R. and F.Z. are Howard Hughes Medical Institute Investigators.

AUTHOR CONTRIBUTIONS

J.A.W. conceived the project. J.A.W. performed all experiments and analysis. J.A.W., A.R., and F.Z. helped guide the project and wrote the manuscript.

DECLARATION OF INTERESTS

The authors are co-inventors on patent applications filed by the Broad Institute related to this work. F.Z. is a scientific founder of and advisor to Arbor Biotechnologies, Beam Therapeutics, Editas Medicine, Pairwise Plants, and Sherlock Biosciences. A.R. is a founder and equity holder of Celsius Therapeutics and an SAB member of ThermoFisher Scientific and Syros Pharmaceuticals.

Received: November 13, 2018
Revised: February 27, 2019
Accepted: May 9, 2019
Published: June 20, 2019

REFERENCES

Achim, K., Pettit, J.B., Saraiva, L.R., Gavriouchkina, D., Larsson, T., Arendt, D., and Marioni, J.C. (2015). High-throughput spatial mapping of single-cell RNA-seq data to tissue of origin. Nat. Biotechnol. *33*, 503–509.

Aspnes, J., Goldenberg, D.K., Whiteley, W., and Anderson, B.D.O. (2006). A theory of network localization. IEEE Trans. Mobile Comput. *5*, 1663–1678.

Chen, K.H., Boettiger, A.N., Moffitt, J.R., Wang, S., and Zhuang, X. (2015). RNA imaging. Spatially resolved, highly multiplexed RNA profiling in single cells. Science *348*, aaa6090.

Greengard, L., and Strain, J. (1991). The fast gauss transform. SIAM J. Sci. Statist. Comput. *12*, 79–94.

Hell, S.W. (2009). Microscopy and its focal switch. Nat. Methods *6*, 24–32.

Herishanu, Y., Pérez-Galán, P., Liu, D., Biancotto, A., Pittaluga, S., Vire, B., Gibellini, F., Njuguna, N., Lee, E., Stennett, L., et al. (2011). The lymph node microenvironment promotes B-cell receptor signaling, NF-kappaB activation, and tumor proliferation in chronic lymphocytic leukemia. Blood *117*, 563–574.

Joyce, J.A., and Fearon, D.T. (2015). T cell exclusion, immune privilege, and the tumor microenvironment. Science *348*, 74–80.

Junker, J.P., Noël, E.S., Guryev, V., Peterson, K.A., Shah, G., Huisken, J., McMahon, A.P., Berezikov, E., Bakkers, J., and van Oudenaarden, A. (2014). Genome-wide RNA Tomography in the zebrafish embryo. Cell *159*, 662–675.

Kinde, I., Wu, J., Papadopoulos, N., Kinzler, K.W., and Vogelstein, B. (2011). Detection and quantification of rare mutations with massively parallel sequencing. Proc. Natl. Acad. Sci. USA *108*, 9530–9535.

Klijn, C., Durinck, S., Stawiski, E.W., Haverty, P.M., Jiang, Z., Liu, H., Degenhardt, J., Mayba, O., Gnad, F., Liu, J., et al. (2015). A comprehensive transcriptional portrait of human cancer cell lines. Nat. Biotechnol. *33*, 306–312.

Lee, J.H., Daugharthy, E.R., Scheiman, J., Kalhor, R., Yang, J.L., Ferrante, T.C., Terry, R., Jeanty, S.S., Li, C., Amamoto, R., et al. (2014). Highly multiplexed subcellular RNA sequencing in situ. Science *343*, 1360–1363.

Lefebvre, J.L., Kostadinov, D., Chen, W.V., Maniatis, T., and Sanes, J.R. (2012). Protocadherins mediate dendritic self-avoidance in the mammalian nervous system. Nature *488*, 517–521.

Lubeck, E., Coskun, A.F., Zhiyentayev, T., Ahmad, M., and Cai, L. (2014). Single-cell in situ RNA profiling by sequential hybridization. Nat. Methods *11*, 360–361.

Moffitt, J.R., Hao, J., Wang, G., Chen, K.H., Babcock, H.P., and Zhuang, X. (2016). High-throughput single-cell gene-expression profiling with multiplexed error-robust fluorescence in situ hybridization. Proc. Natl. Acad. Sci. USA *113*, 11046–11051.

Satija, R., Farrell, J.A., Gennert, D., Schier, A.F., and Regev, A. (2015). Spatial reconstruction of single-cell gene expression data. Nat. Biotechnol. *33*, 495–502.

Schreiner, D., Nguyen, T.M., Russo, G., Heber, S., Patrignani, A., Ahrné, E., and Scheiffele, P. (2014). Targeted combinatorial alternative splicing generates brain region-specific repertoires of neurexins. Neuron *84*, 386–398.

Schumacher, T.N., and Schreiber, R.D. (2015). Neoantigens in cancer immunotherapy. Science *348*, 69–74.

Shi, J., and Malik, J. (2000). Normalized cuts and image segmentation. IEEE Trans. Pattern Anal. Mach. Intell. *22*, 888–905.

Singer, A. (2008). A remark on global positioning from local distances. Proc. Natl. Acad. Sci. USA *105*, 9507–9511.

Ståhl, P.L., Salmén, F., Vickovic, S., Lundmark, A., Navarro, J.F., Magnusson, J., Giacomello, S., Asp, M., Westholm, J.O., Huss, M., et al. (2016). Visualization and analysis of gene expression in tissue sections by spatial transcriptomics. Science *353*, 78–82.

Turchaninova, M.A., Britanova, O.V., Bolotin, D.A., Shugay, M., Putintseva, E.V., Staroverov, D.B., Sharonov, G., Shcherbo, D., Zvyagin, I.V., Mamedov, I.Z., et al. (2013). Pairing of T-cell receptor chains via emulsion PCR. Eur. J. Immunol. *43*, 2507–2515.

Victora, G.D., and Nussenzweig, M.C. (2012). Germinal centers. Annu. Rev. Immunol. *30*, 429–457.

Xu, L., Brito, I.L., Alm, E.J., and Blainey, P.C. (2016). Virtual microfluidics for digital quantification and single-cell sequencing. Nat. Methods *13*, 759–762.

Resource

Cell

A High-Throughput Platform to Identify Small-Molecule Inhibitors of CRISPR-Cas9

Basudeb Maji,[1,2,3] Soumyashree A. Gangopadhyay,[1,2,3,10] Miseon Lee,[1,2,10] Mengchao Shi,[1,2,3,10] Peng Wu,[1,2,3,10] Robert Heler,[4] Beverly Mok,[5,6] Donghyun Lim,[1,2] Sachini U. Siriwardena,[1] Bishwajit Paul,[1,2,3] Vlado Dančík,[1] Amedeo Vetere,[1] Michael F. Mesleh,[7] Luciano A. Marraffini,[4,8] David R. Liu,[5,6,9] Paul A. Clemons,[1] Bridget K. Wagner,[1] and Amit Choudhary[1,2,3,11,*]

[1]Chemical Biology and Therapeutics Science Program, Broad Institute of MIT and Harvard, Cambridge, MA 02142, USA
[2]Department of Medicine, Harvard Medical School, Boston, MA 02115, USA
[3]Divisions of Renal Medicine and Engineering, Brigham and Women's Hospital, Boston, MA 02115, USA
[4]Laboratory of Bacteriology, The Rockefeller University, New York, NY 10065, USA
[5]Merkin Institute of Transformative Technologies in Healthcare, Broad Institute of Harvard and MIT, Cambridge, MA 02142, USA
[6]Department of Chemistry and Chemical Biology, Harvard University, Cambridge, MA 02138, USA
[7]Center for the Development of Therapeutics, Broad Institute of MIT and Harvard, Cambridge, MA 02142, USA
[8]Howard Hughes Medical Institute, The Rockefeller University, 1230 York Avenue, New York, NY 11231, USA
[9]Howard Hughes Medical Institute, Harvard University, Cambridge, MA 02138, USA
[10]These authors contributed equally
[11]Lead Contact
*Correspondence: achoudhary@bwh.harvard.edu
https://doi.org/10.1016/j.cell.2019.04.009

SUMMARY

The precise control of CRISPR-Cas9 activity is required for a number of genome engineering technologies. Here, we report a generalizable platform that provided the first synthetic small-molecule inhibitors of *Streptococcus pyogenes* Cas9 (SpCas9) that weigh <500 Da and are cell permeable, reversible, and stable under physiological conditions. We developed a suite of high-throughput assays for SpCas9 functions, including a primary screening assay for SpCas9 binding to the protospacer adjacent motif, and used these assays to screen a structurally diverse collection of natural-product-like small molecules to ultimately identify compounds that disrupt the SpCas9-DNA interaction. Using these synthetic anti-CRISPR small molecules, we demonstrated dose and temporal control of SpCas9 and catalytically impaired SpCas9 technologies, including transcription activation, and identified a pharmacophore for SpCas9 inhibition using structure-activity relationships. These studies establish a platform for rapidly identifying synthetic, miniature, cell-permeable, and reversible inhibitors against both SpCas9 and next-generation CRISPR-associated nucleases.

INTRODUCTION

SpCas9 is a programmable RNA-guided DNA endonuclease from *S. pyogenes* that has allowed the facile introduction of genomic alterations. The complex of SpCas9 and guide RNA (gRNA) recognizes a substrate sequence via a protospacer adjacent motif (PAM) and base-pairing of the target DNA with gRNA (Chen and Doudna, 2017). The ease of targeting catalytically impaired SpCas9 to any genomic locus has resulted in transformative technologies (Komor et al., 2016; Wang et al., 2016). For example, the fusion of catalytically inactive SpCas9 (dCas9) to transcriptional activators or repressors has enabled gene transcription and repression; the fusion of catalytically impaired SpCas9 to base-modifying enzymes has allowed base conversion (e.g., C→T) at specific genomic sites, a dCas9–GFP fusion has made the imaging of genomic loci possible, and dCas9–acetyltransferases or deacetylases fusion has enabled epigenome editing.

The need for precision control of both wild-type and engineered SpCas9 over the dimensions of dose and time has created a demand for inhibitory anti-CRISPR molecules (Nuñez et al., 2016). SpCas9 is being developed as a gene therapy agent for multiple pathologies, including HIV, muscular dystrophy, and vision and hereditary disorders (Cox et al., 2015; Fellmann et al., 2017). Dose and temporal controls, which are required of all therapeutic agents, are particularly important for SpCas9, as off-target effects, chromosomal translocations, and genotoxicity are observed at elevated activity (Gangopadhyay et al., 2019). Indeed, the timely and partial inhibition of SpCas9 selectively diminishes off-target editing events over on-target ones (Shin et al., 2017). Furthermore, temporal control is important because most delivery systems use constitutively active SpCas9, and this activity must ideally be terminated following on-target editing (Gangopadhyay et al., 2019).

SpCas9 inhibitors will be useful in several other contexts. First, in germline editing, restricting SpCas9 activity to a narrow temporal window is important, as persistent activity in dividing cells contributes to mosaicism (Wang et al., 2013; Yen et al., 2014). Timely SpCas9 degradation reduced mosaicism in non-human primate embryos (Tu et al., 2017). Second, temporarily switching

off gene drives that propagate lethal traits using a SpCas9 inhibitor (Champer et al., 2016; Esvelt et al., 2014; Gantz and Bier, 2016) will allow facile animal husbandry and population expansion for field studies. Furthermore, dose and temporal control of gene drives in a laboratory setting will allow precision population control and propel our understanding of the limits of this technology. Third, inhibiting SpCas9-mediated toxicity to helper cells can enable the efficient packaging of SpCas9 in adeno-associated viruses for delivery (Neve et al., 2005). Fourth, SpCas9 inhibitors could help allay dual-use concerns, where research that is designed to provide a benefit could be co-opted to do harm, from a biosafety perspective in the use of SpCas9 in disease modeling (Wegrzyn et al., 2017). Fifth, SpCas9 inhibitors will propel the fundamental understanding of the biological functions of endogenous SpCas9 and can apply immune-response-based selection pressure on bacteria to evolve new CRISPR-based systems. Finally, dCas9-based technologies, including base editing, will benefit from dose and temporal control.

While several protein-based anti-CRISPR molecules have been reported (Hynes et al., 2017; Pawluk et al., 2016a, 2016b; Rauch et al., 2017; Shin et al., 2017), we focused on small molecules as they complement the protein-based anti-CRISPRs in multiple ways. For example, small-molecule inhibitors can be cell permeable, reversible, proteolytically stable, and non-immunogenic, while protein-based anti-CRISPRs can be highly potent, since they generally possess a greater number of SpCas9 interaction sites. Unlike genetic methods used to express protein-based anti-CRISPRs, small-molecule inhibitors exhibit fast kinetics, inhibiting enzymatic activity in as little as a few minutes (Weiss et al., 2007) and allowing precise temporal control. Small molecules can be synthesized on a large scale at low cost, with little batch-to-batch variability. Unsurprisingly, the pharmacological inhibition of intracellular proteins is usually accomplished using small molecules. Unfortunately, the identification of small-molecule inhibitors of SpCas9 is challenging for multiple reasons. First, inhibitor identification requires robust, orthogonal, sensitive, high-throughput, miniature, and inexpensive SpCas9 assays, which are currently unavailable (Cox et al., 2019). Second, SpCas9 is a single-turnover enzyme that holds on to its substrate with picomolar affinity throughout the biochemical reaction (Sternberg et al., 2014), adding to the challenge of developing such high-throughput assays. Third, the inhibition of SpCas9 activity requires the inactivation of two nuclease domains. Fourth, SpCas9 possesses novel protein folds, limiting the ability to leverage existing rational design approaches (Nishimasu et al., 2014). Finally, SpCas9 is a DNA-binding protein, a class of targets that are often deemed chemically intractable (Koehler, 2010).

Here, we describe a platform for the rapid identification and validation of small-molecule inhibitors of SpCas9. We developed a suite of high-throughput assays for SpCas9 activity, including a fluorescence-polarization-based primary screening assay for probing the SpCas9-PAM interaction. Using this primary screening assay, we sampled a set of small-molecule libraries derived from diversity-oriented synthesis (DOS) (Schreiber, 2000) to identify specific libraries enriched for screening hits. A focused screen of the enriched libraries resulted in the identification of BRD0539 as a SpCas9 inhibitor. We exhaustively validated the activity of BRD0539 in multiple biochemical and cell-based assays and demonstrated target engagement by BRD0539 in cells. Furthermore, BRD0539 is stable in human plasma and reversibly inhibits SpCas9. Finally, we performed structure-activity and stereochemistry-activity relationship studies for BRD0539 to identify its inactive analogs and the pharmacophore required for SpCas9 inhibition. These studies lay the foundation for the rapid identification of cell-permeable, reversible, synthetic anti-CRISPR molecules for contemporary and emerging CRISPR-associated nucleases.

RESULTS

Development of High-Throughput Primary and Secondary Assays

Primary Assay for SpCas9-PAM Binding

We focused on targeting the SpCas9-PAM interaction for several reasons. Mutating the PAM binding site renders SpCas9 inactive (Kleinstiver et al., 2015a), and disrupting PAM binding has been exploited by numerous anti-CRISPR proteins. Furthermore, SpCas9 has a low affinity for the PAM sequence that can be effectively blocked by small molecules. We used fluorescence polarization (FP) to monitor the interaction between SpCas9 and a fluorophore-labeled, PAM-containing, DNA oligonucleotide. The binding of a small-sized PAM-rich DNA to a much larger SpCas9:gRNA complex lowers DNA's tumbling rate, with a concomitant increase in anisotropy (Figure 1A). However, the low-affinity SpCas9-PAM interaction creates a challenge in developing robust binding assays, as the interaction is not strong enough to make a sustained, measurable change in the anisotropy that is detectable over background. To overcome this challenge, we employed a DNA sequence bearing multiple PAM sites (henceforth called 12PAM-DNA) that should increase the association between the DNA and the SpCas9 (Table S1). As expected, the binding of SpCas9:gRNA to 12PAM-DNA resulted in a dose-dependent increase in FP (Figure 1B). We confirmed the PAM dependence of SpCas9:gRNA and 12PAM-DNA interactions in competition experiments using unlabeled DNA sequences containing a varying number of PAM sites. As expected, the decrease in FP of 12PAM-DNA correlated with the density of PAM sites on the competitor DNA (Figure 1C) as well as with the concentration of the competitor DNA. Next, we used differential scanning fluorimetry (DSF), which detects ligand-induced changes in protein stability. The melting temperature of the SpCas9:gRNA complex increased with the number of PAM sites in the DNA sequence (Figure 1D). Finally, using bio-layer interferometry (BLI) (Richardson et al., 2016), we confirmed the increased affinity of SpCas9:gRNA for DNA sequences containing more PAM sites (Figure 1E; Table S1).

Secondary Assays for Cell-Based SpCas9 Activity

We developed several cell-based, orthogonal, and high-throughput assays of SpCas9 activity using either gain or loss of signal. Joung and co-workers previously reported a U2OS.eGFP.PEST cell line in which *eGFP* knockout by SpCas9 led to a loss of fluorescence (Fu et al., 2013; Kleinstiver et al., 2015a); in this cell line, the percentage of eGFP-negative cells correlates with SpCas9 activity. Using automated imaging and counting of eGFP-positive cells, we adapted this

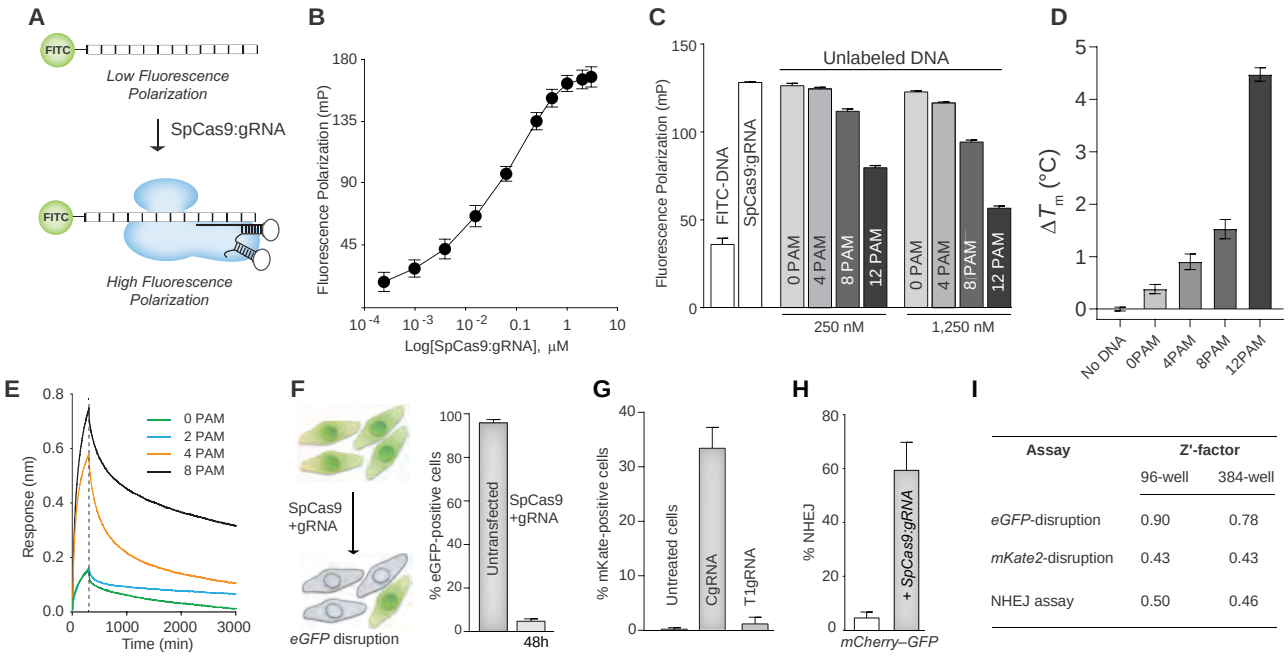

Figure 1. Development of a Screening Workflow for Identification of SpCas9 Inhibitors

(A) Schematic representation of the FP assay for monitoring SpCas9:gRNA and DNA binding.

(B) Dose-dependent increase in the FP signal upon binding of 12PAM-DNA to the SpCas9:gRNA complex. Error bars represent ±SD across technical replicates (n = 3).

(C) Competition experiment demonstrating PAM-specific DNA-SpCas9:gRNA binding wherein 0–12 PAM refers to unlabeled competitor DNA containing the indicated number of PAM sequences. Unlabeled competitor DNA was used in two different ratios: 10 × (250 nM) and 50 × (1,250 nM). Error bars represent ±SD across technical replicates (n = 3).

(D) Differential scanning fluorimetry (DSF) assay showing an increase in the thermal stability of the SpCas9:gRNA complex upon binding to DNA containing an increasing number of PAM sequences. Error bars represent ±SD across technical replicates (n = 3).

(E) Representative BLI sensogram showing the interaction of SpCas9:gRNA with *ds*DNA containing a variable number of PAM sequences. Streptavidin sensors were loaded with 300 nM biotin-*ds*DNA with a variable number of PAM sequences, and the interaction was followed by incubating with 200 nM SpCas9:gRNA complex. Data are for one of the two replicates.

(F) Schematic representation of the eGFP-disruption assay involving the quantification of eGFP disruption by SpCas9 at 48 h post-nucleofection. U2OS.eGFP.PEST cells were nucleofected with SpCas9 and gRNA plasmids followed by incubation for 48 h before imaging. Error bars represent ±SD across technical replicates (n = 4).

(G) Quantification of mKate2-disruption assay in HEK293T cells. Cells were transfected with a plasmid encoding the *mKate2* reporter, SpCas9, and either a non-targeting guide (CgRNA plasmid) or a targeting guide (T1gRNA plasmid). Cells transfected with the CgRNA plasmid showed a high number of mKate2-positive cells, while cells transfected with the T1gRNA plasmid showed a significant reduction in the number of mKate2-positive cells 48 h after transfection. Error bars represent ±SD across technical replicates (n = 4).

(H) Quantification of non-homologous end joining (NHEJ) assay in HEK293T cells. SpCas9-induced NHEJ was quantified by measuring mCherry and GFP expression in HEK293T cells after 48 h. Cells were transfected with the reporter construct encoding either the mCherry-Stop codon (TAG)-GFP, SpCas9, and gRNA or the reporter construct alone. GFP fluorescence observed in the cells transfected with only the reporter indicates the basal level of NHEJ. The GFP fluorescence increases significantly in cells transfected with the reporter, SpCas9, and gRNA indicating an increase in NHEJ following *ds*DNA break by SpCas9. Error bars represent ±SD across technical replicates (n = 4).

(I) Z′-factor values for cell-based secondary assays (eGFP disruption, mKate2 disruption, and NHEJ) in two different plate formats. Assays were performed in 16 technical replicates for 48 h.

See also Figure S1 and Table S1.

eGFP-disruption assay in a 96-well or 384-well format with a Z' = 0.9 or 0.8, respectively (Figures 1F and 1I; Figures S1A and S1D) (Zhang et al., 1999). In a second fluorescence-based assay, we used HEK293T cells expressing a single plasmid construct (Cas9-mKate2-gRNA) encoding both SpCas9 and gRNA components along with their red fluorescent protein target *mKate2* (Figures 1G and S1B) (Moore et al., 2015). We quantified the SpCas9-triggered loss of mKate signal using automated microscopy, yielding an assay with Z' = 0.5 in a 96-well format (Figures 1I and S1D). These two assays, when deployed for inhibitor identification, are gain-of-signal assays that have a lower probability of false positives. We complemented these assays with a loss-of-signal, non-homologous end joining (NHEJ) assay in which cells are transfected with two plasmids in an equimolar ratio: one plasmid expressing out-of-frame *eGFP* downstream of *mCherry*, with the two separated by a stop codon, and the other plasmid expressing SpCas9 and a gRNA that can target the stop codon linker, bringing the *eGFP* gene in-frame (Nguyen et al.,

2016). In this assay, SpCas9-mediated DNA cleavage induced eGFP expression, affording an assay with a $Z' = 0.4$ in a 96-well format (Figures 1H and 1I; Figures S1C and S1D). Unlike the mKate2 assay, we can use mCherry expression in this assay to normalize for transfection efficiency.

Small-Molecule Screening and Identification of Enriched Libraries

Our initial primary screen focused on a 2,652-membered performance-diverse compound collection (Wawer et al., 2014) containing 2,240 small molecules from commercial libraries and 412 from DOS-derived libraries. All screening hits in this experiment were DOS compounds (data not shown). Indeed, DOS libraries of natural-product-like compounds have performed well against microbial targets (Comer et al., 2014; Gerry and Schreiber, 2018). However, screening all available 100,000 DOS compounds across 32 libraries would be inefficient, as compounds *within* a single library are structurally similar and may perform similarly in assays. Instead, we employed a computational approach to assemble 9,549 compounds, a DOS "informer set," which maximally represented the structural diversity across all DOS compounds (Figure S1E). We screened the DOS informer set using the FP assay (Figure 2A), employing 12PAM-DNA lacking a fluorophore as a positive control. Screening hits, which lowered the FP signal by $>3\sigma$ compared to the DMSO vehicle-control distribution, were grouped by library to assess the enrichment (Figure 2B; Table S2). Members of the Pictet-Spengler, spirocyclic azetidine, and Povarov libraries (Comer et al., 2015; Gerard et al., 2012) yielded screening hit rates >1%.

Biochemical and Cellular Validation of the Povarov Scaffold

We chose not to pursue the spirocyclic azetidine library, as the compounds lowered the FP of 12PAM-DNA in the absence of SpCas9:gRNA, suggesting non-specificity (data not shown). Screening additional members of the Pictet-Spengler and Povarov libraries using the FP assay and subsequent counterscreening revealed that most Pictet-Spengler compounds, but not Povarov compounds, exhibited significant fluorescent background, and the hits from the Pictet-Spengler library were also cytotoxic (Figures 2C and S2A). As such, before embarking on activity-guided structure optimization in cells, we decided to validate the binding and inhibitory activity of the Povarov scaffold using small molecules BRD7087 and BRD5779 and their biotinylated analog BRD3539 (Figure S2B). BLI studies using BRD3539 and the SpCas9:gRNA complex suggested a dissociation constant of 0.7 μM (Figures 2D and S2C). No detectable binding was observed in the absence of the Povarov scaffold or in the presence of a 10-fold excess of biotin (Figures S2D and S2E). After confirming that BRD7087 was soluble up to 75 μM in PBS (Figures S2F and S2G), we used ^{19}F NMR spectroscopy to validate the binding of BRD7087 to SpCas9:gRNA. We observed a differential line broadening of the ^{19}F signal upon titration with SpCas9:gRNA (Figure 2E; Table S3; Figure S2H), with significant broadening occurring at protein concentrations as low as 0.75 μM (67-fold excess of BRD7087), indicating tight binding. We confirmed that BRD7087 and BRD5779 were non-cytotoxic (Figures S2I and S2J), demonstrated dose-dependent inhibition of SpCas9 in the eGFP-disruption assay (Figures 2F, S2K, and S2L), and found BRD7087 to inhibit SpCas9 up to ~44% at 10 μM without either affecting eGFP expression (Figure S2M) or inducing notable auto-fluorescence (Figure S2N). BRD7087 and BRD5779 showed a dose-dependent inhibition of SpCas9 in both the mKate2 disruption (Figures S2O and S2P) and NHEJ assays (Figure S2Q). Since BRD7087 and BRD5779 alter PAM binding, they may inhibit technologies that use a catalytically impaired SpCas9, including transcription activation and base editing. The dose-dependent inhibition of dCas9-based transcription activation of *HBG1*, but not of the control gene, was observed using BRD7087 and BRD5779, attaining ~60% inhibition of transcriptional activation at 20 μM (Figures 2G and S2R). Both compounds also inhibited C→T conversion of the *EMX1* gene using the SpCas9(A840H)-cytidine deaminase conjugate (BE3) (Komor et al., 2017; Rees et al., 2017), with close to a 2-fold reduction in C→T conversion at 20 μM (Figure S2S).

Cell-Based Activity-Guided Structure Optimization Identifies BRD0539 as a SpCas9 Inhibitor

Upon biochemical and cellular validation of the Povarov scaffold, we sought to improve the potencies of the identified SpCas9 inhibitors in mammalian cells. To this end, we tested 641 structural analogs of BRD7087 (either synthesized or available from the Broad Institute) at 15 μM in the cell-based eGFP-disruption assay, and several compounds possessed greater potency than BRD7087 (Figure 3A; Table S4). Our hit-triage workflow involved prioritizing compounds based on the absence of cytotoxicity and the presence of dose-dependent inhibition in the eGFP-disruption assay when SpCas9 was provided to the cells as a ribonucleoprotein complex or as a plasmid. From these studies, BRD0539 and BRD3433 emerged as top performers with a 1.8-fold improvement in potency over BRD7087 in the eGFP-disruption assay (Figures 3B–3D and S3A) and an apparent EC_{50} of 11 μM. To confirm that these SpCas9 inhibitions were independent of the DNA repair mechanisms or the optical readout, we employed a HiBiT assay (Schwinn et al., 2018). While the eGFP-disruption assay is a fluorescence-based assay involving error-prone DNA repair, the HiBiT assay involves SpCas9-mediated homology-directed tagging of GAPDH with a short peptide, which produces luminescence upon complementation with a subunit derived from nanoluciferase (Figure 3E). Both compounds exhibited dose-dependent inhibition of SpCas9 in the HiBiT assay with BRD0539 being more active. The inhibitory activity of BRD0539 was further confirmed using fluorescent-activated sorting of eGFP cells (Figure S3B), real-time monitoring of eGFP disruption (Supplementary Videos 1–3 in https://doi.org/10.17632/jpxvnh3n2t.1), the surveyor assay, and next-generation sequencing of the *eGFP* locus (Figures S3C, 3F, S3D). We note that, while BRD0539 is cell permeable, protein-based anti-CRISPRs (e.g., AcrIIA4) are not and require delivery methods like nucleofection (Figure 3G). To demonstrate the reversible inhibition of SpCas9 by BRD0539, we performed eGFP-disruption experiments wherein cells were treated with short pulses of BRD0539 followed by treatment with inhibitor-free media. The cells with media swap at an earlier time point

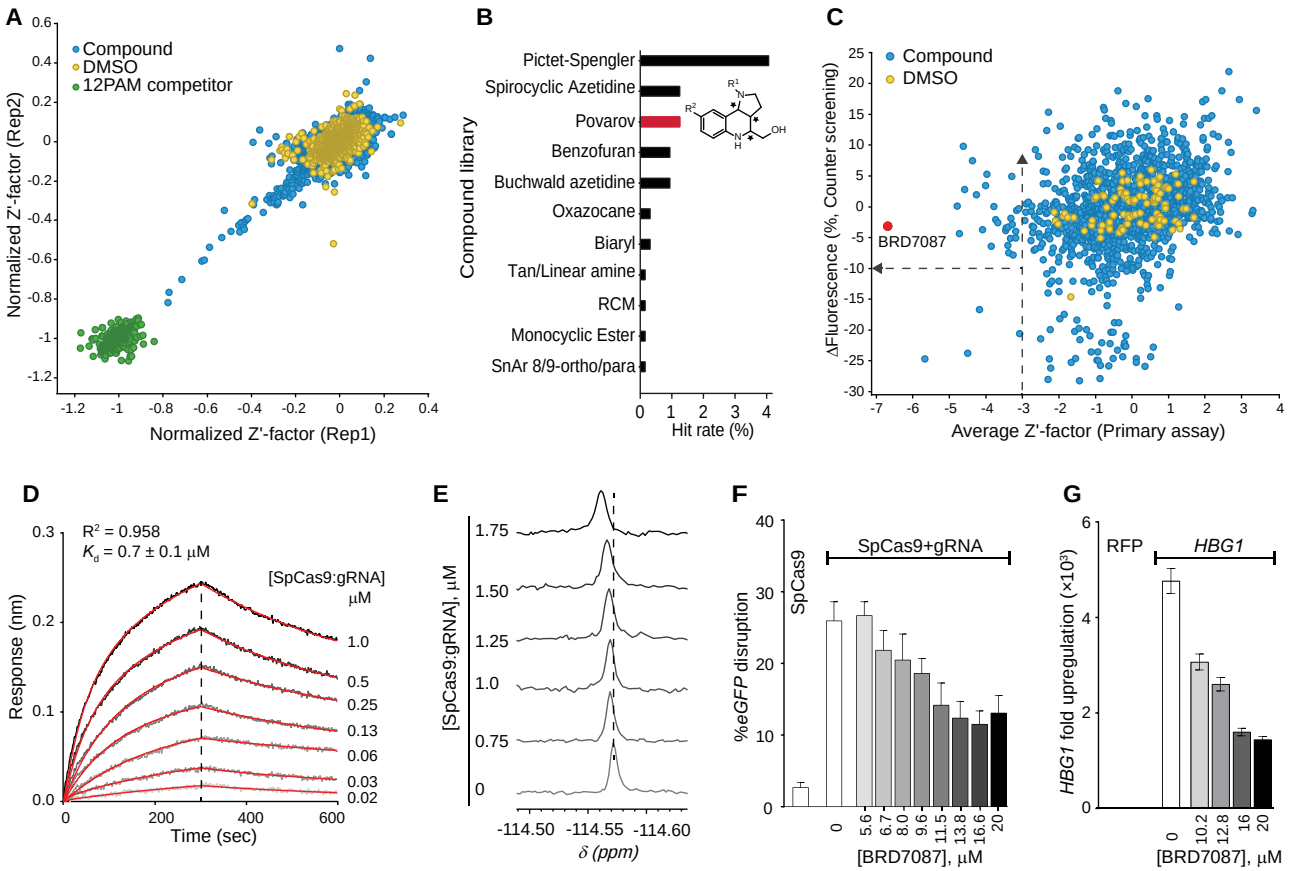

Figure 2. High-Throughput Screening and Identification of Inhibitor Scaffold

(A) Screening results of FP-based assay against 9,549 DOS compounds. Dots in yellow, blue, and green represent DMSO controls, small molecules, and unlabeled 12PAM competitor, respectively.

(B) Hit-rate distribution across the DOS informer set in the FP-based primary assay.

(C) Screening and counterscreening results against the Povarov library. Dots in yellow and blue represent DMSO controls and small molecules, respectively. BRD7087 is indicated in red.

(D) BLI measuring small-molecule binding with the SpCas9:gRNA complex. Streptavidin sensors were loaded with 1 μM of BRD3539, and the interaction was followed by varying the SpCas9:gRNA complex from 0.15 to 1 μM. Global fitting of the response curves against ribonucleoprotein concentration provided the dissociation constant (Figure S2C).

(E) Binding interaction of the BRD7087 and SpCas9:gRNA ribonucleoprotein complex probed via ^{19}F NMR spectrometry. Line broadening in the ^{19}F peak signal indicates the association of BRD7087 with SpCas9.

(F) Dose-dependent inhibition of SpCas9 by BRD7087 in U2OS.eGFP.PEST cells. Compound was tested from 5 to 20 μM. U2OS.eGFP.PEST cells were nucleofected with SpCas9- and gRNA-expressing plasmids and incubated with the compound at the indicated concentration for 24 h before imaging. Error bars represent ±SD across technical replicates (n = 4). *p ≤ 0.0001 for the small molecule at 20 μM compared to DMSO (unpaired t test, two-tailed)

(G) Dose-dependent inhibition of dSpCas9-based transcriptional activation of *HBG1* in HEK293FT cells. Cells were transfected with dSpCas9, MS2.p65.HSF1.GFP, and either *RFP* or *HBG1* plasmids and were incubated in the presence of the small molecule at the indicated concentrations before processing for RT-qPCR. The experiments were performed in three biological replicates, and each biological replicate was processed in six technical replicates. The data represent mean ± SEM for technical replicates. *p ≤ 0.0001 for the small molecule at 20 μM compared to DMSO (unpaired t test, two-tailed).

See also Figures S1 and S2, Tables S1 and S2, and Data S1.

had lower levels of eGFP disruption, suggesting reversible inhibition by BRD0539 (Figure 3H). In contrast, the SpCas9 inhibition by AcrIIA4 was irreversible (Figure 3H). We confirmed binding of the identified compounds to SpCas9:gRNA using BLI (Figures S3E and S3F) following the aforementioned protocol. BRD0539 exhibited a dose-dependent inhibition (apparent IC_{50} = 22 μM) in an *in vitro* DNA cleavage assay, even when the concentration of SpCas9 (5 nM) was much higher than typically present in cells (Figures 3I and S3G). Finally, we confirmed that none of the compounds were auto-fluorescent in cells, none were cytotoxic to multiple cell lines or primary cells (Figures S3H–S3J; Supplementary Item 1 in https://doi.org/10.17632/jpxvnh3n2t.1), and all the compounds were stable in human plasma (Figure 3J) (Di et al., 2005).

Structure-Activity Relationship of BRD0539

To identify the pharmacophore of BRD0539, we examined the activities of structural analogs that differed in R^1 or R^2 groups

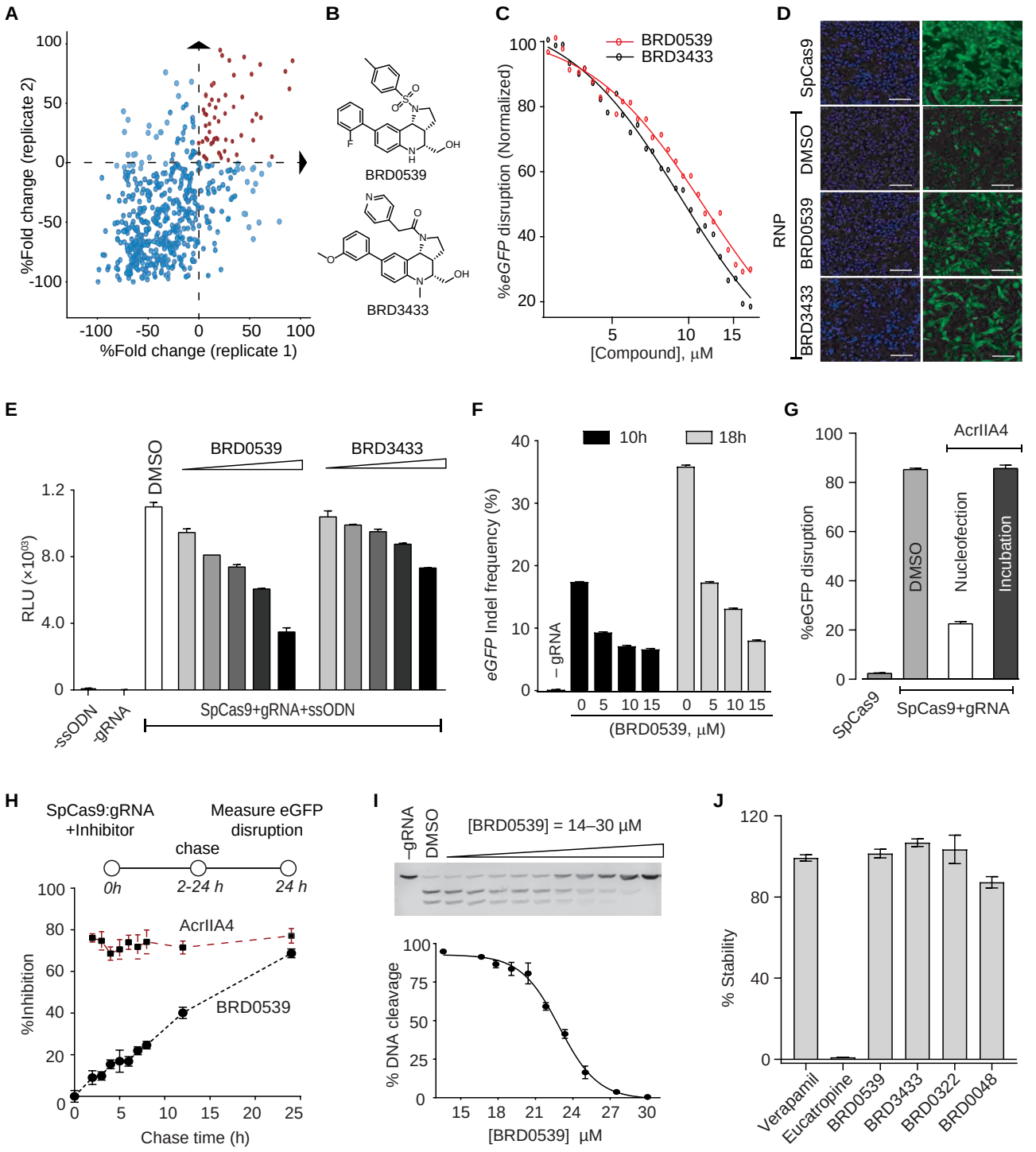

Figure 3. Identification and Validation of Small-Molecule Inhibitors of SpCas9

(A) Scatterplot of activity of BRD7087 analogs in the eGFP-disruption assay. U2OS.eGFP.PEST cells were nucleofected with SpCas9- and gRNA-expressing plasmids and incubated with 15 μM of the compounds for 24 h before imaging. The top-right quadrant represents the compounds with an activity higher than that of BRD7087 in both replicates.

(B) Chemical structures of inhibitors BRD0539 and BRD3433.

(C) Dose-dependent inhibition of SpCas9 by BRD0539 and BRD3433 in U2OS.eGFP.PEST cells with an EC_{50} of 11.5 and 9.3 μM, respectively. Inhibitors were tested from 2.8 to 17.3 μM. U2OS.eGFP.PEST cells were nucleofected with either SpCas9 or preformed SpCas9:gRNA ribonucleoprotein complex and incubated

(legend continued on next page)

but not both (Figure 4A). Keeping R^2 = a and varying R^1 showed that sulfonamides (1–4) were more potent than amides (5–7), perhaps because a sulfonamide can accept two hydrogen bonds while an amide can only accept one. Interestingly, minor changes on R^1 significantly altered the potencies—while 1, 2, or 3 have similar bond connectivity except for the nature of the substituent at the para-position, replacing the methyl group (1) with a fluoro (2) or methoxy (3) group decreased the activity by 18% and 20%, respectively. Furthermore, altering the position of the methyl group from para- (1) to meta- (4) resulted in a 47% reduction in activity. Introducing heteroatoms on the rings (5–8) failed to improve potency—the compound with R^1 = 8 was virtually inactive. Keeping R^1 = 1 and varying R^2 groups showed that alkynl spacers (b or d) lowered the inhibitory activity, which was also observed for an alkenyl moiety. Substituting the relatively small 2-fluoro- (a) with the larger 3-*N,N*-dimethyl-carbamoyl (c) group also led to the loss of activity. We compared the activity of BRD0539 at 12 different dose points in the eGFP-disruption assay with that of BRD3497 and BRD9419, which have a 4-methyl-imidazole or a 2-keto-pyridyl group, respectively, in place of the *p*-tolyl group in BRD0539. While BRD0539 showed dose-dependent inhibitory activity, BRD3497 and BRD9419 barely inhibited SpCas9 (Figures 4B and 4C; Supplementary Videos 4–8 in https://doi.org/10.17632/jpxvnh3n2t.1). The lower inhibitory activity of BRD3497 and BRD9419 was apparent in the HiBiT assay, as well, where BRD0539 showed a greater than 2-fold higher activity (Figure 4D).

In addition to the aforementioned structure-activity relationship, we determined the stereochemical structure-activity relationship for BRD0539 by testing the activities of four stereoisomers in the eGFP-disruption assay (Figures 4E and S4A). Interestingly, among the four stereoisomers, BRD0539 with *RRR* stereochemistry was the most potent, pointing to the specific nature of interactions between SpCas9 and BRD0539. Finally, we also observed some structure-activity relationship with BRD3433. Keeping R^2 = a and systematically varying R^1 showed that the size and nature of the R^1 rings are important: compounds with substituents containing a pyridine (1) or phenyl ring (2,3) are more active than compounds with an imidazole ring (4 or 5), a cyclobutane ring (8), or a benzo[*d*][1,3] dioxole ring (7) (Figure S4B). Furthermore, compounds with aryl rings at R^1 were better inhibitors than those with an aliphatic ring—the compound with R^1 = 8 was virtually inactive. In contrast to BRD0539, introducing a heteroatom on the ring improves the potency (R^1 = 1 versus R^1 = 3). Finally, replacing the aryl ring with bromine led to a drastic 78% reduction in activity.

Mechanism of Inhibition and Specificity of BRD0539

To determine whether BRD0539 disrupted the binding of gRNA to SpCas9, we developed and utilized a FP assay for SpCas-gRNA binding. We monitored the binding of fluorescein isothiocyanate-labeled (FITC)-crRNA:tracrRNA to SpCas9 using FP, observing a sharp increase in the polarization signal upon the addition of SpCas9 to the gRNA (Figure 5A). While the addition of unlabeled competitor gRNA (1 equiv.) caused a drop in polarization signal (Figure 5B), the addition of BRD0539 did not perturb the polarization signal, suggesting that BRD0539 does not interfere with the SpCas9:gRNA interaction (Figure 5C).

Next, we examined whether BRD0539 disrupted the interactions of SpCas9 with DNA using DSF. Briefly, the melting curves of SpCas9 lacking the gRNA (*apo*-SpCas9) suggested the presence of a DNA-bound state upon the addition of DNA with

with the inhibitors at the indicated concentrations for 24 h before imaging. Error bars represent ±SD across technical replicates (n = 3). *$p \leq 0.0001$ for both small molecules at 15 μM compared to DMSO (unpaired t test, two-tailed).

(D) Representative images of the eGFP-disruption assay. U2OS.eGFP.PEST cells were nucleofected with either SpCas9 alone (untreated) or preformed SpCas9:gRNA ribonucleoprotein complex and were treated with the vehicle alone or inhibitors BRD0539 and BRD3433 at 15 μM for 24 h. Left and right panels represent DAPI and GFP channels, respectively.

(E) Dose-dependent inhibition of SpCas9 by BRD0539 and BRD3433 in the HiBiT assay. Inhibitors were tested from 6 to 20 μM. U2OS.eGFP.PEST cells were nucleofected with SpCas9- and gRNA-expressing plasmids along with the single-stranded oligodeoxynucleotides (ssODN) containing the HiBiT tag. The cells were incubated with the inhibitors at the indicated concentrations for 24 h before cell lysis and luminescence measurement. Error bars represent ±SD across technical replicates (n = 2).

(F) Next-generation sequencing analysis of *eGFP* indicating the dose and time-dependent inhibition of SpCas9 by BRD0539 in U2OS.eGFP.PEST cells. Cells were nucleofected with either SpCas9 or preformed SpCas9:gRNA ribonucleoprotein complex targeting the *eGFP* gene and were incubated with BRD0539 at the indicated concentrations for 10 and 18 h before harvesting the genomic DNA. Error bars represent ±SD across technical replicates (n = 2) of two biological replicates.

(G) Cellular impermeability of the anti-CRISPR protein AcrIIA4 assessed by lack of SpCas9 inhibition in the eGFP-disruption assay when AcrIIA4 is incubated in the media. As a positive control for AcrIIA4 activity, the cells were nucleofected with SpCas9:gRNA:AcrIIA4 and incubated for 48 h before imaging. To assess cell permeability, the cells were nucleofected either with SpCas9 or SpCas9:gRNA ribonucleoprotein complex followed by incubation with AcrIIA4 in the media. Error bars represent ±SD across technical replicates (n = 4).

(H) Reversibility of BRD0539- or AcrIIA4-mediated inhibition of SpCas9 in U2OS.eGFP.PEST cells in the eGFP-disruption assay. Cells were nucleofected with either SpCas9 or a preformed SpCas9:gRNA ribonucleoprotein complex or the SpCas9:gRNA:AcrIIA4 ternary complex with an *eGFP* gene targeting guide and then were incubated with either DMSO or 15 μM of BRD0539 followed by a pulse-chase over 2–24 h before imaging. Error bars represent ±SD across technical replicates (n = 2) of two biological replicates.

(I) Inhibition of SpCas9 nuclease activity by BRD0539 in a DNA cleavage assay. SpCas9:gRNA (5 nM) was incubated with BRD0539 at the indicated concentrations for 30 min at room temperature followed by the addition of linear DNA substrate (2,783 bp, puc57) and incubated for an additional 30 min at 37°C. The results were visualized by 1% agarose gel with SYBR Gold staining and were quantified using ImageJ. Error bars represent ±SD across technical replicates (n = 2).

(J) Stability of the compounds in human plasma as determined by ultra-performance liquid chromatography-mass spectrometry (UPLC/MS) using the multiple reaction monitoring (MRM) method. Each compound (5 μM) was incubated with 50% human plasma in PBS for 5 h before being processed for analysis. Error bars represent ±SEM for technical replicates (n = 3).

See also Figure S3, Table S1, and Data S1.

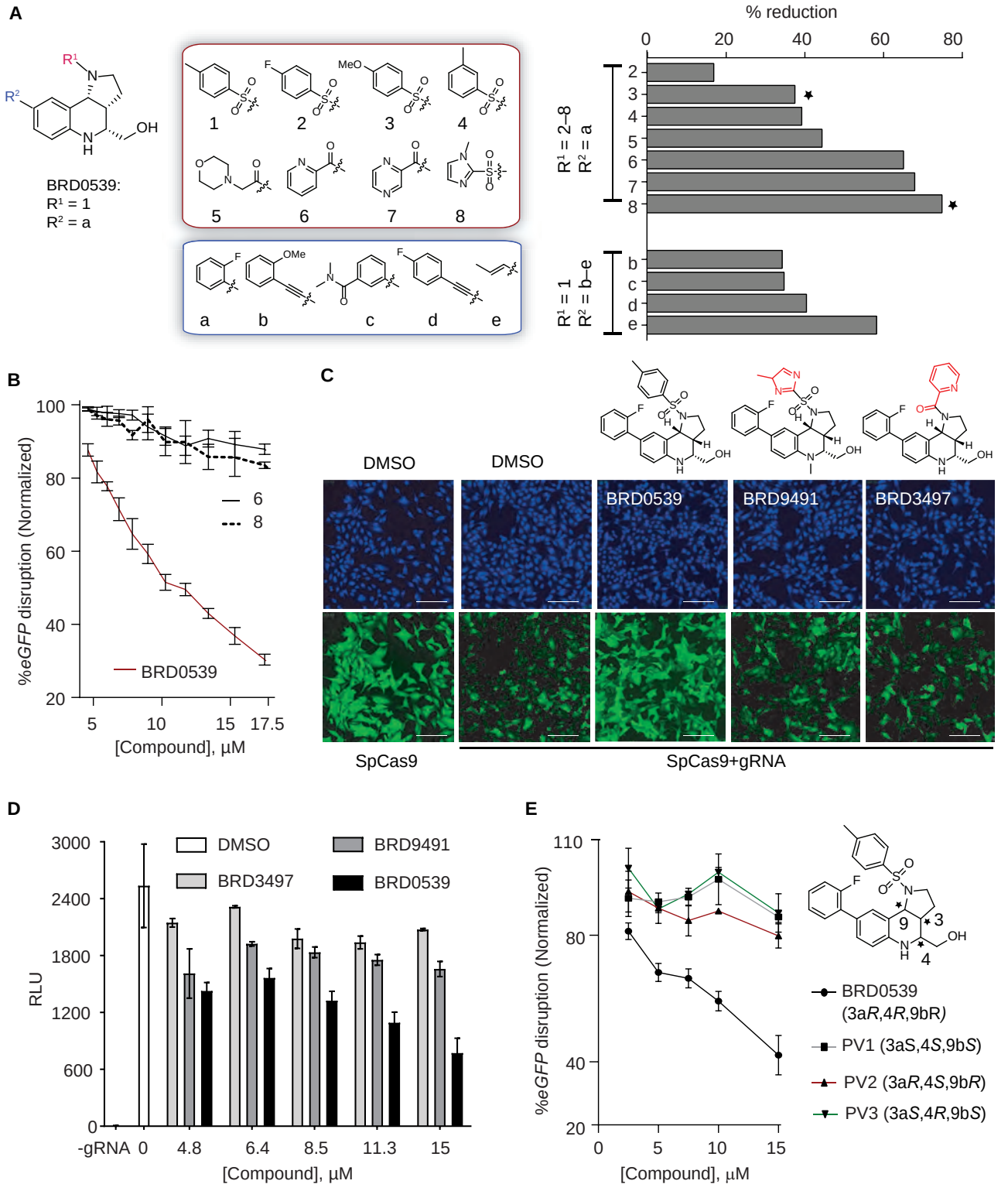

Figure 4. Structure-Activity Relationship

(A) Structure-activity relationship studies of BRD0539 in the eGFP-disruption assay in U2OS.eGFP.PEST cells. The top set of numbered functional groups represents variation at the 1-*N*-cap position (R^1), whereas those in the lettered bottom set represent variation at position 8 (R^2). The bar plot depicts the reduction

(legend continued on next page)

increasing numbers of PAM sequences (0–12 PAM, Figures 5D and S5A) or an increasing concentration of 8PAM DNA (Figures 5E and S5B). BRD0539 dose-dependently blocked the formation of the DNA-bound state in a dose-dependent fashion (Figures 5F and S5C). The SpCas9:gRNA exhibited a multiphasic melting signature that was altered upon the addition of DNA that contained PAM sequences. BRD0539 impaired the perturbation induced by the 4PAM DNA (Figure S5D; Supplementary Items 2 and 3 in https://doi.org/10.17632/jpxvnh3n2t.1). Finally, to confirm target engagement by BRD0539 in cells, we used the cellular thermal shift assay (CETSA), a cellular version of the DSF assay (Martinez Molina and Nordlund, 2016). Since SpCas9:DNA interactions increase the melting temperature of SpCas9, disrupting such interactions by BRD0539 should lower the melting temperature of SpCas9, and we do observe ~2.5°C lowering in cells treated with BRD0539 (Figures 5G and S5E; Supplementary Item 4 in https://doi.org/10.17632/jpxvnh3n2t.1). The interaction between BRD0539 and SpCas9 was further confirmed by pull-down studies in which biotinylated BRD0539 was able to pull down SpCas9 from WM793-SpCas9 cell lysate (Figures 5H and S5F), while no notable non-specific protein pull-down was observed (Supplementary Item 5 in https://doi.org/10.17632/jpxvnh3n2t.1). Finally, while BRD0539 was able to inhibit SpCas9 in the eGFP-disruption assay, BRD0539 was unable to inhibit FnCpf1, a structurally different CRISPR-associated nuclease, in the same assay, further highlighting the specificity of BRD0539 (Figure 5I).

Inhibition of the dCas9-Based Transcription Activation Complex

After optimizing the inhibition of the nuclease activity of the SpCas9:gRNA complex, we sought to optimize for inhibition of the transcriptional activation complex, which consists of dCas9:gRNA and transcription-activating SAM domains (Konermann et al., 2015) that are recruited by the gRNA. Our hit-triage workflow was similar to that for the nuclease activity and involved prioritizing compounds based on the absence of cytotoxicity and the presence of dose-dependent inhibition of transcriptional activation in cells. While the nuclease inhibitors identified above also blocked transcription (Figure S5G), BRD20322 and BRD0048 emerged as the most potent inhibitors of the transcription activation complex, showing a dose-dependent inhibition with an EC_{50} of 12.2 μM and 9 μM, with BRD20322 inhibiting 89% of the transcription at 20 μM (Figures 5J and S5H). None of the inhibitors altered the expression of the control genes.

DISCUSSION

We report a workflow for the rapid identification of small-molecule inhibitors of SpCas9 and demonstrate the utility of this workflow by identifying the first examples of small-molecule inhibitors of SpCas9. Our screening strategy involved disrupting DNA binding by SpCas9, followed by demonstrating activity in multiple mammalian cell lines using gene or protein delivery. Furthermore, we demonstrated inhibition of SpCas9 nuclease and transcription activation in assays with gain of signal (e.g., eGFP-disruption assay), loss of signal (e.g., HiBiT assay), various DNA repair pathways, and a myriad of readouts (e.g., fluorescence, luminescence, next-generation sequencing [NGS], qPCR). Thus, these inhibitors are effective against both wild-type and engineered SpCas9 in mammalian cells with multiple delivery modes, including delivery of the ribonucleoprotein complex. Our inhibitor identification methodology is rapid and cost effective and required testing only ~15,000 compounds to identify potent SpCas9 inhibitors. We envision that the availability of high-throughput assays and a screening workflow will propel the rapid discovery of highly potent inhibitors, not only for SpCas9 but also for next-generation CRISPR-associated nucleases. Finally, the small-molecule inhibitors complement protein-based anti-CRISPRs in that they are cell permeable, reversible, stable in human plasma, and resistant to proteases.

Multiple lines of evidence point to the specific nature of interactions between the inhibitors and the SpCas9:gRNA complex. Small perturbations to the structure or even the stereochemistry of BRD0539 causes loss of inhibitory activity, and FnCpf1 remains uninhibited by BRD0539. Furthermore, the subtle structural variation between inhibitors that block the SpCas9:gRNA complex from those that inhibit the dCas9:gRNA:SAM complex for transcription activation also points to specific interactions. The ability of identified inhibitor BRD0539 to block the formation of the DNA-bound state indicates that the reported inhibitors could either operate by directly competing with the NGG PAM or bind to an allosteric site. Identifying the binding pocket of the inhibitors via structural studies will be key for mechanistic understanding of the aforementioned observations as well as

in activity of different structural analogs with respect to that of BRD0539. Asterisk-labeled compounds have a methyl group at the 4-*N* position, while the others have a proton. The data are an average of two biological replicates.

(B) Dose-dependent inhibition of SpCas9 by BRD0539, BRD3497, and BRD9419 in U2OS.eGFP.PEST cells. The inhibitors were tested from 2.8 to 17.3 μM. U2OS.eGFP.PEST cells were nucleofected with either SpCas9 or preformed SpCas9:gRNA ribonucleoprotein complex and were incubated with the compounds at the indicated concentrations for 24 h before imaging. Error bars represent ±SD across technical replicates (n = 3).

(C) Representative images of the eGFP-disruption assay. U2OS.eGFP.PEST cells were nucleofected with either SpCas9 alone (untreated) or preformed SpCas9:gRNA ribonucleoprotein complex and were treated with either vehicle alone or the indicated compounds at 15 μM for 24 h. The top and bottom panels represent DAPI and GFP channels, respectively.

(D) Dose-dependent inhibition of SpCas9 by BRD0539, BRD3497, and BRD9419 in the HiBiT assay. Inhibitors were tested from 4.8 to 15 μM. U2OS.eGFP.PEST cells were nucleofected with SpCas9- and gRNA-expressing plasmids along with ssODN containing the HiBiT tag. The cells were incubated with compounds at the indicated concentrations for 24 h before cell lysis and luminescence measurements. Error bars represent ±SD across technical replicates (n = 2).

(E) Chemical structures of BRD0539 stereoisomers and their dose-dependent inhibition of SpCas9 in U2OS.eGFP.PEST cells. Inhibitors were tested from 4.6–17.5 μM. Cells were nucleofected with either SpCas9 or preformed SpCas9:gRNA ribonucleoprotein complex and were incubated with the compounds at the indicated concentration for 24 h before imaging. Error bars represent ±SD across technical replicates (n = 3).

See also Figure S4, Table S1, and Data S1.

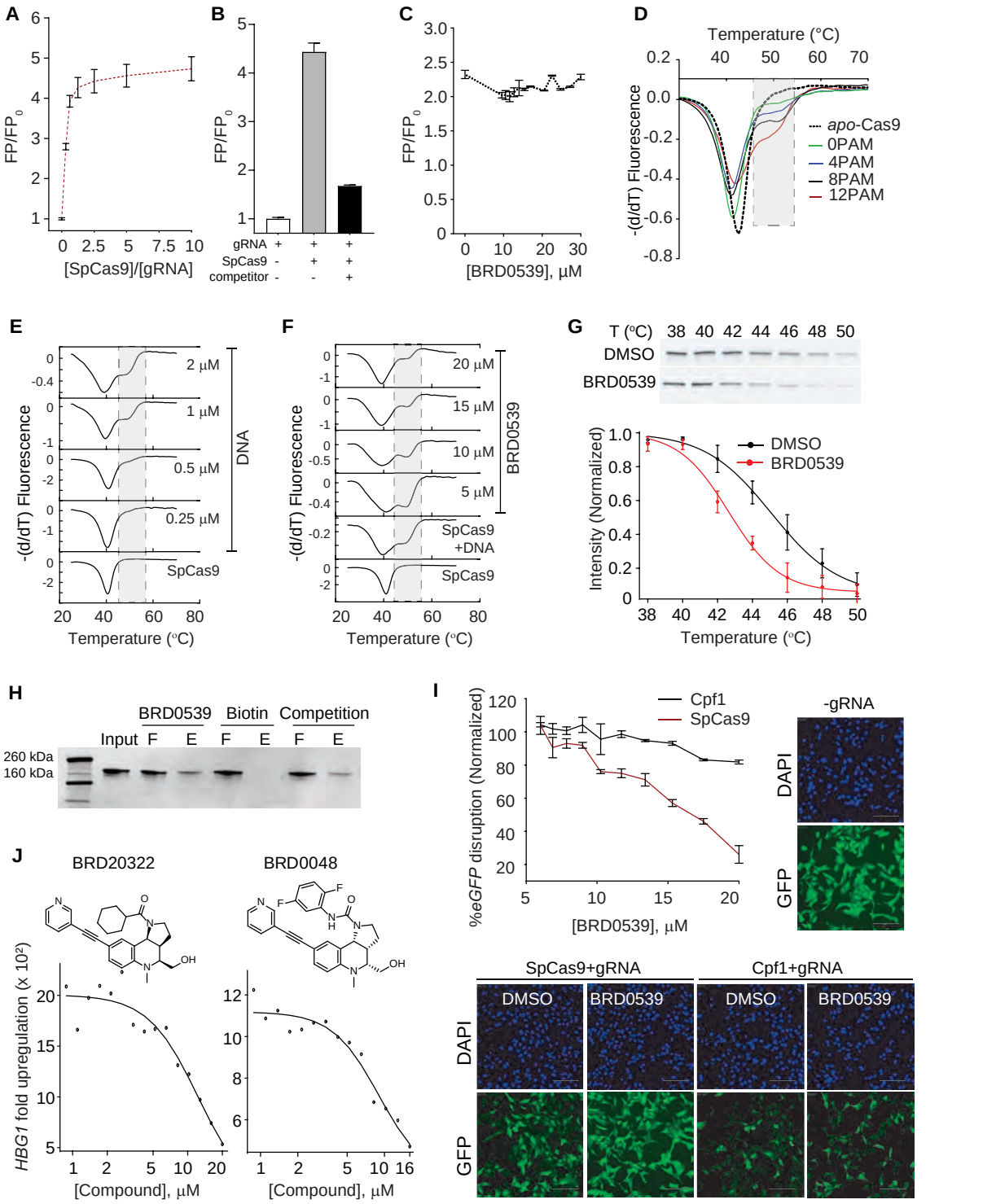

Figure 5. Mechanism of Action and Inhibition of dCas9-Based Transcriptional Upregulation

(A) FP assay for detecting SpCas9-gRNA binding. A FITC-labeled crRNA:tracrRNA (25 nM) was titrated with an increasing amount of SpCas9 (7.5–250 nM). Error bars represent ±SD across technical replicates (n = 3).

(B) Competition experiment demonstrating sequence-specific gRNA-SpCas9 binding. An unlabeled crRNA:tracrRNA (25 nM) was pre-incubated with SpCas9 (25 nM) for 10 min before the addition of FITC-crRNA:tracrRNA (25 nM). Error bars represent ±SD across technical replicates (n = 3).

(legend continued on next page)

potency improvement of the inhibitors. Mechanism-of-action studies involving single-molecule biophysics experiments to examine the effects of the inhibitor on the conformational change of SpCas9 during the catalytic cycle will also provide valuable insight and may explain the molecular mechanism of disruption of DNA binding as suggested by DSF studies. We note that our DSF studies confirm the presence of a flexible conformation of *apo*-SpCas9 that shows a preference for DNA containing PAM sequences (Figure 5D). *Apo*-SpCas9 binds to DNA with an affinity of 25 nM (Sternberg et al., 2014), and high-speed atomic force microscopy studies suggest the presence of a flexible conformation in solution (Shibata et al., 2017) as opposed to the closed conformation observed in crystal structures.

Identifying small-molecule inhibitors of nuclease activity presents similar assay development challenges as we encountered for PAM binding. Our future studies will involve the identification of nuclease inhibitors and an exploration of possible synergies between the two classes of inhibitors. Although our inhibitors are nontoxic to mammalian cells and do not alter transcription and translation of housekeeping genes, it remains to be determined whether these inhibitors or the anti-CRISPR proteins interact with other targets in mammalian cells. Finally, in many applications, degradation of SpCas9 may be required. For example, a recent study has pointed to the existence of antibodies against SpCas9 in humans (Charlesworth et al., 2018), and the SpCas9-specific immune response is construed as a bottleneck in the development of therapeutic applications of SpCas9. Reducing the half-life of SpCas9 may reduce the severity of the immune response. Proteolysis-targeting chimeras (PROTACs) are heterobifunctional small molecules containing a target-protein binder and a ubiquitin-ligase binder joined by a linker (Lai and Crews, 2017). A PROTAC formed by joining our inhibitor to the ubiquitin-ligase binder should recruit ubiquitin ligase to SpCas9, promoting ubiquitination and proteasomal degradation of SpCas9. Furthermore, PROTACs are catalytic and may require a lower dose as they operate by "event-driven pharmacology" as opposed to inhibitors that are stoichiometric and operate by "occupancy-driven pharmacology." Our future efforts will involve the identification of inhibitors for next-generation CRISPR systems and understanding their mode of inhibition as well as the application of such inhibitors. The timely and partial inhibition (~50%) of SpCas9 reduced off-target editing for several genes, including a 5-fold reduction for β-globin (*HBB*)-targeting gRNA that is of therapeutic interest for sickle cell disease (Shin et al., 2017). Partial inhibition of SpCas9 by BRD0539 together with its cellular permeability, reversibility, and plasma stability should afford a facile method for reducing the off-target activity of SpCas9. Together, our studies point to the utility of invocation of chemical biology-based approaches for genome editing and functional genomics studies using CRISPR-based systems.

STAR★METHODS

Detailed methods are provided in the online version of this paper and include the following:

- KEY RESOURCES TABLE
- CONTACT FOR REAGENT AND RESOURCE SHARING
- EXPERIMENTAL MODEL AND SUBJECT DETAILS
  - *Escherichia coli* Rosetta (DE3)
  - *Escherichia coli* BL21 (DE3)
  - Cell culture
- METHOD DETAILS

(C) FP assay for determining the effect of BRD0539 in the SpCas9-FITC-crRNA:tracrRNA binding. SpCas9 (25 nM) was incubated with the indicated amount of BRD0539 (10–30 μM) for 15 min followed by the addition of FITC-crRNA:tracrRNA (25 nM), which was incubated for 30 min before measuring the FP signal. Error bars represent ±SD across technical replicates (n = 3).

(D) Differential scanning fluorimetry studies of the *apo*-SpCas9 interaction with DNA. SpCas9 (1 μM) was incubated with DNA (2 μM) bearing an increasing number of PAM sequences (0–12 PAM). Data are for one of the three biological replicates.

(E) Differential scanning fluorimetry showing the formation of a more stable SpCas9 complex (shaded region) upon binding with increasing concentrations (0.25, 0.5, 1, and 2 μM) of 8PAM DNA. Error bars represent ±SD across technical replicates (n = 2).

(F) Differential scanning fluorimetry depicting the destabilization of SpCas9:8PAM DNA (1 μM:2 μM) complexes (shaded region) upon incubation with increasing concentrations (5, 10, 15, and 20 μM) of BRD0539. Error bars represent ±SD across technical replicates (n = 2).

(G) Cellular thermal shift assay (CETSA) for SpCas9 in WM793 melanoma cells in the absence or presence of BRD0539. WM793 cells stably expressing SpCas9 were incubated with 15 μM BRD0539 for 24 h before performing CETSA and were analyzed by western blot. The top panel is the immunoblot representation of the thermal stability of SpCas9 in WM793 cells treated with either vehicle or BRD0539. The original immunoblot is in the Supplementary Item 4 (https://doi.org/10.17632/jpxvnh3n2t.1). The bottom panel is the quantified thermal stability plot for SpCas9. Error bars represent ±SD across biological replicates (n = 4).

(H) *In vitro* pull-down assay of SpCas9 by the BRD0539-biotin conjugate from WM793-SpCas9 cell lysate. Streptavidin magnetic beads pre-loaded with either BRD0539-biotin or biotin-azide were incubated with WM793-SpCas9 cell lysate for 12 h before processing the samples for western blotting. BRD0539 (20 μM) was used as a competitor. F and E represent the flow-through and eluent, respectively.

(I) Dose-dependent inhibition study of BRD0539 (6–20 μM) against SpCas9 or FnCpf1 in U2OS.eGFP.PEST cells. Cells were nucleofected with SpCas9 or FnCpf1 plasmids and their corresponding gRNA-expressing plasmids and were incubated with the inhibitor at the indicated concentration for 30 h before imaging and analysis. Error bars represent ±SD across technical replicates (n = 4). Representative images of the eGFP-disruption assay for SpCas9 and FnCpf1 in U2OS.eGFP.PEST cells. Cells were nucleofected with either SpCas9 plasmid alone (–gRNA) or either the SpCas9 or FnCpf1 plasmids with their corresponding gRNA-expressing plasmids containing the *eGFP* gene target and were incubated with the inhibitor (15 μM) for 30 h before imaging. The top and bottom panels represent the DAPI and GFP channels, respectively.

(J) Chemical structures of BRD20322 and BRD0048 and their dose-dependent inhibition of dCas9-based transcriptional upregulation of the *HBG1* gene in HEK293FT cells. Cells were transfected with dSpCas9 and MS2.p65.HSF1.GFP plasmids along with either *RFP* or *HBG1* gRNA plasmids and were incubated in the presence of the small molecules at the indicated concentrations before processing for RT-qPCR. The experiments were performed in three biological replicates, and each biological replicate was processed in eight technical replicates. The data represent the mean ± SEM for technical replicates. *$p \leq 0.0001$ for both small molecules at 15 μM and DMSO (unpaired t test, two-tailed).

See also Figure S5, Table S1, and Data S1.

- SpCas9 expression and purification
- In vitro transcription of gRNA
- Fluorescence polarization (FP) assay
- Fluorescence polarization competition assay
- Differential scanning fluorimetry (DSF)
- Bio-layer interferometry (BLI)
- mKate2-disruption assay
- Non-homologous end joining (NHEJ) assay
- Primary assay for compound screening
- Counter-screening assay
- Compound–SpCas9 interaction in BLI
- NMR binding assay
- SpCas9 nuclease activity in eGFP-disruption assay
- Western blot analysis
- Base-editing experiments

- QUANTIFICATION AND STATISTICAL ANALYSIS
- DATA AND SOFTWARE AVAILABILITY

SUPPLEMENTAL INFORMATION

Supplemental Information can be found online at https://doi.org/10.1016/j.cell.2019.04.009.

ACKNOWLEDGMENTS

This work was supported by the Burroughs Wellcome Fund (Career Award at the Scientific Interface to A.C.), DARPA (Brdi N66001-17-2-4055 to A.C.; HR0011-17-2-0049 to D.R.L.), NIH (R21AI126239 to A.C.; RM1HG009490 and R35 GM118062 to D.R.L.), and Army Research Office award W911NF1610586 (to A.C.). We thank Prof. M.D. Shoulders, Dr. K.J. Cox, and Dr. D. Manna for contributive discussions; Prof. J. Keith Joung for providing U2OS.eGFP.PEST cells; and H. Li for providing WM793-SpCas9 cells. D.R.L. and L.A.M. are investigators of the Howard Hughes Medical Institute.

AUTHOR CONTRIBUTIONS

A.C. conceptualized the project and Cas9 assays. B. Maji developed Cas9 assays and performed small-molecule screening, activity optimization, and SAR studies. B. Maji, V.D., B.K.W., and A.C. analyzed the screening data. M.L., M.S., and P.W. performed chemical synthesis. B. Maji, S.A.G., M.L., M.S., P.W., R.H., B. Mok, S.U.S., D.L., B.P., A.V., and M.F.M. performed validation experiments and analyzed data with L.A.M., D.R.L., P.A.C., B.K.W., or A.C. The manuscript was written by B. Maji, S.A.G., M.L., M.S., P.W., B.K.W., and A.C. and was edited by all the authors.

DECLARATION OF INTERESTS

Broad Institute has filed a patent application including work described herein. L.A.M. is a cofounder and Scientific Advisory Board member of Intellia Therapeutics and a co-founder of Eligo Biosciences. D.R.L. is a co-founder and consultant of Editas Medicine, Pairwise Plants, and Beam Therapeutics, companies that use genome editing.

Received: December 14, 2017
Revised: September 17, 2018
Accepted: April 3, 2019
Published: May 2, 2019

SUPPORTING CITATIONS

The following references appear in the Supplemental Information: Tan and Jacobsen (2007); Xu et al. (2014).

REFERENCES

Champer, J., Buchman, A., and Akbari, O.S. (2016). Cheating evolution: engineering gene drives to manipulate the fate of wild populations. Nat. Rev. Genet. *17*, 146–159.

Charlesworth, C.T., Deshpande, P.S., Dever, D.P., Dejene, B., Gomez-Ospina, N., Mantri, S., Pavel-Dinu, M., Camarena, J., Weinberg, K.I., and Porteus, M.H. (2018). Identification of pre-existing adaptive immunity to Cas9 proteins in humans. bioRxiv. https://doi.org/10.1101/243345.

Chen, J.S., and Doudna, J.A. (2017). The chemistry of Cas9 and its CRISPR colleagues. Nat. Rev. Chem. *1*, 0078.

Comer, E., Duvall, J.R., and duPont Lee, M., 4th. (2014). Utilizing diversity-oriented synthesis in antimicrobial drug discovery. Future Med. Chem. *6*, 1927–1942.

Comer, E., Munoz, B., Beaudoin, J.A., Le Quement, S.T., Scherer, C., Duvall, J., Kato, N., Maetani, M., and Braibant, B. (2015). Compounds for the treatment of malaria. WIPO patent WO2015002755, filed June 20, 2014, and granted January 8, 2015.

Cox, D.B.T., Platt, R.J., and Zhang, F. (2015). Therapeutic genome editing: prospects and challenges. Nat. Med. *21*, 121–131.

Cox, K.J., Subramanian, H.K.K., Samaniego, C.C., Franco, E., and Choudhary, A. (2019). A universal method for sensitive and cell-free detection of CRISPR-associated nucleases. Chem. Sci. (Camb.).

Di, L., Kerns, E.H., Hong, Y., and Chen, H. (2005). Development and application of high throughput plasma stability assay for drug discovery. Int. J. Pharm. *297*, 110–119.

Esvelt, K.M., Smidler, A.L., Catteruccia, F., and Church, G.M. (2014). Concerning RNA-guided gene drives for the alteration of wild populations. eLife *3*, e03401.

Fellmann, C., Gowen, B.G., Lin, P.C., Doudna, J.A., and Corn, J.E. (2017). Cornerstones of CRISPR-Cas in drug discovery and therapy. Nat. Rev. Drug Discov. *16*, 89–100.

Fu, Y., Foden, J.A., Khayter, C., Maeder, M.L., Reyon, D., Joung, J.K., and Sander, J.D. (2013). High-frequency off-target mutagenesis induced by CRISPR-Cas nucleases in human cells. Nat. Biotechnol. *31*, 822–826.

Gangopadhyay, S.A., Cox, K.J., Manna, D., Lim, D., Maji, B., Zhou, Q., and Choudhary, A. (2019). Precision Control of CRISPR-Cas9 Using Small Molecules and Light. Biochemistry. Biochemistry *29*, 234–244.

Gantz, V.M., and Bier, E. (2016). The dawn of active genetics. BioEssays *38*, 50–63.

Gerard, B., O'Shea, M.W., Donckele, E., Kesavan, S., Akella, L.B., Xu, H., Jacobsen, E.N., and Marcaurelle, L.A. (2012). Application of a catalytic asymmetric Povarov reaction using chiral ureas to the synthesis of a tetrahydroquinoline library. ACS Comb. Sci. *14*, 621–630.

Gerry, C.J., and Schreiber, S.L. (2018). Chemical probes and drug leads from advances in synthetic planning and methodology. Nat. Rev. Drug Discov. *17*, 333–352.

Hynes, A.P., Rousseau, G.M., Lemay, M.L., Horvath, P., Romero, D.A., Fremaux, C., and Moineau, S. (2017). An anti-CRISPR from a virulent streptococcal phage inhibits Streptococcus pyogenes Cas9. Nat. Microbiol. *2*, 1374–1380.

Jinek, M., Chylinski, K., Fonfara, I., Hauer, M., Doudna, J.A., and Charpentier, E. (2012). A programmable dual-RNA-guided DNA endonuclease in adaptive bacterial immunity. Science *337*, 816–21.

Kleinstiver, B.P., Prew, M.S., Tsai, S.Q., Nguyen, N.T., Topkar, V.V., Zheng, Z., and Joung, J.K. (2015a). Broadening the targeting range of Staphylococcus aureus CRISPR-Cas9 by modifying PAM recognition. Nat. Biotechnol. *33*, 1293–1298.

Kleinstiver, B.P., Prew, M.S., Tsai, S.Q., Topkar, V.V., Nguyen, N.T., Zheng, Z., Gonzales, A.P., Li, Z., Peterson, R.T., Yeh, J.R., et al. (2015b). Engineered CRISPR-Cas9 nucleases with altered PAM specificities. Nature *523*, 481–485.

Koehler, A.N. (2010). A complex task? Direct modulation of transcription factors with small molecules. Curr. Opin. Chem. Biol. *14*, 331–340.

Komor, A.C., Kim, Y.B., Packer, M.S., Zuris, J.A., and Liu, D.R. (2016). Programmable editing of a target base in genomic DNA without double-stranded DNA cleavage. Nature *533*, 420–424.

Komor, A.C., Badran, A.H., and Liu, D.R. (2017). CRISPR-based technologies for the manipulation of eukaryotic genomes. Cell *168*, 20–36.

Konermann, S., Brigham, M.D., Trevino, A.E., Joung, J., Abudayyeh, O.O., Barcena, C., Hsu, P.D., Habib, N., Gootenberg, J.S., Nishimasu, H., et al. (2015). Genome-scale transcriptional activation by an engineered CRISPR-Cas9 complex. Nature *517*, 583–588.

Lai, A.C., and Crews, C.M. (2017). Induced protein degradation: an emerging drug discovery paradigm. Nat. Rev. Drug Discov. *16*, 101–114.

Maji, B., Moore, C.L., Zetsche, B., Volz, S.E., Zhang, F., Shoulders, M.D., and Choudhary, A. (2017). Multidimensional chemical control of CRISPR-Cas9. Nat. Chem. Biol. *13*, 9–11.

Martinez Molina, D., and Nordlund, P. (2016). The Cellular Thermal Shift Assay: A novel biophysical assay for in situ drug target engagement and mechanistic biomarker studies. Annu. Rev. Pharmacol. Toxicol. *56*, 141–161.

Moore, R., Spinhirne, A., Lai, M.J., Preisser, S., Li, Y., Kang, T., and Bleris, L. (2015). CRISPR-based self-cleaving mechanism for controllable gene delivery in human cells. Nucleic Acids Res. *43*, 1297–1303.

Neve, R.L., Neve, K.A., Nestler, E.J., and Carlezon, W.A., Jr. (2005). Use of herpes virus amplicon vectors to study brain disorders. Biotechniques *39*, 381–391.

Nguyen, D.P., Miyaoka, Y., Gilbert, L.A., Mayerl, S.J., Lee, B.H., Weissman, J.S., Conklin, B.R., and Wells, J.A. (2016). Ligand-binding domains of nuclear receptors facilitate tight control of split CRISPR activity. Nat. Commun. *7*, 12009.

Nishimasu, H., Ran, F.A., Hsu, P.D., Konermann, S., Shehata, S.I., Dohmae, N., Ishitani, R., Zhang, F., and Nureki, O. (2014). Crystal structure of Cas9 in complex with guide RNA and target DNA. Cell *156*, 935–949.

Nuñez, J.K., Harrington, L.B., and Doudna, J.A. (2016). Chemical and biophysical modulation of Cas9 for tunable genome engineering. ACS Chem. Biol. *11*, 681–688.

Pattanayak, V., Lin, S., Guilinger, J.P., Ma, E., Doudna, J.A., and Liu, D.R. (2013). High-throughput profiling of off-target DNA cleavage reveals RNA-programmed Cas9 nuclease specificity. Nat. Biotechnol. *31*, 839–843.

Pawluk, A., Amrani, N., Zhang, Y., Garcia, B., Hidalgo-Reyes, Y., Lee, J., Edraki, A., Shah, M., Sontheimer, E.J., Maxwell, K.L., et al. (2016a). Naturally occurring off-switches for CRISPR-Cas9. Cell *167*, 1829–1838.

Pawluk, A., Staals, R.H., Taylor, C., Watson, B.N., Saha, S., Fineran, P.C., Maxwell, K.L., and Davidson, A.R. (2016b). Inactivation of CRISPR-Cas systems by anti-CRISPR proteins in diverse bacterial species. Nat. Microbiol. *1*, 16085.

Rauch, B.J., Silvis, M.R., Hultquist, J.F., Waters, C.S., McGregor, M.J., Krogan, N.J., and Bondy-Denomy, J. (2017). Inhibition of CRISPR-Cas9 with bacteriophage proteins. Cell *168*, 150–158.

Rees, H.A., Komor, A.C., Yeh, W.H., Caetano-Lopes, J., Warman, M., Edge, A.S.B., and Liu, D.R. (2017). Improving the DNA specificity and applicability of base editing through protein engineering and protein delivery. Nat. Commun. *8*, 15790.

Richardson, C.D., Ray, G.J., DeWitt, M.A., Curie, G.L., and Corn, J.E. (2016). Enhancing homology-directed genome editing by catalytically active and inactive CRISPR-Cas9 using asymmetric donor DNA. Nat. Biotechnol. *34*, 339–344.

Schreiber, S.L. (2000). Target-oriented and diversity-oriented organic synthesis in drug discovery. Science *287*, 1964–1969.

Schwinn, M.K., Machleidt, T., Zimmerman, K., Eggers, C.T., Dixon, A.S., Hurst, R., Hall, M.P., Encell, L.P., Binkowski, B.F., and Wood, K.V. (2018). CRISPR-mediated tagging of endogenous proteins with a luminescent peptide. ACS Chem. Biol. *13*, 467–474.

Shibata, M., Nishimasu, H., Kodera, N., Hirano, S., Ando, T., Uchihashi, T., and Nureki, O. (2017). Real-space and real-time dynamics of CRISPR-Cas9 visualized by high-speed atomic force microscopy. Nat. Commun. *8*, 1430.

Shin, J., Jiang, F., Liu, J.-J., Bray, N.L., Rauch, B.J., Baik, S.H., Nogales, E., Bondy-Denomy, J., Corn, J.E., and Doudna, J.A. (2017). Disabling Cas9 by an anti-CRISPR DNA mimic. Sci. Adv. *3*, e1701620.

Sternberg, S.H., Redding, S., Jinek, M., Greene, E.C., and Doudna, J.A. (2014). DNA interrogation by the CRISPR RNA-guided endonuclease Cas9. Nature *507*, 62–67.

Tan, K.L., and Jacobsen, E.N. (2007). Indium-mediated asymmetric allylation of acylhydrazones using a chiral urea catalyst. Angew. Chem. Int. Ed. Engl. *46*, 1315–1317.

Tu, Z., Yang, W., Yan, S., Yin, A., Gao, J., Liu, X., Zheng, Y., Zheng, J., Li, Z., Yang, S., et al. (2017). Promoting Cas9 degradation reduces mosaic mutations in non-human primate embryos. Sci. Rep. *7*, 42081.

Wang, H., Yang, H., Shivalila, C.S., Dawlaty, M.M., Cheng, A.W., Zhang, F., and Jaenisch, R. (2013). One-step generation of mice carrying mutations in multiple genes by CRISPR/Cas-mediated genome engineering. Cell *153*, 910–918.

Wang, H., La Russa, M., and Qi, L.S. (2016). CRISPR/Cas9 in genome editing and beyond. Annu. Rev. Biochem. *85*, 227–264.

Wawer, M.J., Li, K., Gustafsdottir, S.M., Ljosa, V., Bodycombe, N.E., Marton, M.A., Sokolnicki, K.L., Bray, M.A., Kemp, M.M., Winchester, E., et al. (2014). Toward performance-diverse small-molecule libraries for cell-based phenotypic screening using multiplexed high-dimensional profiling. Proc. Natl. Acad. Sci. USA *111*, 10911–10916.

Wegrzyn, R.D., Lee, A.H., Jenkins, A.L., Stoddard, C.D., and Cheever, A.E. (2017). Genome editing: insights from chemical biology to support safe and transformative therapeutic applications. ACS Chem. Biol. https://doi.org/10.1021/acschembio.1027b00689.

Weiss, W.A., Taylor, S.S., and Shokat, K.M. (2007). Recognizing and exploiting differences between RNAi and small-molecule inhibitors. Nat. Chem. Biol. *3*, 739–744.

Xu, H., Zhang, H., and Jacobsen, E.N. (2014). Chiral sulfinamidourea and strong Brønsted acid-cocatalyzed enantioselective Povarov reaction to access tetrahydroquinolines. Nat. Protoc. *9*, 1860–1866.

Yen, S.-T., Zhang, M., Deng, J.M., Usman, S.J., Smith, C.N., Parker-Thornburg, J., Swinton, P.G., Martin, J.F., and Behringer, R.R. (2014). Somatic mosaicism and allele complexity induced by CRISPR/Cas9 RNA injections in mouse zygotes. Dev. Biol. *393*, 3–9.

Zhang, J.H., Chung, T.D., and Oldenburg, K.R. (1999). A simple statistical parameter for use in evaluation and validation of high throughput screening assays. J. Biomol. Screen. *4*, 67–73.

Cell PICTURE SHOW

Sponsored by HAMAMATSU
PHOTON IS OUR BUSINESS

Explore the beauty of microscopy

Cell Picture Show brings you stunning micrographs, images, renderings, and photographs captured by some of the world's leading microscopists.

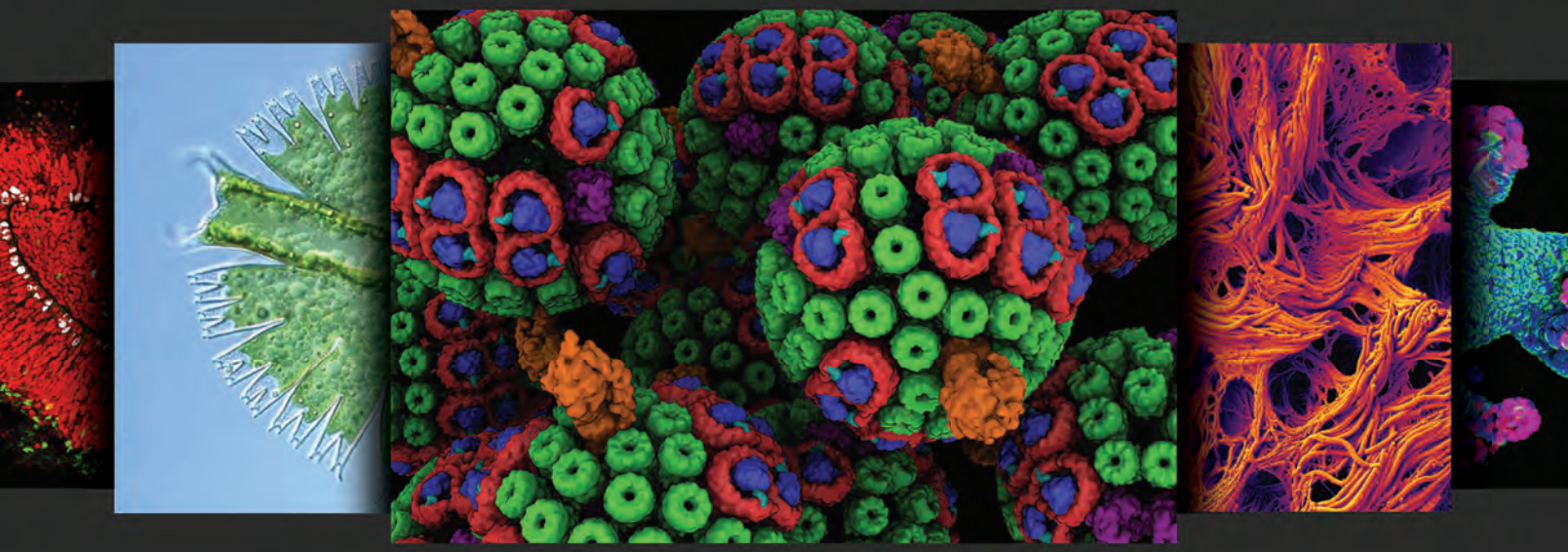

cell.com/pictureshow

CellPress

Cell

Reconstructing the Deep Population History of Central and South America

Cosimo Posth,[1,2,45,*] Nathan Nakatsuka,[3,4,45,*] Iosif Lazaridis,[3] Pontus Skoglund,[3,5] Swapan Mallick,[3,6,7] Thiseas C. Lamnidis,[1] Nadin Rohland,[3] Kathrin Nägele,[1] Nicole Adamski,[3,7] Emilie Bertolini,[8] Nasreen Broomandkhoshbacht,[3,7] Alan Cooper,[9] Brendan J. Culleton,[10,11] Tiago Ferraz,[1,12] Matthew Ferry,[3,7] Anja Furtwängler,[2] Wolfgang Haak,[1] Kelly Harkins,[13] Thomas K. Harper,[10] Tábita Hünemeier,[12] Ann Marie Lawson,[3,7] Bastien Llamas,[9] Megan Michel,[3,7] Elizabeth Nelson,[1,2] Jonas Oppenheimer,[3,7] Nick Patterson,[6] Stephan Schiffels,[1] Jakob Sedig,[3] Kristin Stewardson,[3,7] Sahra Talamo,[14] Chuan-Chao Wang,[1,15] Jean-Jacques Hublin,[14] Mark Hubbe,[16,17] Katerina Harvati,[18,19] Amalia Nuevo Delaunay,[20] Judith Beier,[18] Michael Francken,[18] Peter Kaulicke,[21] Hugo Reyes-Centeno,[18,19] Kurt Rademaker,[22] Willa R. Trask,[23] Mark Robinson,[24] Said M. Gutierrez,[25]

(Author list continued on next page)

[1]Department of Archaeogenetics, Max Planck Institute for the Science of Human History, Jena 07745, Germany
[2]Institute for Archaeological Sciences, Archaeo- and Palaeogenetics, University of Tübingen, Tübingen 72070, Germany
[3]Department of Genetics, Harvard Medical School, Boston, MA 02115, USA
[4]Harvard-MIT Division of Health Sciences and Technology, Boston, MA 02115, USA
[5]Francis Crick Institute, London NW1 1AT, UK
[6]Broad Institute of Harvard and MIT, Cambridge, MA 02142, USA
[7]Howard Hughes Medical Institute, Harvard Medical School, Boston, MA 02115, USA
[8]Dipartimento di Biologia e Biotecnologie, Università di Pavia, Pavia 27100, Italy
[9]Australian Centre for Ancient DNA, School of Biological Sciences and The Environment Institute, Adelaide University, Adelaide, SA 5005, Australia
[10]Department of Anthropology, The Pennsylvania State University, University Park, PA 16802, USA
[11]Institutes of Energy and the Environment, The Pennsylvania State University, University Park, PA 16802, USA
[12]Departamento de Genética e Biologia Evolutiva, Universidade de São Paulo, São Paulo 05508-090, Brazil
[13]UCSC Paleogenomics, University of California, Santa Cruz, Santa Cruz, CA 95064, USA
[14]Department of Human Evolution, Max Planck Institute for Evolutionary Anthropology, Leipzig 04103, Germany
[15]Department of Anthropology and Ethnology, Xiamen University, Xiamen 361005, China
[16]Department of Anthropology, The Ohio State University, Columbus, OH 43210, USA
[17]Instituto de Arqueología y Antropología, Universidad Católica del Norte, San Pedro de Atacama, Región de Antofagasta, Antofagasta CP 1410000, Chile
[18]Institute for Archaeological Sciences, Palaeoanthropology and Senckenberg Centre for Human Evolution and Palaeoenvironment, University of Tuebingen, Tübingen 72070, Germany
[19]DFG Center for Advanced Studies, "Words, Bones, Genes, Tools," University of Tübingen, Tübingen 72070, Germany
[20]Centro de Investigación en Ecosistemas de la Patagonia, Coyhaique 5951601, Chile
[21]Pontifical Catholic University of Peru, San Miguel, Lima 32, Peru
[22]Department of Anthropology, Michigan State University, East Lansing, MI 48824, USA
[23]Central Identification Laboratory, Defense POW/MIA Accounting Agency, Department of Defense, Joint Base Pearl Harbor-Hickam, HI 96853, USA

(Affiliations continued on next page)

SUMMARY

We report genome-wide ancient DNA from 49 individuals forming four parallel time transects in Belize, Brazil, the Central Andes, and the Southern Cone, each dating to at least ~9,000 years ago. The common ancestral population radiated rapidly from just one of the two early branches that contributed to Native Americans today. We document two previously unappreciated streams of gene flow between North and South America. One affected the Central Andes by ~4,200 years ago, while the other explains an affinity between the oldest North American genome associated with the Clovis culture and the oldest Central and South Americans from Chile, Brazil, and Belize. However, this was not the primary source for later South Americans, as the other ancient individuals derive from lineages without specific affinity to the Clovis-associated genome, suggesting a population replacement that began at least 9,000 years ago and was followed by substantial population continuity in multiple regions.

INTRODUCTION

Genetic studies of present-day and ancient Native Americans have revealed that the great majority of ancestry in indigenous people in non-Arctic America derives from a homogeneous

Keith M. Prufer,[26,27] Domingo C. Salazar-García,[14,28] Eliane N. Chim,[29] Lisiane Müller Plumm Gomes,[12] Marcony L. Alves,[29] Andersen Liryo,[30] Mariana Inglez,[12] Rodrigo E. Oliveira,[12,31] Danilo V. Bernardo,[32] Alberto Barioni,[33] Veronica Wesolowski,[29] Nahuel A. Scheifler,[34] Mario A. Rivera,[35,36,37] Claudia R. Plens,[38] Pablo G. Messineo,[34] Levy Figuti,[29] Daniel Corach,[39] Clara Scabuzzo,[40] Sabine Eggers,[12,41] Paulo DeBlasis,[29] Markus Reindel,[42] César Méndez,[20] Gustavo Politis,[34] Elsa Tomasto-Cagigao,[21] Douglas J. Kennett,[10,11,46] André Strauss,[12,18,29,43,46] Lars Fehren-Schmitz,[13,44,46] Johannes Krause,[1,2,46] and David Reich[3,6,7,46,47,*]

[24]Department of Archaeology, Exeter University, Exeter EX4 4QJ, UK
[25]Ya'axché Conservation Trust, Punta Gorda Town, Belize
[26]Department of Anthropology, University of New Mexico, Albuquerque, NM 87131, USA
[27]Center for Stable Isotopes, University of New Mexico, Albuquerque, NM 87131, USA
[28]Grupo de Investigación en Prehistoria IT-622-13 (UPV-EHU), IKERBASQUE-Basque Foundation for Science, Vitoria, Spain
[29]Museu de Arqueologia e Etnologia, Universidade de São Paulo, São Paulo 05508-070, Brazil
[30]Museu Nacional da Universidade Federal do Rio de Janeiro, Rio de Janeiro 20940-040, Brazil
[31]Departamento de Estomatologia, Faculdade de Odontologia, Universidade de São Paulo, São Paulo 05508-000, Brazil
[32]Laboratório de Estudos em Antropologia Biológica, Bioarqueologia e Evolução Humana, Instituto de Ciências Humanas e da Informação, Universidade Federal do Rio Grande, Rio Grande do Sul 96203-900, Brazil
[33]Faculdade de Filosofia Ciencias e Letras, Universidade de São Paulo, São Paulo 05508-080, Brazil
[34]INCUAPA-CONICET, Facultad de Ciencias Sociales, Universidad Nacional del Centro de la Provincia de Buenos Aires, Olavarría 7400, Argentina
[35]Comité Chileno del Consejo Internacional de Monumentos y Sitios, Santiago 8320000, Chile
[36]Field Museum of Natural History, Chicago, IL 60605, USA
[37]Universidad de Magallanes, Punta Arenas 6200000, Chile
[38]Escola De Filosofia, Letras E Ciências Humanas, Universidade Federal de São Paulo, São Paulo 07252-312, Brazil
[39]Servicio de Huellas Digitales Genéticas, School of Pharmacy and Biochemistry, Universidad de Buenos Aires y CONICET, Ciudad Autonoma de Buenos Aires, Junin 954, Argentina
[40]CONICET-División Arqueología, Facultad de Ciencias Naturales y Museo, La Plata 1900, Argentina
[41]Naturhistorisches Museum Wien, Vienna 1010, Austria
[42]German Archaeological Institute, Commission for Archaeology of Non-European Cultures, Bonn 53173, Germany
[43]Centro de Arqueologia Annette Laming Emperaire, Miguel A Salomão, Lagoa Santa, MG 33400-000, Brazil
[44]UCSC Genomics Institute, University of California, Santa Cruz, Santa Cruz, CA 95064, USA
[45]These authors contributed equally
[46]Senior author
[47]Lead Contact
*Correspondence: posth@shh.mpg.de (C.P.), nathan_nakatsuka@hms.harvard.edu (N.N.), reich@genetics.med.harvard.edu (D.R.)
https://doi.org/10.1016/j.cell.2018.10.027

ancestral population. This population was inferred to have diversified 17,500–14,600 calendar years before present (BP) (Moreno-Mayar et al., 2018a) into two branches that have been called "*Southern Native American*" or "*Ancestral A*" (*ANC-A*) and "*Northern Native American*" or "*Ancestral B*" (*ANC-B*) (Moreno-Mayar et al., 2018a; Raghavan et al., 2015; Rasmussen et al., 2014; Reich et al., 2012; Scheib et al., 2018). An individual dating to ~12,900–12,700 BP from the Anzick site in Montana and associated with the Clovis culture was on the *ANC-A* lineage, which is also heavily represented in present-day Central and South Americans and in ancient Californians. In contrast, *ANC-B* ancestry is heavily represented in eastern North Americans and in ancient people from southwest Ontario (Scheib et al., 2018). The original studies that documented these two deep lineages fit models in which Central and South Americans were of entirely *ANC-A* ancestry (Rasmussen et al., 2014; Reich et al., 2012). However, Scheib et al. (2018) suggested that all Central and South Americans harbor substantial proportions of both ancestries (at least ~30% of each).

Recent analyses have also shown that some groups in Brazil share more alleles with Australasians (indigenous New Guineans, Australians, and Andaman Islanders) (Raghavan et al., 2015; Skoglund et al., 2015) and an ~40,000 BP individual from northern China (Yang et al., 2017) than do other Central and South Americans. Such patterns suggest that these groups do not entirely descend from a single homogeneous population and instead derive from a mixture of populations, one of which, *Population Y*, bore a distinctive affinity to Australasians. Notably, our study includes data from individuals such as those from the Lapa do Santo site who have a cranial morphology known as "Paleoamerican," argued to indicate two distinct New-World-founding populations (von Cramon-Taubadel et al., 2017). Here, we test directly the hypothesis that a Paleoamerican cranial morphology was associated with a lineage distinct from the one that contributed to other Native Americans (whether the proposed *Population Y* or another).

Prior to the present study, published data from Central and South America older than the last millennium was limited to two low coverage genomes (Raghavan et al., 2015). Here, we report genome-wide data from 49 individuals from Belize, Brazil, Peru, and the Southern Cone (Chile and Argentina), 41 older than 1,000 years, with each time transect starting between 10,900–8,600 BP (Figure 1; Table S3). To obtain these data, we worked with government agencies and indigenous peoples to identify samples, prepared powder from skeletal material, extracted DNA (Dabney et al., 2013), and generated single and double stranded DNA libraries, most of which we treated with the enzyme uracil-DNA glycosylase (UDG) to reduce characteristic

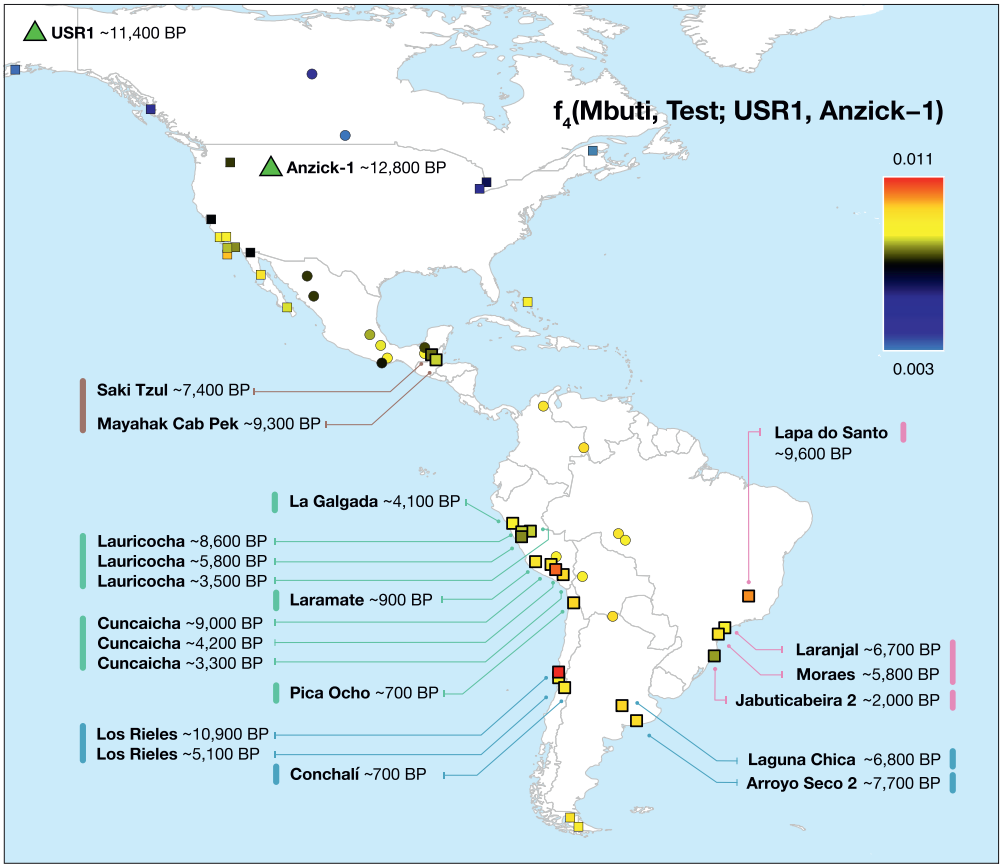

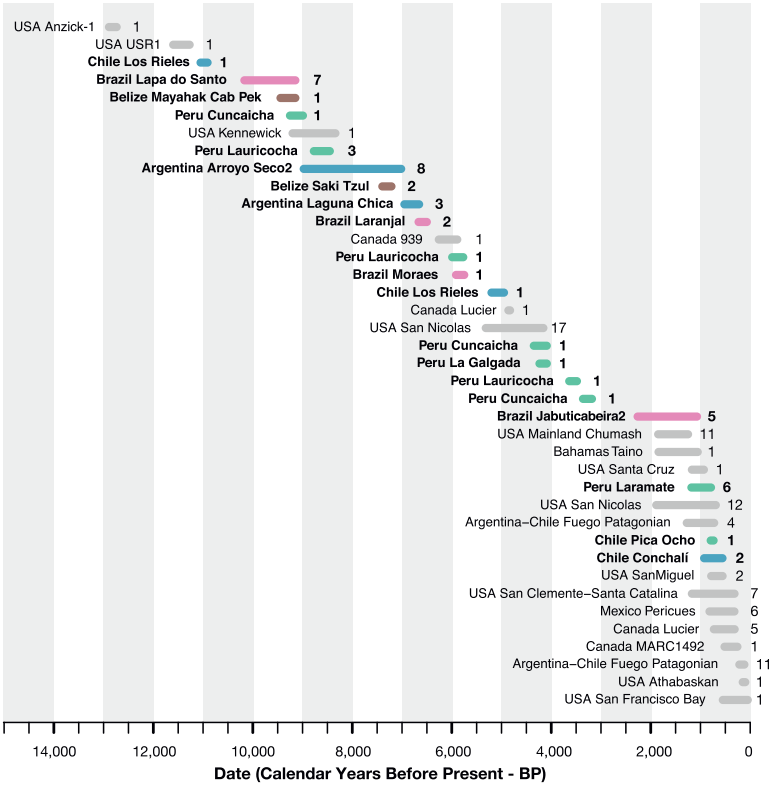

(legend on next page)

errors of ancient DNA (Gansauge and Meyer, 2013; Rohland et al., 2015). We enriched for mtDNA and ~1.2 million SNPs (Fu et al., 2015) and sequenced the enriched libraries on Illumina instruments (Table S3; STAR Methods). We combined ancient and present-day data to study genetic changes over the last 11,000 years.

Ethics Statement

Genetic studies of human history shed light on how ancient and present-day people are biologically related, and it is therefore important to be attentive not just to scientific issues but also to perspectives of indigenous communities when carrying out this work (Bardill et al., 2018). We took a case-by-case approach in each region we studied. In Peru and in some other countries in Central and South America, there is a strong tradition of indigenism in state policy, and governmental officials are recognized as representatives of indigenous perspectives (Herrera, 2011; Silverman, 2006) (Ley General del Patrimonio Cultural de la Nación [Law No. 28296]). We therefore consulted with provincial and state-based offices of the Ministry of Culture to obtain permission for analysis and also incorporated feedback from local community archaeologists to represent indigenous perspectives; permission for sampling was obtained under Resolución Directoral Nacional No. 1346, 545-2011, and RDN No. 092-2016. In Brazil, we obtained research permits from IPHAN (the National Institute of Historical and Artistic Heritage). In Chile and Argentina, in addition to obtaining permits from the local heritage institutions, we sought to determine if any local indigenous group considered the skeletons we analyzed to be ancestors. For most samples, no indigenous community lived near the sites or indicated a connection to the analyzed skeletons, with the exception of a community living near the site of Laguna Chica in Argentina, which approved the study after consultation and participated in the rescue excavation. In Belize, we obtained permission from the National Institute of Culture and History and the Institute of Archaeology, the legal entities responsible for issuing research permits, and we carried out public consultation with local collaborators and communities (see the archaeological site information section in the STAR Methods for additional details).

RESULTS AND DISCUSSION

Authenticity of Ancient DNA

We evaluated the authenticity of the isolated DNA based on its harboring: (1) characteristic cytosine-to-thymine mismatches to the reference genome at the ends of the sequenced fragments, (2) point estimates of contamination in mtDNA below 5% (Renaud et al., 2015), (3) point estimates of X chromosome contamination in males below 3% (Korneliussen et al., 2014), and (4) point estimates of genome-wide contamination below 5% (N.N., Éadaoin Harney, S.M., N.P., and D.R., unpublished data). We removed from analysis two individuals that we genetically determined to be first degree relatives of other individuals with higher DNA yields within the dataset but fully report the data for both here (Table S3; STAR Methods).

Long-Standing Population Continuity in Multiple Regions of South America

We grouped ancient individuals by location, date range, and genetic similarity, for the most part using italicized labels like *Argentina_ArroyoSeco2_7700BP* ("country" followed by "site" followed by a "date" that for us is the average of the midpoint of the date ranges for the individuals in the grouping rounded to the nearest hundred) (Eisenmann et al., 2018). These groupings sometimes span an extensive period of time; for example, the eight Arroyo Seco 2 date estimates range from 8,570 to 7,160 BP. For some analyses, we also lumped individuals into larger clusters, for example grouping individuals from the Andes before and after ~4,200 BP into "*Early Andes*" and "*Late Central Andes*" based on qualitatively different affinities to other individuals in the dataset (STAR Methods).

To obtain an understanding of how the ancient individuals relate to present-day ones, we computed f_3- and f_4-statistics, which estimate allele sharing between samples in a way that is unbiased by population-specific drift (Patterson et al., 2012).

The oldest individuals in the dataset show little specific allele sharing with present-day people. For example, a ~10,900 BP individual from Chile (from the site of Los Rieles) shows only slight excess affinity to later Southern Cone individuals. In Belize, individuals from two sites dating to ~9,300 and ~7,400 BP (Mayahak Cab Pek and Saki Tzul) do not share significantly more alleles with present-day people from the region near Belize than they do with present-day groups elsewhere in Central and South America. In Brazil, genetic data from sites dating to ~9,600 BP (Lapa do Santo) and ~6,700 BP (Laranjal) show no distinctive shared ancestry with present-day Brazilians (Figures 2 and S1; Table S1), although the Laranjal individuals do show potential evidence of shared ancestry with a ~5,800 BP individual from Moraes (Table S4), confirmed by the statistic f_4(*Mbuti*, *Brazil_Laranjal_6700BP*; *Brazil_LapaDoSanto_9600BP*, *Brazil_Moraes_5800BP*), which is Z = 7.7 standard errors from zero.

We detect long-standing continuity between ancient and present-day Native Americans in each of the regions of South America we analyzed beginning at least ~5,800 BP, a pattern that is evident in heatmaps, neighbor-joining trees, and multi-dimensional scaling plots computed on outgroup-f_3 statistics (Figures 2, S1, and S2; Table S1). In Peru, the most ancient individuals dating up to ~9,000 BP from Cuncaicha and Lauricocha share alleles at the highest rate with present-day indigenous groups

Figure 1. Geographic Locations and Time Ranges

(Top) Color coding is based on the value of f_4(*Mbuti*, *Test*; *USR1*, *Anzick-1*), which measures the degree of allele sharing of each *Test* population with *Anzick-1* compared to the Ancient Beringian *USR1* (the latter two plotted as green triangles). All values and standard errors are listed in Table S4. Present-day individuals are circles and ancient individuals are squares (the newly reported individuals are indicated with a thick black outline).

(Bottom) We show previously published (gray) and newly reported ancient data. Magenta, Brazil; brown, Belize; green, Peru/northern Chile; blue, Southern Cone. The numbers give sample size in each grouping.

See also Table S3.

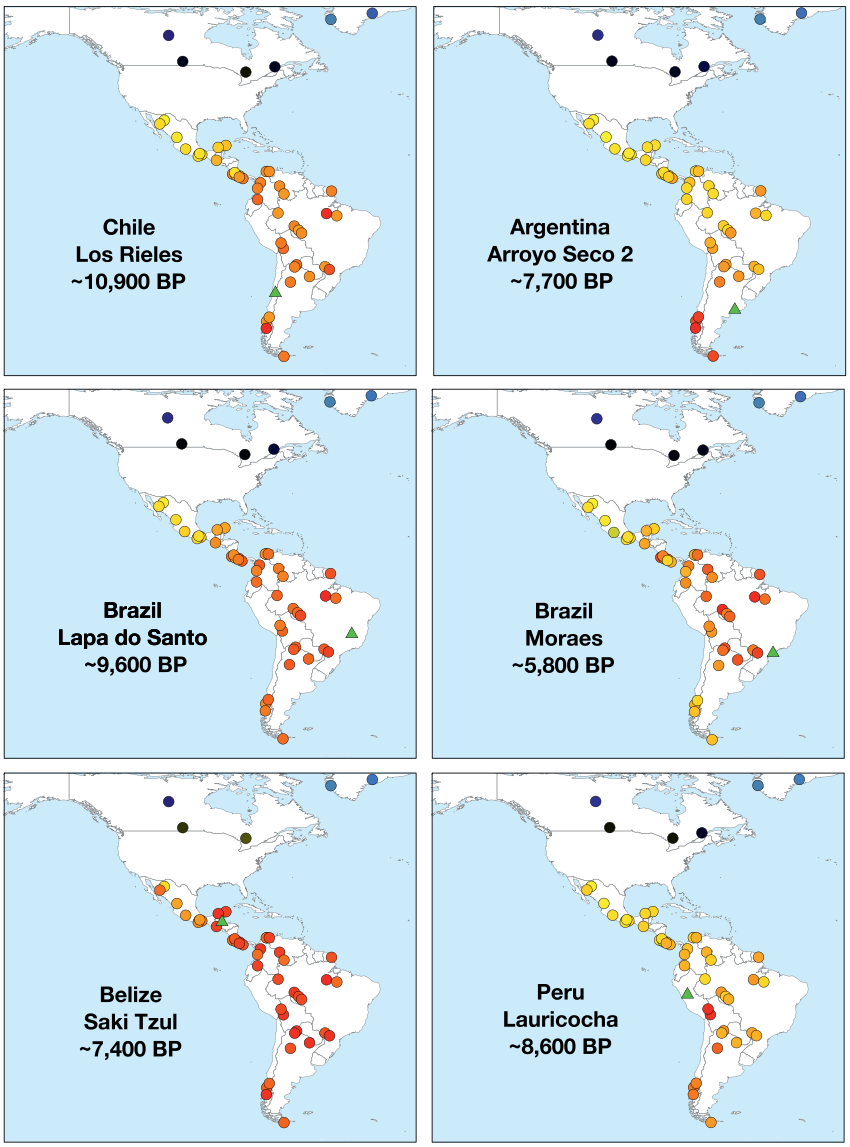

Figure 2. Relatedness of Ancient to Present-Day People

Allele sharing statistics of the form f_3(*Mbuti*; *Test*, *Ancient*), where the "Ancient" individuals represented by a green triangle are *Chile_LosRieles_10900BP*, *Argentina_ArroyoSeco2_7700BP*, *Brazil_LapaDoSanto_9600BP*, *Moraes_Brazil_5800BP*, *Belize_SakiTzul_7400BP*, and *Peru_Lauricocha_8600BP*. The heatmap shows the degree of allele sharing, with red indicating most sharing; yellow, intermediate; and blue, least.

See also Figures S2 and S3 and Table S1.

living in the Central Andes (Lindo et al., 2018; Llamas et al., 2016). Individuals dating up to ~8,600 BP from Arroyo Seco 2 and Laguna Chica also show the strongest allele sharing with some present-day indigenous people in the Southern Cone. In Brazil, the evidence of continuity with present-day indigenous people begins with the Moraes individual at ~5,800 BP. A striking pattern of continuity with present-day people is also observed in the ~2,000 BP Jabuticabeira 2 individuals who were part of the Sambaqui shell-mound building tradition that was spread along the south Brazilian coast from around 8,000–1,000 BP. The Jabuticabeira 2 individuals share significantly more alleles with some Ge-speaking groups than they do with some Tupi-Guarani speaking groups who have been predominant on the coast during the post-Colonial period (Figure S3; Table S1). This supports the theory of shared ancestry between the makers of the Sambaqui culture and the speakers of proto-Ge who are hypothesized to have lived in the region ~2,000 BP (Iriarte et al., 2017). These findings also support the theory of coastal replacement of Ge speakers by Tupi-Guarani speakers after ~1,000 BP (Hubbe et al., 2009) (STAR Methods).

Evidence for at Least Four Genetic Exchanges between South America and Other Regions

Figure 1 plots the excess rate of allele sharing of ancient Central and South Americans with the ~12,800 BP *Anzick-1* individual from Montana compared to the ~11,500 BP *USR1* individual from Alaska, an Ancient Beringian who derives from a lineage that split from the one leading to all other known Native Americans before they separated from each other (Moreno-Mayar et al., 2018a) (Table S4). The distribution of this statistic f_4(*Mbuti*, *Test*; *USR1*, *Anzick-1*) confirms previous findings that *Anzick-1* relatedness is greatest in Central and South Americans and lowest in North American groups (Table S4) (Rasmussen et al., 2014), with the exception of the California Channel Islands, where the earliest individuals from San Nicolas Island around 4,900 BP show some of the highest *Anzick-1* relatedness, consistent with an early spread of *Anzick-1*-related people to these islands followed by local isolation (Scheib et al., 2018) (Figure S2D).

More careful examination reveals significant ancestry variability in the ancient South Americans. The ~10,900 BP Los Rieles individual from Chile, the ~9,600 BP individuals from Lapa do Santo in Brazil, and individuals from southern Peru and northern Chile dating to ~4,200 BP and later ("Late Central Andes" from Cuncaicha, Laramate and Pica Ocho), share more alleles with *Anzick-1* than do other South Americans (Figure 1; Table S4). Many of these signals of asymmetrical relationship to *Anzick-1* are significant as assessed by statistics of the form f_4(*Mbuti*, *Anzick-1*; *Test*$_1$, *Test*$_2$): *Z* score for deviation from zero as high as 3.4 for the (*Test*$_1$, *Test*$_2$) pair (*Early Andes*, *Chile_LosRieles_10900BP*), 3.1 for the pair (*Early Andes,*

Brazil_LapaDoSanto_9600BP), and 3.0 for the pair *(Early Andes*, *Late Central Andes*) (Table S2). We confirmed these findings using *qpWave* (Reich et al., 2012), which evaluates the minimum number of sources of ancestry that must have contributed to a test set of groups relative to a set of outgroups (STAR Methods). We tested all possible pairs of populations and found that none of the three combinations are consistent with being derived from a homogeneous ancestral population: p = 0.0023 for (*Early Andes*, *Brazil_LapaDoSanto_9600BP*), p = 0.0007 for (*Early Andes*, *Late Central Andes*), and p = 0.0000004 for (*Brazil_LapaDoSanto_9600BP*, *Late Central Andes*). We obtained qualitatively similar results replacing *Brazil_LapaDoSanto_9600BP* with *Chile_LosRieles_10900BP* (Figure S4; Table S5). We also obtained similar results for subsets of individuals in each group. Our power to reject models of just two sources of ancestry for the ancient South American individuals depends critically on the use of *Anzick-1* as an outgroup, as when we remove this individual from the outgroup set there is no evidence of a third source of ancestry contributing to *Brazil_LapaDoSanto_9600BP* (p = 0.11) or *Chile_LosRieles_10900BP* (p = 0.35). It also depends critically on the use of California Channel Islands individuals, as when we remove them as outgroups there is no evidence for a third source of ancestry contributing to *Late Central Andes* groups (p = 0.12).

The fact that the three pairs each require two different sources of ancestry in order to produce a model fit could mean that they descend from a total of three (or more) distinct sources of ancestry differentially related to groups outside South America or alternatively that they are mixtures in different proportions of only two sources. To distinguish these possibilities, we used *qpWave*'s ability to test for consistency with the hypothesis that sets of three populations ($Test_1$, $Test_2$, $Test_3$) derive from just two populations relative to the same set of outgroups. *qpWave* rejects the hypothesis of two sources (p = 0.0022), a result that is unlikely to be due to backflow from South America into Central America as the signal persists when we remove present-day Mexicans from the outgroup set (p = 0.001) (Table S5). Further evidence for the robustness of the finding of three source populations comes from the fact that the signal remains significant when we restrict to transversion polymorphisms that are not affected by cytosine-to-thymine errors (p = 0.01). We caution that we did not find significant signals of ancestry heterogeneity relative to North American outgroups when repeating the *qpWave* tests on pairs of present-day populations. We speculate that this may reflect more recent homogenization leading to variation in ancestry proportions too subtle for our methods to detect.

When we add present-day *Surui* individuals into the analysis, there is evidence for a fourth source of ancestry (p = 0.03) (Table S5), likely reflecting the same signal that led to finding "*Population Y*" ancestry in this group (Raghavan et al., 2015; Skoglund et al., 2015).

Modeling the Deep History of Central and South America

We modeled the relationships among diverse ancient Americans using *qpGraph,* which evaluates whether a model of population splitting and admixture is consistent with all *f*-statistics relating pairs, triples, and quadruples of groups (Patterson et al., 2012).

We were able to fit genome-wide data from nine ancient North, Central and South American groups (not including *Anzick-1*) as a star-like radiation from a single source population with negligible admixture between the *ANC-A* and *ANC-B* lineages after their initial bifurcation (maximum $|Z|$ score for a difference between the observed and expected statistics of 2.9 [Figure 3] and 3.2 [Figure S5A]; we represent *ANC-B* by the Ancient Southern Ontario population *Canada_Lucier_4800BP-500BP*). This model is not what would be expected based on the claim of a recent study (Scheib et al., 2018) that major *ANC-A*/*ANC-B* admixture (at least ~30% of each) is necessary to model Central and South Americans. While we confirmed that the model proposed in Scheib et al. (2018) fits the data when restricting to a subset of the populations they analyzed, when we added into the model non-American populations with previously established relationships to Native Americans, the model failed (STAR Methods). To more directly explore whether there is evidence of widespread *ANC-B* ancestry in South America, we tested whether *Canada_Lucier_4800BP-500BP* shares more alleles with a range of Central and South American *Test* populations than with *Anzick-1,* but find no evidence for a statistically significant skew (Table S4). Indeed, the supplementary materials of the previously reported study (Figure S13 of Scheib et al., 2018) show that a model such as the one we favor—without widespread *ANC-B* admixture in South America—fits the data with no differences between observed and expected *f*-statistics greater than $Z > 2$. We also find that when we explicitly model *ANC-B* admixture into the ancestors of South Americans, the inferred genetic drift specific to *Canada_Lucier_4800BP-500BP* is not significantly different from 0, providing evidence against specific affinity to *ANC-B* in South Americans (Figure S6; STAR Methods).

To fit the *Anzick-1* genome associated with the Clovis culture into the admixture graph, we needed to specify additional admixture events. We identified a range of fits for the data. Figure 4 shows the result of manually exploring models guided by common sense principles (geography, time, and archaeology) as well as the genetic data. Figure 5 shows a model obtained by a semi-automated procedure constrained only by the fit to the genetic data (Lazaridis et al., 2018). The most important difference between the two models concerns the question of how the Clovis culture associated *Anzick-1* genome relates to ancient Central and South Americans. Figure 4, which models the lineage leading to *Anzick-1* as unadmixed, seems most plausible because it is natural to expect that the oldest individuals will be least admixed, and because it is simple to explain this model via North-to-South spreads. Figure 5 models some of the ancestry of the Clovis associated genome as deriving from within the radiation of lineages represented in South America, which if true would require a more complex history.

We highlight four points of agreement between the two admixture graphs.

First, both graphs imply a minimum of four genetic exchanges between South America and regions outside South America consistent with the *qpWave* results in the previous section. This includes: (1) a primary source of *ANC-A* ancestry in all South Americans; (2) an *ANC-A* lineage with distinct affinity to *Anzick-1* in *Chile_LosRieles_10900BP*, *Brazil_LapaDoSanto_9600BP*, and

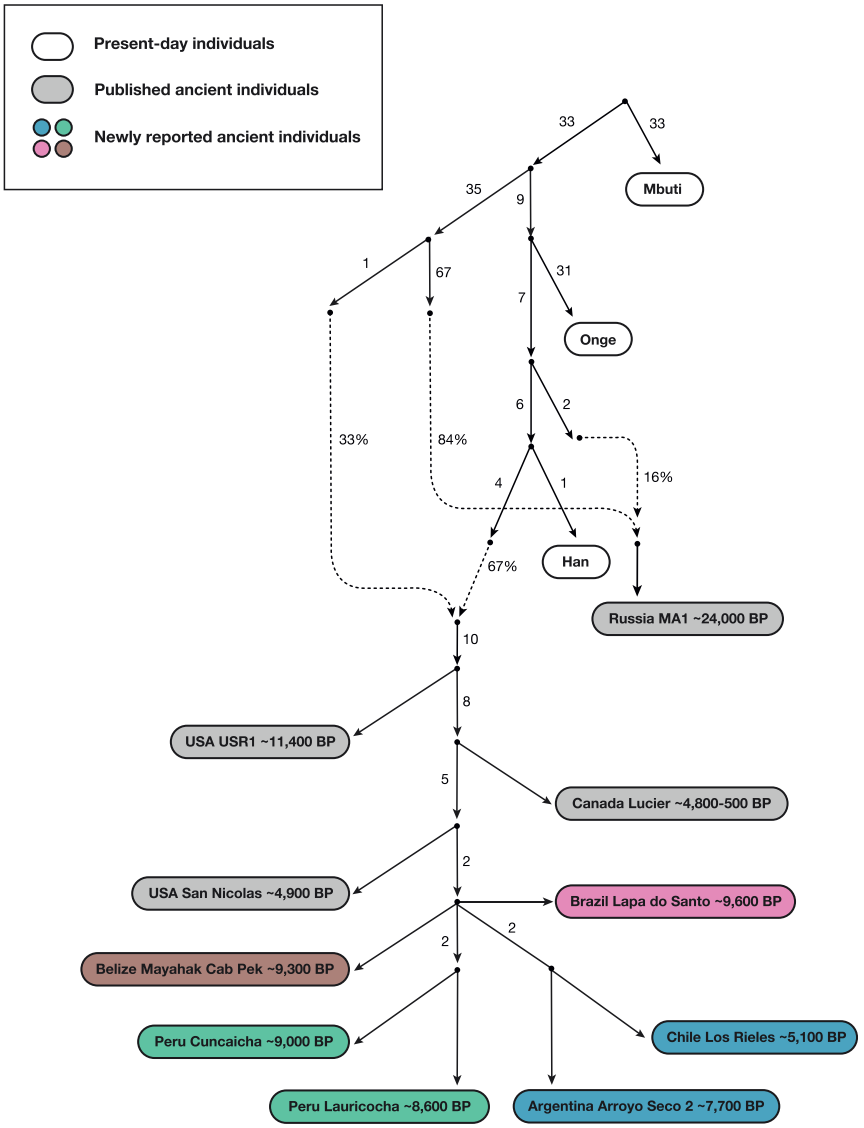

Figure 3. Skeleton Model that Fits the Data with Minimal Admixture

This graph models nine of the ancient North, Central, and South American groups without admixture (branch lengths are in units of F_{ST} × 1,000). The maximum deviation between observed and expected *f*-statistics is $Z = 2.9$ ($Z = 3.1$ when restricting to transversions). Drift lengths in the terminal edges are unlabeled as randomly sampling an allele to represent each individual makes them artifactually long.

See also Figure S6.

some early Southern Cone populations; and (3) *ANC-A* ancestry with a distinctive affinity to ancient individuals from the California Channel Islands (*USA_SanNicolas_4900BP*) present in the Central Andes by ~4,200 BP (Figures S5B and S5C). (4) The final spread of ancestry contributes to present-day Amazonian groups like the *Surui*. In Figures 4 and 5, we do not include the *Surui* but do show such models in Figures S5G–S5I where *Surui* can only be fit by proposing some ancestry differently related to Eurasians than is the case for other Native Americans (as expected if there is *Population Y* ancestry in the *Surui*).

Second, both graphs specify minimal *ANC-B* ancestry in South Americans. While we do find significant allele sharing with a representative *ANC-B* population (*Canada_Lucier_4800BP-500BP*) in people from the Central Andes after ~4,200 years ago—as reflected in significantly positive ($2 < Z < 4$) statistics of the form f_4(*Mbuti*, *Canada_Lucier_4800BP-500BP*; *Brazil_LapaDoSanto_9600BP* or *Brazil_Laranjal_6700BP*, *Late Central* Andes or present-day Aymara and Quechua from Peru) (Tables S2 and S4)—when we fit admixture graph models specifying an *ANC-B* contribution to *Late Central Andes* groups, the *ANC-B* proportion is never more than 2% (Figures S5D–S5F).

Third, both graphs infer little genetic drift separating the lineages leading to the different ancient groups in each major region of South America. This can be seen in our inferred five-way split whose order we cannot resolve involving lineages leading to: (1) the early Belizeans, (2) early Peruvians, (3) early Southern Cone populations, (4) the main lineage leading to *Brazil_LapaDoSanto_9600BP*, and (5) the lineage leading to *Chile_LosRieles_10900BP* (Figure S5A). This suggests rapid human radiation of the main lineage ancestral to later South Americans (Raghavan et al., 2015; Reich et al., 2012).

Fourth, both graphs agree that there is distinctive shared ancestry between the Clovis culture associated *Anzick*-1 and the earliest South American individuals from Lapa do Santo in Brazil and Los Rieles in Chile. We also detect evidence of ancestry related to *Anzick-1* in the oldest Central American genome, as the most ancient individual from Belize has evidence of more *Anzick-1* relatedness than later Belize individuals as reflected in the weakly significant statistic f_4(*Mbuti, Anzick-1*; *Belize_SakiTzul_7400BP*, *Belize_MayahakCabPek_9300BP*) ($Z = 2.1$). Taken together, these results support the hypothesis that an expansion of a group associated with the Clovis culture left an impact far beyond the geographic region in which this culture was spread (Fiedel, 2017). At the same time, both classes of models provide evidence against a stronger version of this hypothesis, which is that an expansion of a homogeneous population associated with the Clovis culture was the primary source of the ancestry of later Central and South Americans. Specifically, both models find that the overwhelming majority of the ancestry of most Central and South Americans derives from one or more lineages

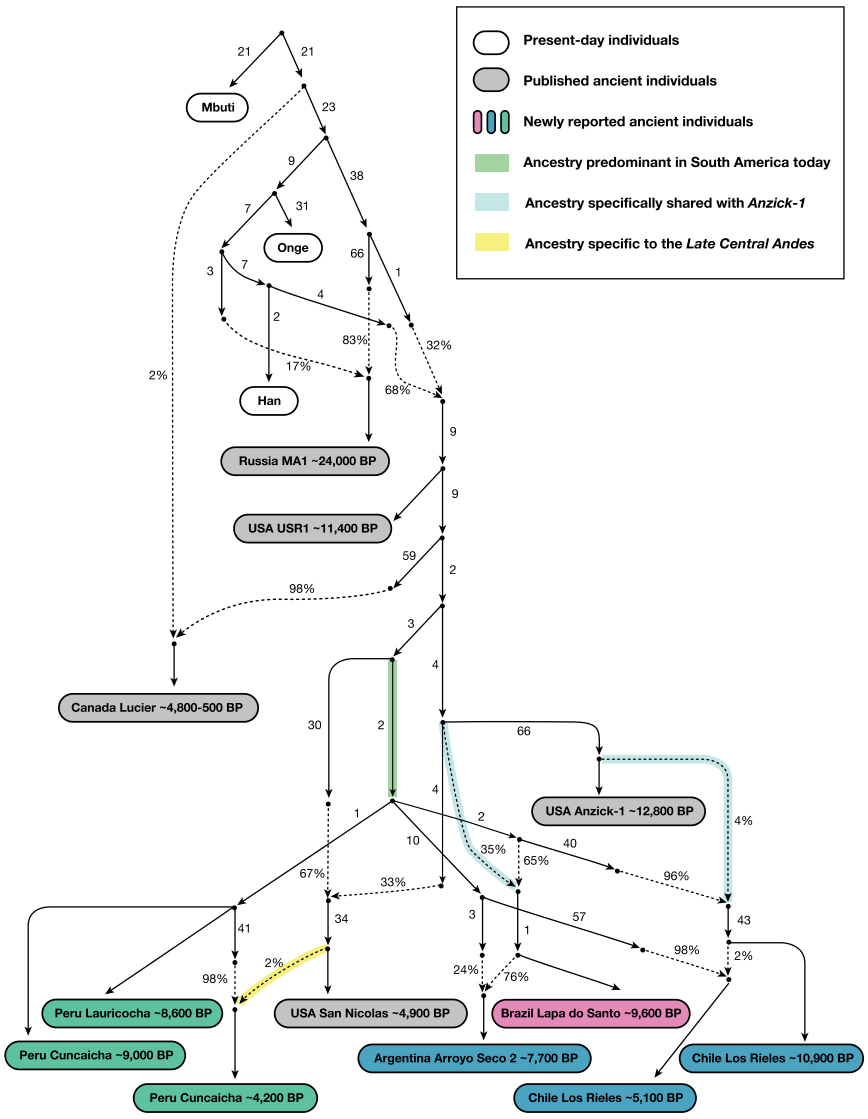

Figure 4. Adding in the ~12,800 BP Anzick-1 and ~10,900 BP Los Rieles

We used Figure 3 that models all analyzed Native Americans as unadmixed as a framework graph (excluding *Belize_MayahakCabPek_9300BP* because of relatively low coverage). We then added in *Anzick-1 and Chile_LosRieles_10900BP*. This model specifies three sources of North American related ancestry in South America, indicated by color-coding (*Population Y* ancestry is not included but Figures S5B–S5I show related fits some of which do include it). The maximum deviation between observed and expected *f*-statistics is $Z = 3.4$ ($Z = 3.0$ when restricting to transversions). The inferred 2% West Eurasian admixture into *Canada_Lucier_4800BP-500BP* is most likely explained by contamination in these samples by people of European ancestry.

See also Figure S6 and Tables S4 and S5.

without the *Anzick-1* affinities present at Lapa do Santo. Thus, a different *ANC-A* lineage from the one represented in *Anzick-1* made the most important contribution to South Americans, and there must have been a population turnover in the mid-Holocene that largely replaced groups such as the ones represented by the ~10,900 BP individual at Los Rieles in Chile and the ~9,600 BP individuals at Lapa do Santo in Brazil. This genetic evidence of a major population turnover correlates with the findings from morphological studies of a population turnover in Brazil around this time (Hubbe et al., 2014).

It is tempting to hypothesize that the early branching *ANC-A* lineages that we have shown contributed most of the ancestry of Central and South Americans today—and that harbor no specific *Anzick-1* association—contributed to the people who lived at the site of Monte Verde in southern Chile and whose material artifacts have been dated to a pre-Clovis period at least ~14,500 BP (Dillehay et al., 2008). However, because all the earliest Central and South American individuals show affinities to *Anzick-1*, our results could also be consistent with a scenario in which nearly all the ancestry of the South American genomes derives from population movements from North America that began no earlier than the Clovis period. In either case, we demonstrate that the non-*Anzick-1* associated ancestry type began to spread in South America by at least ~9,000 BP, the date of the oldest genomes that have no specific Anzick-1 affinity (from Cuncaicha and Lauricocha in the Central Andes).

All the Ancient South Americans Descend from the Same Eurasian Source Population

Previous studies have suggested that present-day groups like *Surui* from Amazonia harbor ancestry from a source termed "*Population Y*" (Raghavan et al., 2015; Skoglund et al., 2015), which shared alleles at an elevated rate with Australasian groups (*Onge*, *Papuan*, and *Australians*) as well as the ~40,000 BP Tianyuan individual from China (Yang et al., 2017). We tested for this signal in the ancient South American individuals with statistics of the form f_4(*Mbuti, Australasian*; *X*, *Mixe or ancient South American*), and while we replicated the originally reported signal when *X* was present-day *Karitiana* or *Surui*, we could not detect a signal when *X* was any of the ancient South Americans (Table S6). We also studied the statistic f_4(*Mbuti*, *Tianyuan*; $Ancient_1$, $Ancient_2$) to test if any ancient individual is differentially related to Tianyuan (Yang et al., 2017), but no statistic was significant (Table S6). We finally applied *qpWave* to all pairs of South American groups, testing whether they were homogeneously related to a set of diverse non-Native American outgroups (*Mbuti*, *Han*, *Onge*, *French*, and *Papuan*) and found no pair of ancient South Americans that consistently gave significant signals ($p < 0.01$), as expected if all the ancient South Americans

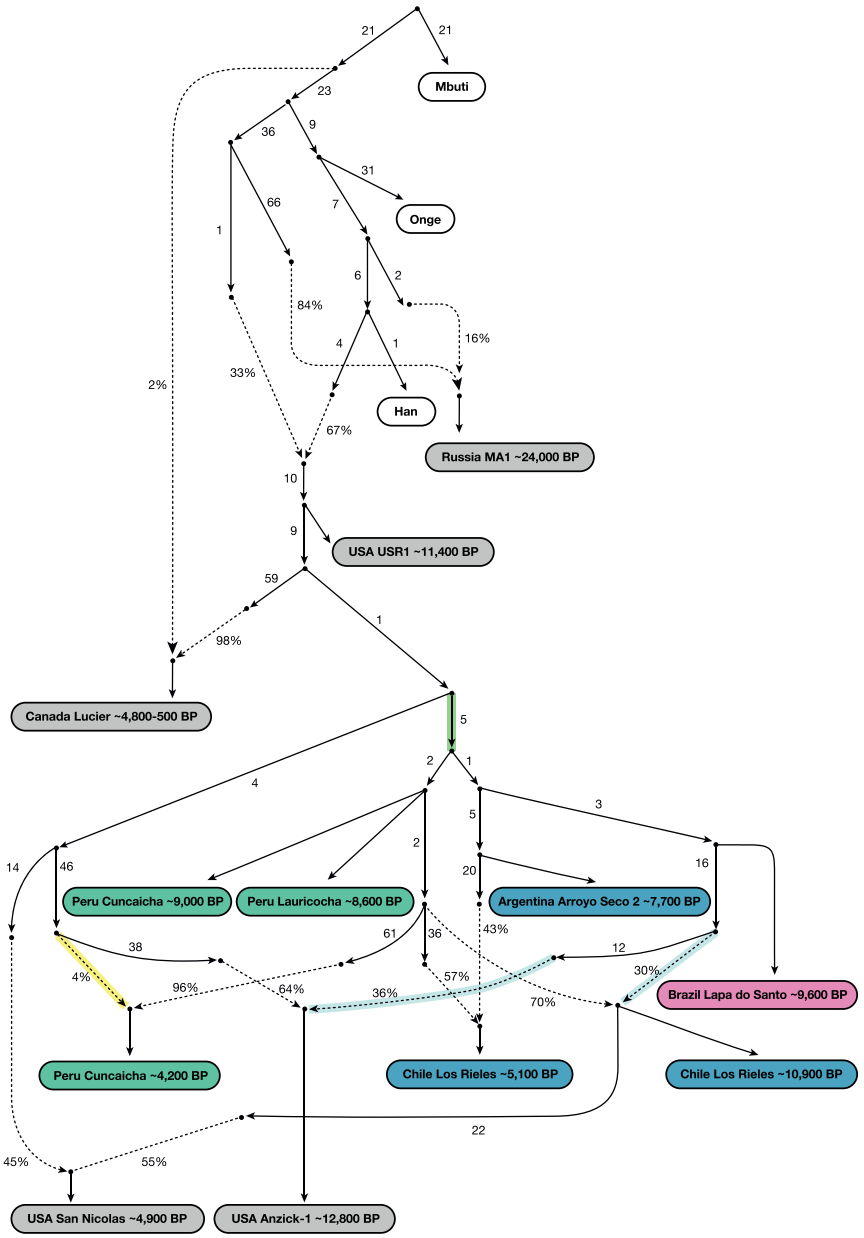

Figure 5. An Alternative Fitting Admixture Graph Obtained by a Semi-automated Method

We also applied a semi-automated approach that aims to fit population relationships while minimizing the number of admixture events (STAR Methods) (Lazaridis et al., 2018). This is less plausible than Figure 4 on archaeological grounds, but it has a lower maximum Z score for the same number of admixture edges ($Z = 2.9$ for all sites, $Z = 2.9$ when restricting to transversions). Like Figure 4, this model specifies a minimum of three genetic exchanges between North and South America, indicated here by color-coding (please see Figure 4 color legend). See also Figure S6 and Table S5.

we analyzed derived from the same stem Native American population (Table S6). Our failure to find significant evidence of Australasian or Paleolithic East Asian affinities in any of the ancient Central and South American individuals raises the question of what ancient populations could have contributed the *Population Y* signal in *Surui* and other Amazonian groups and increases the previously small chance that this signal—despite the strong statistical evidence for it—was a false-positive. A priority is to search for the *Population Y* signal in additional ancient genomes.

Our finding of no excess allele sharing with non-Native American populations in the ancient samples is also striking as many of these individuals—including those at Lapa do Santo—have a "Paleoamerican" cranial morphology that has been suggested to be evidence of the spread of a substructured population of at least two different Native American source populations from Asia to the Americas (von Cramon-Taubadel et al., 2017). Our finding that early Holocene individuals with such a morphology are consistent with deriving all their ancestry from the same homogeneous ancestral population as other Native Americans extends the finding of Raghavan et al. (2015) who came to a similar conclusion after analyzing Native Americans inferred to have Paleoamerican morphology who lived within the last millennium.

Single Locus Analysis

The D4h3a mtDNA haplogroup has been hypothesized to be a marker for an early expansion into the Americas along the Pacific coast (Perego et al., 2009). However, its presence in two Lapa do Santo individuals and *Anzick-1* (Rasmussen et al., 2014) makes this hypothesis unlikely (Figure S7; Table S3; STAR Methods).

The patterns we observe on the Y chromosome also force us to revise our understanding of the origins of present-day variation. Our ancient DNA analysis shows that the Q1a2a1b-CTS1780 haplogroup, which is currently rare, was present in a third of the ancient South Americas. In addition, our observation of the currently extremely rare C2b haplogroup at Lapa do Santo disproves the suggestion that it was introduced after 6,000 BP (Roewer et al., 2013).

The patterns of variation at phenotypically significant variants are also notable. Our data show that a variant in *EDAR* that affects tooth shape, hair follicles and thickness, sweat, and mammary gland ductal branching and that occurs at nearly 100% frequency in present day Native Americans and East Asians (Kamberov et al., 2013) was not fixed in *USR1*, *Anzick-1*, a *Brazil_LapaDoSanto_9600BP* individual and a *Brazil_Laranjal_6700BP* individual, all of whom carry the ancestral allele (Table S7). Thus, the derived allele rose in frequency in parallel

in both East Asians and in Native Americans. In contrast at *FADS2*, one of the variants at a polymorphism (rs174570) associated with fatty acid desaturase 2 levels is derived in all the ancient individuals, supporting the hypothesis that the selective sweep that drove it to near fixation was complete prior to the peopling of the Americas (Amorim et al., 2017).

DISCUSSION

Our finding of two previously undocumented genetic exchanges between North and South America has significant implications for models of the peopling of the Americas.

Most important, our discovery that the Clovis-associated *Anzick-1* genome at ~12,800 BP shares distinctive ancestry with the oldest Chilean, Brazilian, and Belizean individuals supports the hypothesis that an expansion of people who spread the Clovis culture in North America also affected Central and South America, as expected if the spread of the Fishtail Complex in Central and South America and the Clovis Complex in North America were part of the same phenomenon (direct confirmation would require ancient DNA from a Fishtail-context) (Pearson, 2017). However, the fact that the great majority of ancestry of later South Americans lacks specific affinity to *Anzick-1* rules out the hypothesis of a homogeneous founding population. Thus, if Clovis-related expansions were responsible for the peopling of South America, it must have been a complex scenario involving arrival in the Americas of sub-structured lineages with and without specific *Anzick-1* affinity, with the one with *Anzick-1* affinity making a minimal long-term contribution. While we cannot at present determine when the non-*Anzick*-1 associated lineages first arrived in South America, we can place an upper bound on the date of the spread to South America of all the lineages represented in our sampled ancient genomes as all are *ANC-A* and thus must have diversified after the *ANC-A*/*ANC-B* split estimated to have occurred ~17,500–14,600 BP (Moreno-Mayar et al., 2018a).

A second notable finding of this study is our evidence that the ancient individuals from the California Channel Islands have distinctive and significant allele sharing with groups that became widespread over the Central Andes after ~4,200 BP. There is no archaeological evidence of large-scale cultural exchange between North and South America around this time, but it is important to recognize that ~4,200 BP is a minimum date for the exchange between North and South American that drove this pattern; the gene flow itself could have occurred thousands of years before and the ancestry deriving from it could have persisted in a region of South America not yet sampled with ancient DNA. The evidence of an expansion of this ancestry type in the Central Andes by ~4,200 BP is notable in light of the increasing density of sites in this region at approximately this time, a pattern that is consistent with a demographic expansion of a previously more restricted population (Goldberg et al., 2016).

We conclude by highlighting several limitations of this study. First, all the individuals we newly report have a date less than ~11,000 BP and thus we could not directly probe the initial movements of people into Central and South America. Second, from the period between 11,000–3,000 BP that includes most of our individuals, we lacked ancient data from Amazonia, northern South America, and the Caribbean and thus cannot determine how individuals from these regions relate to the ones we analyzed. Third, because we reported few individuals from after 3000 BP, this study provides just a glimpse of the power of this type of analysis to reveal more recent events. Regionally focused studies with large sample sizes are needed to realize the potential of ancient DNA to reveal how the human diversity of this region came to be the way it is today.

STAR★METHODS

Detailed methods are provided in the online version of this paper and include the following:

- KEY RESOURCES TABLE
- CONTACT FOR REAGENT AND RESOURCE SHARING
- EXPERIMENTAL MODEL AND SUBJECT DETAILS
  - Archaeological site information
  - Samples from Argentina
  - Samples from Belize
  - Samples from Brazil
  - Samples from Chile
  - Samples from Peru
  - Grouping ancient samples into analysis clusters
- METHOD DETAILS
  - Direct AMS ^{14}C bone dates
  - PSUAMS and UCIAMS Protocols and Pretreatment
  - PSUAMS and UCIAMS Quality Control and Measurement
  - PSUAMS Acid Etch/Hydrolysis
  - MAMS Protocols and Pretreatment
  - Calibration of radiocarbon dates
  - Ancient DNA sample processing
- QUANTIFICATION AND STATISTICAL ANALYSIS
  - Contamination estimation in mitochondrial DNA, the X chromosome, and the autosomes
  - Present-day human data
  - Y chromosome and mitochondrial DNA analyses
  - Principal component analysis
  - Symmetry statistics and admixture tests (f-statistics)
  - *qpWave* analyses
  - Admixture graph modeling
  - Analyses of phenotypically relevant SNPs
  - Insights into more recent history of Brazil based on Jabuticabeira 2 individuals
- DATA AND SOFTWARE AVAILABILITY

SUPPLEMENTAL INFORMATION

Supplemental Information includes seven figures and seven tables and can be found with this article online at https://doi.org/10.1016/j.cell.2018.10.027.

ACKNOWLEDGMENTS

In Belize, we thank the Institute of Archaeology, our Maya collaborators, and the Ya'axché Conservation Trust for providing opportunities to consult with their community. In Argentina, we thank the Comunidad Indígena Mapuche-Tehuelche Cacique Pincen for supporting sampling of skeletal material from Laguna Chica. In Peru, we thank Johny Isla-Cuadrado and the National Museum of Archaeology, Anthropology and

History for permission to sample skeletal material. In Brazil, we thank all of the individuals who participated in the Lagoa Santa studies; J. Hein, R. Tavares de Oliveira, J. Bárbara Filh; and institutional support from the IEF, IPHAN IBAMA, and the cities of Matozinhos, Lagoa Santa and Pedro Leopoldo. We thank S. Fiedel, Q. Fu, C. Jeong, T. Kivisild, M. Lipson, V. Narasimhan, I. Olalde, B. Potter, A. Scally, C. Scheib, O. Semino, A. Torroni, and T. Stafford for critical comments. We are grateful to M. O'Reilly for graphic design help. We thank the wet laboratory and computational teams at MPI-SHH and at Harvard Medical School. L.F.-S. was supported by the Wenner-Gren Foundation (SC-14-62), a Hellman Foundation fellowship, and the NSF (A15-0187-001). N.N. was supported by the NIGMS (GM007753). P.S. was supported by Cancer Research UK (FC001595), the UK Medical Research Council (FC001595), and the Wellcome Trust (FC001595). C.M. and A.N.D. were supported by FONDECYT #1170408 and CONICYT R17A10002. Archaeological research in Argentina was funded by the National Geographic Society (9773-15), ANPCYT (PICT 2014-2070), and CONICET (PIP 0414). B.L., W.H., and A.C. were supported by the ARC and received sequencing support funding from The Environment Institute at Adelaide University. Funding for the Belize research to K.M.P. and D.J.K. came from the NSF (BCS1632061, BCS1632144), to K.M.P. from the Alphawood Foundation, and to D.J.K. and B.J.C. from the NSF Archaeometry program (BCS-1460369). The Cuncaicha work was supported by an Alexander von Humboldt Foundation fellowship (K.R.), the DFG (FOR 2237, INST 37/706, FOR 2237), the Pontifical Catholic University of Lima, and Northern Illinois University. D.C. is Superior Researcher of CONICET. Financial support for research in Brazil was provided by FAPESP (99/12684-2, 04/01321-6, 04/11038-0, 2016/1237-1, and 2017/16451-2). D.R. was supported by the NSF (BCS-1032255), the NIGMS (GM100233), by an Allen Discovery Center grant, and is an Investigator of the Howard Hughes Medical Institute. We refer readers to two other manuscripts that are being published simultaneously with this one for independent analyses of ancient DNA samples from the Americas (Moreno-Mayar et al., 2018b; Lindo et al., 2018). This manuscript is dedicated to the National Museum of Brazil, whose irreplaceable collections of natural and cultural material were lost in the fire of September 2, 2018.

AUTHOR CONTRIBUTIONS

Conceptualization, C.P., N.N., I.L., P.S., A.C., T.F., T.H., N.P., S.S., J.S., M.H., A.S., L.F.-S., J.K., and D.R.; Formal Analysis, C.P., N.N., I.L., P.S., T.C.L., E.B., and C.C.-W.; Investigation, C.P., N.R., K.N., N.A., N.B., B.J.C., M. Ferry, A.F., W.H., K. Harkins, T.K.H., A.M.L., B.L., M.M., E.N., J.O., K.S., S.T., and L.F.-S.; Resources, J.-J.H., K. Havarti, A.N.D., J.B., M. Francken, P.K., H.R.-C., K.R., W.R.T., M. Robinson, S.M.G., K.M.P., D.C.S.-G., E.N.C., L.M.P.G., M.L.A., A.L., M.I., R.E.O., D.V.B., A.B., V.W., N.A.S., M.A.R, C.R.P., P.G.M., L.F., D.C., C.S., S.E., P.D.B., M. Reindel, C.M., G.P., E.T.-C., D.J.K., and A.S.; Data Curation, C.P., N.N., S.M., and D.R.; Writing, C.P., N.N., A.S., L.F.-S., and D.R.; Supervision, D.J.K., A.S., L.F-S., J.K., and D.R.

DECLARATION OF INTERESTS

The authors declare no competing interests.

Received: August 30, 2018
Revised: September 15, 2018
Accepted: October 11, 2018
Published: November 8, 2018

REFERENCES

Amorim, C.E.G., Nunes, K., Meyer, D., Comas, D., Bortolini, M.C., Salzano, F.M., and Hünemeier, T. (2017). Genetic signature of natural selection in first Americans. Proc. Natl. Acad. Sci. USA *114*, 2195–2199.

Bardill, J., Bader, A.C., Garrison, N.A., Bolnick, D.A., Raff, J.A., Walker, A., and Malhi, R.S.; Summer internship for INdigenous peoples in Genomics (SING) Consortium (2018). Advancing the ethics of paleogenomics. Science *360*, 384–385.

Briggs, A.W., Stenzel, U., Meyer, M., Krause, J., Kircher, M., and Pääbo, S. (2010). Removal of deaminated cytosines and detection of in vivo methylation in ancient DNA. Nucleic Acids Res. *38*, e87.

Cardich, A. (1964). Lauricocha: Fundamentos para una prehistoria de los Andes centrales, *Volume 3* (Centro Argentino de Estudios Prehistóricos).

Chala-Aldana, D., Bocherens, H., Miller, C., Moore, K., Hodgins, G., and Rademaker, K. (2018). Investigating mobility and highland occupation strategies during the Early Holocene at the Cuncaicha rock shelter through strontium and oxygen isotopes. J. Archaeol. Sci. Rep. *19*, 811–827.

Crawford, J.E., Amaru, R., Song, J., Julian, C.G., Racimo, F., Cheng, J.Y., Guo, X., Yao, J., Ambale-Venkatesh, B., Lima, J.A., et al. (2017). Natural selection on genes related to cardiovascular health in high-altitude adapted Andeans. Am. J. Hum. Genet. *101*, 752–767.

Dabney, J., Knapp, M., Glocke, I., Gansauge, M.T., Weihmann, A., Nickel, B., Valdiosera, C., García, N., Pääbo, S., Arsuaga, J.L., and Meyer, M. (2013). Complete mitochondrial genome sequence of a Middle Pleistocene cave bear reconstructed from ultrashort DNA fragments. Proc. Natl. Acad. Sci. USA *110*, 15758–15763.

DeBlasis, P., Kneip, A., Scheel-Ybert, R., Giannini, P.C., and Gaspar, M.D. (2007). Sambaquis e paisagem: dinâmica natural e arqueologia regional no litoral do sul do Brasil. Arqueologia suramericana *3*, 29–61.

Dillehay, T.D., Ramírez, C., Pino, M., Collins, M.B., Rossen, J., and Pino-Navarro, J.D. (2008). Monte Verde: seaweed, food, medicine, and the peopling of South America. Science *320*, 784–786.

Edgar, R.C. (2004). MUSCLE: multiple sequence alignment with high accuracy and high throughput. Nucleic Acids Res. *32*, 1792–1797.

Eisenmann, S., Bánffy, E., van Dommelen, P., Hofmann, K.P., Maran, J., Lazaridis, I., Mittnik, A., McCormick, M., Krause, J., Reich, D., and Stockhammer, P.W. (2018). Reconciling material cultures in archaeology with genetic data: The nomenclature of clusters emerging from archaeogenomic analysis. Sci. Rep. *8*, 13003.

Fehren-Schmitz, L., and Georges, L. (2016). Ancient DNA reveals selection acting on genes associated with hypoxia response in pre-Columbian Peruvian Highlanders in the last 8500 years. Sci. Rep. *6*, 23485.

Fehren-Schmitz, L., Llamas, B., Lindauer, S., Tomasto-Cagigao, E., Kuzminsky, S., Rohland, N., Santos, F.R., Kaulicke, P., Valverde, G., Richards, S.M., et al. (2015). A re-appraisal of the early Andean human remains from Lauricocha in Peru. PLoS ONE *10*, e0127141.

Felsenstein, J. (1989). PHYLIP-Phylogeny Inference Package (Version 3.2). Cladistics *5*, 164–166.

Fiedel, S.J. (2017). The Anzick genome proves Clovis is first, after all. Quat. Int. *444*, 4–9.

Fu, Q., Hajdinjak, M., Moldovan, O.T., Constantin, S., Mallick, S., Skoglund, P., Patterson, N., Rohland, N., Lazaridis, I., Nickel, B., et al. (2015). An early modern human from Romania with a recent Neanderthal ancestor. Nature *524*, 216–219.

Fumagalli, M., Moltke, I., Grarup, N., Racimo, F., Bjerregaard, P., Jørgensen, M.E., Korneliussen, T.S., Gerbault, P., Skotte, L., Linneberg, A., et al. (2015). Greenlandic Inuit show genetic signatures of diet and climate adaptation. Science *349*, 1343–1347.

Gansauge, M.-T., and Meyer, M. (2013). Single-stranded DNA library preparation for the sequencing of ancient or damaged DNA. Nat. Protoc. *8*, 737–748.

Goldberg, A., Mychajliw, A.M., and Hadly, E.A. (2016). Post-invasion demography of prehistoric humans in South America. Nature *532*, 232–235.

Grieder, T., Mendoza, A.B., Smith, E.E., Jr., and Malina, R.M. (1988). La Galgada, Peru. A Preceramic Culture in Transition (University of Texas).

Herrera, A. (2011). Indigenous Archaeology…in Peru? (New York: Routledge).

Hogg, A.G. (2013). SHCal13 Southern Hemisphere calibration, 0–50,000 years cal BP. Radiocarbon *55*, 1889–1903.

Hubbe, M., Neves, W.A., de Oliveira, E.C., and Strauss, A. (2009). Postmarital residence practice in southern Brazilian coastal groups: continuity and change. Lat. Am. Antiq. *20*, 267–278.

Hubbe, M., Okumura, M., Bernardo, D.V., and Neves, W.A. (2014). Cranial morphological diversity of early, middle, and late Holocene Brazilian groups: implications for human dispersion in Brazil. Am. J. Phys. Anthropol. *155*, 546–558.

Iriarte, J., DeBlasis, P., De Souza, J.G., and Corteletti, R. (2017). Emergent complexity, changing landscapes, and spheres of interaction in southeastern South America during the middle and late Holocene. J. Archaeol. Res. *25*, 251–313.

Jackson, D., Méndez, C., and Aspillaga, E. (2012). Human remains directly dated to the Pleistocene-Holocene transition support a marine diet for early settlers of the Pacific Coast of Chile. J. Island Coast. Archaeol. *7*, 363–377.

Jónsson, H., Ginolhac, A., Schubert, M., Johnson, P.L., and Orlando, L. (2013). mapDamage2.0: fast approximate Bayesian estimates of ancient DNA damage parameters. Bioinformatics *29*, 1682–1684.

Jostins, L., Xu, Y., McCarthy, S., Ayub, Q., Durbin, R., Barrett, J., and Tyler-Smith, C. (2014). YFitter: maximum likelihood assignment of Y chromosome haplogroups from low-coverage sequence data. arXiv, arXiv:14077988.

Kamberov, Y.G., Wang, S., Tan, J., Gerbault, P., Wark, A., Tan, L., Yang, Y., Li, S., Tang, K., Chen, H., et al. (2013). Modeling recent human evolution in mice by expression of a selected EDAR variant. Cell *152*, 691–702.

Kennett, D.J., Plog, S., George, R.J., Culleton, B.J., Watson, A.S., Skoglund, P., Rohland, N., Mallick, S., Stewardson, K., Kistler, L., et al. (2017). Archaeogenomic evidence reveals prehistoric matrilineal dynasty. Nat. Commun. *8*, 14115.

Korlević, P., Talamo, S., and Meyer, M. (2018). A combined method for DNA analysis and radiocarbon dating from a single sample. Sci. Rep. *8*, 4127.

Korneliussen, T.S., Albrechtsen, A., and Nielsen, R. (2014). ANGSD: Analysis of Next Generation Sequencing Data. BMC Bioinformatics *15*, 356.

Lazaridis, I., Belfer-Cohen, A., Mallick, S., Patterson, N., Cheronet, O., Rohland, N., Bar-Oz, G., Bar-Yosef, O., Jakeli, N., Kvavadze, E., et al. (2018). Paleolithic DNA from the Caucasus reveals core of West Eurasian ancestry. bioRxiv. https://doi.org/10.1101/423079.

Lazaridis, I., Patterson, N., Mittnik, A., Renaud, G., Mallick, S., Kirsanow, K., Sudmant, P.H., Schraiber, J.G., Castellano, S., Lipson, M., et al. (2014). Ancient human genomes suggest three ancestral populations for present-day Europeans. Nature *513*, 409–413.

Lazaridis, I., Nadel, D., Rollefson, G., Merrett, D.C., Rohland, N., Mallick, S., Fernandes, D., Novak, M., Gamarra, B., Sirak, K., et al. (2016). Genomic insights into the origin of farming in the ancient Near East. Nature *536*, 419–424.

Letunic, I., and Bork, P. (2011). Interactive Tree Of Life v2: online annotation and display of phylogenetic trees made easy. Nucleic Acids Res. *39*, W475-8.

Li, H. (2011). A statistical framework for SNP calling, mutation discovery, association mapping and population genetical parameter estimation from sequencing data. Bioinformatics *27*, 2987–2993.

Li, H., and Durbin, R. (2009). Fast and accurate short read alignment with Burrows–Wheeler transform. Bioinformatics *25*, 1754–1760.

Li, H., Handsaker, B., Wysoker, A., Fennell, T., Ruan, J., Homer, N., Marth, G., Abecasis, G., and Durbin, R.; 1000 Genome Project Data Processing Subgroup (2009). The Sequence Alignment/Map format and SAMtools. Bioinformatics *25*, 2078–2079.

Lindo, J., Haas, R., Hofman, C., Apata, M., Moraga, M., Verdugo, R., Watson, J.T., Llave, C., Witonsky, D., Pacheco, E., et al. (2018). The genetic prehistory of the Andean highlands 7,000 Years BP through European contact. Sci. Adv. *4*, eaau4921.

Lindo, J., Achilli, A., Perego, U.A., Archer, D., Valdiosera, C., Petzelt, B., Mitchell, J., Worl, R., Dixon, E.J., Fifield, T.E., et al. (2017). Ancient individuals from the North American Northwest Coast reveal 10,000 years of regional genetic continuity. Proc. Natl. Acad. Sci. USA *114*, 4093–4098.

Lipson, M., and Reich, D. (2017). A working model of the deep relationships of diverse modern human genetic lineages outside of Africa. Mol. Biol. Evol. *34*, 889–902.

Llamas, B., Fehren-Schmitz, L., Valverde, G., Soubrier, J., Mallick, S., Rohland, N., Nordenfelt, S., Valdiosera, C., Richards, S.M., Rohrlach, A., et al. (2016). Ancient mitochondrial DNA provides high-resolution time scale of the peopling of the Americas. Sci. Adv. *2*, e1501385.

Lohse, J.C., Madsen, D.B., Culleton, B.J., and Kennett, D.J. (2014). Isotope paleoecology of episodic mid-to-late Holocene bison population expansions in the Southern Plains, USA. Quat. Sci. Rev. *102*, 14–26.

Mallick, S., Li, H., Lipson, M., Mathieson, I., Gymrek, M., Racimo, F., Zhao, M., Chennagiri, N., Nordenfelt, S., Tandon, A., et al. (2016). The Simons Genome Diversity Project: 300 genomes from 142 diverse populations. Nature *538*, 201–206.

Moreno-Mayar, J.V., Potter, B.A., Vinner, L., Steinrücken, M., Rasmussen, S., Terhorst, J., Kamm, J.A., Albrechtsen, A., Malaspinas, A.S., Sikora, M., et al. (2018a). Terminal Pleistocene Alaskan genome reveals first founding population of Native Americans. Nature *553*, 203–207.

Moreno-Mayar, J.V., Vinner, L., de Barros Damgaard, P., de la Fuente, C., Chan, J., Spence, J.P., Allentoft, M.E., Vimala, T., Racimo, F., Pinotti, T., et al. (2018b). Early human dispersals within the Americas. Science. https://doi.org/10.1126/science.aav2621.

Patterson, N., Price, A.L., and Reich, D. (2006). Population structure and eigenanalysis. PLoS Genet. *2*, e190.

Patterson, N., Moorjani, P., Luo, Y., Mallick, S., Rohland, N., Zhan, Y., Genschoreck, T., Webster, T., and Reich, D. (2012). Ancient admixture in human history. Genetics *192*, 1065–1093.

Pearson, G.A. (2017). Bridging the gap: an updated overview of Clovis across Middle America and its techno-cultural relation with fluted point assemblages from South America. PaleoAmerica *3*, 203–230.

Peltzer, A., Jäger, G., Herbig, A., Seitz, A., Kniep, C., Krause, J., and Nieselt, K. (2016). EAGER: efficient ancient genome reconstruction. Genome Biol. *17*, 60.

Perego, U.A., Achilli, A., Angerhofer, N., Accetturo, M., Pala, M., Olivieri, A., Hooshiar Kashani, B., Ritchie, K.H., Scozzari, R., Kong, Q.P., et al. (2009). Distinctive Paleo-Indian migration routes from Beringia marked by two rare mtDNA haplogroups. Curr. Biol. *19*, 1–8.

Plens, C.R. (2007). Sítio Moraes, uma biografia não autorizada: análise do processo de formação de um sambaqui fluvial (Universidade de São Paulo).

Plens, C.R. (2010). Animals for humans in life and death. Museu de Arqueologia e Etnologia *20*, 31–52.

Politis, G.G., Gutiérrez, M.A., Rafuse, D.J., and Blasi, A. (2016). The Arrival of Homo sapiens into the Southern Cone at 14,000 years ago. PLoS ONE *11*, e0162870.

Pucciarelli, H.M., Perez, S.I., and Politis, G.G. (2010). Early Holocene human remains from the Argentinean Pampas: additional evidence for distinctive cranial morphology of early South Americans. Am. J. Phys. Anthropol. *143*, 298–305.

Racimo, F., Gokhman, D., Fumagalli, M., Ko, A., Hansen, T., Moltke, I., Albrechtsen, A., Carmel, L., Huerta-Sánchez, E., and Nielsen, R. (2017). Archaic Adaptive Introgression in TBX15/WARS2. Mol. Biol. Evol. *34*, 509–524.

Rademaker, K., Hodgins, G., Moore, K., Zarrillo, S., Miller, C., Bromley, G.R., Leach, P., Reid, D.A., Álvarez, W.Y., and Sandweiss, D.H. (2014). Paleoindian settlement of the high-altitude Peruvian Andes. Science *346*, 466–469.

Raghavan, M., Steinrücken, M., Harris, K., Schiffels, S., Rasmussen, S., DeGiorgio, M., Albrechtsen, A., Valdiosera, C., Ávila-Arcos, M.C., Malaspinas, A.S., et al. (2015). POPULATION GENETICS. Genomic evidence for the Pleistocene and recent population history of Native Americans. Science *349*, aab3884.

Ramsey, C.B., and Lee, S. (2013). Recent and planned developments of the program OxCal. Radiocarbon *55*, 720–730.

Rasmussen, M., Anzick, S.L., Waters, M.R., Skoglund, P., DeGiorgio, M., Stafford, T.W., Jr., Rasmussen, S., Moltke, I., Albrechtsen, A., Doyle, S.M., et al.

(2014). The genome of a Late Pleistocene human from a Clovis burial site in western Montana. Nature *506*, 225–229.

Reich, D., Thangaraj, K., Patterson, N., Price, A.L., and Singh, L. (2009). Reconstructing Indian population history. Nature *461*, 489–494.

Reich, D., Patterson, N., Campbell, D., Tandon, A., Mazieres, S., Ray, N., Parra, M.V., Rojas, W., Duque, C., Mesa, N., et al. (2012). Reconstructing Native American population history. Nature *488*, 370–374.

Reimer, P.J., and Reimer, R.W. (2001). A marine reservoir correction database and on-line interface. Radiocarbon *43*, 461–463.

Reimer, P.J., Bard, E., Bayliss, A., Beck, J.W., Blackwell, P.G., Ramsey, C.B., Buck, C.E., Cheng, H., Edwards, R.L., and Friedrich, M. (2013). IntCal13 and Marine13 radiocarbon age calibration curves 0–50,000 years cal BP. Radiocarbon *55*, 1869–1887.

Renaud, G., Slon, V., Duggan, A.T., and Kelso, J. (2015). Schmutzi: estimation of contamination and endogenous mitochondrial consensus calling for ancient DNA. Genome Biol. *16*, 224.

Roewer, L., Nothnagel, M., Gusmão, L., Gomes, V., González, M., Corach, D., Sala, A., Alechine, E., Palha, T., Santos, N., et al. (2013). Continent-wide decoupling of Y-chromosomal genetic variation from language and geography in native South Americans. PLoS Genet. *9*, e1003460.

Rohland, N., Harney, E., Mallick, S., Nordenfelt, S., and Reich, D. (2015). Partial uracil-DNA-glycosylase treatment for screening of ancient DNA. Philos. Trans. R. Soc. Lond. B Biol. Sci. *370*, 20130624.

Scheib, C.L., Li, H., Desai, T., Link, V., Kendall, C., Dewar, G., Griffith, P.W., Mörseburg, A., Johnson, J.R., Potter, A., et al. (2018). Ancient human parallel lineages within North America contributed to a coastal expansion. Science *360*, 1024–1027.

Scheifler, N.A. Pincen, I.A., Estévez, J.J., Fehren-Schmitz, L., González, M., Grub, A., and Politis, G. (2017). Primeros estudios arqueológicos y antiguas reivindicaciones indígenas del sitio Laguna Chica (Sistema Lagunar Hinojo-Las Tunas, área Oeste de la subregión Pampa Húmeda). Resúmenes del VIII Congreso de Arqueología de la Región Pampeana. (Universidad Nacional de Lujan, Lujan (Prov. Buenos Aires)), pp. 39.

Schubert, M., Lindgreen, S., and Orlando, L. (2016). AdapterRemoval v2: rapid adapter trimming, identification, and read merging. BMC Res. Notes *9*, 88.

Silverman, H. (2006). Cultural resource management and heritage stewardship in Peru. CRM: Journal of Heritage Stewardship *3*, 57–72.

Skoglund, P., Northoff, B.H., Shunkov, M.V., Derevianko, A.P., Pääbo, S., Krause, J., and Jakobsson, M. (2014). Separating endogenous ancient DNA from modern day contamination in a Siberian Neandertal. Proc. Natl. Acad. Sci. USA *111*, 2229–2234.

Skoglund, P., Mallick, S., Bortolini, M.C., Chennagiri, N., Hünemeier, T., Petzl-Erler, M.L., Salzano, F.M., Patterson, N., and Reich, D. (2015). Genetic evidence for two founding populations of the Americas. Nature *525*, 104–108.

Stenzel, U. (2018). https://bitbucket.org/ustenzel/biohazard.

Strauss, A., Oliveira, R.E., Villagran, X.S., Bernardo, D.V., Salazar-García, D.C., Bissaro, M.C., Pugliese, F., Hermenegildo, T., Santos, R., Barioni, A., et al. (2016). Early Holocene ritual complexity in South America: the archaeological record of Lapa do Santo (east-central Brazil). Antiquity *90*, 1454–1473.

Talamo, S., and Richards, M. (2011). A comparison of bone pretreatment methods for AMS dating of samples >30,000 BP. Radiocarbon *53*, 443–449.

Tamm, E., Kivisild, T., Reidla, M., Metspalu, M., Smith, D.G., Mulligan, C.J., Bravi, C.M., Rickards, O., Martinez-Labarga, C., Khusnutdinova, E.K., et al. (2007). Beringian standstill and spread of Native American founders. PLoS ONE *2*, e829.

Tamura, K., Stecher, G., Peterson, D., Filipski, A., and Kumar, S. (2013). MEGA6: molecular evolutionary genetics analysis version 6.0. Mol. Biol. Evol. *30*, 2725–2729.

Torroni, A., Rengo, C., Guida, V., Cruciani, F., Sellitto, D., Coppa, A., Calderon, F.L., Simionati, B., Valle, G., Richards, M., et al. (2001). Do the four clades of the mtDNA haplogroup L2 evolve at different rates? Am. J. Hum. Genet. *69*, 1348–1356.

Vianello, D., Sevini, F., Castellani, G., Lomartire, L., Capri, M., and Franceschi, C. (2013). HAPLOFIND: a new method for high-throughput mtDNA haplogroup assignment. Hum. Mutat. *34*, 1189–1194.

Villagran, X.S., Strauss, A., Miller, C., Ligouis, B., and Oliveira, R. (2017). Buried in ashes: Site formation processes at Lapa do Santo rockshelter, east-central Brazil. J. Archaeol. Sci. *77*, 10–34.

von Cramon-Taubadel, N., Strauss, A., and Hubbe, M. (2017). Evolutionary population history of early Paleoamerican cranial morphology. Sci. Adv. *3*, e1602289.

Ward, G.K., and Wilson, S.R. (1978). Procedures for comparing and combining radiocarbon age determinations: a critique. Archaeometry *20*, 19–31.

Williams, A.L., Jacobs, S.B., Moreno-Macías, H., Huerta-Chagoya, A., Churchhouse, C., Márquez-Luna, C., García-Ortíz, H., Gómez-Vázquez, M.J., Burtt, N.P., Aguilar-Salinas, C.A., et al.; SIGMA Type 2 Diabetes Consortium (2014). Sequence variants in SLC16A11 are a common risk factor for type 2 diabetes in Mexico. Nature *506*, 97–101.

Yang, M.A., Gao, X., Theunert, C., Tong, H., Aximu-Petri, A., Nickel, B., Slatkin, M., Meyer, M., Paabo, S., Kelso, J., et al. (2017). 40,000-year-old individual from Asia provides insight into early population structure in Eurasia. Curr. Biol. *27*, 3202–3208.

slas 2020
INTERNATIONAL CONFERENCE & EXHIBITION

TECHNOLOGY
INNOVATION
RESEARCH

LEVEL UP YOUR SCIENCE

JANUARY 25 › 29
SAN DIEGO CONVENTION CENTER | CA

SLAS2020.ORG › #SLAS2020

SLAS2020 CONFERENCE HIGHLIGHTS

SLAS2020 KEYNOTE SPEAKERS

Jackie Hunter, Ph.D.
BenevolentAI

Opening Keynote

BenevolentAI uses AI to augment the research capability of drug scientists, radically changing the way R&D is done — from target identification and validation, through medicinal chemistry and lead optimization to clinical proof of concept.

Leroy Cronin, Ph.D.
University of Glasgow

Closing Keynote

With one of the largest multidisciplinary chemistry-based research teams in the world, Dr. Cronin's group at the University of Glasgow is developing the concept of 'Chemputing', which enables the universal digitalization of chemistry to understand how information can be encoded into chemicals and construct chemical computers.

TEN SCIENTIFIC EDUCATIONAL TRACKS

- 144 Podium Presentations & 22 Short Courses
- 2020 Innovation Award Announced on January 29
- SLAS Ignite Special Programming
- Hundreds of Poster Presentations and Three Student Poster Awards

slas
Come Transform Research

HIGH SCORING EXHIBITION

- More Than 300 Innovation Providers
- SLAS New Product Award and SLAS Ignite Award
- Innovation Ave*NEW* for Start-up and Emerging Companies
- Two Theaters: Solutions Spotlight and Ignite Academic Collaboration Presentations
- SLAS Journal Recognition and Meet the Editors

NETWORKING FOR THE WIN!

- Student and Early-Career Events and Mentoring Program
- Networking Party at Seaport Village
  Sponsored by: HAMILTON
- SLAS Booth: Connect, Relax and Recharge
- Ignite Partnership Program
- 10th Anniversary FUNd Run
  Sponsored by: TECAN.

NEVER STOP

ACCELERATING REGENERATIVE MEDICINE

We're applying our photographic film innovations to help advance new treatments in the revolutionary field of regenerative medicine. Over the last 80-plus years, we've developed advanced technology that controls complex chemical reactions in photographic film that's a mere 20 microns[*1] thick. And today, that technology is being applied to research and the world's first clinical trial[*2] of medical treatments that use high-quality iPS cells. And in the future, we'll strive to help those suffering from a range of medical conditions, such as those of the eyes, nerves, heart and more. Of course, the challenges are endless, but so are the possibilities. Which is why we'll never stop accelerating regenerative medicine to help build a stronger, healthier future for all.

FUJIFILM
Value from Innovation

Follow Fujifilm Life Sciences at

*1 Thickness of layers excluding the base.
*2 Fujifilm's iPS cells are being utilized in the world's first clinical trial using iPS cells conducted in the UK by the Australian company Cynata.

NIS-Elements AI

Intelligent Imaging with Deep Learning

NIS-Elements AI

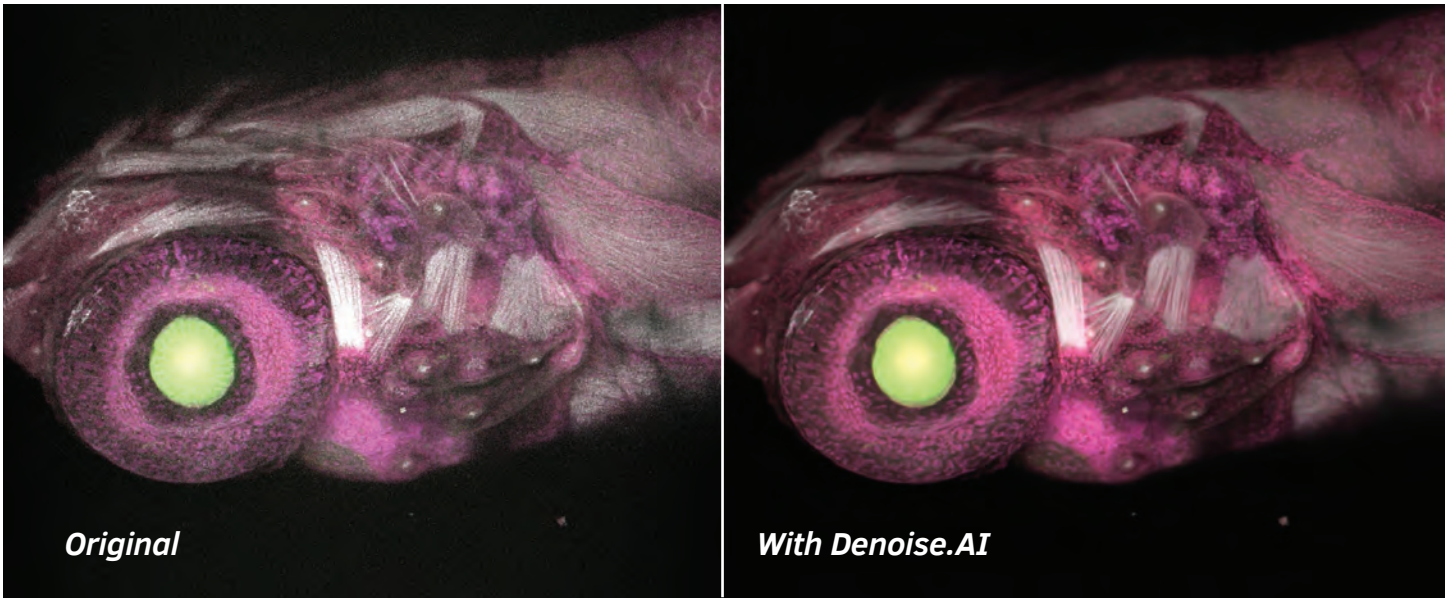

Nikon's new Artificial Intelligence (AI) feature for its NIS-Elements imaging software leverages deep learning to remove shot noise from resonant confocal images in real-time, resulting in breathtakingly clear images using minimal excitation power.

See Nikon at the ASCB|EMBO 2019 Meeting
Booth #900

To see how Nikon is using AI to transform your imaging,
visit www.microscope.healthcare.nikon.com/nis-elements-ai

Nikon Instruments Inc. | www.microscope.healthcare.nikon.com | nikoninstruments@nikon.net